# Study of the initiation and propagation phases of chloride induced corrosion in reinforced concrete structures

Chantal Chalhoub


# THÈSE

**En vue de l'obtention du**

## DOCTORAT DE L'UNIVERSITÉ DE TOULOUSE

**Délivré par :**

Université Toulouse 3 Paul Sabatier (UT3 Paul Sabatier)

---

**Présentée et soutenue par :**
**Chantal CHALHOUB**

**le** jeudi 30 janvier 2020

**Titre :**

Study of the initiation and propagation phases of chloride induced corrosion in reinforced concrete structures

---

**École doctorale et discipline ou spécialité :**
ED MEGEP : Génie civil

**Unité de recherche :**
LMDC - Laboratoire Matériaux et Durabilité des Constructions de Toulouse

**Directeur/trice(s) de Thèse :**

Raoul FRANCOIS et Myriam CARCASSES

**Jury :**
M. Ueli ANGST, Rapporteur
Mme Valerie L'HOSTIS, Rapporteure
M. Joost GULIKERS, Examinateur
Mme Mette GEIKER, Examinatrice
M. Lionel LINGER, Examinateur
M. Philippe TURCRY, Examinateur
M. Raoul FRANCOIS, Directeur de thèse
Mme Myriam CARCASSES, Co-directrice de thèse

# Acknowledgments

I would like to acknowledge the financial support of the ANR MODEVIE project, grant ANR-14-CE22-0018 of the French National Research Agency (ANR) and the French National Federation of Public Works (FNTP) which made this work possible. I would like to thank the laboratory Materials and Durability of Constructions (LMDC) and the University Paul Sabatier (UPS) for welcoming me in Toulouse during these 3 years.

My supervisor Raoul François is acknowledged for sharing his profound knowledge and his inspiring ideas which contributed a lot to the development of my research work. I appreciated his constructive criticism and helpful instructions which increased the scientific quality of this Ph.D. thesis. Myriam Carcasses my supervisor and the project manager of ANR MODEVIE is warmly acknowledged for trusting in me to achieve this research project and for allowing me to work on such an ambitious and innovative topic. I appreciated her positive feedback which helped in the development of the work. I thank both supervisors for encouraging me to share and present my work in tens of meetings and for giving me the chance to participate in several workshops and conferences.

My sincere thanks must also go to Stephane Laurens for his helpful contribution in the field of electrochemistry which helped me develop a broader perspective on my thesis. I appreciated his pedagogical approach, his attention to details and his passion. Thanks to David Garcia for his competent genuine support and his participation in a part of the numerical work. I would also like to thank Zarbita Noureddine for his hard work, his positive and encouraging attitude, for his help during the preparation and casting of test samples especially his good welding capability. Further thanks are due to Elie Sassine for all the discussions we had about corrosion and concrete which helped to enrich the work.

I would also like to express my gratitude to all the FNTP members and all the partners of the ANR MODEVIE project for their valuable discussions. Special thanks to François Cussigh, Lionel Linger and Valérie L'Hostis for their interest in my work and their fruitful criticisms and advice. They generously gave their time to offer me valuable comments toward improving my work.

Thanks to the laboratory technical team and the administrative staff for their prompt support and kind care, especially Vanessa Mazars, Ghislaine Dupouey and Nathalie Attanasio who warmly welcomed me whenever I asked for their assistance.

All the Ph.D. students and interns deserve a special thanks for the good work atmosphere they created each day, for their sympathy and concern. Special thanks to my brilliant friends and colleagues Mohamed Ibro, Faten Abi Farraj, Pierre Morenon, Bernard Salesses, Marie Giroudon and Duc Long Tran for their exceptional support.

I cannot forget my best friends Joanna, Rana, Yara, Mélanie, Lucas, Géraud, and Charbel and my cousins Roula, Rachel and Amine who cheered me up and celebrated with me each accomplishment. I thank with love my great companion and best friend Raphael for his love and positive support, for his interest in my Ph.D. work and his help for practicing my oral presentations. I would like to express my gratitude for my dog Orage for his cuteness and his positive energy.

Last but certainly not least, I deeply thank my family in Lebanon. My parents Moni and Grace, my sisters Gretta and Jana and my brother Yorgo who supported me despite the hard times and difficult moments they went through. For all the time we spent apart, we were separated in distance but never in heart.

Finally, I dedicate my work to my hometown Lebanon, to my lovely Beirut. I dedicate it for the voice, the unity of Lebanese people, for hope, peace and new beginnings.

## Abstract

It is commonly accepted that chloride-induced corrosion of steel is one of the most documented causes leading to the deterioration of reinforced concrete structures. The Ph.D. study aimed at the improvement of the understanding of chloride-induced corrosion in concrete during the transition phase between initiation and propagation and during the corrosion propagation phase.

Traditionally, chloride-induced corrosion is initiated when the chloride content reaches a threshold value called critical chloride content or Ccrit. In spite of much research invested in this domain, there is still no agreement on an accurate method for the determination of the chloride threshold value initiating corrosion. The first objective of this work was to develop a new test set-up that considers the localized character of corrosion initiated by chlorides. This approach was based on a physical separation between the anode, contaminated with chlorides, and the cathode, which is chloride free. The experimental protocol will allow quantifying the galvanic corrosion current, making it possible to determine, in a second step, the chloride threshold values for corrosion initiation. The criterion for corrosion initiation was a threshold corrosion current defined as a current that is independent of the cathode/anode surface ratio and subsequently independent of the area of passive steel. This criterion was considered as an anodic control of corrosion during the transition stage from the initiation phase to the propagation phase. This test protocol was applied to mortar and concrete formulations with several types of binders (CEM I cement, CEM III cement and CEM I with silica fume) with different water/binder ratios embedding ribbed steel bars with different steel surface conditions (as received, chemically cleaned, chemically cleaned than oxidized with humidity or high temperature). It was found that the test protocol is rapid and applicable to all formulations. The experimental results provide an understanding of the influence of binder type, w/b ratio and porosity on the susceptibility of steel to chloride-induced corrosion initiation. The steel surface condition was found to have an important overall effect on corrosion initiation but this effect is dependent on the type of binder used.

Several literature studies considered that chloride-induced corrosion initiation is under anodic control which could mean that corrosion is controlled by the electrochemical parameters of steel. The parameters of passive steel can be directly derived from experimental measurements owing to the uniform passive state of rebars. However, because of the non-uniform nature of chloride-induced corrosion in concrete, it is not possible to experimentally obtain uniformly active steel. In this thesis, the determination of the electrochemical properties of active steel was achieved based on inverse numerical modeling focusing on the dependence of these properties on chloride contamination. All the experimental observations coupled with the numerical modeling approach highlighted the dependency of the electrochemical properties of active steel on chloride content.

When dealing with macrocell corrosion, it is crucial to consider the geometry and size of the structure, including the mobilizable cathode-anode distance and the cathode to anode surface ratio. In this work, the mobilizable cathode-anode distance was investigated. It was found that macrocell corrosion current could be provided by cathode bars at large distances from the anode, the distance being dependent on the electrical resistivity of the structure. These findings support the assumption that corrosion in the submerged zone with lack of oxygen could be due to coupling with a cathodic zone in the aerated parts of structures and not necessarily associated with pitting phenomenon linked to water reduction under very negative potential in submerged area.

Corrosion propagation is affected by several parameters like electrical resistivity which is known to be inversely proportional to the corrosion rate according to several empirical reported studies. An

inversely proportional relationship between macrocell current and electrical resistivity was also found in our experimental investigations which consisted of a cathode permutation technique where the same anode was connected to two different cathodes with different electrical resistivity.

Last but not least, it was experimentally observed that steel embedded in mortar with a high substitution level of slag (80%) presented a particular behavior. Highly negative potentials were measured despite the absence of chlorides which was considered as an indication of the absence of dissolved oxygen at the steel/mortar interface. It was assumed that these negative potentials were associated with the reaction of water reduction, while, in the presence of oxygen the reaction is the reduction of oxygen. During the galvanic coupling between highly negative cathodes and chloride contaminated anodes, corrosion currents were, in some cases, negative and then became positive. The change in sign of the measured current was always associated with the increase in the potentials of cathodes to more positive values which was considered as an indication of the oxidation of iron with a significant polarization for a weak current and therefore a rapid reduction of the galvanic current. Indeed at such low potential, the passive layer has disappeared but the anodic polarization of cathode led to both the increase of the potential of the cathode and the reformation of the passive layer. These statements were only assumptions and needed further investigations.

Finally, a part of the thesis work was devoted to the development of a simplified empirical model of relevance to the engineer used for the prediction of corrosion propagation duration in the case of chloride-induced macrocell corrosion in uncracked reinforced concrete structures. This model was mainly based on the experimental results obtained during the thesis. The duration of the acceptable corrosion propagation period was defined as the one corresponding to the appearance of the first corrosion cracks. The developed approach will allow predicting the duration of the propagation phase, according to the chosen service limit criteria, in case of new reinforced concrete structures under the risk of chloride-induced corrosion.

**Keywords:**

Chloride induced corrosion; Macrocell corrosion; Localized corrosion; Reinforced concrete; Critical chloride content; Cathode over anode ratio; Binder type; Steel surface; Porosity; Active steel; Passive steel; Electrochemical properties; anodic control; Cathode-Anode distance; Electrical resistivity; Numerical simulation; Blast furnace slag; Oxygen; Cathodic reaction; Corrosion current density; Propagation phase; Cross-section reduction; Performance-based approach.

## Résumé

Il est communément admis que la corrosion des aciers par les chlorures est la cause principale de la détérioration des structures en béton armé. L'objectif de cette thèse est de contribuer à l'amélioration de la compréhension de la corrosion induite par les chlorures dans le béton pendant la phase de transition entre l'initiation et la propagation et pendant la phase de propagation de la corrosion.

Traditionnellement, la corrosion induite par les chlorures est initiée lorsque la teneur en chlorure atteint une valeur critique appelée seuil critique en chlorure ou Ccrit. Malgré de nombreuses recherches dans ce domaine, il n'existe toujours pas d'accord sur une méthode précise pour la détermination de la valeur seuil initiant la corrosion. Le premier objectif de ce travail était de développer un nouveau montage expérimental prenant en compte le caractère localisé de la corrosion initiée par les chlorures. Cette approche se basait sur une séparation physique entre l'anode contaminée par des chlorures et la cathode sans chlorure. Le protocole expérimental permettra de quantifier le courant de corrosion galvanique, permettant ainsi de déterminer, dans un deuxième temps, les valeurs de seuils critiques en chlorure. Le critère d'initiation de la corrosion était un courant de corrosion seuil défini comme un courant indépendant du rapport de surface cathode/anode et, par la suite, indépendant de la surface de l'acier passif. Ce critère a été considéré comme un contrôle anodique de la corrosion pendant la phase de transition de la phase d'initiation à la phase de propagation. Ce protocole d'essai a été appliqué à des formulations de mortier et de béton avec plusieurs types de liants (ciment CEM I, ciment CEM III et CEM I avec fumée de silice), différents rapports eau/liant, incorporant des barres d'acier HA torsadés avec différentes conditions de surface d'acier (tels que reçus, nettoyés chimiquement et nettoyé chimiquement puis oxydé avec humidité ou à haute température). Il a été constaté que le protocole expérimental est rapide et applicable à toutes les formulations. Les résultats expérimentaux permettent de comprendre l'influence du type de liant, du rapport E/L et de la porosité sur la sensibilité de l'acier à l'initiation de la corrosion induite par les chlorures. Il a été constaté que l'état de la surface de l'acier avait un effet global important sur l'initiation de la corrosion, mais cet effet dépend du type de liant utilisé.

Plusieurs études de la littérature ont considéré que le déclenchement de la corrosion induite par les chlorures est sous contrôle anodique, ce qui pourrait signifier que la corrosion est contrôlée par les paramètres électrochimiques de l'acier. Les paramètres de l'acier passif peuvent être directement dérivés des mesures expérimentales grâce à l'état passif uniforme des barres d'armature. Cependant, en raison de la nature non uniforme de la corrosion induite par les chlorures dans le béton, il n'est pas possible d'obtenir expérimentalement de l'acier uniformément actif. Dans cette thèse, la détermination des propriétés électrochimiques de l'acier actif a été réalisée sur la base d'une modélisation numérique inverse se concentrant sur la dépendance de ces propriétés vis-à-vis de la contamination par les chlorures. Toutes les observations expérimentales associées à l'approche de modélisation numérique ont mis en évidence la dépendance des propriétés électrochimiques de l'acier actif sur la teneur en chlorure.

Lorsqu'il s'agit de la corrosion par macro pile, il est crucial de prendre en compte la géométrie et la taille de la structure, y compris la distance mobilisable cathode-anode et le rapport surfacique cathode/anode. Dans ce travail, la distance mobilisable cathode-anode a été étudiée. Il a été constaté que le courant de corrosion par macro pile pouvait être fourni par des barreaux de cathode éloignés de l'anode, cette distance dépendant de la résistivité électrique de la structure. Ces résultats confirment l'hypothèse selon laquelle la corrosion dans la zone submergée avec un manque d'oxygène pourrait être due au couplage avec la zone cathodique dans les parties aérées de la structure et non

nécessairement au phénomène de piqûre lié à la réduction de l'eau suite à un potentiel très négatif en zone submergée.

La propagation de la corrosion est influencée par plusieurs paramètres comme la résistivité électrique connue, selon plusieurs études empiriques rapportées, par sa relation inversement proportionnelle à la vitesse de corrosion. Cette relation inversement proportionnelle entre le courant de macro pile et la résistivité a également été trouvée dans nos investigations expérimentales qui consistaient en une technique de permutation de cathode dans laquelle la même anode était connectée à deux cathodes différentes avec des résistivités électriques différentes.

Enfin, il a été observé expérimentalement que l'acier dans des mortiers composés de taux de substitution élevés en laitier (80%) présentait un comportement particulier. Des potentiels fortement négatifs ont été mesurés malgré l'absence de chlorures, ce qui a été considéré comme une indication de l'absence d'oxygène à l'interface acier/mortier. On a supposé que ces potentiels négatifs étaient associés à la réaction de réduction de l'eau, alors qu'en présence d'oxygène, la réaction est la réduction de l'oxygène. Lors du couplage galvanique entre des cathodes fortement négatives et des anodes contaminées par des chlorures, les courants de corrosion étaient, dans certains cas, négatifs puis positifs. Le changement de signe du courant mesuré a toujours été associé à l'augmentation des potentiels des cathodes à des valeurs plus positives. Ce qui a été considérée comme une indication de l'oxydation du fer avec une polarisation importante pour un courant faible et donc une réduction rapide du courant galvanique. En effet à un potentiel aussi faible, la couche passive a disparu mais la polarisation anodique de la cathode a conduit à la fois à l'augmentation du potentiel de la cathode et à la reformation de la couche passive. Ces déclarations ne sont que des hypothèses et nécessitent des investigations supplémentaires.

Enfin, une partie du travail de thèse a été consacrée au développement d'un modèle empirique simplifié pour l'ingénieur utilisé pour la prédiction de la durée de propagation de la corrosion induite par les chlorures dans les structures en béton armé non fissurées. Ce modèle était principalement basé sur les résultats expérimentaux obtenus au cours de la thèse. La durée de la période de propagation de la corrosion acceptable a été définie comme celle correspondant à l'apparition des premières fissures de corrosion. L'approche développée permettra de prédire la durée de la phase de propagation, selon les critères de limite de service choisis, dans le cas de nouvelles structures en béton armé exposées au risque de corrosion induite par les chlorures.


## Mots clés:

Corrosion induite par les chlorure; Corrosion par macro pile; Corrosion localisée; Béton armé; Seuil critique en chlorures; Rapport cathode/anode; Type de liant; Surface d'acier; Porosité; Acier actif; Acier passif; Propriétés électrochimiques; contrôle anodique; Distance cathode-anode; Résistivité électrique; Simulation numérique; Laitier de haut fourneau; Oxygène; Réaction cathodique; Densité de corrosion; Phase de propagation; Réduction de la section transversale; Approche performantielle.

# Table of Contents

## Part I – Extended summary

## Part II - Appended papers

## Part III - Appendices

## Part II - List of appended papers

**Paper I -** Determination of chloride threshold initiating corrosion: A new set-up taking the localized aspect of corrosion into account
Cement and Concrete Research 124 (2019) 105825
Chantal Chalhoub*, Raoul François, Myriam Carcasses

**Paper II -** Macrocell corrosion of steel in concrete: characterization of anodic behavior in relation to the chloride content
Materials and corrosion (2020)
Chantal Chalhoub*, Raoul François, David Garcia, Stéphane Laurens, Myriam Carcasses

**Paper III -** Critical chloride threshold values as a function of cement type and steel surface condition
Cement and Concrete Research 134 (2020) 106086
Chantal Chalhoub*, Raoul François, Myriam Carcasses

**Paper IV -** Anodic control of the initiation of macrocell chloride-induced corrosion in concrete structures
To be submitted
Chantal Chalhoub*, Raoul François, Myriam Carcasses

**Paper V -** Effect of Cathode-Anode distance and electrical resistivity on macrocell corrosion currents and cathodic response in cases of chloride-induced corrosion in reinforced concrete structures
Construction and Building Materials 245 (2020) 118337
Chantal Chalhoub*, Raoul François, Myriam Carcasses

**Paper VI -** Influence of concrete electrical resistivity on corrosion propagation and its relationship with cathode/anode ratio and chloride contamination
To be submitted
Chantal Chalhoub*, Raoul François, Myriam Carcasses

**Paper VII -** Influence of ground granulated blast furnace slag on chloride-induced corrosion of steel in reinforced mortar
To be submitted
Chantal Chalhoub*, Raoul François, Myriam Carcasses

**Paper VIII -** Lifetime prediction model of reinforced concrete structures under the risk of corrosion based on service limit state criteria associated with a corrosion current density corresponding to the appearance of the first corrosion-induced cracking
To be submitted
Chantal Chalhoub*, Raoul François, Myriam Carcasses

## Declaration of authorship

Chantal Chalhoub planned and conducted all the experiments in the laboratory LMDC, Toulouse, France (preparation of samples, electrochemical measurements, chemical analyses, characterization tests, scanning electron microscopy and backscattered electron analysis) and some experiments at CEA, Saclay, France (RAMAN observations). Chantal Chalhoub did all the numerical simulations using the software Comsol Multiphysics, evaluated the results, and wrote all the appended papers.

The co-authors Raoul François and Myriam Carcasses contributed, in all the appended papers, with constructive criticism and helpful instructions which increased the scientific quality of the report. They also helped in the evaluation and discussion of the results and evaluated the writing.

In paper II, David Garcia developed the optimization numerical model using the software Comsol Multiphysics. Chantal Chalhoub realized all the experiments and the rest of the numerical simulations. Chantal Chalhoub wrote all the manuscript and Stéphane Laurens assisted in the writing process. Both Stéphane Laurens and David Garcia contributed a lot in the discussion and evaluation of the numerical results of paper II.

In paper IV, Chantal Chalhoub and Zarbita Noureddine prepared the test samples and ran the experiments. Chantal Chalhoub evaluated the results and wrote the manuscript. Anode and cathode concrete samples were prepared in the VINCI construction Laboratory in Paris, France with the assistance of the technical team. Chantal Chalhoub participated in the design and preparation of these samples.

During the FNTP conferences and the ANR MODEVIE meetings, François Cussigh and Lionel Linger gave helpful guidance for the evaluation and discussion of the results in paper VIII.

# List of symbols and abbreviations

| Abbreviation | Meaning | Unit (SI) |
|---|---|---|
| I | Corrosion current | A |
| $I_g$ | Galvanic (macrocell) corrosion current | A |
| $i_{corr}$ | Corrosion current density | $A/m^2$ |
| $S_a$ | Surface area of active steel | $m^2$ |
| $R_p$ | Polarization resistance | Ω |
| w/c(b) | Water/cement (binder) | |
| s/c | Sand/cement | |
| Cl | Chloride content | |
| Ccrit | Critical chloride content | |
| C-I cracks | corrosion-induced crack | |
| M | Precedes mortar formulations | |
| B | Precedes concrete formulations | |
| OPC | Ordinary Portland cement | |
| PC | Portland cement | |
| FA | Fly ash | |
| SF | Silica fume | |
| S | Slag | |
| BFS | Blast furnace slag | |
| RH | Relative humidity | |
| T | Temperature | |
| ZRA | Zero Resistance ammeter | |
| LPR | Linear polarization resistance | |
| C/A ratio | Cathode to anode ratio | |
| C-A distance | Cathode-anode distance | |
| GR | Guard Ring | |
| WE | Working Electrode | |
| CE | Counter Electrode | |
| RE | Reference Electrode | |

# Part I- Extended Summary

# 1. Introduction

Reinforced concrete is one of the most common materials used by the construction industry all over the world. The idea of reinforced concrete was born in 1850 by Joseph Monier. It is until 1920 that history of reinforced concrete and architecture coincide and several great architects exploit it in their work. The popularity of reinforced concrete is due to the complementarity between steel and concrete. Concrete has a high compressive strength and a lower tensile strength that will be compensated by the incorporation of steel reinforcement. The raw materials needed for its production are usually low-cost and available. The alkaline environment provided by the concrete allows the passivation of steel bars which protects the steel by constituting an electrochemical barrier increasingly slowing down the corrosion phenomenon in which corrosion rates are mainly negligible. Additionally, the concrete cover acts as an obstacle for aggressive agents and delays their time of arrival to the reinforcement bars. Reinforced concrete is used for the construction of several types of structures form small private buildings, to civil engineering infrastructures, like bridges and tunnels, to offshore platforms and dams, which have an important range of exposure conditions including marine and severe environments. Some exposure conditions or inefficiently selected raw materials can lead to the early deterioration of the structures which is a huge economic and ecological problem.

It is widely accepted that reinforcement corrosion is the first cause of the deterioration mechanism. According to a study published by NACE (National Association of Corrosion Engineers) in 2016 [1] the annual universal cost of corrosion is estimated at $ 2.5 trillion, which is equivalent to 3.4% of global GDP. The indirect cost of corrosion due to traffic delays and loss in productivity should be in the same order of magnitude [2]. In reinforced concrete, corrosion is the principal cause of early deterioration of the structures. Nowadays, the study of the corrosion process in reinforced concrete structures is developing day by day. The two main causes of reinforcement corrosion in concrete are carbonation and chloride contamination of concrete, both leading to the breakdown of the passivation film protecting the steel.

The service life of reinforced concrete structures is the sum of the corrosion initiation phase and corrosion propagation phase. During the initiation phase, the aggressive species like chlorides penetrate through the concrete moving towards reinforcement. During this phase, reinforcement does not suffer from corrosion. The initiation period ends when reinforcement is depassivated. Today's regulation defines the end of the initiation phase regarding chloride-induced corrosion when chlorides at the level of rebars reach a critical threshold value ($C_{crit}$). During the initiation phase, the chloride threshold value is one of the most important input parameters that govern the outcome of the prediction of the initiation stage. However, there is still no agreement on a reliable method for its determination and several mechanisms are still not well understood [3]. Nevertheless, from a fundamental and practical perspective, corrosion initiation, also known as corrosion onset, does not correspond to an instantaneous event but is more like a gradual phase until corrosion becomes stable [4–7]. In other words, the critical chloride content is the amount of chlorides at the steel surface necessary to sustain a local depassivation of steel and so induce corrosion initiation.

Most methods for lifetime prediction only discuss the initiation stage which is a safe approach concerning the design of structures. However, recently, several works mentioned the importance of incorporating a part of the propagation period in the life of the structure ($t_{prop}$). Hence, the attention of the scientific community has shifted to the propagation phase, but without neglecting the initiation period. To limit the damages due to corrosion of concrete structures during $t_{prop}$, additional steps need to be taken to minimize the corrosion rate succeeding initiation stage. The localized nature of corrosion in concrete leads to the propagation stage of corrosion with a corrosion rate that depends on numerous elements and several processes: anodic, cathodic, ohmic and geometric. In the propagation phase, the corrosion is said to be active. The duration of the propagation phase must be associated with a level of deterioration related to a pre-defined limit state corresponding to structural or durability performance.

The propagation phase can also be divided into several sub-phases that correspond each to predefined limit criteria. The damages caused by corrosion can be related to steel cross-section loss, loss in ductility or damage of the steel/concrete interface bond, cracking of the concrete cover and also the collapse of the structure. The limit states of a structure are either service limit states (SLS) or ultimate limit states (ULS). However, it is more suitable to adopt an adequate service limit state related to an acceptable damage indicator in case of the propagation phase such as the longitudinal corrosion-induced crack openings on the concrete surface or the cross-section loss corresponding to the appearance of the first corrosion-induced crack.

This Ph.D. study focuses on chloride-induced reinforcement corrosion in concrete and mortar in the case of different types of binders. It addresses the transition phase between initiation and propagation and investigates several aspects of the propagation phase of corrosion.

## 1.1. Project framework

The work is part of the ANR MODEVIE research program which represents the modeling part of French National Project PERFDUB aiming at setting up a methodology for justifying the durability of concrete structures using a performance-based approach which was developed since 2005. According to this approach, the materials must meet performance requirements, which translate into expectations of certain properties of the material. The tools used to evaluate these performances are sustainability indicators, performance tests or sustainability models. Sustainability indicators can correspond to general indicators such as electrical resistivity, water porosity, mechanical resistance, etc.

The field of research of ANR MODEVIE concerns new structures but is interested in old constructions to link pathologies or observed aging to the type of concrete used and its durability indicators. Starting from scientific models available for the different phenomena in play, its output is an overall engineering model able to provide a reliable assessment of service life concrete structures subjected to corrosion by chloride and carbonation. The service lifetime of the structures was determined by calculating the sum of the initiation period and the propagation period. This is done by providing experiments and modeling tools to predict the long-term behavior of structures. MODEVIE gathers 10 partners (Fig. 1) which are experts in the fields of mass transfer and corrosion, all involved in the development of the performance-based approach for concrete structures under risk of corrosion.


*Fig. 1. ANR MODEVIE-PERFDUB partners*

## 1.2. Objectives

The objective of the Ph.D. study was to contribute to the improvement of the understanding of chloride-induced corrosion in concrete. The following objectives were identified:

1. **Development of a new laboratory test set-up that considers the localized character of corrosion initiated by chlorides for the determination of the critical chloride content initiating corrosion**
    1.1. Derive a test protocol that is expected to allow the detection of corrosion initiation and to quantify the galvanic corrosion current.
    1.2. Select an approach for the determination of the critical chloride content.
    1.3. Study the impact of binder type and steel surface condition on the critical chloride content.

2. **Characterization of the anodic behavior in relation to the chloride content**
    2.1. Use the experimental setup described in objective no. 1 to investigate the impact of chloride contamination on macrocell corrosion current.
    2.2. Characterize the electrochemical behavior of passive steel on non-contaminated samples.
    2.3. Develop a numerical optimization for quantifying active steel parameters focusing on chloride's effect on the iron anodic Tafel coefficient.

3. **Corrosion propagation**
    3.1. Use the experimental setup that evolves from objective no. 1 to study the chloride-induced corrosion propagation phase.
    3.2. Identify the impact of the cathode to anode ratio and cathode-anode distance on macrocell corrosion current.
    3.3. Study the role of electrical resistivity on macrocell corrosion propagation.
    3.4. Investigate the influence of ground granulated blast furnace slag on macrocell corrosion of steel in reinforced mortar

4. **Development of an engineering model practical for end-users for the prediction of the propagation phase of reinforced concrete structures adapted to the performance-based approach**
    4.1. Identify the limitations of previously reported corrosion rate predictive models
    4.2. Review the different parameters impacting corrosion propagation
    4.3. Develop an empirical simplified model calibrated from experimental results derived from objectives no. 1, 2 and 3.
    4.4. Define a limit state associated with reinforcement corrosion corresponding to an acceptable corrosion state.

## 1.3. Research approach and limitations

- This study focuses on chloride-induced corrosion in reinforced mortar/concrete; the effect of carbonation is not considered and the experimental tests are achieved under laboratory conditions.

- <u>In experiments:</u>
  The size of the anode rebar in all the experimental campaigns was chosen to be small with lengths of 1 and 2 cm and diameters of 6 and 12 mm). The reason behind this choice is to have an anode steel bar that is, as much as possible, in an active state. However, in real structures, the anode forms spontaneously on larger rebar surfaces. Consequently, the factors that decide where corrosion starts on the steel surface, also known as the “weakest spot”, could be induced by the rebar damages after

manufacturing for instance during the handling or during the assembly of the bars on construction site. It could also be related to size effect in the casting process, for instance, the heterogeneity of the steel/concrete interface. In such cases, this limitation cannot be resolved in a laboratory experimental test even if a bigger length of anode rebar was used. Knowing that, in reality, the length of the bars is approximately 6m whereas the length of the bars used as anodes, in experimental works, usually do not exceed 0.1 m.

Also, the non-uniformity of mill scale could lead to the concept of the weakest spot which is related to the geometry of the rebar such as the presence of ribs which can induce different cooling kinetics during the industrial process.

This limitation was resolved by using different types of steel surface conditions. For instance, it is possible to use a certain treatment that eliminates the effects of the formation of mill scale during the cooling of rebars by using an acid cleaning technique followed with a heating treatment that allows the formation of a new layer of corrosion products that is supposed to be more uniform than mill scale. This allowed indicating whether the presence of the weakest point was only related to the presence of ribs.

Also, in reality, the cathode to anode ratio is very high at the beginning of the corrosion process because of the multiple layers of reinforcement bars that are still initially in the passive state. For this reason, in all of the tests, high C/A ratios were tested from 10 to 2950.

The method used to determine the levels of free and total chlorides is a destructive traditional technique consisting of the measurements of chlorides in powder samples dissolved with nitric acid for total chlorides and water for free chlorides.

- In numerical simulations:
  It must be noted that the scale of this study concerns the macro-level of the corrosion process of rebars in concrete. As a result, a cohesion of matter is described in terms of stress and strain and their interaction via the constitutive law, the corrosion of steel in concrete is described in terms of potential and current and their interaction via the Butler Volmer equation.

  Also, knowing that the cathodic reaction and subsequently the cathodic electrochemical parameters vary according to the nature of the chemical reaction and the oxygen availability at the steel-concrete interface, it must be noted that these assumptions are considered in the case of unlimited oxygen availability. This implies that the corrosion process is not limited by the flow of oxygen. Moreover, it has to be considered that, at the corrosion dynamic equilibrium, the anodic current produced by the oxidation of the Fe electrode is balanced by the cathodic current relative to the oxygen reduction.

## 1.4. Organization of the thesis

The thesis consists of three parts:
Part I Extended summary
Part II Appended papers
Part III Appendices

# 2. Theoretical background

In this section, chloride-induced corrosion in concrete is briefly discussed.

## 2.1. Oxidation of steel during its formation

Steel reinforcement bars in reinforced concrete structures are often covered with a non-uniform layer of mill scale which is formed during the manufacture of steel at high temperatures (greater than 575 ° C).
Mill scale is generally composed of three layers:

- An inner layer in contact with iron formed of ferrous oxide (FeO);
- An intermediate layer formed of magnetite ($Fe_3O_4$);
- An outer layer, the most oxidized formed of hematite ($Fe_2O_3$).

Indeed, steel is an alloy formed largely of iron with a little carbon. When it is manufactured at high temperature, pure iron at surface reacts with oxygen to form ferrous oxide (FeO) which is transformed into pure iron (Fe) and magnetite ($Fe_3O_4$), once the steel is air-cooled. Magnetite is then oxidized to hematite ($Fe_2O_3$).

The calamine layer may or may not be associated with a layer of corrosion products formed during the storage of steels at the construction site.

In the 1970s, thermomechanical reduction processes of reinforcement were developed and their use in place of cold-hardened reinforcement began in many countries.

## 2.2. Atmospheric oxidation of steel

When stored on site, the steel undergoes natural climatic conditions. It is then possible to identify several types of oxides and hydroxides of iron present in the oxidation layer formed during its exposure to air:

- Magnetite ($Fe_3O_4$) (dry air) ;
- Goethite (α-FeOOH) and lepidocrocite (γ-FeOOH) (moist air or rain) [8] ;
- Maghemite ($\gamma Fe_2O_3$) if the time of its exposure is long [9].

## 2.3. Passivation phenomenon of steel

Reinforcement bars are then placed in formwork before concrete casting. Once the steel is in contact with the concrete, a thin layer of corrosion products is formed on the steel-concrete interface. This phenomenon is called "passivation" of steel, so it is said that steel is "passivated" or "passive". The thin layer formed is called “passivation film” which acts as a barrier slowing down the corrosion process by reducing corrosion kinetics to negligible values.

## 2.4. Formation and thermodynamic stability of the passivation film

The interstitial solution of concrete constitutes a strongly alkaline environment with a pH between 12 and 13 depending on the nature of the cement.

The potential-pH Pourbaix equilibrium diagram of Fe / $H_2O$ system [10] demonstrates the possibility of the formation of oxides on the surface of the steel in alkaline solutions.

As shown in Fig. 2, it is possible to see several possible thermodynamic domains in this diagram:

- Passivation: zones governed by $Fe_2O_3$ and $Fe_3O_4$ species;
- Corrosion: zones governed by $Fe^{2+}$ and $Fe^{3+}$ ions;
- Immunity: dominance area of iron stability (the metal does not react);
- Thermodynamic stability of water at atmospheric pressure: zone delimited by parallel dashed lines.

The Pourbaix diagram corresponds to the pure iron and water system, whereas, in reinforced concrete, steel is an alloy and the interstitial solution of concrete, which contains cations, is much more complex than pure water. Moreover, this diagram does not take into account the kinetics of the chemical reactions, though, it allows to explain qualitatively the passivation of steel in concrete

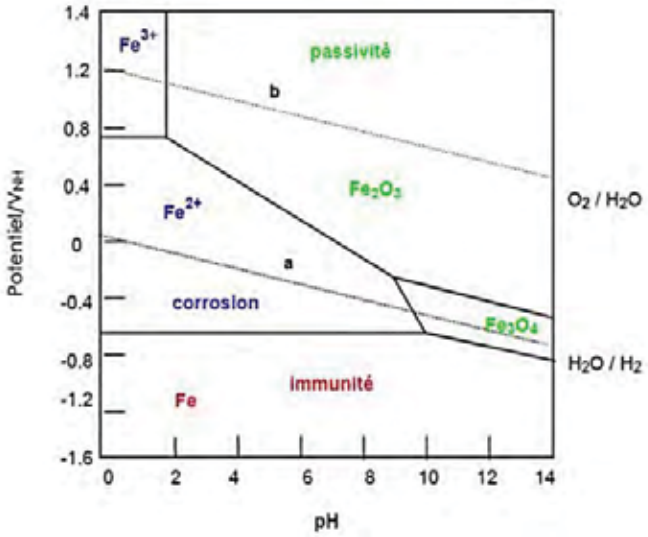


*Fig. 2. Simplified E-pH POURBAIX diagram of iron in an aqueous medium under standard temperature and pressure conditions (T = 25 °C, et P = 1 atm) [10]*

## 2.5. Composition and structure of passivation film

### 2.5.1. Composition of the passivation layer

The thickness of the passive film formed in the case of tests in solution is in the order of a few nm [11–13]. In the case of steel coated with a cement matrix, the layer was found to have a thickness of about ten µm [14,15] which could be associated with the thickness of the passivation film formed.

The exact nature and structure of the passivation layer are still largely controversial. The passivation film is often described as a double layer consisting of a relatively dense inner layer adjacent to the steel and an outer layer which is most often porous.

- The inner layer of the film is formed of iron oxides mainly magnetite. Several authors have reported the presence of $Fe^{2+}$ in the inner layer of the passivation film.
- The outer layer in contact with the electrolyte probably consists of iron oxy-hydroxides.

The nature and structure of the passivation film were mainly studied in the case of steels immersed in alkaline solution simulating the interstitial solution of concrete and little work was done in case of steels embedded in cementitious materials. Table 1 represents some of the observations obtained by different authors on the composition of the passivation layer.

*Table 1. Different observations concerning the composition of the passivation film.*

| The inner part of the passivation film | | The external part of the passivation film | |
|---|---|---|---|
| Observations | References | Observations | References |
| Rich in $Fe^{2+}$ | [11,16–18] | Rich in $Fe^{3+}$ | [16] |
| Dense three-dimensional layer of Iron(III) oxide | [19] | Local formation of hematite, presence of hydroxides and maghemite | [14] |
| Dense inner bilayer spinel phase ($\gamma$-$Fe_2O_3$ /$Fe_3O_4$) | [15] | The porous outer layer mainly formed of goethite ($\alpha$-FeOOH) and nodules of $Ca(OH)_2$ crystals | [15] |
| Mainly formed of magnetite ($Fe_3O_4$) | [12] | Presence of precipitate of $Ca(OH)_2$ | [11,20] |
| | | Mainly composed of Iron(III) oxide ($\gamma$-$Fe_2O_3$) | [12] |

The overall analysis of all the results obtained by the various authors goes in the direction of a bilayer model with an inner layer of magnetite and an outer layer consisting of more or less hydrated iron oxyhydroxides. Whatever the environmental conditions (aerated or non-aerated), the corrosion products seem to stabilize from 1 month to 3 years [21].

### 2.5.2. Kinetics of passive corrosion

In aerated conditions, several authors have estimated average passive corrosion rates to be less than 1 µm / year [21–24]. These measured passive corrosion rates are equivalent with or without interfacial defects [25]. The basic interstitial solution of concrete is, therefore, a protective medium for reinforcement. The steel is coated with a passivation film and dissolves at a very low speed (uniform corrosion). Under certain conditions, this passive film is destabilized causing the initiation of corrosion. Depassivation of reinforcement can be induced by the carbonation from atmospheric carbon dioxide ($CO_2$) and/or by chloride ions ($Cl^-$). In the present thesis, only chloride-induced corrosion is considered.

## 2.6. Corrosion initiation

### 2.6.1. Sources of chlorides in reinforced concrete

Chlorides in reinforced concrete come from 2 types of sources: external and internal. The external source essentially results from 2 origins [26,27]:

- Marine environment (case of XS exposure classes) with different levels of contamination summarized in Table 2.
- De-icing salts used in severe winter conditions (case of XD exposure classes).

*Table 2. Different chloride exposure classes in marine environments.*

| Exposure class | Methods of contamination |
|---|---|
| XS1 | Parts of the structure exposed to sea spray |
| XS2 | Parts of the structure permanently immersed in seawater |
| XS3 | Tidal areas, areas subject to sea projections or sea spray |

The penetration of chlorides from the external source requires the presence of a liquid phase. It is done either by diffusion as a result of a concentration gradient in case of a saturated concrete, or by a combination of capillary absorption and convection in case of an unsaturated concrete. The transfer takes place from regions with high concentrations (surfaces subjected to sea spray, de-icing salts) to regions with lower concentrations (concrete core).

The internal origin of chlorides comes from concrete compounds (cement, aggregates, water, and cement additives). These initial chlorides are mainly fixed to the cement matrix. Thus, the standard NF EN 206, published in 2016, limits the maximum amount of chlorides initially present in the mix ($C_0$) for different types of concrete structures and different types of binders. However, these limits are not chloride threshold values initiating corrosion, but rather practical guidelines for the production of fresh concrete (Table 3).

*Table 3. Acceptable initial levels of total chlorides according to EN 206: 2016*

| Type of structure | $C_0$ total Cl (%/wt. binder) |
|---|---|
| Reinforced concrete | 0.2 - 0.4 |
| Prestressed concrete | 0.1 - 0.2 |
| Reinforced concrete with CEM III | 0.4 (depends on national application) |
| | 0.65 for FRANCE |
| Unreinforced concrete | 1.0 |

### 2.6.2. Types of chlorides in concrete

Two types of chlorides exist in concrete: bound chlorides which are fixed to the cement matrix and free chlorides which are present in the interstitial solution of concrete and are mainly responsible for the initiation of corrosion (depassivation of steel) [28]. The sum of free and bound chlorides represents total chlorides.

The measurement of chloride content in cementitious materials is a very important topic especially in the domain of chloride-induced corrosion in reinforced concrete structures. This measurement is a very challenging task because of the high heterogeneity of concrete [29]. The determination of the level of chloride contamination in concrete is documented in different technical documents [30] and standards [31–33]. Yet, many laboratories have developed their procedures, for instance, the recommendations of GranDuBé [34]. The determination of chlorides is very complex and the measurement techniques produce large uncertainty between the different laboratories [35]. Moreover, the results obtained from the same procedure performed by the same laboratory showed a high scatter with uncertainty in the range of 10–25% (with the highest uncertainty at low chloride contents) even for constant method and laboratory [36].

There are several destructive and non-destructive methods for the assessment of chloride content in cementitious materials. The traditional method consists of the measurements of chlorides on powder samples dissolved with nitric acid for total chlorides and water for free chlorides. The main problem is that the experimental measurement of the concentration of free chlorides is more delicate than that of total chlorides. For example, the determination of the content of free chlorides by dissolution with water is very dependent on the conditions of the experimental protocol adopted such as the temperature, the amount of water added and the stirring time. Besides, it has been shown that measurement of the free chloride content by extraction of the interstitial solution can overestimate the actual free chloride content since a certain amount of fixed chlorides may be released due to applied pressure [37,38]. The same problem can occur when determining by dissolution with water. All this makes it possible to understand the reason why, in standards and norms, one often prefers to use criteria based on total chlorides.

It is also important to note that during corrosion, some of the bound chlorides may be released under the influence of the increase in temperature above 55 °C [39] or because of the local acidification near a corrosion pit [40]. This means that some of the bound chlorides may be involved in the corrosion process. It is, therefore, necessary, when studying the corrosion process, to determine both free and total chlorides.

Before proceeding to the process of depassivation of steel, it is first important to understand the chloride/concrete interaction mechanism which is the process of chloride binding in concrete.

### 2.6.3. Chloride binding in concrete

Portland cement consists mainly of clinker to which is added gypsum. Portland cement clinker is mainly composed of tricalcium and dicalcium silicates with a lower amount of calcium and iron-calcium aluminates and other minor components. When mixed with water, clinker and gypsum react with water to form mineral species from which the main types are:

- Portlandite ($Ca(OH)_2$) ;
- C-S-H or Calcium silicate hydrate ($Ca_xSi_yO_z(OH)_{m.nH2O}$) ;
- AFm or hydrated calcium aluminates ($Ca_4Al_2(SO_4)(OH)_{12}.6H_2O$) et/ou ($Ca_4Al_2(CO_3)_x(OH)_y.nH_2O$) ;
- AFt ou ettringite ($Ca_6Al_2(SO_4)_3(OH)_{12}.26H_2O$) et le tricarboaluminate ($Ca_6Al_2(CO_3)_3(OH)_{12}.26H_2O$);
- Hydrogrossular $Ca_3Al_2\ (SiO_4)_{3-x}\ (OH)_{4x}$.

Chlorides from the external source pass through the concrete cover before reaching the steel bars. As a result, some of these chlorides will be fixed to the cement matrix according to one of the two chlorides binding mechanisms: physical binding and chemical binding.

Physical binding is the result of the adsorption of chlorides by mineral species of concrete in particular by C-S-H. Physical adsorption can be explained by Stern's double layer model.

Chemical binding is the result of the chemical reaction of chlorides with anhydrous or hydrated aluminates such as AFm leading to the precipitation of salts:

- Friedel's salt ($Ca_4Al_2(OH)_{12.05}Cl_{1.95}.4H_2O$) ;
- Kuzel's salt ($Ca_4Al_2(SO_4)_{0.5}Cl(OH)_{12}.6H_2O$) ;
- Oxychloride salts ($3CaO.CaCl_2.H_2O$, $3CaO.CaCl_2.2H_2O$, $3CaO.CaCl_2.10H_2O$, $CaO.CaCl_2.12H_2O$, $CaO.CaCl_2.15H_2O$) which are formed in the case of very high chloride concentrations (3 to 8 mol/L of solution) [41,42].

The chloride binding capacity is dependent on several factors [43–52] related to binder type, the content of calcium and iron-calcium aluminates, the content of C-S-H gel, pH and temperature. The

unfixed part of chlorides will be responsible for the initiation of corrosion [28] once it reaches an amount called threshold chloride content. A local depassivation of the steel will take place and corrosion is initiated between the depassivated zone and the rest of the passive reinforcement. Chloride binding capacity of concrete is thus an important resistant parameter against chloride-induced corrosion. It also impacts the critical chloride content when expressed in terms of total chlorides.

### 2.6.4. Depassivation of steel

Until now, the mechanism of steel depassivation by chlorides remains uncertain. There are 3 main mechanisms which can explain the local degradation of the passivation film with the possibility of interacting:

Mechanism of adsorption (physical and chemical):

The mechanism of physical adsorption, first addressed in 1964 [53], considers that the adsorption of chlorides on the surface of the passivation film increases the transfer of ferrous and ferric ions towards the interstitial solution of concrete (see Fig. 3).

The chemical adsorption mechanism discussed later [54], requires the dissolution of the passive film by chlorides (see Fig. 4).

These two mechanisms can interact. Indeed, cations existing in the passivation layer can bind to the chlorides, thus reducing the positive charge concerning the metal cations. Therefore, the transfer of metal cations to the electrolyte will be favored.

Also, the accumulation of metal cations at the passivation film/concrete interface can cause a decrease in pH leading to the dissolution of the passivation film. On the other hand, the concrete can buffer the pH by the dissolution of portlandite which makes it possible to repassivate the steel [55].

Penetration mechanism:

According to this mechanism proposed in 1965 [56], chlorides penetrates through the defects of the passivation film up to the metal/passivation film interface (see Fig. 5). Steel will then be in direct contact with chlorides and will dissolve into ferrous ions $Fe^{2+}$ which reacts with hydroxyl ions $OH^-$ to produce the ferrous hydroxide $Fe(OH)_2$ will be further oxidized to $Fe_3O_4$ or $Fe_2O_3$ [57], depending on oxygen availability. These more expansive products can cause cracking of the passivation film [58] (see Fig. 6).

Mechanism of failure of the film by electrostriction

This mechanism suggests the breaking of the passivation layer under the effect of electrostriction due to the reduction of the superficial tension of the oxide layer caused by the adsorption of chlorides.

The interdependence of 2 or more mechanisms

According to several authors [58,59], the three proposed mechanisms can influence each other or even interact. For example, the chemical adsorption mechanism may favor the mechanism of failure under the effect of electrostriction.

The local and random nature of corrosion induced by chlorides can be explained by the presence of defects in the passivation film which can create favorable locations for the depassivation of steel regardless of the type of mechanism involved.

These different mechanisms justify the existence of a threshold value in chlorides from which the steel would be depassivated and thus the "active corrosion" would be initiated.

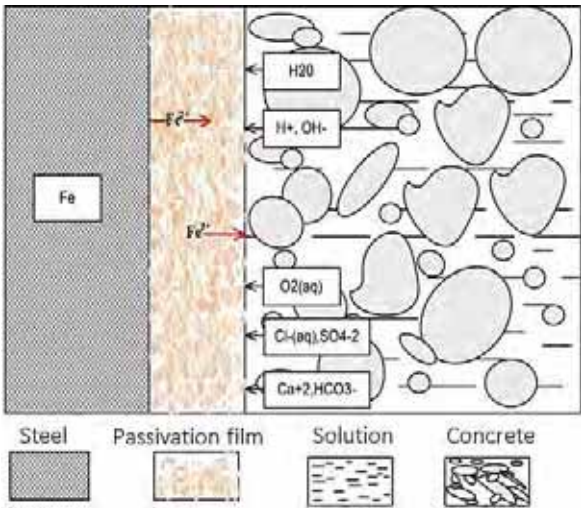


*Fig. 3. Physical adsorption of chlorides at the surface of the passivation film [60]*

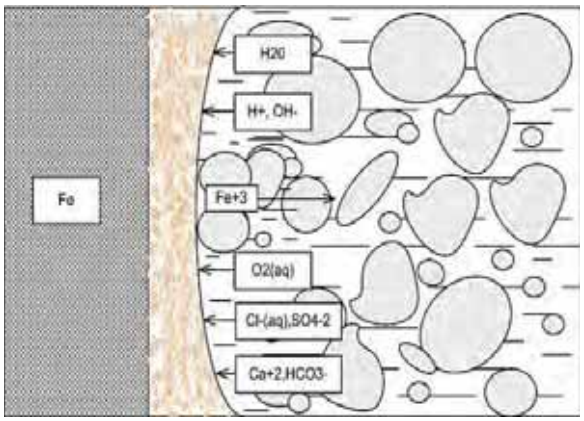


*Fig. 4. Chemical adsorption leading to the dissolution of the passivation film [60]*

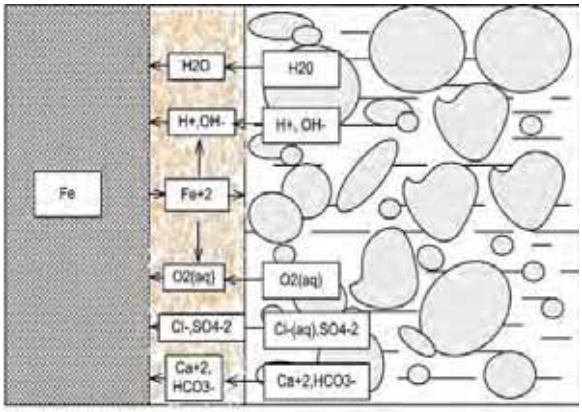


*Fig. 5. Diffusion of chlorides through the passivation film [60]*

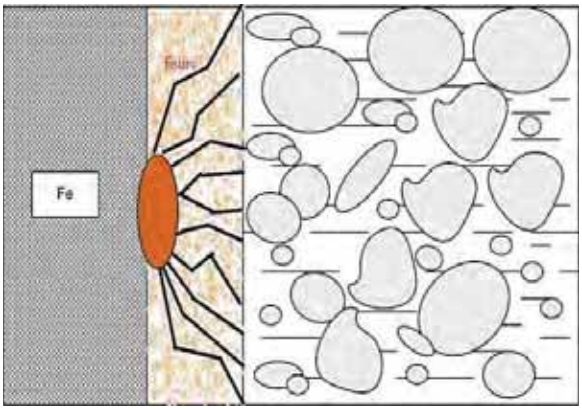


*Fig. 6. Cracking of the passive film induced by the formation of oxy-hydroxide [60]*

## 2.7. Questionable concept of threshold critical chloride content ''Ccrit''

The common assumption is that the chloride concentration at the surface of the steel embedded in concrete is the most important parameter for predicting the initiation of corrosion. This concept has received considerable attention from researchers in recent decades. As a result, great efforts have been made to determine the chloride threshold value by measuring and modeling chloride infiltration. The adopted concept reduces the whole problem of initiation to a question of chloride only and ignores the important effect of a large number of parameters. It is, therefore, necessary to understand the relevant elements governing the initiation of corrosion in concrete before continuing to apply this concept to modern materials [61]. The first step needed is to establish a clear definition of the concept of critical chloride content.

### 2.7.1. Definitions of critical chloride content ''Ccrit''

There are several definitions of the critical chloride threshold value. In literature, these definitions are often mixed. It is, therefore, necessary to be aware when comparing and evaluating the published results of Ccrit [3].

Definition1:
From a scientific point of view, according to some authors, such as Tutti [62], the critical chloride threshold (Ccrit) is defined as the minimum chloride content necessary for the depassivation of steel. This threshold corresponds to the chloride content measured at the level of the reinforcing bar corresponding only to the corrosion initiation phase. Conceptually, this means that, below the critical content, there is no corrosion, and above it, corrosion occurs.

Definition2:
Other authors have pointed out that, under certain conditions, depassivation is not an instantaneous event but must be considered as a time during which the initial formation of the corrosion spot takes place until the stability of the corrosion [62]. This definition does not contradict the first approach, but, it adds that the transition from a passive to an active state takes place, in many cases, over a long period, but also a range of chloride concentrations rather than a single value. The chloride concentration may be high enough to initiate pitting, but may not be sufficient to support the growth of stable corrosion [62].

Definition3:
From a practical point of view, some researchers define Ccrit as the chloride content associated with an acceptable degree of reinforcement corrosion correlated to an acceptable degree of deterioration of reinforced concrete structures. The Ccrit values obtained from this approach are dependent on the acceptable degradation term which is not precisely defined and especially on the corrosion rate which is influenced by a large number of parameters such as electrical resistivity of concrete cover, oxygen content, etc. According to this definition, Ccrit corresponds to the phase of corrosion propagation which, apart from chloride content, depends on several parameters. Consequently, the results of Ccrit using this approach are widely scattered and difficult to justify from a scientific point of view [3].

After comparing the different definitions of the critical chloride content, it is important to understand the different expressions used to determine Ccrit. These expressions translate the competition between aggressive species (total or free chlorides) and inhibiting agents. It is especially the choice of the inhibiting agents which is responsible for the diversity of existing expressions of Ccrit.

### 2.7.2. Expressions of the critical chloride content (Ccrit)

Generally, there are 4 different expressions of Ccrit:

Expression 1: Total chloride content expressed according to the weight of binder or concrete
The critical chloride content is most often expressed as a mass percentage of total chlorides versus the weight of binder (cement + additions + substitutions) or to the weight of concrete since in some cases the quantification of binder in hardened concrete can be difficult.

Expression 2: Free chloride content expressed according to the weight of binder or concrete or as a concentration of chlorides in the interstitial solution
It makes more sense to determine Ccrit in terms of free chlorides since they are responsible for initiating corrosion. This approach can be adopted by assuming that there is no risk that bound chlorides are released into the interstitial solution. It is important to keep in mind that the experimental measurement of free chlorides is less reliable than that of total chlorides. Free chlorides can be expressed either in the form of a mass percentage relative to the weight of binder or concrete or in the form of a concentration of chloride ions relative to the volume of the solution present in the pores.

Expression 3: $[Cl^-]/[OH^-]$ ratio

This ratio makes it possible to integrate the interactions between the penetration of chlorides (increase in the concentration of free chlorides ($Cl^-$)) and carbonation (reduction of the concentration of hydroxides ($OH^-$)). The ratio links the activity of $Cl^-$ to the pH of the interstitial solution and assumes that only free chlorides are involved in the corrosion process and that the inhibiting effect of concrete is due to the concentration of $OH^-$ of the solution in pores.

The results obtained by the various authors using this expression of Ccrit are very scattered and contradictory:

- Some authors found a constant $Cl^-/OH^-$ ratio [63];
- Others found this ratio constant $(Cl^-)^{0.83}/(OH^-)$ [64];
- Several authors indicate that the ratio $Cl^-/OH^-$ increases with pH of simulating and storing solutions [44,65];
- Others, on the contrary, have found that Ccrit increases with decreasing pH (case of concretes with silica fume in particular) [66].

This dissonance of the results can be explained by the difficulty of determining, in a reliable way, the concentration of $OH^-$ ions or the pH of the porous concrete solution. Also, the inhibiting properties of the concrete cover do not depend exclusively on the hydroxide ions but a large number of factors [40]. This means that a higher $Cl^-/OH^-$ ratio does not have to be associated with a higher risk of corrosion initiation.

Expression 4: $[Cl^-]/[H^+]$ ratio

This expression translates the relationship between total chlorides and the ability of the hydration products to neutralize the acid i.e. to buffer the pH [67].

By comparing these different expressions, it is possible to assume that the expression 1 presents the most common, the simplest and therefore the most reliable method widely used to express Ccrit in literature [3,68,69]. Expression 2, even though it is criticized by the fact that bound chlorides can be released due to phenomena like carbonation [70], it is more correct, since only free chlorides are responsible for initiating corrosion. In the thesis, this expression of Ccrit was mainly used.

### 2.7.3. Ccrit in literature

Lots of research has been devoted to the identification of a critical chloride threshold likely to initiate corrosion of reinforcement. A considerable number of documents have been published presenting values of critical chloride contents in reinforced concrete. Despite the multitude of undertaken studies, Ccrit values found in the literature are widely scattered and are not unanimous. Many aspects of chloride-induced reinforcement corrosion in concrete are still poorly understood and no consensus on Ccrit has yet been found. Currently, there is no accepted or standardized test protocol for measuring Ccrit. Thus, conservative threshold values are often used (Table 4).

*Table 4. Conservative values of existing Ccrit*

| Ccrit (total Cl in %/wt. binder) | Reference |
|---|---|
| 0.3 - 0.5 | [71] |
| 0.3 - 0.5 | [72] |
| 0.2 - 0.6 | [73] |

A comparative study and literature evaluation conducted by Angst et al. [3] groups the various results of Ccrit obtained experimentally for the different definitions and expressions of Ccrit presented

previously, for several test conditions and several types of steel and types of the binder. From an overall perspective, a wide scattering of Ccrit is observed. Ccrit values expressed in the form of $Cl^-/OH^-$ vary up to 3 orders of magnitude from 0.01 to 45, whereas, Ccrit values expressed as the total chloride contents relative to the weight of binder vary up to two orders of magnitude from 0.04% to 8.34%.
This large scatter of the critical chloride content is related to the different experimental procedures adopted and to many parameters that affect the corrosion induced by chlorides in reinforced concrete.

Many parameters affect the value of Ccrit and many of them are correlated [62,74]. As a result, applying a single Ccrit value to a wide range of structures seems to be complicated. According to a recently published paper by the RILEM Technical Committee 262-SCI [75], the parameters influencing Ccrit at the steel/concrete interface can be classified as factors related to reinforcement bars, concrete, and interfacial concrete voids, and other factors like temperature and moisture content.

## 2.8. Corrosion propagation phase: corrosion control mechanisms

The corrosion propagation phase is the stage that follows corrosion initiation once stable corrosion has established. Corrosion of steel in concrete structures exposed to chlorides (seawater, de-icing salts, etc.) is non-uniform corrosion which refers to the macroscopic aspect of localized or macrocell corrosion. This type of corrosion corresponds to the electrical connection of cathode (passive steel) and anode (active steel) which are spatially separated on the surface of the steel reinforcement network with a distance than can easily reach decimeters or even meters [76].

In the anodic areas, the oxidation reaction occurs consisting of the dissolution of irons. At the cathodic areas, in presence oxygen at the steel/concrete interface, the oxygen reduction reaction takes place. An electronic current circulates through the metal from active steel towards passive steel and ionic current flows through the interstitial solution of concrete. As a result, macrocell corrosion is a function of the anodic reactions, the cathodic reactions, and the ionic and electronic current flows. Indeed, it is commonly believed that to achieve and sustain the "dynamic equilibrium" of a galvanic corrosion system, all these reactions must occur at the same rate [77–79] which makes each of these processes possible rate-limiting factor. The electronic control associated with the transport of electrons through reinforcement bars is considered negligible when compared to the other rate-limiting factors.

In the presence of oxygen, the cathodic current corresponds to the reduction of dissolved oxygen along with the formation of hydroxyl ions at the steel-concrete interface. Therefore, the cathodic control is usually associated with the restrictions of the kinetics of the cathodic reaction. This reaction is conditioned by oxygen availability determined by its diffusion kinetics through the cement matrix. This situation is usually encountered when the structure is in submerged conditions where chloride contamination happens relatively easily but oxygen availability is limited by its slow diffusion through saturated concrete and its low concentration in solution. Cathodic control can also be encountered in sulfide containing materials like slag

The anodic reaction is governed by the anodic charge transfer which is influenced by the very local aspects of the inhomogeneous matrix of the concrete. In other terms, the anodic control is dependent on the microstructure of concrete associated with the nature of the porous network of concrete, the form of the corrosion pit and the presence of corrosion products. Anodic control might also be dependent on the type of steel used and the type of steel surface condition according to findings in [80]. In the passive state, the anodic Tafel coefficient is relatively high which presents a controlling factor of corrosion since it limits corrosion current. While, in the active state, corrosion could be limited anodically by mass transport also known as anodic diffusion control which is the result of several parameters like the geometry of the corrosion pit [81] and the microstructure of concrete [82].

the extent to which ohmic control contributes to the limitation of macrocell corrosion is mainly dependent on the size of anode [76], geometrical configuration (size and location of cathode) and the electrical resistivity of concrete. In the case of large anodes and large structures where the cathode-anode distance is relatively important (in orders of decimeters to meters), the mobilizable cathode surface can be limited by the ohmic resistance making the electrochemical system under ohmic control. It must be noted that in the early phase of the corrosion process, the size of the anode is relatively small and the available cathode area is usually very high giving C/A ratios as high as 200,000 [80,82]. As a result, the ohmic control is supposed insignificant since the anodic ohmic resistance at the anode dominates the ohmic and cathodic control owing to the concentration of current in small anodes [83]. Indeed, The small size of active steel is, hence, associated with high local current densities [82] as high as 100 $\mu A/cm^2$ [article 6]. This indicates that, at the initiation stage, it is possible to exclude that the corrosion rate is limited by the C/A ratio and consequently on the ohmic control. The electrical resistivity of concrete can be significantly affected by several parameters [84] like water content [85–92], the concentration of chlorides in the interstitial solution increases [93–98], carbonation level [99], type of binder [100–102] and temperature [103].

It appears that the early phase of the corrosion stage is governed by anodic control, while, later stages appear to be dominated by cathodic/ohmic control [82].

## 2.9. Uniformity paradigm

It is clear and quite unanimously recognized that, despite several decades of research on the topic of chloride-induced corrosion in concrete, a part of the scientific community is still unable to propose any reliable technique for measuring corrosion rates. The reason behind this failure is related to the uniformity paradigm which was adopted by generations of researchers and engineers, most often without even being aware of it. The uniformity paradigm is responsible for the failure of the scientific community in providing reliable technologies for measuring, predicting and protecting steel-reinforced concrete structures affected by corrosion. The uniformity paradigm is expressed by two fundamental assumptions which are not true:

- Uniformity of the electrochemical state of steel in concrete;
- Uniformity of the electrochemical perturbation applied in cases of corrosion measurement or cathodic protection.

Regarding steel corrosion systems in concrete, nothing is ever uniform, neither the electrochemical state of steel nor the electrochemical perturbation applied for measuring it [104,105]. That's why it is not possible to use methods and equations originally derived for uniform corrosion and apply to localized corrosion [106,107].

As a result, the development of reliable technologies requires a drastic paradigm shift, by addressing the real 3D nature of the physical problem [105,108,109] which is now possible thanks to easily-available computational resources.

## 3. Overview of the work

Table 5 presents an overview of the Ph.D. study which is structured in eight sections according to the objectives and topics discussed in each appended paper.

Table 6 presents a summary of the different experimental setups concerning the test samples and the materials used according to each paper. The detailed preparation of the test samples (anode, cathode, wall, and beam) is presented in Appendix II. The technical sheets of the materials used for the preparation of the samples are presented in Appendix I. The steel bar used in the Ph.D. study was ribbed steel mainly in as received conditions. Yet, several steel surface conditions were also used and their preparation is detailed in Appendix IV. In all the experimental work, characterization tests of all the formulations were realized, for instance, water porosity, electrical resistivity, chloride migration coefficient, compression strength, etc. These tests are described in Appendix III. The pH of the interstitial solution was measured for some formulations and the measurement technique was shown in Appendix VII.

Also, Table 6 presents the different measurements achieved in the thesis according to each paper. Chloride measurements were realized in most of the experimental work. The methodology adopted for the measurements of the contents of total and free chlorides in concrete and mortar is detailed in Appendix V. The steady-state polarization test was also used in several papers. The test setup and the analysis of the measurement are shown in Appendix VI.

Some of the results of the scanning electron microscopy, Backscattered electron analysis, and Raman spectroscopy realized in Paper I are presented in Appendix Paper I.

Table 7 presents a summary of the different numerical studies achieved in each paper of the thesis. These numerical simulations were explained in the papers. The concept of the Nelder Mead optimization used in the numerical analysis in Paper II is explained in Appendix Paper II.

*Table 5. Summary of the Ph.D. study*

| Paper | Title | Objective |
|---|---|---|
| **I** | Determination of chloride threshold initiating corrosion: A new set-up taking the localized aspect of corrosion into account. | - Development of a new experimental protocol for the determination of the chloride threshold Ccrit initiating corrosion taking into account the intrinsic localized aspect of chloride-induced corrosion and allowing to quantify macrocell current. |
| **II** | Macrocell corrosion of steel in concrete: characterization of anodic behavior in relation to the chloride content. | - Determination of electrochemical properties of active steel in mortar based on inverse numerical modeling taking into consideration the influence of chloride contamination level on iron anodic coefficient and subsequently on electrochemical properties of active steel. |
| **III** | Critical chloride threshold values as a function of cement type and steel surface condition. | - Application of the experimental protocol developed in the Paper I for determining threshold values of chloride initiating corrosion in reinforced samples made with different mortars and concrete compositions. |
| **IV** | Anodic control of the initiation of macrocell chloride-induced corrosion in concrete structures. | - Numerical analysis of the process controlling chloride-induced corrosion initiation using numerical modeling based on Butler-Volmer equation and electrochemical parameters of steel determined from Paper II. |
| **V** | Effect of Cathode-Anode distance and electrical resistivity on macrocell corrosion currents and cathodic response in cases of chloride-induced corrosion in reinforced concrete structures. | - Experimental and numerical investigation of the influence of the cathode-anode distance on the macrocell current in the case of chloride-induced corrosion.<br>- Determination of geometrical factors in case of unidimensional geometry showing the impact of resistivity. |
| **VI** | Influence of concrete electrical resistivity on corrosion propagation and its relationship with cathode/anode ratio and chloride contamination. | -Study of the impact of electrical resistivity of concrete on the macrocell corrosion current during the corrosion propagation phase.<br>-Investigation of the influence of chloride contamination on electrical resistivity in the case of different types of binders and study of the effect of electrical resistivity on the Cathode/Anode surface ratio and the mobilizable cathode surface contributing to macrocell current. |
| **VII** | Influence of ground granulated blast furnace slag on macrocell corrosion of steel in reinforced mortar. | - Study of the influence of oxygen availability on the kinetics of the cathodic reaction.<br>- Investigation of the behavior of compositions with high levels of slag on macrocell current. |
| **VIII** | Lifetime prediction model of reinforced concrete structures under the risk of corrosion based on service limit state criteria associated with a corrosion current density corresponding to the appearance of the first C-I cracking. | - Development of an empirical model to predict the duration of corrosion propagation corresponding to the appearance of first corrosion cracks in structures under the risk of chloride-induced corrosion. |

*Table 6. Description of the different experimental setups used in the thesis*

| Paper | Samples | Materials | Analysis methods |
|---|---|---|---|
| I | Anode<br>Cathode | Mortar CEMI<br>Ribbed steel $\varphi$ 6 mm<br>(As received, Cleaned, Cleaned then pre-oxidized) | -Galvanic coupling, ZRA measurements (potentiostat and multimeter)<br>-Chloride content measurements (chloride titrator)<br>-Gravimetric measurements<br>-Microscopic observations<br>-Scanning electron microscopy (SEM)<br>-Backscattered electron analysis (BSE)<br>-Raman spectroscopy |
| | Wall | Concrete CEMI<br>Ribbed steel $\varphi$ 12 mm<br>(As received) | |
| II | Anode<br>Cathode | Mortar CEMI<br>Ribbed steel $\varphi$ 6 mm<br>(As received) | -Galvanic coupling, ZRA measurements (potentiostat)<br>-Chloride content measurements (chloride titrator)<br>-Steady-state polarization tests (potentiostat) |
| III | Anode<br>Cathode | Mortar CEMI, CEMI+10%SF<br>Concrete CEMI, CEM III<br>Ribbed steel $\varphi$ 6 mm<br>(As received, Cleaned, Cleaned then pre-oxidized) | -Galvanic coupling, ZRA measurements (potentiostat and multimeter)<br>-Chloride content measurements (chloride titrator)<br>-Gravimetric measurements<br>-Microscopic observations |
| | Wall | Concrete CEMI, CEMI+15%SF<br>Ribbed steel $\varphi$ 12 mm<br>(As received) | |
| V | Beam | Mortar CEMI<br>Ribbed steel $\varphi$ 12 mm<br>(As received) | -Galvanic coupling and ZRA measurements (acquisition system and multimeter) |
| VI | Anode<br>Cathode | Mortar CEMI, CEMI+10%SF<br>Concrete CEMI, CEM III<br>Ribbed steel $\varphi$ 6 mm<br>(As received) | -Galvanic coupling, ZRA measurements (potentiostat and multimeter)<br>-Cathode permutation technique<br>-Chloride content measurements (chloride titrator)<br>-Electrical resistivity measurements (resistivity meter and potentiostat) |
| | Wall | Concrete CEMI, CEMI+15%SF, CEMI+80%S<br>Ribbed steel $\varphi$ 12 mm<br>(As received) | |
| VII | Anode<br>Cathode | Mortar CEMI, CEMI+10%SF, CEMI+40%S, CEMI+80%S<br>Ribbed steel $\varphi$ 6 mm<br>(As received) | -Galvanic coupling, ZRA measurements (potentiostat)<br>-Chloride content measurements (chloride titrator)<br>-Steady-state polarization tests (potentiostat)<br>-Microscopic observations |
| VIII | Anode<br>Cathode | Mortar CEMI<br>Ribbed steel $\varphi$ 6 mm<br>(As received) | -Galvanic coupling and ZRA measurements (potentiostat)<br>-Temperature monitoring (thermometer) |

*Table 7. Description of the numerical work achieved in the thesis*

| Paper | Software | Numerical study |
|---|---|---|
| II | Comsol Multiphysics | -Numerical optimization for the characterization of the active state of steel<br>-Numerical simulation of galvanic coupling tests<br>-Indirect resistivity measurement by inverse numerical modeling |
| IV | Comsol Multiphysics | -Numerical simulation of galvanic coupling tests |
| V | Comsol Multiphysics | -Numerical simulation of galvanic coupling tests |
| VI | Comsol Multiphysics | -Indirect resistivity measurement by inverse numerical modeling |
| VIII | Excel | -Fitting numerical models with experimental results<br>-Development of Excel spreadsheets designed for engineering calculations based on the corrosion propagation prediction model |

# 4. Main findings

The main findings are discussed according to the objectives presented in part 1.2 and reported below.

1. **Development of a new laboratory test set-up that considers the localized character of corrosion initiated by chlorides for the determination of the critical chloride content initiating corrosion**

    1.1. Derive a test protocol that is expected to allow the detection of corrosion initiation and to quantify the galvanic corrosion current.
    1.2. Select an approach for the determination of the critical chloride content.
    1.3. Study the impact of binder type and steel surface condition on the critical chloride content.

2. **Characterization of the anodic behavior in relation to the chloride content**

    2.1. Use the experimental setup described in objective no. 1 to investigate the impact of chloride contamination on macrocell corrosion current.
    2.2. Characterize the electrochemical behavior of passive steel on non-contaminated samples.
    2.3. Develop a numerical optimization for quantifying active steel parameters focusing on chloride's effect on the iron anodic Tafel coefficient.

3. **Corrosion propagation**

    3.1. Use the experimental setup that evolves from objective no. 1 to study the chloride-induced corrosion propagation phase.
    3.2. Identify the impact of the cathode to anode ratio and cathode-anode distance on macrocell corrosion current.
    3.3. Study the role of electrical resistivity on macrocell corrosion propagation.
    3.4. Investigate the influence of ground granulated blast furnace slag on macrocell corrosion of steel in reinforced mortar

4. **Development of an engineering model practical for end-users for the prediction of the propagation phase of reinforced concrete structures adapted to the performance-based approach**

    4.1. Identify the limitations of previously reported corrosion rate predictive models
    4.2. Review the different parameters impacting corrosion propagation
    4.3. Develop an empirical simplified model calibrated from experimental results derived from objectives no. 1, 2 and 3.
    4.4. Define a limit state associated with reinforcement corrosion corresponding to an acceptable corrosion state.

## 4.1. Development of a new laboratory test set-up that considers the localized character of corrosion initiated by chlorides for the determination of the critical chloride content initiating corrosion

### 4.1.1. The general principle of the experimental protocol

A new test protocol was developed in [Paper I] to reproduce the localized chloride-induced corrosion found in real structures. This developed method consists of the same components found in other experimental protocols (such as the steel bar surface condition, the alkaline environment, the procedure to introduce and measure the chlorides and the exposure conditions) but with the addition of another component which is the macrocell corrosion current. Indeed, the test set-up is based on a physical separation of the anode part, contaminated with chlorides, from the cathode part, which is chloride free allowing the measurement of the macrocell (galvanic) corrosion current between anodic and cathodic zones, which was impossible to do in tests performed on single bar specimens. The surface of the rebar at the anode is 1.88 $cm^2$ and that of the rebars of the cathode is 30.16 $cm^2$.

The anode and cathode samples were placed in a sodium hydroxide solution and were connected by a potentiostat using the ZRA (Zero Resistance Ammeter) electrochemical technique to measure the galvanic coupling current between them. The measurement of the current was maintained for 7 days to reach the steady-state (stabilization of the measured galvanic current). All the electrochemical experiments were carried out at a constant temperature of 20 $^oC$ in a controlled room. The macrocell current was calculated from the integral of the current signal over a duration of 7 days.

After the end of the test, the anodes were split in the middle, the steel bars were removed and the total chloride contents were measured on solutions prepared from mortar powders with the Ti amo software by precipitation with a silver nitrate solution. Since the total chlorides are the sum of free and fixed chlorides, the transition from total chlorides to free chlorides was achieved using empirical adsorption isotherm equations that were determined. It should be noted that such isotherms, corresponding to the imbibition process, do not correspond to classical isotherms of massive samples, where chlorides penetrate through the concrete by diffusion, which could partially explain the low bound chloride contents found. Hence, total and free chloride contents were measured on reference samples for the determination of adsorption isotherm equations described by the Freundlich model calibrated to experimental results which allows the shift from total chloride to the free chlorides. The preparation of the solutions for total and free chlorides was performed according to standard NF-EN-14629 [31] and the procedure recommended by GranDuBé [34], respectively.

The spatial variation in chloride contamination in anode samples was evaluated in Appendix V where a reinforced anode sample was soaked in a saline solution with a concentration of 280 g/L for a duration of 48 hours. Then, the specimen was split in half and one of the parts of the anode was used to collect mortar powder form different areas. This part was divided into 6 parts and 6 mortar powders were collected and tested. The level of total chloride contents was measured with the titrator and the percentages of chloride contents were calculated versus the level of chloride measured in the sampling area (surrounding the rebar). The obtained results indicated a variation of chlorides between 91 and 113% versus the chloride content measured in the area near the rebar. This observation is an indication of the reproducibility of the adopted procedure and most importantly the homogeneous distribution of the total chloride content inside the tested samples. This result is consistent with observations from the study realized by Sbartaï et al. [96] where the same preconditioning of samples was used. The authors [96] stated that this preconditioning technique (oven drying before contamination) allows, first, to accelerate chloride intrusion throughout the material by capillary processes, and also, to have a

homogeneous distribution of the total chloride content inside the tested samples. This last statement was supported by a chemical investigation achieved according to (AFPC-AFREM) recommendations [110].

All the corrosion measurements made up form anode-cathode coupling were linked to a predefined geometric factor, the cathode/anode (C/A) apparent ratio, which was equal to 16. To reach very high C/A ratios, a concrete wall was used to represent the cathodic part. The network of frames in the wall was completely electrically disconnected but could be electrically connected from the outside. The anode was placed in a PVC pipe containing a sodium hydroxide solution that was connected to the wall allowing the ionic current to circulate. Smaller C/A ratios were also tested. Each anode was connected to 3 cylindrical cathodes (ϕ11x22cm3) with three different lengths of steel (1, 5 and 16 cm) embedded in them to test C/A ratios of 1, 5 and 16 respectively. Then, the anode was electrically connected to the steel bar(s) of the wall, connecting a different number of bars each time, with different lengths presenting cathode/anode ratios from 200 to 2950. Current measurements were made using an Agilent multimeter and the values of the currents were recorded after they had stabilized to a steady-state condition.

The test was firstly achieved on samples made with a CEMI mortar mixture with a w/b ratio of 0.55 [Paper I]. Four different types of steel surface were used in this study: As Received Steel, "ARS" (steel without treatment), Cleaned Steel, "CS" (steel cleaned with an acid solution), Cleaned Steel Pre-oxidized by high Temperature, "CSPT" (steel cleaned then oxidized with a heat treatment), and Cleaned Steel Pre-oxidized by exposure to Humid environment "CSPH" (steel cleaned then oxidized for two weeks in a humid environment). This experimental protocol was then used in [Paper III] for the assessment of the critical chloride contents for different types of binder and steel surface conditions in mortar and concrete formulations. In addition to CEMI mortar formulation, another mortar formulation M10SF-043 was used with 10% of silica fume with a w/b ratio of 0.43. Three concrete formulations were also used where the first one B1-15L-049 was made with CEMI with 15% of limestone addition and a w/b ratio of 0.49, and B3-15L-051 and B3-041 formulations were made with the cement CEM III/A, which contained 64% of blast furnace slag (S). The formulation B3-041 has a w/b ratio of 0.41 and B3-15L-051 had 15% of limestone additions and w/b ratio of 0.51.

### 4.1.2. Approach for the determination of the critical chloride content initiating corrosion

The corrosion current was independent of the C/A ratio for a certain range of chloride content. Beyond this chloride content, an increase in the C/A ratio led to an increase in the galvanic current, which is in agreement with the fundamental galvanic coupling concepts. The experimental results also showed that the current growth rate decreased with increasing cathodic surface area, which could mean that the current would reach its maximum value and stabilize for a given C/A ratio [Paper I].

As a result, the critical chloride content initiating corrosion ($Ccrit$) was determined based on a limiting macrocell current called threshold corrosion current. This current is defined as a current that is independent of the cathode/anode surface ratio and was found equal to 3 µA [Paper I]. This finding indicates that the corrosion initiation must be linked to a threshold current that is not affected by surface ratio between cathode and anode which supports the concept of a rate-limiting step of corrosion initiation linked to the anodic controlling process found in other literature studies [80,82,111–114].

### 4.1.3. Influence of steel surface condition on $Ccrit$

In the case of CEMI mortar formulation, it was found that the total and free chloride threshold values for CEMI in the case of ARS, CSPT, and CSPH specimens were found respectively 0.6 and 0.5 %/wt. cement. However, in the case of cleaned steel, the free Cl content is 1.9%/wt. cement corresponding to a total chloride content of 2%/wt. cement [Paper I]. This means that the absence of mill scale and pre-existing corrosion products (when the rebars were chemically cleaned) had a mainly positive impact on $Ccrit$ in the case of CEMI mortar formulation. This result was found to be consistent with the literature, where the presence of mill scale or corrosion products on the steel surface has a negative effect on corrosion initiation [75].

A Scanning Electron Microscope (SEM) JEOL JSM 6380 operating in Backscattered Electron (BSE) mode was used to study the steel-mortar interface. A Bruker Energy Dispersive Spectrum analyzer (EDS) was used to quantify Iron, Oxygen, and Chloride in the observation zones along an analytical line. The elementary composition analysis of the interface in ARS, CSPT and CSPH samples revealed the presence of chlorides in the corrosion products. Furthermore, the chloride-containing corrosion deposits were circular and located at the steel/oxide interface. This means that the chloride ions penetrated through the oxide film formed on the surface of the bars to produce a chemical compound composed of Cl, Fe, and O. On the other hand, in CS samples, the thickness of the layer formed on the surface of the steel was less than 50 nm. Therefore, it was not possible to quantify the elements formed at the interface even with magnification higher than 500x [Paper I].

The corrosion products present at the steel/mortar interface were identified by Raman micro-spectroscopy with a Horiba spectrometer at the CEA lab at Saclay, France. Raman analysis was not possible in the case of CS samples because of the very thin layer of oxides. It was found that some chloride-containing corrosion products located at the steel/mortar interface on the steel side were composed of akaganeite and iron hydroxychloride β-$Fe_2(OH)_3Cl$, which could explain the presence of the circular shapes containing Cl that were observed and analyzed with the SEM. Hematite and magnetite corrosion products were also found and may have been corrosion products resulting from the pre-corrosion process carried out before casting [Paper I]. Some of the results of the scanning electron microscopy, Backscattered electron analysis and Raman spectroscopy realized are presented in Appendix Paper I.

It was concluded that the similarity of behavior between as received steel, ARS, and cleaned pre-oxidized steel, may be attributed to the resemblance in the composition of the mill scale layer found on the ARS and the layer of corrosion products formed on the cleaned pre-oxidized steel. The macrocell currents obtained in the absence of mill scale (cleaned steel specimens) were relatively weak. This phenomenon may be attributable to a less porous passive film formed on the cleaned steel making it harder for the chloride ions to diffuse through [Paper I].

On the other hand, in the case of M10SF-043, no clear effect of steel surface condition on $Ccrit$ was observed [Paper III].

### 4.1.4. Impact of the type of binder and water porosity on $Ccrit$

It was found that including 10 % of silica fume in the mortar formulation with a lower w/b ratio improved $Ccrit$ compared to a mortar formulation made only with CEMI [Paper III].

On the other hand, the use of CEMIIIA instead of CEMI in concrete formulations for the same w/b ratio presented higher $Ccrit$ values. Moreover, in CEMIIIA concrete formulations, the decrease of w/b

seemed to increase $Ccrit$ values. These results agree on the fact that a lower w/b ratio increases $Ccrit$ [Paper III].

It was quite interesting to see that critical chloride content expressed in terms of free chloride content in the porosity is the same for the mortar cast with CEM I (M1-055) and the concrete cast with CEM I (B1-15L-049). The porosity of the cement paste was also calculated and it was found to be similar in both the previous compositions (45% for M1 and 51% for B1-15L-049), considering that there is less paste in the concrete mix than in mortar mix. It was found that if there is a decrease in porosity, the chloride threshold expressed in terms of free chloride contents increased strongly.

The expression of chloride threshold in terms of free chloride content in the porosity seemed more reliable for comparing different compositions of concrete. It would also be possible to propose a model of variation of chloride threshold $Free\ [Cl]$ according to the water porosity of cement paste if more concrete compositions were tested.

It was concluded that a relationship may exist between the free chloride threshold concentration in porosity and the water porosity of cement paste. For 0 % porosity, the threshold concertation is supposed infinite since no corrosion occurs and, for 100 % porosity, the results from steel in solution show lower critical concentrations. The results of the different formulations studied in this work showed the same trend, where lower porosity formulations were associated with higher critical chloride concentrations, the concentrations being slightly higher in the case of CEM III mixes. This statement remains to be confirmed by further studies, however.

## 4.2. Characterization of the anodic behavior in relation to the chloride content

Because of the non-uniform nature of chloride-induced corrosion in concrete, it is not possible to experimentally obtain uniformly active steel. Consequently, the determination of the electrochemical properties of active steel cannot be directly measured from electrochemical experiments since some parts of the steel bar tested are still in a passive state. [Paper II] represents a first step in the measurement of the electrochemical properties of active steel areas in mortar (100% CEMI with a w/b ratio of 0.55) based on inverse 3D numerical modeling and considering their dependency on chloride contamination.

The scale of this study concerned the macro-level of the corrosion process of rebars in concrete. As a result, as cohesion of matter was described in terms of stress and strain and their interaction via the constitutive law, the corrosion of steel in concrete was described in terms of potential and current and their interaction via the Butler-Volmer equation. To achieve relevant results, the physical description has been conducted at two different levels: the fundamental reversible electrodes level and the corrosion system level.

Preliminary, an experimental campaign was carried out based on the experimental protocol developed in [Paper I], consisting of measuring galvanic corrosion currents between anode samples contaminated by chlorides and cathode samples which are free of chlorides. Several chloride pollution levels of the anode specimens were applied to investigate the consequence of the galvanic corrosion current exchanged. It was found that for chloride contents lower than 0.5 %/wt. cement, galvanic currents exchanged between anode and cathode were constant and negligible, while, for higher chloride concentrations, galvanic currents increased quite linearly with chloride pollution levels. The clear transition observed in this experimental relationship confirms the existence of a chloride-threshold effect.

Polarization tests were conducted separately on anode and cathode samples to get the polarization curves. Since the steel at the cathode is in a uniform passive state, polarization tests realized on cathode samples allowed for directly determining the electrochemical parameters of passive steel at the fundamental reversible electrodes level and the corrosion system level, which contributed to enrich the database of electrochemical properties of passive steel [Paper II].

On the other hand, autopsies of the anode samples showed that the steel was not entirely in an active state, hence, parameters of active steel could not be directly deduced from the polarization test. Therefore, a numerical optimization approach, based on the fundamental effect of the iron anodic Tafel coefficient, was then developed to quantify the optimal set of parameters of ''pure'' active steel. Particular attention was focused on the effect of the chloride content of the anode samples on the iron anodic Tafel coefficient and, subsequently, on the rest of the electrochemical properties of active steel which are fundamentally dependent on anodic Tafel coefficient [Paper II].

To validate the global set of electrochemical parameters of steel, numerical simulations were performed to reproduce the galvanic coupling test between cathode and anode specimens. By considering various corrosion spot morphologies, a quite good quantitative correlation was observed between the experimental points and numerical results. A complementary set of numerical simulations conducted by considering constant (chloride independent) anodic Tafel coefficient of active steel showed that the numerical results do not fit the experimental ones [Paper II].

All these experimental observations coupled with the numerical modeling approach highlight the dependency of the electrochemical properties of active steel on chloride content [Paper II].

The electrochemical parameters of active and passive steel deduced from [Paper II] were used in paper [Paper IV] to simulate the early phase of corrosion propagation. The aim of [Paper IV] was to investigate, from the perspective of numerical analysis, the mechanism of chloride-induced corrosion initiation in reinforced concrete structures. This paper did not try to explain the physical aspects of corrosion initiation or find a physical meaning of the depassivation mechanism. The main focus consisted of finding numerical calculations allowing to simulate the transition from the corrosion initiation phase to the early stage of corrosion propagation and to test whether corrosion initiation is controlled by the anodic process.

The interface of rebars with the electrolyte was simulated using the equations of the Butler-Volmer model as boundary conditions. The input data of the Butler-Volmer equations are the electrochemical parameters of active and passive steel deduced from [Paper II].

Two different numerical models were achieved to simulate two different sizes of the cathode, and subsequently, to simulate different cathode/anode surface ratio. The first model consisted of simulating the anode-cathode coupling experiment which was presented in [Paper I and II] and the second model consisted of simulating the anode-wall experiment which was also realized in the experimental protocol achieved in [Paper I].

To simulate the early stages of chloride-induced corrosion, the surface of active steel was kept very small (0.05 $cm^2$) which only represents 2.5 % of the surface of the anode rebar (1.88 $cm^2$). The surface of the anode in an active state was considered constant and independent of the chloride level.

The numerical results showed that for chloride levels lower than the critical chloride content which was determined in [Paper I], the galvanic current flowing between anodic and cathodic areas was negligible and independent of the cathode/anode ratio. Beyond the critical chloride content, the currents became significant and increased when the cathode/anode ratio increased [Paper IV]. These numerical simulations were confronted with experimental results from [Paper I] where the same behaviors were observed.

The numerical results showed that the phenomenon of depassivation of steel due to chloride ingress can be described numerically by an anodic Tafel coefficient which is chloride dependent, and subsequently, by parameters of active steel which change with chloride contamination [Paper IV]. This approach was tested in the case of CEMI mortar formulation but could be further developed for other types of binders.

These results allow confirming using numerical modeling the concept of an anodic control of the early chloride-induced corrosion propagation phase which was previously stated in [Paper I] and reported in other literature studies [80,82,111–114].

## 4.3. Corrosion propagation

### 4.3.1. Mobilizable cathode and influence of the electrical resistivity

When dealing with macrocell corrosion, it is crucial to consider the electrical resistivity of concrete and the geometry and size of the structure, including the cathode to anode surface ratio (C/A ratio) and the mobilizable cathode-anode distance.

The cathode-anode distance is the maximum distance where passive reinforcement bars exchange current with corroding active sites. An application of the mobilizable cathode-anode distance is the corrosion of submerged regions of reinforced concrete structures where very high local anodic current densities were reported with no visual manifestation making this type of corrosion very dangerous. One possible explanation for these observations is that active steel (anode) bars in the submerged region could be coupled with a cathodic aerated zone located far away from the anode.

[Paper V] studies the influence of cathode-anode distance on the macrocell current. Experimental campaigns were developed to test the effect of the cathode-anode distance on the cathodic reaction regardless of the C/A ratio. For this purpose, the corresponding set-up must allow the distance between the anode and cathode to vary, for a fixed C/A ratio. Experimental investigations were carried out on a 10 m long reinforced beam consisting of 20 segments of rebars: an anode where corrosion was initiated with chloride diffusion, and 19 identical cathodes. Different electrical connections were made between cathodes and corrosion currents were measured to test the impact of the cathode-anode distance on the evolution of corrosion current and the attenuation of the cathodic reaction concerning the distance between anode and cathode.

Experimental investigations were followed by numerical analyses of the experiments allowing to confirm the experimental results and to test the impact of electrical resistivity on the limits of the mobilizable cathode. The 3D numerical modeling has proved to be a powerful tool for macrocell corrosion analysis. Qualitative and quantitative agreements between experimental measurements and numerical results based on this approach were also found in other studies [115–117]. Furthermore, the findings of this paper show that numerical simulation allows performing parametric studies rapidly which helps in a second step the enrichment of the available database as well as the coherent development of further experiments and the opportunity to substitute laboratory experiments by numerical computer simulations

It was found that whatever the electrical resistivity, in the absence of closer bars acting cathodically and connected to the anode, the macrocell corrosion current can be provided by cathode bars at large distances from the anode [Paper V]. This could mean that, in cases of partly immersed structures where corrosion is initiated in an immersed region of the structure, the mobilized cathodic area could be far away from the anode in aerated parts of the structure, where oxygen is available. These results are supported by the observations regarding localized corrosion in submerged regions of structures [118].

While traditional prospects for corrosion in submerged region proclaim that corrosion rate is limited by the absence of cathodic regions due to the restricted oxygen availability at the steel/concrete interface, the present work complements previously reported studies in the domain of chloride-induced macrocell corrosion in concrete and shows that corrosion can be provided by cathodes distant from the anode [Paper V]. This work also brings added values to efforts previously made by allowing to test experimentally and numerically the impact of large cathode-anode distances on macrocell corrosion for the same anode and the same cathode/anode ratio [Paper V].

According to the numerical results obtained in [Paper V], it was found that the increase in electrical resistivity reduces the cathode-anode distance allowing a significant current flow (mobilizable C-A distance). As a result, a higher resistivity would restrain the extent of the reinforcement area in the submerged zone where anodic sites could be developed.

If closer bars are present next to the anode and are acting cathodically, then these cathodes receive more current than the more distant ones. The attenuation of cathodic current with the distance from the anode is strong and depends on the electrical resistivity of the concrete [Paper V].

It was found that the electrical resistivity influences the distribution of macrocell current along with the rebar network in such a way that the proportion of corrosion current received by the closest cathode area increases with electrical resistivity and so the cathodic area involved in the macrocell corrosion process decreases [Paper V].

Furthermore, [ Paper V] proposed an analytical approach to describe the mathematical relationship between the electrical resistivity and the mobilizable cathode-anode distance in the case of unidimensional geometries to give an understanding of the relationship between the geometrical factor and the macrocell current.

As shown above, the electrical resistivity of concrete is an important durability indicator affecting macrocell corrosion. Electrical resistivity depends on several parameters like the chloride content. It was found, as expected, that the increase in chloride levels in mortar or concrete leads to the decrease of electrical resistivity. A possible intrinsic relationship may exist between free chloride content and electrical resistivity whatever the concrete or mortar formulation in case of saturated conditions [ Paper VI] . This relationship between electrical resistivity and chloride content is an indication of the presence of a time-dependent resistivity gradient in real structures, since, parts of the structure will be contaminated with chlorides while the rest remains intact. This statement is another argument for the need to use numerical simulations when modeling the corrosion propagation of reinforced concrete structures which allows taking into consideration the spatial variability of several parameters like electrical resistivity.

In [Paper VI], an experimental test was carried out, consisting in the measurement of galvanic corrosion currents between anodes and cathodes from the same composition, similar to the experimental protocol developed in [Paper I] . The originality of the experimental campaign of [Paper VI] is that another galvanic coupling test is achieved consisting of keeping the same anode but replacing the cathodes with other cathodes from different formulations. This technique was called, ''cathode permutation'' since only the cathode is changed or replaced and the anodes are kept the same. This technique allows studying the impact of the parameters at the cathode on macrocell current which is usually associated with the kinetics of the cathodic reaction and most importantly with the electrical resistivity of the cathode. A proportional relationship was found between macrocell corrosion current and the electrical resistivity [Paper VI].

Additionally, [Paper VI] studied the effect of electrical resistivity on the cathode/anode (C/A) ratio and the mobilizable cathode surface contributing to macrocell current. Results showed that corrosion current increased with C/A ratio but tended to stabilize for lower C/A ratio when electrical resistivity increases which could be linked to an ohmic control of corrosion limiting the mobilizable cathode surface. Finally, macrocell currents decreased with the increase in electrical resistivity and the results show an asymptotic behavior of current when electrical resistivity is very high.

### 4.3.2. Atypical behavior of mortar with a high level of slag

Formulations with a high level of slag (substitution level of 80%) showed an atypical behavior when compared to slag-free formulations or formulations with lower slag content. The atypical behavior corresponds to a highly negative potential, which could be found for some cathodes [Paper VII].

Galvanic coupling experiments were achieved between anode samples contaminated with chlorides and cathode specimens without any chlorides. These tests were realized on samples made with mortar with 80% of slag and 20% of CEMI (w/b=0.47) and they based on the test protocol developed in [Paper I] which was applied on mortar samples with 100% of CEMI.

During the galvanic coupling between cathodes with highly negative potentials and chloride contaminated anodes, corrosion currents were, in some cases, negative and then became positive. When the macrocell current is positive, it means that the electrons are provided by the oxidation reaction at the anode and received by the cathode where the reduction reaction takes place. Conversely, a negative macrocell current indicates that the electrons are provided by the oxidation reaction at the cathode and received by the anode when the reduction reaction happens. The change in sign of the measured current was always associated with the increase in the potentials of cathodes, which were initially highly negative, to more positive values which became comparable to the potentials measured on CEMI. Based on these results, it was found that when the potential of the cathode is higher (more positive) than that of the anode, the measured current was positive indicating that the oxidation reaction takes place at the anode and the reduction reaction at the cathode. This behavior was similar to that encountered in the case of formulations without slag (100% of CEMI) and lower slag content (40% of slag). On the other hand, when the potential of the cathode is lower than that of the anode, the macrocell current is positive which means that the electrons are provided by the oxidation of iron at the anode and received by the cathode where the reduction of oxygen takes place.

Polarization test was achieved on chloride-free cathode specimens with 80% of slag and the deduced polarization curves were compared to polarization curves of cathodes form different formulations and different curing conditions. The results showed that, in the case of the cathode samples with moderately negative potentials, the corrosion potential and the kinetics of the reduction reaction at the cathode decreased when the water/binder ratio decreased or when the water porosity or the size of pores decreased. This behavior was associated with the case where oxygen is still available at the cathode. The modification of the kinetics of the cathodic reaction observed can only be explained by a limitation in oxygen availability which could be caused by a denser cement matrix resulting in a lower effective steel surface area accessible for the cathodic reduction reaction[Paper VII].

However, in the case of the cathode samples with highly negative potentials despite the absence of chlorides, the measured cathodic and anodic kinetics, due to external polarization, were high compared to cathodes with more positive potentials. This behavior was associated with the absence of oxygen at the steel/mortar interface which is probably induced by the oxidation of oxygen by the high amount of sulfide in a mortar with high slag contents and also the refinement of the porous network. It was assumed that these negative potentials were associated with the reaction of water reduction, while, in the presence of oxygen the reaction is the reduction of oxygen. This statement was only an assumption and needed further investigations [Paper VII].

## 4.4. Development of an empirical engineering model for the prediction of the duration of the propagation phase

In [Paper VIII], a literature review of some empirical models developed for the prediction of corrosion current densities in reinforced concrete structures was prepared followed by a literature overview of the different parameters influencing corrosion propagation.

[Paper VIII] addresses the prediction of the duration of the corrosion propagation phase based on the observation that in a concrete structure before the appearance of corrosion-induced cracks, the preponderant component of corrosion is that related to the macro-cell process (localized corrosion). This work contributed to the objectives of the French ANR Modevie project aiming for the development of an overall engineering model for the assessment of the service life of concrete structures by calculating the sum of initiation period and propagation period.

This first step consisted of developing a model for the assessment of the corrosion current density which was considered constant during the early phase of corrosion propagation before the appearance of the first corrosion-induced cracks. The proposed model must take into consideration the parameters affecting the corrosion propagation phase which are related to anodic, cathodic and ohmic processes governing chloride-induced corrosion propagation.

The proposed model takes into consideration the impact of parameters related to:

- The anodic behavior like the concentration in free chlorides and the steel/concrete interface [Paper I];
- The influence of parameters related to cathodic behavior like oxygen availability [Paper V];
- The parameters related to the ohmic interaction between anodic zones and cathodic zones, in particular, the electrical resistivity of the concrete, the surface ratio between cathode and anode (very high in real structures), and the distance between aerated cathode and anode (important parameter for XS2 type exposures).
- The influence of temperature.

The model was initially expressed in terms of macrocell corrosion current and was calibrated from experimental results obtained from previous studies, mainly from an experimental test that physically separates the anode contaminated with chlorides from the cathode which is chloride-free [80]. After calibration, the transition from corrosion current to corrosion current density was achieved. These current densities were considered as apparent densities since they were calculated by considering the entire surface of the anode.

It must be noted that several definitions of corrosion current density models annotated “$i_{corr}$" exist in the literature, where most of them assume a uniform corrosion state. In this paper, the developed model takes explicitly into account the localized aspect of corrosion. Hence, the developed corrosion current density model was initially called "$i_{ge}$” but was later on annotated “$i_{corr}$” to simplify the notations.

The service limit criterion chosen in this study was the appearance of the first corrosion-induced cracks which was considered as a conservative and practice-related approach. The link between loss of local section and the appearance of corrosion cracks was deduced from other literature studies but was updated to take into account the fluid nature of corrosion products in submerged regions. The model is empirical and allows the determination of the steel cross-section loss initiating cracking knowing the diameter of the reinforcement bar and the concrete cover.

After the determination of the corrosion current density and the steel cross-section loss initiating cracking in concrete, it was possible to calculate the duration of the propagation phase before the

appearance of the first corrosion cracks using Faraday's law. The originality of the model is that the corrosion current density is taken into account only partly to obtain a local reduction of the reinforcement section, the other part of the corrosion current density is used for the extension of the anodic zones in their length.

The output of the model was compared to values found in literature according to AFNOR normalization documents [119,120] where the corrosion propagation duration was considered from experts' opinion. A series of tests were carried out to evaluate the sensitivity of the model and to estimate the lifetime of real structures in various environments with classical rebar cover design and concrete complying with corresponding exposure class.

The developed model is only studied on lab specimens, therefore, its calibration using data from long-term field tests is a need. The model does not consider the influence of service cracks on corrosion rate and it is only applied to non-carbonated concretes. The limitations and assumptions of the model were also highlighted. Future corrosion studies, as well as developments towards predicting the duration of corrosion propagation in concrete, would benefit from considering those aspects.

# 5. Conclusion

The following conclusions were drawn:

### Development of a new laboratory test set-up that considers the localized character of corrosion initiated by chlorides for the determination of the critical chloride content initiating corrosion

- The test protocol allows to reproduce the localized chloride-induced corrosion by inducing a physical separation of the anode part, contaminated with chlorides, from the cathode part, which is chloride free allowing the measurement of the macrocell (galvanic) corrosion current between anodic and cathodic zones, which was impossible to do in tests performed on single bar specimens.

- The critical chloride content initiating corrosion was determined based on a limiting macrocell current called threshold corrosion current that is independent of the cathode/anode surface ratio which supports the concept of a rate-limiting step of corrosion initiation linked to the anodic control of corrosion at this stage.

- The absence of mill scale and pre-existing corrosion products (when the rebars were chemically cleaned) had a mainly positive impact on $Ccrit$ in the case of CEMI mortar formulation.

- A potential relationship could exist between the free chloride threshold concentration in the porosity and the water porosity of cement paste, where lower porosity formulations are associated with higher critical chloride concentrations, the concentrations being slightly higher in the case of CEM III mixes. This statement remains to be confirmed by further studies, however.

### Characterization of the anodic behavior in relation to the chloride content

- The determination of the electrochemical parameters of passive steel in chloride-free samples can be directly deduced from experimental polarization curves owing to the uniform passive state of samples without chlorides.

- The determination of the electrochemical properties of active steel embedded in concrete or mortar polluted with chlorides could not be directly deduced from the polarization test owing to the non-uniform aspect of chloride-induced corrosion.

- 3D numerical optimization approach, based on the fundamental effect of the iron anodic Tafel coefficient, is an option that can be used to quantify the parameters of ''pure'' active steel.

- Anodic Tafel coefficient and subsequently electrochemical properties of active steel appear to be dependent on the level of chloride contamination.

- The macrocell (galvanic) corrosion can be numerically simulated using the equations of the Butler-Volmer model as boundary conditions to represent the interface of rebars with the electrolyte, using as input data the electrochemical parameters of active (deduced form numerical optimization and experience) and passive (deduced experimentally) steel.

Corrosion propagation

- Macrocell corrosion current can be provided by cathodes distant from the anode. This could mean that, in cases of partly immersed structures where corrosion is initiated in an immersed region of the structure, the mobilized cathodic area could be far away from the anode in aerated parts of the structure, where oxygen is available. If close bars are present next to the anode and are acting cathodically, these cathodes receive more current than the more distant ones.

- The electrical resistivity influences the distribution of macrocell current along with the rebar network in unidimensional geometries such a way that the increase in electrical resistivity reduces the mobilizable cathode-anode distance.

- A proportional relationship was found between macrocell corrosion current and the electrical resistivity.

- A possible intrinsic relationship may exist between free chloride content and electrical resistivity whatever the concrete or mortar formulation in case of saturated conditions.

- The increase in electrical resistivity leads to the stabilization of corrosion current for lower cathode/anode ratios which could be linked to an ohmic control of corrosion limiting the mobilizable cathode surface.

- Formulations with high levels of slag (substitution level of 80%) showed an atypical behavior when compared to aerated samples made with slag-free formulations or with formulations with lower slag content. This behavior was associated with the absence of oxygen at the steel/mortar interface which is probably induced by the oxidation of oxygen by the high amount of sulfide present in slag and also by the refinement of the porous network.

- When highly negative free potentials were measured, high kinetics of anodic and cathodic reactions were also measured when the steel was polarized externally. It was assumed that the reduction reaction is that of water reduction, while, in the presence of oxygen, the reaction is the reduction of oxygen. It was also assumed that the oxidation reaction at the anode is that of iron, while, in the presence of oxygen, the oxidation of iron in passive conditions takes place. All these statements were only assumptions and needed further investigations.

- This could mean that if a part of a structure made with a high level of slag, appears to have a very negative potential due to the lack of oxygen, there is no real risk of corrosion since an eventual macrocell current could be established with another part of the structure with a higher potential, which will lead to polarization and then an increase of the potential and the reformation of the passive layer. Hence, the binder with a high level of slag usually known for its atypical behavior would, in the long term and aerated conditions, behave like an ordinary slag-free binder (such as CEMI). As a result, when studying the phase of corrosion propagation of steel in concrete with high levels of slag, it would be more conservative to consider that the slag inhibitory property is mainly linked to his higher electrical resistivity.

Development of an engineering model practical for end-users for the prediction of the propagation phase of reinforced concrete structures adapted to the performance-based approach

- The service limit criterion chosen for the determination of the service life of reinforced concrete structures was the appearance of the first corrosion-induced cracks. The prediction of the duration of the corrosion propagation phase is based on the observation that in a concrete structure before the appearance of corrosion-induced cracks, the preponderant component of corrosion is that related to the macro-cell process (localized corrosion).

- The model developed to estimate the corrosion current density takes into consideration parameters related to the anodic, cathodic, and ohmic mechanisms and environmental parameters.

- Only a part of the corrosion current density is supposed to contribute to the local reduction of the reinforcement section, the other part of the corrosion current density is used for the extension of the anodic zones in their length.

# 6. Future research

Some aspects of this Ph.D. study were not fully achieved or fully understood. Further investigations would benefit from considering these aspects:

### Characterization of the anodic behavior in relation to the chloride content

In this thesis, the electrochemical parameters of active steel in a mortar made with M1-055 formulation (100% of CEM I, w/b ratio of 0.55) was achieved using inverse numerical modeling. A relationship was found between the chloride contamination level and the iron anodic Tafel coefficient, and subsequently, the electrochemical properties of active steel. This investigation was achieved in case of CEM I mortar formulation embedding as received ribbed steel bars.

A similar investigation on other formulations with different types of binders and w/b ratios would be interesting. Most of the data required for such investigation, like the polarization curves of cathodes and anodes contaminated with different levels of chlorides, were achieved during this thesis on different mortar and concrete formulations (M1-055, M10SF-043, B1-15L-049, B3-15L-051, and B3-041), but the numerical optimization was only achieved in case of M1-055. In the end, it would be interesting, if possible, to determine an intrinsic equation of the anodic Tafel coefficient which could be dependent on the chloride level and some properties linked to materials, for instance, water porosity.

### Mobilizable cathode

In this work, an analytical approach was proposed to describe the mathematical relationship between the electrical resistivity and the mobilizable cathode-anode distance in the case of unidimensional geometries to give an understanding of the relationship between the geometrical factor and the macrocell current. However, in actual reinforced concrete structures, the reinforcement network is usually three dimensional. Future experimental and numerical investigations could be achieved on three-dimensional structures allowing to test the mobilizable cathode along with the impact of electrical resistivity.

### Formulations with high levels of slag

Formulations with a high level of slag (substitution level of 80%) showed an atypical behavior when compared to slag-free formulations or formulations with a lower slag content [Paper VII]. Highly negative free potentials were measured along with high kinetics of anodic and cathodic reactions. It was assumed that the reduction reaction is that of water reduction, while, in the presence of oxygen, the reaction is the reduction of oxygen.

The reduction of water as a cathodic reaction is a well-known result for the uniform corrosion of Magnesium embedded in cementitious materials, because of the highly negative potential of Magnesium. In the case of cathodic polarization of Magnesium, the response seems comparable to the one of slag cathode with highly negative potential and could be a way of development to conclude on the behavior of high level of slag formulation.

## Assumptions and limitations of the engineering model for the prediction of the duration of the propagation phase of reinforced concrete structures subjected to chlorides

A limitation of empirical models is that they are, in most cases, dependent on the conditions of the experimental set-up used. The developed model was based on experiments achieved on lab specimens in controlled environments which engenders the isolation of some parameters from the others leading to the neglect of possible interaction between them. Therefore, its calibration using data from long-term field tests is a need. Despite being limited to some conditions, such models can be enhanced using numerical approaches.

Besides, the model was based on several (strong) assumptions related to:

- The percentage of corrosion current leading to the reduction of the steel cross-section loss;
- The shape of the corrosion pit when calculating the steel cross-section loss initiating cracking;
- The quantification of the influence of the top-bar effect on the macrocell current during corrosion propagation;
- The ratio between the pressures of corrosion products formed in aerated conditions versus the ones formed in submerged conditions.

The assessment of these parameters is important and relevant for modeling the propagation stage of corrosion.

## An engineering model for the prediction of the duration of propagation phase of reinforced concrete structures subjected to carbonation

In this thesis, was proposed a simplified empirical model for the prediction of the duration of the propagation phase of chloride-induced corrosion based on the observation that in a concrete structure before the appearance of corrosion-induced cracks, the preponderant component of corrosion is that related to the macro-cell process (localized corrosion).

Further development of this model towards predicting corrosion propagation in carbonated concrete would benefit from considering this work. The development of a simplified engineering model for the estimation of the propagation duration of reinforced concrete structures subjected to carbonation is currently under development. The model will be calibrated with a similar experimental protocol based on the separation of cathode and anode. The only difference between both protocols is the preconditioning of anode samples which are carbonated instead of being contaminated with chlorides.

Indeed, after curing, the anodes were stored in an oven for 14 days at 45 ° C followed by 7 days at 20 ° C and 65% relative humidity. The contamination of the test samples with carbon dioxide was carried out in a 50% carbonation chamber. Once carbonated (verification with Phenolphthalein test), the samples will be placed in NaOH solution with cathode samples for the galvanic coupling experiment. For each formulation, 3 control specimens (without reinforcement) 40 mm in diameter and 220 mm in length were extracted from specimens with 110 mm in diameter and 220 mm in length by coring. These specimens underwent the same preconditioning of the test samples and were used to control the progress of the carbonation front.

## References


[1] G. Koch, N. Thompson, O. Moghissi, J. Payer and J. Varney, *IMPACT (International Measures of Prevention, Application, and Economics of Corrosion Technologies)*, APUS310GKOCH (AP110272), NACE International, Houston, 2016.

[2] M. Yunovich, N.G. Thompson, T. Balvanyos and L. Lave, *Corrosion cost and preventive strategies in the United States- appendix D: highway bridges*, Office of Infrastructure Research and Development, Federal Highway Administration, United States, 2001.

[3] U. Angst, B. Elsener, C. K. Larsen and Ø. Vennesland, *Critical chloride content in reinforced concrete — A review*, Cement and Concrete Research, 39 (2009), pp. 1122–1138.

[4] U. Angst, B. Elsener, C. Larsen and Ø. Vennesland, *Chloride Induced Reinforcement Corrosion: Electrochemical Monitoring of Initiation Stage and Chloride Threshold Values*, Vol. 53, 2011.

[5] G. Burstein, P. Pistorius and S. Mattin, *The nucleation and growth of corrosion pits on stainless steel*, Corrosion Science 35 (1993), pp. 57–62.

[6] P. Pistorius and G. Burstein, *Metastable pitting corrosion of stainless steel and the transition to stability*, Philosophical Transactions of the Royal Society of London. Series A: Physical and Engineering Sciences 341 (1992), pp. 531–559.

[7] N. Laycock and R. Newman, *Localised dissolution kinetics, salt films and pitting potentials*, Corrosion science 39 (1997), pp. 1771–1790.

[8] M. Stratmann and H. Streckel, *On the Atmospheric Corrosion of Metals Which Are Covered with Thin Electrolyte Layers—I. Verification of the Experimental Technique*, Vol. 30, 1990.

[9] R.M. Cornell and U. Schwertmann, *The Iron Oxides: Structure, Properties, Reactions, Occurrence and Uses*, Wiley-VCH, 2003.

[10] M.J.N. Pourbaix and N. de Zoubov, *Atlas d'equilibres electrochimiques*, Gauthier-Villars, Paris, 1963.

[11] P. Ghods, O. Isgor, J.R. Brown, F. Bensebaa and D. Kingston, *XPS Depth Profiling Study on the Passive Oxide Film of Carbon Steel in Saturated Calcium Hydroxide Solution and the Effect of Chloride on the Film Properties*, Vol. 257, 2011.

[12] K. Noda, T. Tsuru and S. Haruyama, *The Impedance Characteristics of Passive Films on Iron*, Vol. 31, 1990.

[13] B. Huet, V. L'Hostis, F. Miserque and H. Idrissi, *Electrochemical Behavior of Mild Steel in Concrete: Influence of PH and Carbonate Content of Concrete Pore Solution*, Vol. 51, 2005.

[14] C. Andrade, M. Keddam, X.R. Nóvoa, M. Pérez, C. Rangel and H. Takenouti, *Electrochemical Behaviour of Steel Rebars in Concrete: Influence of Environmental Factors and Cement Chemistry*, Vol. 46, 2001.

[15] K. K. Sagoe-Crentsil and F. Glasser, *Steel in Concrete: Part II Electron Microscopy Analysis*, Vol. 41, Magazine of Concrete Research, 1989.

[16] L. Freire, X.R. Nóvoa, M. Montemor and M. Carmezim, *Study of Passive Films Formed on Mild Steel in Alkaline Media by the Application of Anodic Potentials*, Vol. 114, 2009.

[17] F. Miserque, B. Huet, G. Azou, D. Bendjaballah and V. L'Hostis, *X-Ray Photoelectron Spectroscopy and Electrochemical Studies of Mild Steel FeE500 Passivation in Concrete Simulated Water*, Vol. 136, 2006.

[18] A. Carnot, I. Frateur, S. Zanna, B. Tribollet, I. Dubois-Brugger and P. Marcus, *Corrosion Mechanisms of Steel Concrete Moulds in Contact with a Demoulding Agent Studied by EIS and XPS*, Vol. 45, 2003.

[19] H. T. Cao, L. Bucea and V. Sirivivatnanon, *Corrosion Rates of Steel Embedded in Cement Pastes*, Vol. 23, 1993.

[20] M. Montemor, A. Simões and M. Ferreira, *Analytical Characterization of the Passive Film Formed on Steel in Solutions Simulating the Concrete Interstitial Electrolyte*, Vol. 54, 1998.

[21] L. Chomat, V. L'Hostis, E. Amblard and L. Bellot-Gurlet, *Long Term Study of Passive Corrosion of Steel Rebars in Portland Mortar in Context of Nuclear Waste Disposal*, Vol. 49, 2014.

[22] W. Hauser and R. Koester, *Corrosion behavior of nodular cast iron casks for low and intermediate level wastes*, Materials Research Society Symposia Proceedings (1986), pp. 437–444.

[23] R. Grauer, B. Knecht, P. Kreis and J. P. Simpson, *Die Langzeit-Korrosionsgeschwindigkeit Des Passiven Eisens in Anaeroben Alkalischen Lösungen*, Vol. 42, 1991.
[24] F. Foct and I. Petre-Lazar, *Experimental Study of Carbon Steel General and Localised Corrosion in Concrete*, EUROCORR 2004 Conf., Nice, France, September 2004, CAFRACOR and SCI, 11-0-485 [CDROM]., 2004.
[25] A. Nasser, *La corrosion des aciers dans le béton à l'état passif et par carbonatation : prise en compte des courants galvaniques et des défauts d'interface acier-béton*, 2010.
[26] A. Neville, *Chloride attack of reinforced concrete: an overview*, Materials and Structures 28 (1995), pp. 63.
[27] M.F. Montemor, A.M.P. Simões and M.G.S. Ferreira, *Chloride-induced corrosion on reinforcing steel: from the fundamentals to the monitoring techniques*, Cement and Concrete Composites 25 (2003), pp. 491–502.
[28] C.L. Page, N. Short and W.R. Holden, *A reply to discussion by B. B. Hope, A. Ip and J. A. Page of the paper "the influence of different cements on chloride-induced corrosion of reinforcing steel,"* Cement and Concrete Research - CEM CONCR RES 16 (1986), pp. 977–979.
[29] N.F. da Silva, *Chloride Induced Corrosion of Reinforcement Steel in Concrete - Threshold Values and Ion Distributions at the Concrete-Steel Interface*, 2013.
[30] RILEM TC 178-TMC, *RILEM TC 178-TMC: 'Testing and modelling chloride penetration in concrete'Analysis of total chloride content in concrete*, Mater. Struct. 35 (2002), pp. 583–585.
[31] *NF EN 14629 - Produits et systèmes pour la protection et la réparation des structures en béton - Méthodes d'essais - Mesurage du taux de chlorure d'un béton durci*. 2007.
[32] *European Standard EN196-21, Methods for testing cement: determination of the chloride, carbon dioxide and alkali content of cement, European Committee for Standardization.* 1989.
[33] *AASHTO-T260, Standard method of test for sampling and testing for chloride ion in concrete and concrete raw materials, American Association of State Highway and Transportation Officials.* 1997.
[34] G. Arliguie and H. Hornain, *GranDuBé: grandeurs associées à la durabilité des bétons*, Presses des Ponts, 2007.
[35] M. Castellote and C. Andrade, *Round-Robin test on chloride analysis in concrete—Part I: Analysis of total chloride content*, Materials and structures 34 (2001), pp. 532–549.
[36] U. Angst, A. Rønnquist, B. Elsener, C.K. Larsen and Ø. Vennesland, *Probabilistic considerations on the effect of specimen size on the critical chloride content in reinforced concrete*, Corrosion Science 53 (2011), pp. 177–187.
[37] G. K. Glass, Y. Wang and N. Buenfeld, *An Investigation of Experimental Methods Used to Determine Free and Total Chloride Contents*, Vol. 26, Cement and Concrete Research, 1996.
[38] K. Byfors, C.M. Hansson and J. Tritthart, *Pore Solution Expression as a Method to Determine the Influence of Mineral Additives to Cement on Chloride Binding*, Vol. 16, Cement Concrete Research, 1986.
[39] M. Maslehuddin, C. L. Paget and Rasheeduzzafar, *Temperature Effect on the Pore Solution Chemistry in Contaminated Cements*, Vol. 49, 1997.
[40] G.K. Glass and N. Buenfeld, *The Presentation of the Chloride Threshold Level for Corrosion of Steel in Concrete*, Vol. 39, 1997.
[41] M.Y. Hobbs, *Solubilities and Ion Exchange Properties of Solid Solutions between the OH, Cl and CO3 End Members of the Monocalcium Aluminate Hydrates*, University of Waterloo, 2001.
[42] D. Damidot, F. Glasser and U. A. Birnin-Yauri, *Thermodynamic Investigation of the CaO-Al2O3-CaCl2-H2O System at 25°C and the Influence of Na2O*, Vol. 4, 1994.
[43] J. Tritthart, *Chloride binding in cement I. Investigations to determine the composition of porewater in hardened cement*, Cement and Concrete Research 19 (1989), pp. 586–594.
[44] J. Tritthart, *Chloride Binding in Cement II. The Influence of the Hydroxide Concentration in the Pore Solution of Hardened Cement Paste on Chloride Binding*, Vol. 19, 1989.
[45] H. Justnes, *A review of chloride binding in cementitious systems*, NORDIC CONCRETE RESEARCH-PUBLICATIONS- 21 (1998), pp. 48–63.

[46] C.K. Larsen, *Chloride binding in concrete*, Dr. Ing. Thesis, Report No 1998:101, Norwegian University of Science and Technology, NTNU, 1998.
[47] C. ARYA, N. Buenfeld and J.B. Newman, *Factors Influencing Chloride-Binding in Concrete*, Cement and Concrete Research 20 (1990), pp. 291–300.
[48] C. L. Page and Ø. Vennesland, *Pore Solution Composition and Chloride Binding Capacity of Silica Fume Cement Pastes*, Materials and Structures 16 (1983), pp. 19–25.
[49] R. Luo, Y. Cai, C. Wang and X. Huang, *Study of chloride binding and diffusion in GGBS concrete*, Cement and Concrete Research 33 (2003), pp. 1–7.
[50] R. Dhir, M. El-Mohr and T. Dyer, *Chloride binding in GGBS concrete*, Cement and Concrete Research 26 (1996), pp. 1767–1773.
[51] K. Kopecskó and G.L. Balázs, *Concrete with improved chloride binding and chloride resistivity by blended cements*, Advances in Materials Science and Engineering 2017 (2017), .
[52] T. Luping and L.-O. Nilsson, *Chloride binding capacity and binding isotherms of OPC pastes and mortars*, Cement and Concrete Research 23 (1993), pp. 247–253.
[53] Y. M Kolotyrkin, *Pitting Corrosion of Metals*, Vol. 19, 1963.
[54] *Corrosion localisée editeurs scientifiques F. Dabosi, G. Beranger, B. Baroux*. Available at http://bibliotheque.bordeaux.fr/in/details.xhtml?id=mgroup%3A9782868832405.
[55] E.E.D. Abd El Aal, S. Abd El Wanees, A. Diab and S. Abd El Haleem, *Environmental Factors Affecting the Corrosion Behavior of Reinforcing Steel III. Measurement of Pitting Corrosion Currents of Steel in Ca(OH)2 Solutions under Natural Corrosion Conditions*, Vol. 51, 2009.
[56] T.P. Hoar, D.C. Mears and G.P. Rothwell, *The Relationships Between Anodic Passivity, Brightening and Pitting*, Vol. 5, 1965.
[57] M. Pourbaix, *Lectures on Electrochemical Corrosion*, Plenum Press, New York and London (1973), .
[58] H.-H. Strehblow, *Mechanisms of Pitting Corrosion*, in *Corrosion Mechanisms in Theory and Practice*, 1995, .
[59] H.-H. Strehblow, *Nucleation and Repassivation of Corrosion Pits for Pitting on Iron and Nickel*, Vol. 27, 1976.
[60] T. Van Quan, *Contribution à la compréhension des mécanismes de dépassivation des armatures d'un béton exposé à l'eau de mer : théorie et modélisation thermochimique*, 2016.
[61] U.M. Angst and B. Elsener, *Chloride threshold values in concrete–a look back and ahead*, Special Publication 308 (2016), pp. 1–12.
[62] *COST Action 521 : corrosion of steel in reinforced concrete structures : final report.*. Available at https://publications.europa.eu/en/publication-detail/-/publication/c122c980-b071-4eb7-8ac8-fc8353a502be/language-en.
[63] D.A. Hausmann, *STEEL CORROSION IN CONCRETE -- HOW DOES IT OCCUR?*, Materials Protection 6 (1967), pp. 19–23.
[64] V. Gouda and W. Halaka, *Corrosion and Corrosion Inhibition of Reinforcing Steel: I. Immersed in Alkaline Solutions*, British Corrosion Journal 5 (1970), pp. 204–208.
[65] L. Li and A. Sagues, *Chloride Corrosion Threshold of Reinforcing Steel in Alkaline SolutionsOpen-Circuit Immersion Tests*, Vol. 57, 2001.
[66] C. L. Page and J. Havdahl, *Electrochemical Monitoring of Corrosion of Steel in Microsilica Cement Paste*, Vol. 18, Materials and Structures, 1985.
[67] G. Sergi and G.K. Glass, *A Method of Ranking the Aggressive Nature of Chloride Contaminated Concrete*, Vol. 42, 2000.
[68] M. Thomas, *Chloride thresholds in marine concrete*, Cement and concrete research 26 (1996), pp. 513–519.
[69] C. Alonso, C. Andrade, M. Castellote and P. Castro, *Chloride threshold values to depassivate reinforcing bars embedded in a standardized OPC mortar*, Cement and Concrete research 30 (2000), pp. 1047–1055.

[70] G. Glass and N. Buenfeld, *Chloride threshold levels for corrosion induced deterioration of steel in concrete*, 1st RILEM workshop on Chloride Penetration into Concrete St Rémy lès Chevreuse, France (1995), pp. 429–440.
[71] *Rilem, Draft recommendation for repair strategies for concrete structures damaged by reinforcement corrosion*, Materials and Structures 27 (1994), pp. 415–436.
[72] ACI Committee 222, *Corrosion of Metals in Concrete*, Journal Proceedings 82 (1985), .
[73] *Model Code for Service Life Design, fib Bulletins No. 34*. Available at https://www.fib-international.org/publications/fib-bulletins/model-code-for-service-life-design-pdf-detail.html.
[74] J. Mietz, *Corrosion Books: Corrosion of Steel in Concrete. By: Luca Bertolini, Bernhard Elsener, Pietro Pedeferri, Rob Polder*, Vol. 55, 2004.
[75] U.M. Angst, M.R. Geiker, M.C. Alonso, R. Polder, O.B. Isgor, B. Elsener et al., *The effect of the steel–concrete interface on chloride-induced corrosion initiation in concrete: a critical review by RILEM TC 262-SCI*, Materials and Structures 52 (2019), pp. 88.
[76] K. Hornbostel, U.M. Angst, B. Elsener, C.K. Larsen and M.R. Geiker, *Influence of mortar resistivity on the rate-limiting step of chloride-induced macro-cell corrosion of reinforcing steel*, Corrosion Science 110 (2016), pp. 46–56.
[77] K. Tutti, *Corrosion of steel in concrete*, Swedish Cement and Concrete Research Institute (1982), pp. 17–21.
[78] C. Page and K. Treadaway, *Aspects of the electrochemistry of steel in concrete*, Nature 297 (1982), pp. 109–114.
[79] L. Bertolini, B. Elsener, P. Pedeferri, E. Redaelli and R.B. Polder, *Corrosion of Steel in Concrete: Prevention, Diagnosis, Repair*, 2nd editionWiley-VCH VerlagGmbH & Co., 2013.
[80] C. Chalhoub, R. François and M. Carcasses, *Determination of chloride threshold initiating corrosion: A new set-up taking the localized aspect of corrosion into account*, Cement and Concrete Research 124 (2019), pp. 105825.
[81] U. Angst, *Chloride induced reinforcement corrosion in concrete: Concept of critical chloride content – methods and mechanisms*, Norwegian University of Science and Technology Faculty of Engineering Science and Technology Department of Structural Engineering, 2011.
[82] U. Angst, B. Elsener, C.K. Larsen and Ø. Vennesland, *Chloride induced reinforcement corrosion: rate limiting step of early pitting corrosion*, Electrochimica Acta 56 (2011), pp. 5877–5889.
[83] K. Hornbostel, U. Angst, B. Elsener, C. Larsen and M. Geiker, *On the limitations of predicting the ohmic resistance in a macro-cell in mortar from bulk resistivity measurements*, Cement and Concrete Research 76 (2015), pp. 147–158.
[84] O.E. Gjørv, Ø.E. Vennesland and A.H.S. El-Busaidy, Electrical Resistivity Of Concrete In The Oceans, in OTC-2803-MS, 1977, pp. 8.
[85] M. Fares, *Evaluation de gradients de teneur en eau et en chlorures par méthodes électromagnétiques non-destructives.*, Université Nantes Angers Le Mans, France., 2015.
[86] S. Feliu, C. Andrade, J. González and C. Alonso, *A new method forin-situ measurement of electrical resistivity of reinforced concrete*, Materials and structures 29 (1996), pp. 362–365.
[87] R. Sriravindrarajah and R. Swamy, *Development of a conductivity probe to monitor setting time and moisture movement in concrete*, Cement, Concrete and Aggregates 4 (1982), pp. 73–80.
[88] S. Millard, Reinforced concrete resistivity measurement techniques, 91 (1991).
[89] R.L. Du Plooy, *The development and combination of electromagnetic non-destructive evaluation techniques for the assesment of cover concrete condition prior to corrosion*, Université Nantes Angers Le Mans, 2013.
[90] G. Villain, Z.M. Sbartaï, J.-F. Lataste, V. Garnier, X. Dérobert, O. Abraham et al., Characterization of water gradients in concrete by complementary NDT methods, 2015.
[91] S. Naar, *Evaluation non destructive du béton par mesures de résistivité électrique et thermographie infrarouge passive*, Bordeaux 1, 2006.
[92] K. Hornbostel, C.K. Larsen and M.R. Geiker, *Relationship between concrete resistivity and corrosion rate–a literature review*, Cement and Concrete Composites 39 (2013), pp. 60–72.

[93] M. Saleem, M. Shameem, Er.G. Hussain and M. Maslehuddin, *Effect of moisture, chloride and sulphate contamination on the electrical resistivity of Portland cement concrete*, Construction and Building Materials 10 (1996), pp. 209–214.
[94] M. Fares, G. Villain, S. Bonnet, S.P. Lopes, B. Thauvin and M. Thiery, *Determining chloride content profiles in concrete using an electrical resistivity tomography device*, Cement and Concrete Composites 94 (2018), pp. 315–326.
[95] J. Enevoldsen, C. Hansson and B. Hope, *The influence of internal relative humidity on the rate of corrosion of steel embedded in concrete and mortar*, Cement and concrete research 24 (1994), pp. 1373–1382.
[96] Z. Sbartaï, S. Laurens, J. Rhazi, J. Balayssac and G. Arliguie, *Using radar direct wave for concrete condition assessment: Correlation with electrical resistivity*, Journal of applied geophysics 62 (2007), pp. 361–374.
[97] F. Hunkeler, *The resistivity of pore water solution—a decisive parameter of rebar corrosion and repair methods*, Construction and Building Materials 10 (1996), pp. 381–389.
[98] I.-S. Yoon, *Effect of Water and Chloride Content on Electrical Resistivity in Concrete*, NOT PEER-REVIEWED (2019), .
[99] C. Alonso, C. Andrade and J.A. González, *Relation between Resistivity and Corrosion Rate of Reinforcement in Carbonated Mortar Made with Several Cement Types*, Vol. 18, 1988.
[100] A. Neville, *Propriétés des Bétons» Editions Eyrolles*, Paris 806 (2000), .
[101] V. Lakshminarayanan, P. Ramesh and S. Rajagopalan, *A new technique for the measurement of the electrical resistivity of concrete*, Magazine of Concrete research 44 (1992), pp. 47–52.
[102] J. Cabrera and P. Ghoddoussi, *Influence of Fly Ash on the Resistivity and Rate of Corrosion of Reinforced Concrete*, Special Publication 145 (1994), pp. 229–244.
[103] M. Castellote, C. Andrade and M.C. Alonso, *Standardization, to a reference of 25 C, of electrical resistivity for mortars and concretes in saturated or isolated conditions*, Materials Journal 99 (2002), pp. 119–128.
[104] M. Raupach, *Chloride-induce macrocell corrosion of steel in concrete—Theoretical background and practical consequences*, Construction and Building Materials 10 (1996), pp. 329–338.
[105] R. Francois, S. Laurens and F. Deby, *Corrosion and Its Consequences for Reinforced Concrete Structures*, Elsevier, 2018.
[106] A. Clément, S. Laurens, G. Arliguie and F. Deby, *Numerical Study of the Linear Polarisation Resistance Technique Applied to Reinforced Concrete for Corrosion Assessment*, Vol. 16, 2012.
[107] U. Angst and M. Büchler, *On the applicability of the Stern–Geary relationship to determine instantaneous corrosion rates in macro-cell corrosion*, Materials and Corrosion 66 (2014), pp. 1017–1028.
[108] J. Gulikers and M. Raupach, *Numerical models for the propagation period of reinforcement corrosion - Comparison of a case study calculated by different researchers*, Materials and Corrosion 57 (2006), pp. 618–627.
[109] J. Warkus, M. Raupach and J. Gulikers, *Numerical Modelling of Corrosion – Theoretical Backgrounds –*, Vol. 57, 2006.
[110] Z.M. Sbartaï, *Caractérisation physique des bétons par radar: approche neuromimétique de l'inversion*, Paul Sabatier University (France) and Sherbrooke University (Canada)., 2005.
[111] G. Glass, C. Page and N. Short, *Factors affecting the corrosion rate of steel in carbonated mortars*, Corrosion Science 32 (1991), pp. 1283–1294.
[112] J.A. Gonzalez, J. Algaba and C. Andrade, *Corrosion of reinforcing bars in carbonated concrete*, British Corrosion Journal 15 (1980), pp. 135–139.
[113] C. Page and J. Havdahl, *Electrochemical monitoring of corrosion of steel in microsilica cement pastes*, Materials and Structures 18 (1985), pp. 41–47.
[114] P. Lambert, C. Page and P. Vassie, *Investigations of reinforcement corrosion. 2. Electrochemical monitoring of steel in chloride-contaminated concrete*, Materials and Structures 24 (1991), pp. 351–358.

[115] J. Warkus and M. Raupach, *Modelling of reinforcement corrosion – Corrosion with extensive cathodes*, Materials and Corrosion 57 (2006), pp. 920–925.
[116] S. Jäggi, H. Böhni and B. Elsener, *Macrocell corrosion of steel in concrete-Experiments and numerical modelling*, European Federation of Corrosion (2001), .
[117] J. Warkus and M. Raupach, *Modelling of reinforcement corrosion–geometrical effects on macrocell corrosion*, Materials and corrosion 61 (2010), pp. 494–504.
[118] M. Walsh and A. Sagues, *Steel Corrosion in Submerged Concrete Structures - Part 1: Field Observations and Corrosion Distribution Modeling*, Corrosion -Houston Tx 72 (2016), pp. 518–533.
[119] *CEN/TC 250/SC 2/WG 1/TG 10 _ Summary for Reliability analysis of German & Spanish DtS Rules for Durability vs Maximum Corrosion Threshold*. AFNOR/P18B/GE CR, 2018.
[120] *Béton – Classes de résistance aux expositions _ Contribution française aux travaux du TG 10, préparée par François TOUTLEMONDE*. AFNOR/P18B/GE CR, 2019.

# Part II- Appended Papers

# Paper I

## Determination of chloride threshold initiating corrosion: A new set-up taking the localized aspect of corrosion into account

Chantal Chalhoub*, Raoul François, Myriam Carcasses

Cement and Concrete Research 124 (2019) 105825

Cement and Concrete Research 124 (2019) 105825

Contents lists available at ScienceDirect

Cement and Concrete Research

journal homepage: www.elsevier.com/locate/cemconres

# Determination of chloride threshold initiating corrosion: A new set-up taking the localized aspect of corrosion into account

Chantal Chalhoub*, Raoul François, Myriam Carcasses

*LMDC, INSA, UPS, Université de Toulouse, France*

A B S T R A C T

In spite of much research invested in the study of concrete reinforcement corrosion induced by chlorides, there is still no agreement on an accurate method for determining the chloride threshold value initiating corrosion. The objective of this work is to present a new test set-up that considers the localized character of corrosion initiated by chlorides. This approach is based on a physical separation between the anode, contaminated with chlorides, and the cathode, which is chloride free. This approach will allow to quantify the galvanic corrosion current, making it possible to determine, in a second step, the chloride threshold values for corrosion initiation. The criteria for corrosion initiation was a threshold corrosion current defined as a current that is independent of the cathode/anode surface ratio. It was then important to test the influence of the geometric surface ratio on the galvanic corrosion current. It was found that it is an important parameter that needs to be taken into account when studying corrosion in the presence of chlorides. Preliminary results of threshold values were determined based on this criterion for CEMI and for several types of steel surface conditions. The preliminary results also give an idea of the influence of chloride contents on the galvanic corrosion currents.

## 1. Introduction

Traditionally, concrete reinforcement corrosion induced by chlorides is initiated when the chloride content reaches a certain threshold Ccrit. After investing much time and effort in this field, researchers have still not reached agreement on an accurate and reliable method for the determination of this threshold value [1]. Corrosion initiated by chlorides is macrocell corrosion (also known as localized or non-uniform corrosion). This means that the anodic (active steel) and cathodic (passive steel) sites are distant from one another.

Two traditional electrochemical techniques are commonly used for analysing corrosion initiation: measurement of the linear polarization resistance, and measurement of the reinforcement potential, where a potential drop would indicate the start of corrosion.

The first electrochemical method, the measurement of linear polarization resistance of steel in concrete, is supposed to provide quantitative information on corrosion kinetics, unlike the potential measurements. It is based on polarizing the reinforcement in order to shift the corrosion system from its equilibrium state. The polarization resistance obtained is then converted into corrosion current density by means of the Stern-Geary equation [2,3], which was originally established for the uniform corrosion state [4]. Unfortunately, application of the Stern–Geary [2] equation to localized corrosion found in real structures is unsuitable since it is not fundamentally correct to apply the mixed potential concept established by Wagner and Traud [5] when anode and cathode are some distance apart.

Several problems in understanding polarization measurements and their application to macrocell corrosion have been reported [6,7]. In fact, the behaviour of the macrocell system has been found to depend on the polarization direction (anodic or cathodic) and magnitude. Laurens et al. [8] proved that, when a macrocell system was polarized cathodically, the polarizing current was spread over passive areas. Conversely, it was spread over active areas in the case of anodic polarization. This means that, in localized corrosion systems, the apparent linear polarization range is underestimated when this technique is employed. Additionally, Elsener et al. [9] found that the response of a macrocell system is not the same as that of a microcell system. Recently, Angst and Büchler [10] questioned the applicability of the Stern–Geary equation for quantifying the corrosion rate using linear polarization resistance measurements in the case of macrocell systems. All the arguments mentioned above show that the linear polarization resistance measurement does not take account of the intrinsic localized aspect of corrosion in concrete reinforcement. Consequently, it is not possible to apply this method to reinforced structures in the aim of quantifying corrosion kinetics [11].

The second method employs a technique for corrosion initiation that is commonly used because of its low cost and its ease of execution. The diagnosis of corrosion initiation cannot be made with an absolute value of reinforcement potential [12,13] as presented in the ASTM standard C876-91 [14], where the absolute potential measurement is interpreted and expressed in terms of corrosion risk. A better way is to monitor potential over time in order to identify corrosion initiation [12].

* Corresponding author.
*E-mail address:* chantal.chalhoub@insa-toulouse.fr (C. Chalhoub).

https://doi.org/10.1016/j.cemconres.2019.105825
Received 11 February 2019; Received in revised form 26 June 2019; Accepted 19 July 2019

Several experimental studies were realized based on this approach. Recently, a RILEM technical committee (TC) 235-CTC [15] was formed in order to realize an appropriate test method capable of giving information related to Ccrit with tolerable measurement uncertainty. However, its ultimate aim was not achieved. Concrete samples (water/binder = 0.45) embedding vertical steel bars were used. The bars were chemically cleaned followed by a pre-rusting procedure in humid environment in order to create a practice-related and reproducible steel type. The introduction of chlorides was realized with a pre-drying procedure in a drying environment followed by an immersion in a 3.3% NaCl solution in order to accelerate the chloride ingress. Yet, the test duration was found much longer than expected. The open circuit potential of the rebars was monitored and the criteria of corrosion initiation was a potential drop of at least 150 mV in a period < 24 h with a condition that the potential remains at its level or lower for a minimum period of 7 days in order to make sure that stable corrosion takes place. The measured total chloride threshold values varied from 0.6% to 1.6% /wt. binder with an average value of 1.05%.

An experimental protocol, developed by Angst et al. [16], consists on taking a number of samples from real reinforcing concrete structures where corrosion has not yet initiated and expose them to controlled laboratory corrosion testing. The main advantage of this method is that it guarantees real conditions regarding factors that significantly impact Ccrit, such as the steel-concrete interface, the type and the age of the concrete and the type and surface condition of steel. The method also allows to prevent false corrosion initiation and steel bar effects. The corrosion initiation criteria was based on the method developed by RILEM technical committee TC 235 [15].

Another experimental work, developed by Pacheco and Polder [17], was also based on this RILEM Committee work. The test specimens were formed of ordinary Portland cement (PC) and ground granulated blast furnace slag (CEMIII/B) cement with a water/binder ratio equal to 0.45 for both formulations. The surface condition of the bars was as received steel with possible presence of oxidation products on some areas. The critical total chloride contents of the PC specimens ranged between 0.3 and 1%/wt. binder with an average value of 0.56%.

V. Nygaard and Geiker [18] developed an experimental method that allows to accelerate chloride ingress decreasing the time needed to initiate corrosion. The chloride ingress was realized by a sample drying followed by their immersion in saline solution. The authors stated that there can be adverse effects of the conditioning used, mainly for the drying part (such as the non-saturated pores and/or coarsening of the pore system) which can lead to lower Ccrit. In this case, the corrosion activity of the bars was monitored by potentiostatic control. In fact, a current was applied to the steel electrodes to maintain their fixed potentials and corrosion initiation was defined as an increase of the applied current to > 50 μA. The critical chloride found on CEMI concrete samples (Water/binder = 0.45) ranged from 0.52 to 0.74 wt% binder. However, galvanostatic or potentiostatic control prevents repassivation which can occur under site conditions. The polarization method is then considered to be non-representative and conservative [15].

Garcia et al. [19] used the same corrosion initiation criteria presented earlier and found, in case of CEMI, Ccrit values that ranged between 0.6% and 0.9% per weight of cement.

This technique, also implemented in others several studies [20–23], does not provide any quantitative information about corrosion kinetics. Moreover, the results obtained by Garcia et al. [19] indicate that it is no longer useful in cases of formulations with slag and pozzolanic additives. It was found that, for formulations with high substitution levels of slag, the potential values were very low from the beginning of the potential monitoring (between −600 and −700 mV/SCE), despite the absence of corrosion, and that no potential drop occurred with the initiation of corrosion. This implies that the detection of corrosion initiation using a potential drop could be difficult in cases where the potential is highly negative, for example in slag cements or in other binders containing sulfide [16].

It was therefore necessary to propose a new test protocol that would reproduce the localized chloride-induced corrosion found in real structures. This test method consists on the same components found in the other protocols discussed earlier (such as the steel bar surface condition, the alkaline environment, the procedure to introduce and measure the chlorides and the exposure conditions) but with the addition of another component which is the galvanic corrosion current. Hence, the test set-up described here is based on a physical separation of the anode part, contaminated with chlorides, from the cathode part, which is chloride free. In order to estimate corrosion rates and predict lifetime of reinforced concrete structures subjected to chloride-induced corrosion, the macrocell current is of main concern. This new experimental approach will allow the galvanic corrosion current to be quantified, thus making it possible to determine in a forthcoming work the chloride threshold values for corrosion initiation for all kind of binders including high slag contents. Preliminary results of threshold values were determined based on a threshold corrosion current that is considered independent of the surface ratio between cathode and anode. It was then important to test the influence of the geometric surface ratio on the galvanic corrosion current. It was confirmed that it is an important parameter that needs to be taken into account when studying corrosion in presence of chlorides.

With this test, it is also possible to study the influence of several parameters on corrosion propagation: anodic, cathodic, ohmic, geometric and environmental mechanisms. The preliminary results presented in this paper provide an idea of how chloride contents and the nature of the steel surface influence the galvanic corrosion currents.

## 2. Electrochemical background on the macrocell corrosion system

Corrosion initiated by chlorides is an electrochemical phenomenon involving two mechanisms, one of oxidation and the other of reduction. The anode, where the oxidation of the steel takes place, generates electrons needed for the reduction reaction of dissolved oxygen at the cathode. In the case where the anode and cathode are spatially combined, the corrosion is said to be uniform and is also known as microcell corrosion. In this case, the potential field is uniform and there is no current flowing in the concrete volume.

On the other hand, when the anode and cathode are spatially separated, the corrosion is said to be macrocell or non-uniform. This type of corrosion, also known as galvanic or localized corrosion, is encountered in reinforced concrete structures exposed to aggressive agents such as chlorides. In fact, the reinforcing steel in concrete is naturally protected against corrosion by a passivation phenomenon consisting of the fast formation of a dense oxide film on the steel surface. Nevertheless, this passive film may be locally destroyed by chloride ions, causing a local activation of the steel and leading to macrocell corrosion conditions.

In macrocell systems, anodic and cathodic potentials at equilibrium are different, which leads to a non-uniform electrochemical state of the steel with the presence of a potential gradient. Consequently, an ionic current circulates through the interstitial solution of the concrete between anodic (active) and cathodic (passive) areas. This ionic current is influenced by the electrical resistivity of the concrete, which consequently affects the macrocell electronic current flowing through the metallic network. This makes the electrical resistivity of the concrete a possible control factor of the macrocell system.

A macrocell corrosion system can be defined as the electrical connection of two uniform corrosion systems: one active, representing the anode, and the other passive, representing the cathode, which results in their mutual polarization.

## 3. Experimental test protocol

The experimental set-up recreated localized corrosion by imposing a physical separation between the anode and cathode, which allowed the

galvanic corrosion current to be measured. This was done by preparing two types of samples: the anode, representing the sample contaminated with chlorides, and the cathode, representing the sample without chlorides. To avoid the diffusion phase of chlorides and reduce the time needed for them to reach the steel surface, anodes were dried to constant weight then soaked in saline solutions.

This two-piece test set-up enabled the galvanic corrosion current to be quantified, thus making it possible to determine the chloride threshold values for corrosion initiation. It was also possible to test the influence of several parameters and mechanisms on corrosion propagation, such as the influence of anodic parameters and the ratio between cathodic and anodic surface areas (noted C/A ratio). The size of the anode was chosen to be small despite the fact that, in reality, the anode forms spontaneously on larger rebar surfaces. The reason behind this is to have an anode steel bar that is, as much as possible, in an active state. In real structures, the C/A ratio is very high at the beginning of the corrosion process because of the multiple layers of reinforcement bars that are still initially in the passive state. For this reason, in the present test, a high C/A ratio, of 16, was chosen. Moreover, it was important to choose a sufficiently large C/A ratio that is equal to 16 because lower C/A values may lead to corrosion currents that are difficult to measure.

### 3.1. Description of test specimens

#### 3.1.1. Specimen characteristics

The cathodic samples were cylindrical (ϕ110 x 220 mm) with a cover of 5.2 cm. At the centre of each sample was a 160 mm long Fe-500 ribbed steel bar 6 mm in diameter. The anodic samples were also cylindrical (ϕ33 x 70 mm) with a steel bar of 10 mm length and 6 mm diameter embedded at the centre of each one, thus having a cover of 1.35 cm (Fig. 1).

Two electrical wires were tin welded to each steel bar, one to the upper part and one to the lower, leaving only the lateral surface of the steel uncovered. The upper wire was used to guarantee a good electrical connection during electrochemical testing. Each wire was held in place by a hole made in the middle of the upper and lower part of the plastic mould. The rebar was thus maintained in the middle of the specimen. The lower wire was fixed to the hole of the base of the mould with a knot, which was then covered in silicone.

#### 3.1.2. Mortar composition and its characterization

The use of reinforced mortar specimens instead of reinforced concrete allowed small samples to be made without recourse to core cutting. The mortar formulation used and its characteristics are presented in Tables 1 and 2, respectively. The water/cement ratio used was 0.55 and the sand/cement ratio was 2.75.

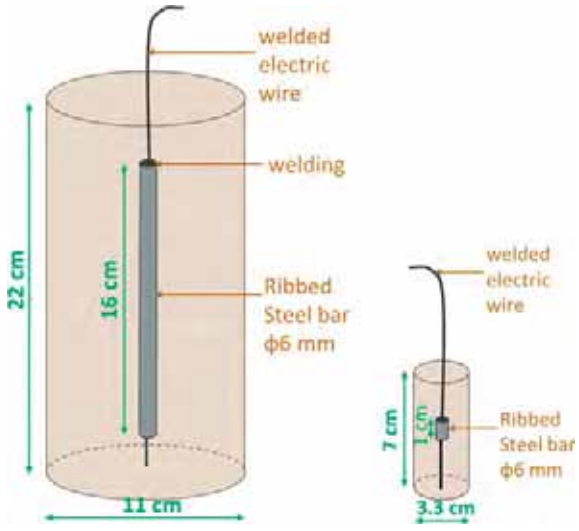


**Fig. 1.** Dimensions of the cathodic (left) and anodic (right) test specimens.

**Table 1**
Mortar formulation.

| Materials | Quantity (kg/m3) |
|---|---|
| Siliceous sand 0/4 | 1408 |
| CEMI 52.5 R (Lafarge factory) | 512 |
| Water | 281.4 |

#### 3.1.3. Steel bar reinforcement types

It is essential to understand the effect of the surface condition of steel on rebar corrosion. In fact, reinforcement bars are often covered with a layer of mill scale (high temperature phase formed during the cooling of iron) which may or may not be combined with a layer of corrosion related to the action of rainwater or formed during prolonged outdoor exposure on site.

The non-uniformity of mill scale could lead to the concept of weakest spot. The weakest spot could be related to the geometry of the rebar such as the presence of ribs which can induce different cooling kinetics during the industrial process. On the other hand, the weakest spot could be related to damages after manufacture for instance during the handling or during the assembly of the bars on construction site. It could also be related to size effect in casting process for instance the heterogeneity of the steel/concrete interface.

If the weakest point is induced by the rebar damages or size effect, this limitation cannot be resolved in a laboratory experimental test even if a bigger length of anode rebar was used. Knowing that, in reality, the length of the bars is approximately 6 m whereas the length of the bars used as anodes, in experimental works, usually do not exceed 0.1 m.

However, if the weakest point is associated with the geometry, it is possible to resolve this issue by using different types of steel surface conditions. For instance, it is possible to use a certain treatment that eliminates the effects of formation of mill scale during the cooling of rebars by using an acid cleaning technique followed with a heating treatment that allows the formation of a new layer of corrosion products that is supposed to be more uniform than mill scale.

Four different types of steel surface were used in this study (Fig. 2):

- As Received Steel, “ARS”: steel without treatment presenting a non-uniform layer of mill scale, which is the case for many reinforcement bars on site.
- Cleaned Steel, “CS”: steel cleaned with a chemical cleaning procedure based on standard ISO 8407 [24], which uses an acid solution

**Table 2**
Characterization results on the mortar obtained at 10, 28 and 90 days of curing age.

| Characterization tests | CEMI | | | | | |
|---|---|---|---|---|---|---|
| | 10 days | | 28 days | | 90 days | |
| Compressive strength (MPa) (NF EN 196–1) | 59<br>54<br>56 | $\overline{X}=56$<br>$\sigma=2$ | 65<br>68<br>65 | $\overline{X}=66$<br>$\sigma=1$ | 78<br>75<br>74 | $\overline{X}=75$<br>$\sigma=2$ |
| Water porosity (%) (AFREM) | 21.5<br>21.7<br>22 | $\overline{X}=21.7$<br>$\sigma=0.20$ | 21.3<br>21.5<br>20.7 | $\overline{X}=21.2$<br>$\sigma=0.34$ | 20.86<br>21.06<br>21.22 | $\overline{X}=21.0$<br>$\sigma=0.15$ |
| Chloride migration coefficient (10–12 m2/s) (NtBuild 492) | 20.15<br>19.79<br>20.38 | $\overline{X}=20.11$<br>$\sigma=0.24$ | 20.22<br>19.48<br>19.33 | $\overline{X}=19.68$<br>$\sigma=0.39$ | 17.16<br>17.02<br>16 | $\overline{X}=16.73$<br>$\sigma=0.52$ |
| Electrical resistivity (Ω·m) (RILEM TC-154 EMC) | 106<br>111 | $\overline{X}=109$<br>$\sigma=3$ | 114<br>132 | $\overline{X}=123$<br>$\sigma=9$ | 120<br>135 | $\overline{X}=128$<br>$\sigma=8$ |

**Fig. 2.** Different types of steel bars used: ARS, CS, CSPT and CSPH.

to remove the mill scale layer. The weight difference of the steel bar before and after the cleaning treatment was measured on 96 different bars and had an average value of 2.2 mg with a coefficient of variation (CV) of 28.8%. This value could represent the weight of the mill scale layer at the steel surface.

- Cleaned Steel Pre-oxidized by high Temperature, "CSPT": steel cleaned then oxidized with a heat treatment of 72 h at 400 °C in order to obtain a homogeneous layer of corrosion products having a composition close to that of the mill scale found in the case of ARS bars, which is made up mostly of magnetite with a little hematite. The weight difference after cleaning of the samples was measured before and after the heat treatment on 48 different steel bars. The weight difference was around 0.67 mg (CV = 38.4%) and represented the weight of the layer of corrosion products formed at the surface of the steel bars during the heating treatment.
- Cleaned Steel Pre-oxidized by exposure to Humid environment "CSPH": steel cleaned then oxidized for two weeks in a humid environment (relative humidity = 95%) in order to study a non-uniform oxidation layer formed in the absence of mill scale.

The steel type abbreviations explained in this section are used in the rest of the paper. The weight of the anodic steel bars was measured with a precision of 0.0001 g before the wires were welded, in order to quantify the steel weight loss before and after corrosion.

#### 3.1.4. Preparation of mortar samples

Once prepared and mixed, the fresh mortar was poured into the corresponding moulds in two layers, each of them being vibrated for approximately 30 s in order to eliminate air voids. During the vibration, it was important to keep the steel in the middle of the mould by pulling the electrical wire vertically. After casting, the surface of the specimens was covered with a plastic cover to prevent the evaporation of water. The upper wire was inserted in the hole of the cover and fixed with adhesive tape. Then, the specimens were placed in a curing room where the relative humidity was approximately 95%. All the specimens were unmoulded after 24 h and then cured for 28 days in the same wet curing room.

### 3.2. Processing of anodic specimens

This section will present the diffrent steps of the processing of anodic samples that are illustrated in Fig. 3.

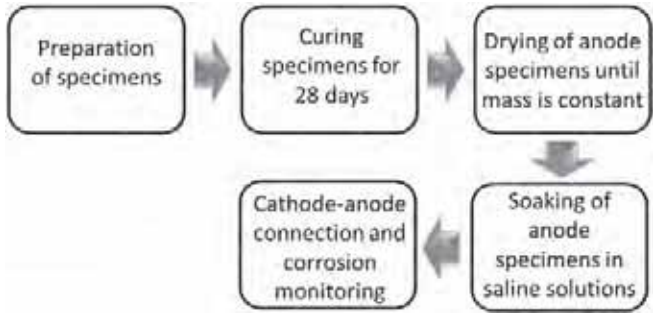


**Fig. 3.** Schematic representation of the specimen processing.

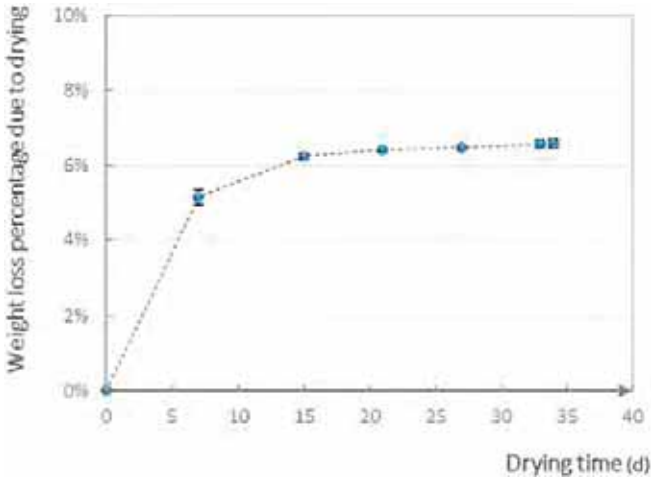


**Fig. 4.** Stabilization of the weight loss of anodes during their drying in the oven.

#### 3.2.1. Drying of anodic specimens

After the end of the wet cure, the anodic specimens were dried at a constant temperature of 45 °C and a controlled relative humidity of 25% until their mass was constant, i.e. until 2 successive weighings before and after 24 h in the oven did not differ by > 0.05%. The temperature was limited to 45 °C to avoid the destabilization of hydrates and cracking. The drying time necessary for the stabilization of the mass of the anodes and consequently the extraction of all the existing water in the connected pores was between 25 and 35 days (Fig. 4). The average volume of dried water was calculated with equation (Eq. (1)). It corresponded to 15.7% of the apparent total volume of the mortar specimen and represented almost 75% of the water porosity of the formulation used.

$$V_{dried}\,(L) = \frac{W_{dried}}{\rho_{Water\ meas}} \tag{1}$$

$W_{dried}$:Weight of the water dried from connected pores determined by the mass difference found when measuring the anodic sample before and after complete drying (g); $\rho_{Water\ meas}$: Density of water measured experimentally at 20 °C, with a value of 995 g/L.

During their drying period, anode specimens could be subjected to carbonation. It was then important to see if the anode specimens were carbonated during drying. For this reason, some dummy specimens having the same dimensions of the anode but without reinforcement, were dried in the same environment of the anode specimens. After more than one year of drying, phenolphthalein solution was sprayed onto the freshly cut surfaces of those samples in order to determine the carbonation depth. A solid purple coloration was observed on the entire surface indicating that there was no carbonation during the drying of anode samples.

#### 3.2.2. Immersion of anodic specimens in saline solutions

After the end of drying, the chlorides were introduced by soaking the anodes in 1 L of sodium chloride solutions having controlled chloride contents using demineralized water. The electrical wires welded to the bars were coated with silicone to avoid chloride penetration into the samples through the wires. The samples were entirely immersed for 48 h in saline solutions with 5 different concentrations of NaCl: 12.25, 22.75, 70, 140 and 280 g/L. Hence, a priori, known quantities of chlorides were present in the anode samples. Their quantities were also measured a posteriori, after the destruction of the specimens to check the corrosion state. On the other hand, the cathodes, which were chloride free, remained intact and could thus be reused.

5 reference samples identical to the anode samples but without steel

**Table 3**
Weight percentage of absorbed saline solution according to duration of soaking.

| [NaCl] (g/L) | $W_{abs}/W_{initial}$ (%) | | | | | | |
|---|---|---|---|---|---|---|---|
| | Imbibition duration (h) | | | | | | |
| | 0 | 5 | 24 | 48 | 72 | 96 | 168 |
| 280 | 0% | 6.9% | 7.6% | 7.7% | 7.7% | 7.7% | 7.8% |
| 140 | 0% | 7.0% | 7.2% | 7.2% | 7.2% | 7.2% | 7.3% |
| 70 | 0% | 7.0% | 7.0% | 7.0% | 7.0% | 7.1% | 7.2% |
| 22.75 | 0% | 6.6% | 6.6% | 6.7% | 6.7% | 6.7% | 6.8% |
| 12.25 | 0% | 6.9% | 6.9% | 6.9% | 6.9% | 7.0% | 7.1% |

bars were contaminated with the different saline solutions for a period of 168 h. The weight of the samples was measured before and after soaking at different imbibition durations. After 48 h of soaking, the weight of saline solution absorbed by the sample ($W_{abs}$) according to the initial weight of the sample ($W_{initial}$) had almost stabilized (Table 3). This means that a period of 48 h of soaking is an optimal duration for the immersion of anode samples in saline solutions.

### 3.3. Methods for corrosion assessment

At the end of the corrosion test, a steady state polarization test was performed on samples. This test is not presented and not used in this paper but will be exploited in a forthcoming work. Then, the chloride contents were determined for all the anode samples. All of the CS, CSPT and CSPH and some of the ARS specimens were used for the characterization of the steel/mortar interface. Most of the ARS specimens were used for visual and optical inspection and gravimetric measurements. Each of the analysis methods presented in Fig. 5 is detailed below.

#### 3.3.1. Anode-cathode coupling and measurement of galvanic corrosion current

After two days of immersion in the saline solution, each anodic specimen was placed, with the corresponding cathode, in a sodium hydroxide solution (NaOH). The anode and cathode samples were separated by a distance of 30 cm, leaving 1 cm of the anode and 3 cm of the cathode not immerged in the alkaline solution. The pH and

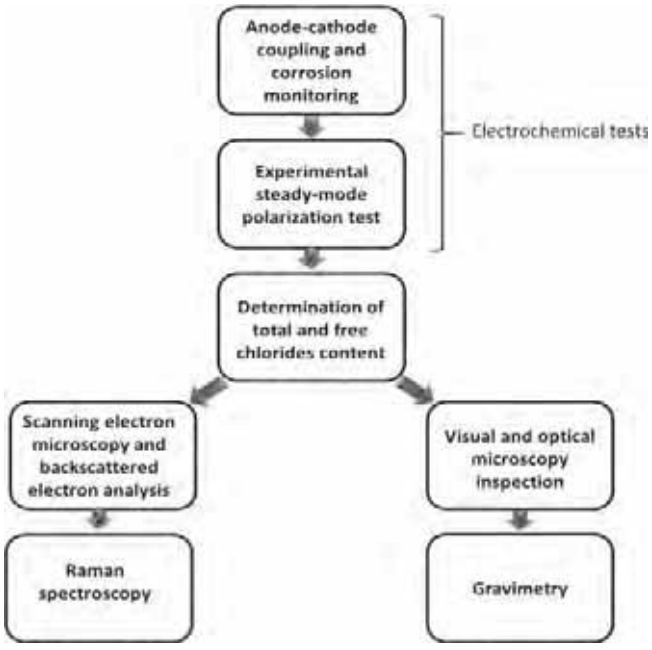


**Fig. 5.** Summary of the corrosion analysis methods used.

**Table 4**
pH and electrical conductivity of NaOH solution measured at different ages.

| Age (days) | pH | Electrical conductivity (mS/cm) |
|---|---|---|
| 0 | 12.31 | 57.1 |
| 7 | 12.21 | 26.42 |
| 7 | 12.20 | 27.47 |

electrical conductivity of the sodium hydroxide solution were measured with a pH meter and a conductivity meter, respectively (Table 4). Since NaOH reacts with carbon dioxide from the air, each solution prepared for the test was renewed after 7 days in order to maintain the same concentration and thus the same pH.

The anode and cathode samples were connected by a potentiostat controlled by EC-Lab® software using the ZRA (Zero Resistance Ammeter) electrochemical technique to measure the galvanic coupling current between them (Fig. 6). The measurement of the current was maintained for 7 days in order to reach the steady state (stabilization of the measured galvanic current). All the electrochemical experiments were carried out at a constant temperature of 20 °C in a controlled room.

It is important to note that, if the anode was left alone after chloride soaking, intrinsic localized corrosion due to chlorides led to non-uniform corrosion on the anode (called inside macrocell), which was assumed to be negligible in comparison with the galvanic corrosion. Further research will be needed to assess the proportion of inside macrocell corrosion of the anode in comparison with the galvanic current measured.

This two-specimen system allowed the galvanic current between anodic and cathodic areas to be quantified, which has not been possible in the single-specimen systems developed in the literature [15]. This galvanic corrosion current was evaluated according to the chloride contents and the nature of the steel surface.

The potentials of the anode and cathode were measured before the two samples were connected and the potential was tracked for 1 h after the samples had been disconnected at the end of the corrosion test. Generally, the potentials measured with respect to a reference electrode located on the surface of the concrete do not represent the real potential of the reinforcement. These potentials depend on the position of the reference electrode because of different phenomena such as junction potential at all interfaces, gradient of concentration in the embedding mortar, etc. In this test, the geometry of the anode specimens and cathode samples was the same and the samples were symmetrical, with a constant cover thickness regardless of the position of the reference electrode. Hence, it was possible to compare the potential measurements.

#### 3.3.2. Determination of total and free chloride contents per mass of cement

Total and free chloride (Cl) contents were measured at the end of the corrosion test in all of the anode samples to relate the measured chloride levels to the experimental galvanic currents. The dissolution of powders for the determination of total chlorides (free and bound) was carried out according to standard NF-EN-14629 [25] and the preparation of solutions for the free chlorides followed the procedure recommended by GranDuBé [26]. The determination of chlorides in mortar powder requires a sample weighing between 1 and 5 g. Thus, mortar was taken at the level of the steel bar after splitting the sample in the middle and removing a thickness of 5 mm of mortar from either side (Fig. 7) to obtain almost 6 g of powder. Approximately 2 g was used for the quantification of total chlorides and 4 g for the free chlorides. The volumetric analysis was performed with the Ti amo software by precipitation with a silver nitrate solution.

In order to confirm whether the soaking procedure led to the estimated chloride contents in the vicinity of the rebar, these measurements were also made on 6 reinforced reference samples directly after 48 h of soaking, without their coupling with a cathode (hence avoiding

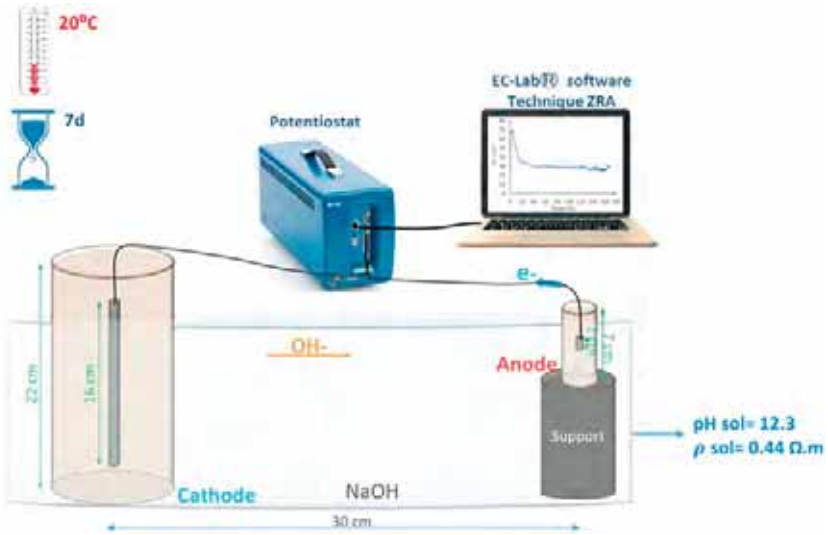


**Fig. 6.** Cathode-anode coupling and measurement of the galvanic current.

possible chloride accumulation induced by the potential gradient resulting from the corrosion test). These control specimens were soaked in 5 different saline solutions with the 5 concentrations mentioned in part 3.2.2, and in demineralized water. To make sure that this sampling method was reliable and repetitive, we also measured the free chlorides on 4 g of powder with the GranDuBé method, then the remaining chlorides, which represented the fixed chlorides, with the NF-EN-14629 standard. The results presented in Table 5 show that the sum of the free and fixed chlorides was almost equal to the level of total chlorides.

Knowing that the total chlorides are the sum of free and fixed chlorides, the shift from total to free chlorides could also be theoretically achieved using adsorption isotherm equations, which are empirical relations between the concentrations of a solute on the surface of an adsorbent and the concentration of the solute in the liquid with which it is in contact. The relationship between bound and free chlorides can be described by the Freundlich isotherm for high free chloride concentrations (Fig. 8). This relation (Eq. (2)) is often used to describe isotherms because it correlates well with the experimental data.

$$\text{Fixed Cl} = \alpha\ \text{Free Cl}^{\delta} \quad (2)$$

with:

- Fixed Cl (%/wt. cement): Quantity of bound chlorides in the solid phase;
- Free Cl (%/wt. cement): Quantity of free chlorides in the pore solution;
- α and δ: Empirical coefficients.

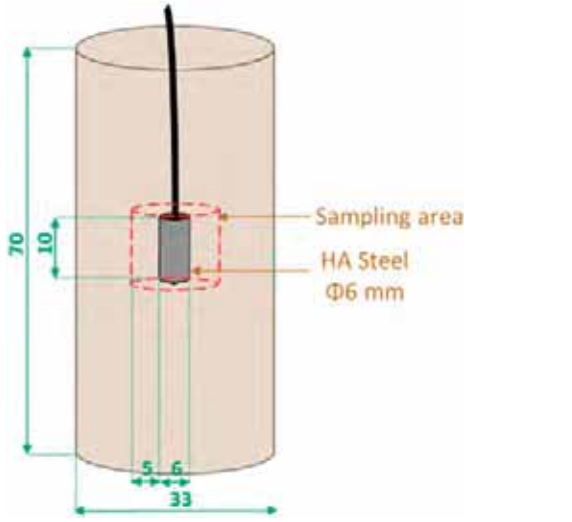


**Fig. 7.** Sampling area for the determination of chloride content (dimensions in mm).

**Table 5**
Application of the titration procedure on 6 reference samples.

| [NaCl] (g/L) | Experimental results (%/wt. cement) | | | | calculation |
|---|---|---|---|---|---|
| | 2 g of powder | 4 g of powder | 4 g of powder | | Free Cl + Remaining fixed Cl |
| | Total Cl (NF-EN-14629) | Free Cl (GranDuBé) | Free Cl (GranDuBé) | Remaining fixed Cl (NF-EN-14629) | |
| 0 | 0.09 | 0.03 | 0.03 | 0.06 | 0.09 |
| 12.25 | 0.29 | 0.16 | 0.17 | 0.12 | 0.29 |
| 22.75 | 0.43 | 0.30 | 0.28 | 0.12 | 0.41 |
| 70 | 1.03 | 0.89 | 0.88 | 0.18 | 1.05 |
| 140 | 2.80 | 2.59 | 2.50 | 0.31 | 2.81 |
| 280 | 5.03 | 4.68 | 4.69 | 0.38 | 5.07 |

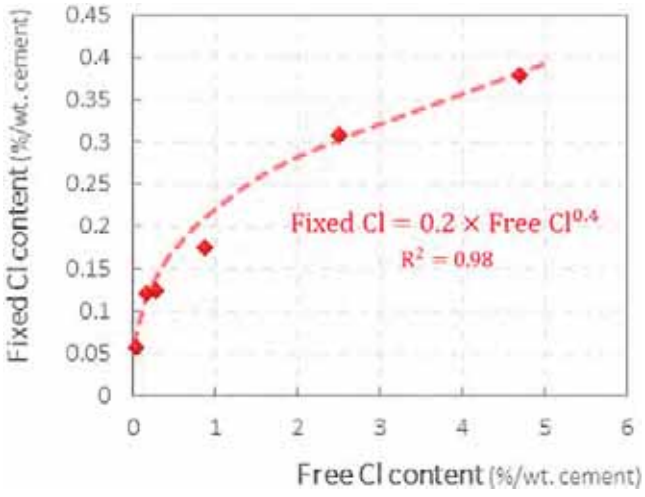


**Fig. 8.** Freundlich isotherm for the fixation of chlorides after 48 h in the case of the formulation presented in Table 11.

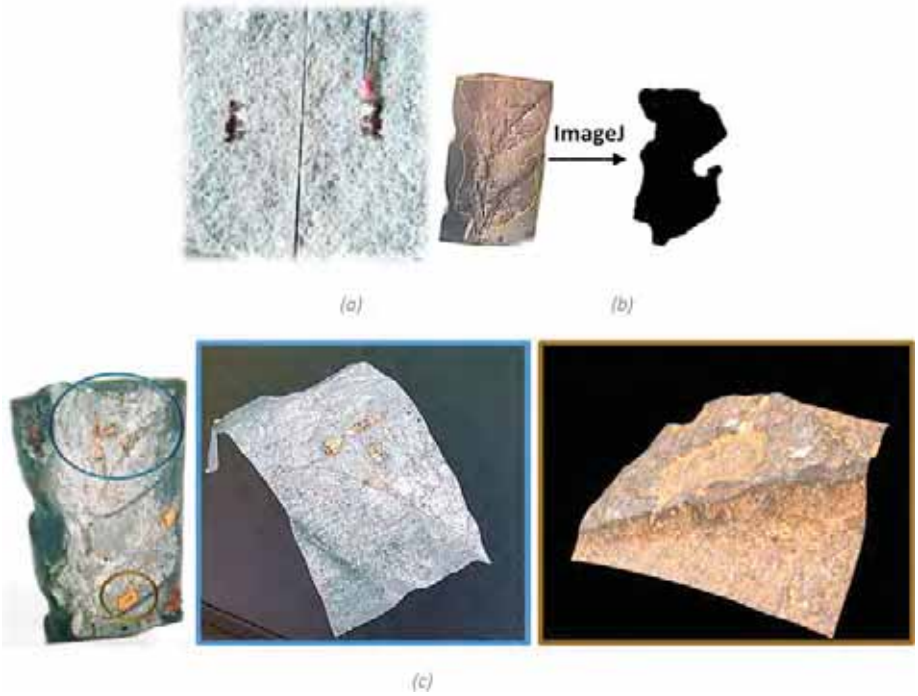


**Fig. 9.** (a) Splitting of the anode and visual detection of corrosion products. (b) Image processing of 1 side of a steel bar using ImageJ. (c) 3D observation with KEYENCE digital microscope of a steel bar corroded for 70 days.

The empirical coefficients are determined by fitting the Freundlich equation (Eq. (2)) with the results obtained with the reference samples mentioned above, giving $\alpha = 0.2$ and $\delta = 0.4$ with a correlation coefficient of 0.98.

*3.3.3. Visual and optical microscopy inspection*

Once the anode had been split in the middle, it was simple to remove the steel. Then, the steel bar could be observed visually and with a microscope to detect the presence of corrosion products (Fig. 9a). The steel bar was then cleaned to remove all the corrosion products at the steel surface, following the ISO 8407 standards [24]. This cleaning method consists of light mechanical cleaning treatment combined with a chemical cleaning procedure using a solution of hydrochloric acid, antimony trioxide and tin (II) chloride. The steel was then directly observed with a microscope and 4 images were taken on 4 different sides of each sample in order to cover the whole cylinder. The area of the corroded steel surface was estimated on the images using ImageJ software (Fig. 9b), which is an open source image processing program designed for scientific multidimensional images. The error involved when moving from a 3D object to 2D images was considered negligible even though the diameter of the steel bar is small (6 mm).

*3.3.4. Gravimetric measurements*

After the cleaning treatment and the microscopic inspection, the steel was weighed. The difference between the initial mass (weight of the steel measured before mortar casting) and the final one (weight after experiment and cleaning) gave the total mass loss of the steel. However, it was important to exclude the metal loss resulting from cleaning. This was determined using 96 different control specimens of steel bar. The average mass loss of the control specimens was around 2.23 mg (Coefficient of Variation CV = 28.8%), which reflected the mass lost by test specimens in the cleaning procedure. Gravimetric measurements were only performed on ARS steel, since all of the CS, CSPT and CSPH and some of the ARS specimens were used for the characterization of the steel/mortar interface. Hence, there was no need to correct the mass loss to take account of that associated with the pre-cleaning and pre-corrosion treatment. The steel mass loss resulting from the polarization test, when realized, was also calculated using Faraday's law and subtracted from the total weight loss.

## 4. Results and discussion

### 4.1. Experimental macrocell corrosion current

*4.1.1. Determination of the average corrosion current*

As mentioned previously, the localized aspect of corrosion initiated by chlorides was even observed on the small anode (Fig. 9). This means that the anode was partially active and therefore behaved as a localized corrosion system. Consequently, it was necessary to separate the three types of current presented in Fig. 10, where $I_g$ is the measured corrosion current exchanged between anode and cathode, $I_a$ is the corrosion current exchanged between active and passive zones of the anode, and $I_{micro}$ is the microcell corrosion current at anodic sites of the anode which was considered negligible because of the polarization of the anode during the corrosion test [11].

In a first approach, $I_a$ was neglected because the passive area in the anode, also called the internal cathodic area, was much smaller than that of the external cathodic area, i.e. the passive area at the cathode.

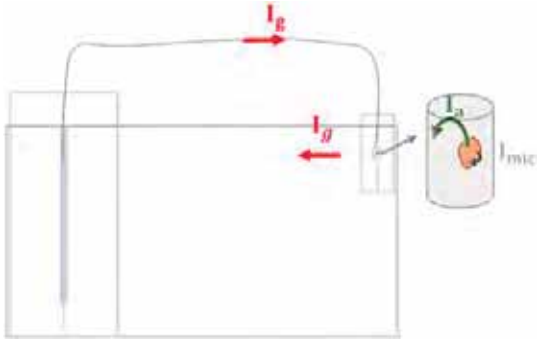


**Fig. 10.** Simplified schematic illustration of anode-cathode coupling showing the different types of currents.

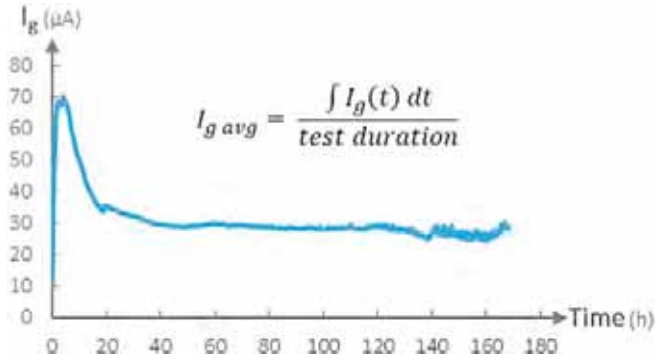


**Fig. 11.** Monitoring of a galvanic current measured between the anode and cathode samples.

Further developments will be done to characterize this internal current $I_a$.

In the anode-cathode coupling tests, the galvanic corrosion current $I_g$ was measured for 7 days. Fig. 11 shows the tracking of the measured corrosion current over time. Two main values of corrosion currents were considered: the instantaneous current at 7 days and the average current $I_{g\ avg}$ calculated from the integral of the current signal over a duration of 7 days. However, since the average current is more representative of the corrosion process, this value is used in the rest of this paper.

#### 4.1.2. Influence of chloride content and steel surface condition on galvanic corrosion current

Fig. 12 presents the average corrosion currents, $I_{g\ avg}$, measured when connecting the anode and cathode according to the free chloride levels expressed in %/weight of cement and calculated from the measured total chloride contents using the isotherm presented in Fig. 8. The results are presented for the 4 types of steel described in section 3.1.3.

An increase of the corrosion current with the chloride level was observed for the case of as received steel, cleaned steel pre-oxidized in a humid environment, and cleaned steel pre-oxidized with high temperature. The similarity in the composition of the mill scale layer found on the as received steel and the layer of corrosion products formed on cleaned pre-oxidized steel could explain the resemblance of behaviour between these 3 types of steel. The non-uniformity of these layers may justify the presence of some scatter in the results obtained. Ghods and al. [27] found that the presence of micro cracks in the mill scale layer could lead to cavernous corrosion, which could partially explain the dispersion of the chloride threshold values for steel bars with presence of mill scale.

In contrast, the corrosion currents obtained for cleaned steel were weak compared to the results obtained with the other 3 types of steel. Yet, only for chloride levels higher than 2%, $I_{g\ avg}$ became significant and above 10 µA (samples CS9 and CS11). Nevertheless, Fig. 13 shows that the currents measured in the case of high chloride contents were negligible during the first few days or hours and then increased sharply. This could be attributed to a time being necessary for chlorides to diffuse through the passivation layer formed on the cleaned steel. It should be noted that the average current for those 2 test pieces was also calculated by dividing the current signal surface by the total test duration.

The results obtained on the different steel surface samples allowed to make the assumption that the oxides formed on steel in the absence of mill scale (case of cleaned steel) are less porous to chloride ingress than those formed in the presence of mill scale (case of as received steel) and those formed on cleaned pre-oxidized steel.

This result is consistent with the work of E. Mahallati et al. [28] who studied the impact of the presence of mill scale on steel bars using cyclic polarization experiments. It was found that the formation, development and maintenance of the passive layer was determined by the accessibility of the metal cations to combine with oxygen and hydroxide ions. Hence, the mill scale layer could create an obstacle disrupting the formation of the passive layer. Horne et al. [29] also showed that the amount of portlandite near the reinforcement was almost 30% higher in the case of polished steel than in the case of steel with a mill scale layer. This phenomenon could have the effect of enhancing the buffering capacity of concrete at the steel-concrete interface.

A similarity is observed between the results obtained in case of ARS, which has a non-uniform surface condition, and the CSPT, which has a more uniform surface condition. This would indicate that the presence of a weakest point is not only related to the presence of ribs.

### 4.2. Nature of corrosion products

#### 4.2.1. SEM observation and BSE results

A Scanning Electron Microscope (SEM) JEOL JSM 6380 operating in Backscattered Electron (BSE) mode was used to study the steel-mortar interface. A Bruker Energy Dispersive Spectrum analyzer (EDS) was used to quantify Iron (Fe in blue), Oxygen (O in red) and Chloride (Cl in green) in the observation zones along an analytical line. Fig. 14 and Fig. 15 show examples of SEM images at the steel-mortar interface for CSPH and CS anode samples, respectively. The analysis is then displayed as a graph in which the horizontal axis represents the distance from the starting point of the analytical line and the vertical axis characterizes the normalized mass percentages reflecting the Fe, O and Cl content. The thickness of the steel-mortar interface layer was also measured and the maximum thickness of the non-uniform layer was recorded for each steel type (Table 6).

The elementary composition analysis of the interface in ARS, CSPT and CSPH samples revealed the presence of chlorides in the corrosion products. Furthermore, the Cl-containing corrosion deposits were circular and located at the steel/oxide interface. This means that the chloride ions penetrated through the oxide film formed on the surface of the bars to produce a chemical compound composed of Cl, Fe and O. On the other hand, in CS samples, the thickness of the layer formed on the surface of the steel was < 50 nm. Therefore, it was not possible to quantify the elements formed at the interface even with magnifation higher than 500×.

#### 4.2.2. Raman results

The corrosion products present at the steel/mortar interface were identified by Raman micro-spectroscopy with a Horiba spectrometer at the CEA lab at Saclay, France. The microanalyses in this study were performed with the 100× objective using the green visible radiation wavelength of 532 nm. Over the entire optical path and the detection system, the spectral resolution was about 2 $cm^{-1}$. Spectra were calibrated by means of a silicon crystal. The excitation laser power was filtered at 1% (acquisition time: 300 s) then 10% (acquisition time: 20s) in order to avoid potential thermal transformation of sensitive iron oxides and (oxy)hydroxide [30,31]. Finally, the spectra were acquired and processed using the LabSpec software and the phases were identified by comparison with spectra existing in the literature [30,32–34]. Raman analysis was not possible in the case of CS samples because of the very thin layer of oxides. Fig. 16 summarizes the corrosion products that were found in the Raman analysis. In this figure, it can be seen that some Cl-containing corrosion products (akaganeite and iron hydroxychloride β-$Fe_2(OH)_3Cl$) were found at the steel/mortar interface on the steel side, which could explain the presence of the circular shapes containing Cl that were observed and analysed with the SEM. The hematite and magnetite may have been corrosion products resulting from the pre-corrosion process carried out before casting.

### 4.3. Gravimetric and surface measurements

The corrosion current, $I_{Faraday}$, could be calculated theoretically

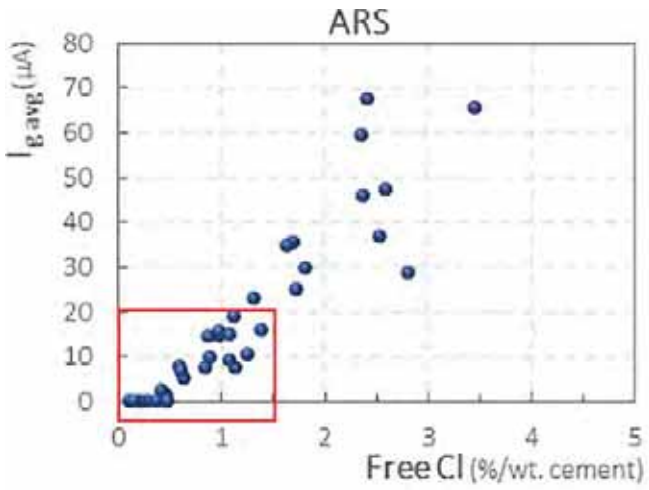


(a1)

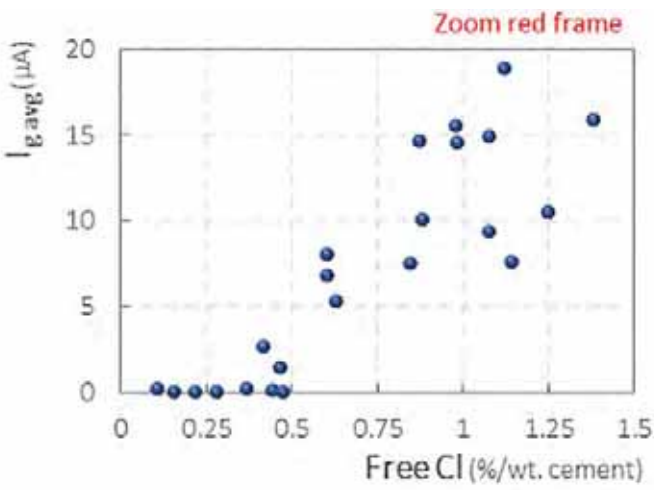


(a2)

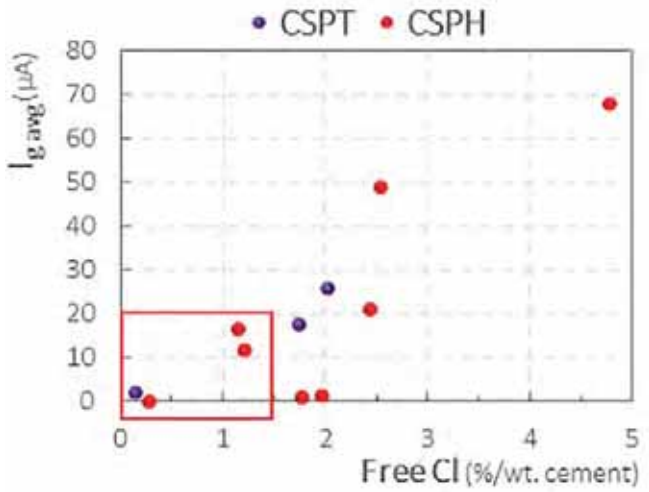


(b1)

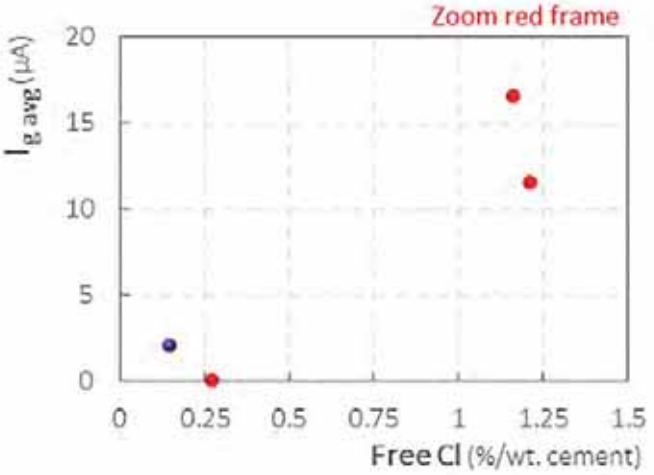


(b2)

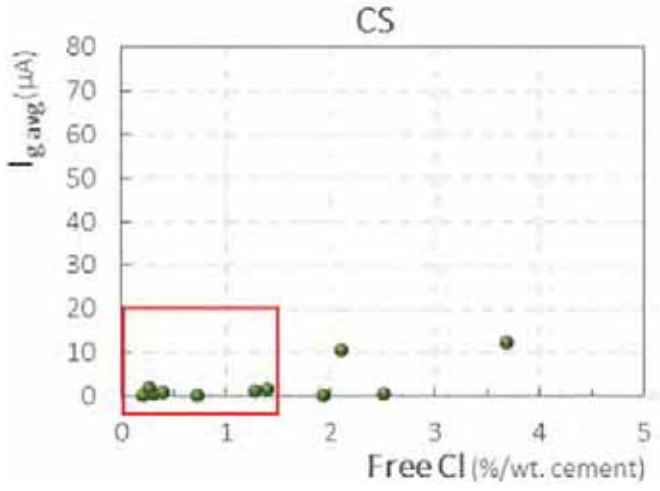


(c1)

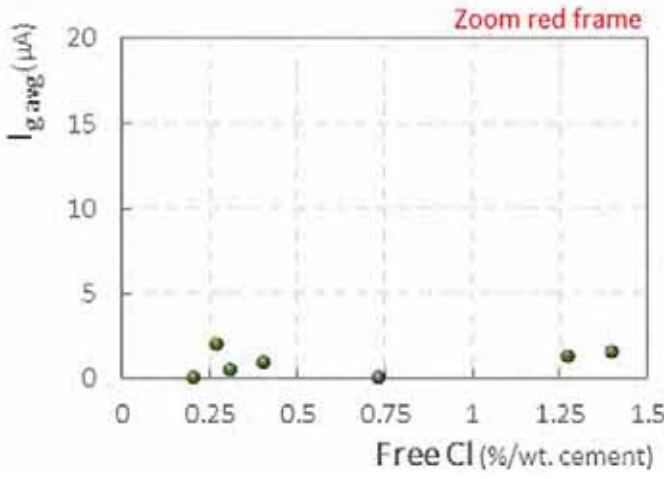


(c2)

**Fig. 12.** Average corrosion currents according to free chloride contents (a1-2) As received steel; (b1-2) cleaned steel pre-oxidized by high temperature and cleaned steel pre-oxidized in a humid environment and (c1-2) cleaned steel.

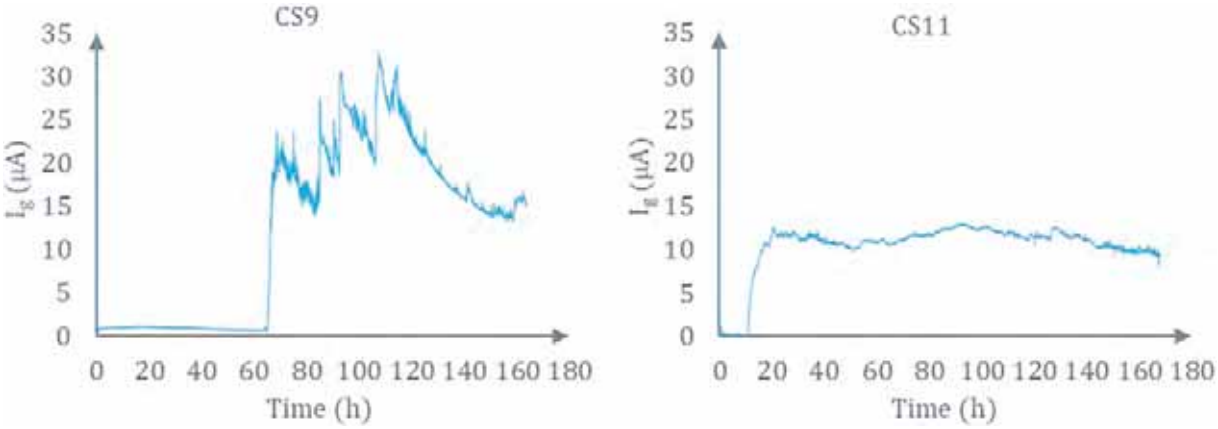


**Fig. 13.** Corrosion current measured in the case of cleaned steel for samples CS9 and CS11.

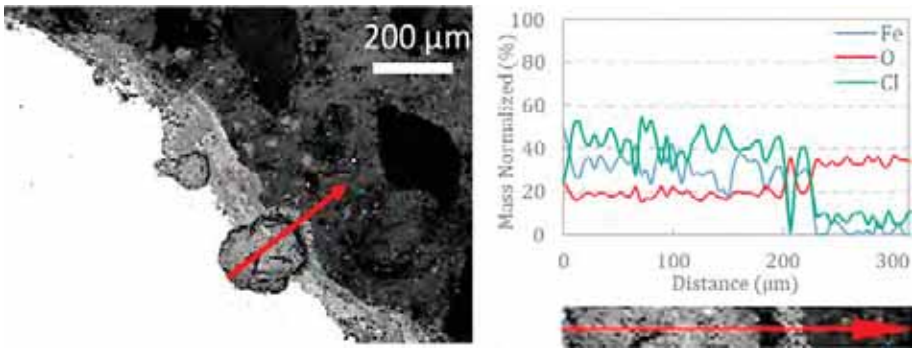


**Fig. 14.** Example of SEM observation and BSE analysis on a CSPH anode sample (magnifications: 110×).

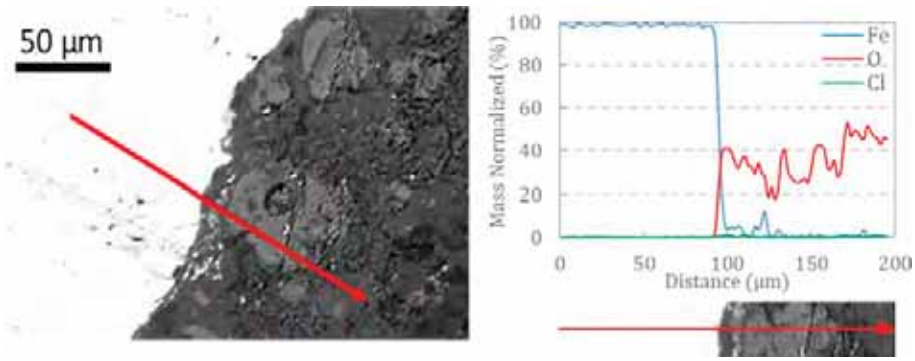


**Fig. 15.** Example of SEM observation and BSE analysis on a CS anode sample (magnifications: 500×).

**Table 6**
Maximum thickness of the steel-mortar interface layer measured on anode samples.

| Steel type | ARS | CSPT | CSPH | CS |
|---|---|---|---|---|
| Maximum thickness of the steel-mortar interface layer | 100 µm | 90 µm | 300 µm | < 50 nm |

from the measured loss of steel mass, using Faraday's law (Fig. 17). The mass loss of test specimens from the cleaning procedure and the steel mass loss resulting from the polarization test, when realized, were subtracted from the total weight loss. Looking at Fig. 17 we can see that the calculated currents deduced from the mass loss were slightly higher than the average galvanic currents, $I_{g\ avg}$, measured in the experiment between anode and cathode.

This mass gap can be explained by our inability to measure the internal macrocell corrosion current $I_a$ of the anode. Despite the scatter between the two values, the measured and calculated currents showed the same trend and were relatively close, which means that $I_a$ was relatively negligible. An increase was also observed in the active steel surface measured after 7 days of corrosion with the free Cl levels (Fig. 18).

The experimental protocol presented in this work is based on the quantification of galvanic corrosion current for a C/A ratio sufficiently large that is equal to 16. This method allows to determine the chloride threshold values based on a threshold corrosion current that is independent of the area of passive steel. This current is defined as a current that does not change when the C/A ratio is higher than 16. In other words, the chloride threshold value was associated with a corrosion state that is the same whether this ratio is 16 or higher.

Knowing that the corrosion current can be influenced by the cathode/anode surface ratio, it was crucial to study the effect of this geometric parameter. In the next section, the influence of this ratio is

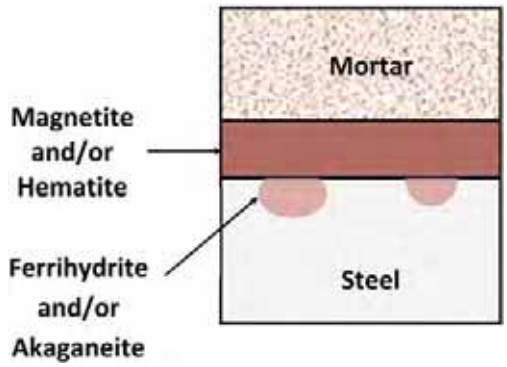


**Fig. 16.** Summary of the corrosion products found on CSPT and CSPH samples.

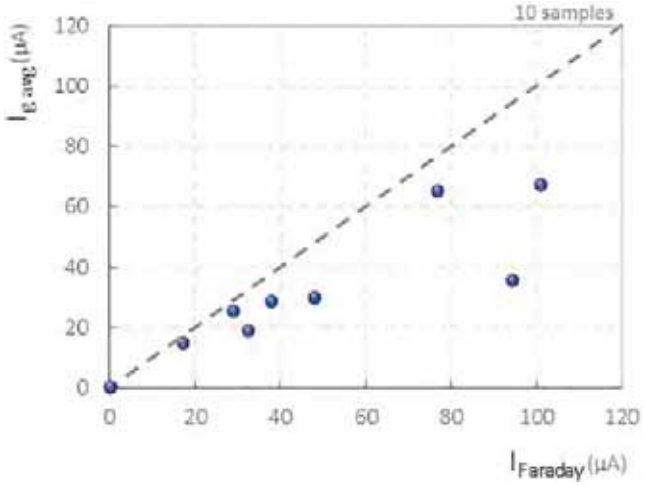


**Fig. 17.** Measured corrosion currents versus calculated currents with Faraday's law.

studied and the threshold current is fixed which allows to determine the chloride threshold values of the results presented earlier (part 4).

## 5. Cathode/anode ratio "C/A"

The C/A ratio is generally defined as the fraction representing the surface area of passive steel divided by that of active steel. On real structures, the formation of new anodic sites linked to chloride ingress will lead to a decrease of the C/A ratio, which is initially very high. It is thus very important to characterize the relationship between the geometric C/A ratio and the corrosion current $I_g$.

Several authors have studied the impact of this factor on the galvanic corrosion current. Warkus and Raupach [35] studied experimentally and numerically the influence of the C/A ratio by changing the amount of passive reinforcement in chloride-free part of reinforced structures. They found that increasing the cathodic area leads to an increase in macrocell current.

Considering that in the initiation stage of corrosion C/A ratios are extremely high, it was crucial to determine, in this work, the galvanic corrosion current, in case of very large cathodic area. It is important to recall that all the corrosion measurements made up to now were linked to a predefined geometric factor, the C/A apparent ratio, which was equal to 16. To reach very high C/A ratios, a concrete wall was used to represent the cathodic part. The dimensions of the wall are presented in Fig. 19 and its formulation is given in Table 7. The wall was a concrete parallelepiped of 75 × 20 × 100 cm containing 18 embedded steel bars of 12 mm diameter: 10 horizontal bars each having a length of 70 cm and 8 vertical bars having a length of 102 cm with 5 cm emerging from

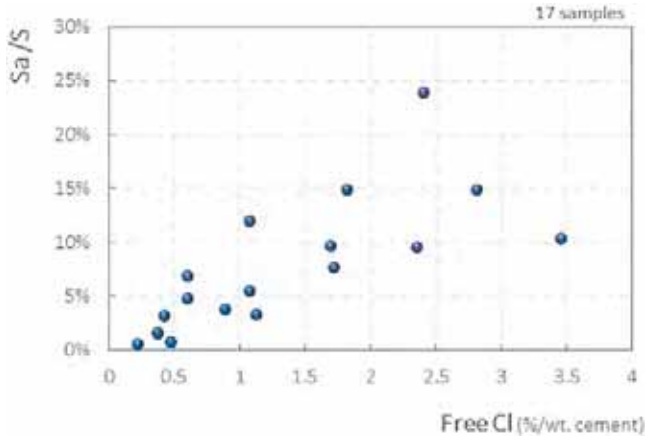


**Fig. 18.** Measured corroded surface area percentages according to free chloride contents.

the concrete. The network of frames was completely electrically disconnected but could be electrically connected from the outside. The anode was placed in a PVC pipe containing a sodium hydroxide solution that was connected to the wall allowing the ionic current to circulate. Smaller C/A ratios were also tested. In fact, each anode was connected to 3 cylindrical cathodes ($\phi 11 \times 22\ cm^3$) with three different lengths of steel (1, 5 and 16 cm) embedded in them so as to test C/A ratios of 1, 5 and 16 respectively.

Then, the anode was electrically connected to the steel bar(s) of the wall, connecting a different number of bars each time, with different lengths presenting surface area ratios from 200 to 2950. Ten different tests were carried out using 10 different anodes that were geometrically identical but had been soaked in different concentrations of sodium chloride. Current measurements were made using an Agilent multimeter and the values of the currents were recorded after they had stabilized to a steady-state condition.

It must be noted that the C/A ratios are presented, in this work, in terms of apparent ratios. The effective C/A ratios are based on the real anodic areas measured after splitting the samples presenting even higher ratios. Fig. 20 presents the currents measured for different C/A ratios for different free Cl levels. The free chloride levels of the samples tested are shown in the legend of the graph and are expressed in %/weight of cement. The results shown in Fig. 20 indicate that, for the same active surface area, an increase of the passive area led to an increase of the corrosion kinetics. This allows one to conclude that an increase in the C/A ratio leads to an increase in the corrosion current, which is in agreement with the localized corrosion concepts mentioned above.

In fact, for a given active surface area mobilized for the anodic reaction, the intensity of the corrosion current is a function of the passive surface area mobilized for the cathodic reaction. This means that the larger the passive area is, the stronger is the corrosion anodic current [11]. Moreover, the experimental results show that the current growth rate decreases with increasing cathodic surface area, which could mean that the current will reach its maximum value and stabilize for a certain C/A ratio. Thus, it can be reciprocally concluded that the corrosion currents are high at the beginning (when the C/A ratio is high) and fall continuously when the anodic surface increases (when the C/A ratio decreases). The maximum corrosion current and the threshold stabilization ratio are associated with the chloride levels. For $Cl^-$ levels lower than 1%, the C/A ratio does not have much influence on corrosion currents. The maximum corrosion current is also a function of the electrical resistivity of the wall. This parameter will be studied in a further step of the research.

Looking at the results obtained, we can assume that for "low" C/A ratios, corrosion is cathodically controlled. This means that corrosion

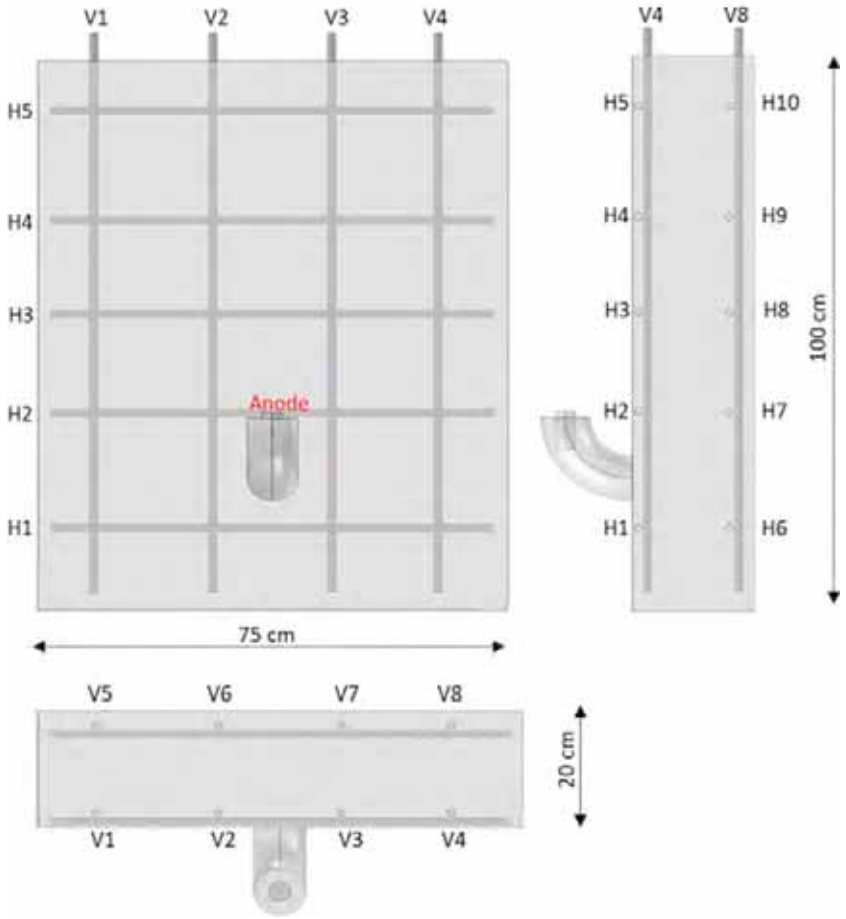


**Fig. 19.** Description of the concrete wall.

**Table 7**
Formulation of the concrete wall.

| | |
|---|---|
| Cement | CEM I 52.5 N CE CP2 NF |
| Sand | 0/4R ALL SIL CE |
| Gravel | 4/10 SR ALL SIL CE |
| Water/Cement | 0.55 |
| Sand/Cement | 2 |

current depends on dioxygen availability which is, in our case, a function of the size of cathode. On the other hand, for "high" C/A ratios, corrosion current is limited by the steel consumption, which is a function of the chloride content. An ohmic control of corrosion is also present in this case because, when the C/A ratio increases, the cathode becomes more distant from the anode.

With this experiment, given the small size of anode and the large cathodic area, it was possible to test very high apparent C/A ratios compared to the ones studied by other authors. It was also possible to experimentally test at least 14 different C/A ratios for each anode specimen. This means that, this set-up makes it possible to determine galvanic currents for different C/A and different chloride contents.

The effective C/A ratios were also estimated and reached very high values (almost 200,000). Yet, the influence of the effective ratio on corrosion current was found the same to that obtained when dealing with the apparent ratios.

In the next part, the results obtained with both apparent C/A ratios 16 and 2950 will be presented according to the different free chloride contents. This will allow to determine the threshold galvanic current which will be the criteria for the determination of the chloride threshold value in case of a formulation formed with an ordinary Portland cement.

## 6. Chloride threshold values based on a chloride threshold current

Fig. 21 presents the corrosion currents exchanged between anode and cathode for different free chloride contents for the apparent C/A ratios of 16 and 2950 in case of ARS specimens.

The concept of initiation of corrosion is set according to a limit current. This implies that the initiation criteria is related to a certain limiting galvanic current that is independent of the area of passive steel. This threshold current must then be independent of the C/A ratio.

The limiting current was found equal to 3 µA. For galvanic currents lower than 3 µA, all the obtained currents are almost the same independently from the C/A ratio. On the other hand, for galvanic currents higher than 3 µA, the galvanic currents obtained with a ratio of 2950 are 3 times bigger than the ones obtained with a C/A ratio equal to 16.

Consequently, the total and free chloride threshold values for CEMI in the case of ARS, CSPT and CSPH specimens are respectively 0.6 and 0.5%/wt. cement. However, in the case of cleaned steel, the free Cl content is 1.9%/wt. cement corresponding to a total chloride content of 2%/wt. cement.

Indeed, in Fig. 12, the galvanic corrosion current was a linear function of chloride content, with a slope change of around 0.5% of free chlorides by weight of cement in case of ARS, CSPT and CSPH specimens and 1.9%/wt. cement in case of CS specimens. The chlorides threshold values are in agreement with the discussion made earlier about the influence of the steel type condition on corrosion (part 4).

Using this approach, it would be possible to compare different types of binders, which would constitute a further step in the research.

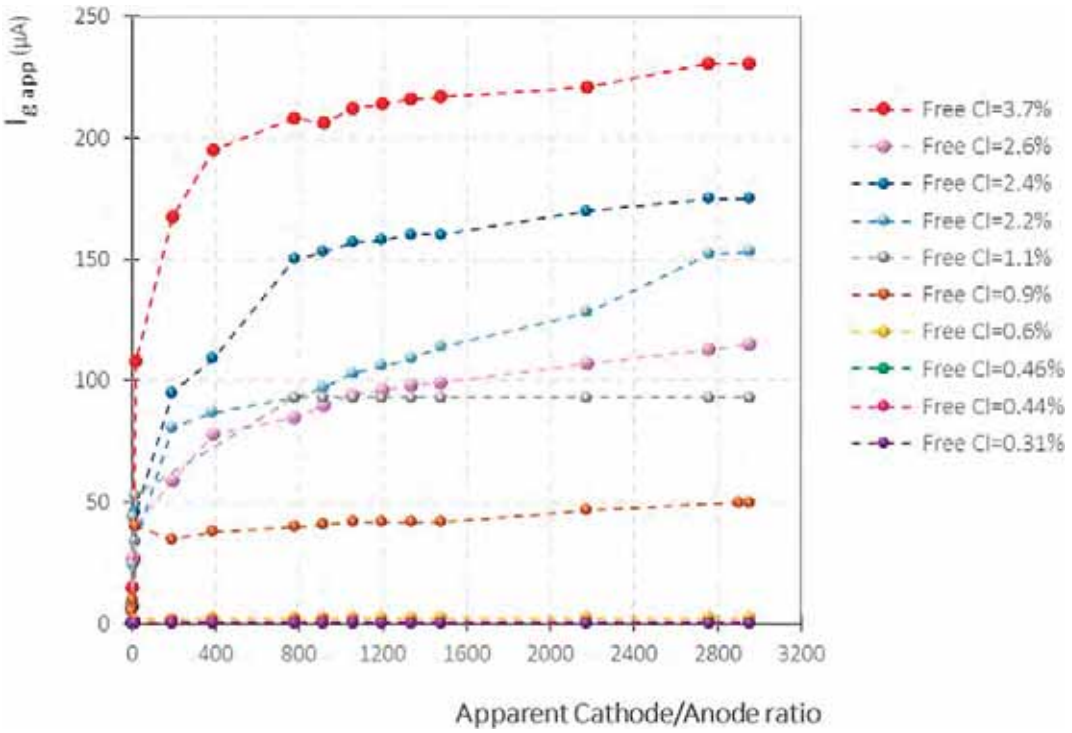


**Fig. 20.** Results of the experimental C/A ratio test.

## 7. Conclusion

This paper has presented a new test set-up established on the localized aspect of chloride- induced corrosion in reinforced concrete structures. This two-piece system first allows the galvanic corrosion current between anodic (with chlorides) and cathodic (without chlorides) zones to be measured, which was impossible to do in tests performed on single bar specimens.

The first results presented in this paper are limited to CEM I samples. These preliminary results highlight the influence of chloride content and steel surface on the corrosion rate. It was deduced that an increase in chloride levels led to an increase in the number of "corroded sites", leading to an increase in the galvanic currents measured. The role of mill scale on corrosion kinetics was also highlighted when comparing results obtained with 4 different steel types. The similarity of behaviour between as received steel, ARS, and cleaned pre-oxidized steel, CSP, may be attributed to the resemblance in the composition of the mill scale layer found on the ARS and the layer of corrosion products formed on CSP. The non-uniformity of these layers may justify the presence of some irregular current densities obtained. The corrosion kinetics obtained in the absence of mill scale (cleaned steel specimens) were relatively weak. This phenomenon may be attributable to a less porous passive film making it harder for the chloride ions to diffuse through.

With this test, it is possible to determine the chloride threshold values initiating corrosion and also the corrosion current during the propagation stage. The criteria for corrosion initiation was set as a limiting galvanic current called threshold corrosion current. This current is defined as a current that is independent of the cathode/anode surface ratio and was found equal to 3 µA. This indicates that the

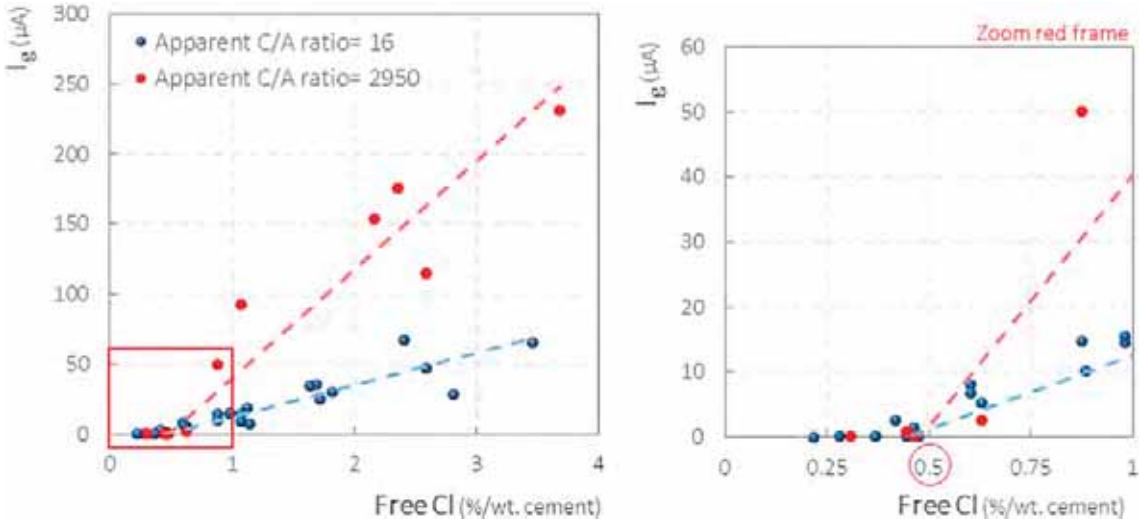


**Fig. 21.** Ig measured for different free chloride contents for apparent C/A ratios of 16 and 2950.

corrosion initiation must be linked to a threshold current that is not affected by surface ratio between cathode and anode. The total and free chloride threshold values for CEMI in case of ARS, CSPT and CSPH specimens are respectively 0.6 and 0.5%/wt. cement. However, in case of cleaned steel, the free Cl content is 1.9%/wt. cement corresponding to a total chloride content of 2%/wt. cement.

Furthermore, it was confirmed that an increase in the C/A ratio led to an increase in the galvanic current, which is in agreement with the fundamental galvanic coupling concepts. The experimental results also showed that the current growth rate decreased with increasing cathodic surface area, which could mean that the current would reach its maximum value and stabilize for a given C/A ratio.

With this method, it is also possible to compare different types of binders which will be the next step of the study.

## Acknowledgements

This work was supported by the ANR MODEVIE project, grant ANR-14-CE22-0018 of the French Agence Nationale de la Recherche and by the French National Federation of Public Works (FNTP).

## References

[1] U. Angst, B. Elsener, C.K. Larsen, Ø. Vennesland, Critical chloride content in reinforced concrete — a review, Cem. Concr. Res. 39 (2009) 1122–1138.
[2] M. Stern, A.L. Geary, Electrochemical Polarization I. A Theoretical Analysis of the Shape of Polarization Curves, 104 (1957).
[3] C. Andrade, C. Alonso, J. Gulikers, R. Polder, R. Cigna, Ø. Vennesland, et al., Test Methods for On-site Corrosion Rate Measurement of Steel Reinforcement in Concrete by Means of the Polarization Resistance Method, 37 (2004).
[4] A. Clément, S. Laurens, G. Arliguie, F. Deby, Numerical Study of the Linear Polarisation Resistance Technique Applied to Reinforced Concrete for Corrosion Assessment, 16 (2012).
[5] C. Wagner, W. Traud, Über die Deutung von Korrosionsvorgängen durch Überlagerung von elektrochemischen Teilvorgängen und über die Potentialbildung an Mischelektroden, Zeitschrift für Elektrochemie und angewandte physikalische Chemie, 44 (1938), pp. 391–402.
[6] A. Sagues, S.C. Kranc, On the Determination of Polarization Diagrams of Reinforcing Steel in Concrete, 48 (1992).
[7] J. Gulikers, Numerical Simulation of Corrosion Rate Determination by Linear Polarization, (2015).
[8] S. Laurens, P. Hénocq, N. Rouleau, F. Deby, E. Samson, J. Marchand, et al., Steady-state polarization response of chloride-induced macrocell corrosion systems in steel reinforced concrete — numerical and experimental investigations, Cem. Concr. Res. 79 (2016) 272–290.
[9] B. Elsener, Macrocell Corrosion of Steel in Concrete - Implications for Corrosion Monitoring, 24 (2002).
[10] U. Angst, M. Büchler, On the Applicability of the Stern–Geary Relationship to Determine Instantaneous Corrosion Rates in Macro-cell Corrosion, 66 (2014).
[11] R. Francois, S. Laurens, F. Deby, Corrosion and Its Consequences for Reinforced Concrete Structures, Elsevier, 2018.
[12] B. Elsener, C. Andrade, J. Gulikers, R. Polder, M. Raupach, Half-cell Potential Measurements – Potential Mapping on Reinforced Concrete Structures, 36 (2003).
[13] R. Francois, G. Arliguie, D. Bardy, Electrode Potential Measurements of Concrete Reinforcement for Corrosion Evaluation, 24 (1994).
[14] G01 Committee, Test Method for Corrosion Potentials of Uncoated Reinforcing Steel in Concrete, ASTM International.
[15] L. Tang, J.M. Frederiksen, U. Angst, R. Polder, M. Cruz Alonso, B. Elsener, et al., Experiences From RILEM TC 235-CTC in Recommending a Test Method for Chloride Threshold Values in Concrete, 3 (2018).
[16] U. Angst, C. Boschmann, M. Wagner, B. Elsener, Experimental Protocol to Determine the Chloride Threshold Value for Corrosion in Samples Taken From Reinforced Concrete Structures, (2017).
[17] J. Pacheco, R. Polder, Critical Chloride Concentrations in Reinforced Concrete Specimens With Ordinary Portland and Blast Furnace Slag Cement, 61 (2016).
[18] P.V. Nygaard, M. Geiker, A Method for Measuring the Chloride Threshold Level Required to Initiate Reinforcement Corrosion in Concrete, 38 (2005).
[19] V. Garcia, R. Francois, M. Carcasses, P. Gegout, Potential Measurement to Determine the Chloride Threshold Concentration That Initiates Corrosion of Reinforcing Steel Bar in Slag Concretes, 47 (2014).
[20] P. Sandberg, Chloride Initiated Reinforcement Corrosion in Marine Concrete, Division of Building Materials, LTH, Lund University, 1998.
[21] U. Angst, B. Elsener, C. Larsen, Ø. Vennesland, Chloride Induced Reinforcement Corrosion: Electrochemical Monitoring of Initiation Stage and Chloride Threshold Values, 53 (2011).
[22] N.R. Jarrah, O. Al-Amoudi, M. Maslehuddin, O.A. Ashiru, A. Ibrahim Al-Mana, Electrochemical Behaviour of Steel in Plain and Blended Cement Concretes in Sulphate and/or Chloride Environments, 9 (1995).
[23] V. Bouteiller, C. Cremona, V. Baroghel-Bouny, A. Maloula, Corrosion Initiation of Reinforced Concretes Based on Portland or GGBS Cements: Chloride Contents and Electrochemical Characterizations Versus Time, 42 (2012).
[24] ISO 8407, Corrosion of Metals and Alloys — Removal of Corrosion Products From Corrosion Test Specimens, (2009).
[25] NF EN 14629, Produits et systèmes pour la protection et la réparation des structures en béton - Méthodes d'essais - Mesurage du taux de chlorure d'un béton durci, (2007).
[26] H. Hornain, GranDuBé: grandeurs associées à la durabilité des bétons, Presses des Ponts, 2007.
[27] P. Ghods, O. Isgor, G.A. McRae, J. Li, G.P. Gu, Microscopic investigation of mill scale and its proposed effect on the variability of chloride-induced depassivation of carbon steel rebar, Corr. Sci. 53 (2011) 946–954.
[28] E. Mahallati, M. Saremi, An Assessment on the Mill Scale Effects on the Electrochemical Characteristics of Steel Bars in Concrete under DC-Polarization, 36 (2006).
[29] A.T. Horne, I.G. Richardson, R.M.D. Brydson, Quantitative Analysis of the Microstructure of Interfaces in Steel Reinforced Concrete, 37 (2007).
[30] D. Neff, S. Réguer, L. Bellot-Gurlet, P. Dillmann, R. Bertholon, Structural Characterisation of Corrosion Products on Archaeological Iron: An Integrated Analytical Approach to Establish Corrosion Forms, 35 (2004).
[31] D.L. de Faria, S. Venáncio Silva, M.T. de Oliveira, Raman Microspectroscopy of Some Iron Oxides and Oxyhydroxides, 28 (1997).
[32] S. Réguer, D. Neff, L. Bellot-Gurlet, P. Dillmann, Deterioration of Iron Archaeological Artefacts: Micro-Raman Investigation on Cl-containing Corrosion Products, 38 (2007).
[33] D. Neff, P. Dillmann, L. Bellot-Gurlet, G. Beranger, Corrosion of Iron Archaeological Artefacts in Soil: Characterisation of the Corrosion System, 47 (2005).
[34] M. Hanesch, Raman Spectroscopy of Iron Oxides and (Oxy)Hydroxides at Low Laser Power and Possible Applications in Environmental Magnetic Studies, 177 (2009).
[35] J. Warkus, M. Raupach, Modelling of reinforcement corrosion – geometrical effects on macrocell corrosion, Mater. Corros. 61 (2009).

# Appendix Paper I

## SEM observation, BSE analysis, and Raman spectroscopy

Appendix in: Study of the initiation and propagation phases of chloride induced corrosion in reinforced concrete structures

Realized by: Chantal Chalhoub

Thesis for the degree of Philosophiæ doctor

Université Toulouse 3 Paul Sabatier (UT3 Paul Sabatier)

Laboratoire Matériaux et Durabilité des Constructions de Toulouse

Appendix Paper I

# Contents

# 1. Introduction

This report presents a part of the results of a Scanning Electron Microscope (SEM) observation, BSE analysis, and Raman spectroscopy that were achieved during the thesis.

These analyses were conducted during the work achieved in [Paper I]. The results correspond to the mortar formulation M1-055 which is made with 100 % of CEM I with a w/b ratio of 0.55.

In [Paper I], different steel surface conditions were prepared :

- As received steel annotated “ARS”
- Cleaned steel pre-oxidized with high temperature annotated “CSPT”
- Cleaned steel pre-oxidized in humid environment annotated “CSPH”
- Cleaned steel annotated “CS”

## 2. SEM observation

In this section, some microscopic observations achieved with the Scanning Electron Microscope (SEM) JEOL JSM 6380 are presented for several anodes with different types of steel surface conditions.

### Anode samples with cleaned pre-oxidized steel in a humid environment

CSPH 3

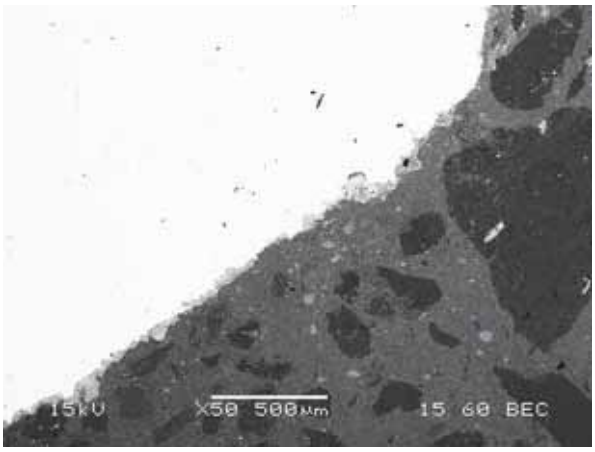


CSPH 4

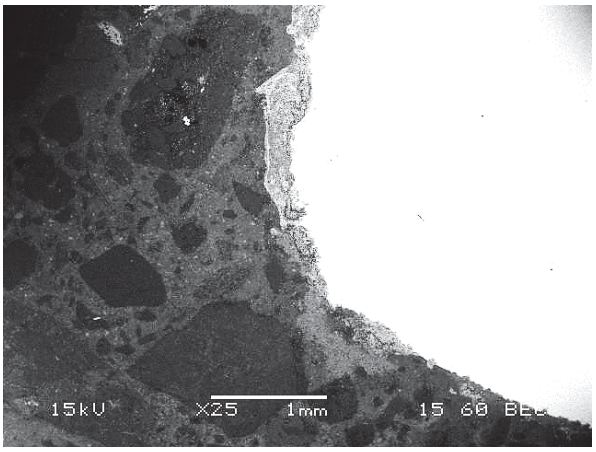


CSPH 5

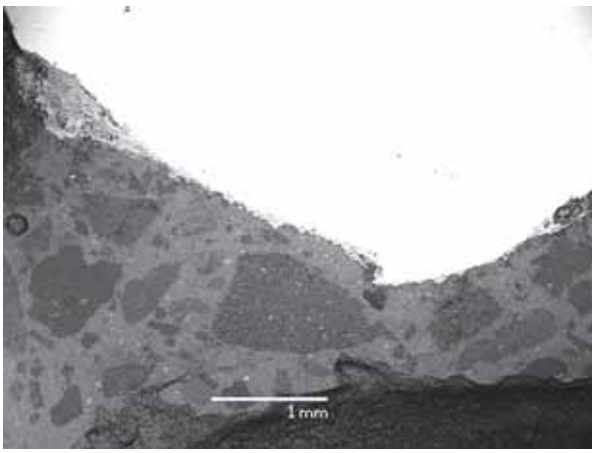


CSPH 6

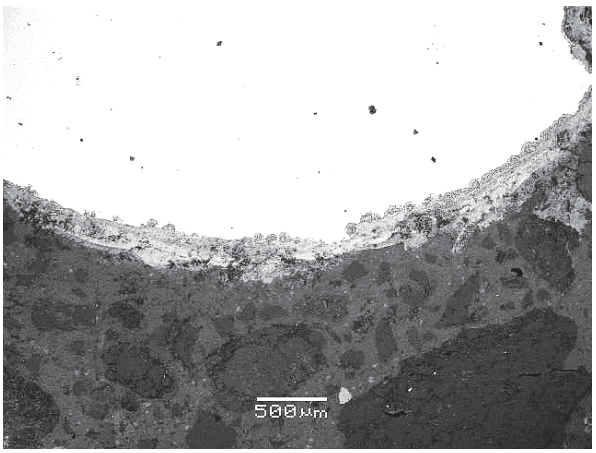


*Fig. 1. Example of SEM observation of CSPH anode samples*

## Anode samples with cleaned steel

CS 4

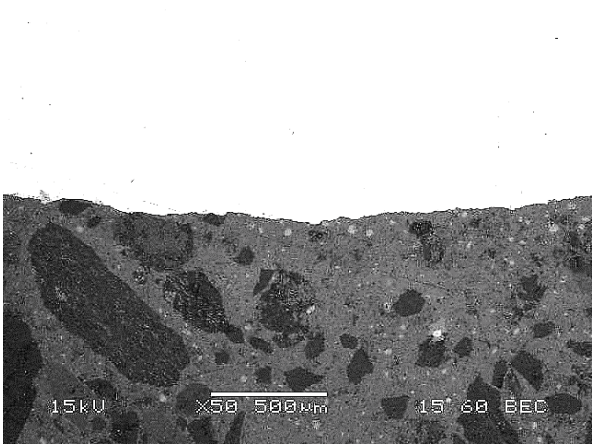


CS 5

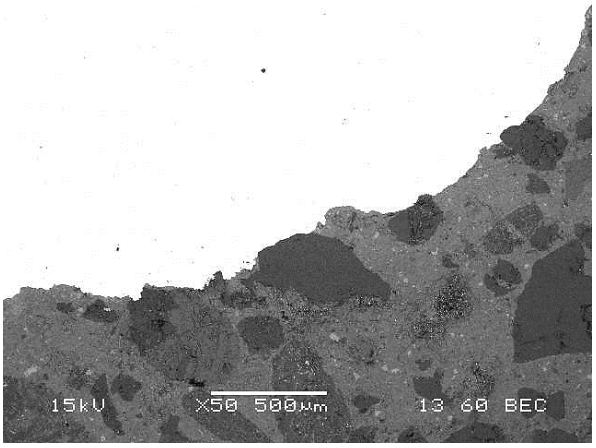


CS 9

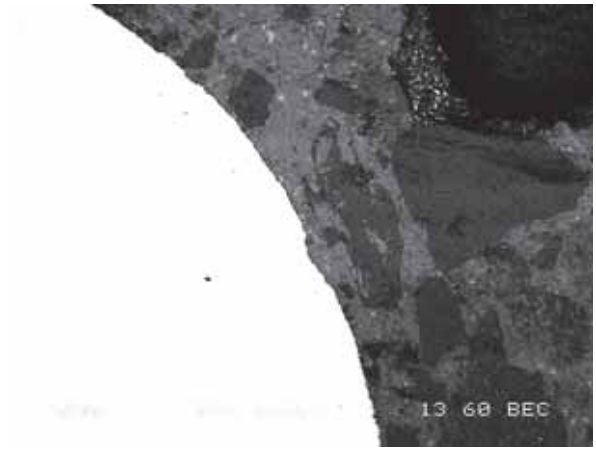


CS 10

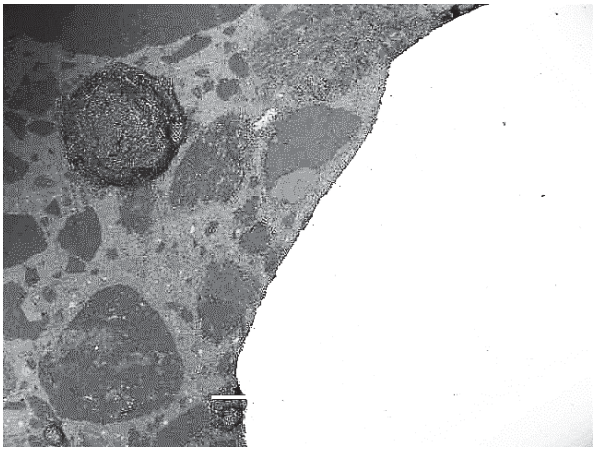

*Fig. 2. Example of SEM observation of CS anode samples*

## 3. BSE analysis

This section presents some results of the Scanning Electron Microscope (SEM) JEOL JSM 6380 operating in Backscattered Electron (BSE) mode which was used to investigate the steel-mortar interface. A Bruker Energy Dispersive Spectrum analyzer (EDS) was used to quantify Iron (Fe in blue), Oxygen (O in red) and Chloride (Cl in green) in the observation zones along an analytical line. The analysis is then displayed as a graph in which the horizontal axis represents the distance from the starting point of the analytical line and the vertical axis characterizes the normalized mass percentages reflecting the Fe, O and Cl content. BSE Mapping was also achieved on some samples.

### Anode samples with as received steel

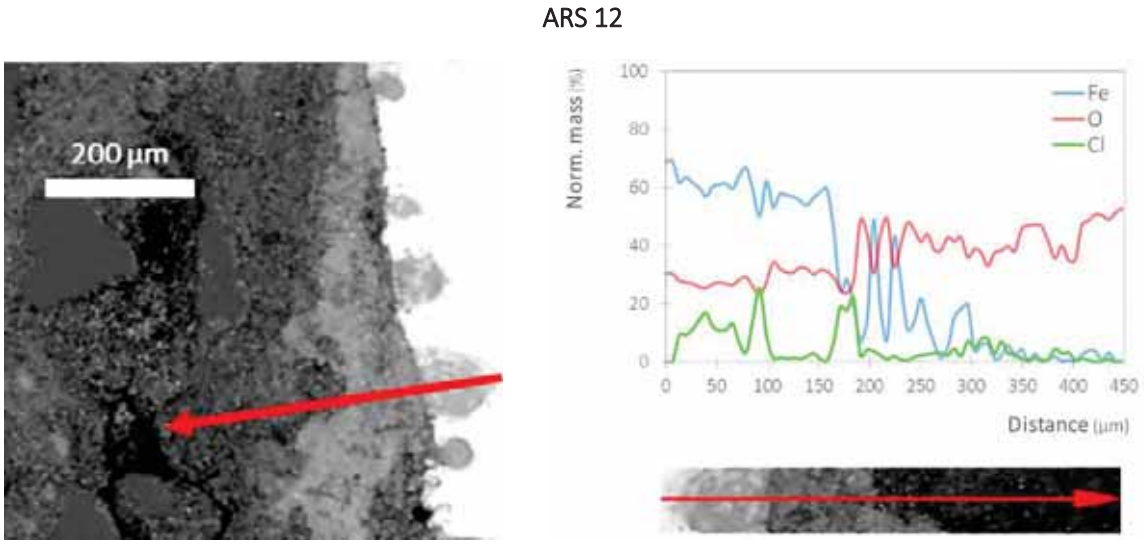


*Fig. 3. Example of SEM observation and BSE analysis on ARS anode samples*

### Anode samples with cleaned steel pre-oxidized with high temperature

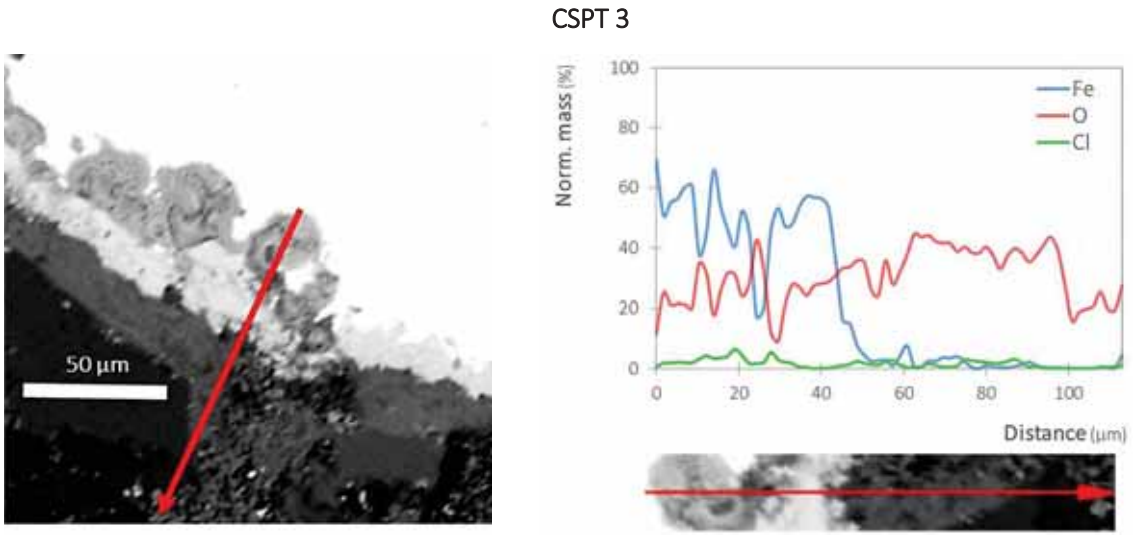


*Fig. 4. Example of SEM observation and BSE analysis of CSPT anode samples*

## Anode samples with cleaned pre-oxidized steel in a humid environment

### CSPH 3

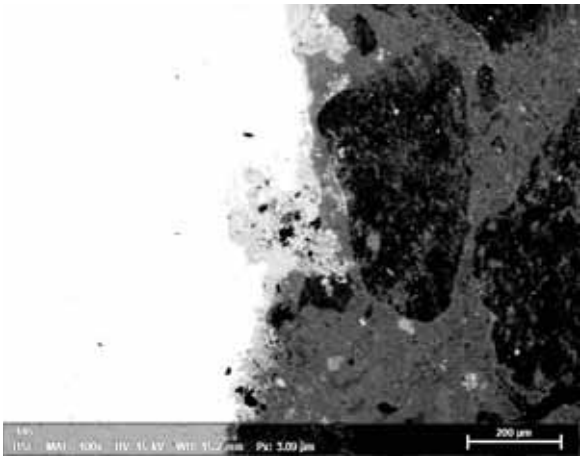

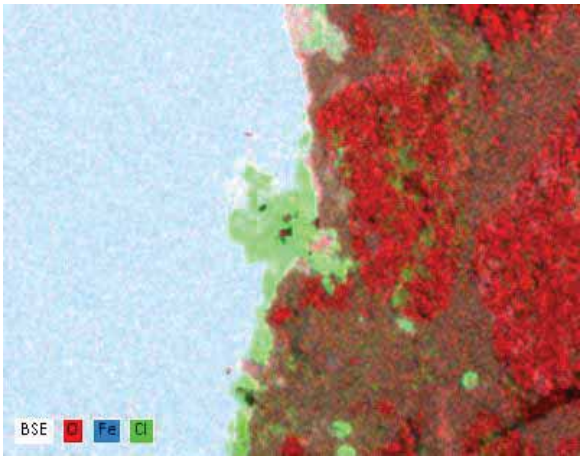


### CSPH 4

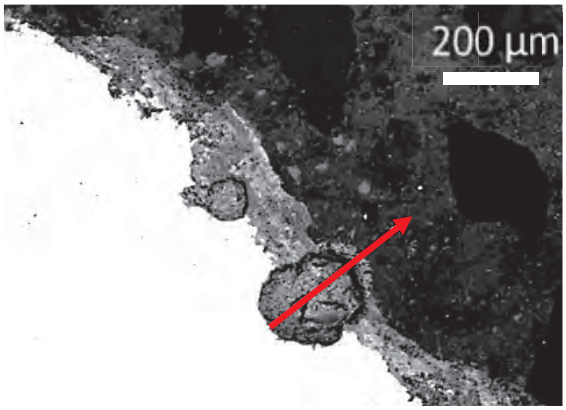


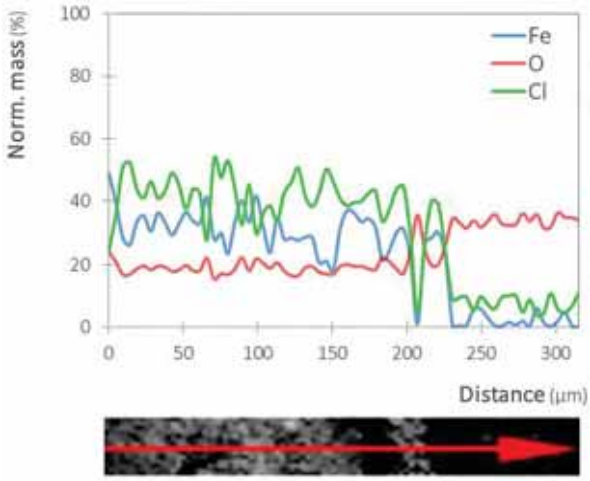


### CSPH 5

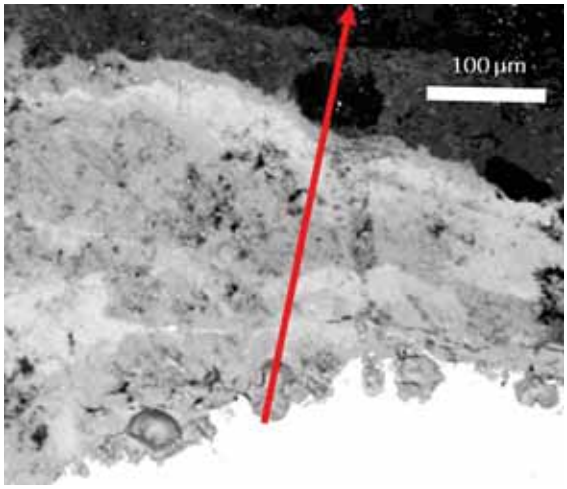


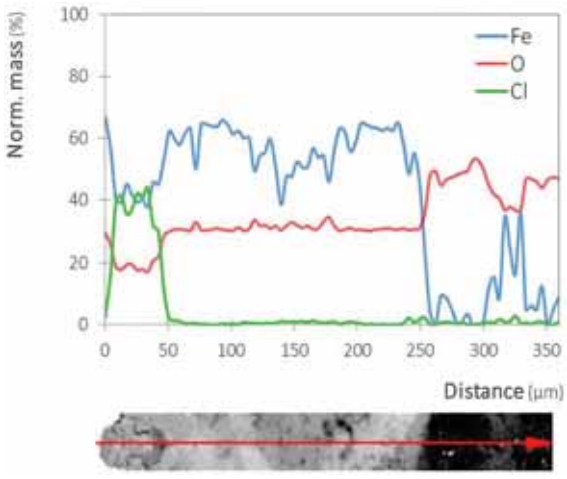

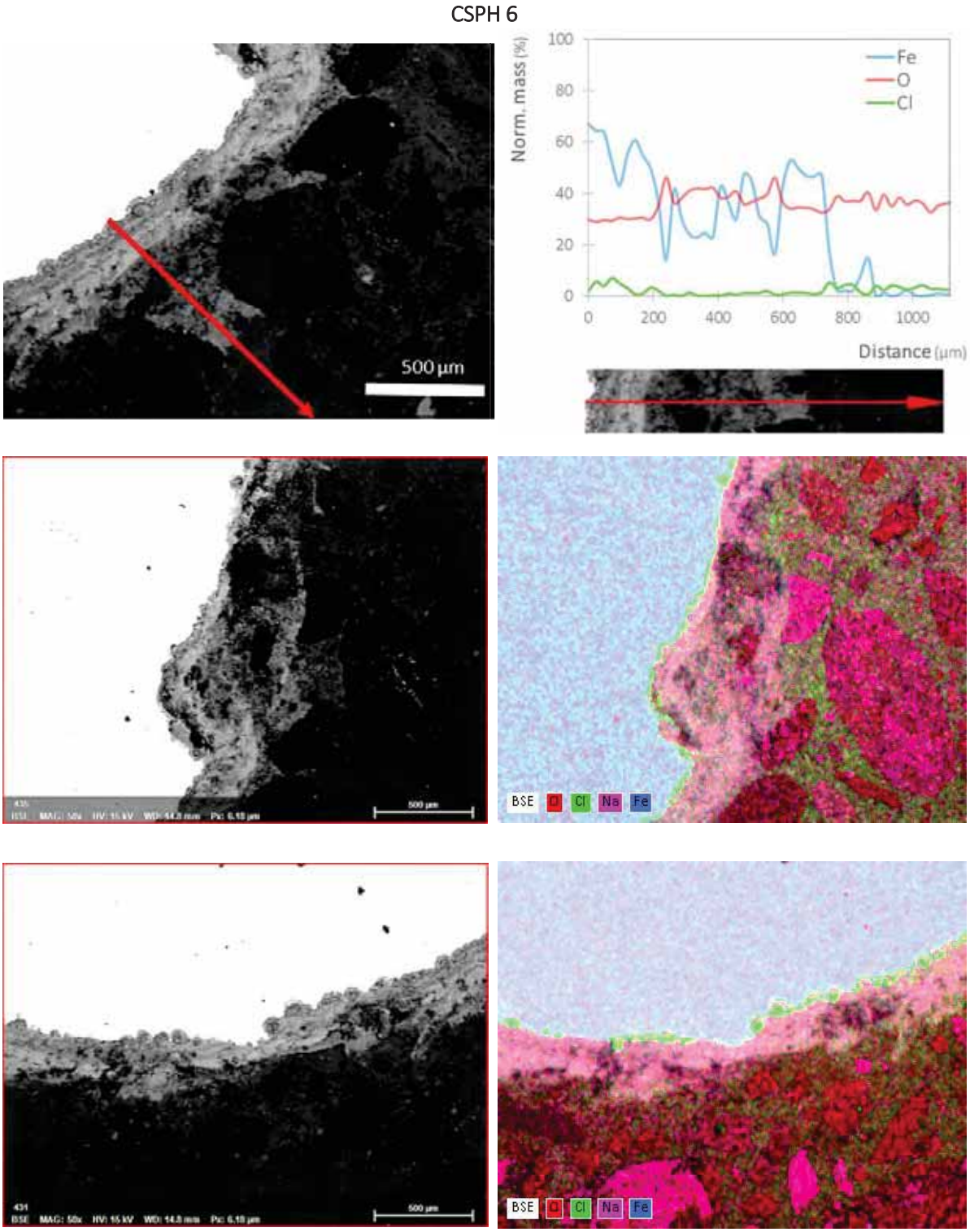


*Fig. 5. Example of SEM observation and BSE analysis of CSPH anode samples*

## Anode samples with cleaned steel

CS 2

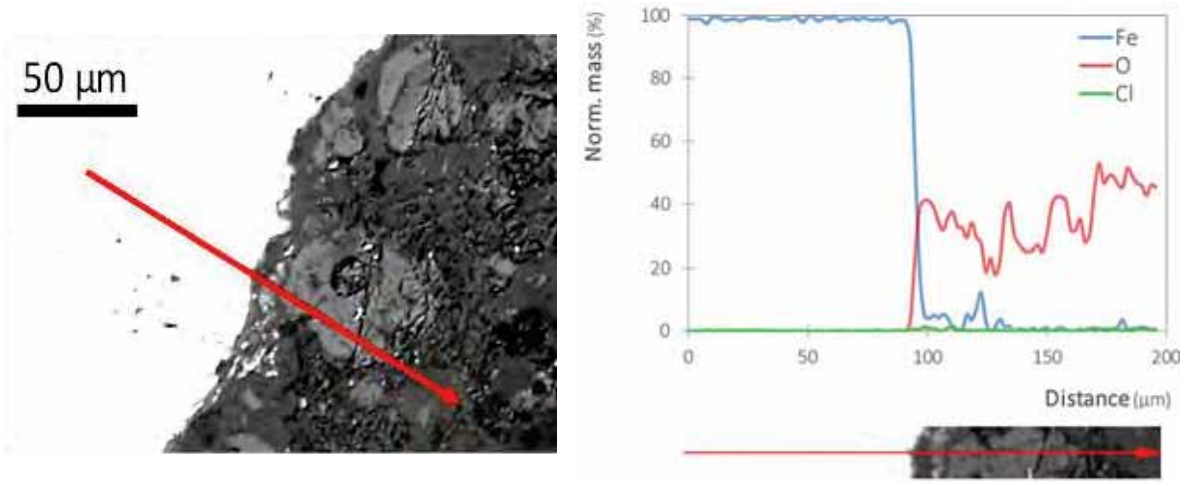


CS 3

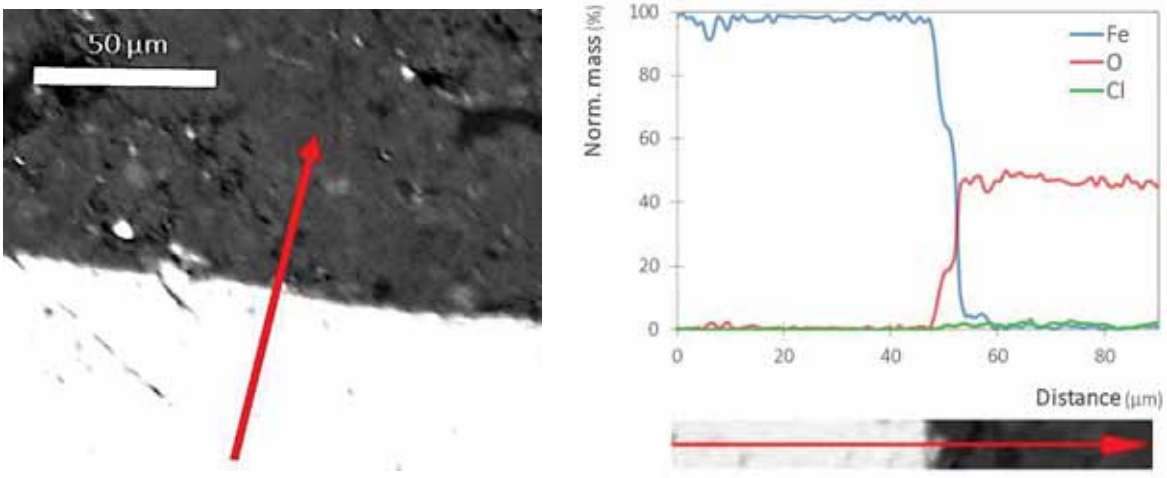


CS 7

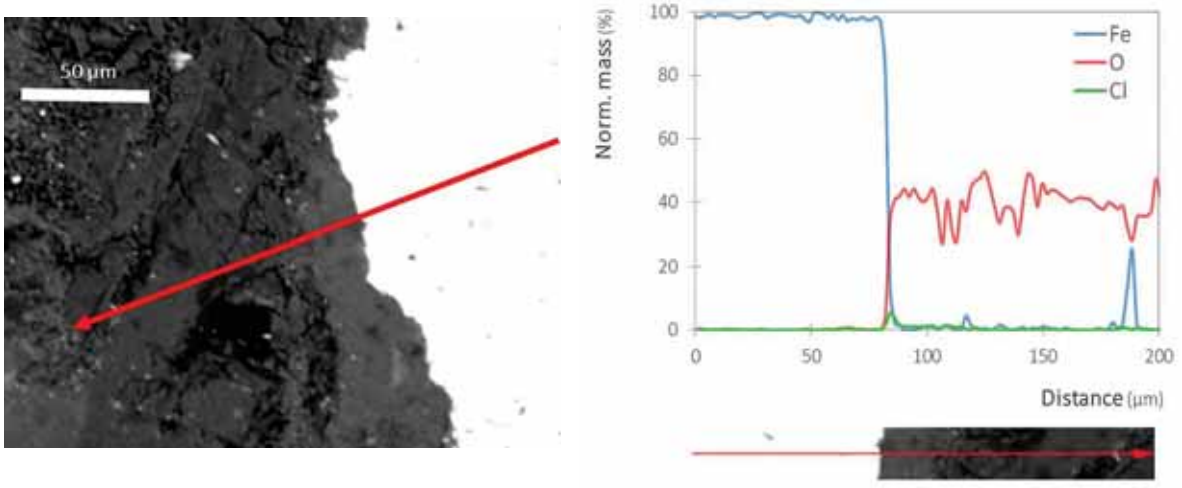

CS 8

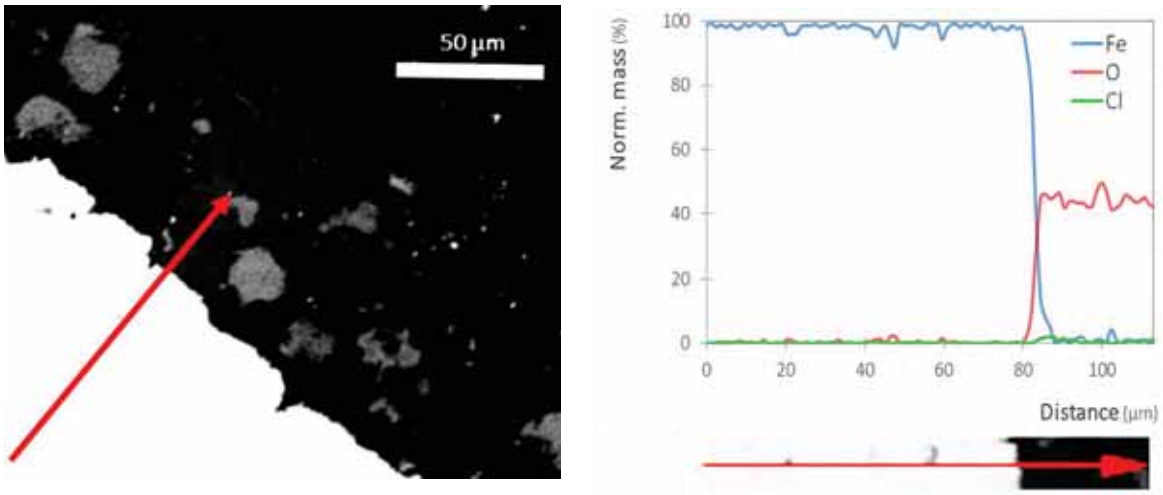


*Fig. 6. Example of SEM observation and BSE analysis of CS anode samples*

## 4. Raman spectroscopy

The corrosion products present at the steel/mortar interface were identified by Raman micro-spectroscopy with a Horiba spectrometer (Fig. 7) at the CEA lab at Saclay, France. The microanalyses in this study were performed with the 100x objective using the green visible radiation wavelength of 532 nm. Over the entire optical path and the detection system, the spectral resolution was about 2 $cm^{-1}$. Spectra were calibrated by means of a silicon crystal. The excitation laser power was filtered at 1% (acquisition time: 300s) then 10% (acquisition time: 20s) in order to avoid potential thermal transformation of sensitive iron oxides and (oxy)hydroxide [1,2]. Finally, the spectra were acquired and processed using the LabSpec software and the phases were identified by comparison with spectra existing in the literature [1,3–5].

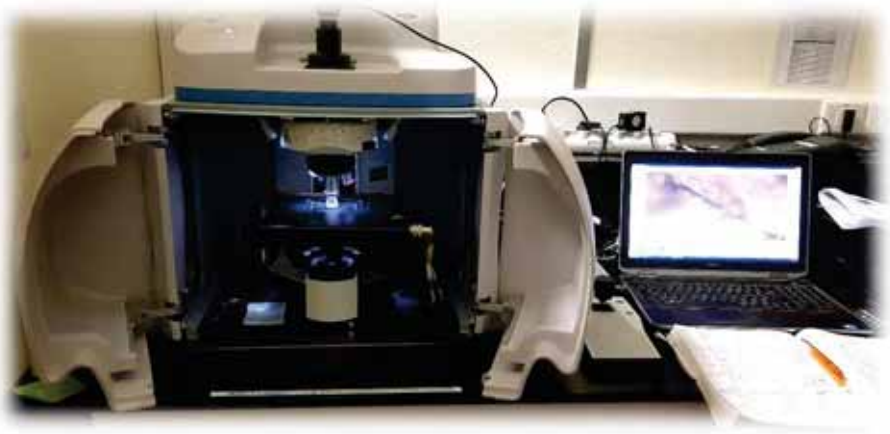

*Fig. 7. Raman micro-spectroscopy with a Horiba spectrometer*

Table 1 shows a list of wavenumber that characterizes different iron oxides and (oxy)hydroxides according to [1,3–5] and their characteristics according to [6–8]. The wavenumbers with the biggest intensity are shown in bold in each corrosion product type.

*Table 1. List of wavenumber of different corrosion products*

| Corrosion product type | Chemical Formula | Wavenumbers | Color |
|---|---|---|---|
| Goethite | $\alpha - FeOOH$ | 247, **301**, **388,** 416, 482, 552, 685, 1003 | Yellow-brown |
| Lepidocrocite | $\gamma - FeOOH$ | 223, **257,** 284, 310, 355, 380, 532, 657, 1300 | Orange |
| Hematite | $\alpha - Fe_2O_3$ | **223,** 241, **289,** 404, 494, 604, 1310 | Black; sliver-gray; brown, red |
| Maghemite | $\gamma$-$Fe_2O_3$ | 350, 512, **670, 710,** 1400 | Brown, bluish-black; brown to yellow; white to bluish-gray |
| Magnetite | $Fe_3O_4$ | 308, 542, **669** | Dark gray |
| Ferrihydrite | $5Fe_2O_3.9H_2O$ | 370, 510, **710** | Dark brown Yellow-brown |
| Akaganeite | $\beta - FeOOH$ | 310, **390**, 490, 540, 610, **720**, 1300-1500, 3227-3509 | Red-brown |
| Iron hydroxychloride | $\beta - Fe_2(OH)_3Cl$ | **127**, **160**, 200, 318, **423**, 618, 804, 3552, 3564 | Light grey-blue color |

## CSPT2

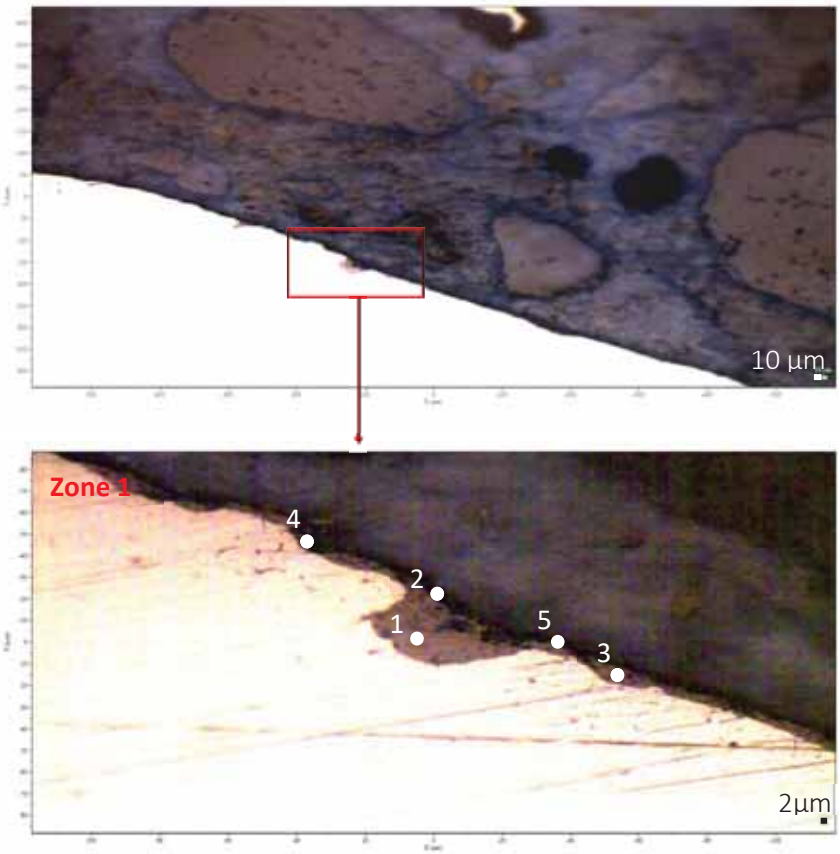


**Zone 1:**

1: 300, 548, **669**
: Magnetite

2: **225**, **291**, 408, 1317
: Hematite

3: 300, 540, **669**
: Magnetite

4: 300, 540, **669**
: Magnetite

5: **223**, **291**, 407, 544, 669, 1319
: Hematite

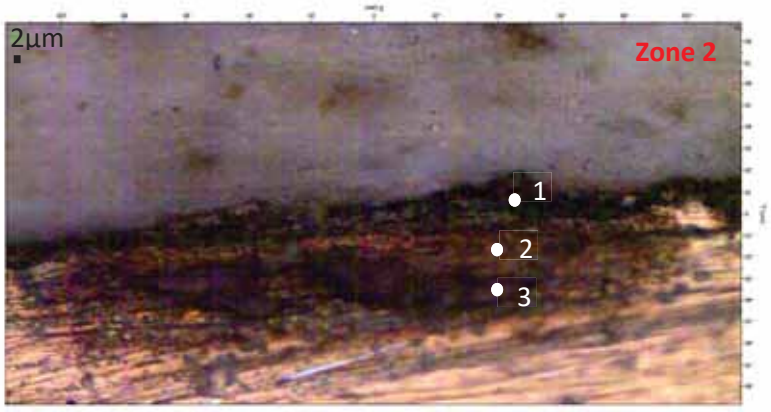


**Zone 2:**

1: 309, 540, **667**
: Magnetite

2: 147, 346, 510, **710**
: Ferrihydrite

3: 147, 383, 510, **710**
: Ferrihydrite

## CSPT3

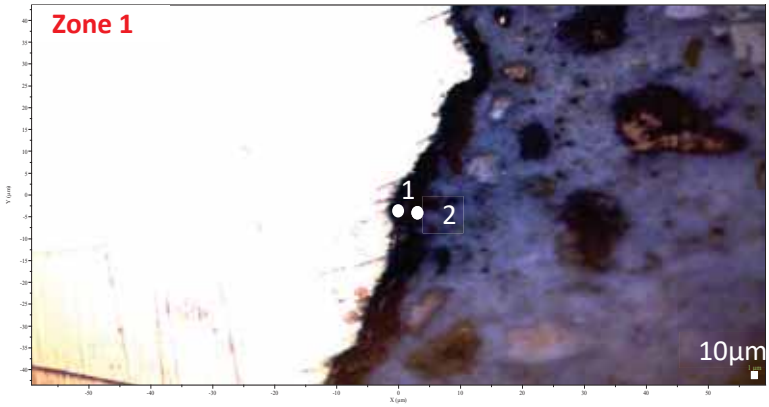


Zone 1:

1: 313, 540, **669**
: Magnetite

2: **224**, 247, **292**, 410, 498, 612, 667, 1325
: Hematite

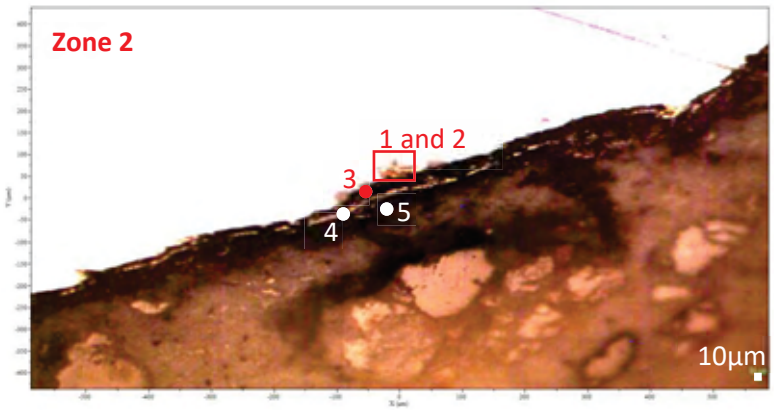


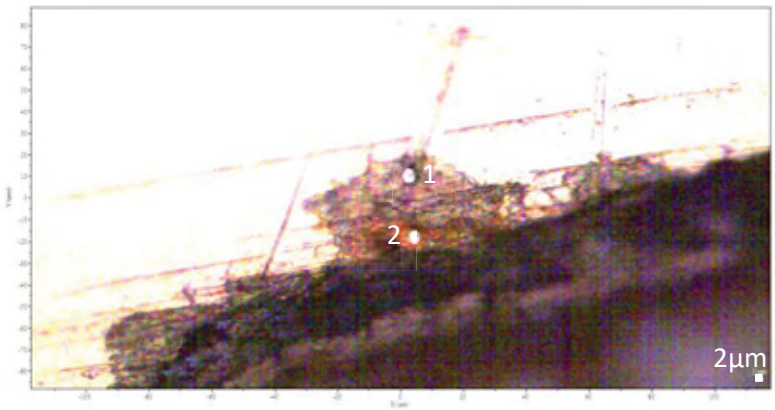


Zone 2:

1: 134, 188,215, **423**, **504**, **3411**
: Possible presence of Iron hydroxychloride

2: 319, **399**, 497,539, 710, 1379, **2930**
: Akaganeite

3: 400, 511, **680**
: Magnetite

4: 307, 540, **667**
: Magnetite

5: **220**, 317, 518, 696, 1365
: Hematite

## CSPH6

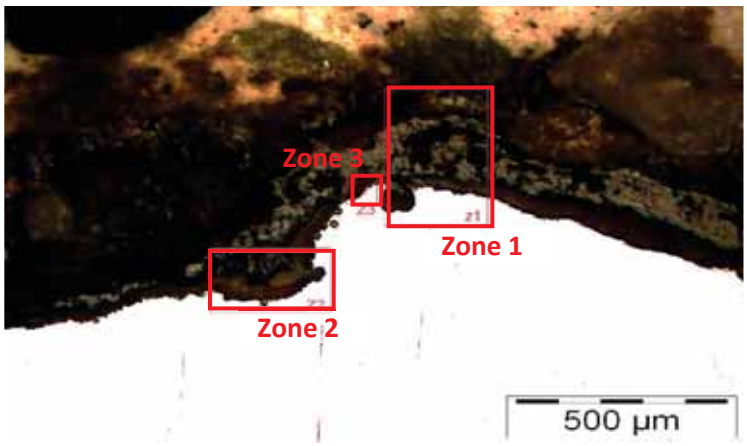


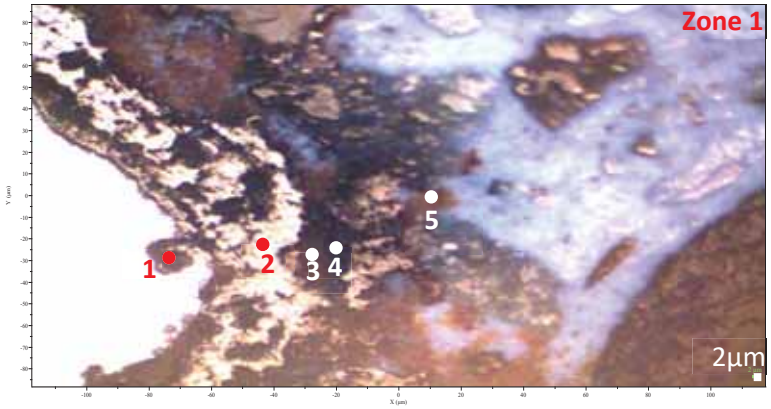


Zone 1:

1: 348, 511, **694**
: Ferrihydrite

2: 319, 537, **673**
= Magnetite

3: 319, 540, **669**
: Magnetite

4: 317, 539, **669**
: Magnetite

5: 126, 202, 352, 383, 395, **463**
: unidentified product

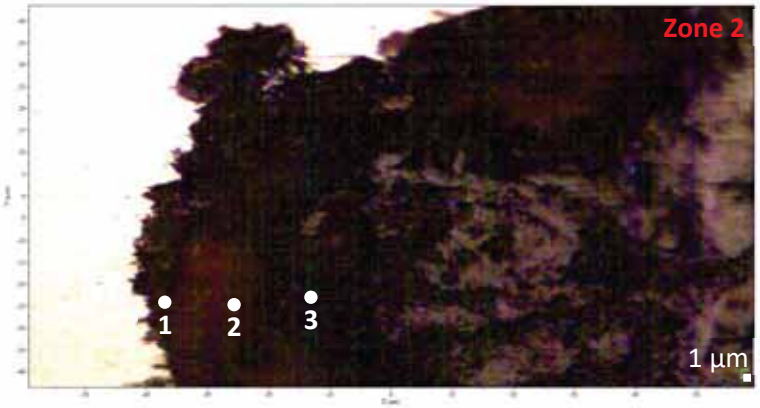


Zone 2:

1: 138, 318, 400, **717**, 1401, 1586
: Akaganeite + unidentified product

2: 135, **307**, **383**, 494, 534, 606, **717**, 1387
: Akaganeite

3: **319**, 381, 540, **667**, 719, 1400
: Akaganeite + Magnetite

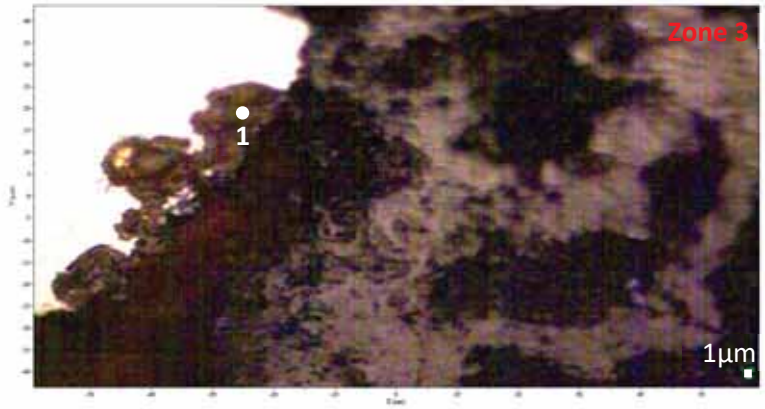


## Zone 3:

1: 138, **307**, **386**, 494, 534, 607, **717**, 1368
: Akaganeite

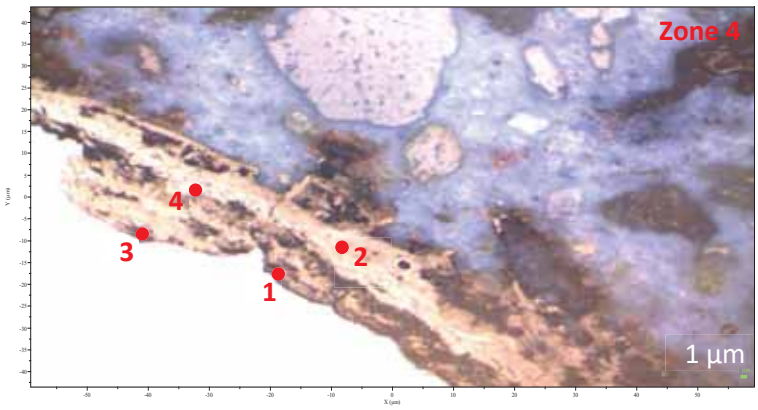


## Zone 4:

1: 310, **389**, 492, 540, 611, **720**, 1405
: Akaganeite

2: 320, 340, 496, **669**, 1400
: Magnetite + unidentified product

3: 317, **387**, 540, 697, **720**, 1384
: Akaganeite

4: 320, 340, 540, **669**
: Magnetite

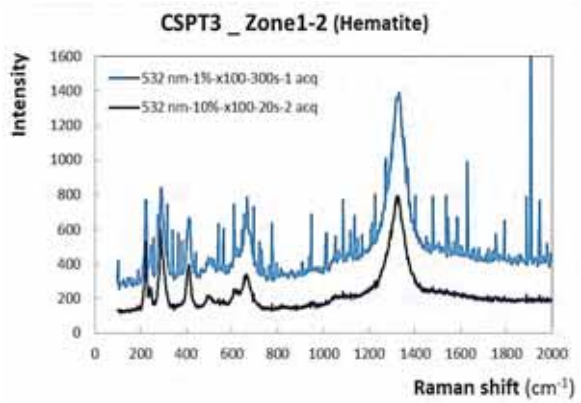
CSPT3 _ Zone1-2 (Hematite)
532 nm-1%-x100-300s-1 acq
532 nm-10%-x100-20s-2 acq
Intensity
Raman shift (cm-1)

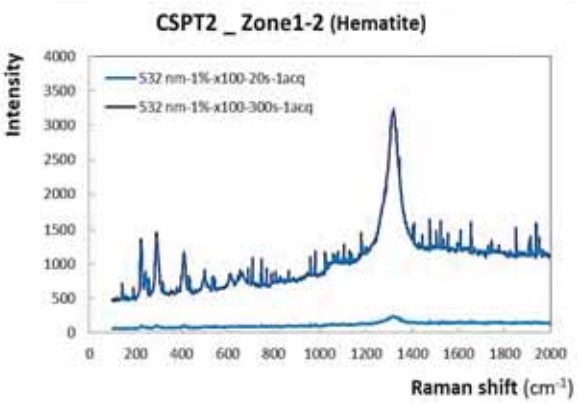
CSPT2 _ Zone1-2 (Hematite)
532 nm-1%-x100-20s-1acq
532 nm-1%-x100-300s-1acq
Intensity
Raman shift (cm-1)

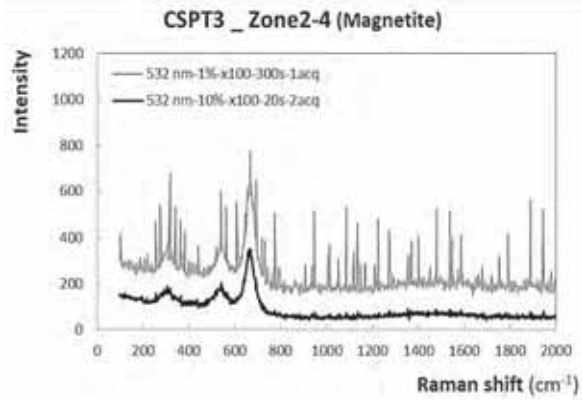
CSPT3 _ Zone2-4 (Magnetite)
532 nm-1%-x100-300s-1acq
532 nm-10%-x100-20s-2acq
Intensity
Raman shift (cm-1)

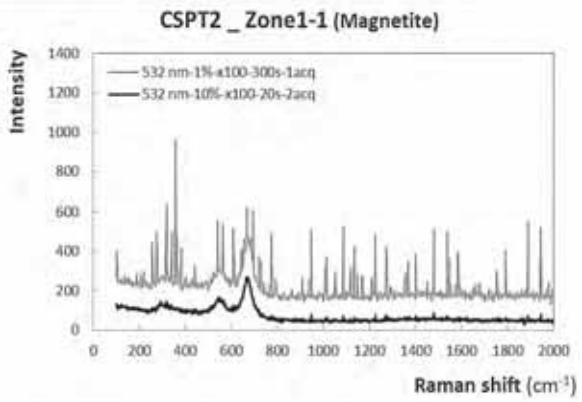
CSPT2 _ Zone1-1 (Magnetite)
532 nm-1%-x100-300s-1acq
532 nm-10%-x100-20s-2acq
Intensity
Raman shift (cm-1)

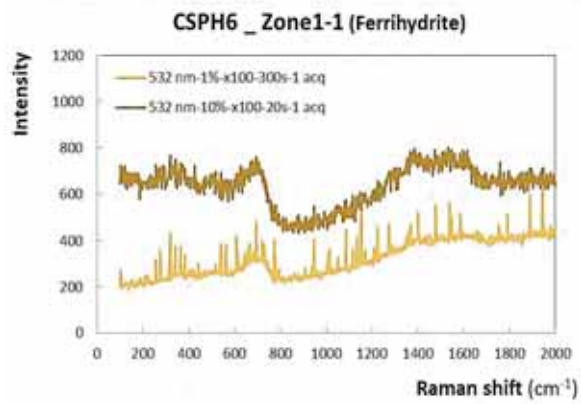
CSPH6 _ Zone1-1 (Ferrihydrite)
532 nm-1%-x100-300s-1 acq
532 nm-10%-x100-20s-1 acq
Intensity
Raman shift (cm-1)

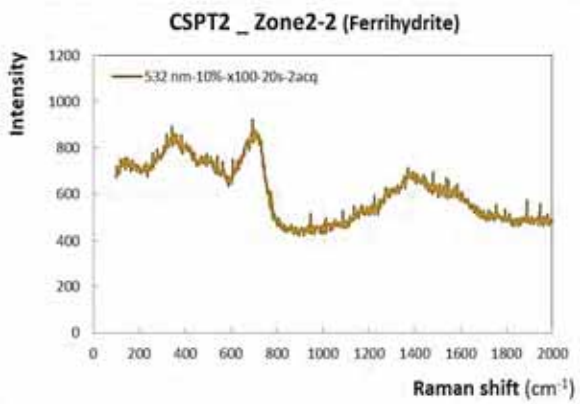
CSPT2 _ Zone2-2 (Ferrihydrite)
532 nm-10%-x100-20s-2acq
Intensity
Raman shift (cm-1)

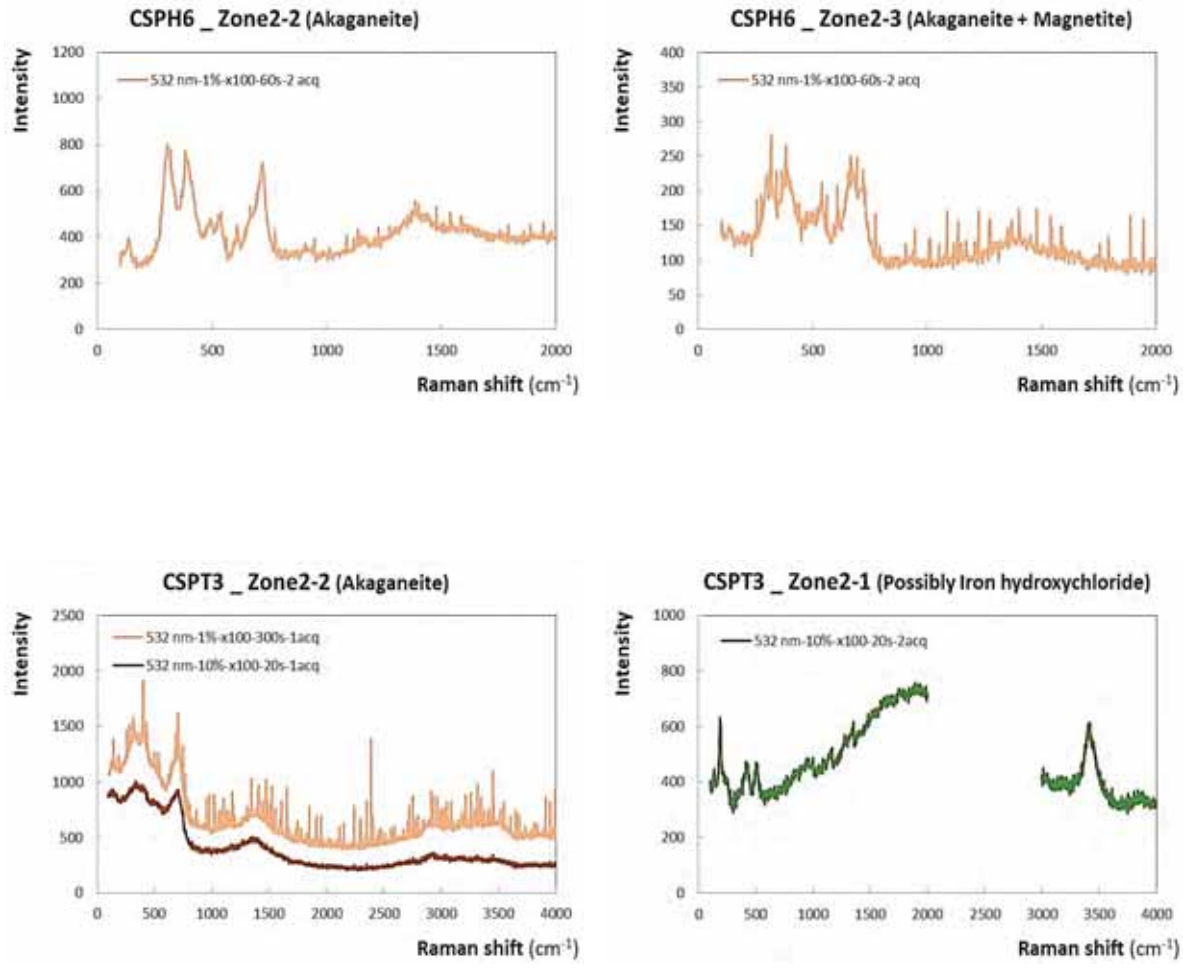


*Fig. 8. Some Raman spectra of corrosion products obtained on specimens*

## 5. References


[1] D. Neff, S. Réguer, L. Bellot-Gurlet, P. Dillmann and R. Bertholon, *Structural Characterisation of Corrosion Products on Archaeological Iron: An Integrated Analytical Approach to Establish Corrosion Forms*, Vol. 35, 2004.

[2] D. L. a. de Faria, S. Venáncio Silva and M. T. de Oliveira, *Raman Microspectroscopy of Some Iron Oxides and Oxyhydroxides*, Vol. 28, 1997.

[3] S. Réguer, D. Neff, L. Bellot-Gurlet and P. Dillmann, *Deterioration of Iron Archaeological Artefacts: Micro-Raman Investigation on Cl-Containing Corrosion Products*, Vol. 38, 2007.

[4] D. Neff, P. Dillmann, L. Bellot-Gurlet and G. Beranger, *Corrosion of Iron Archaeological Artefacts in Soil: Characterisation of the Corrosion System*, Vol. 47, 2005.

[5] M. Hanesch, *Raman Spectroscopy of Iron Oxides and (Oxy)Hydroxides at Low Laser Power and Possible Applications in Environmental Magnetic Studies*, Vol. 177, 2009.

[6] R.M. Cornell and U. Schwertmann, *The Iron Oxides: Structure, Properties, Reactions, Occurrences and Uses, 2nd, Completely Revised and Extended Edition*, Vol. 703 Pages, 2003.

[7] B. Jegdić, S. Polić-Radovanović, S. Ristić and A. Alil, *Corrosion processes, nature and composition of corrosion products on iron artefacts of weaponry*, Scientific Technical Review 61 (2011), pp. 50–56.

[8] P. Refait and J.-M.R. Génin, *The mechanisms of oxidation of ferrous hydroxychloride β-Fe2(OH)3Cl in aqueous solution: The formation of akaganeite vs goethite*, Corrosion Science 39 (1997), pp. 539–553.

# Paper II

**Macrocell corrosion of steel in concrete: characterization of anodic behavior in relation to the chloride content**

**Chantal Chalhoub*, Raoul François, David Garcia, Stephane Laurens, Myriam Carcasses**

**Materials and corrosion (2020)**

Received: 20 November 2019 | Accepted: 2 March 2020

DOI: 10.1002/maco.201911398

ARTICLE

Materials and Corrosion

# Macrocell corrosion of steel in concrete: Characterization of anodic behavior in relation to the chloride content

**Chantal Chalhoub** | **Raoul François** | **David Garcia** | **Stephane Laurens** | **Myriam Carcasses**

Laboratoire Matériaux et Durabilité des Constructions (LMDC), Institut National des Sciences Appliquées (INSA), Université Paul Sabatier (UPS), Université de Toulouse, Toulouse, France

**Correspondence**
Chantal Chalhoub, LDMC, INSA-UPS Génie Civil, 135, Avenue de Rangueil 31400 Toulouse 31062, France.
Email: chantal.chalhoub@insa-toulouse.fr

**Funding information**
Agence Nationale de la Recherche, ANR MODEVIE Project; French National Federation of Public Works

**Abstract**

This study presents the determination of electrochemical properties of active steel in mortar, based on inverse numerical modeling that focuses on their dependency on chloride content. An experimental campaign, consisting of galvanic coupling tests between anode samples contaminated with different chloride concentrations and cathode samples without chlorides, was carried out. Cathode polarization tests allowed for directly determining passive steel electrochemical parameters. Anode polarization tests coupled with a numerical optimization were then performed for quantifying active steel parameters and focusing on chloride's effect on the iron anodic Tafel coefficient. Furthermore, the steel electrochemical properties were successfully used as input parameters to model the galvanic experiments.

**KEYWORDS**

active steel, chloride-induced corrosion, electrochemical properties, passive steel

## 1 | INTRODUCTION AND THEORETICAL BACKGROUND

Chloride-induced corrosion of steel is one of the most documented causes leading to the deterioration of reinforced concrete structures. In fact, once the steel is in contact with the concrete, a thin layer of corrosion products is formed at the steel–concrete interface, which restrains further oxidation. This phenomenon is called "passivation" of steel, which means that the steel is in a passive state. However, in the presence of chlorides, the steel can become locally active due to the breakdown of the thin passivation layer that creates a local active corrosion site. Therefore, macrocell or galvanic corrosion is established, as the remaining steel area is still in a passive condition.

It must be noted that the scale of this study concerns the macro-level of the corrosion process of rebars in concrete. As a result, a cohesion of matter is described in terms of stress and strain and their interaction via the constitutive law, and the corrosion of steel in concrete is described in terms of potential and current, and their interaction via the Butler–Volmer equation.

Chloride-induced corrosion of steel in concrete is an electrochemical phenomenon involving two main reactions: the oxidation of iron at the anode (Equation 1) generating electrons needed for the reduction reaction of dissolved oxygen at the cathode (Equation 2):

$$\mathrm{Fe} \rightarrow \mathrm{Fe}^{2+} + 2\mathrm{e}^{-}, \tag{1}$$

$$\frac{1}{2}\mathrm{O}_2 + \mathrm{H}_2\mathrm{O} + 2\mathrm{e}^{-} \rightarrow 2\mathrm{OH}^{-}. \tag{2}$$

In a galvanic system, an electronic current circulates through the metal, as electrons are transported from the anodic sites (active steel) toward the cathodic sites (passive steel). Concomitantly, an ionic current flows through the concrete electrolyte that is the interstitial solution of concrete.

  

Generally speaking, according to spatial considerations, two corrosion mechanisms can be distinguished: Microcell (or uniform) corrosion and macrocell (or localized, galvanic) corrosion. The definition of a corrosion system is based on the concept of the reversible electrode. In fact, corrosion occurs from the electrical coupling of two reversible electrodes: One playing the role of the anode and the other is the cathode of the global electrochemical cell. The electrochemical polarization behavior of a single reversible electrode is usually modeled by the Butler–Volmer equation (Equation 3), which was independently derived by John Alfred Valentine Butler (1899–1977) in 1924, Max Volmer in 1930 (1885–1965), and Tibor Erdey-Grúz (1902–1976) in 1930:

$$i = i_0\left(\exp\left(\frac{\log(10)}{\beta_a}(E - E_{rev})\right) - \exp\left(-\frac{\log(10)}{\beta_c}(E - E_{rev})\right)\right), \quad (3)$$

where $i$ is the net current density of the reversible electrode at the metal–electrolyte interface ($A/m^2$); $E$ is the potential of the reversible electrode under polarization (V vs. ref); $i_0$ is the exchanged current density of the electrode at reversible equilibrium ($A/m^2$); $E_{rev}$ is the reversible potential of the electrode at reversible equilibrium (V vs. ref); $\beta_a$ is the anodic Tafel slope of the reversible electrode, expressing the oxidation reaction (V/dec); and $\beta_c$ is the cathodic Tafel slope of the reversible electrode, expressing the reduction reaction (V/dec).

Microcell corrosion corresponds to the electrical coupling of two infinitely close reversible electrodes characterized by different reversible potentials ($E_{rev}$). In other words, the anode and cathode sites are spatially combined, and the resistance between both sites can thus be overlooked. In this case, the potential field of the system is uniform and its value equals the mixed potential of the two electrodes involved. This mixed potential is referred to as the corrosion potential $E_{corr}$. Regarding corrosion problems affecting steel in concrete, the two involved reversible electrodes are formed by the redox couples $Fe^{2+}/Fe$ (labeled Fe in the following discussion) and $O_2/OH^-$ (labeled $O_2$ in the following discussion). Figure 1 illustrates the typical polarization curves of iron and oxygen, as well as the electrochemical behavior of the resulting corrosion system when these two reversible electrodes are coupled in uniform conditions. As the reversible potential $E_{rev,Fe}$ is lower than $E_{rev,O_2}$, the coupling leads to oxidation of iron (anode) and reduction of oxygen (cathode). Due to the uniform potential field, there is no current flowing in the concrete volume. In reinforced concrete, there may be only uniform corrosion, even if the steel is entirely passive or entirely active. The net current density at the interface of each uniform system is the algebraic sum of the current densities associated with the oxidation (anodic) and reduction (cathodic) reactions. At the corrosion potential $E_{corr}$, both reversible electrodes are actually out of equilibrium, but the anodic current density is counterbalanced by the cathodic current density. Therefore, corrosion can still be regarded as some dynamic equilibrium between two different electrodes. As anodic and cathodic reactions do not involve the same chemical species, and even though there is no net current at the electrochemical interface, this dynamic equilibrium is accompanied by the irreversible consummation of the anodic electrode (corrosion). The anodic current density of the corrosion

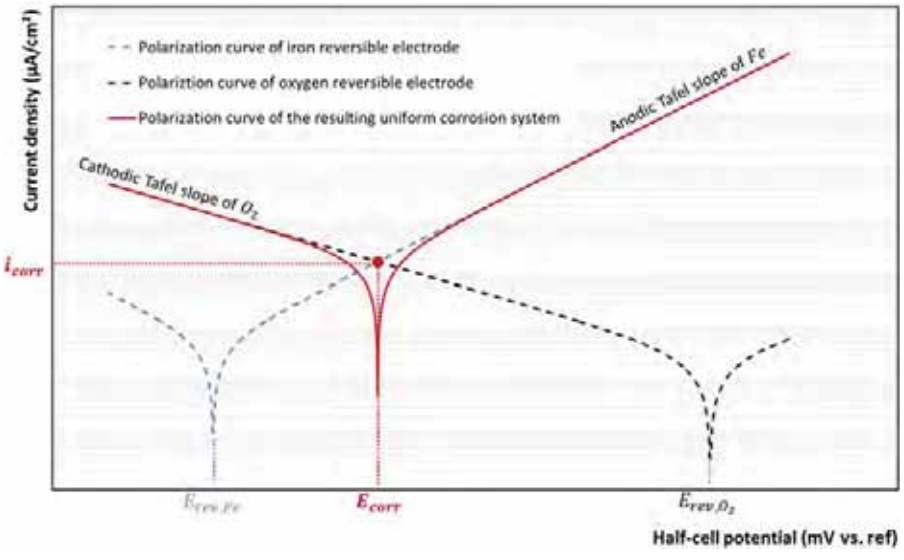


**FIGURE 1** Typical polarization curves of iron and oxygen, and polarization curve of the associated uniform corrosion system [Color figure can be viewed at wileyonlinelibrary.com]

system at its natural equilibrium is, therefore, referred to as the corrosion current density $i_{corr}$.

From the electrochemical behaviors of both reversible electrodes Fe and $O_2$, the corrosion potential and the corrosion current density can be exactly determined. First, knowing that the cathodic reaction and subsequently the cathodic electrochemical parameters vary according to the nature of the chemical reaction and the oxygen availability at the steel–concrete interface, it must be noted that these assumptions are considered in the case of unlimited oxygen availability. This implies that the corrosion process is not limited by the flow of oxygen. Moreover, it has to be considered that, at the corrosion dynamic equilibrium, the anodic current $i_{corr}$ produced by the oxidation of the Fe electrode is balanced by the cathodic current relative to the oxygen reduction as follows:

$$\begin{aligned} i_{corr} &= i_{0,Fe} \times \exp\left(\frac{\log(10)}{\beta_{a,Fe}}(E_{corr} - E_{rev,Fe})\right) \\ &= i_{0,O_2} \times \exp\left(-\frac{\log(10)}{\beta_{c,O_2}}(E_{corr} - E_{rev,O_2})\right). \end{aligned} \quad (4)$$

This balance relation allows for the exact determination of $E_{corr}$, providing that all electrochemical properties of the reversible electrodes are known:

$$E_{corr} = \frac{-\frac{\log\left(\frac{i_{0,Fe}}{i_{0,O_2}}\right)}{\log(10)} + \frac{E_{rev,O_2}}{\beta_{c,O_2}} + \frac{E_{rev,Fe}}{\beta_{a,Fe}}}{\frac{1}{\beta_{c,O_2}} + \frac{1}{\beta_{a,Fe}}}. \quad (5)$$

Once $E_{corr}$ is calculated, the corrosion current density $i_{corr}$ is then deduced from Equation (4). As observed in Figure 1, the polarization behavior of a uniform corrosion system may also be modeled by the Butler–Volmer equation (Equation 6), which relies on the relation between the system potential $E$ under polarization and the associated net current density $i$ produced at the steel–electrolyte interface:

$$\begin{aligned} i = i_{corr}\Bigg(&\exp\left(\frac{\log(10)}{\beta_a}(E - E_{corr})\right) \\ &- \exp\left(-\frac{\log(10)}{\beta_c}(E - E_{corr})\right)\Bigg), \end{aligned} \quad (6)$$

where $i$ is the net current density produced by the uniform corrosion system at the metal–electrolyte interface ($A/m^2$); $E$ is the potential of the uniform corrosion system under polarization (V vs. ref); $i_{corr}$ is the corrosion current density ($A/m^2$); $E_{corr}$ is the potential of the uniform corrosion system at equilibrium (V vs. ref); $\beta_a = \beta_{a,Fe}$ is the anodic Tafel slope of the electrochemical system, expressing the oxidation reaction of iron (V/dec); and $\beta_c = \beta_{c,O_2}$ is the cathodic Tafel slope of the electrochemical system, expressing the reduction reaction of oxygen (V/dec).

Providing particular sets of electrochemical parameters, both the polarization behaviors of uniform active and passive states of steel in concrete may be described by the Butler–Volmer model. In the following sections, parameters relative to active or passive steel will be annotated with "a" or "p" indices, respectively. Actually, in case of a free flow of oxygen, the usual difference in electrochemical behaviors of active steel and passive steel may be entirely described by varying only the anodic Tafel coefficient $\beta_{a,Fe}$ of the iron reversible electrode, with all other reversible electrode properties being maintained as constant. In the literature, the anodic Tafel coefficient

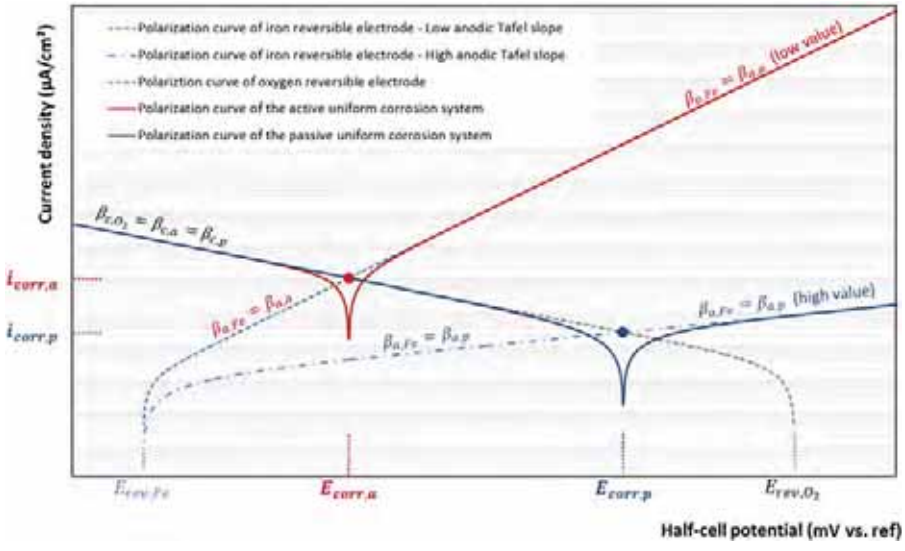


**FIGURE 2** Impact of the anodic Tafel coefficient of the iron reversible electrode on the polarization curve of the iron–oxygen corrosion system [Color figure can be viewed at wileyonlinelibrary.com]

of active steel is always found lower than that of passive steel. Figure 2 highlights the impact of $\beta_{a,Fe}$ on the polarization curve of a corroding system. Two simple simulations are performed here by using two values of the anodic Tafel coefficient $\beta_{a,Fe}$, labeled $\beta_{a,a}$ and $\beta_{a,p}$, such that $\beta_{a,a} < \beta_{a,p}$.

As illustrated in Figure 2, from the simple assumption that the anodic Tafel coefficient of the iron reversible electrode is smaller in active steel compared with passive steel ($\beta_{a,a} < \beta_{a,p}$) and considering all the other reversible electrode parameters as constant, some usual knowledge regarding the electrochemical features of corrosion of steel in concrete may be deduced naturally from Equations (4) and (5) as follows:

$$E_{corr,a} < E_{corr,p}, \tag{7}$$

$$i_{corr,a} > i_{corr,p}. \tag{8}$$

Taking account of these observations, it appears to be relevant and highly parsimonious to build a fundamental description of active and passive steel only on the basis of the modification of the anodic Tafel coefficient of steel. In such a vision of the problem, all the other electrochemical properties of the reversible electrodes involved ($E_{rev,Fe}$, $E_{rev,O_2}$, $i_{0,Fe}$, $i_{0,O_2}$, and $\beta_{c,O_2}$) are considered as independent and constant with respect to the active or passive nature of steel.

As exposed above, macrocell corrosion takes place when active and passive steel areas are electrically connected, as different areas of the same bar or of a globally connected steel network (Figure 3). Therefore, macrocell corrosion corresponds here to the electrical coupling of two uniform corrosion systems (active and passive) that are spatially distant on the surface of the steel network. This type of corrosion, also known as galvanic or localized corrosion, is systematically encountered in reinforced concrete structures exposed to aggressive agents such as chlorides. Moreover, the multilayered reinforcing bars favor the macrocell aspect of corrosion, because deeper layers are still passive when depassivation occurs in the first layers due to the ingress of aggressive species from the external concrete surface. This nonuniform corrosion is characterized by a nonuniform electrochemical state of steel, a nonuniform potential field, and therefore an ionic current flow that circulates between active (anode) and passive (cathode) sites in concrete.

Once electrically connected to the passive steel, the active steel undergoes an anodic polarization from its equilibrium potential ($E_{corr,a}$) toward a higher potential ($E_a$), which causes the creation of a global positive net current ($I_M$) at the active interface, defined as the macrocell or galvanic corrosion current. Conversely, passive steel undergoes a cathodic polarization from its potential at equilibrium ($E_{corr,p}$) toward a lower potential value ($E_p$), which generates a negative current associated with oxygen reduction ($-I_M$).

As active and passive zones are distant, the potential at the anode ($E_a$) remains lower than the potential at the cathode ($E_p$) due to the ohmic resistance of concrete. The ohmic potential drop is equal to the potential difference between passive and active areas. Ohm's law links the ohmic drop ($E_a - E_p$), the electrolytic resistance ($R_e$), and the galvanic corrosion current ($I_M$) flowing between the anode and cathode (Equation 9). This relationship highlights the influence of the electrical resistivity of concrete on the corrosion current, which is also known as the ohmic control of corrosion:

$$E_a - E_p = R_e \times I_M. \tag{9}$$

Despite the galvanic coupling of active and passive steel areas, a residual microcell activity can take place. Hence, the intensity of the total corrosion current ($I_{CORR}$) is the sum of the intensity of the macrocell current ($I_M$) and the intensity of the residual microcell current ($I_{micro}$) (Equation 10). This residual current depends on the

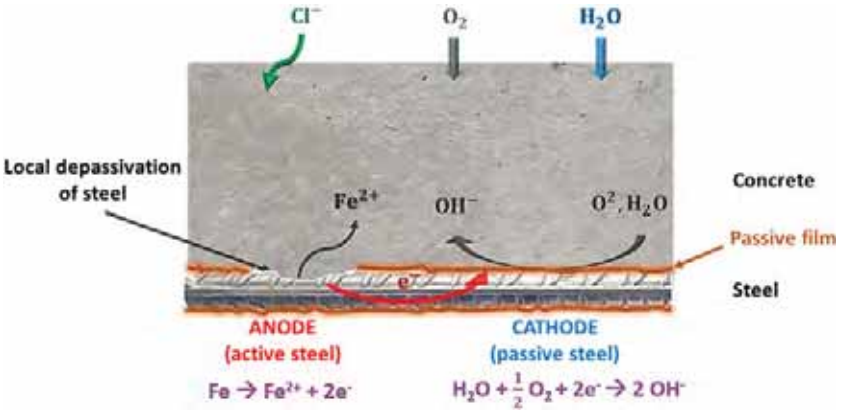


**FIGURE 3** Simplified scheme of the mechanism of chloride-induced corrosion of steel in reinforced concrete [Color figure can be viewed at wileyonlinelibrary.com]

magnitude of the anodic polarization of the active steel induced by its coupling with the passive steel. For strong polarization, the residual microcell current can be neglected:

$$I_{CORR} = I_M + I_{micro}. \quad (10)$$

It should be noted that actual macrocell systems are three-dimensional (3D) problems requiring a 3D analysis. For a 3D galvanic system, the equilibrium is determined as a boundary problem with Ohm's law and charge conservation as volume equations and Butler–Volmer's equations as boundary conditions. This results in anodic polarization fields of active areas and cathodic polarization fields of passive areas. Therefore, numerical methods are needed for the resolution of 3D galvanic problems.

Electrochemical properties of steel in reinforced concrete encountered in the literature vary significantly from one author to another.[1]

Table 1 presents ranges of these parameters that are commonly used by different authors.[1-7] A significant scatter is observed. Moreover, none of these authors takes into account the influence of chlorides on the electrochemical parameters at the active state.

A number of numerical models developed for the study of the propagation period of reinforcement corrosion involve these parameters as input data. Regarding the exponential nature of the Butler–Volmer model, the observed scatter in electrochemical properties may produce very significant differences in numerical simulations. It is then important to accurately characterize the parameters for active or passive steel to properly simulate the corrosion propagation.

The great variability observed in the literature regarding electrochemical properties of steel in concrete may be explained in various ways and linked to the difficulty in generating uniformly active steel. The electrochemical parameters of passive steel can be directly derived from experimental measurements, owing to the uniform passive state of rebars. Therefore, it is easy to proceed to the experimental assessment of passive steel electrochemical properties.

Conversely, uniformly active steel is quite impossible to obtain experimentally, especially in the case of chloride-induced corrosion. The determination of the Butler–Volmer polarization parameters of active steel is difficult[8] and cannot be directly measured from electrochemical experiments, as some parts of the active steel bar tested are still in the passive state. Moreover, it is probably ambiguous to measure these parameters in solutions, as reaction kinetics differs from those in concrete.[8] In addition, these parameters appear to be changing with pit growth over time.[8] Consequently, the response of active steel to polarization tests always expresses the behavior of a galvanic system (coupled with active and passive areas).

Several studies considered that the chloride-induced corrosion initiation is under anodic control,[8-13] which means that corrosion is controlled by the electrochemical parameters of steel like the anodic Tafel coefficients, anodic potential, and current.[10]

Therefore, to infer the electrochemical properties of active steel, an inverse modeling procedure is necessary. The study must also take into consideration the possible impact of factors like chloride contamination on electrochemical parameters.

In 2008, Maekawa et al.[14] indicated that the breakdown of passive film induced by chloride ions can be translated by an anodic Tafel slope $\beta_{a,Fe}$ dependent on chloride content. The authors suggested to multiply the anodic Tafel coefficient with a semiempirical theoretical factor, considering the level of chloride contamination.

In this study field, this paper represents a first step in the measurement of the electrochemical properties of active steel areas on the basis of 3D inverse numerical modeling, which is an original feature of this study. It also investigates the influence of chloride content on these electrochemical properties. To achieve relevant results, the physical description has been conducted at two different levels: The fundamental reversible electrode level and the corrosion system level.

An experimental campaign was carried out, which consisted of measuring galvanic corrosion currents between a cathode (sample without chlorides) and an anode (sample contaminated by chlorides). Several chloride pollution levels of the anode specimens were applied to investigate the consequence of the galvanic corrosion current exchanged.

Polarization tests were conducted separately on anode and cathode samples to obtain the polarization curves.

**TABLE 1** Ranges of the electrochemical parameters used as input data for numerical simulation by different authors

| Active state | | | | Passive state | | | |
|---|---|---|---|---|---|---|---|
| $E_{corr,a}$ (mV/SCE) | $i_{corr,a}$ ($\mu A/cm^2$) | $\beta_{a,a}$ (mV/dec) | $\beta_{c,a}$ (mV/dec) | $E_{corr,p}$ (mV/SCE) | $i_{corr,p}$ ($\mu A/cm^2$) | $\beta_{a,p}$ (mV/dec) | $\beta_{c,p}$ (mV/dec) |
| [−1,200; −660] | [0; 10] | [0; 91] | [116; ∞] | [−100; 400] | [$10^{-4}$; $10^{-2}$] | [75; ∞] | [116; 200] |

The electrochemical parameters of passive steel at the reversible electrode level were directly measured, as the steel at the cathode was in uniform electrochemical conditions. However, autopsies of the anode samples showed that the steel was not entirely in an active state. Hence, parameters of active steel could not be directly deduced from the polarization test. Therefore, a numerical optimization approach based on the fundamental effect of the iron anodic Tafel coefficient, as described above, was then developed to quantify the optimal set of parameters of "pure" active steel. Particular attention was focused on the effect of the chloride content of the anode samples on the iron anodic Tafel coefficient and subsequently on the deduced electrochemical properties of active steel. The electrochemical properties of active and passive steel were then used as input parameters of numerical simulations, aimed at reproducing the experimental anode–cathode galvanic coupling.

## 2 | EXPERIMENTAL DETAILS AND PRELIMINARY RESULTS

### 2.1 | Measurement of galvanic corrosion current between a small anodic specimen and a large cathodic specimen

Experimental work was setup to recreate localized corrosion by connecting a cathode sample to an anode sample (Figure 4). A CEMI mortar formulation was used to prepare the samples and the steel used was not submitted to any treatment. Table 2 presents the composition of the mortar used and Table 3 summarizes its usual physical properties according to standard protocols.

The cathode mortar sample (ϕ110 × 220 mm) was free of chloride, whereas the anode mortar sample (ϕ33 × 70 mm)

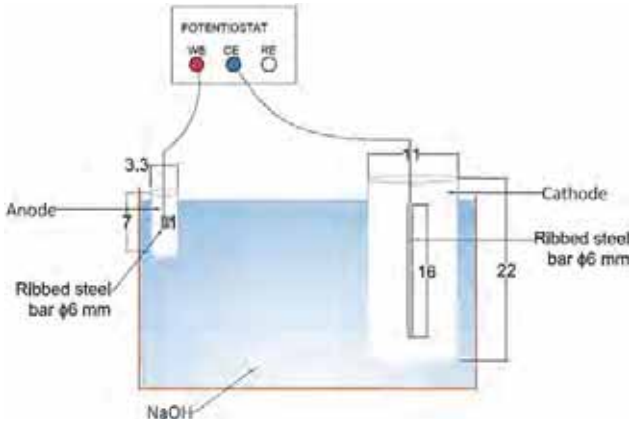


**FIGURE 4** Experimental setup for the measurement of galvanic corrosion current (dimensions are in cm) [Color figure can be viewed at wileyonlinelibrary.com]

**TABLE 2** Mortar composition

| Materials | Quantity (kg/m$^3$) |
|---|---|
| CEMI 52.5R | 512 |
| Siliceous sand 0/4 | 1,408 |
| Water | 281.4 |
| Sand/cement | 2.75 |
| Water/cement | 0.55 |

was polluted with chlorides by using a procedure that consisted of drying the samples to constant weight, followed with 48 hr of soaking in saline solution. Several chloride pollution levels were involved by using saline solutions with various NaCl concentrations.

A cathode sample contains, at its center, a ϕ6 × 160 mm Fe-500 ribbed steel bar. The anode sample embeds, at its center, a ϕ6 × 10 mm steel bar. Steel bars are tin welded to electrical wires that allow for the connection of both samples to a BioLogic SP-50 galvanostat–potentiostat. The SP-50 ZRA function was used for measuring the galvanic corrosion current. This test was realized for 7 days at a constant temperature of 20°C. The average galvanic current $I_g$ was then calculated from the integral of the current signal over the duration of the test.

After the galvanic corrosion test, total and free chloride contents were measured in the anode samples according to standard NF-EN-14629[17] and the GranDuBé procedure,[18] respectively.

### 2.2 | Polarization tests

To measure the electrochemical properties of passive and active steel, polarization tests were performed on cathode specimens and anode specimens, respectively, owing to a BioLogic SP-50 potentiostat. The experimental setup is described in Figure 5 for cathode specimens, and the same setup was also applied to anode specimens. To achieve a real steady-state measurement, a reversible potentiostatic step protocol introduced by Laurens et al.[6] was implemented to obtain the polarization curves. In such a protocol, the instantaneous responses for each step allowed for estimating the electrical properties of the mortar, whereas the asymptotic response qualified the polarization behavior of the steel. Depending on the level of polarization applied, the time required to achieve a steady state can be very long. The reversible potentiostatic step protocol allows for quickly and accurately estimating asymptotic responses and consequently for building polarization curves in a real steady-state condition.

The polarization cycle programmed in the software consists of applying potential increments and drops of

**TABLE 3** Mortar general properties

| Characterization tests at 28 days | Average value | Standard deviation |
|---|---|---|
| Electrical resistivity (Ω·m) (RILEM TC-154 EMC)[15] | 123 | 9.0 |
| Water porosity (%) (AFREM)[16] | 21.2 | 0.34 |
| Chloride migration coefficient ($10^{-12}$ $m^2/s$) (NT Build 492) | 19.68 | 0.39 |
| Compressive strength (MPa) (NF EN 196-1) | 66 | 1.0 |
| pH at a temperature of 21.9°C | 13.04 | – |

10, 20, 40, and then three steps of 80 mV with respect to the open-circuit potential. For each potential step, a waiting time of 360 s was chosen with an acquisition frequency of 1 Hz. Therefore, with respect to the free potential, a polarization range of ±310 mV was explored.

As the reference electrode was located in the solution near the counter electrode (CE), an ohmic drop correction was generally applied to get the actual potential response of steel. However, ohmic drop correction was applied here only for passive steel specimens (cathodes), as their electrochemical state may be considered as uniform. This correction was derived from the ohmic resistance achieved from the instantaneous responses at each step of the reversible polarization test.

As the cathode samples are free of chloride, the steel is indeed entirely in a passive state. Therefore, the characterization of passive behavior can be directly deduced from the experimental polarization test by fitting a Butler–Volmer model on the polarization curve. It has to be highlighted here that the fitting of electrochemical parameters is performed on the reversible electrode level, and the parameters associated with the corrosion system level are deduced from Equations (4) and (5).

Conversely, as discussed in Section 1, the steel in the anode specimens cannot be considered uniformly active despite the chloride presence. Therefore, regarding the anode specimen, the polarization response expresses the behavior of a galvanic system in which only a part of the steel surface is active. In this condition, the usual ohmic drop correction is no longer valid, as the electrochemical solicitation, as well as the electrochemical state, is not uniform. Consequently, no ohmic drop correction was applied to the polarization measurements relative to the anode specimens. As expressed in the preceding section, the polarization behavior of the anode specimens was used to infer active steel electrochemical properties from an optimization procedure based on inverse numerical modeling.

## 2.3 | Estimation of the area of active steel

The inverse numerical modeling to be implemented for active steel characterization requires knowledge of the

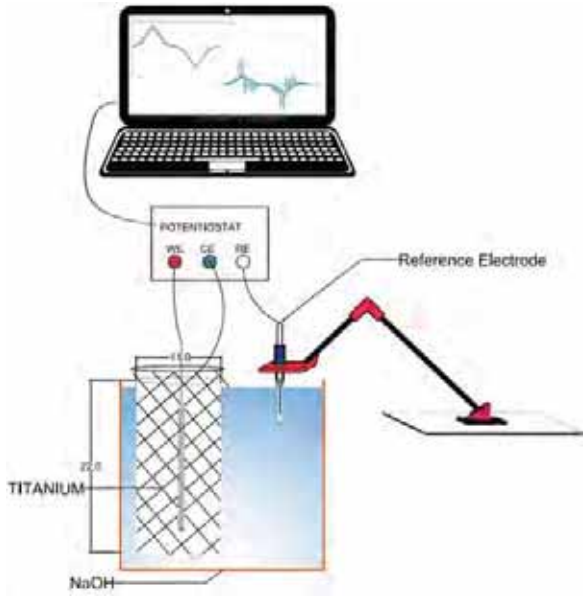


**FIGURE 5** Assembly of the steady-state polarization test on a cathode specimen [Color figure can be viewed at wileyonlinelibrary.com]

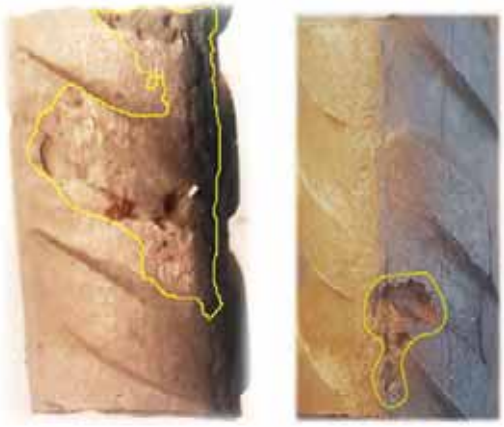

**FIGURE 6** Examples of microscopic inspections on the anode steel bars showing the localized corroded areas [Color figure can be viewed at wileyonlinelibrary.com]

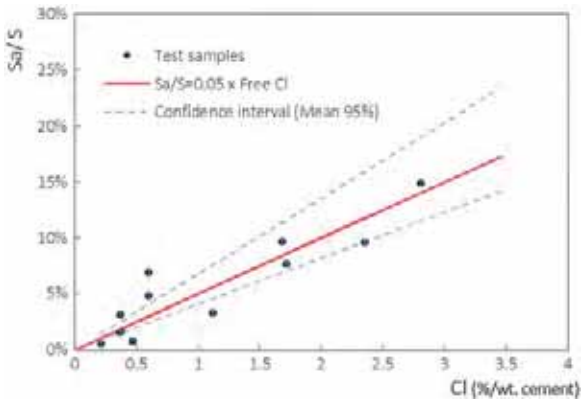


**FIGURE 7** Linear relation between $S_a/S$ and free Cl content [Color figure can be viewed at wileyonlinelibrary.com]

actual active steel surface. After the galvanic corrosion tests, the corrosion products were removed from the steel surface of anodic steel bars with a cleaning procedure according to the ISO 8407 standards.[19] Then, microscopic inspections of the steel surface of the anode samples were carried out. As expected, these observations confirmed that the steel bars were not completely in an active state, but represented a mix of passive and active sites (Figure 6). In fact, corroding (active) sites were distributed on the steel surface in a random manner. The total surface of active steel ($S_a$) was estimated as the sum of all the small active areas observed.

These autopsies performed on anode samples revealed that the corroding active area increases with the increase in the free chloride content. The experimental relation obtained between both variables can be modeled with an empirical linear model (Equation 11). The obtained linear relationship has a correlation coefficient ($R^2$) equal to 0.83, and it is presented in Figure 7. This relation was then used as an input parameter in further developments involving numerical simulations of polarization tests and galvanic current experiments:

$$\frac{S_a}{S} = 0.05 \times Cl, \tag{11}$$

where $S_a$ is the total area of active steel at the anode ($cm^2$); $S$ is the total area of the steel at the anode ($S = \pi \times 0.6 \times 1 \approx 1.88\,cm^2$); Cl is the free chloride content (%/wt. cement).

## 2.4 | Electrical resistivity of specimens as a function of chloride content

In this study, two approaches to the measurement of electrical resistivity were implemented. The first approach consisted of performing direct measurement on two different nonreinforced reference samples according to RILEM TC-154 EMC[15] and using a resistivity meter (direct transmission mode). The reference samples, having a diameter of 11 cm and a thickness of 5 cm, were tested at the age of 90 days.

The second approach consisted of using the electrical resistance obtained during the polarization tests of steel-reinforced specimens (from the instantaneous responses at each polarization step) and converting it into electrical resistivity by inverse numerical modeling. In other words, a numerical model was involved to assess the specimen geometrical factor, linking resistance, and resistivity, which will be referred to as indirect resistivity measurement.

Figure 8 presents the comparison of the two approaches of resistivity measurement applied to free chloride specimens: Two reference specimens for the first approach and six cathode specimens for the second. It can be observed that the electrical resistivity by using the indirect approach on chloride-free mortar samples is in the same order of magnitude of the direct measurement (transmission mode).

Figure 9 shows the electrical resistivity estimated using the indirect numerical approach on 17 different anode samples that were polluted by chloride solutions with various concentrations. It also presents the electrical resistivity measured directly with a resistivity meter on 10 different reference samples that were contaminated with different levels of chlorides. The reference samples

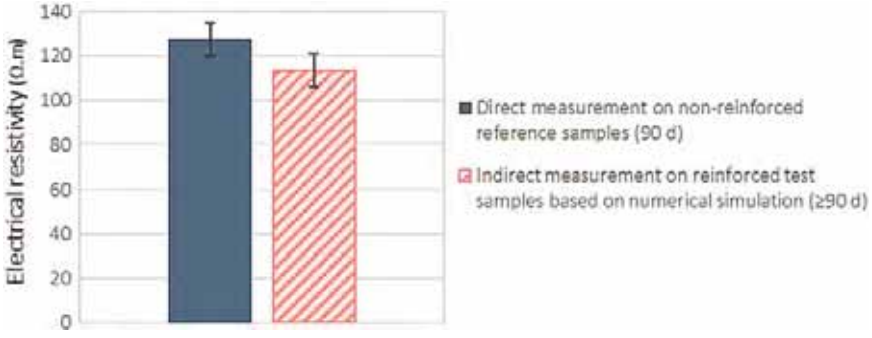


**FIGURE 8** Measured and estimated electrical resistivity of CEMI chloride-free mortar formulation [Color figure can be viewed at wileyonlinelibrary.com]

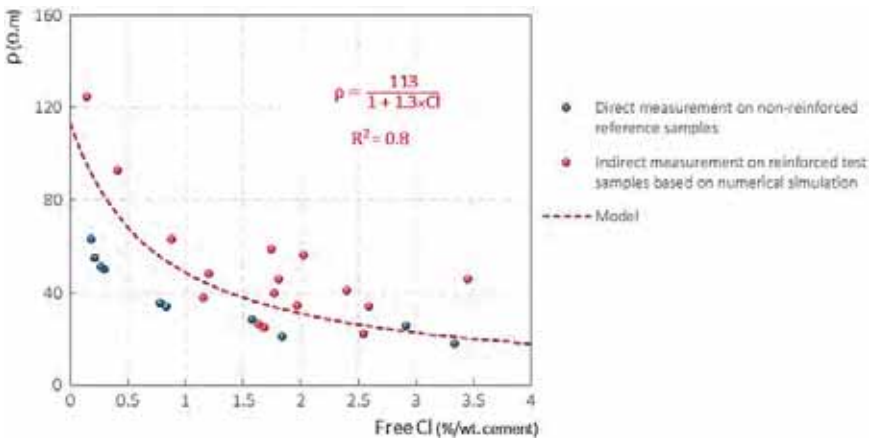


**FIGURE 9** Effect of the chloride content on the electrical resistivity of the CEMI mortar [Color figure can be viewed at wileyonlinelibrary.com]

are identical to the anode samples, but with no reinforcement. As expected, it can be observed from both results that the increase in the chloride content leads to a decrease in the electrical resistivity of mortar. This is well known and caused due to the high impact of chlorides on the ionic conductivity of the pore solution of the mortar. An empirical relationship was deduced between the estimated electrical resistivity and the free chloride content (Equation 12). This relation was then used as an input parameter in further developments involving numerical simulations of polarization tests and galvanic current experiments:

$$\rho = \frac{113}{1 + 1.3 \times \mathrm{Cl}} = \frac{\rho_0}{1 + 1.3 \times \mathrm{Cl}}, \tag{12}$$

where $\rho$ is the electrical resistivity of the chloride-polluted mortar (Ω·m); Cl is the free chloride content (%/wt. cement); $\rho_0$ is defined as the electrical resistivity of chloride-free mortar (Ω·m).

## 3 | NUMERICAL OPTIMIZATION PROCEDURE FOR THE CHARACTERIZATION OF THE ACTIVE STATE OF STEEL

As discussed above, it is impossible to generate purely active steel in cementitious materials, especially in the case of chloride-induced corrosion. Therefore, it is also impossible to directly extract the electrochemical properties of active steel from a polarization test on the anode specimens, as a part of the bar is still in a passive state. Consequently, the polarized system and the collected response actually concern a galvanic system established between the active part of the bar and the passive one. To extract the proper electrochemical properties of the active steel area from the global polarization response of an anode sample, a complementary inverse modeling procedure is required, given the following:

1. The electrochemical properties of passive steel have been determined previously and directly from polarization tests applied to the free chloride cathode samples;
2. The active surface $S_a$ is inferred from Equation (11), depending on the free chloride content of the anode specimen;
3. The mortar resistivity is inferred from Equation (12), depending on the free chloride content of the anode specimen.

Regarding the actual active surface to be involved in the simulation, it is relevant to address the issue of the possible impacts of the location and the morphology of the corroding spot at the steel surface (monospot or multispots scenarios for the same global active surface). To test the sensitivity of the numerical results to these possible effects, some simulations of the galvanic coupling between a small anode and a large cathode were performed by varying only the location and morphology of the active surface; the global active surface was the same for each case. Figure 10 shows the results in terms of galvanic corrosion current exchanged between the anode and cathode specimens, with respect to the galvanic current, labeled $I_0$, obtained for the first scenario (central spot, left side, Figure 10). It is observed that the currents obtained for different active surface positions and morphologies do not vary more than 18% with respect to $I_0$ obtained. This result indicates that location and morphology of the spot appear as second-order influencing parameters. Therefore, in the further inverse modeling approach, the active surface $S_a$ will be systematically modeled as the first scenario, that is, central monospot (Figure 10, left scenario).

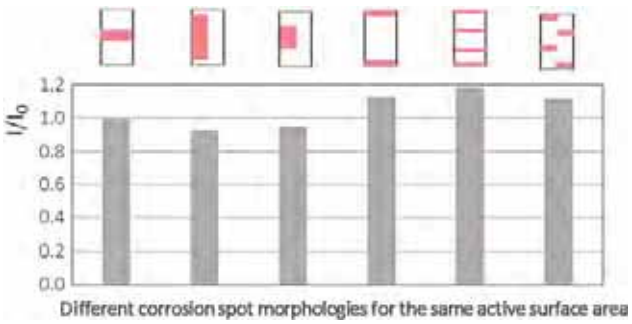


**FIGURE 10** Effect of the position and morphology of active sites on the galvanic corrosion current [Color figure can be viewed at wileyonlinelibrary.com]

## 3.1 | Direct numerical model and boundary conditions

The numerical simulations were performed by using the COMSOL Multiphysics software, based on the finite element method. The "electric currents" option of the COMSOL AC/DC toolbox was implemented to address the physical problem as a purely electrical model in a steady-state condition. Electrochemical behavior of active and passive steel areas was then implemented by using Butler–Volmer equations as boundary conditions.

The geometric model relative to the polarization tests applied to the anode specimens is presented in Figure 11. The model is composed of the anode mortar specimen, embedding the steel bar that is actually the working electrode (WE) of the measurement system. The anode is surrounded by a CE that represents the titanium mesh. The NaOH solution between the CE and the anode specimen is represented by an intermediate volume characterized by an electrical resistivity that was measured experimentally ($\rho_{sol} = 0.43\ \Omega{\cdot}m$).

In the experimental test, oxygen is considered to be available in sufficient quantity at the steel–concrete interface due to free access through the emerged part of the sample. In this configuration, the electrochemical reactions at the interface are considered to be not subjected to cathodic control.

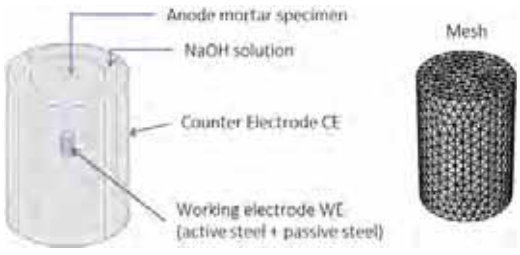


**FIGURE 11** Geometric model involved in the numerical simulation. CE, counter electrode; WE, working electrode [Color figure can be viewed at wileyonlinelibrary.com]

Mortar is considered as a homogeneous and isotropic environment with a uniform electrical resistivity ($\rho$) deduced from Equation (10), according to the level of chloride pollution in the simulated anode. The electric transport in the concrete volume is governed by local Ohm's law (Equation 13) coupled with charge conservation (Equation 14):

$$i = -\frac{1}{\rho}\nabla E, \tag{13}$$

$$\nabla . i = 0, \tag{14}$$

where $i$ is the local current density vector ($A/m^2$); $E$ is the potential field (V); $\rho$ is the electrical resistivity of mortar ($\Omega{\cdot}m$).

To simulate the polarization test applied on an anode specimen, specific boundary conditions must be locally applied, as illustrated in Figure 12. It has to be noted that the WE representing the steel bar is not properly modeled, but only its electrochemical response expressed by the Butler–Volmer equation, used as boundary conditions at the steel–mortar interface. Active and passive states are only distinguished by using different sets of electrochemical properties. Passive steel properties were deduced directly from the polarization tests applied to cathode specimens. Active steel properties are actually the subject of the present fitting procedure to be presented in the next section.

Regarding the CE, an inward current density ($i_{CE}$) is applied. This current is equal to the asymptotic current ($I_{CE}$) collected experimentally, divided by the CE area ($A_{CE}$). This makes it possible to numerically simulate the polarization of the WE.

## 3.2 | Inverse modeling approach

The inverse modeling procedure aims at measuring the proper electrochemical properties of active steel. For each level of chloride contamination, it consists of fitting the simulated polarization response of a properly defined galvanic system to the experimental polarization curve of anode specimen composed of active and passive steel areas.

As discussed above, the electrochemical characteristics of the passive area of the anode specimen were directly extracted from polarization tests realized on cathode samples. Moreover, the equivalent anodic surface and the electrical resistivity relative to each level of chloride contamination were deduced from the empirical relationships defined in Equations (11) and (12), respectively, which means that, in the numerical simulations, the active steel surface area and electrical resistivity of the anodes are considered to be changing with the level of chloride contamination.

It must be stated that, in the inverse modeling procedure, the equivalent anodic surface area is considered

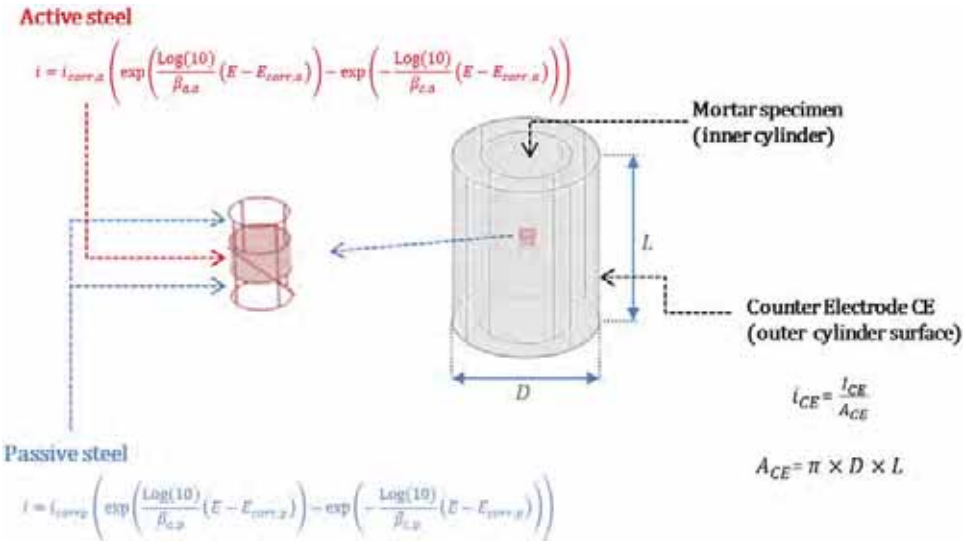


**FIGURE 12** Boundary conditions involved in the inverse simulations [Color figure can be viewed at wileyonlinelibrary.com]

active during the complete experiment, which means that the model neglects the pit growth or formation of corrosion products insulating parts of the pits.

All these properties were used as constant input parameters for each anode sample simulated, and only the active steel properties were submitted to the optimization process through the Butler–Volmer boundary condition defined for active steel (Equation 15):

$$i = i_{\text{corr,a}}\left(\exp\left(\frac{\log(10)}{\beta_{\text{a,a}}}(E - E_{\text{corr,a}})\right) - \exp\left(-\frac{\log(10)}{\beta_{\text{c,a}}}(E - E_{\text{corr,a}})\right)\right), \quad (15)$$

where $\beta_{\text{c,a}} = \beta_{\text{c,p}} = \beta_{\text{c,O}_2}$ is the cathodic Tafel coefficient of oxygen measured from the polarization tests on large cathode specimens.

In this study, the fundamental assumption adopted is that the iron anodic Tafel coefficient $\beta_{\text{a,a}}$ is sufficient to describe the electrochemical nature (active or passive) of steel in cementitious materials. Therefore, a physically constrained optimization procedure was developed in which only the iron Tafel coefficient $\beta_{\text{a,a}}$ was computed for each anode sample. The physical constraints applied to the optimization of $\beta_{\text{a,a}}$ are imposed by the deterministic relationships to be verified between $E_{\text{corr,a}}$, $i_{\text{corr,a}}$, and all the reversible electrode properties (Equations 16 and 17):

$$E_{\text{corr,a}} = \frac{-\frac{\log\left(\frac{i_{0,\text{Fe}}}{i_{0,\text{O}_2}}\right)}{\log(10)} + \frac{E_{\text{rev,O}_2}}{\beta_{\text{c,O}_2}} + \frac{E_{\text{rev,Fe}}}{\beta_{\text{a,a}}}}{\frac{1}{\beta_{\text{c,O}_2}} + \frac{1}{\beta_{\text{a,a}}}}, \quad (16)$$

$$i_{\text{corr,a}} = i_{0,\text{Fe}} \times \exp\left(\log(10)\frac{E_{\text{corr,a}} - E_{\text{rev,Fe}}}{\beta_{\text{a,a}}}\right). \quad (17)$$

The objective function of the optimization procedure is the mean square error (MSE) between the experimental and simulated polarization curves of an anode specimen characterized by a specific level of chloride contamination. A first semiarbitrary value of $\beta_{\text{a,a}}$ is set, and the associated numerical solution is computed and confronted with the experimental polarization curve to extract the MSE. The Nelder–Mead algorithm[20] is then involved in the fitting procedure of $\beta_{\text{a,a}}$ with the aim of minimizing the MSE. The Nelder–Mead algorithm does not require any derivative calculations (gradient-free), and it is widely used to solve parameters in similar statistical problems, in which the function values are uncertain or subject to noise.

The optimization procedure is reproduced for various anode specimens with various chloride contents. The methodology of the numerical optimization used for each anode sample is illustrated in a flowchart in Figure 13. This protocol allows investigating the relationship between the anodic Tafel coefficient and the level of chloride pollution in the anode samples.

## 4 | RESULTS AND DISCUSSION

### 4.1 | Experimental relationship between the chloride contamination of small anodes and the macrocell current exchanged with large cathodes

Figure 14 presents the average galvanic corrosion currents measured during the galvanic coupling experiments, with

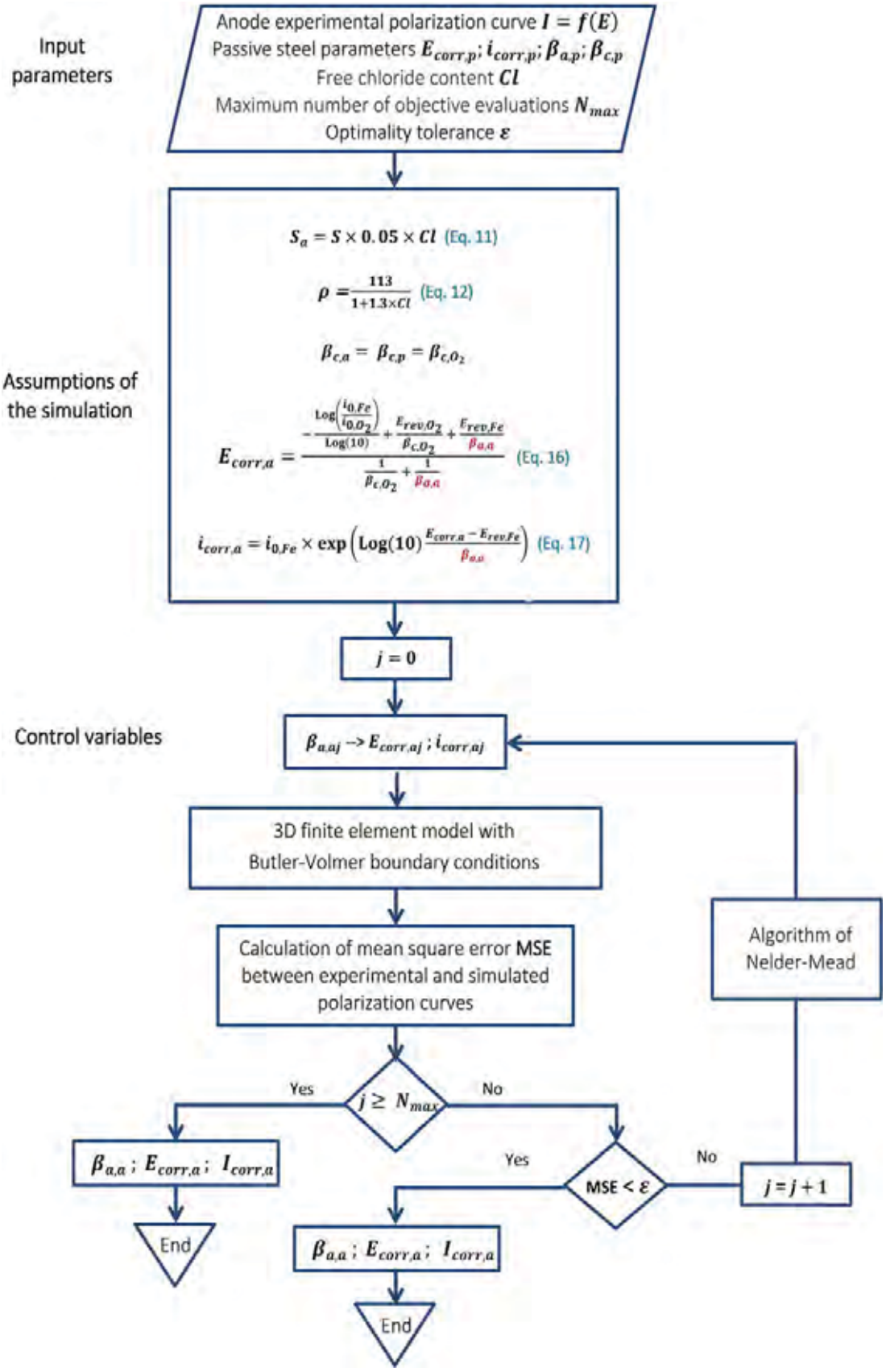


**FIGURE 13** Flowchart of the numerical optimization used for each anode specimen [Color figure can be viewed at wileyonlinelibrary.com]

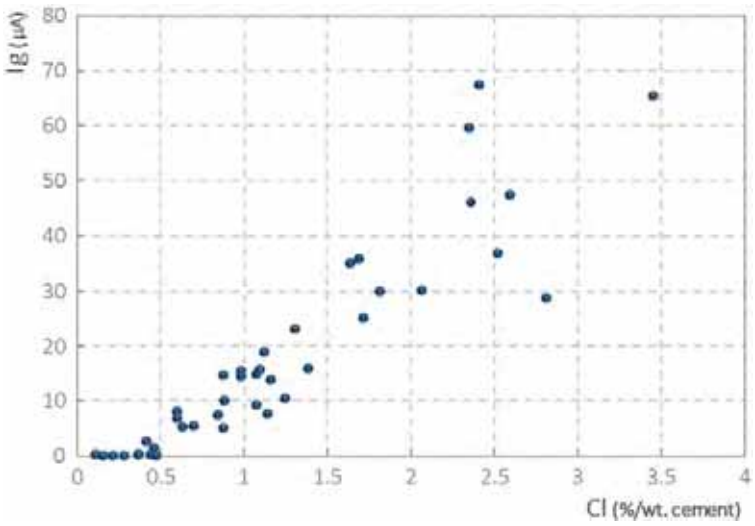


**FIGURE 14** Experimental results of the galvanic coupling [Color figure can be viewed at wileyonlinelibrary.com]

respect to the free chloride content in the anode samples (Section 2.1). A total of 41 galvanic tests, corresponding to 41 different anode samples with different levels of chloride contamination, were involved to build this experimental relationship.

First, the results illustrated in Figure 14 indicate that for chloride concentrations lower than 0.5%/wt. cement, the galvanic current exchanged between the small anode mortar specimen and the large cathode remains quite constant and negligible. For higher chloride concentrations, the galvanic current exchanged increases quite linearly with the chloride pollution level in the anode mortar specimens and reaches almost 70 μA for chloride contents of about 3%/wt. cement.

**TABLE 4** Butler–Volmer parameters of reversible electrodes fitted from polarization curves of passive steel specimens

| Reversible electrode | $E_{rev}$ (V/Ag–AgCl–KCl sat) | $i_0$ (A/m$^2$) | Tafel coefficient (V/dec) |
|---|---|---|---|
| $Fe^{2+}/Fe$ | −0.890 | $4.5 \times 10^{-8}$ | $\beta_{a,Fe} = 0.240$ |
| $O_2/OH^-$ | 0.019 | $2.5 \times 10^{-6}$ | $\beta_{c,O_2} = 0.115$ |

The clear transition observed in this experimental relationship highlights the probable existence of a chloride threshold effect. Therefore, a critical chloride content ($C_{crit}$) could then be associated with a value of 0.5%/wt. cement.[9]

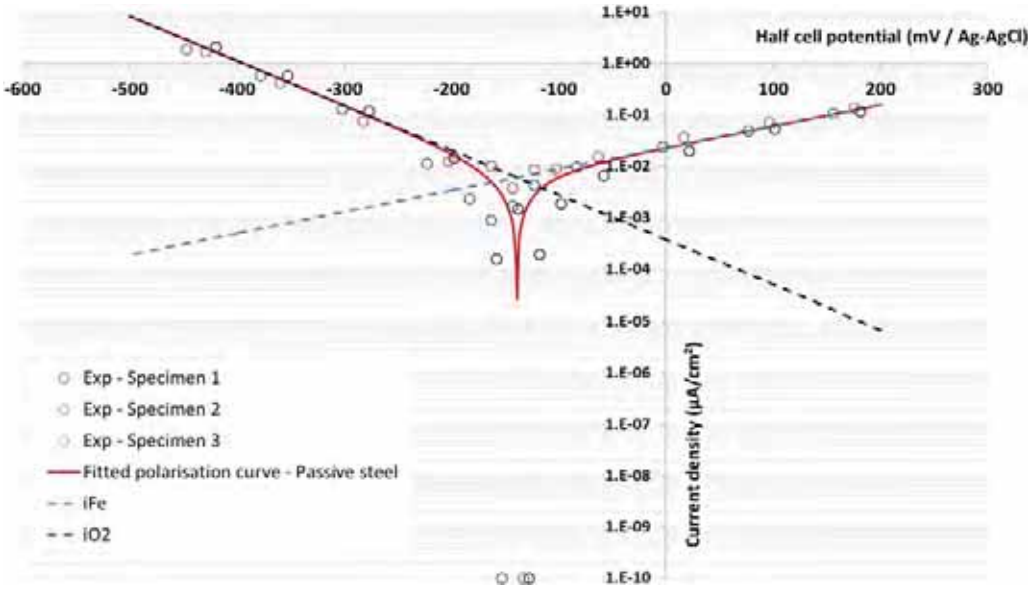


**FIGURE 15** Polarization curves of passive steel (CEMI cathodes) [Color figure can be viewed at wileyonlinelibrary.com]

**TABLE 5** Butler–Volmer parameters of passive steel specimens

| $E_{corr,p}$ (V/Ag–AgCl–KCl sat) | $i_{corr,p}$ (A/m$^2$) | $\beta_{a,p} = \beta_{a,Fe}$ (V/dec) | $\beta_{c,p} = \beta_{c,O_2}$ (V/dec) |
|---|---|---|---|
| −0.138 | $5.6 \times 10^{-5}$ | 0.240 | 0.115 |

The increase in the galvanic current exchanged with the pollution level could be simply explained by the effect of chlorides on the electrical resistivity (decrease) and on the global active surface (increase). However, the results to be presented in Section 4.3 reveal the third cause of this experimental behavior.

## 4.2 | Electrochemical properties of passive steel

Figure 14 presents the passive steel polarization curves collected experimentally on three cathode specimens (chloride-free) after ohmic drop correction. A quite good homogeneity is observed, allowing for the global fitting of one single electrochemical model on the three experiments, as shown in Figure 15.

The anodic and cathodic Tafel slopes $\beta_{a,Fe}$ ($=\beta_{a,p}$) and $\beta_{c,O_2}$ ($=\beta_{c,p}$) were extracted graphically from the well-defined anodic and cathodic branches of the experimental polarization curve. Then, the reversible potentials ($E_{rev,Fe}$ and $E_{rev,O_2}$) and the exchange current densities ($i_{0,Fe}$ and $i_{0,O_2}$) were simply optimized with the aim of minimizing the MSE between the experimental points and the fitted Butler–Volmer model. Table 4 summarizes the achieved electrochemical properties of the two reversible electrodes at the passive state.

From these reversible electrode parameters, the passive corrosion potential $E_{corr,p}$ and the passive corrosion current density $i_{corr,p}$ are deduced as follows:

$$E_{corr,p} = \frac{-\frac{\log\left(\frac{i_{0,Fe}}{i_{0,O_2}}\right)}{\log(10)} + \frac{E_{rev,O_2}}{\beta_{c,O_2}} + \frac{E_{rev,Fe}}{\beta_{a,Fe}}}{\frac{1}{\beta_{c,O_2}} + \frac{1}{\beta_{a,Fe}}} \quad (18)$$

and

$$i_{corr,p} = i_{0,Fe} \times \exp\left(\log(10)\frac{E_{corr,p} - E_{rev,Fe}}{\beta_{a,Fe}}\right). \quad (19)$$

Given that anodic and cathodic Tafel slope coefficients of passive steel ($\beta_{a,p}$ and $\beta_{c,p}$) are directly provided by $\beta_{a,Fe}$ and $\beta_{c,O_2}$, respectively, the measured electrochemical properties of passive steel are listed in Table 5.

## 4.3 | Electrochemical properties of active steel

The numerical fitting procedure aiming at extracting the purely active electrochemical behavior from experimental polarization tests (Section 3) was applied on 10 anode specimens with 8 different levels of chloride contamination. Table 6 presents the anode labels and the associated levels of chloride pollution selected for this study.

Figure 16 shows the anodic part of the experimental polarization curves realized on those anode samples. These curves were collected from steady-state polarization tests that were performed after the end of the galvanic coupling tests (after anode depolarization). Current intensities were used, as the polarizing current was not uniformly distributed over the steel surface. It should also be considered that no ohmic drop correction was applied due to the galvanic nature of the tested specimens. Nevertheless, for each of these 10 polarization curves, a simulated curve resulting from the optimization of $\beta_{a,a}$ was built, which takes into account the proper electrical resistivity (empirical Equation 12) and the active surface (empirical Equation 11) relative to the anode specimen tested. Therefore, electrochemical cell resistance effects are reproduced by numerical simulation. In other words, it can be considered that an implicit ohmic correction is done in the numerical simulation.

Figure 17 illustrates the results of the numerical optimization of $\beta_{a,a}$ in relation with the level of chloride contamination. An eleventh point was added for Cl = 0%, corresponding to the iron anodic coefficient at a passive state (Section 4.2). The chloride threshold effect discussed in Section 4.1 regarding the galvanic coupling tests is also visible in this experiment. However, even if a steep variation is observed around Cl = 0.5%, the transition of $\beta_{a,a}$ from the passive state (Cl = 0%) to the active state with the increase in chloride content appears as a

**TABLE 6** Information about the 10 anodes used for numerical optimization

| Anode sample | A1 | A2 | A3 | A4 | A5 | A6 | A7 | A8 | A9 | A10 |
|---|---|---|---|---|---|---|---|---|---|---|
| Cl (%/wt. cement) | 0.22 | 0.37 | 0.37 | 0.47 | 0.60 | 0.60 | 0.63 | 1.71 | 2.81 | 3.45 |

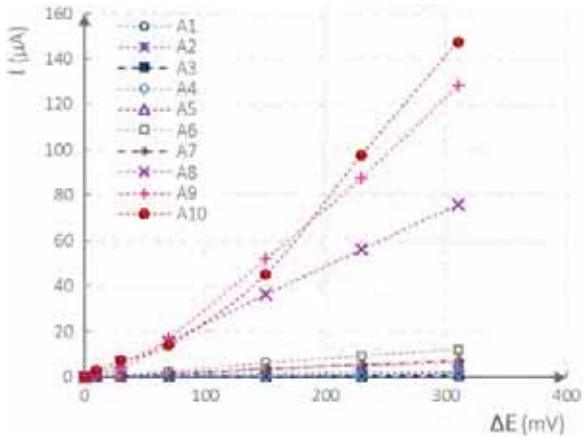


**FIGURE 16** Anodic polarization curves of 10 anode specimens [Color figure can be viewed at wileyonlinelibrary.com]

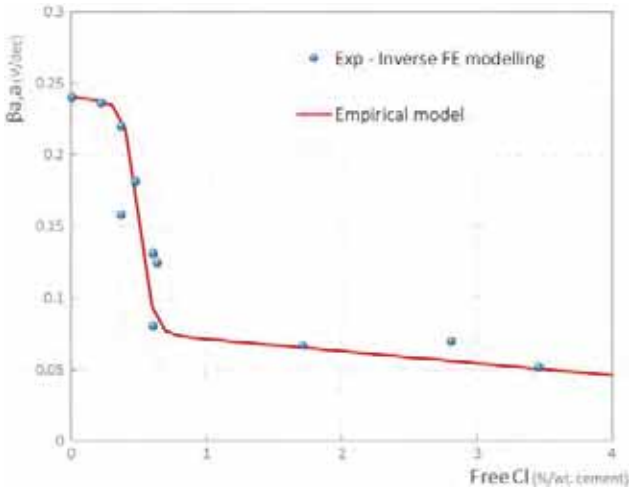


**FIGURE 17** Optimized values of $\beta_{a,a}$ according to chloride contamination [Color figure can be viewed at wileyonlinelibrary.com]

quite continuous phenomenon. Moreover, for chloride contents greater than 1%, the anodic Tafel slope seems to decrease quite linearly.

This experimental relationship between the chloride content and the iron anodic Tafel coefficient was modeled as an empirical pseudo-sigmoidal behavior (Equation 20), which is displayed as the red continuous curve in Figure 17:

$$\beta_{a,a} = 0.08 + \frac{0.16}{1 + \exp(20 \times (Cl - 0.5))} - 0.0085 \times Cl. \quad (20)$$

Figure 18 displays the effect of the chloride contamination on the values of $E_{corr,a}$ and $i_{corr,a}$ deduced from Equations (16) and (17), respectively, associated with the fitted values of $\beta_{a,a}$. The so-called semiempirical models displayed as red curves are built by mixing the pseudo-sigmoidal model (Equation 20) and the physically funded models expressed by Equations (16) and (17). The same, quite smooth, chloride threshold effect appears on the corrosion potential behavior (left). This threshold appears weaker regarding the effect of chlorides on the corrosion current density.

## 4.4 | Numerical simulation of the galvanic coupling tests

To validate the global set of electrochemical parameters of steel presented above, numerical simulations were performed to reproduce the galvanic coupling tests between the large cathode specimens and the small anode specimens for various chloride contamination levels (Section 4.1).

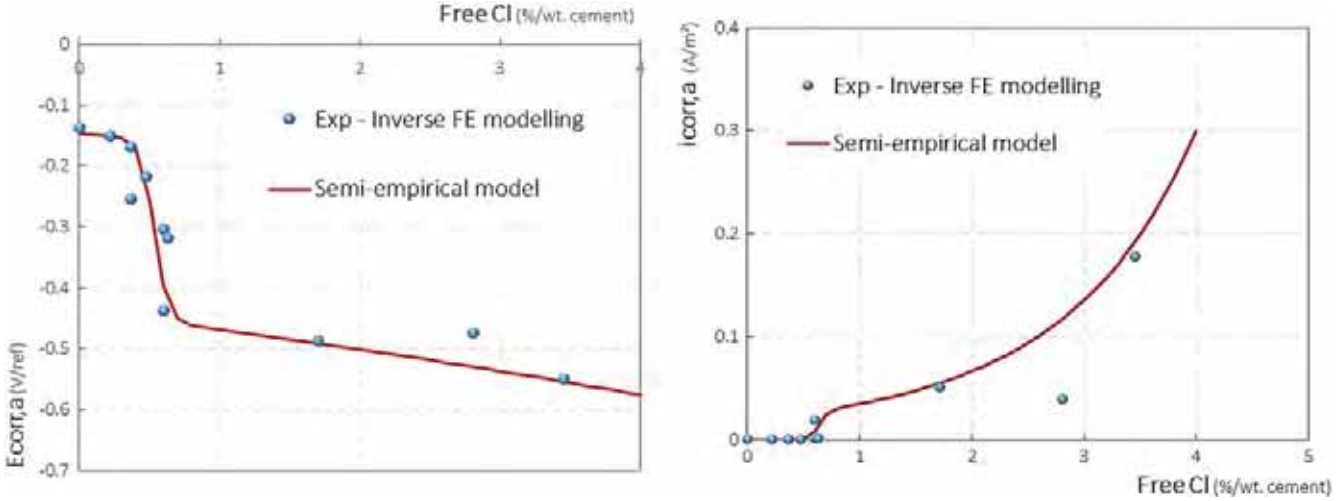


**FIGURE 18** Values of $E_{corr,a}$ and $i_{corr,a}$ according to chloride contamination deduced from Equations (16) and (17), respectively [Color figure can be viewed at wileyonlinelibrary.com]

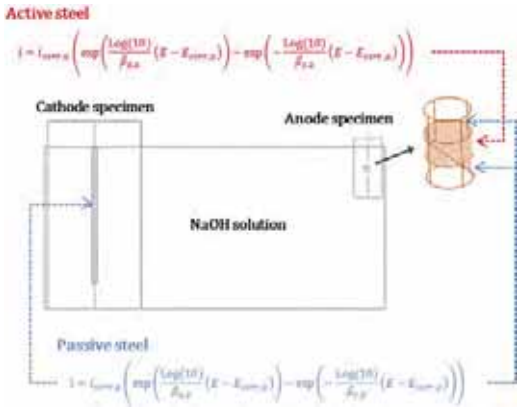


**FIGURE 19** Numerical model of galvanic coupling tests [Color figure can be viewed at wileyonlinelibrary.com]

The 3D model has the same dimensions as the experimental setup (Figure 19). The Butler–Volmer equations were applied locally on passive and active steel areas using electrochemical parameters presented in Sections 4.2 and 4.3, respectively.

The galvanic corrosion current is calculated by the integration of the normal current density produced by the active area or by the passive area at the steel–concrete interface. In the numerical postprocessing, it is necessary to verify that these currents are equal to ensure that the numerical convergence is achieved.

Figure 20 presents the experimental and numerical galvanic currents obtained, relative to the anode–cathode coupling tests for different chloride contents. The single-centered spot simulated scenario is displayed as the red curve. A quite good qualitative correlation is observed between the experimental points and this scenario, but the simulation slightly underestimates the averaged galvanic current. Therefore, taking account of the visual observations and measurements of the actual active surfaces in the anode specimens (Section 2.3), as well as the second-order effect of the spot morphology on the galvanic current produced (Section 3), two additional simulated scenarios were added:

- The anodic surface is +urve in Figure 20);
- The anodic surface is distributed over nine distinct corroding spots (green curve in Figure 20).

These two added numerical scenarios allowed achieving the quantitative correlation between experimental and simulated data. The quantitative agreement observed here between experimental and simulated galvanic currents highlights the relevance of the passive and active electrochemical properties presented in Sections 4.2 and 4.3.

Regarding the final comment formulated at the end of Section 3.1, the increase in the galvanic current for Cl values higher than 0.5% is only partly due to the effect of chloride on electrical resistivity and the active surface. Indeed, the dependence of the anodic Tafel coefficient of active steel on chlorides also plays a great role in the observed experimental behavior. To prove this statement, a complementary set of numerical simulations was

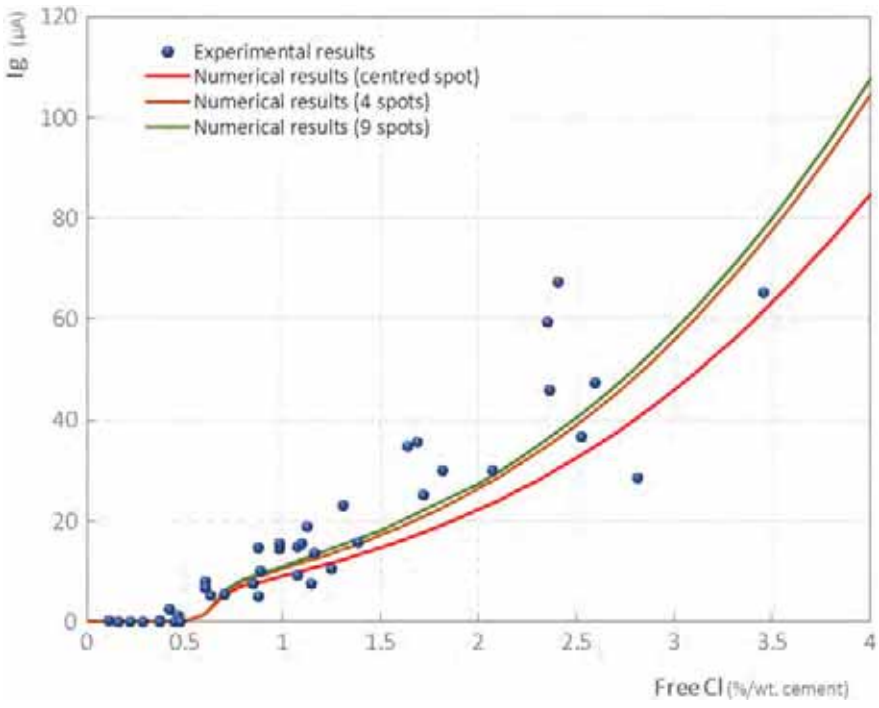


**FIGURE 20** Experimental results of the galvanic coupling and numerical outcomes for the obtained active parameters [Color figure can be viewed at wileyonlinelibrary.com]

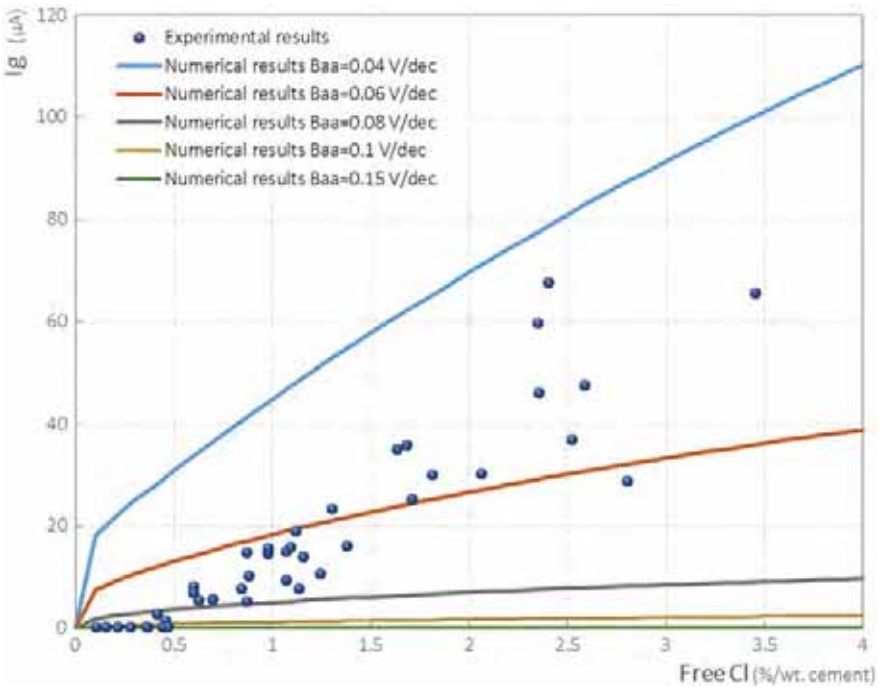


**FIGURE 21** Experimental results of the galvanic coupling and numerical outcomes in case of constant $\beta_{a,a}$ [Color figure can be viewed at wileyonlinelibrary.com]

conducted by considering constant anodic Tafel slopes of active steel (chloride-independent) instead of using the empirical model. Here, only the electrical resistivity and the active surface were set as chloride-dependent. Figure 21 presents the results of such a simulation procedure. It is obvious that the numerical results do not fit the experimental ones.

These experimental observations coupled with the numerical modeling approach highlight the chloride dependence on the electrochemical properties of active steel. More generally, the numerical modeling of steel corrosion in reinforced concrete requires taking account of the effects of the chloride contamination level on the following:

- The active surface;
- The electrical resistivity of concrete or mortar;
- The iron anodic Tafel coefficient $\beta_{a,a}$, and on the subsequent properties $E_{corr,a}$ and $i_{corr,a}$.

## 5 | CONCLUSION

Due to the nonuniform nature of chloride-induced corrosion in concrete, it is not possible to experimentally obtain uniformly active steel. Consequently, the determination of the electrochemical properties of active steel cannot be directly measured from electrochemical experiments, as some parts of the steel bar tested are still in a passive state.

This study presents the determination of the electrochemical properties of active steel, based on inverse numerical modeling that focuses on their dependency on chloride contamination.

An experimental campaign was conducted, consisting of measuring galvanic corrosion currents between small anode mortar samples contaminated with different chloride concentrations and large cathode mortar samples that are free of chlorides. It was found that for chloride contents lower than 0.5%/wt. cement, galvanic currents exchanged between anode and cathode were constant and negligible, whereas, for higher chloride concentrations, galvanic currents increased quite linearly with chloride pollution levels. The clear transition observed in this experimental relationship confirms the existence of a chloride threshold effect.

As the steel at the cathode is in a uniform passive state, polarization tests realized on cathode samples allowed for directly determining the electrochemical parameters of passive steel at the fundamental reversible electrodes level and the corrosion system level, which contributed to enrich the database of electrochemical properties of passive steel.

However, autopsies of the anode samples revealed that the steel was not entirely in an active state. As a result, parameters of active steel could not be directly deduced from polarization tests. Consequently, a numerical optimization approach was developed to quantify the optimal set of parameters of "pure" active steel. The numerical simulation focused on the influence of chloride contamination on the iron anodic Tafel coefficient

and, subsequently, on the rest of the electrochemical properties of active steel that are fundamentally dependent on anodic Tafel coefficient.

To validate the global set of electrochemical parameters of steel, numerical simulations were performed to reproduce the galvanic coupling test between cathode and anode specimens. By considering various corrosion spot morphologies, a quite good quantitative correlation was observed between the experimental points and numerical results. A complementary set of numerical simulations conducted by considering constant (chloride-independent) anodic Tafel coefficient of active steel showed that the numerical results do not fit the experimental ones.

All these experimental observations coupled with the numerical modeling approach highlight the dependency of the electrochemical properties of active steel on chloride content.

## ACKNOWLEDGMENTS

This study was supported by the ANR MODEVIE project, Grant No. ANR-14-CE22-0018 of the French Agence Nationale de la Recherche, and by the French National Federation of Public Works.

## DATA AVAILABILITY STATEMENT

The raw/processed data required to reproduce these findings cannot be shared at this time, as the data also form a part of an ongoing study.

## ORCID

*Chantal Chalhoub* http://orcid.org/0000-0002-8588-732X

## REFERENCES

[1] J. Gulikers, M. Raupach, *Mater. Corros.* **2006**, *57*, 618.
[2] A. M. Hassanein, G. K. Glass, N. R. Buenfeld, *Cem. Concr. Compos.* **2002**, *24*, 159.
[3] R. Polder, W. H. A. Peelen, F. Lollini, E. Redaelli, L. Bertolini, *Mater. Corros.* **2009**, *60*, 130.
[4] S. C. Kranc, A. A. Sagüés, *Corros. Sci.* **2001**, *43*, 1355.
[5] J. Warkus, M. Brem, M. Raupach, *Mater. Corros.* **2006**, *57*, 636.
[6] S. Laurens, P. Hénocq, N. Rouleau, F. Deby, E. Samson, J. Marchand, B. Bissonnette, *Cem. Concr. Res.* **2016**, *79*, 272.
[7] C. Cao, *Constr. Build. Mater.* **2014**, *72*, 434.
[8] U. Angst, B. Elsener, C. K. Larsen, Ø. Vennesland, *Electrochim. Acta* **2011**, *56*, 5877.
[9] C. Chalhoub, R. François, M. Carcasses, *Cem. Concr. Res.* **2019**, *124*, 105825.
[10] G. Glass, C. Page, N. Short, *Corros. Sci.* **1991**, *32*, 1283.
[11] J. A. Gonzalez, J. Algaba, C. Andrade, *Br. Corros. J.* **2013**, *15*, 135.
[12] C. Page, J. Havdahl, *Mater. Struct.* **1985**, *18*, 41.
[13] P. Lambert, C. Page, P. Vassie, *Mater. Struct.* **1991**, *24*, 351.
[14] K. Maekawa, T. Ishida, T. Kishi, *Multi-Scale Modeling of Structural Concrete*, CRC Press, Boca Raton **2008**.
[15] RILEM TC 154-EMC, *Acad. Search Engine* **2000**, *33*, 603.
[16] J.P. Ollivier, *Durabilité Des Bétons*. Compte Rendu Des Journées Techniques AFPC-AFREM, Toulouse **1997**.
[17] NF EN 14629, Produits et systèmes pour la protection et la réparation des structures en béton—Méthodes d'essais—Mesurage du taux de chlorure d'un béton durci, **2007**.
[18] G. Arliguie, H. Hornain, *GranDuBé: grandeurs associées à la durabilité des bétons*, Presses des Ponts, Paris **2007**.
[19] ISO 8407:2009, Corrosion of metals and alloys—Removal of corrosion products from corrosion test specimens, **2009**.
[20] S. Singer, J. Nelder, *Scholarpedia* **2009**, *4*, 2928.

**How to cite this article:** Chalhoub C, François R, Garcia D, Laurens S, Carcasses M. Macrocell corrosion of steel in concrete: Characterization of anodic behavior in relation to the chloride content. *Materials and Corrosion*. 2020;1–18. https://doi.org/10.1002/maco.201911398

# Appendix Paper II

## Nelder-Mead optimization

Appendix in: Study of the initiation and propagation phases of chloride induced corrosion in reinforced concrete structures

Realized by: Chantal Chalhoub

Thesis for the degree of Philosophiæ doctor

Université Toulouse 3 Paul Sabatier (UT3 Paul Sabatier)

Laboratoire Matériaux et Durabilité des Constructions de Toulouse

Appendix Paper II

Appendix Paper II

# Contents

# 1. Introduction

This report presents a very superficial presentation of the Nelder-Mead algorithm which was used in the numerical optimization presented in paper II which is involved in the fitting procedure of $\beta_{a,a}$ with the aim of minimizing the Mean Square Error "MSE". A more detailed explanation can be found in the cited references [1–3].

# 2. Nelder-Mead algorithm

The optimization method used is the Nelder-Mead algorithm which is one of the best-known algorithms for multidimensional optimization without derivatives (gradient-free). It is widely used to solve the estimation of parameters and similar statistical problems, in which the function values are uncertain or subject to noise [1].

The basic algorithm is simple enough to understand, very easy to use and often faster than other methods. On the other hand, the absence of a convergence theory often results in a numerical decomposition of the algorithm, even for smooth and well-behaved functions. The method can take a lot of iterations with a negligible improvement in the value of the function, although it is far from the minimum. This usually leads to premature termination of the iterations. A heuristic approach dealing with such cases is to restart the algorithm multiple times, with a reasonably small number of iterations for each run [1].

The used algorithm is a simplex method (generalized N-dimensional triangle with N+1 vertices) used to find the minimum of a function of N variables [2]. For example, in the case of one variable, the simplex is a line and in the case of two variables, a simplex is a triangle, and the technique is a pattern search that associates function values at the three vertices of a triangle [2,3]. It modifies or moves the simplex, one vertex at a time, to an optimal region in the search space which is associated with the optimal objective value.

Fig. 1 summarizes the steps of the Nelder-Mead method. The first step consists of determining the indices of the worst, second-worst and the best vertex. The second step consists of calculating the centroid of the best side which is the one opposite the worst vertex. The third step consists of transforming the simplex by substituting only the worst vertex with a better one using reflection, expansion or contraction according to the best side. If the transformation succeeds by giving a better objective value, the accepted point becomes the new vertex of the simplex. On the other hand, if the transformation fails by giving a worse objective value, a shrink transformation of the simplex towards the best vertex is achieved. Finally, the last step is the termination which is typically reached when:

- A given number of iterations is reached
- The simplex reaches a minimum 'size' limit.
- The current best solution reaches a satisfactory limit.

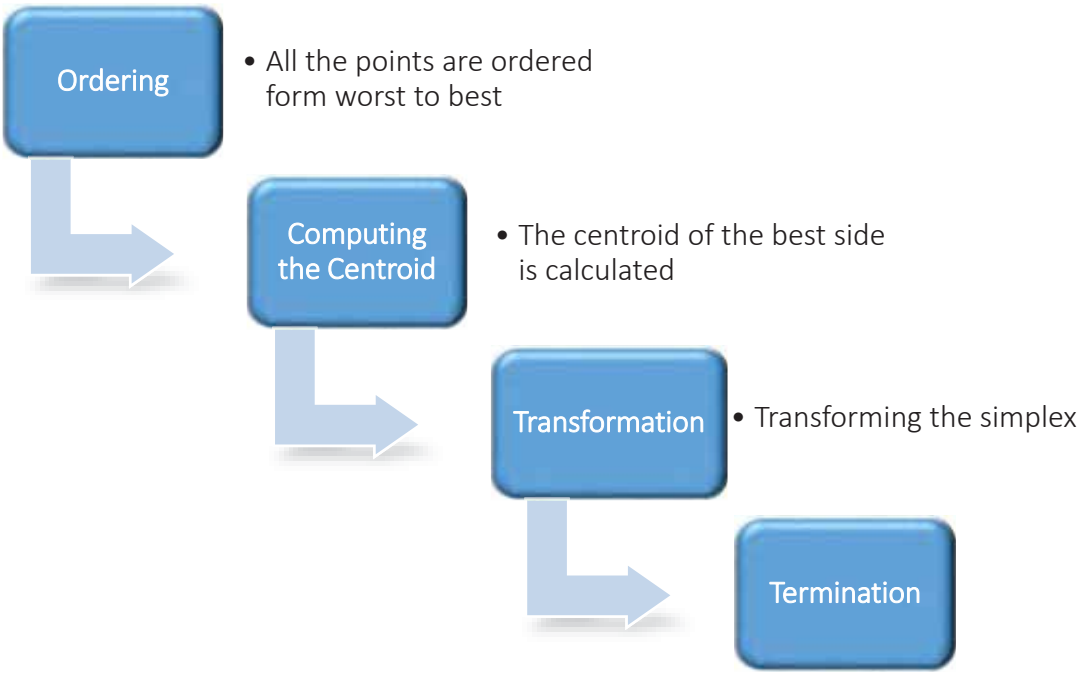


*Fig. 1. Steps of the Nelder-Mead method*

The different possible simplex transformations (Reflection, Expansion, Contraction, and Shrink) are illustrated in Fig. 2 in the case of a triangle simplex.

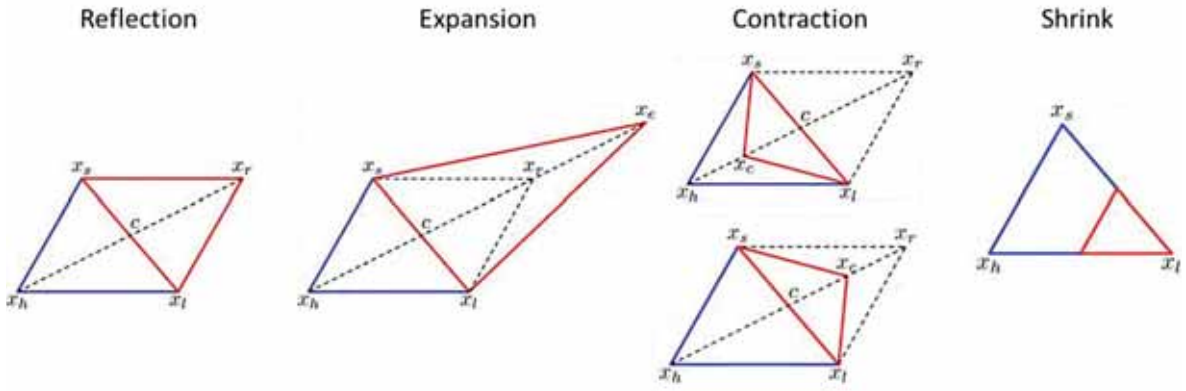


*Fig. 2. Simplex transformations (taken from [1])*

## 3. References

[1] S. Singer and J. Nelder, *Nelder-Mead algorithm*, Scholarpedia 4 (2009), pp. 2928.
[2] John H. Mathews and Kurtis K. Fink, *Numerical Methods Using Matlab, 4th Edition*, 2004.
[3] srjoglekar246, *Nelder-Mead Optimization*, Sachin Joglekar's blog, 2016.

# Paper III

**Critical chloride threshold values as a function of cement type and steel surface condition**

**Chantal Chalhoub*, Raoul François, Myriam Carcasses**

**Cement and Concrete Research 134 (2020) 106086**

Cement and Concrete Research 134 (2020) 106086

Contents lists available at ScienceDirect

Cement and Concrete Research

journal homepage: www.elsevier.com/locate/cemconres

# Critical chloride threshold values as a function of cement type and steel surface condition

Chantal Chalhoub*, Raoul François, Myriam Carcasses

*LMDC, INSA, UPS, Université de Toulouse, France*

ARTICLE INFO

*Keywords:*
Chloride-induced localized corrosion
Critical chloride content
Binder type
Porosity

ABSTRACT

This paper presents the application of a new test protocol developed for determining chloride threshold values initiating corrosion in reinforced concrete. The experimental set-up was described in previous work and is based on the intrinsic localized aspect of chloride-induced corrosion. The test protocol is also based on the concept of anodic control of corrosion initiation, and therefore independent of the area of passive steel. The test method is applied to mortar and concrete formulations with different binders and steel surface conditions. Chloride-binding isotherms were also determined to allow the transition from total to free chlorides. It is found that the test protocol is rapid and applicable to all formulations. The experimental results provide an understanding of the influence of binder type, w/b ratio and porosity on chloride-induced corrosion initiation. As expected, the steel surface condition is shown to have an important overall effect on corrosion initiation.

## 1. Introduction

Chloride-induced corrosion is the leading cause of deterioration of reinforced concrete structures and chlorides in reinforced concrete originate from two types of source: an external source resulting from the marine environment and de-icing salts [1,2] and an internal source resulting from concrete compounds. Several standards, such as EN 206: 2016, limit the maximum amount of chlorides initially present in the mix ($C_0$) according to the type of reinforcement, as shown in Table 1.

There are 2 types of chlorides: bound chlorides, which are fixed to the binder matrix, and free chlorides, which are present in the interstitial solution of concrete and are mainly responsible for initiating the corrosion of steel. The sum of free and bound chlorides gives the total chlorides.

These 2 types of chlorides can be measured experimentally but the main problem is that the experimental measurement of the concentration of free chlorides by dissolution with water is very dependent on the conditions adopted for the experimental protocol, such as the temperature, the amount of water added and the stirring time. In addition, it has been shown that measurement of the free chloride content by extraction of the interstitial solution or dissolution with water can overestimate the actual free chloride content since a certain amount of fixed chlorides may be released because of the pressure applied [3,4]. It is also important to note that, during corrosion, some of the bound chlorides may be released because of the increase in temperature to above 55 °C [5] or local acidification near a corrosion pit [6]. It is, therefore, necessary, during the study of corrosion initiation, to determine both free and total chlorides.

Practically, it is assumed that corrosion initiation occurs when the chloride content at the depth of the rebars reaches a critical threshold value called *Ccrit*. However, several interpretations of "corrosion initiation" exist, leading to different determinations of *Ccrit* [7]. Some associate the initiation of corrosion with the depassivation of steel in concrete, which is close to the shift from the initiation to the propagation stage as described in Tuutti's model [8], while others associate it with an acceptable degree of corrosion, which is part of the propagation stage of corrosion. Nevertheless, from a fundamental and practical perspective, corrosion initiation, also known as corrosion onset, does not correspond to an instantaneous event but is more like a gradual phase until corrosion becomes stable [9–12]. In other words, the critical chloride content is the quantity of chlorides at the steel surface necessary to sustain a local depassivation of steel and so induce corrosion initiation.

When studying the diffusion rate of chloride in the pore network, it is important to consider the total chloride content since the fixation of chloride is a dominant parameter affecting the service life of concrete [13]. However, bound chlorides do not affect the threshold *Ccrit* [13], hence it is more appropriate to express the chloride threshold in terms of free chlorides.

*Ccrit* is one of the most important input parameters for corrosion

* Corresponding author.
*E-mail address:* chantal.chalhoub@insa-toulouse.fr (C. Chalhoub).

https://doi.org/10.1016/j.cemconres.2020.106086
Received 21 October 2019; Received in revised form 27 February 2020; Accepted 15 April 2020

**Table 1**
Acceptable initial levels of total chlorides according to EN 206: 2016.

| Type of structure | $C_0$ (% /wt. binder) |
|---|---|
| Reinforced concrete | 0.40 |
| Pre-stressed concrete | 0.20 |
| Reinforced concrete with CEM III | 0.4 (depends on national application) |
| Reinforced concrete with CEM III | 0.65 for FRANCE |
| Unreinforced concrete | 1.00 |

initiation models in cases of chloride ingress. Its accurate determination allows the service life of new reinforced concrete structures to be appropriately designed and evaluated and the residual service life of existing structures to be predicted. However, there is still no appropriate method for its determination and *Ccrit* values found in the literature are very scattered [7,14–21]. Moreover, the *Ccrit* values used in several service life design model codes for concrete structures vary considerably [22–25]. In Europe and North America, it is common to use a *Ccrit* equal to 0.40%/wt. cement for acid-soluble chlorides or 0.15% %/wt. cement for water-soluble chlorides [26].

Many research reviews have gathered together *Ccrit* values published in Western (European and North-American) data [7,14–20] and a large number of Chinese published articles have also been evaluated recently, considering only publications regarding carbon steel [21]. From all these reported data, it was found that *Ccrit* values were considerably scattered over 2 orders of magnitude [7,14–21]. Given the large uncertainties, it is still not possible to adopt a consistent range of *Ccrit* values for engineering life design models and differences in the procedures and test protocols used make it hard to compare the published values of *Ccrit*. Nevertheless, it has been possible to find a literature agreement on the qualitative impact of some influencing factors [7].

Numerous experimental test set-ups have been developed for *Ccrit* evaluation. An innovative protocol developed by Angst et al. [27] consists of determining *Ccrit* for the actual structure, which presents a practice-related method for existing structures at risk of corrosion and ensures real conditions concerning factors that significantly influence *Ccrit*, like the steel-concrete interface and the type and surface condition of the steel. The technique most commonly used by several researchers [27–29] to detect corrosion initiation is a potential drop based on the process developed by RILEM technical committee TC 235 [30]. However, the authors state that criteria used to detect corrosion initiation may be difficult to fulfill in situations where the potential is usually negative, for instance in slag cements or with other binders containing sulfide [27,28].

Recently, a new experimental protocol taking the localized aspect of corrosion in concrete into consideration has been developed by Chalhoub et al. [31] based on a galvanic coupling between two physically separated samples: an anode contaminated with chlorides and a cathode, which is chloride free. The test set-up allows the chloride threshold initiating corrosion to be determined on the basis of a criterion corresponding to a threshold corrosion current that is independent of the cathode/anode surface ratio. As described in the test procedure in [31], the limit current $I_{crit}$ is independent of the passive steel surface area and hence independent of the C/A ratio and it was found equal to 3 μA.

Besides the determination of the chloride threshold values initiating corrosion, the test protocol also allows to study the corrosion current during the propagation stage. In this study [31], the experimental test was applied to CEMI mortar samples and for different types of steel surface conditions. The role of mill scale on chloride-induced corrosion was highlighted and it was found that the corrosion kinetics obtained in the absence of mill scale (cleaned steel specimens) were relatively weak. The result was attributed to a less porous passive film formed in absence of mill scale layer making it harder for the chloride ions to diffuse through [31].

In the present paper, this protocol will be used to assess the critical chloride contents for different types of binder and steel surface conditions in mortar and concrete formulations. The details of the test procedures, the experimental conditions of the preconditioning of anode samples to initiate corrosion, and the electrochemical galvanic coupling test can be found elsewhere [31].

## 2. Literature review of the factors influencing *Ccrit*

Corrosion initiation in concrete under chloride attack is a complex phenomenon and is influenced by several parameters, such as factors related to the Steel Concrete Interface (SCI) and the impact of the test procedure used among others. It has been found that *Ccrit* values depend significantly on the procedures used in the experimental test set-ups developed for detecting corrosion initiation, which could override the influence of the influencing parameters under study [6]. Yet, when corrosion initiation was inspected at the same scale as in the experimental test, the SCI was found to be a dominating parameter.

Knowing the complexity of the SCI, it was important to analyze the local influence of its different characteristics [32]. This section presents a brief overview of several aspects of the SCI and their individual impact on the initiation of chloride-induced corrosion in concrete. For this purpose, several research papers were revisited [7,21,32] in addition to a recently published paper based on the work of the RILEM Technical Committee 262-SCI [33], which inspired the structure of the following overview. According to this paper [33], the influencing parameters can be classified as factors related to reinforcement bars, concrete, and interfacial concrete voids, and other factors like temperature and moisture content. In the next section, the influence of elements related to rebars and concrete on *Ccrit* will be briefly discussed, based on data mostly collected from the papers mentioned above.

### 2.1. Factors related to reinforcement bars

#### 2.1.1. Type of reinforcing steel

There are few studies concerning the effect of metallurgy on the initiation of chloride-induced corrosion of steel in concrete or alkaline environments [34–36] and the existing data are contradictory and vary significantly [33]. The strong impact of the microstructure of the rebar surface cannot be neglected when dealing with corrosion initiation in concrete.

The geometry of rebars is also an important parameter that may impact the SCI locally. This parameter mainly corresponds to the diameter of rebars, the presence or absence of ribs, the presence or absence of bends on the rebars, and their shape. Few published works have investigated the impact of rebar geometry on corrosion initiation [37–42] and the data are not consistent overall [33].

#### 2.1.2. Surface condition of reinforcing steel

The surface condition of the reinforcing steel and the method used for their preparation have a significant impact on *Ccrit*. On site, the type of rebars used is as-received, which means that rebars are generally covered with a non-uniform layer of mill scale or pre-rusted when the mill scale layer is combined with rust products. It is then important to understand the impact of these layers on corrosion initiation.

The mill scale mostly encountered on rebars used for construction is non-uniform and irregular with cracks and crevices [43,44]. In most studies, the presence of a mill scale layer on the surface of carbon steel and even stainless steel appears to stimulate corrosion initiation and thus to lower *Ccrit* compared to when it is removed with polishing, sandblasting or cleaning and pickling [31,45–54]. In particular, Mahallati and Saremi [55] established that the formation and protecting features of the passive layer are reduced by the presence of mill scale. However, a few studies [46] have shown that the presence of a dense, continuous mill scale layer raises *Ccrit*, presenting a corrosion-protective characteristic.

When investigating chloride-induced corrosion in concrete, it is advisable to use practice-related rebars, such as as-received or pre-rusted bars. It is also possible to use sandblasted or polished rebars as corrosion monitoring sensors in structures. Moreover, most of the research has been carried out on CEMI samples and has not studied the impact of the steel surface in the case of other binders.

### 2.2. Factors related to concrete

#### 2.2.1. Cement type and additions

The cement type is a factor that is thought to impact corrosion initiation by changing the microstructure at the steel-concrete interface [32] and by influencing the pH of the pore solution and the chloride binding capacity. Also, the replacement of CEMI with other binder types has an influence on the composition of the pore solution and consequently on *Ccrit*. The level of chloride binding is dependent on several factors related to the binder type [56], such as the of C-S-H gel content [57], which impacts the physical binding of chlorides, and also the C3A and C4AF content, which influences the chemical binding of chlorides. This binding capacity impacts *Ccrit* when expressed in terms of total chlorides. The impact of several types of cements and mineral additions is presented below.

a) Silica fume (SF):

The partial substitution of SF for ordinary Portland cement (CEM I) decreases the quantity of aluminate phases, which reduces the chemical binding of chlorides but also causes a refinement of the pore structure of the cement matrix, thus improving the physical adsorption of chlorides. Yet, C-S-H formed in the presence of SF could have weaker chloride sorption than those formed in CEM I [58]. Consequently, in SF-containing materials, the chloride binding capacity is lower than that of CEM I [58–60].

Byfors [61] measured the pH of pore solutions pressed out of cement pastes and found that increasing the silica fume substitution level seemed to decrease the pH of the pore solution. This result was also found by Page and Vennesland [59], who studied specimens of the capillary pore solution of hardened cement pastes formed with different substitution levels of silica-fume and sodium chloride. They also found that, when the pH of pore solution reached a certain level, the stability of the passive film protecting the steel was reduced, as was the stability of Friedel's salt [59].

Lower critical chloride contents have frequently been reported in cases of SF-containing cement in comparison with CEM I [51,62–67].

However, in his work, Scott [42] found that the inclusion of SF (with a level of 7%) in concrete resulted in a *Ccrit* similar to the one obtained in CEM I specimens. This result contradicts the previously reported papers and also the common view established by Frederiksen [68]. Scott [42] stated that the use of a superplasticizer may have ensured a better distribution of SF in the concrete matrix and around the rebar, which may have reduced the degree of porosity or voids in the interfacial zone, leading to higher *Ccrit*. Kayyali and Haque [69] found that the use of a superplasticizer increased the concentration of free chloride and raised the value of the Cl -/OH - ratio in different tested concretes. Scott [42] also added that including SF contributed to the densification of the SCI, which could counterbalance the decrease of pH and limit the exposed area of steel initially accessible for corrosion.

b) Slag (S):

The partial substitution of ground granulated blast-furnace slag (GGBFS) for ordinary Portland cements (CEM I) increases the chloride binding capacity through the increase in physical and chemical chloride binding [60,70–72]. Yet, it is reported that the presence of Slag reduces the pH of the pore solution [73] (The method used to measure the pH and the age of the samples tested are not indicated in this paper).

Some published papers found lower *Ccrit* in case of specimens containing slag in comparison with OPC specimens [42,66,67,74,75], while others reported higher *Ccrit* [63,67,76–78] or did not find any important impact [79–81].

Scott [42] tested different substitution levels of slag, 25, 50 and 75%, and found that the reduction in *Ccrit* did not vary uniformly with the substitution level. In fact, it occurred in the following order 25% S > 75%S > 50%S. The author [42] added that the results obtained with 75% of S were possibly a result of the more open pore structure, which may have promoted the oxidation of sulfides. Subsequently, if this oxidation took place before chlorides reached the steel, it could have inhibited possible damage to the passive layer by sulfides.

Kosalla and Raupach [82] investigated potential differences and polarization states on reinforced concrete specimens with CEMI and blast furnace slag cement (BFSC, CEMIII). They studied the impact of binder type in the case of rebars in a passive state and found that steel in BFSC responded more strongly to variations in oxygen availability than CEM I did. This may indicate that, in BFSC, a different passive film is formed, having different polarizability and reactivity.

c) Limestone addition (L):

Several experimental studies show that increasing the limestone (L) content in concrete with the same water/cement ratio (w/c) leads to an increase of chloride ingress into the concrete [83–86]. Nevertheless, this effect of limestone addition in concrete mixes designed for an equal w/c basis is more pronounced than its effect in concrete mixes designed to achieve equal strength compared to Portland cement concrete formulations [85].

Some researchers have found that the presence of L in concrete mixes is associated with a reduction in the chloride binding capacity [85]. The latter could be attributed to a lower alumina content due to the reaction of L with constituents that bind chlorides, most importantly C3A and possibly C4AF [85,86].

Fagerlund stated that, in presence of L additions, the pore structure and the permeability of concrete are considered to be unaffected, while the chloride binding capacity is reduced, which could explain this higher chloride ingress when L is added [87].

On the other hand, some researchers, like Kopecskó and Balázs [72], found that L behaved as an inert material when chloride binding was considered.

The influence of L addition on chloride-induced corrosion of steel reinforcement in concrete is not commonly reported [85]. Few studies have evaluated Portland limestone cement concretes (PLC) [85] and suggest that the corrosion rate is moderate to considerably increased when PLC concrete is used [88–97]. Diab et al. [98,99] proposed that the impact of PLC concrete on corrosion depends on w/c, fineness of L and the cement content.

#### 2.2.2. Water/binder ratio

When studying the effect of concrete on corrosion initiation, it is important to discuss the impact of the water/binder (w/b) ratio, known for its impact on the porosity of concrete and hence on the pore structure of the steel-concrete interface. Consequently, the w/b ratio influences moisture content and oxygen concentration in the steel-concrete interfacial zone. Based on several works [18,62,79,100–104] where w/b ratio used ranges from 0.30 to 0.75, it was found that decreasing the w/b ratio below 0.5 generates an increase of almost 30% in *Ccrit* [33]. This result is supported by Poupard et al. [105], who determined the depassivation of rebars experimentally but quantified the chloride content using an electrodiffusion model. On the other hand, the authors of [33] state that, in cases where w/b ratio is higher than 0.5, its effect is inconsistent and generally insignificant. This is somewhat in agreement with the Chinese literature [21], where numerous published papers based on Portland cement have studied w/b ratios between 0.30 and 0.60. It has been found that the increase of w/b ratio

leads to a decrease of *Ccrit* [63,76,80,81].

In summary, it appears that the steel type condition is one of the most dominant parameters of the SCI, impacting the initiation of chloride-induced corrosion. The influence of factors related to concrete, such as w/b ratio and cement type is apparently small but the reported results are contradictory.

This paper focuses on inspecting the effect of steel surface condition and binder type on chloride-induced corrosion in mortar and concrete samples by using a test protocol that is based on macrocell corrosion. The main objective is to analyze the effect of these factors on *Ccrit* and compare the results thus obtained with results from the literature. Results of formulation with a large replacement level of cement by slag (80%) will not be presented here because of the specific effect of very high slag content. A further paper will be dedicated to chloride-induced corrosion in cases of mortar with a high substitution level of slag.

## 3. Materials and methods

### 3.1. Formulation composition

Two mortar formulations (M1-055 and M10SF-043) and three concrete formulations (B1-15L-049, B3-041, and B3-15L-051) were used in this work and their composition is detailed in Table 2. The formulation M1-055 was made of 100% of CEMI 52.5R with a w/b ratio of 0.55. It is the same formulation as presented in [31] but was used, in this paper, for the purpose of comparison. The other mortar formulation, noted M10SF-043, was made with the same cement but included partial replacement with silica fume at a substitution level of 10% and had a lower w/b ratio, of 0.43.

The concrete formulations were made in the framework of a Benchmark partially funded by IREX and the concrete samples were produced in the VINCI Construction Laboratory in Nanterre, France.

The mass percentage of binder (*Mbp*) was determined from the following equation:

$$Mbp\ [\%] = \frac{C_b \times 100}{\rho} \quad (1)$$

where:

- $C_b$ is the binder content (kg/m$^3$);
- ρ is the theoretical density (kg/m$^3$).

Table 3 presents the silicate and aluminate compositions of the cements used in the mortar and concrete formulations.

Table 4 presents the chloride and sulfide contents in binders of each formulation, which were determined from technical sheets of the materials used.

### 3.2. Characterization tests

Several characterization tests were performed on these formulations for different ages and the results are presented in the following sections and in Table 5. It must be noted that the age of mortar or concrete in this work is calculated from the day of preparation and mixing of the

**Table 3**
Silicate and aluminate compositions of cements.

| | | M1-055 M10SF-043 | B1-15L-049 | B3-041 B3-15L-051 |
|---|---|---|---|---|
| Cement type | | CEMI 52.5R | CEM I 52,5 N CECP2 NF | CEM III A 52.5 L CE PM-ES-CP1 NF |
| **Slag percentage** | | 0% | 0% | 64% |
| **Clinker percentage** | | 95% | 97% | 36% |
| **Clinker composition** | **C3S** (%) | 67 | 61 | 68 |
| | **C2S** (%) | 10 | 16 | 11 |
| | **C3A** (%) | 9 | 9 | 10 |
| | **C4AF** (%) | 8 | 11 | 8 |

**Table 2**
Composition of mortar and concrete formulations.

| | Mass of constituents in kg/m$^3$ | | | | |
|---|---|---|---|---|---|
| | M1-055 | M10SF-043 | B1-15L-049 | B3-041 | B3-15L-051 |
| **Sand** | 1408 (0-4mm RL) | 1457 (0-4mm RL) | 818 (0-4 R) | 830 (0-4 All) | 818 (0-4 R) |
| **Gravel** | 0 | 0 | 957 (6-20 SC) | 309 (4-11.2 All SCL) | 957 (6-20 SC) |
| | | | | 696 (11.2-22.4 All SCL) | |
| **Cement** | 512 (52.5 R) | 477 (52.5 R) | 280 (CEM I 52,5 N CECP2 NF) | 380 (CEM III A 52,5 L CE PM-ES-CP1 NF) | 280 (CEM III A 52.5 L CE PM-ES-CP1 NF) |
| **Addition** | 0 | 53 Silica fume (CONDENSIL S95 DM) | 50 (Betocarb HP Gy) | 0 | 50 (Betocarb HP Gy) |
| **Binder** $C_b$ | 512 | 530 | 330 | 380 | 330 |
| **Plasticizer** | 0 | 3.18 (CHRYSO®Fluid Optima 175) | 1.6 (SIKA Techno 348) | 4.6 (Optima 372) | 2.1 (OMEGA 144) |
| **Effective water** | 281.4 | 225.25 | 163 | 155 | 169 |
| **Theoretical density** ρ | 2223 | 2232 | 2315 | 2390 | 2320 |
| **Apparent density** | — | — | 2090 | 2280 | 2130 |
| **Measured density** at 28d | — | — | 2319 | 2439 | 2332 |
| ***Mbp*** (%) | 23.03 | 23.75 | 14.25 | 15.9 | 14.22 |
| **Slump** (mm) | — | — | 160 | 170 | 190 |
| **Temperature of concrete** (°C) | — | — | 25 | — | 23 |
| **Water/cement** | 0.55 | 0.47 | 0.58 | 0.41 | 0.60 |
| **Water/Binder** | 0.55 | 0.43 | 0.49 | 0.41 | 0.51 |
| **Paste volume** (L) | 467 | 425 | 320 | 300 | 329 |

**Table 4**
Chloride and sulfide contents in binders used in each formulation determined from technical sheets of materials.

| Formulation | Composition of binder | Chlorides (%/wt. binder) | Sulfides (%/wt. binder) |
|---|---|---|---|
| **M1-055** | 100% CEMI 52.5R | 0.04 | 0.01 |
| **M10SF-043** | 90% CEMI 52.5R + 10% Silica Fume S95 DM | 0.04 | 0.02 |
| **B1-15L-049** | 85% CEMI 52.5N + 15% Betocarb GY | 0.06 | 0.02 |
| **B3-041** | 100% CEM III A 52.5 L | 0.26 | 0.56 |
| **B3-15L-051** | 85% CEM III A 52.5 L + 15% Betocarb GY | 0.22 | 0.48 |

formulation until the day of testing.

As shown in Table 5, the compressive strength of the mortar formulations was measured at 28 days according to NF EN 196-1 [106] and the results show that M10SF-043 had higher compressive strength than M1-055. Compressive strength results of concrete formulations, measured according to NF EN 206-1 [107], show a higher strength for B3-041 compared to B1-15L-049 and B3-15L-051 at 28 days.

Water porosity tests for mortar and concrete formulations were carried out according to standard NF P18-459 [108] and it was found that water porosity decreased when substituting silica fume for 10% of the CEMI and when the w/b ratio was reduced. It was also found that the water porosity of concrete B3-15L-051 at 90 days was slightly higher than that of B1-15L-049 at 28 days and that the porosity of B3-041 was much lower than that of B1-15L-049 and B3-15L-051 due to the lower w/b ratio of this formulation.

The chloride migration coefficient was measured, according to standard NtBuild 492 [109] for mortar mixes, and according to the French standard XP P18-462 [110] for concrete mixes. It can be clearly seen that the migration coefficients were largely reduced when CEMI was replaced by silica fume. This was a result of the much lower overall porosity. The results also show that the chloride migration coefficients for slag-containing concrete mixtures, B3-041, and B3-15L-051, were much lower than that of B1-15L-049.

The electrical resistivity of mortar formulations was measured on 2 (for M1-055) and 3 (for M10SF-043) non-reinforced reference samples at different ages according to the RILEM TC-154 EMC procedure and gave the results presented in Fig. 1. The electrical resistivity of M1-055 was almost 100 Ω·m and did not evolve significantly with time. On the other hand, the resistivity of M10SF-043 increased with time to reach values as high as 700 Ω·m at 90 days and almost 1000 Ω·m at 317 days.

A more interesting feature of the galvanic coupling experiment is the electrical resistivity of the samples at the time of the test. Consequently, an indirect measurement method was used for the assessment of the electrical resistivity using at least four reinforced cathode samples subjected to an external polarization test coupled with 3D numerical simulation with Comsol Multiphysics software. This test is usually used to characterize the electrochemical behavior of an electrode/electrolyte system using the steady-state electrochemical response of the system, while the instantaneous response of the system allows the ohmic drop correction to be made. Hence, the numerical simulation that reproduces this test uses the instantaneous response to determine the electrical resistivity of the mortar or concrete under test. The details of the electrochemical testing and numerical simulation used to assess electrical resistivity will be detailed in an unpublished work by Chalhoub et al.

Table 6 presents the average values of electrical resistivity of all the mixes with the coefficient of variation (CV) and the ages of the samples when tested. It can be seen that the resistivity of mortar mixes are consistent with the values measured on reference samples (Fig. 1). It can also be seen that slag cement formulations (B3-041 and B3-15L-051) present higher resistivities than the concrete without slag (B1-15L-049), B3-041 having a higher resistivity than B3-15L-051 due to its lower w/b ratio.

### 3.3. Steel bar reinforcement types

All the steel bars used in this study were cold rolled ribbed steel bars (manufacturer: Fimurex, France) with a diameter of 6 mm and were taken from the same batch. No intended deformation was applied to the rebars and no bent parts were observed on them.

Four different types of steel surface conditions were investigated in this study, as summarized and explained in Table 7:

### 3.4. Preparation of samples

For each formulation, two types of samples were prepared according to the test procedure described in [31]. Samples were:

- Anode samples (shown in Fig. 2): These were reinforced samples with diameters, ϕ, of 33 mm and heights, h, of 70 mm having one steel bar embedded at their center, with dimensions of ϕ = 6 mm and h = 10 mm. These samples were contaminated with chlorides before being used either as test samples for corrosion tests or as reference samples for chloride-binding isotherms or for imbibition duration verification tests. For anode concrete samples, cylindrical concrete specimens with a diameter of 110 mm instead of 33 mm and a height of 70 mm were made because of the size of aggregates. After curing, the final anode (ϕ 33 × h 70 mm) was extracted from the cylindrical specimen by coring.
- Cathode samples (shown in Fig. 3): These were reinforced samples with dimensions of ϕ = 110 and h = 220 mm having one steel bar with dimensions of ϕ = 6 and h = 160 mm embedded at their center. These samples were chloride-free and are used as cathodes for galvanic coupling tests.

The formworks of all the samples were removed 24 h after casting. In both samples, the casting direction was parallel to the reinforcement bar. Both ends of rebars in all specimens used were protected with tin welding which was used to achieve the cable connections.

Table 8 presents the number of test and reference samples used for each mortar and concrete formulation and for the different steel surface

**Table 5**
Characterization tests results of the mortar and concrete formulations.

| | Compressive strength at 28 days $f_{c\,28}$ (Wet cure) | | Water porosity $p_w$ | | | Coefficient of migration of chlorides | | |
|---|---|---|---|---|---|---|---|---|
| | Average value (MPa) | Standard | Average value (%) | Age (days) | Norm | Average value ($10^{-12}$ $m^2/s$) | Age (days) | Standard |
| **M1-055** | 66 | NF EN 196-1 | 21.2 | 28 | NF | 19.68 | 28 | Nt Build 492 |
| **M10SF-043** | 91 | (4 × 4 × 16 *cm*) | 14.9 | 28 | P18-459 | 2.81 | 28 | |
| **B1-15L-049** | 40 | NF EN 206-1 | 16.3 | 28 | | 43.67 | 29 | XP P18-462 |
| **B3-041** | 74 | (φ11 × 22 *cm*) | 11.4 | 90 | | 0.83 | 92 | |
| **B3-15L-051** | 41 | | 17.2 | 90 | | 3.14 | 93 | |

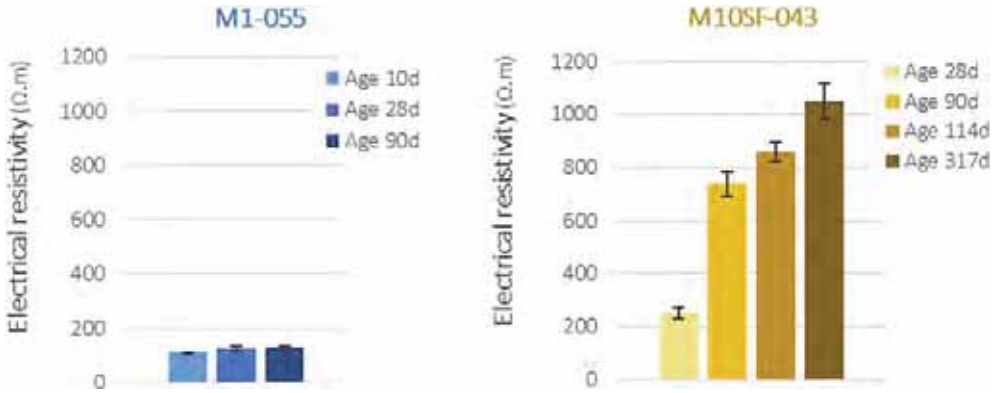


**Fig. 1.** Monitoring of electrical resistivity of M1-055 and M10SF0-43 according to RILEM TC-154 EMC.

**Table 6**
Electrical resistivity of the mortar and concrete formulations.

| | Electrical resistivity | | |
|---|---|---|---|
| | Average value (Ω.m) | CV (%) | Age (days) |
| **M1-055** | 113 | 7 | 40-300 |
| **M10SF-043** | 737 | 10 | 80-108 |
| **B1-15L-049** | 69 | 10 | 98 |
| **B3-041** | 718 | 2 | 255 |
| **B3-15L-051** | 267 | 1 | 289 |

conditions.

### 3.5. Preconditioning of anodes

After the preparation of samples, the specimens were unmoulded and wet cured (relative humidity RH = 95%) with the curing durations given in Table 9. After wet curing, anode samples were dried to constant weight and then submerged in saline solutions to initiate corrosion.

The anode samples were dried to constant weight in an oven at a controlled temperature of 45 °C and constant relative humidity of 25%. The samples were weighed regularly and the drying was stopped when the weight difference between 2 successive weighings at least 24 h apart did not exceed 0.05%.

Fig. 4 shows the evolution of the weight percentage of water removed according to the drying duration for each formulation. It can be seen that formulations M1-055 and B1-15L-049 needed almost 30 days to reach the predetermined weight loss criteria, whereas M10SF-043 needed 46 days and the formulations B3-15L-051 and B3-041 needed 72 and 140 days respectively.

Table 9 summarizes information about curing durations and the drying of anode samples. It was decided to wait at least 28 days for CEMI based formulations and 60 days for slag-containing formulations

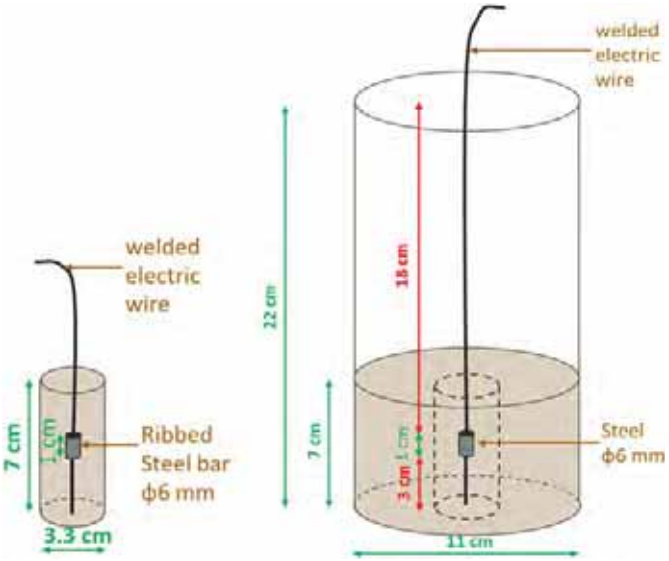


**Fig. 2.** Description of mortar (on the left from [31]) and concrete (on the right) anode samples

before starting their drying, in order to minimize the effect of hydration as much as possible.

$p_{dried}$ represents the average value of the porosity that is dried and it is calculated through weight loss measurements on all the test and reference samples. $p_w$ presents the measured water porosity of the formulations. The age of samples when characterized is also recalled. It is then possible to calculate the percentage of porosity that is dried by dividing $p_{dried}$ by $p_w$ and it can be seen that concrete samples were relatively more dried than mortar samples.

After anode drying, reference samples were immersed for 7 days to make sure that the imbibition duration of 48 h was sufficient to complete saturation in all the formulations. Then, test samples were soaked

**Table 7**
Types of reinforcement rebars used in this experimental set-up.

| Type of steel | Abbr | Treatment | Characteristics |
|---|---|---|---|
| **As Received Steel** | **ARS** | Without treatment | Presence of a non-uniform layer of mill scale |
| **Cleaned Steel** | **CS** | Cleaning with a chemical cleaning procedure based on standard ISO 8407 | Removal of the mill scale layer |
| **Cleaned Steel Pre-oxidized by high Temperature** | **CSPT** | Cleaning with a chemical cleaning procedure based on standard ISO 8407 followed by heat treatment of 72 h at 400 $^0$C | Removal of the mill scale layer and formation of a more homogeneous layer of corrosion products with a composition close to that of mill scale |
| **Cleaned Steel Pre-oxidized in a Humid environment** | **CSPH** | Cleaning with a chemical cleaning procedure based on standard ISO 8407 followed by exposure in a humid environment (relative humidity = 95%) | Removal of the mill scale layer and formation of a non-uniform oxidation layer |

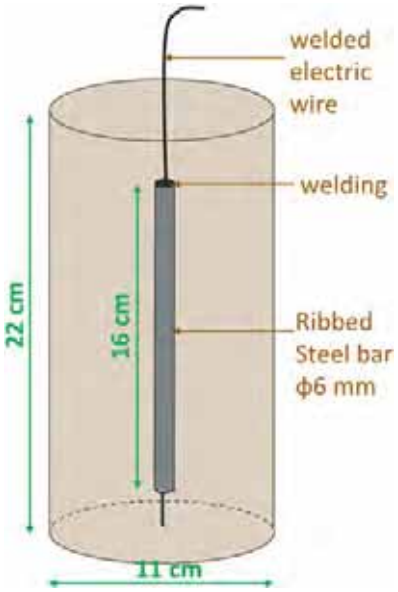


**Fig. 3.** Description of cathode samples.
(Taken from [31].)

in NaCl solutions with different concentrations for 48 h.

### 3.6. Transition from total to free chlorides

In studies of chloride-induced corrosion initiation, the chloride threshold content is usually expressed in the form of total chloride content rather than free chloride content. However, it is possible to link the two values with a relationship between bound chlorides and free chlorides, which is described by a Freundlich model in cases of high free chloride concentrations and a Langmuir model when dealing with low free chloride concentrations [57]. Hence, the Freundlich model was chosen for chloride binding in the reference samples soaked for 48 h in different concentrations of salt solutions.

The free and total chloride contents were measured as described in standard NF-EN-14629 [111] and the procedure recommended by GranDuBé [112], respectively, and these measured chloride contents are expressed as %/wt of concrete or mortar. It should be mentioned that the unit used for bound chloride (mg/g binder) is usually different from the unit used for free chloride (g/L) but, in this work, the same units were chosen for bound and free chlorides. In order to express the chloride contents in %/wt of binder, the measured chloride contents were divided by the mass percentage of binder (Mpb). The level of bound chlorides was calculated by subtracting the measured free chloride content from the measured total chloride content. The initial

**Table 9**
Information about curing and drying mortar and concrete anodes.

| Formulation | Duration of wet curing (d) | $p_{dried}$ (%) | Drying duration (d) | $p_w$ (%) | Age (days) | $p_{dried}$ /$p_W$ (%) |
|---|---|---|---|---|---|---|
| **M1-055** | 28 | 16.1 | 34 | 21.2 | 28 | 75 |
| **M10SF-043** | 28 | 11.7 | 46 | 14.9 | 28 | 78 |
| **B1-15L-049** | 28 | 16.0 | 34 | 16.3 | 28 | 98 |
| **B3-041** | 60 | 11.1 | 142 | 11.4 | 90 | 97 |
| **B3-15L-051** | 60 | 17.1 | 72 | 17.2 | 90 | 99 |

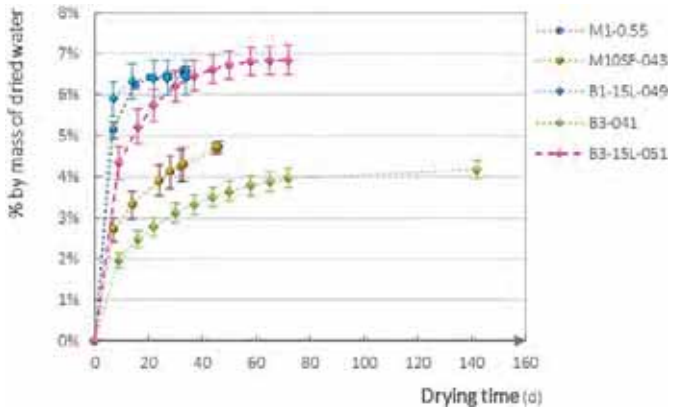


**Fig. 4.** Percentage by mass of water removed according to the drying time.

amounts of total and free chlorides were determined from chloride measurements made on reference samples that were soaked in demineralized water only. For concrete samples, these contents were taken as the average values of the chloride contents measured on three different reference samples.

### 3.7. Measurement of macrocell current

After the preconditioning of anode samples, cathodes were taken from the curing room and placed with the anodes in a sodium hydroxide solution in a room where the temperature was controlled at 20 °C. Then, galvanic connections were made between anodes and cathodes and corrosion currents were measured for 168 h. The apparent C/A ratio in this case is equal to 16.

The average galvanic currents, noted $I_{g\ avg}$, were then calculated and total chloride contents at the level of the rebars were measured experimentally. For this purpose mortar powder was taken at the level of the steel bar after splitting the sample in the middle and removing a thickness of 5 mm of mortar from either side (illustrated in a previously reported study [31]). The free chloride contents were deduced from the

**Table 8**
Number of test and reference samples.

| | Formulation | Steel type | Number of test samples | | | | Number of reference samples | |
|---|---|---|---|---|---|---|---|---|
| | | | Anode samples | | Cathode samples | | Chloride-binding isotherms | Imbibition duration test |
| **Mortar** | **M1-055** | ARS | 41 | 63 | 6 | 12 | 7 | 5 |
| | | CS | 11 | | 3 | | | |
| | | CSPT | 3 | | 2 | | | |
| | | CSPH | 8 | | 1 | | | |
| | **M10SF-043** | ARS | 19 | 47 | 5 | 15 | 6 | 5 |
| | | CS | 13 | | 5 | | | |
| | | CSPT | 15 | | 5 | | | |
| **Concrete** | **B1-15L-049** | ARS | 14 | 43 | 8 | 24 | 11 | 5 |
| | **B3-041** | ARS | 16 | | 8 | | 15 | 5 |
| | **B3-15L-051** | ARS | 13 | | 8 | | 10 | 4 |

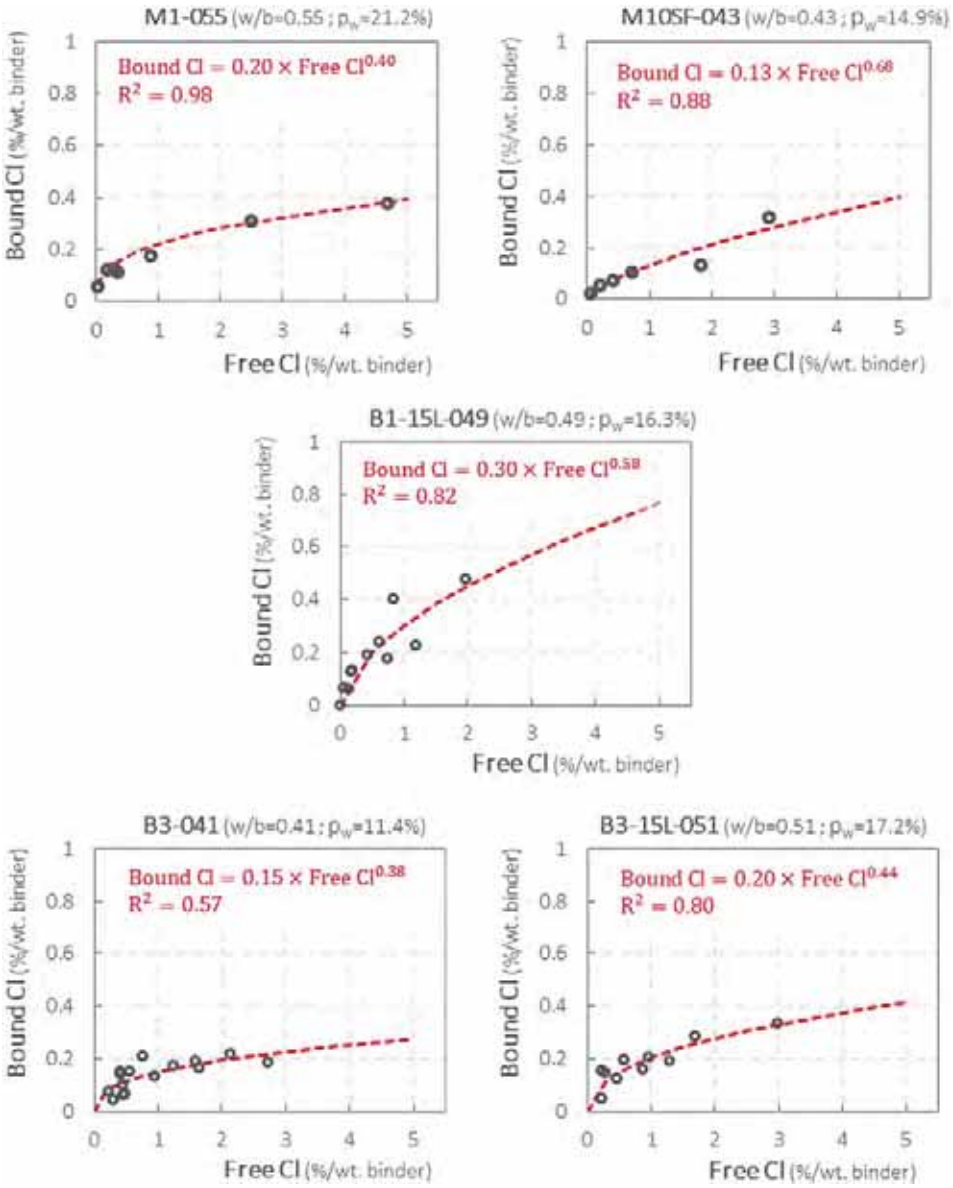


**Fig. 5.** Chloride-binding isotherms for all the formulations.

**Table 10**
Initial free and total chloride contents measured experimentally on reference samples.

| Formulations | Initial total Cl content (%/wt. binder) | Initial free Cl content (%/wt. binder) |
|---|---|---|
| **M1-055** | 0.09 | 0.03 |
| **M10SF-043** | 0.09 | 0.07 |
| **B1-15L-049** | 0.13[a] | 0.07[a] |
| **B3-041** | 0.41[a] | 0.32[a] |
| **B3-15L-051** | 0.35[a] | 0.25[a] |

[a] Average value of chloride contents from 3 different samples.

total chloride contents using the chloride-binding isotherm relations presented in Fig. 5.

The critical chloride contents, expressed in terms of free chlorides per weight of binder, were determined for each formulation and steel type according to the criterion developed in [31], which is based on a critical limiting current $I_{crit}$ of 3 µA.

The anode samples were then connected to larger cathodes which consisted of reinforced walls presenting an apparent C/A ratio of 2950. The dimensions of the walls and the details of this experiment can be found elsewhere [31]. The objective of this test was to highlight the concept of chloride threshold, which is based on a limiting current independent of the C/A ratio.

### 3.8. Measurement of the surface area of active steel

After the end of electrochemical measurements, the anode is split in the middle and the steel bar was removed and cleaned to remove all the corrosion products at the steel surface using the ISO 8407 standards [113]. The surface area of corroded steel was measured using the software ImageJ on the images taken from microscopic observations of the rebar.

## 4. Results

### 4.1. Chloride-binding isotherms

Fig. 5 shows all the isotherms for all the formulations. The corresponding Freundlich relation is indicated in red on each graph with the

a) M1-055 results

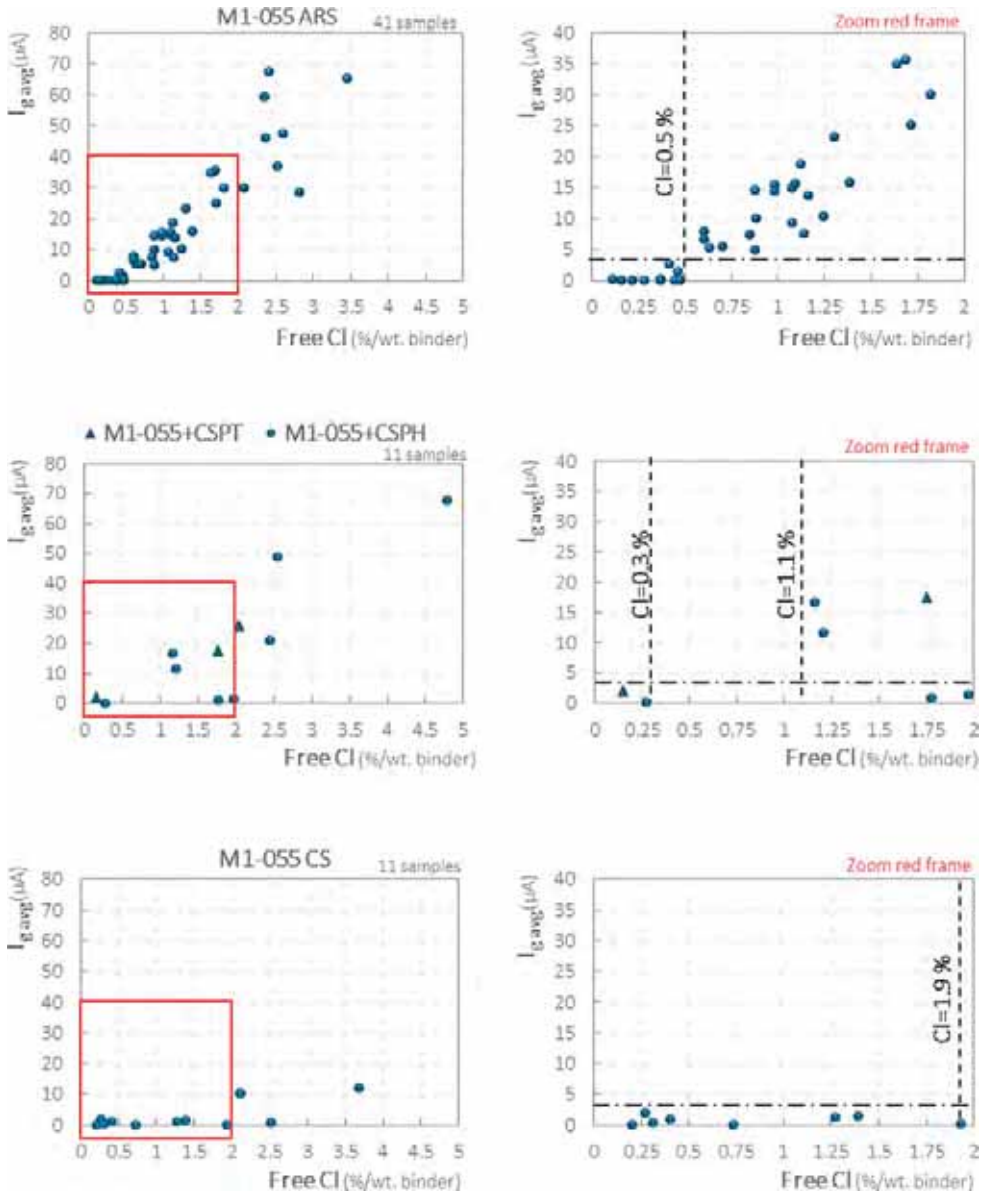


**Fig. 6.** M1-055 results for the 4 types of steel from [31].

corresponding coefficient of determination, $R^2$. It should be noted that these isotherms, corresponding to the imbibition process, do not correspond to classical isotherms of massive samples, where chlorides penetrate through the concrete by diffusion, which could partially explain the low bound chloride contents found.

These results show that the binding of chlorides decreases in presence of slag, which is contradictory to the observations found in the literature [60,70,71]. Also, binding decreases with w/b ratio and decreases slightly in presence of silica fume. When comparing B1-15L-049 and M1-055, it can be seen that B1-15L-049 bound almost twice as much chloride as M1-055.

The initial free and total chloride contents that were measured on reference samples soaked only in demineralized water are presented in Table 10. The results clearly show that the formulations B3-041 and B3-15L-051 presented the highest amounts of initial chlorides, while the other formulations presented almost the same amount of chlorides, around 0.1%/wt. binder.

The results in Table 10 were qualitatively in agreement with the initial chloride levels measured experimentally. It should be noted that the initial chloride contents in B3-041 and B3-15L-051 are in agreement with the French application of the European standard EN 206, since their initial chloride contents are below the limit of 0.65%/wt. binder for CEM III concrete (Table 1).

### 4.2. Galvanic coupling between anodes and cathodes

This section presents the results of galvanic coupling tests between anodes and cathodes. In each graph, *Ccrit* is mentioned and is indicated with a black vertical dashed line while $I_{crit}$ is indicated with a black horizontal dashed line. The number of tested samples is also stated.

It was proposed to use margins of variation of *Ccrit* in case of a lack of tested samples for certain chloride contents.

### 4.3. Galvanic coupling between anodes and extremely large cathodes

Fig. 9 shows the results of corrosion currents obtained for the

a) M10SF-043 results

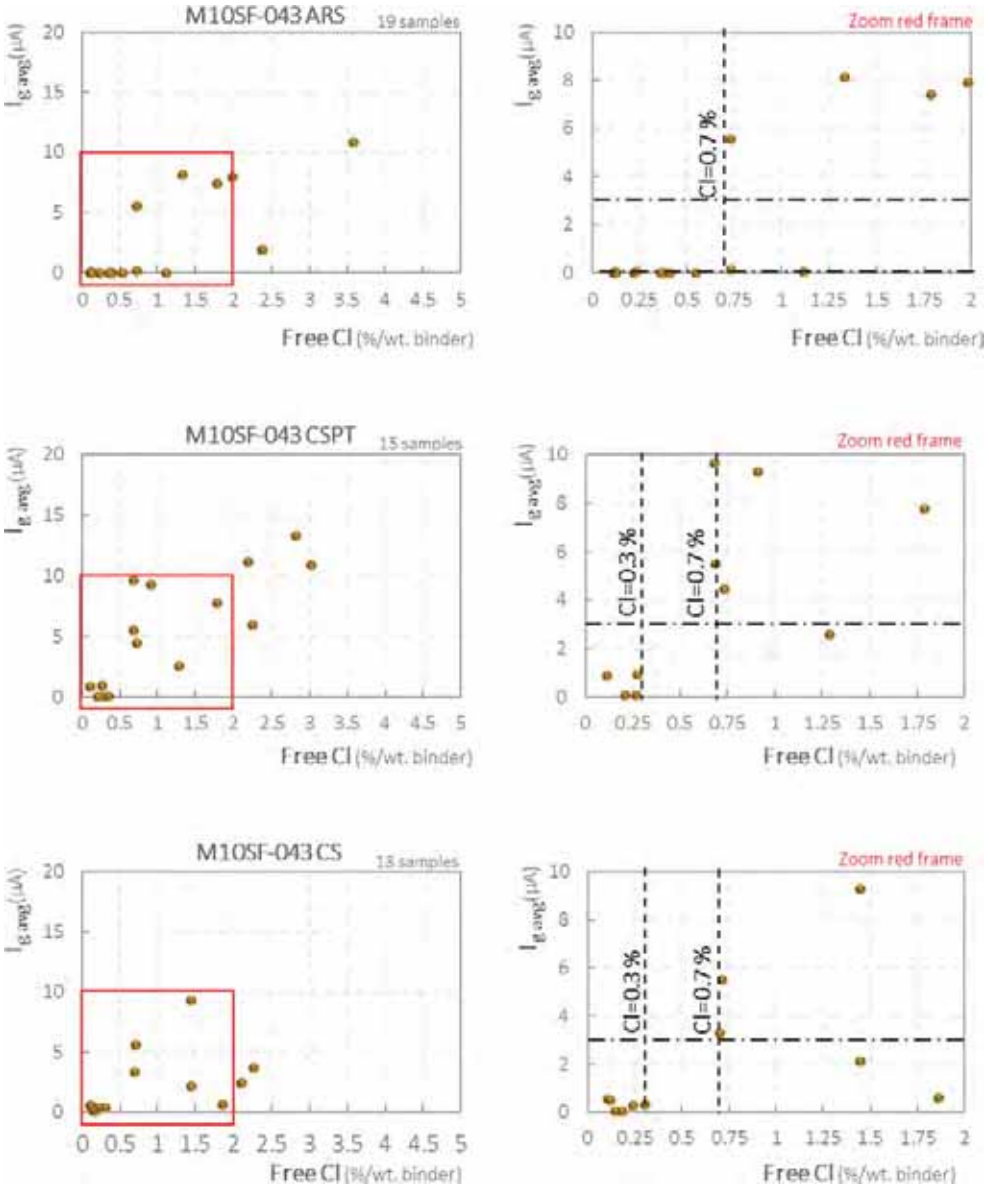


**Fig. 7.** M10SF-043 results for the 3 types of steel.

apparent C/A ratio of 2950 (when the anode is connected to the wall) and compares them with the results when the C/A ratio is 16 (when the anode is connected to the cylindrical cathode).

For chloride contents lower than 0.5% in M1-055 and 0.7% in M10SF-043, corrosion currents are almost the same and lower than $I_{crit}$ whatever the apparent C/A ratio.

As mentioned in [31], the apparent C/A ratios are different from the effective C/A ratios, which are considerably higher since they are calculated from the real anodic areas measured after splitting the samples. Despite the difference between the orders of magnitude of the two C/A ratios, their influence on corrosion current according to chloride contamination was found to be the same.

### 4.4. Autopsy and measurement of surface area of corroded steel

Some of the anodes of mortar formulations with ARS bars were split and the steel bars were cleaned, then observed with a microscope in order to measure the surface area of steel that was corroded. Fig. 10 shows a 3D visualization with X-ray tomography obtained at CEA Saclay, France of two anode samples made with the M1-055 formulation that were contaminated with chloride contents of 0.37% (photograph on the left) and 2.07%/wt. binder (two photographs on the right). These photographs clearly show that the rebar of the anode sample with a low chloride level is in a passive state, whereas the one with the higher chloride level presents a mixed surface condition of active (corroded) and passive areas.

As stated in [31], the measured corroded area increased with chloride content. The variation of the ratio between active surface areas, Sa, and the total surface area of the anode, S, could be approached by a linear regression model as shown in Fig. 11.

### 4.5. Steel weight loss measurements

Gravimetric measurements were also made on some anode samples. Fig. 12 shows the percentage of steel weight loss (Δw/wt. steel) according to the level of chloride content for all the formulations (graphs

b) Results of concrete formulations with ARS

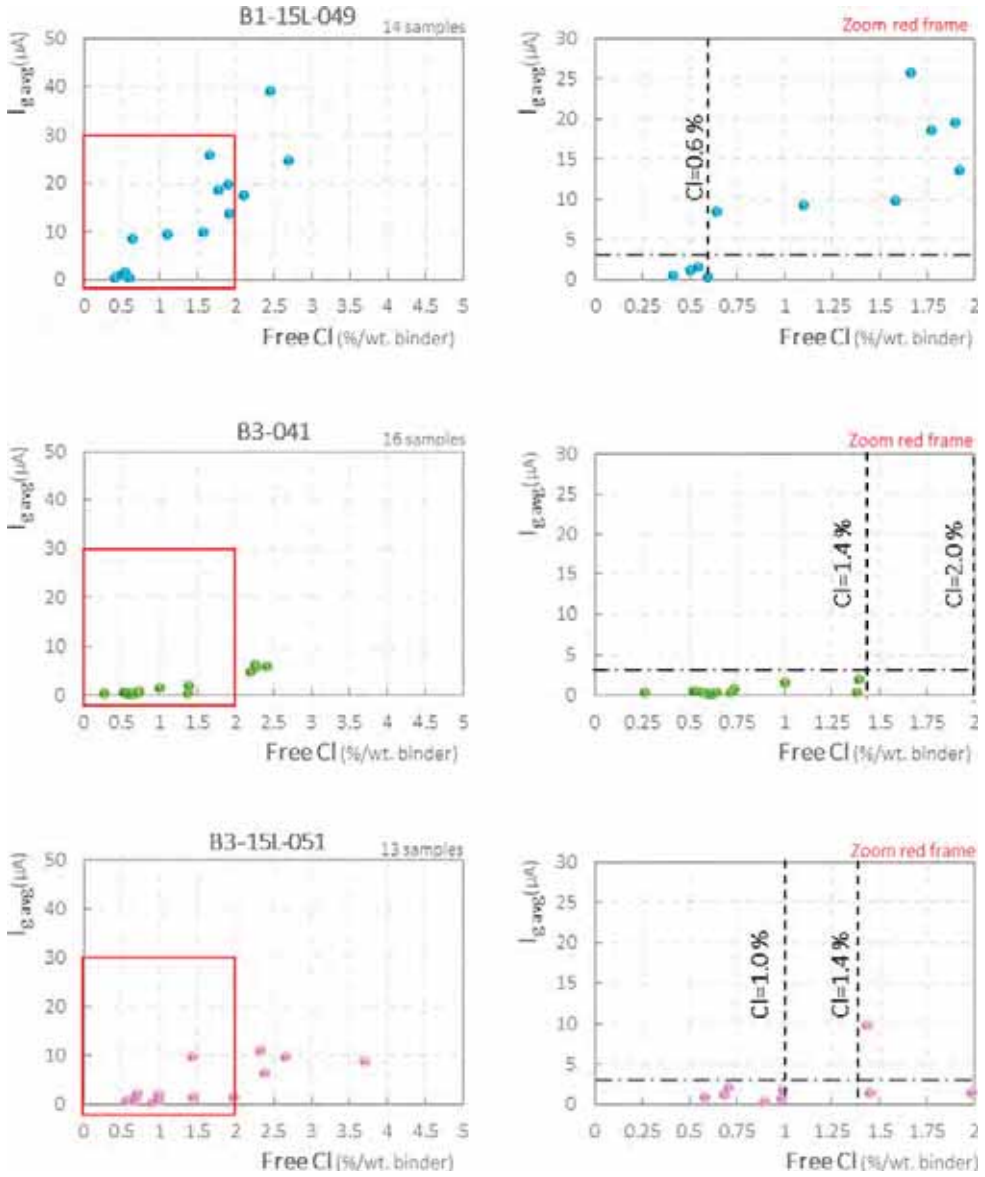


**Fig. 8.** B1-15L-049, B3-041 and B3-15L-051 results.

on the left) except B3-15L-051 and B3-041. The weight loss measurements of these last mentioned formulations are not presented because the steel weight losses were relatively too low and close to the measurement error. The steel weight loss of M10SF-043 was also relatively low but is presented here for purposes of comparison.

Fig. 12 also shows the relationship between the measured corrosion current $I_{g\ avg}$ and the corrosion current, $I_{Faraday}$, calculated from Faraday's law by using the weight loss measured (graphs on the right).

The mean and maximum values of the steel weight loss of B1-15L-049 are between 1.5 and 2 times smaller than the ones measured in M1-055, which is qualitatively consistent with the corrosion current results of both formulations.

In addition, the steel weight loss measurements of M10SF-043 are > 3 times lower than those of M1-055, which is also in agreement with the very low corrosion currents obtained with M10SF-043.

Furthermore, the calculated $I_{Faraday}$ were generally higher than the measured $I_{g\ avg}$, although both currents showed the same trend and the difference between them can be partly attributed to both internal macrocell corrosion and microcell corrosion currents at the anode, which cannot be measured experimentally with galvanic coupling set-ups.

It must be noted, however, that weight loss measurements are subject to uncertainties, which means that most of the results are simply indicative.

## 5. Discussion

In the previous section, the corrosion currents versus chloride content data were plotted separately for different mortar and concrete mixes with different types of steel surface conditions.

An overall analysis shows that corrosion currents increase with chloride content.

When considering mortar mixes, it is clear that corrosion currents in M10SF-043 (Fig. 7) are lower than the currents obtained with M1-055 (Fig. 6) because of the higher electrical resistivity in presence of silica fume.

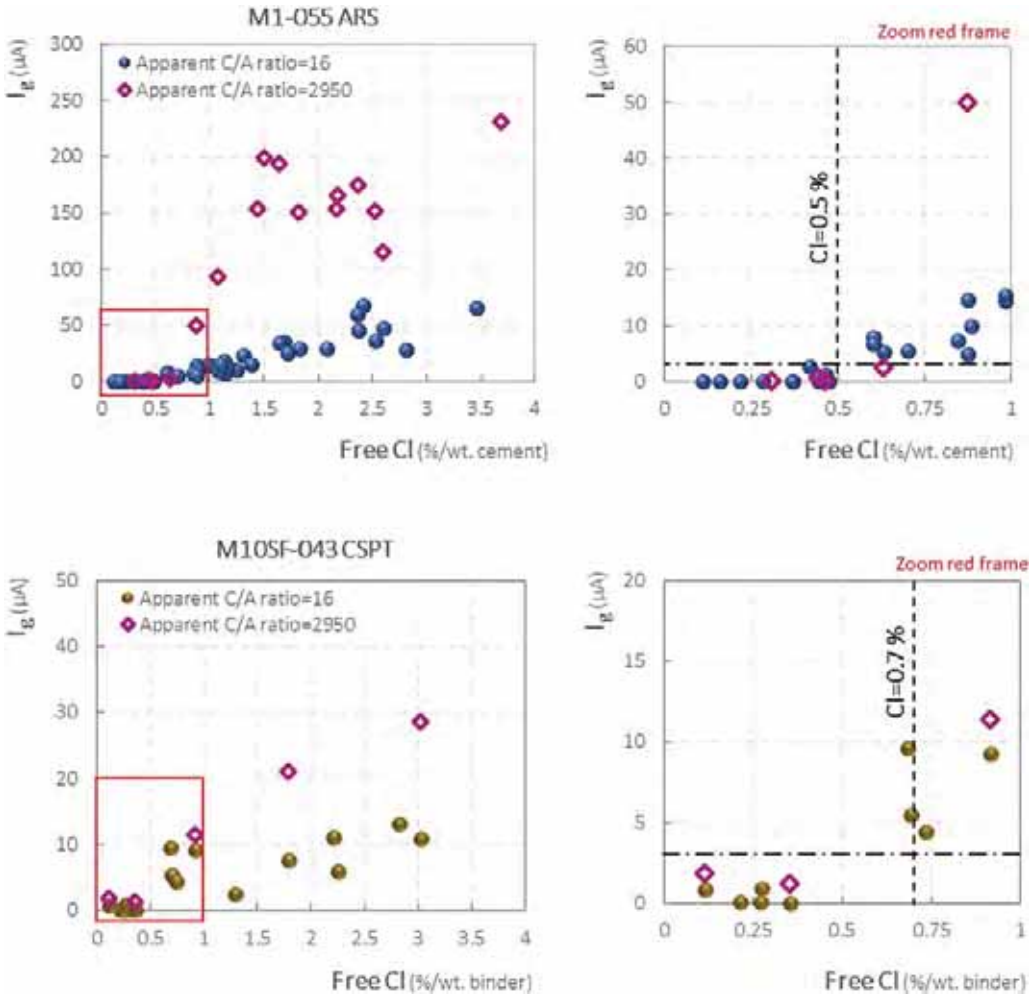


**Fig. 9.** Ig measured for different free chloride contents for apparent C/A ratios of 16 and 2950.
Most of the M1-055 results are taken from [31].

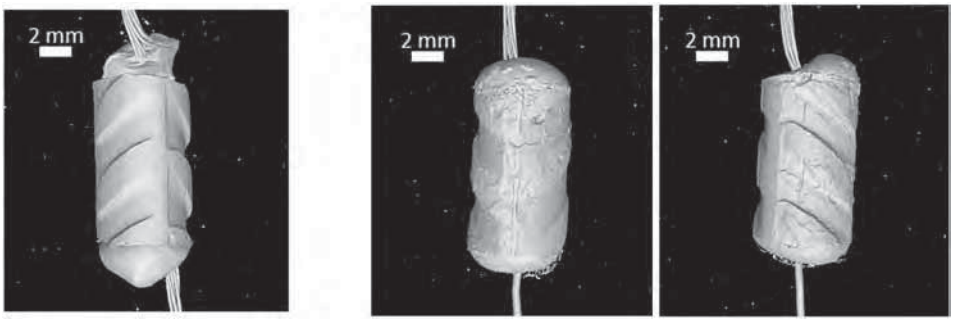


**Fig. 10.** 3D visualization of 2 anode samples made with the formulation M1-055.
The first sample is contaminated with a free Cl content of 0.37%/wt. binder (photograph on the left).
The second sample (shown from different angles) is contaminated with a free Cl content of 2.07%/wt. binder (2 photographs on the right) (X-ray Tomography (CEA Saclay, France)).

As shown in Fig. 6, a very high *Ccrit* value and lower currents were found for M1-055 with CS rebars compared to ARS rebars and almost the same behavior was observed between M1-055 samples with ARS and CSPT.

In case of M10SF-043 samples presented in Fig. 7, despite the lack of tested samples in the case of CS rebars, especially for chloride contents between 0.3 and 0.7%/ wt. binder, it is possible to argue that currents obtained in case of CS samples were somewhat lower than the ones obtained with the ARS samples. The CSPT samples of M10SF-043 appeared to have a behavior similar to that of ARS samples but the corrosion currents were slightly higher. This result could be explained by the nature of oxides formed on steel in the absence of mill scale (case of CS) which could be less porous to chloride ingress than those formed in the presence of mill scale (case of ARS) and those formed on CSPT.

When considering concrete mixes, presented in Fig. 8, in which only ARS rebars were embedded, formulations with slag cements, B3-041 and B3-15L-051, presented lower corrosion currents than concrete without slag, B1-15L-049, due to their higher electrical resistivity. Also, the macrocell currents obtained with B3-041 appear to be lower than the ones obtained with B3-15L-051 which could be explained by the lower w/b ratio of the formulation B3-041. Additionally, both formulations B3-041 and B3-15L-051 had higher *Ccrit* values than B1-15L-049 with the B3-041 formulation having the highest *Ccrit* value.

Nevertheless, as the binder compositions and binder amounts were different, it is difficult to compare the different *Ccrit* values obtained.

It seems reasonable to suppose that the onset of corrosion at the SCI

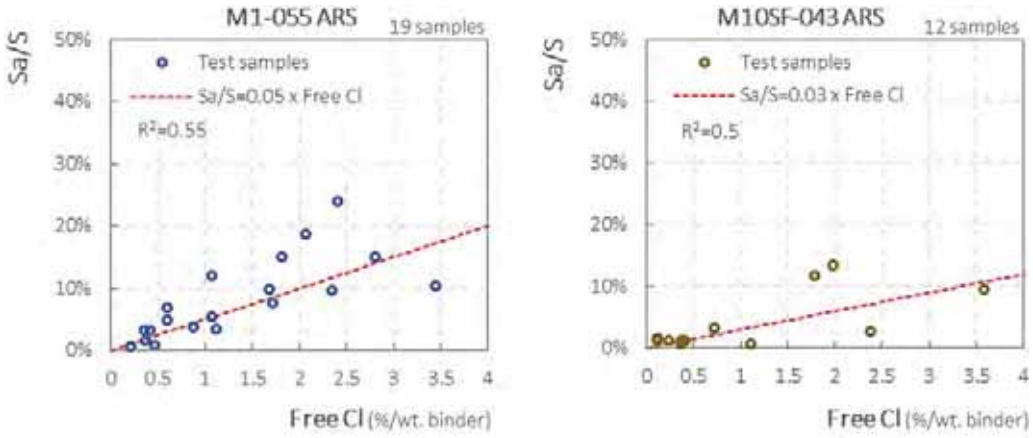


**Fig. 11.** Area of corroded surface at anode bars as a function of free Cl contents in case of mortar formulations.
Most of M1-055 results are taken from [31].

is dependent on the free chloride concentration in the pore solution and that the onset of corrosion could also be linked to the porosity.

We therefore propose to calculate the free chloride content *Free* [*Cl*] in the porosity to compare the results obtained on the different compositions of mortar or concrete.

Table 11 summarizes the different critical chloride contents of the mixes studied, showing only the ARS sample results that were presented earlier in Section 4.2. It also shows the initial chloride contents measured experimentally on reference samples that were presented previously in Section 4.1.

*Ccrit* values are presented in Table 11 according to different expressions:

- *Total* $Ccrit_b$ is the total critical chloride content per weight of binder expressed in %/wt. binder;
- *Free* $Ccrit_b$ is the free critical chloride content per weight of binder expressed in %/wt. binder;
- *Total* $Ccrit_m$ is the total critical chloride content per weight of material (mortar or concrete) expressed in %/wt. material;
- *Free* $Ccrit_m$ is the free critical chloride content per weight of material (mortar or concrete) expressed in %/wt. material;
- *Free* [*Cl*] represents the critical concentration of free chlorides expressed in g per litre of pore water and calculated with the following equation:

$$Free\ [Cl] = \frac{Free\ Ccrit_m \times \rho}{p_w} = \frac{Free\ Ccrit_b \times C_b}{p_w} \quad (2)$$

where:

- $p_w$ is the water porosity (%);
- ρ is the theoretical density of material (mortar or concrete);
- $C_b$ is the binder content (kg/m$^3$ of material).

Since a margin of variation of *Ccrit* was proposed for B3-041 and B3-15L-051 due to the lack of tested samples, it was found more appropriate to adopt a conservative approach by choosing the lower *Ccrit* values for each case.

It is quite interesting to see that critical chloride content expressed in terms of free chloride content in the porosity is the same for the mortar cast with CEM I (M1-055) and the concrete cast with CEM I (B1-15L-049). The porosity of the cement paste was also calculated and it was found to be similar in both the previous compositions (45% for M1 and 51% for B1-15L-049), considering that there is less paste in concrete mix than in mortar mix.

If there is a decrease in porosity, the chloride threshold expressed in terms of free chloride contents increases strongly: there is a factor of 2 between the mortar including SF (M10SF-0.43) and the ordinary mortar (M1-055). In this case, the porosity ratio is 1.4. It is then interesting that, for an equivalent porosity ratio and the same binder, 1.5 between the concretes B3-041 and B3-15L-051, the difference between chloride thresholds is also equivalent: 2.35 compared to 2.

The expression of chloride threshold in terms of free chloride content in the porosity then seems more reliable for comparing different compositions of concrete. It would also be possible to propose a model of variation of chloride threshold *Free* [*Cl*] according to the water porosity of cement paste if more concrete compositions were tested.

Fig. 13 presents the *Free* [*Cl*] threshold values that were found in this study for CEMI samples (M1-055, M10SF-043 and B1-15L-049) and CEMIII samples (B3-04 and B3-15L-051) according to the calculated water porosity of the cement paste. It also shows published critical *Free* [*Cl*] results from the literature [48,114–116] obtained from laboratory experiments using steel directly immersed in solutions. These were considered to be associated with a porosity of 100%, which could simulate, in this case, a steel–solution interface. It must be noted that the investigations all used different surface conditions of steel, such as cleaned, polished or, in one study, not reported [114]. Additionally, different pH values were tested and the results showed a strong influence of pH on the critical chloride concentration [116].

Despite the scatter observed, it seems that *Free* [*Cl*] values obtained from tests dealing with steel embedded in mortar or concrete, where the porosity is far below 100%, present higher *Free* [*Cl*] values than those found in experiments in solution, where porosity is assumed equal to 100%.

This result is also consistent with observations from Angst et al. [7], who found that critical chloride content of steel in solutions varied between 0.0056 and 0.42 mol/L (equivalent to 0.2 and 15 g/L).

All these observations confirm the importance of considering the steel–concrete interface as a first-order influencing factor [7] which could explain why it is commonly agreed that experiments in alkaline solutions are not appropriate to simulate experiments in concrete.

It can be concluded that a relationship may exist between the free chloride threshold concentration in porosity and the water porosity of cement paste. For 0% porosity, the threshold concentration is supposed infinite since no corrosion occurs and, for 100% porosity, the results from steel in solution show lower critical concentrations. The results of the different formulations studied in this work show the same trend, where lower porosity formulations are associated with higher critical chloride concentrations and concentrations are slightly higher in the

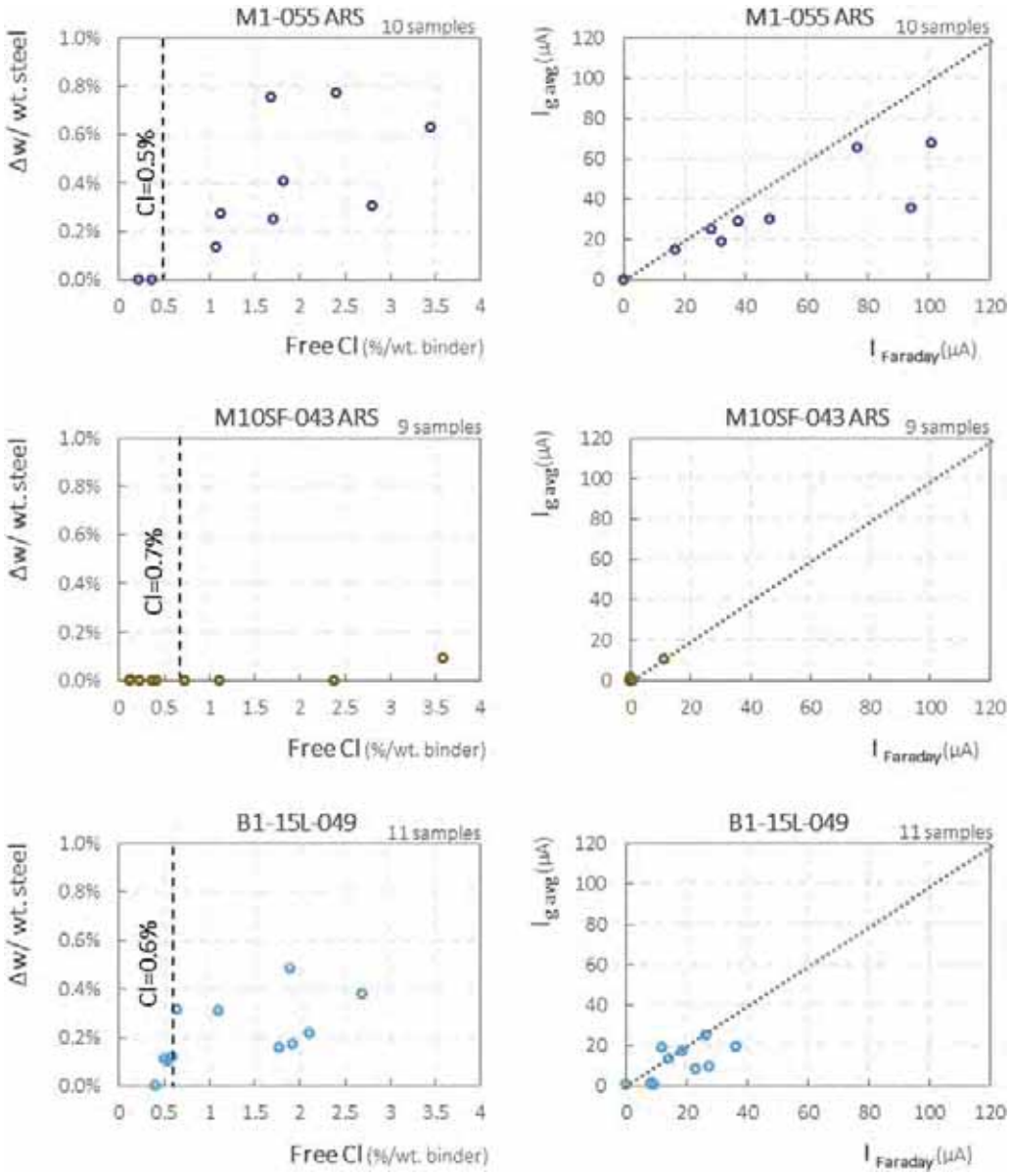


**Fig. 12.** Gravimetric measurements (on the left) and (on the right).
M1 results taken from [31].

case of CEMIII mixes. This statement needs to be confirmed by further investigations, however.

In addition, it is possible to assess the impact of binder type on *Ccrit* using an equation established in the RILEM TC 262-SCI paper [33]. The chosen equation (Eq. (3)) allows chloride-induced corrosion to be evaluated in the absence or presence of a certain predefined criterion. The equation normalizes the effect and thus allows the impact of the influencing elements to be compared between different test protocols. Moreover, the sign of the effect shows whether the characteristic has a positive or negative effect on *Ccrit*. This method is based on the assumption that the parameters influencing *Ccrit* are independent. It should be noted that the expression for *Ccrit* used in this study is the concentration of free chloride in the pore solution, *Free* [*Cl*].

$$E_{x,j} = \frac{C_{crit}^{x,j} - C_{crit}^{Ref,j}}{min\{C_{crit}^{x,j}, C_{crit}^{Ref,j}\}} \quad (3)$$

where:

- x is the characteristic under study;
- $E_{x,\,j}$ is the effect of a particular characteristic x;
- $C_{crit}^{x,\,j}$ is *Ccrit* of the characteristic x stated in a study j;
- $C_{crit}^{Ref,\,j}$ is *Ccrit* of the reference case in the same study j.

Fig. 14 presents the effect of silica fume (SF) inclusion and w/b ratio on corrosion initiation, according to Eq. (3), for mortar formulations. The reference case is the formulation M1-055 and the studied case is M10SF-043, for which 19 samples were tested. It can be seen that reducing the w/b ratio by 22% and replacing cement with 10% of silica fume have a positive effect ($E_{x,\,j} = 1.0$) on corrosion initiation.

Fig. 15 presents the effect of cement type on corrosion initiation. The reference case is the formulation B1-15L-049 made with *CEMI* and the studied case is the formulation B3-15L-051 made with *A*, where 13 samples were tested. Both formulations have the same w/b ratio and contain 15% of limestone additions, the only difference is the cement type. The presence of slag in concrete can be seen to have a positive effect ($E_{x,\,j} = 0.7$) on the resistance to corrosion initiation.

Fig. 16 presents the effect of w/b ratio on corrosion initiation. The reference case is the formulation B3-15L-051 made with *CEMIII A* and

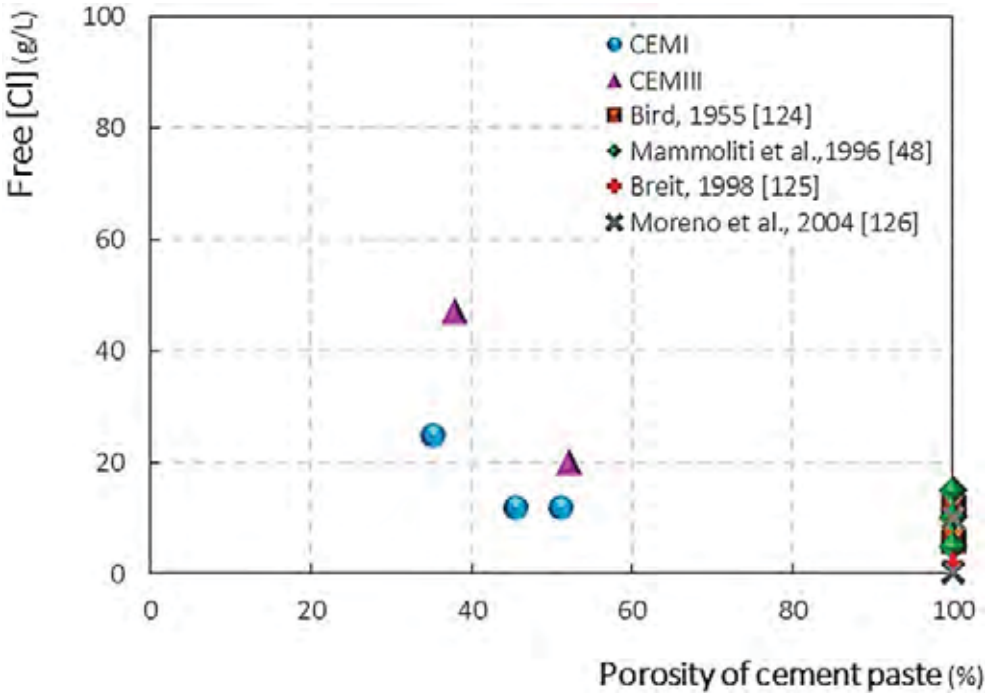


**Fig. 13.** Critical chloride concentrations according to water porosity of cement paste.

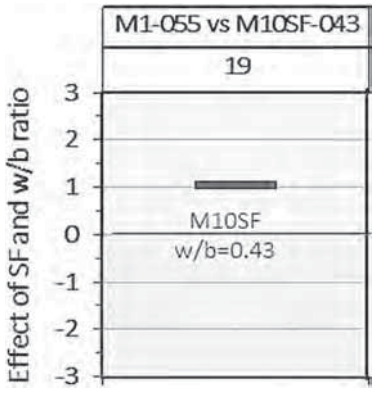


**Fig. 14.** Influence of SF and w/b ratio based on [33].
(Reference case is M1-055).
(Studied case is M10SF-043).

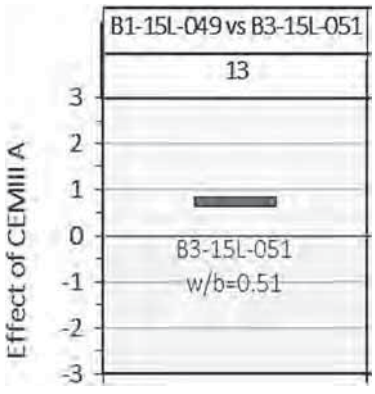


**Fig. 15.** Influence of CEMIII based on [33].
(Reference case is B1-15L-049).
(Studied case is B3-15L-051).

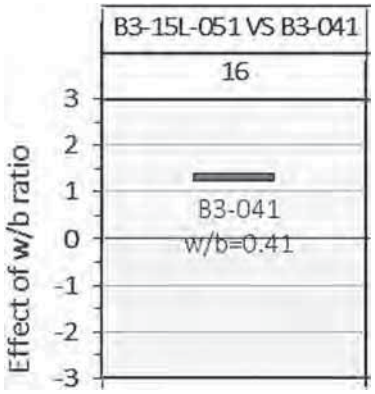


**Fig. 16.** Influence of w/b ratio based on [33].
(Reference case is B3-15L-051).
(Studied case is B3-041).

the studied case is the formulation B3-041 also made with *A*, where 16 samples were tested. Both formulations have the same cement type but have different w/b ratios and only B3-15L-051 contains limestone additions. It can be deduced that reducing the w/b ratio by 20% has a positive effect ($E_{x,\ j} = 1.3$) on corrosion initiation.

This presentation makes it possible to qualitatively compare the results shown in this paper with those published in the literature. In the RILEM TC 262-SCI paper [33], it was found that the effect of binder type on the susceptibility of steel to chloride-induced corrosion initiation was still unclear, with a weak overall effect on Ccrit ($< \pm 1.5$). It was also found that decreasing the w/b to below 0.5 had a slight positive effect ($0 \leq E_{x,\ j} \leq 1$) on corrosion initiation with an increase of critical chloride contents by approximately 30% [33].

As for the effect of steel surface condition, it was found that, in M1-055, the presence of mill scale alone on the steel bars had a negative impact on Ccrit. For instance, in this case, the Ccrit value obtained with the CS rebars was found to be 1.9%/ wt. binder, whereas Ccrit obtained in ARS samples was 0.5%/ wt. binder. It can be assumed that this result is consistent with the literature, where the presence of mill scale or corrosion products on the steel surface has a negative effect on

**Table 11**
Summary of critical chloride contents according to the different types of formulations in the case of ARS.

| Formulation | Initial Cl content (%/wt. binder) | | $Ccrit_b$ (%/wt. binder) | | $Ccrit_m$ (%/wt. material) | | *Free* [Cl] (g/L) |
|---|---|---|---|---|---|---|---|
| | Total Cl | Free Cl | Total $Ccrit_b$ | Free $Ccrit_b$ | Total $Ccrit_m$ | Free $Ccrit_m$ | |
| **M1-055** | 0.09 | 0.03 | 0.65 | 0.50 | 0.15 | 0.12 | 12 |
| **M10SF-043** | 0.09 | 0.07 | 0.80 | 0.70 | 0.19 | 0.17 | 25 |
| **B1-15L-049** | 0.13 | 0.07 | 0.82 | 0.60 | 0.12 | 0.09 | 12 |
| **B3-041** | 0.41 | 0.32 | 1.58 | 1.4 | 0.25 | 0.22 | 47 |
| **B3-15L-051** | 0.35 | 0.25 | 1.20 | 1.0 | 0.17 | 0.14 | 20 |

corrosion initiation [33].

On the other hand, M10SF-043 samples with CS and CSPT presented certain ranges of Ccrit instead of one fixed value. Hence, it was difficult to quantitatively define the effect of the steel surface condition on corrosion initiation. However, given the results, it can be argued that, in the case of M10SF-043, the effect of the steel type condition on corrosion initiation was almost inexistent.

## 6. Conclusion

This paper is based on an experimental test protocol developed by Chalhoub et al. [31] that takes the localized aspect of chloride induced corrosion in concrete into account and allows the critical chloride content to be determined on the basis of a limit corrosion current that is independent of the C/A ratio. In this work, several mortar and concrete formulations were tested and different types of steel surface condition were also investigated.

It was found that including 10% of silica fume in the mortar formulation with a lower w/b ratio improved *Ccrit* compared to a mortar formulation made only with CEMI.

On the other hand, the use of CEMIIIA instead of CEMI in concrete formulations for the same w/b ratio presented higher *Ccrit* values. Moreover, in CEMIIIA concrete formulations, the decrease of w/b seemed to increase *Ccrit* values. These results agree on the fact that a lower w/b ratio increases *Ccrit*.

It was also found that the absence of mill scale and pre-existing corrosion products (when the rebars were chemically cleaned) had a mainly positive impact on *Ccrit* in the case of CEMI mortar formulation. However, the effect of steel surface type seems to depend on other factors such as the w/b ratio and the binder type since, in the CEMI formulation with 10% of silica fume, no clear effect of steel surface condition on *Ccrit* was observed.

Additionally, it is important to state that the EN 206 standard allows for a significant initial chloride level present at mixing for CEMIII concrete, which seems adequate since the critical chloride contents were relatively high for CEMIII concrete. Moreover, the value of the total chlorides present initially in CEMIII concretes was found to be 0.41%/wt. cement, which is slightly higher than many maximum initial chloride limits applied in several countries, except, for example, in France, which allows 0.65% wt. cement.

Finally, a potential relationship could exist between the free chloride threshold concentration in the porosity and the water porosity of cement paste, where lower porosity formulations are associated with higher critical chloride concentrations, the concentrations being slightly higher in the case of CEMIII mixes. This statement remains to be confirmed by further studies, however.

## CRediT authorship contribution statement

**Chantal Chalhoub:**Investigation, Resources, Writing - original draft, Writing - review & editing.**Raoul François:**Supervision, Validation.**Myriam Carcasses:**Supervision, Validation

## Declaration of competing interest

The authors declare that they have no known competing financial interests or personal relationships that could have appeared to influence the work reported in this paper.

## Acknowledgments

This work was supported by the ANR MODEVIE project, grant ANR-14-CE22-0018 of the French National Research Agency (ANR) and by the French National Federation of Public Works (FNTP).

This work was also a part of a project partially financed by IREX.

## References

[1] A. Neville, Chloride attack of reinforced concrete: an overview, Mater. Struct. 28 (1995) 63.
[2] M.F. Montemor, A.M.P. Simões, M.G.S. Ferreira, Chloride-induced corrosion on reinforcing steel: from the fundamentals to the monitoring techniques, Cem. Concr. Compos. 25 (2003) 491–502.
[3] G.K. Glass, Y. Wang, N. Buenfeld, An investigation of experimental methods used to determine free and total chloride contents, Cem. Concr. Res. 26 (1996).
[4] K. Byfors, C.M. Hansson, J. Tritthart, Pore solution expression as a method to determine the influence of mineral additives to cement on chloride binding, Cement Concrete Research 16 (1986).
[5] M. Maslehuddin, C.L. Paget, Rasheeduzzafar, Temperature Effect on the Pore Solution Chemistry in Contaminated Cements, vol. 49, (1997).
[6] G.K. Glass, N. Buenfeld, The presentation of the chloride threshold level for corrosion of steel in concrete, 39 (1997).
[7] U. Angst, B. Elsener, C.K. Larsen, Ø. Vennesland, Critical chloride content in reinforced concrete—a review, Cem. Concr. Res. 39 (2009) 1122–1138.
[8] K. Tuutti, Corrosion of Steel in Concrete, Swedish Cement and Concrete Research Institute, 1982.
[9] U. Angst, B. Elsener, C. Larsen, Ø. Vennesland, Chloride Induced Reinforcement Corrosion: Electrochemical Monitoring of Initiation Stage and Chloride Threshold Values, vol. 53, (2011).
[10] G. Burstein, P. Pistorius, S. Mattin, The nucleation and growth of corrosion pits on stainless steel, Corros. Sci. 35 (1993) 57–62.
[11] P. Pistorius, G. Burstein, Metastable pitting corrosion of stainless steel and the transition to stability, Philosophical Transactions of the Royal Society of London. Series A: Physical and Engineering Sciences 341 (1992) 531–559.
[12] N. Laycock, R. Newman, Localised dissolution kinetics, salt films and pitting potentials, Corros. Sci. 39 (1997) 1771–1790.
[13] G. Fagerlund, The Threshold Chloride Level for Initiation of Reinforcement Corrosion in Concrete: Some Theoretical Considerations, Division of Building Materials, Lund Institute of Technology, 2011.
[14] K.Y. Ann, H.-W. Song, Chloride threshold level for corrosion of steel in concrete, Corros. Sci. 49 (2007) 4113–4133.
[15] L. Jiang, S. Bai, J. Xu, Y. Zhang, H. Chu, Review on Research of Threshold Chloride Concentration of Reinforcing Steel Corrosion in Concrete, 35 (2015).
[16] M.C. Alonso, M. Sanchez, Analysis of the variability of chloride threshold values in the literature, Mater. Corros. 60 (2009) 631–637.
[17] G.K. Glass, N.R. Buenfeld, The presentation of the chloride threshold level for corrosion of steel in concrete, Corros. Sci. 39 (1997) 1001–1013.
[18] W. Breit, Critical Corrosion Inducing Chloride Content – State of the Art and New Investigation Results, Verein Deutscher Zementwerke e.V., Verlag Bau+Technik, 2001, pp. 631–637.
[19] G. Glass, N. Buenfeld, Chloride threshold levels for corrosion induced deterioration of steel in concrete, 1st RILEM Workshop on Chloride Penetration Into Concrete St Rémy lès Chevreuse, France, 1995, pp. 429–440.
[20] U. Angst, Ø. Vennesland, Critical Chloride Content in Reinforced Concrete - State of the Art, (2008), pp. 149–150.
[21] Y. Cao, C. Gehlen, U. Angst, L. Wang, Z. Wang, Y. Yao, Critical chloride content in reinforced concrete—an updated review considering Chinese experience, Cem.

Concr. Res. 117 (2019) 58–68.
[22] F. fib, Model code for service life design, 110 International Federation for Structural Concrete (FIB), Switzerland, 2006.
[23] P. Beverly, Fib Model Code for Concrete Structures 2010, Ernst & Sohn, 2013.
[24] ISO 16204, Durability – Service Life Design of Concrete Structures, (2012).
[25] GB50010-2010, Code for Design of Concrete Structures, (2010).
[26] Rilem, Draft recommendation for repair strategies for concrete structures damaged by reinforcement corrosion, Mater. Struct. 27 (1994) 415–436.
[27] U. Angst, C. Boschmann, M. Wagner, B. Elsener, Experimental Protocol to Determine the Chloride Threshold Value for Corrosion in Samples Taken From Reinforced Concrete Structures, (2017).
[28] V. Garcia, R. Francois, M. Carcasses, P. Gegout, Potential Measurement to Determine the Chloride Threshold Concentration That Initiates Corrosion of Reinforcing Steel Bar in Slag Concretes, vol. 47, (2014).
[29] J. Pacheco, R. Polder, Critical chloride concentrations in reinforced concrete specimens with, Ordinary Portland and Blast Furnace Slag Cement 61 (2016).
[30] L. Tang, J.M. Frederiksen, U. Angst, R. Polder, M. Cruz Alonso, B. Elsener, et al., Experiences from RILEM TC 235-CTC in Recommending a Test Method for Chloride Threshold Values in Concrete, vol. 3, (2018).
[31] C. Chalhoub, R. François, M. Carcasses, Determination of chloride threshold initiating corrosion: a new set-up taking the localized aspect of corrosion into account, Cem. Concr. Res. 124 (2019) 105825.
[32] U. Angst, M. Geiker, A. Michel, C. Gehlen, H.S. Wong, O. Isgor, et al., The Steel–Concrete Interface, vol. 50, (2017).
[33] U.M. Angst, M.R. Geiker, M.C. Alonso, R. Polder, O.B. Isgor, B. Elsener, et al., The effect of the steel–concrete interface on chloride-induced corrosion initiation in concrete: a critical review by RILEM TC 262-SCI, Mater. Struct. 52 (2019) 88.
[34] D. Trejo, R. Pillai, Accelerated Chloride Threshold Testing: Part I - ASTM A 615 and A 706 Reinforcement, vol. 100, (2003).
[35] D. Trejo, R. Pillai, Accelerated Chloride Threshold Testing - Part II: Corrosion-resistant Reinforcement, vol. 101, (2004).
[36] U.M. Angst, B. Elsener, Forecasting chloride-induced reinforcement corrosion in concrete—effect of realistic reinforcement steel surface conditions, Proceedings of the 4th International Conference on Concrete Repair, Rehabilitation and Retrofitting (ICCRRR), 2015, pp. 177–184.
[37] C. Alonso, C. Andrade, M. Castellote, P. Castro, Chloride threshold values to depassivate reinforcing bars embedded in a standardized OPC mortar, Cem. Concr. Res. 30 (2000) 1047–1055.
[38] L. Michel, U. Angst, Towards Understanding Corrosion Initiation in Concrete – Influence of Local Electrochemical Properties of Reinforcing Steel, 199 (2018), p. 04001.
[39] I. Zafar, T. Sugiyama, Laboratory investigation to study the corrosion initiation of rebars in fly ash concrete, Mag. Concr. Res. 66 (2014) 1051–1064.
[40] C.B. Käthler, U.M. Angst, B. Elsener, Towards Understanding Corrosion Initiation in Concrete – Influence of Local Concrete Properties in the Steel-concrete Interfacial Zone, 199 (2018), p. 04002.
[41] P. Sandberg, The Effect of Defects at the Steel-concrete Interface, Exposure Regime, and Cement Type on Pitting Corrosion in Concrete, Lund University, Division of Building Materials, 1998 TVBM-3081.
[42] A.N. Scott, The Influence of Binder Type and Cracking on Reinforcing Steel Corrosion in Concrete, (2004).
[43] P. Ghods, O. Isgor, G.A. McRae, J. Li, G.P. Gu, Microscopic investigation of mill scale and its proposed effect on the variability of chloride-induced depassivation of carbon steel rebar, Corr. Sci. 53 (2011) 946–954.
[44] F. YANG, Corrosion Protection of Steel Embedded in New Sustainable Cementitious Materials, Politechnico Milano, 2018.
[45] L. Li, A. Sagues, Chloride Corrosion Threshold of Reinforcing Steel in Alkaline SolutionsOpen-circuit Immersion Tests, vol. 57, (2001).
[46] R. Pillai, D. Trejo, Surface Condition Effects on Critical Chloride Threshold of Steel Reinforcement, vol. 102, (2005).
[47] T. Mohammed, H. Hamada, Corrosion of steel bars in concrete with various steel surface conditions, ACI Mater. J. 103 (2006).
[48] L.T. Mammoliti, L.C. Brown, C.M. Hansson, B.B. Hope, The influence of surface finish of reinforcing steel and pH of the test solution on the chloride threshold concentration for corrosion initiation in synthetic pore solutions, Cem. Concr. Res. 26 (1996) 545–550.
[49] P. Ghods, O. Isgor, G.A. McRae, G.P. Gu, Electrochemical investigation of chloride-induced depassivation of black steel rebar under simulated service conditions, Corros. Sci. 52 (2010) 1649–1659.
[50] D. Boubitsas, L. Tang, The influence of reinforcement steel surface condition on initiation of chloride induced corrosion, Mater. Struct. 48 (2014) 2641–2658.
[51] M. Manera, Ø. Vennesland, L. Bertolini, Chloride threshold for rebar corrosion in concrete with addition of silica fume, Corros. Sci. 50 (2008) 554–560.
[52] M. Hurley, J. Scully, Threshold chloride concentrations of selected corrosion resistant rebar materials compared to carbon steel, Corrosion 62 (2006) 892–904.
[53] L. Bertolini, M. Gastaldi, Corrosion resistance of low-nickel duplex stainless steel rebars, Mater. Corros. 62 (2011) 120–129.
[54] R. Figueira, A. Sadovski, A. Melo, E. Pereira, Chloride threshold value to initiate reinforcement corrosion in simulated concrete pore solutions: the influence of surface finishing and pH, Constr. Build. Mater. 141 (2017) 183–200.
[55] E. Mahallati, M. Saremi, An Assessment on the Mill Scale Effects on the Electrochemical Characteristics of Steel Bars in Concrete Under DC-polarization, vol. 36, (2006).
[56] H. Justnes, A review of chloride binding in cementitious systems, Nordic Concrete Research-Publications 21 (1998) 48–63.
[57] T. Luping, L.-O. Nilsson, Chloride binding capacity and binding isotherms of OPC pastes and mortars, Cem. Concr. Res. 23 (1993) 247–253.
[58] C.K. Larsen, *Chloride Binding in Concrete*, Dr. Ing. Thesis, Report No 1998:101, Norwegian University of Science and Technology, NTNU, 1998.
[59] C.L. Page, Ø. Vennesland, Pore solution composition and chloride binding capacity of silica fume cement pastes, Mater. Struct. 16 (1983) 19–25.
[60] C. ARYA, N. Buenfeld, J.B. Newman, Factors influencing chloride-binding in concrete, Cem. Concr. Res. 20 (1990) 291–300.
[61] K. Byfors, Influence of silica fume and flyash on chloride diffusion and pH values in cement paste, Cem. Concr. Res. 17 (1987) 115–130.
[62] C.M. Hansson, B. Sorensen, The threshold concentration of chloride in concrete for the initiation of reinforcement corrosion, in: N.S. Berke, V. Chaker, D. Whiting (Eds.), Corrosion Rates of Steel in Concrete. ASTM STP 1065, 1990, pp. 3–16.
[63] H. Ba, M. Zhang, Study of critical concentration of chloride ion on concrete reinforcement corrosion, Eighth Natl. Symp. Durab. Concr. (2012) 485–492.
[64] K. Pettersson, Chloride Threshold Value and the Corrosion Rate in Reinforced Concrete, (1994), pp. 257–266.
[65] X.-B. Chen, M.-X. Tang, H.-S. Hu, K.-L. Ma, Chloride ion threshold for underground structure durability estimation exposured to chloride ions invading in Guangzhou, J. Cent. S. Univ. (Sci. Technol.) 43 (2012) 4840–4849.
[66] J. Ryou, K. Ann, Variation in the chloride threshold level for steel corrosion in concrete arising from different chloride sources, Mag. Concr. Res. 60 (2008) 177–187.
[67] W. Breit, Kritischer korrosionsauslösender Chloridgehalt - Neuere Untersuchungsergebnisse (Teil 2). 8:511, Beton, 48 (1998).
[68] J.M. Frederiksen, Chloride threshold values for service life design, in: C. Andrade, J. Kropp (Eds.), Testing and Modelling the Chloride Ingress into Concrete, 2000, pp. 397–414.
[69] O. Kayyali, M. Haque, The Cl−/OH− ratio in chloride-contaminated concrete—a most important criterion, Mag. Concr. Res. 47 (1995) 235–242.
[70] R. Luo, Y. Cai, C. Wang, X. Huang, Study of chloride binding and diffusion in GGBS concrete, Cem. Concr. Res. 33 (2003) 1–7.
[71] R. Dhir, M. El-Mohr, T. Dyer, Chloride binding in GGBS concrete, Cem. Concr. Res. 26 (1996) 1767–1773.
[72] K. Kopecskó, G.L. Balázs, Concrete with improved chloride binding and chloride resistivity by blended cements, Adv. Mater. Sci. Eng. 2017 (2017).
[73] A. Cheng, R. Huang, J.-K. Wu, C.-H. Chen, Influence of GGBS on durability and corrosion behavior of reinforced concrete, Mater. Chem. Phys. 93 (2005) 404–411.
[74] V. Gouda, W. Halaka, Corrosion and corrosion inhibition of reinforcing steel: II. Embedded in concrete, Br. Corros. J. 5 (1970) 204–208.
[75] Q. Zhang, W. Sun, J. Shi, Influence of mineral admixtures on chloride threshold level for corrosion of steel in mortar, Guisuanyan Xuebao(Journal of the Chinese Ceramic Society) 38 (2010) 633–637.
[76] Z. Meng, Research on Chloride Threshold Level for Reinforcement Corrosion in Concrete and the Impact of Corrosion Inhibitor, Ph.D. Master thesis Harbin Institute of Technology, 2012.
[77] P.-F. Wang, M.-T. Tsai, Y.-W. Chan, A study on critical chloride ion concentration for corrosion of reinforcing steel in mortar, J. Chin. Inst. Civil Hydraul. Eng. 26 (2014) 211–214.
[78] P. Schiessl, W. Breit, Local Repair Measures at Concrete Structures Damaged by Reinforcement Corrosion-aspect of Durability, (1996), pp. 525–534.
[79] B. Oh, S. Jang, Y. Shin, Experimental investigation of the threshold chloride concentration for corrosion initiation in reinforced concrete structures, Mag. Concr. Res. 55 (2003) 117–124.
[80] Y. Li, Y. Zhu, J. Fang, Experimental study of chloride ion's critical content causing reinforcement corrosion in concrete, Hydro-Science and Engineering (2004) 24–28.
[81] Y. Li, The Study of Chloride Ions Penetration Capacity and Critical Content Concrete, Master thesis Nanjing Hydraulic Research Institute, 2003.
[82] M. Kosalla, M. Raupach, Potential differences between passive reinforcement segments in concrete components in dependency of binder type, aeration conditions and quality of the steel/concrete-interface, Mater. Corros. 67 (2016) 639–651.
[83] B. Persson, Assessment of the chloride migration coefficient, internal frost resistance, salt frost scaling and sulphate resistance of self-compacting concrete: with some interrelated properties, Report TVBM 3100 (2001).
[84] D. Boubitsas, Studies of the Efficiency of Granulated Blast Furnace Slag and Limestone Filler in Mortars-long Term Strength and Cloride Penetration, (2005).
[85] A.A. Elgalhud, R.K. Dhir, G. Ghataora, Chloride ingress in concrete: limestone addition effects, Mag. Concr. Res. 70 (2018) 292–313.
[86] V. Bonavetti, V. Rahhal, E. Irassar, Studies on the carboaluminate formation in limestone filler-blended cements, Cem. Concr. Res. 31 (2001) 853–859.
[87] G. Fagerlund, *Imaginable Effects of Limestone Filler on Chloride Transport*, TVBM-7187, Lund Institute of Technology, Lund, 2005.
[88] L. Bertolini, M. Gastaldi, M. Pedeferri, E. Redaelli, Prevention of steel corrosion in concrete exposed to seawater with submerged sacrificial anodes, Corros. Sci. 44 (2002) 1497–1513.
[89] L. Bertolini, Comparison of Resistance to Chloride Penetration of Concretes and Mortars for Repair, (2004), pp. 165–168.
[90] F. Bolzoni, S. Goidanich, L. Lazzari, M. Ormellese, Corrosion inhibitors in reinforced concrete structures part 2–repair system, Corros. Eng. Sci. Technol. 41 (2006) 212–220.
[91] F. Bolzoni, A. Brenna, G. Fumagalli, S. Goidanich, L. Lazzari, M. Ormellese, et al., Experiences on corrosion inhibitors for reinforced concrete, International Journal of Corrosion and Scale Inhibition 3 (2014) 254–278.
[92] Z. Evgenia, Z. Aggeliki, S. Atteyeh, B. George, T. Sotirios, Effect of corrosion inhibitors in limestone cement, Mater. Sci. Appl. (2013) 2013.

[93] A. Brenna, F. Bolzoni, S. Beretta, M. Ormellese, Long-term chloride-induced corrosion monitoring of reinforced concrete coated with commercial polymer-modified mortar and polymeric coatings, Constr. Build. Mater. 48 (2013) 734–744.
[94] M. Ormellese, M. Berra, F. Bolzoni, T. Pastore, Corrosion inhibitors for chlorides induced corrosion in reinforced concrete structures, Cem. Concr. Res. 36 (2006) 536–547.
[95] I. Fayala, L. Dhouibi, X. Nóvoa, M.B. Ouezdou, Effect of inhibitors on the corrosion of galvanized steel and on mortar properties, Cem. Concr. Compos. 35 (2013) 181–189.
[96] P. Garcés, M.S. De Rojas, M. Climent, Effect of the reinforcement bar arrangement on the efficiency of electrochemical chloride removal technique applied to reinforced concrete structures, Corros. Sci. 48 (2006) 531–545.
[97] E. Sistonen, A. Cwirzen, J. Puttonen, Corrosion mechanism of hot-dip galvanised reinforcement bar in cracked concrete, Corros. Sci. 50 (2008) 3416–3428.
[98] A.M. Diab, A.A. Aliabdo, I.A. Mohamed, Corrosion behaviour of reinforced steel in concrete with ground limestone partial cement replacement, Mag. Concr. Res. 67 (2015) 747–761.
[99] A.M. Diab, I.A. Mohamed, A.A. Aliabdo, Impact of organic carbon on hardened properties and durability of limestone cement concrete, Constr. Build. Mater. 102 (2016) 688–698.
[100] K. Pettersson, Corrosion threshold value and corrosion rate in reinforced concrete, CBI REPORT 2 (1992) 92.
[101] Y. Li, Y. Zhu, X. Zhu, Y. Ge, S. Laura, Chloride ion critical content in reinforced concrete, J. of Wuhan Univ. of Techn.-Mater. Sci. Ed. 22 (2007) 737–740.
[102] P. Sandberg, K. Pettersson, H. Sørensen, H. Arup, Critical chloride concentrations for the onset of active reinforcement corrosion, Proc. of the RILEM International Workshop on Chloride Penetration into Concrete, 1995, pp. 453–459.
[103] R. Polder, Critical chloride content for reinforced concrete and its relationship to concrete resistivity, Mater. Corros. 60 (2009) 623–630.
[104] G.R. Meira, C. Andrade, E.O. Vilar, K.D. Nery, Analysis of chloride threshold from laboratory and field experiments in marine atmosphere zone, Constr. Build. Mater. 55 (2014) 289–298.
[105] O. Poupard, A. Aït-Mokhtar, P. Dumargue, Corrosion by chlorides in reinforced concrete: determination of chloride concentration threshold by impedance spectroscopy, Cem. Concr. Res. 34 (2004) 991–1000.
[106] NF EN 196-1, Méthodes d'essais des ciments-Partie 1: détermination des résistances mécaniques (Methods of testing cements–part 1: determination of mechanical strengths), (2006).
[107] Standard NF EN 206, Béton – Spécification, Performances, Production et Conformité, (2014).
[108] NF P18-459, Essai Pour Béton Durci-Essai de Porosité et de Masse volumique, French Standard, 2010 (NF P18-459, Mars (2010)).
[109] N. Build, Concrete, mortar and cement-based repair materials: chloride migration coefficient from non-steady-state migration experiments, Nordtest method 492 492 (1999).
[110] XP P18-462, Test on Hardened Concrete – Chloride Migration Accelerated Test in Non-steady State – Determination of the Apparent Chloride Diffusion Coefficient (in French), French standard, 2012.
[111] NF EN 14629, Produits et systèmes pour la protection et la réparation des structures en béton - Méthodes d'essais - Mesurage du taux de chlorure d'un béton durci, (2007).
[112] G. Arliguie, H. Hornain, GranDuBé: grandeurs associées à la durabilité des bétons, Presses des Ponts, 2007.
[113] ISO 8407:2009(en), Corrosion of Metals and Alloys—Removal of Corrosion Products From Corrosion Test Specimens.
[114] D. Lewis, W. Copenhagen, Corrosion of reinforcing steel in concrete in marine atmospheres, Corrosion 15 (1959) 60–66.
[115] W. Breit, Kritischer Chloridgehalt–Untersuchungen an Stahl in chloridhaltigen alkalischen Lösungen, Mater. Corros. 49 (1998) 539–550.
[116] M. Moreno, W. Morris, M. Alvarez, G. Duffó, Corrosion of reinforcing steel in simulated concrete pore solutions: effect of carbonation and chloride content, Corros. Sci. 46 (2004) 2681–2699.

# Paper IV

## Anodic control of the initiation of macrocell chloride-induced corrosion in concrete structures

**Chantal Chalhoub*, Raoul François, Myriam Carcasses**

**To be completed and submitted**

# Anodic control of the initiation of macrocell chloride-induced corrosion in concrete structures

Chantal Chalhoub*, Raoul François, Myriam Carcasses
LMDC, INSA, UPS, Université de Toulouse, France
* Corresponding author: chantal.chalhoub@insa-toulouse.fr

## Abstract

This work investigated, from the perspective of numerical modeling, the mechanism of chloride-induced corrosion initiation in reinforced concrete structures. This paper did not explain the physical aspects of corrosion initiation and steel depassivation. It consisted of simulating the transition from the corrosion initiation phase to the early stage of corrosion propagation to examine the process controlling the initiation of corrosion. The interface of rebars with the electrolyte was simulated using the equations of the Butler-Volmer model as boundary conditions. The input data of the Butler-Volmer equations are the electrochemical parameters of passive steel and active steel. The latter being dependent on the level of chloride contamination. Two different numerical models were achieved to simulate two different sizes of the cathode, and subsequently, to simulate different cathode/anode (C/A) surface ratio. The size of active steel was kept very small and was considered constant and independent of the chloride level. The numerical results showed that for chloride levels lower than the critical chloride content, the galvanic current flowing between anodic and cathodic areas was negligible and independent of the cathode/anode ratio. Beyond the critical chloride content, the currents became significant and increased when the cathode/anode ratio increased. These observations showed that the phenomenon of depassivation of steel due to chloride ingress can be described by an anodic Tafel coefficient which is chloride dependent, and subsequently, by parameters of active steel which change with chloride contamination. This statement supports the concept of anodic control of the early phase of chloride-induced corrosion propagation.

## Keywords

Chloride-induced corrosion; corrosion initiation; anodic control; cathode to anode ratio.

## 1. Introduction

Concrete presents a non-aggressive environment for steel bars due to its alkaline solution. When reinforcement rebars are in contact with the concrete interstitial solution, they are in a passive state. However, aggressive species like chlorides could induce a local depassivation of reinforcing steel. Corrosion is initiated when the level of chlorides at the steel surface reaches a threshold value called critical chloride content. Corrosion initiation is not an instantaneous occurrence but rather a gradual period until stable corrosion [1–4].

After the corrosion initiation, comes the corrosion propagation phase where a corrosion system is established. Corrosion of steel in concrete structures exposed to chlorides (seawater, de-icing salts, etc.) is localized also known as macrocell corrosion. This type of corrosion corresponds to the electrical connection between passive steel and active steel which are spatially separated with a distance than can easily reach decimeters or even meters [5]. At the beginning of corrosion propagation, very small local corrosion pits are formed, while, the bigger part of the steel remains in a passive state.

In the anodic areas, the oxidation reaction of iron takes place. At the cathodic areas, in presence oxygen at the steel/concrete interface, the oxygen reduction reaction takes place. An electronic current circulates through the metal from active steel towards passive steel and ionic current flows through the interstitial solution of concrete. As a result, macrocell corrosion is a function of the anodic reactions, the cathodic reactions, and the ionic and electronic current flows. Indeed, it is commonly believed that to achieve and sustain the "dynamic equilibrium" of a galvanic corrosion system, all these reactions must occur at the same rate [6–8] which makes each of these processes possible rate-limiting factor. The electronic control associated with the transport of electrons through reinforcement bars is considered negligible when compared to the other rate-limiting factors.

It is usually assumed that the corrosion rate in concrete is controlled by the slowest process which can be either the anodic, the cathodic or the ohmic process involving implicitly the impact of the cathode/anode ratio and cathode-anode distance. A recent study by Hornbostel et al. [5] showed that there is no one rate-limiting process governing the corrosion rate but rather a combination of at least two or all the processes. Nevertheless, according to different experimental studies investigating corrosion initiation induced by chlorides and carbonation [9–14], it appears that corrosion initiation is mostly under anodic control.

Before proceeding to the content of this paper, the different types of corrosion control need to be addressed separately and linked to the observations found in the literature. Also, the influence of these controlling mechanisms on the initiation of chloride-induced macrocell corrosion needs to be discussed.

## Cathodic control

In the presence of oxygen, the cathodic current corresponds to the reduction of dissolved oxygen along with the formation of hydroxyl ions at the steel-concrete interface. Therefore, the cathodic control is usually associated with the restrictions of the kinetics of the cathodic reaction (oxygen reduction). The cathodic reaction depends on several influencing parameters such as the binder type and concrete composition (water/binder ratio, pore solution chemistry), saturation state, cover depth, temperature, type of steel (carbon steel, galvanized, etc.) and steel surface condition (polished, as received, pre-passivated, pre-oxidized, etc.). On the other hand, no correlation exists between the cathodic reaction kinetics and the concrete resistivity [5]. An example of the impact of binder type on cathodic reaction is the lower current density provided by cathodes in fly ash mortar compared to Portland cement mortars [5]. One explanation of this observation may be related to the lower $OH^-$ concentration present in the pore solution of fly ash mortar [5] known for its impact on oxygen reduction reaction [15]. Another explanation is the denser mortar matrix in fly ash mortar resulting in a lower effective steel surface area accessible for the cathodic reduction reaction. [5]

The cathodic reaction is conditioned by oxygen availability determined by its diffusion kinetics through the cement matrix. This situation is usually encountered when the structure is in submerged conditions where chloride contamination happens relatively easily but oxygen availability is limited by its slow diffusion through saturated concrete and its low concentration in solution. This condition of cathodic corrosion control is another evidence that cathodic kinetics is not correlated with concrete resistivity. In fact, in water-saturated concrete where the concrete resistivity is low, corrosion currents are usually low and sometimes even non-existent [8] since the corrosion rate can be controlled by the rate at which oxygen will reach the steel surface hence the expression of cathodic control [16].

Another example of cathodic control is when the porous network is refined in cases of concrete with slag cement (CEM II and CEM III) or concrete with mineral additions like slag or silica fume, which limits the accessibility of rebars to oxygen [Paper VII]. Besides, sulfides present in the pore solution of

concrete are unstable in the presence of oxygen [17], meaning that they are subjected to oxidation which may reduce the level of oxygen in the interstitial solution.

In the case of unsaturated concrete structures, it is improbable that corrosion initiation is limited by the oxygen diffusion which means that no cathodic control limits the early pitting corrosion [9]. Similarly, the corrosion of large-scale systems characterized by an infinitely large cathode/anode (C/A) ratio is never under cathodic control. This statement highlights a limitation of small-scale laboratory corrosion experiments with low C/A ratios which do not represent reality [5].
[18–20][18–20][9][9][9][9][9]

## Ohmic control:

As presented earlier, macrocell corrosion is characterized by the spatial separation between anodic sites and cathodic sites. Accordingly, the flow of ionic current through the concrete electrolyte is conditioned by the ohmic resistance between active and passive sites.

The extent to which ohmic control contributes to the limitation of macrocell corrosion is mainly dependent on the size of anode [5], the size and location of the cathode, and the electrical resistivity of concrete.

In the case of large anodes and large structures where the cathode-anode distance is relatively important (in orders of decimeters to meters), the mobilizable cathode surface can be limited by the ohmic resistance making the electrochemical system under ohmic control.
However, in the early phase of the corrosion process, the size of the anode is relatively small and the available cathode area is usually very high giving C/A ratios as high as 200,000 [9,10]. Hence, the small size of active steel is associated with high local current densities [9] as high as 100 µA/cm2 [article 6]. This indicates that, at the initiation stage, the ohmic control is supposed insignificant since the anodic resistance dominates the ohmic and cathodic control [23].

The reason why, in some studies [21]0–22], it was found that corrosion is under cathodic/ohmic control, is that often very high levels of chloride contamination are used in experiments that induce relatively large anodes, or, severely large anodes are simulated in case of numerical modeling. As a result, the studied conditions represent a corrosion phase far after corrosion initiation [9]. Until now, the occurrence of the switch from anodic control to cathodic/ohmic control is still unidentified [9].

## Anodic control:

The anodic reaction is governed by the anodic charge transfer which is influenced by the very local aspects of the inhomogeneous matrix of concrete and this why it must not be correlated to the bulk electrical resistivity of concrete [5]. The anodic control is dependent on the microstructure of concrete associated with the nature of the porous network of concrete, the form of the corrosion pit and the presence of corrosion products. Anodic control might also be dependent on the type of steel used and the type of steel surface condition according to findings in [10].

The anodic resistance control must not be mistaken with the ohmic control. Indeed, a lower resistivity increases the Influx of chloride ions which supposedly maintains the development of corrosion pit, yet, it also supports the mobility of hydroxyl ions which may reduce the corrosion pit activity by increasing the pH [22]. Nevertheless, it must be noted that the mobility of hydroxyl ions is higher than that of chlorides [23]. This means that, if the hydroxide ion concentrations dominate the chloride concentration, hydroxide ions will preferentially migrate into the depassivated region which highlights the importance of the $Cl/OH^{-}$ ratio when dealing with corrosion initiation [9].

The initial step of corrosion in concrete appears to be, according to several studies [9–14], to a large degree, under anodic control. In these experiments, relatively small anodes were investigated presenting a corrosion state in the early and intermediate stages of corrosion propagation [5].
Glass et al [11] investigated the corrosion of steel in a carbonated mortar and proposed the term anodic resistance control to represent the anodic control of corrosion with the anodic reaction being indirectly influenced by the mortar or concrete resistivity by limiting the mobility of ions close to corrosion pit. The authors also stated that the risk of corrosion is considerably higher in presence of chlorides in a way that low chloride contents reduce the mortar resistivity, while higher contents promote moisture retention and decelerate drying effects [11].

Page and Havdahl [13] found that the presence of micro silica in cement pastes embedding steel bars limited the anodic reaction due to the fine microstructure of the material which restricted the chloride ions transport to the steel surface.
Angst et al [9] launched an experimental campaign on different compositions of reinforced concrete samples embedding 2 rebars with a diameter of 8 mm presenting each a cover of 10 mm and an exposed area of 17.6 $cm^2$. The samples were contaminated with chloride through partial immersion in chloride solutions. Frequent measurements of potentials, polarisation resistance, concrete resistivity, and measurements of the galvanic current between the working electrode and cathode in addition to polarisation curves, were realized throughout the depassivation progression. The results found indicate that the early chloride-induced corrosion initiation is under mixed anodic/ohmic control and becomes with time completely under anodic control [9].
Recently, an experimental test protocol to detect chloride threshold contents was published by the present authors where the criteria used to detect corrosion initiation is based on the concept of anodic control [10]. The authors determined the critical chloride content using a criterion based on a limiting galvanic current which is independent of the area of the cathode and subsequently independent of the C/A ratio [10].

Angst et al [9] stated that [18,25][18,25][18,25][18,25][18,25]in the early stage of localized corrosion, it is difficult to measure the anode-cathode galvanic current because of the small size of the anode which means that it is more accurate to study this mechanism using numerical simulation [9]. This implies that it is possible to evaluate corrosion initiation through numerical simulation.

As mentioned above, the corrosion initiation under chloride attack is reported to be under anodic control. Additionally, the reaction at the anode depends on the electrochemical parameters of active steel which appears to be, according to several studies [Paper II] [26], dependent on the chloride pollution level.

This work aims at investigating, from the point of view of numerical analysis, the mechanism of chloride-induced corrosion initiation in reinforced concrete structures. This paper does not try to explain the physical aspects of corrosion initiation or find a physical meaning of the depassivation mechanism. The main focus consists of numerically simulating the transition from the corrosion initiation phase to the early stage of corrosion propagation and to test whether corrosion initiation is controlled by the anodic process.

The scale of this study concerns only the macro-level of the corrosion process of rebars in concrete. Explaining the depassivation and initiation mechanisms at a micro-level is not the objective of this work. Therefore, a cohesion of matter is described in terms of stress and strain and their interaction via the constitutive law; the corrosion of steel in concrete is described in terms of potential and current and their interaction via the Butler-Volmer model. The interface of rebars with the electrolyte was simulated using the equations of the Butler-Volmer model as boundary conditions. The input data of the Butler-

Volmer equations are the electrochemical parameters of active and passive steel which were deduced from [Paper II].

Two different numerical models were achieved to simulate two different sizes of the cathode, and subsequently, to simulate different cathode/anode (C/A) surface ratio. The first model consisted of simulating the anode-cathode coupling experiment corresponding to a C/A ratio of 16 which was presented in [10] and [Paper II]. The second model consisted of simulating the anode-wall experiment corresponding to higher C/A ratios up to 2950 which was also realized in the experimental protocol achieved in [10].

To simulate the early stages of chloride-induced corrosion, the size of active steel was kept very small (0.05 $cm^2$) which only represents 2.5 % of the size of the anode rebar (1.88 $cm^2$). The size of the anode in the active state did not change with the chloride contamination level like the simulation achieved in [Paper II], but instead, it was considered constant and independent of the chloride level.

## 2. Electrochemical parameters of steel

The polarization behavior of a uniform corrosion system can be modeled by the Butler-Volmer equation (Eq. 1), which relies on the relation between the system potential $E$ under polarization and the associated net current density $i$ produced at the steel-electrolyte interface.

$$i = i_{corr}\left(\exp\left(\frac{\mathrm{Log}(10)}{\beta_a}(E - E_{corr})\right) - \exp\left(-\frac{\mathrm{Log}(10)}{\beta_c}(E - E_{corr})\right)\right) \qquad \text{Eq. 1}$$

Where:
- $i$ is the net current density produced by the uniform corrosion system at the metal-electrolyte interface ($A/m^2$);
- $E$ is the potential of the uniform corrosion system under polarization (V/ref);
- $i_{corr}$ is the corrosion current density ($A/m^2$);
- $E_{corr}$ is the potential of the uniform corrosion system at equilibrium (V/ref);
- $\beta_a$ is the anodic Tafel slope of the electrochemical system, expressing the oxidation reaction of iron (V/dec);
- $\beta_c$ is the cathodic Tafel slope of the electrochemical system, expressing the reduction reaction of oxygen (in presence of oxygen) (V/dec).

These parameters are the input data needed to simulate numerically the behavior of passive and active steel. The properties of passive and active steel will be annotated with the letters "$p$" and "$a$", respectively. Since the cathode samples are chloride-free, the steel is indeed entirely in a passive state. Therefore, the characterization of passive behavior can be directly deduced from the experimental polarization test by fitting a Butler-Volmer model on three experimental polarization curves per formulation.

This characterization was achieved in [Paper II] on chloride-free cathode samples (with a surface of 30.16 $cm^2$) made with mortar based on CEMI with a w/b ratio of 0.55. The details of the polarization test achieved to obtain the polarization curves are presented in [Paper II] and detailed in Appendix VI. The anodic and cathodic Tafel slopes $\beta_{a,p}$ and $\beta_{c,p}$ were extracted graphically from the well-defined anodic and cathodic branches of the experimental polarization curve. The rest of the parameters were simply optimized to minimize the MSE between the experimental points and the fitted Butler-Volmer

model. The measured electrochemical parameters of passive steel are listed in Table 1. The parameters will be used in this work as input data to characterize the behavior of passive steel.

*Table 1. Butler-Volmer parameters of passive steel specimens (taken from [Paper II])*

| Formulation | $E_{corr,p}$ (V / Ag-AgCl-KCl sat) | $i_{corr,p}$ (A/m²) | $\beta_{a,p}$ (V/dec) | $\beta_{c,p}$ (V/dec) |
|---|---|---|---|---|
| M1-055 | $-0.138$ | $5.60 \times 10^{-5}$ | 0.240 | 0.115 |

On the other hand, not a lot of data about the anodic polarization curves of localized active steel in concrete exist in the literature [5] and the determination of the electrochemical behavior of anode is complicated [9]. Indeed, the determination of these parameters cannot be directly deduced from experimental polarization curves because of the non-uniform aspect of chloride-induced corrosion.

Maekawa et al [26] stated that the breakdown of the passive film by chloride ions can be described by varying the anodic Tafel slope $\beta_{a,a}$ with chloride content. Indeed, the anodic Tafel coefficient is multiplied with a semi-empirical theoretical factor which accounts for changes in chlorides levels as follows:

$$\beta_{a,a} = \left(\frac{2.303 \times R \times T}{0.5 \times z_{Fe} \times F}\right) \times f_p \qquad \text{Eq. 2}$$

$$f_p = \begin{cases} 10^4 & if\ Cl \leq 0.04 \\ 0.4/Cl & if\ 0.04 < Cl < 0.4 \\ 1 & if\ Cl \geq 0.4 \end{cases} \qquad \text{Eq. 3}$$

Where:

- $\beta_{a,a}$ is the anodic Tafel coefficient of steel (V/dec);
- $R$ is the universal gas constant (8.314 J/mol/K);
- $T$ is the temperature (Kelvin);
- $z_{Fe}$ is the number of charge of Fe ions (2);
- $F$ is the Faraday constant (96500 A.s/mol)
- $f_p$ is the anodic Tafel gradient factor;
- $Cl$ is the free chloride content (%/wt. binder).

According to this model, for low chloride contents (lower than a numerically predefined value of 0.04% by mass of binder), the anodic Tafel coefficient is very high approaching infinity. The depassivation phase is described by a decrease of the factor $f_p$ until the chloride content reaches the critical chloride content (which is fixed in the study as 0.4% by mass of binder). That authors suppose that when the level of chlorides is higher than the critical threshold value, the passive film is destroyed, as a result, the anodic Tafel coefficient becomes equal to the Tafel gradient given by Nernst's equation [26].

The authors [26] realized experimentation on mortar and concrete formulations based on ordinary Portland cement with a w/c ratio of 0.45. Deformed carbon steel bars were used and were polished then degreased with acetone before being placed in the mold. The test specimens embedded two rebars; one for weight loss measurements and the other one for electrochemical measurements. Samples were contaminated with chlorides by adding different contents of NaCl in mixing water. Half-cell potential measurements were realized every 2 days using an external reference electrode. Finally, the samples were split to measure gravimetric steel weight loss. They found that the model developed by incorporating the effect of chlorides in the anodic Tafel coefficient underestimates the experimental results. Therefore, it was decided to enhance the model by including the effect of chlorides on the anodic potential by introducing a semi-empirical factor that accounts for the variation of anodic potential with chloride content [26]. The experimental results were used to calibrate both factors.

With these chloride dependent parameters, the authors succeed to find a good correlation between numerical and experimental results for both corrosion currents and potentials [26]. It is assumed that for chloride content higher than the threshold value, the corrosion rate is constant and equivalent to the corrosion rate of active steel [26].

Recently, a study was developed based on inverse numerical simulation consisting of quantifying the electrochemical parameters of active steel [Paper II]. The investigation highlighted the dependency of the iron anodic Tafel coefficient and, consequently the rest of the electrochemical parameters of active steel on the chloride contamination level [Paper II]. An empirical pseudo-sigmoidal relationship was found between anodic Tafel coefficient and free chloride content (Eq. 4).

$$\beta_{a,a} = 0.08 + \frac{0.16}{1 + \exp\big(20 \times (Cl - 0{,}5)\big)} - 0.0085 \times Cl \qquad \textit{Eq. 4}$$

where:

- $\beta_{a,a}$ is the anodic Tafel coefficient (V/dec);
- $Cl$ is the free chloride content (%/wt. binder).

The originality of this approach is that it links directly the anodic Tafel coefficient $\beta_{a,a}$ to chloride content. The other parameters, the corrosion potential $E_{corr,a}$ and current $i_{corr,a}$ , are deduced from deterministic relationships based on the reversible electrode properties of iron and oxygen and dependent on $\beta_{a,a}$. A detailed explanation of this procedure can be found in [Paper II]. Also, the reversible electrode properties of iron will not be presented in this paper but can be found in [Paper II].

Both empirical models presented above claimed to predict well corrosion currents and take both into account the effect of free chloride content on the electrochemical parameters of steel.

Fig. 1 shows the empirical model of the anodic Tafel coefficient $\beta_{a,a}$ determined according to both approaches presented above as a function of free chloride content. It can be seen that both models have a clear transition between an active and passive state which corresponds to a chloride-threshold effect. In other terms, both models describe the phenomenon of depassivation and the progress of corrosion using the impact of chlorides on the electrochemical parameters of steel.

In both models, when the chloride level is zero or negligible, the anodic Tafel slope is relatively high. In case of the model developed by Maekawa et al [26], the anodic Tafel coefficient is extremely high approaching infinity, whereas, in case of Chalhoub et al [Paper II], the anodic Tafel coefficient is equal to that of steel in the passive state that was measured experimentally. The transition from passive to active state is translated with a steeper variation of $\beta_{a,a}$ in the case of Maekawa et al [26]. Furthermore, when chloride level exceeds the threshold value, $\beta_{a,a}$ becomes constant in the case of the model

developed by Maekawa et al [26], while, it decreases linearly in the case of the model developed in [Paper II]. Another difference between the models is that, in [Paper II], $E_{rev,Fe}$ was considered constant, while, it decreases with chloride content in the case of the model of Maekawa et al [26].

Besides, in Maekawa et al's model [26], the critical chloride content was considered, by the authors, equal to 0.4% by mass of binder. This critical content was explicitly presented in their model. On the other side, in Chalhoub et al's model [Paper II], the critical chloride content which is equal to 0.5% by weight of cement was implicitly introduced in the equation of $\beta_{a,a}$.

The electrochemical parameters of active steel and the $\beta_{a,a}$ model presented in [Paper II] will be used in this work as input data to characterize the behavior of active steel.

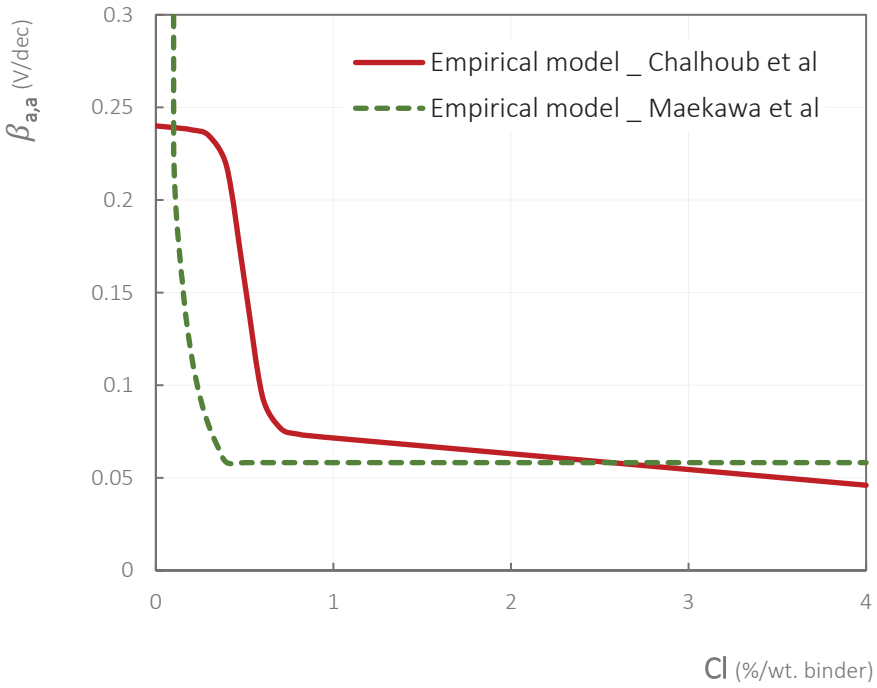


*Fig. 1. Comparison between both models of the anodic Tafel coefficient*

## 3. Numerical simulation

In previous work [10], anode samples were firstly connected to large cathodes (cylindrical specimens) which corresponds to an apparent C/A ratio of 16. Anodes were also connected to the rebars of a wall presenting C/A ratios from 200 to 2950. The determination of the critical chloride content was done with a critical current that does not change even if the size of the cathode increases. In the case of CEMI mortar formulation (M1-055) embedding as received rebars, a critical chloride content of 0.5% by mass of cement was found.

This section aims at verifying numerically if, at initiation, corrosion is independent of the size of the cathode which confirms the criterion used in the experimental protocol in [10] to detect corrosion initiation and supports the concept of anodic control of corrosion initiation. The numerical simulation was realized with the software Comsol Multiphysics. Two different numerical models were developed having the same dimensions as the two experimental set-ups mentioned earlier. The first model corresponding to the anode-cathode coupling experiment is presented in Fig. 2.

The Butler-Volmer equations were applied locally on passive and active steel areas using electrochemical parameters presented in section 2 which are detailed in [Paper II] where the electrochemical parameters of active steel were dependent on chlorides. To simulate the early stages of chloride-induced corrosion, the size of active steel was kept very small (0.05 $cm^2$) which only represents 2.5 % of the size of the anode rebar (1.88 $cm^2$).

The size of the anode in the active state did not change with the chloride contamination level like the simulation achieved in [Paper II], but instead, it was considered constant and independent of the chloride level. For the small anode, only a part of the steel surface is considered as active and the rest is associated with a passive state due to the intrinsic localized characteristic of corrosion induced by chlorides which do not allow a whole active surface of the anode.

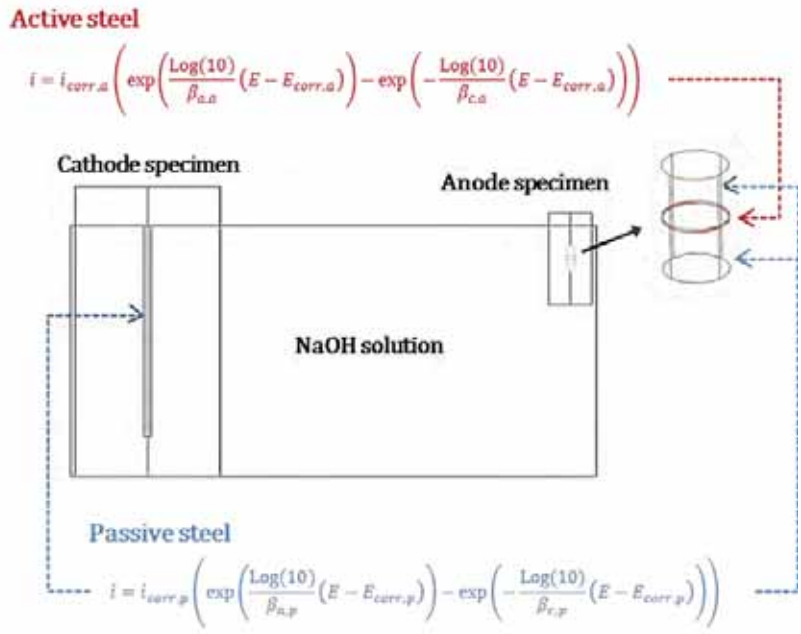


*Fig. 2. The numerical model of anode-cathode galvanic coupling test*

The second model corresponding to the anode-wall coupling experiment is presented in Fig. 3. All the horizontal and vertical rebars of the wall were associated with Butler-Volmer boundary conditions relative to a passive state.

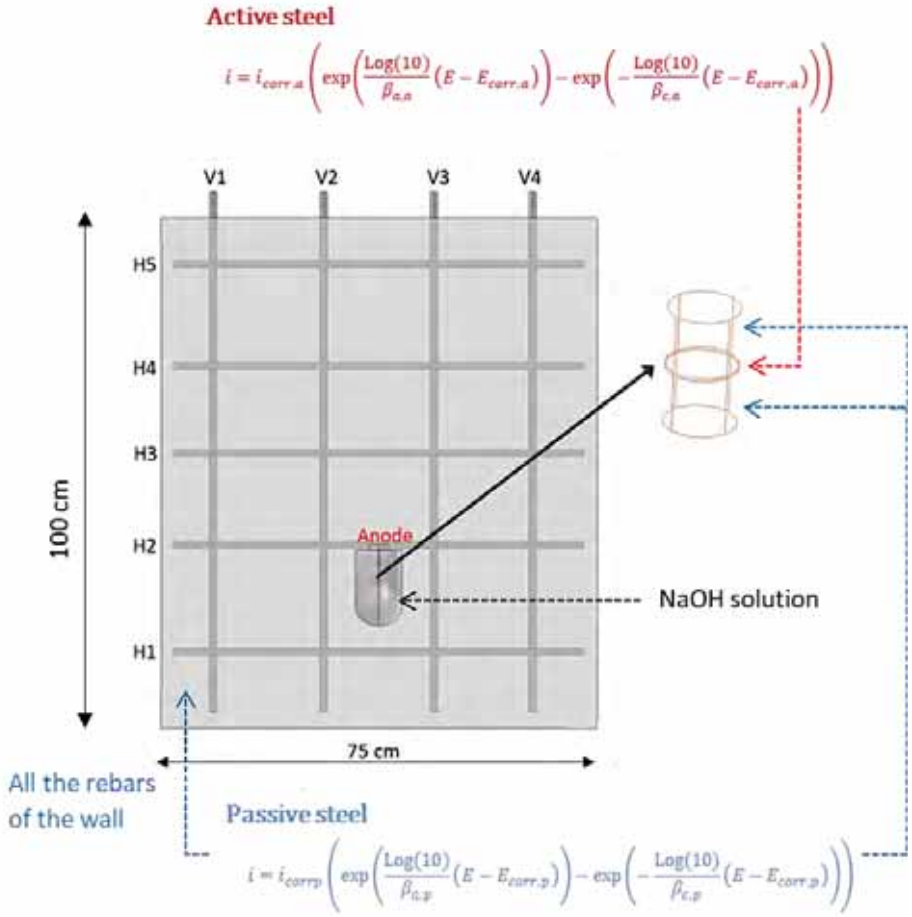


*Fig. 3. The numerical model of anode-wall galvanic coupling test*

## 4. Results

Fig. 4 shows the experimental results taken from [10] which consists of the macrocell corrosion currents measured according to the free chloride contents in case of the C/A ratios of 16 and 2950. In this paper, we are only interested in the results corresponding to low and moderate chloride contamination between 0 and 1 %/wt. cement.

Fig. 4 also introduces the numerical results obtained in the case of the numerical simulations realized according to the numerical models presented earlier, corresponding to both C/A ratios of 16 and 2950, and keeping in mind that the size of the anode did not change with chloride contamination.

It can be seen between that for chloride levels lower than 0.5% / wt. cement, the macrocell currents were negligible even if the size of the cathode increase. However, beyond the critical chloride content, macrocell currents increased with the C/A ratio and became 4 to 5 times higher.

These observations allow confirming that the early stage of corrosion propagation is under anodic control since it is controlled by the electrochemical parameters of active steel. Corrosion initiation was found to be, as expected, independent of the size of the cathode. Indeed, owing to the small size of active steel in the early stage of corrosion, the cathode is usually large enough to provide enough current to sustain the corrosion process.

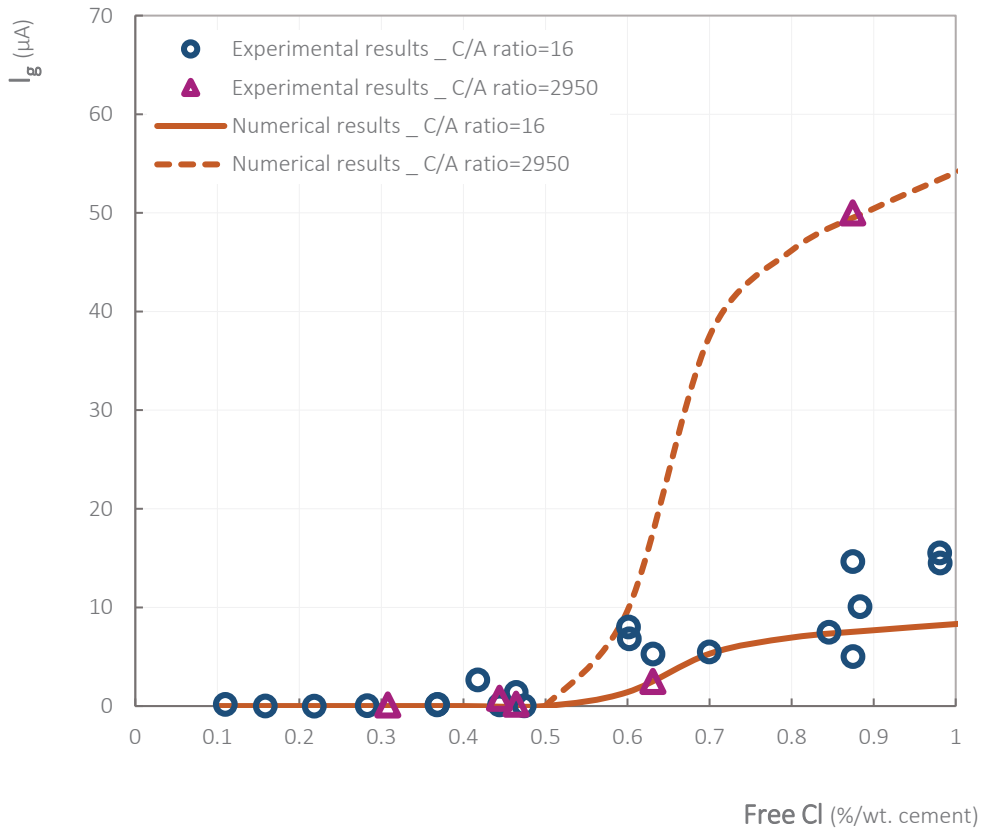


*Fig. 4. Experimental and numerical results of the galvanic coupling in case of C/A ratios of 16 and 2950*

From a numerical perspective, it is possible to say that the breakdown of the passivation film in the case of chloride-induced corrosion can be described by changing the anodic Tafel slope $\beta_{a,a}$ as a function of chlorides.

Indeed, as the level of chlorides increases, the anodic Tafel coefficient decreases – a process simulating the beginning of the depassivation of steel. When the steel is locally depassivated, the increase in chloride content leads to an increase in the macrocell current.

## 5. Future research

This work was achieved in case of a formulation based on 100% of CEMI with a w/b ratio of 0.55. A similar investigation on other formulations with different types of binders and w/b ratios would be interesting. Most of the data required for such investigation, like the polarization curves of cathodes and anodes contaminated with different levels of chlorides, were achieved on several mortars and concrete formulations (M10SF-043, B1-15L-049, B3-15L-051, and B3-041) which were presented in [Paper III].

In the end, it would be interesting, if possible, to determine an intrinsic equation of the anodic Tafel coefficient $\beta_{a,a}$ which could be a function of the chloride level and some properties linked to materials, for instance, water porosity.

As shown in part 2, when the chloride level is zero or negligible, the anodic Tafel slope is equal to that of steel in the passive state $\beta_{a,p}$. Also, the model of $\beta_{a,a}$ is a function of the chloride content and

implicitly considers the critical chloride content expressed in weight percentage versus the mass of cement.

Since the model is based on the amount of free chloride per weight of cement, conversion to a concentration of free chlorides in the interstitial solution in pore water can be achieved knowing the water porosity of the formulation.

$[Cl]$ represents the concentration of free chlorides expressed in g per liter of pore water as shown in Eq. 5. When $Cl$ is equal to $Ccrit$ , $[Cl]$ is annotated $[Cl_{crit}]$.

$$[Cl] = \frac{Cl \times C_b}{p_w} \qquad \text{Eq. 5}$$

where:

- $Cl$ is the chloride content (%/ wt. binder);
- $p_w$ is the water porosity (%);
- $C_b$ is the binder content (kg/m$^3$ of material).

Fig. 5 shows a schematic representation of an intrinsic model of the anodic Tafel coefficient which appears to be a function of $[Cl]$, $[Cl_{crit}]$ and $\beta_{a,p}$. These variables could be linked to the water porosity of the formulations and the type of binder.

Indeed, in [Paper III], it was found that when the porosity of cement paste decreases, higher critical chloride concentrations $[Cl_{crit}]$ were obtained, the concentrations were slightly higher in the case of CEM III mixes. Also, when the porosity or the type of binder is changed, the anodic Tafel coefficient of steel in a passive state $\beta_{a,p}$ could increase.

All these statements are only suggestions based on observations from previous studies, thus they need further investigations.

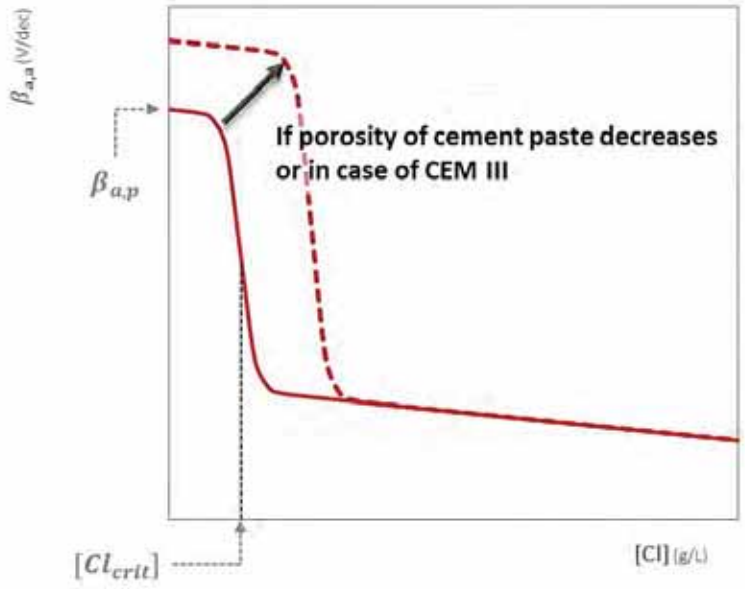


*Fig. 5. Schematic representation of an intrinsic model of the anodic Tafel coefficient*

## 6. Conclusion

This work investigated, from the perspective of numerical modeling, the mechanism of chloride-induced corrosion initiation in reinforced concrete structures. It consisted of simulating the transition from the corrosion initiation phase to the early stage of corrosion propagation to examine the process controlling the initiation of corrosion. This paper did not explain the physical aspects of corrosion initiation and steel depassivation.

The interface of rebars with the electrolyte was simulated using the equations of the Butler-Volmer model as boundary conditions. The input data of the Butler-Volmer equations are the electrochemical parameters of active and passive steel which were deduced from [Paper II].

Two different numerical models were achieved to simulate two different sizes of the cathode, and subsequently, to simulate different cathode/anode (C/A) surface ratio. The first model consisted of simulating the anode-cathode coupling experiment corresponding to a C/A ratio of 16 which was presented in [10] and [Paper II]. The second model consisted of simulating the anode-wall experiment corresponding to higher C/A ratios up to 2950 which was also realized in the experimental protocol achieved in [10].

To simulate the early stages of chloride-induced corrosion, the size of active steel was kept very small (0.05 $cm^2$) which only represents 2.5 % of the size of the anode rebar (1.88 $cm^2$). The size of the anode in an active state did not change with the chloride contamination level like the simulation achieved in [Paper II], but instead, it was considered constant and independent of the chloride level.

The numerical results showed that for chloride levels lower than the critical chloride content, the galvanic current flowing between anodic and cathodic areas was negligible and independent of the cathode/anode ratio. Beyond the critical chloride content, the currents became significant and increased when the cathode/anode ratio increased.

These observations showed that the phenomenon of depassivation of steel due to chloride ingress can be described by an anodic Tafel coefficient which is chloride dependent, and subsequently, by parameters of active steel which change with chloride contamination. This statement supports the concept of anodic control of the early phase of chloride-induced corrosion propagation which was stated in previous work [10] and reported in other literature studies [9–14].

This work was achieved in the case of a mortar formulation based on 100% of CEMI with a w/b ratio of 0.55. A similar investigation on other formulations with different types of binders and w/b ratios would be interesting.

## Acknowledgments

This work was supported by the ANR MODEVIE project, grant ANR-14-CE22-0018 of the French Agence Nationale de la Recherche and by the French National Federation of Public Works (FNTP).

## References


[1] U. Angst, B. Elsener, C. Larsen and Ø. Vennesland, *Chloride Induced Reinforcement Corrosion: Electrochemical Monitoring of Initiation Stage and Chloride Threshold Values*, Vol. 53, 2011.

[2] G. Burstein, P. Pistorius and S. Mattin, *The nucleation and growth of corrosion pits on stainless steel*, Corrosion Science 35 (1993), pp. 57–62.

[3] P. Pistorius and G. Burstein, *Metastable pitting corrosion of stainless steel and the transition to stability*, Philosophical Transactions of the Royal Society of London. Series A: Physical and Engineering Sciences 341 (1992), pp. 531–559.

[4] N. Laycock and R. Newman, *Localised dissolution kinetics, salt films and pitting potentials*, Corrosion science 39 (1997), pp. 1771–1790.

[5] K. Hornbostel, U.M. Angst, B. Elsener, C.K. Larsen and M.R. Geiker, *Influence of mortar resistivity on the rate-limiting step of chloride-induced macro-cell corrosion of reinforcing steel*, Corrosion Science 110 (2016), pp. 46–56.

[6] K. Tutti, *Corrosion of steel in concrete*, Swedish Cement and Concrete Research Institute (1982), pp. 17–21.

[7] C. Page and K. Treadaway, *Aspects of the electrochemistry of steel in concrete*, Nature 297 (1982), pp. 109–114.

[8] L. Bertolini, B. Elsener, P. Pedeferri, E. Redaelli and R.B. Polder, *Corrosion of Steel in Concrete: Prevention, Diagnosis, Repair*, 2nd editionWiley-VCH VerlagGmbH & Co., 2013.

[9] U. Angst, B. Elsener, C.K. Larsen and Ø. Vennesland, *Chloride induced reinforcement corrosion: rate limiting step of early pitting corrosion*, Electrochimica Acta 56 (2011), pp. 5877–5889.

[10] C. Chalhoub, R. François and M. Carcasses, *Determination of chloride threshold initiating corrosion: A new set-up taking the localized aspect of corrosion into account*, Cement and Concrete Research 124 (2019), pp. 105825.

[11] G. Glass, C. Page and N. Short, *Factors affecting the corrosion rate of steel in carbonated mortars*, Corrosion Science 32 (1991), pp. 1283–1294.

[12] J.A. Gonzalez, J. Algaba and C. Andrade, *Corrosion of reinforcing bars in carbonated concrete*, British Corrosion Journal 15 (1980), pp. 135–139.

[13] C. Page and J. Havdahl, *Electrochemical monitoring of corrosion of steel in microsilica cement pastes*, Materials and Structures 18 (1985), pp. 41–47.

[14] P. Lambert, C. Page and P. Vassie, *Investigations of reinforcement corrosion. 2. Electrochemical monitoring of steel in chloride-contaminated concrete*, Materials and Structures 24 (1991), pp. 351–358.

[15] H. Kaesche, *Corrosion of Metals: Physicochemical Principles and Current Problems*, Springer Science & Business Media, Berlin, 2012.

[16] J.P. Broomfield, *Corrosion of steel in concrete: Understanding*, Investigation and Repair, E&FN, London (1997), pp. 1–15.

[17] S. Stephant, *Etude de l'influence de l'hydratation des laitiers sur les propriétés de transfert gazeux dans les matériaux cimentaires*, 2015.

[18] S. Jäggi, *Experimentelle und numerische Modellierung der lokalen Korrosion von Stahl in Beton unter besonderer Berücksichtigung der Temperaturabhängigkeit*, (2001), .

[19] M. Raupach, *Zur chloridinduzierten Makroelementkorrosion von Stahl in Beton*, Deutscher Ausschuss für Stahlbeton (1992), .

[20] J. Gulikers, *Experimental investigations on macro cell corrosion in chloride-contaminated concrete*, HERON, 41 (2), 1996 (1996), pp. 107–123.

[21] K. Hornbostel, U. Angst, B. Elsener, C. Larsen and M. Geiker, *On the limitations of predicting the ohmic resistance in a macro-cell in mortar from bulk resistivity measurements*, Cement and Concrete Research 76 (2015), pp. 147–158.

[22] R. Polder, *Critical chloride content for reinforced concrete and its relationship to concrete resistivity*, Mater. Corros. 60 (2009), pp. 623–630.

[23] A.J. Bard and L.R. Faulkner, *Electrochemical Methods, Fundamentals and Applications*, 2nd edJohn Wiley & Sons, 2001.
[24] U. Angst, *Chloride induced reinforcement corrosion in concrete: Concept of critical chloride content – methods and mechanisms*, Norwegian University of Science and Technology Faculty of Engineering Science and Technology Department of Structural Engineering, 2011.
[25] P. Garces, M. Andrade, A. Saez and M. Alonso, *Corrosion of reinforcing steel in neutral and acid solutions simulating the electrolytic environments in the micropores of concrete in the propagation period*, Corrosion Science 47 (2005), pp. 289–306.
[26] K. Maekawa, T. Ishida and T. Kishi, *Multi-Scale Modeling of Structural Concrete*, CRC Press, 2008.

# Paper V

**Effect of Cathode-Anode distance and electrical resistivity on macrocell corrosion currents and cathodic response in cases of chloride induced corrosion in reinforced concrete structures**

**Chantal Chalhoub*, Raoul François, Myriam Carcasses**

**Construction and Building Materials 245 (2020) 118337**

Construction and Building Materials 245 (2020) 118337

Contents lists available at ScienceDirect

Construction and Building Materials

journal homepage: www.elsevier.com/locate/conbuildmat

# Effect of Cathode–Anode distance and electrical resistivity on macrocell corrosion currents and cathodic response in cases of chloride induced corrosion in reinforced concrete structures

Chantal Chalhoub *, Raoul François, Myriam Carcasses

*LMDC, INSA, UPS, Université de Toulouse, France*

## HIGHLIGHTS

- Influence of the cathode–anode distance on the macrocell current in case chloride induced corrosion in mortar.
- Attenuation of the cathodic reaction according to the cathode–anode distance and the impact of electrical resistivity.
- Experimental investigations followed by numerical analyses of the experiments.

## ARTICLE INFO

*Article history:*
Received 29 September 2019
Received in revised form 13 January 2020
Accepted 1 February 2020

*Keywords:*
Chloride-induced corrosion
Steel reinforcement
Mortar
Localized corrosion
Cathode-Anode distance
Electrical resistivity
Numerical simulation

## ABSTRACT

When dealing with macrocell corrosion, it is crucial to consider the geometry and size of the structure, including the mobilizable cathode–anode distance, which is the maximum distance where passive reinforcement bars exchange current with corroding active sites. An application of the mobilizable cathode–anode distance is the corrosion of submerged regions of reinforced concrete structures where very high local anodic current densities were reported with no visual manifestation making this type of corrosion very dangerous. One possible explanation for these observations is that active steel (anode) bars in the submerged region could be coupled with a cathodic aerated zone located far away from the anode. This paper aims to study the influence of cathode–anode distance on the macrocell current. Experimental investigations were carried out on a 10 m long reinforced beam consisting of 20 segments of rebars: an anode where corrosion was initiated with chloride diffusion, and 19 identical cathodes. Different electrical connections were made between cathodes and corrosion currents were measured in order to test the impact of the cathode–anode distance on the evolution of corrosion current and the attenuation of the cathodic reaction in relation to the distance between anode and cathode. The experimental campaign was supported by numerical simulations, which confirmed the experimental results and tested the impact of electrical resistivity on the mobilizable cathode–anode distance. By connecting the anode to each cathode alone, it was found that macrocell corrosion current could be provided by cathode bars at large distances from the anode, the distance being dependent on the electrical resistivity of the structure. It was also found that, when all the cathodes were connected to the anode, the closest bar received the highest proportion of the total current, which increased with electrical resistivity, whereas the most distant bars received very limited amounts of current.



## 1. Introduction

Reinforcement bars are protected from corrosion by a thin layer of passive film that forms in the alkaline environment. However, this film can be destroyed by carbonation or locally damaged when the chloride content reaches a critical level. Steel switches to an active state and acts anodically, while the rest of the bars (besides the active spot or in the other layers of reinforcement), still in the passive state, act cathodically.

In cases of microcell corrosion, anodic and cathodic parts are located directly next to each other and their position can vary with time. On the other hand, if the anode and cathode are far apart, the corrosion is called macrocell and the difference in the electrochemical state between the two parts generates the flow of an electric current through the reinforcing steel and ionic current through

* Corresponding author.
*E-mail address:* chantal.chalhoub@insa-toulouse.fr (C. Chalhoub).

https://doi.org/10.1016/j.conbuildmat.2020.118337
0950-0618/

the surrounding electrolyte. Chloride-induced corrosion in reinforced concrete structures is localized and becomes equivalent to a macrocell or galvanic corrosion [1].

The equilibrium of such a system is established on the basis of the dynamic equilibrium between oxidation of steel at the anode and the reduction of oxygen at the cathode. Thus, the geometry of the structure is a crucial parameter in macrocell corrosion. One of the most important geometric parameters that could significantly influence corrosion is the mobilizable cathode–anode distance, also known as the "distance of influence", which limits the throwing power of the anode which is defined as the ability of the corrosion current to reach areas distant from the anode [2]. Furthermore, when dealing with partially submerged reinforced structures in marine environments, it is essential to understand the limits of the mobilizable cathode–anode distance.

Raupach [3] stated that coating the steel before applying a repair patch in cracked concrete structures did not prevent the corrosion mechanism. It could be reduced slightly but not stopped. In fact, the cathodic reaction rate could be reduced considerably in the coated area but other, more distant, passive steel surfaces acted cathodically and constituted the driving force of the macrocell corrosion. This statement clearly supports the localized aspect of corrosion in concrete with the idea of a mobilizable cathode area that can be at a large distance from the anode.

Several research works have studied the effect of the cathode–anode distance on the macrocell current [4–8]. Raupach and Gulikers [6] made 2 reinforced concrete beams with a length of 2 m using a coplanar arrangement of 20 reinforcing bars, each with a length of 10 cm. They measured the macrocell currents with an ammeter and stated that the cathodic reaction could still occur at 2 m from the anode in cases of low resistivity and well-aerated concrete. Warkus and Raupach [4] performed experimental investigations on a beam with a length of 1.5 m and found that the galvanic current decreases sharply with the cathode–anode distance. However, the cathodic reaction at a distance 7 times greater than that of the closest cathode bar could still provide a current density equal to 35% of the maximum current delivered by the closest bar. Cavalier and Vassie [7] carried out half-cell potential studies on bridge decks and also found that the potentials of steel reinforcement bars at distances exceeding a meter from the anodic site were polarized, which indicates the contribution of distant cathodes to the macrocell current corrosion. Jäggi et al. [8] achieved macrocell investigations using a segmented one-dimensional model bar and found that the current decreased with the increase in distance from the anode. In addition, Jäggi et al. [8] modeled the experiments using input data measured experimentally to calculate the current distribution and found a good correlation between experimental and numerical results. Furthermore, the authors [8] realized two-dimensional macrocell arrangements and the numerical results showed that the current distribution is symmetrical with a gradual decrease in current from the closet cathode to the more distant cathodes for all four directions and the current density at the end of bars is unquestionably not negligible [8]. Arya and Vassie [5] studied the effect of cathode–anode distance by using a unidimensional cell consisting of a 4 m long beam and found that the current was reduced when the cathode–anode distance increased but that cathode bars the most distant from the anode still contributed significantly to the galvanic corrosion current. This indicates that the throwing power of the anode exceeded a distance of one meter. They also found that currents obtained with the denser concrete beam were much lower than those with the more porous beam, which implies that the resistivity of concrete would significantly reduce the throwing power of the anode.

Elsener [9] investigated the impact of the resistivity on potential profiles at the surface and macrocell current distribution with a zero resistance ammeter in solutions and Portland cement mortar specimens contaminated with 3% of chloride as NaCl added to the mixing water. The current distribution was found symmetrical along with the cathode segments and the currents provided by close cathodes were highest but were reduced with the increase in the cathode–anode distance [9]. Elsener [9] stated that, when using potential mapping technique in high resistive concrete, the small corroding spots can be only located with a very small grid size, whereas, in concrete with low resistivity, a much larger cathodic area is polarized making the location of small anode possible with large grid size. Hence, in case of unlimited oxygen availability, in mortar or concrete, the macrocell current is controlled by the resistance distribution only at high concrete resistivity [9].

One application of the mobilizable cathode–anode distance is the throwing power of galvanic (sacrificial) anode in case of cathodic protection of metallic structures like pipelines addressed by Pedeferri [2] and Lazzari [10]. They developed theoretical analytical equations to calculate the throwing power in terms of a maximum distance $L_{max}$ for simple typical geometries. The throwing power is a function of the current density, electrical resistivity, ohmic drop and some parameters taking into consideration the characteristic dimension and type of geometry, for instance, pipes or plates 2, [10].

Another application of the mobilizable cathode–anode distance is the corrosion of submerged regions of reinforced concrete structures, which has traditionally received little attention since it was generally assumed that corrosion in submerged zones was less probable than corrosion in splash zones of concrete. This assumption of lower probability is partly justified by the limited availability of oxygen for the cathodic reaction at the surface of the steel in submerged regions. One of the probable reasons why there are few reports of underwater corrosion is the absence of corrosion-induced cracking despite significant steel cross-section loss and/or loss of bond. In fact, in high-humidity conditions with low oxygen content, fluid or non-expansive corrosion products are more generally expected, which may not induce concrete cracking, so there is no visual manifestation of corrosion during a usual design service period [11–13]. For example, Walsh and Sagüés [14] showed that severe corrosion of steel could occur in parts of reinforced concrete structures submerged in marine environments. Corroded regions were not only near the waterline but were even encountered at large distances below the mud line. Field studies on pilings taken from actual marine bridges showed multiple instances of strong local corrosion associated with significant local loss of steel cross-section. They concluded that cathodic reaction rates under the limitation of diffusion of oxygen, which are considered negligible in cases of uniform corrosion, are, conversely, significant in cases of non-uniform corrosion. In fact, active steel bars in the submerged region could be coupled with a cathodic aerated zone, which would induce high corrosion rates in a small active area. These observations were also consistent with reports made in other works [15,16] indicating the necessity for further detailed investigations and research. With their numerical model, the authors [14] also found that eliminating corrosion in the splash/evaporation zone might, in some cases, increase corrosion of steel in the submerged region. In fact, the absence of corrosion in the above-water zones favors a cathodic action that can cause an aggravation of corrosion in the submerged region.

Macrocell corrosion results in very high local anodic current densities [17–19] making this topic a major concern in the domain of reinforced concrete construction. The resulting local cross-sections are very dangerous especially if there is no visual manifestation like cracking or spalling of the concrete cover, for instance, in cases of partially submerged structures where corrosion products are soluble [11–13,20]. As a result, the subject of submerged region corrosion deserves closer examination knowing the need

for better durability objectives for reinforced concrete structures especially in case of marine infrastructures. This analysis must, primarily, start with understanding the phenomenon of macrocell corrosion followed by proving that the mobilizable cathode zone could reach cathodes located at important distances from the anode in order to confirm the assumptions that anodes in submerged regions could be coupled with cathodes located in atmospheric regions.

The literature is scarce regarding the extensive cathodic response in reinforced concrete structures in the case of macrocell corrosion and its dependence on electrical resistivity. This topic is more popular in the domain of cathodic protection of pipelines placed most likely in soil, where, the throwing power of sacrificial anode is determined by theoretical equations or models using FEM simulations [2,10]. Yet, when dealing with chloride-induced corrosion in reinforced concrete structures, this issue is very important especially when it comes to understanding the macrocell process and its implications on the corrosion monitoring techniques and cathodic protection methods. In other terms, the determination of equations for the evolution of the mobilizable cathode in macrocell corrosion of rebars in concrete would be beneficial for understanding the phenomenon and identifying the role of electrical resistivity.

Additionally, when testing experimentally the cathode–anode distance, it is usually coupled with the cathode/anode ratio annotated 'C/A ratio', which is the ratio between anode and cathode surface areas; a change in cathode–anode distance is usually linked to an increase in C/A ratio. The separation between cathode–anode distance and C/A ratio would allow understanding the separate effect of cathode–anode distance on macrocell corrosion.

An exception to this is the study realized by Arya and Vassie [5] where the effect of the separation distance was tested independently from the C/A ratio. However, the cathode–anode distances tested in this paper [5], as well as in other reported studies [4,6], are limited to a certain range (less than 4 m).

These concerns led to the present study, which focused on investigating the influence of cathode–anode distance on the macrocell current. Experimental campaigns were developed in order to test the effect of the cathode–anode distance on the cathodic reaction regardless of the C/A ratio. For this purpose, the corresponding set-up must allow the distance between the anode and cathode to vary, for a fixed C/A ratio, over a large range, up to 10 m, in order to determine the limits imposed by this geometrical element on localized corrosion. The attenuation of the cathodic reaction according to the cathode–anode distance was also tested. Experimental investigations were followed by numerical analyses of the experiments allowing to confirm the experimental results and to test the impact of electrical resistivity on the limits of the mobilizable cathode.

## 2. Experimental campaign

### 2.1. Description of the mortar beam

A mortar beam was cast to perform the experimental test. The geometry of the beam is illustrated in Fig. 1. Note that the scale in the horizontal direction is different from that in the vertical direction to make the scheme clearer. The beam had a length of 10 m and a square cross-section of 10x10 $cm^2$. It contained a single bed of reinforcement bars that was composed of 20 ribbed steel bars with a diameter of 12 mm, 19 of which had a length of 20 cm and one a length of 2 cm. This last bar, representing the anode, was exposed to chloride contamination in order to initiate its corrosion. The length of this bar was kept short in order to limit the cathodic area within the anode.

All the 19 bars of 20 cm length were aligned, centered and parallel to the length of the beam and were in an entirely passive state: they acted as cathodes. The total area of cathode bars is approximately 1,433 $cm^2$. The first bar on the left was centered but transversal to the direction of the other bars. It formed the anode with a surface of 7.5 $cm^2$. The spacing (s) between two consecutive bars was 30 cm and the last bar at each extremity of the beam was 24.4 cm from the end.

The electrical contact was made with electrical wires that were tin welded to each bar. A piece of wood was fixed above the anode bar before casting, to leave a space of only 1 cm between its lower part and the upper part of the anode bar. This was done in order to reduce the cover thickness to 1 cm instead of 4.4 cm at the level of the anode bar.

Given the large span of the beam, it was decided to keep it in its formwork throughout all the tests to avoid any damage that demolding might have caused.

The formulation of the beam is summarized in Table 1 and its characterization in Table 2.

### 2.2. Method of corrosion initiation

At the age of 7 days, the wooden block placed above the anode was removed and replaced with sodium chloride (NaCl) solution (Fig. 2). This operation reduced the time needed for the chloride to diffuse to the bars and enabled corrosion to start. Before the saline solution was added, two supports were sealed with silicone sealant to securely close both ends of the notch. As shown in Fig. 3, silicone was also placed on the other two side faces to make sure the diffusion of chlorides only took place in one direction. The concentration of the NaCl solution was 280 g/L.

The potential of the anode was measured, with a reference electrode Ag/AgCl/KCl (sat), each day after the addition of the saline solution in order to detect the beginning of the depassivation process of the anode (see Fig. 4). Almost 7 days after the solution was added, the potential of the anode dropped by 100 mV.

The potential (E) of all the bars was also measured to make sure that the rest of the bars were all in a passive state (Fig. 5). The potentials of rebars in a passive state are usually expected to reach stable values, in a range indicating steel passivity which is usually around −100 to +200 mV vs. Ag/AgCl/KClsat [21] in case of cement without slag or other sulfide containing binders [22]. This criterion of passivation of rebars was used in this study and it was also applied in other studies, for instance, in the experimental protocol developed by Angst et al. [22] where the chloride threshold value initiating corrosion was determined in samples taken from reinforced concrete structures.

The corrosion measurements started at the age of 15 days, which means 7 days after the saline solution was added.

### 2.3. Methods of corrosion measurement

#### 2.3.1. Connection of anode to each cathode separately

Corrosion current annotated '$I_{Ci}$' was measured with an Agilent Multimeter between the anode and each cathode annotated '$C_i$' with $i \in [1; 19]$. The measurement was made for each anode–cathode connection separately for a duration of 10 min. Each current measured corresponded to the same C/A ratio, which was 10, but to a different cathode–anode distance. A waiting time of 20 min between connections was needed for the depolarization of the anode and corresponding cathode to take place.

Fig. 6 shows an example of the corrosion measurement connection between the anode and each of the cathode bars $C_1$, $C_5$ and $C_{10}$ respectively.

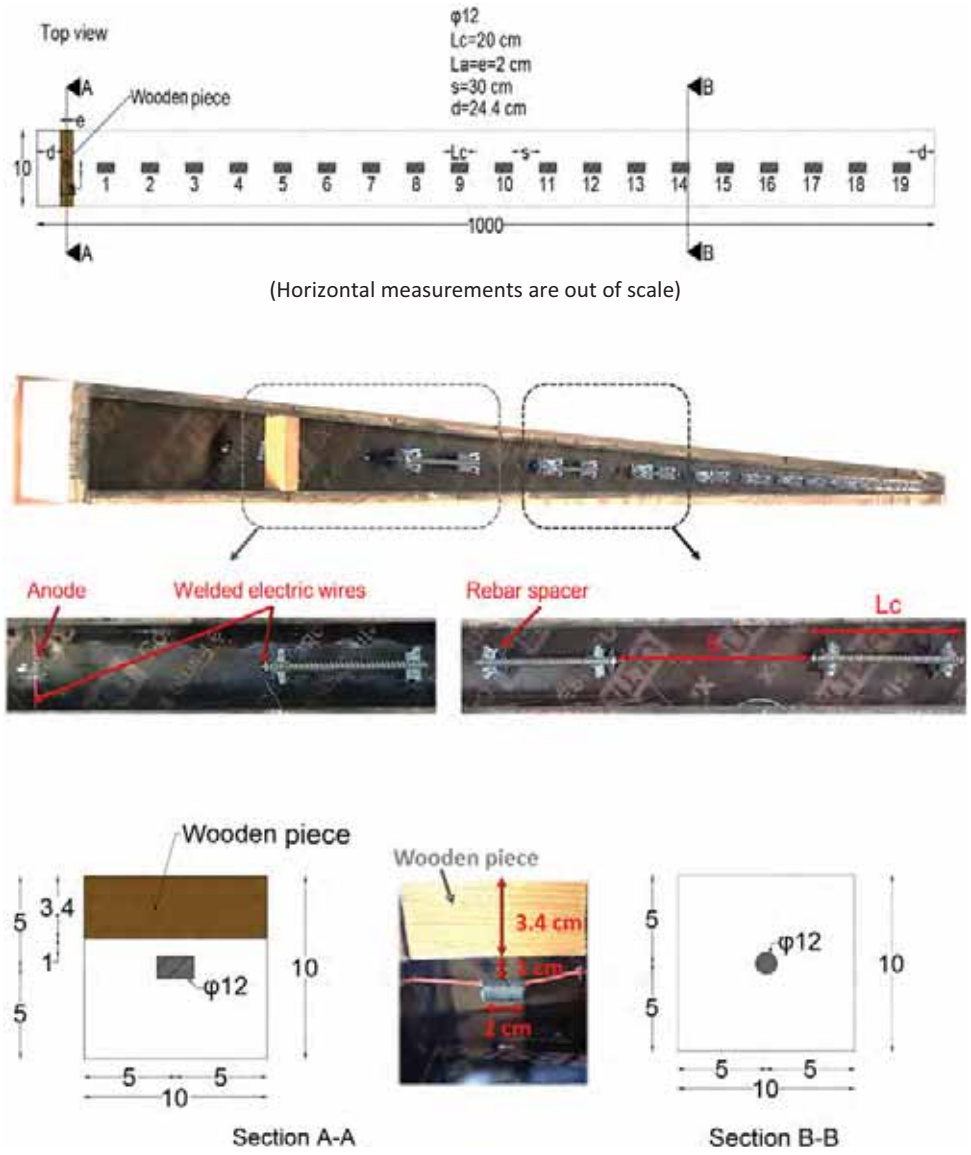


**Fig. 1.** Details of reinforcement of the mortar beam (dimensions are in cm except for ϕ12 in mm).

**Table 1**
Composition of mortar formulation.

| Materials | Quantity (kg/m3) |
|---|---|
| CEMI 52.5 R | 512 |
| Siliceous sand 0/4 | 1408 |
| Water/Cement | 0.55 |

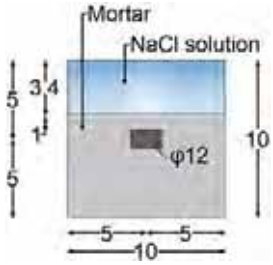


**Fig. 2.** Side view at anode level after addition of the saline solution.

**Table 2**
Characterization results of the beam formulation at the age of 28 days.

| Characterization tests | Average value | Standard deviation | Number of samples tested |
|---|---|---|---|
| Electrical resistivity (Ω·m) [RILEM TC-154 EMC] | 87 | 0.8 | 3 |
| Water porosity (%) [AFREM] | 23.4 | 0.25 | 3 |
| Chloride migration coefficient (10–12 m2/s) [NtBuild 492] | 12.1 | 0.6 | 3 |


**Fig. 3.** Top view at anode level after addition of the saline solution.

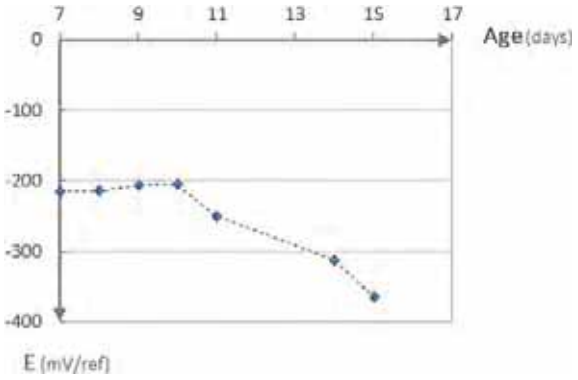


**Fig. 4.** Monitoring of the potential of the anode.

Because of the considerable length of the beam, it was not possible to make the measurements in a temperature-controlled room. However, the temperature was measured with a thermometer (Testo) at both ends of the beam to make sure there was no important temperature difference between both ends of the beam. The average temperature at the first end (the one on the anode side) was 18.9 °C and the other end was at 18.3 °C. This implies that there was no relative effect of temperature on the corrosion currents measured independently between the anode and each cathode. However, this is only an indicative result since the temperature was only measured in two positions along the beam.

The duration of measurement of each connection was limited to 10 min so that all the measurements could be performed within a day. At the end of the test, the current of the first cathode was checked again to be sure that the anodic activity had remained stable all day.

### 2.3.2. Connection of anode to all cathodes simultaneously

In this experiment, the same beam presented in Fig. 1 was used to test the effect of cathode–anode distance on the reduction of the cathodic reaction. The anode was connected to all the identical cathode bars located at different distances from the anode and the C/A ratio remained constant. The system under test was thus composed of the anode and the 19 cathodes aligned along the length of the beam. The apparent C/A ratio was then equal to 190.

In order to determine the distribution of currents received by the cathodes, it was necessary to simultaneously measure all the currents received from the anode by the different cathode bars. An MW 100 YOKOGAWA acquisition system was used for this purpose.

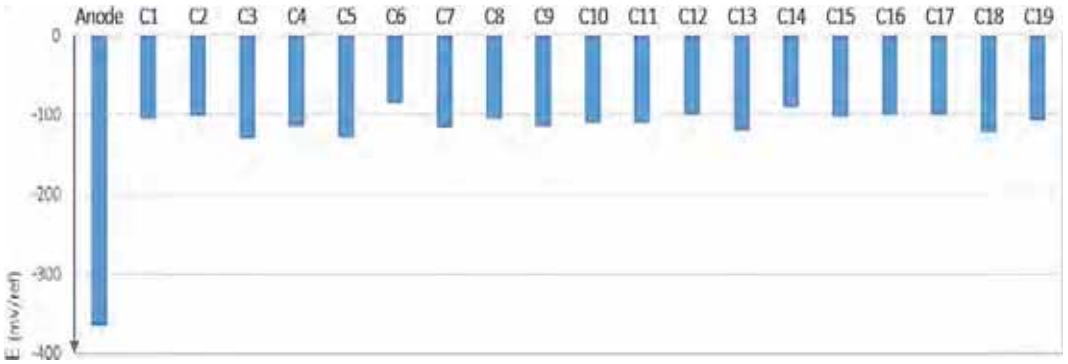


**Fig. 5.** Potential of the different bars before corrosion measurement (C stands for cathode).

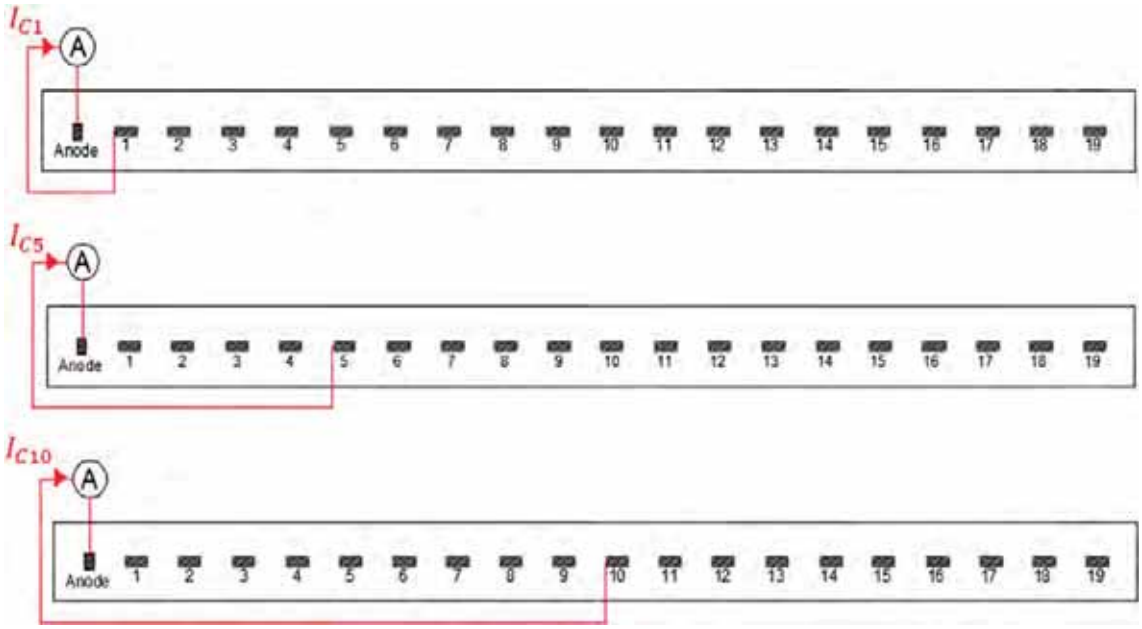


**Fig. 6.** Experimental set up when the anode is connected to each of cathodes $C_1$ , $C_5$ and $C_{10}$ respectively.

Fig. 7 illustrates the connections of the acquisition system coupled with the reinforcement bars of the beam. The device comprised 19 input terminals, each containing a precision resistor. This made it possible to measure the voltage at the level of each cathode segment and then determine the current received by the same bar using Ohm's law as shown in Eq. (1):

$$I_{Ci} = \frac{U_i \times 10^6}{R} \tag{1}$$

where:

$U_i$ is the voltage measured by the acquisition device at the terminals of resistor $R$ of the reinforcement bar $C_i$ (V);

$R$ is the resistance connected to the reinforcement bar $C_i$ which is the same for all the cathodes (Ω);

$I_{Ci}$ is the current received by reinforcement bar $C_i$ (μA) when the anode is connected to all cathodes with $i \in [1; 19]$.

Resistors of 250 Ω and 1 Ω were used. Both resistors are negligible in comparison with concrete resistance and they gave the same results, which means that a high resistance of 250 Ω does not affect the current measurements. So, the 250 Ω resistance was chosen for the rest of the measurements since it allows us to measure a higher difference of electrical potential which provided better measurement precision.

A multimeter was connected in series with the system to measure the total current of the system $I$ and to verify that it was equal to the sum of the currents $I_{Ci}$ received by each cathode bar and determined by the acquisition system (Eq. (2 )).

$$I = \sum_{i=1}^{19} I_{Ci} \tag{2}$$

The monitoring of the currents was maintained for 6 h even though the current stabilized after less than 10 min of connection. In this experiment, the temperature was also measured at both ends of the beam during the current monitoring. Fig. 8 shows the variation of temperature measured at both ends of the beams.

## 3. Numerical study

### 3.1. Theoretical fundamentals of the simulation

The software used for the 3D numerical simulation was Comsol Multiphysics and the model adopted was a steady-state electrical model.

The geometrical numerical model used the same dimensions for the reinforced beam as presented earlier. The steel–concrete interface of each reinforcement bar was modeled as a cylinder of diameter 1.2 cm and length 20 cm for the cathodes and 2 cm for the anode.

In the experiment, oxygen was considered to be available in limitless quantities at the steel–concrete interface. Consequently, an electrical model was considered adequate to simulate the electrochemical behavior of steel. The numerical simulation was governed by the local Ohm's law (Eq. (3)) and electric charge conservation (Eq. (4)) in the volume of mortar.

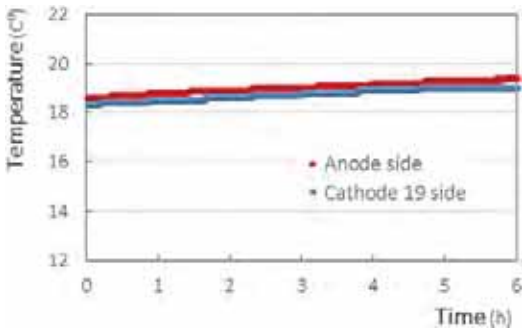


**Fig. 8.** The temperature at the two ends of the beam during the measurement.

Since the measurements were made 15 days after casting and since the beam was kept in its formwork, it can be assumed that the mortar constituting the beam was a homogeneous, isotropic environment with uniform electrical resistivity.

$$i = -\frac{1}{\rho}\nabla E \tag{3}$$

$$\nabla . i = 0 \tag{4}$$

where:

$E$ is the potential field (V);

$i$ is the local current density vector (A/m$^2$);

$\rho$ is the electrical resistivity (Ω.m).

### 3.2. Boundary conditions and input parameters

In the numerical model, steel bars were represented by their interface with the electrolyte and modeled by the Butler–Volmer equation presented in Eq. (5), using active Butler–Volmer parameters in the case of active steel and passive parameters in the case of passive steel. The electrical connection between active and passive zones could thus be simulated, allowing electrons to move from active to passive areas. The rest of the domain was associated with electrical isolation conditions.

$$i = i_{corr}\left(exp\left(\frac{log(10)}{\beta_a}(E - E_{corr})\right) - exp\left(-\frac{log(10)}{\beta_c}(E - E_{corr})\right)\right) \tag{5}$$

where:

$i_{corr}$ is the equilibrium corrosion current density (A/m$^2$);

$E_{corr}$ is the equilibrium potential (V/ref);

$\beta_a$ and $\beta_c$ are the anodic and cathodic Tafel slopes respectively (V/dec).

In the following section, parameters relative to active or passive steel will be annotated with 'a' or 'p' indices, respectively. All the cathode bars from $C_1$ to $C_{19}$ were either associated with passive boundary conditions or with electrical isolation conditions, depending on the galvanic connection system. The interfaces of all cathode bars were considered identical but, in reality, they


**Fig. 7.** Connections of the acquisition system when all cathodes are connected to the anode.

could differ slightly from one bar in the passive state to another, due to the casting process.

At the anode, the actual active surface areas were not known. The aim of the simulation was to determine the relative cathodic current (percentage of current received by the cathode) according to the distance of the cathode for a given constant anodic state. Then, it was not indispensable to know the real area of the anodic surface. Hence, the active anodic surface was calibrated to fit the experimental current measured when the cathode $C_{10}$, located in the middle of the beam, was connected to the anode.

The input parameters of the simulation are summarized in Table 3 and the changes in these parameters did not modify the qualitative aspect of the numerical results.

All the numerical simulations were performed for five different electrical resistivities: 1, 80, 300, 500 and 1000 Ω·m. An electrical resistivity of 80 Ω·m was chosen because it was close to the one measured for the experimental test, and the other four values were chosen to test the impact of resistivity on the relative currents as a function of the cathode–anode distance.

In the context of soil mapping, electrical resistivity shows a large range of values from 1 Ω·m for saline soil to $10^5$ Ω·m for dry soil overlaying crystalline rocks [23,24]. Therefore, it was decided to test very low electrical resistivity with the aim of comparing the throwing power in concrete with the ones usually encountered in the domain of cathodic protection of pipelines embedded in saline soils.

The first set of numerical simulations consisted of modeling the connection of the anode separately to each cathode. In such cases, the passive boundary conditions are applied to the connected cathode, while, the rest of the cathodes is associated with electrical isolation conditions. 19 Numerical simulations were realized in order to reproduce the first experiment presented in part 2.3.1.

**Table 3**
Input parameters of the numerical simulation.

| Name of parameter | Value | Unit | |
|---|---|---|---|
| Butler-Volmer parameters for passive steel | $E_{corr,p}$ | −0.110 | V vs. Ag/AgCl/KCl (sat) |
| | $i_{corr,p}$ | 6E−05 | A/m$^2$ |
| | $\beta_{a,p}$ | 0.24 | V/dec |
| | $\beta_{c,p}$ | 0.3 | V/dec |
| Butler-Volmer parameters for active steel | $E_{corr,a}$ | −0.576 | V |
| | $i_{corr,A}$ | 0.3 | A/m$^2$ |
| | $\beta_{a,a}$ | 0.046 | V/dec |
| | $\beta_{c,a}$ | 0.3 | V/dec |
| Electrical resistivity of the beam | ρ | {1; 80; 300; 500; 1000} | Ω.m |

As an illustration, Fig. 9 shows a zoomed image of the side view of the beam near the anode and the Butler-Volmer boundary conditions applied for active and passive steel when simulating the connection of anode to cathode $C_1$.

The second numerical simulation consisted of modeling the connection of the anode simultaneously to all the cathode bars. The numerical simulation was based on the same geometrical model of the beam, keeping the same input parameters of the model presented above in Table 3. In this case, the passive boundary conditions are applied to all the 19 cathodes since they were all connected to the anode. The same anode surface as chosen in the first simulation was also used in this one.

The total current exchanged between the anode and the 19 cathode bars was determined by integrating the normal current density at the surface of the anode. The current received by each cathode bar was determined by integrating the current density at the surface of the corresponding cathode.

## 4. Results and discussion

### 4.1. Effect of the Cathode-Anode distance on macrocell corrosion current

The following results correspond to the experiment detailed in part 2.3.1 where the anode was connected separately to each cathode. Fig. 10 presents the monitoring of the corrosion current $I_g$ measured between the anode and each of the cathode bars $C_1$, $C_5$ and $C_{10}$. It can be seen that the measured corrosion current stabilized after a duration of 10 min. The currents $I_{Ci}$ corresponding to the different (Anode − Cathode$C_i$) systems are the currents measured after 10 min of connection.

It is possible to see that the current measured decreased when the anode was connected to the more distant cathode, for instance, when connecting the anode to cathode $C_{10}$, the current was reduced to almost half the current measured when the anode was connected to the cathode $C_1$.

Fig. 11 presents the different currents measured experimentally versus the center-to-center cathode–anode distance. The closest cathode $C_1$ is located at a center-to-center distance of 41 cm from the anode and the more distant cathode $C_{19}$ at a distance of 941 cm. It can be seen that the measured current decreased with the increase of the separation distance between the anode and connected cathode. The decrease in current was due to the ohmic effect caused by the increased path length for negative ions transporting charge from cathode to anode through the concrete volume. It is interesting that increasing the cathode–anode distance

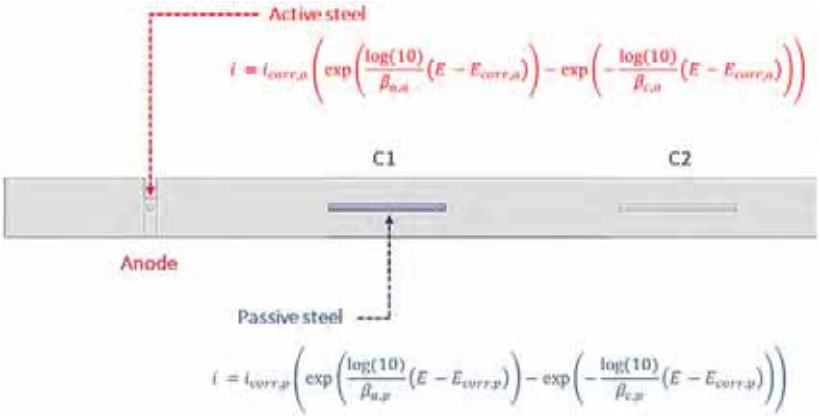


**Fig. 9.** Boundary conditions of the reinforcement bars of the beam for the anode–cathode $C_1$ connection system (side view of the first end of the simulated beam).

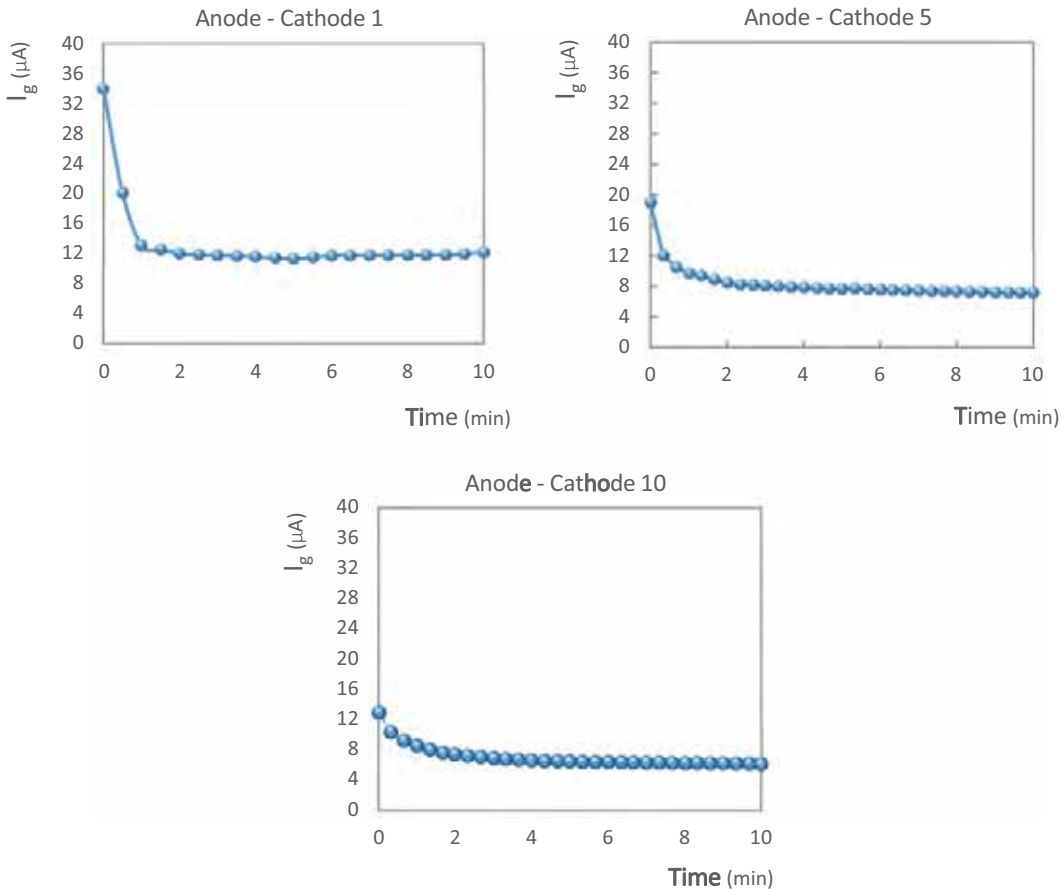


**Fig. 10.** Measurement of corrosion current between the anode and each of the cathodes $C_1$, $C_5$ and $C_{10}$.

23 times between $C_1$ and $C_{19}$ led to a decrease of only 65% of current.

It was important to check if a numerical simulation of the experimental work could fit the experimental results concerning the effect of the cathode–anode distance. It was also interesting to test the influence of electrical resistivity on the cathode–anode distance effect.

The corrosion current was calculated by integrating the normal current density at the steel/concrete interface. Each numerical current associated with a cathode corresponded only to corrosion current exchanged between the active surface of the anode and the corresponding cathode.

Fig. 12 illustrates the streamlines of the currents exchanged between the active surface of the anode and each of cathode $C_1$ and $C_5$. The exchanged currents are: the electronic current (grey arrow) which is the current produced by the flow of electrons in the electric cables and the ionic current (red lines) flowing through the beam. The distribution of the streamlines representing ionic current was extracted from numerical simulations.

Indeed, at the anode, the oxidation of iron generates electrons needed for the reduction reaction of dissolved oxygen at the connected cathode (which is in this case $C_1$ or $C_5$).

This experimental and numerical coupling system, corresponds, in real life, to a macrocell corrosion system where an electronic current circulates through the metal since electrons are transported from the anodic sites (active steel) towards the cathodic sites (passive steel). Concomitantly, an ionic current flows through the mortar electrolyte which is the interstitial solution of mortar.

To simplify the presentation of the currents obtained numerically with the different connections made between the anode and each cathode bar, the results were presented in terms of percentage of current exchanged between the anode and the corresponding cathode versus the corrosion current obtained when connecting the anode with the first cathode bar $C_1$ (Eq. (6)).

$$\delta_{i/C1} = \frac{I_{Ci} \times 100}{I_{C1}} \tag{6}$$

where:

$\delta_i/C1$ is the percentage of current exchanged between the anode and the cathode $C_i$ versus $I_{C1}$ (%);

$I_{ci}$ is the macrocell current obtained when coupling the anode with the cathode $C_i$ (μA);

$I_{C1}$ is the macrocell current obtained when coupling the anode with the first cathode $C_i$ (μA).

The experimental relative percentages were also calculated according to the macrocell current $I_{C1}$ obtained numerically which gave the same percentage value for cathode $C_{10}$ as the numerical one (i.e. 40%).

The relative macrocell corrosion currents obtained numerically between the anode and the different cathodes are presented in Fig. 13 for different electrical resistivities and compared with the relative values of the currents measured experimentally that were presented earlier in Fig. 11.

Arya and Vassie [5] are one of the rare authors who studied the impact of cathode–anode distance on corrosion current independently from the C/A ratio. Therefore, the experimental results obtained by Arya and Vassie [5] on beam A (made with OPC with a w/c of 0.65 and 3% of chlorides by weight of cement added din mixing water) were also added to Fig. 13 in term of current percentages versus the current provided by the closest cathode and

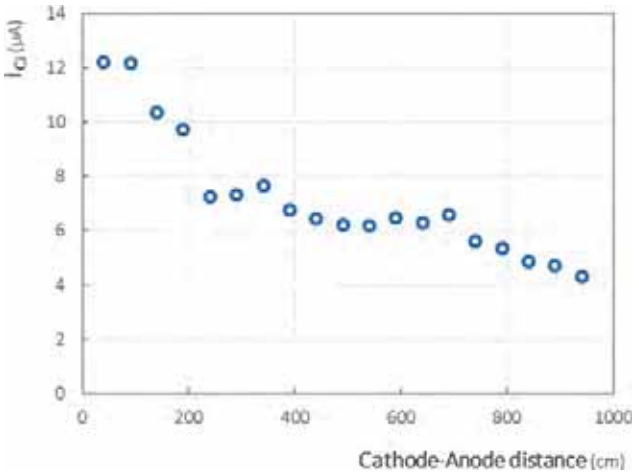


**Fig. 11.** Experimental results of corrosion currents according to the cathode–anode distance.

were showed according to the center to center cathode–anode distance. The electrical resistivity of the beam was not presented in their research paper.

Quite a good correlation is observed between the experimental points and the numerical results for the electrical resistivity of 80 Ω·m, which is the closest to the resistivity of the beam at 28 days (87 Ω·m). A good agreement is also observed between the results obtained in this paper and the ones found in Arya and Vassie [5].

It is possible to see that the current at a distance of 941 cm from the anode represented almost 30% of the current obtained at a distance of 41 cm. In both experimental and numerical results, the anode is intact, hence, the decrease in current with distance could only be explained by the increase in cathode–anode distance induced by the increase in electrical resistance also known as the 'ohmic resistance effect'. A qualitative agreement can be seen between experimental and numerical results for the effect of cathode–anode distance. The closest cathode bar received the highest current and the most distant one received about 30% of this current. Some differences can be observed between experimental and numerical results. These could be due to the effect of the steel-mortar interface, which could vary from one cathode to another one but was considered identical in the simulation.

Also, it is possible to see that the relationship between the corrosion currents and cathode–anode distance is not linear but depends on the geometry of the system.

From all the results, it can be concluded that the effect of distance on the cathodic reaction is related to electrical resistance. Both experimental and numerical results show that the macrocell current can be provided by cathode bars that are located at a considerable distance from the anode, in this case, a distance of 9.4 m. This means that the cathodic reduction reaction can occur at places significantly distant from the anode in the absence of less distant cathodes.

Fig. 14 shows the numerical results obtained for the different electrical resistivity ranging from 1 to 1000 Ω·m. It can be seen that, whatever the electrical resistivity, the increase in the cathode–anode distance led to a decrease in the corrosion current. Moreover, the reduction in current with distance is more pronounced with the higher electrical resistivity. Indeed, when the electrical resistivity is increased for the same cathode–anode distance, the relative current is reduced.

To infer the mobilizable distance in case of the first campaign (when each cathode is connected separately), a relative current threshold is fixed and the cathode–anode distance (called mobilizable C-A distance) corresponding to this criterion is determined for the different electrical resistivities.

As an example, a threshold relative current of 20% (gray horizontal line in Fig. 14) is used in the following discussion and the corresponding maximum mobilizable C-A distances annotated '$d_{max}$' are presented in Table 4 according to different resistivities '$\rho$'.

According to numerical results, in the case of the lowest resistivity of 1 Ω·m, the mobilizable cathode surface area corresponding to a relative current threshold of 20% could reach 80 m. This result is only indicative and was calculated with a linear extrapolation by assuming that for low electrical resistivity the evolution of the current with the distance is linear.

Then, the mobilizable cathode–anode distance decreases strongly with increasing electrical resistivity. In the case of resistivity of 80 Ω·m, the mobilizable cathode surface area is greater than 10 m and could be equal to 11.2 m if using a logarithmic extrapolation.

Fig. 15 presents the evolution of $d_{max}$ with the electrical resistivity and the corresponding fitting model. The latter was determined by a power equation optimized with the aim of minimizing the Mean Square Error 'MSE' between the points in red and the fitted model.

This Eq. (8) describes the relationship between $d_{max}$ and resistivity giving a correlation coefficient of 1.00 and an MSE equal to 4.

$$d_{max} = \frac{80}{\rho^{0.42}} \tag{7}$$

where:

$d_{max}$ is the mobilizable distance corresponding to a relative current threshold of 20% (m);

$\rho$ is the electrical resistivity (Ω.m).

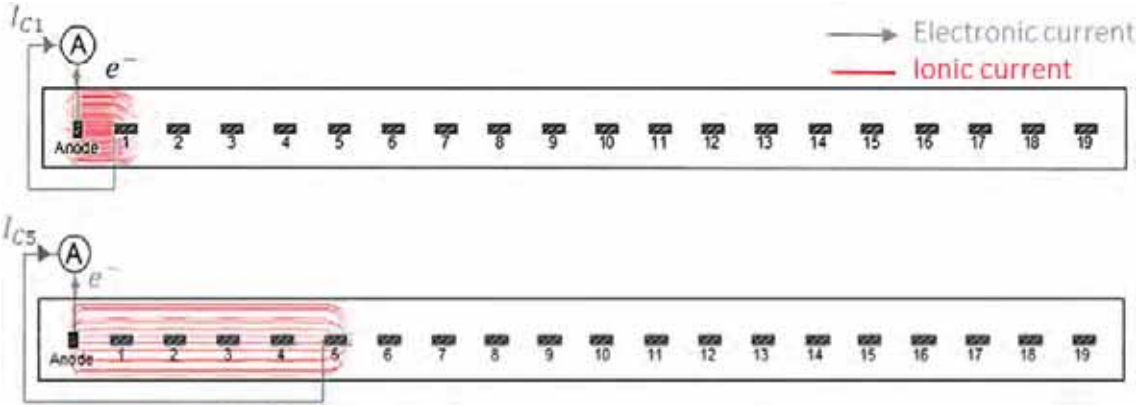


**Fig. 12.** Streamlines of the currents exchanged between the anode and each of the cathodes $C_1$ and $C_5$.

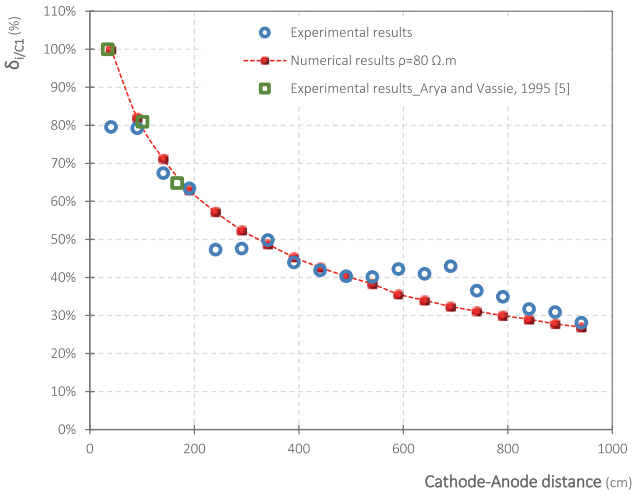


**Fig. 13.** Effect of cathode–anode distance on relative corrosion currents (experimental and numerical results).

According to this investigation, it can be concluded that, in the absence of closer cathodes acting cathodically, the macrocell corrosion current can be provided by cathode bars at large distances from the anode up to 80 m for very low resistivity (1 Ω·m) and 5 m for very high resistivity (1000 Ω·m).

Nevertheless, it must be noted that the results correspond to the geometry of the test beam presenting a one-dimensional reinforcement arrangement, while, in actual reinforced concrete structures, the reinforcement network could be three dimensional.

Even though, the results show that, in cases of partly immersed structures where corrosion is initiated in an immersed region of the structure, the mobilized cathodic area could be far away from the anode in aerated parts of the structure, where oxygen is available. These results are supported by the severe localized corrosion observed in submerged regions of reinforced structures [14–16].

Moreover, the findings of this campaign present an additional argument for the statement deduced by Walsh and Sagues [14] which is that eliminating corrosion in the splash/evaporation zone might in some cases increase corrosion of steel in the submerged region. Indeed, corrosion in the splash zone would be expected to reduce corrosion in the submerged zone because of beneficial macrocell coupling by making the potential of the submerged steel more negative hence delaying the initiation of corrosion underwater [14]. This experiment supports the assumption that corrosion in the submerged zone with lack of oxygen could be due to coupling with a cathodic zone in the aerated parts of structures and not necessarily associated with pitting phenomenon linked to water reduction under very negative potential in submerged area.

In addition, the results show that the development of a good quality concrete mixture that limits the throwing power of the anode would engender an obvious reduction in the area of the mobilizable cathode and subsequently reduce the corrosion current in concrete structures. This statement was also mentioned in the conclusions deduced by Arya and Vassie [5].

Finally, the good correlation between numerical and experimental results show that numerical simulations of reinforcement corrosion assure comprehensive results. This means that 3D numerical analysis based on a finite element method allows the quantification of the macrocell current for a simple geometry of the corrosion system and must also be used for more complicated geometries [4,25]. It also allows testing the effect of changes in single parameters, such as, in this case, the electrical resistivity of the beam.

### *4.2. Attenuation of the cathodic response as a function of the cathode–anode distance*

The following results correspond to the experiment detailed in part 2.3.2 where the anode was connected to all the cathodes. Fig. 16 shows the total corrosion current exchanged between the anode and all the cathode bars, and examples of currents received by the cathodic bars $C_1 - C_6$ and $C_{17} - C_{19}$.

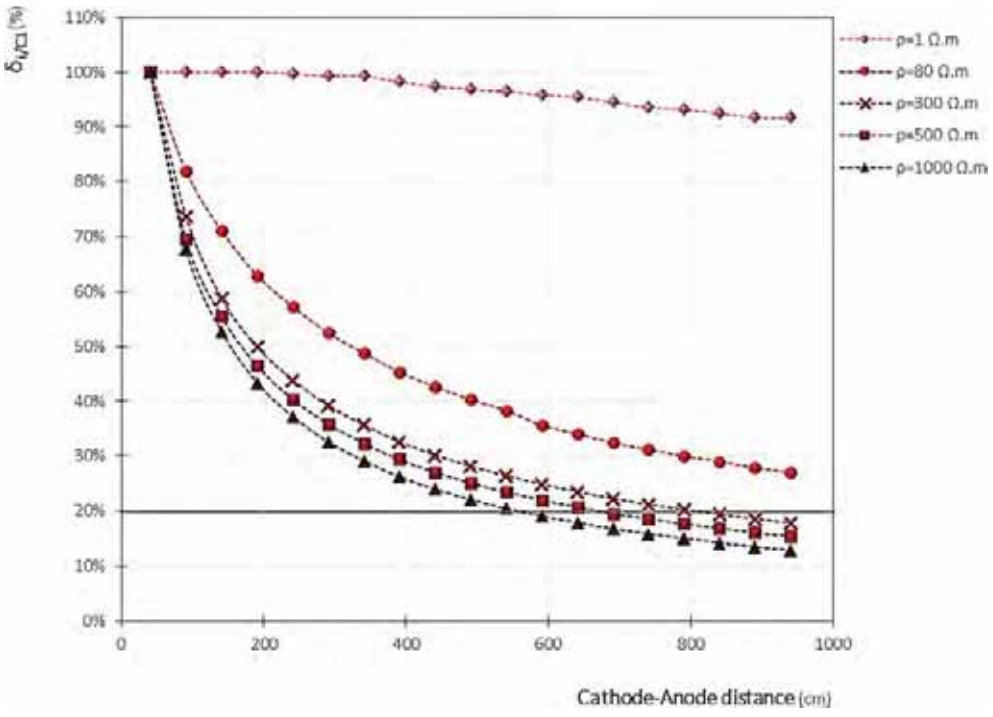


**Fig. 14.** Numerical results on the effect of cathode–anode distance and electrical resistivity.

**Table 4**
Cathode-anode distances at which relative current reaches 20%

| Electrical resistivity '$\rho$' (Ω.m) | Mobilizable distance $d_{max}$ corresponding to a relative current threshold of 20% (m) |
|---|---|
| 1 | Could reach 80 m (calculated with linear extrapolation) |
| 80 | ≈11.5 (calculated with a logarithmic extrapolation) |
| 300 | 7.9 |
| 500 | 6.9 |
| 1000 | 5.4 |

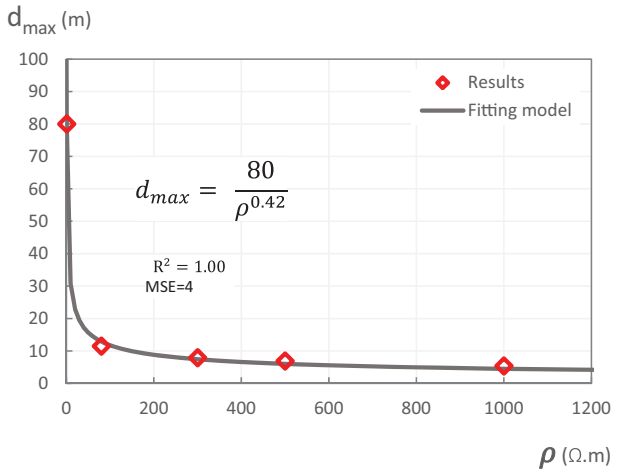


**Fig. 15.** Maximum mobilizable cathode–anode distance $d_{max}$ as a function of electrical resistivity.

It can be observed that currents in the passive reinforcement bars remained almost constant versus time.

In order to compare the currents received by the different cathode bars, the results are presented in terms of percentages of current received by each bar according to the total current of the system as in Eq. (8):

$$\alpha_{Ci} = \frac{I_{Ci} \times 100}{I} \tag{8}$$

where

$\alpha_{Ci}$ is the percentage of the current received by cathode bar $C_i$ (%);

$I_{Ci}$ is the current received by the cathode bar $C_i$ (μA), $i \in [1; 19]$;

$I$ is the total current flowing through the system (μA).

Table 5 summarizes the distribution of the current in the reinforcement passive bars. From the experimental results obtained, it can be concluded that the distribution of the macrocell current is mostly a function of the distance between the anode and the different passive bars. Cathode 1 receives the greatest part of the current (almost 30%) since the distance that separates it from the corroded steel is the smallest compared to the other bars. Conversely, cathodes 17 and 19 receive a smaller part of the current (almost 1%) because they are more distant from the anode. This indicates that cathodic activity is mostly involved close to the anode and then there is a strong decrease with the increase of the cathode–anode distance.

Fig. 17 shows the distribution of the corrosion currents obtained numerically and experimentally. It is clear that the numerical and experimental results are qualitatively similar. The same active anodic surface as chosen in the first simulation was also used in this one and the current of the total system was equal to the experimental one. Some differences may be observed, especially in the currents received by the bars $C_{14}$, $C_{15}$, $C_{16}$, $C_{17}$ and $C_{19}$, where the experimental currents are higher than those calculated in the simulation.

Despite the small differences, it can be deduced that the current received by each bar is strongly affected by the cathode–anode distance. The closest bar receives the largest part of the current whereas the most distant bars receive a very limited part.

Using numerical simulation, it was possible to calculate corrosion currents for different electrical resistivities of the beam. The numerical results, shown in Fig. 18, clearly show that the electrical resistivity has an impact on the distribution of macrocell currents along the beam since the closest cathode bar received more corrosion current when the electrical resistivity was higher. Conversely, the more distant cathodes received lower corrosion currents when resistivity increased. It can be seen that, for resistivity of 80 Ω·m, corrosion currents became relatively negligible (around 1%) at a distance of 5.8 m, whereas, when the resistivity was 500 or 1000 Ω·m they became comparatively low from 3.8 m and 3.3 m respectively. On the other hand, in case of a very low resistivity of 1 Ω·m, the current slowly decreases with distance and the distribution is more uniform along the beam.

Fig. 19 compares current distributions within the beam provided by cathodes located at both ends of the beam when all cathodes are connected to the anode in case of electrical resistivity of 80 Ω·m (upper image) and 1000 Ω·m (lower image). The current distribution within the beam is illustrated with the red lines where a high number of lines are an indication of a higher current received by the cathode and a lower corrosion current is illustrated by a lower concentration of lines. As expected, a higher fraction of

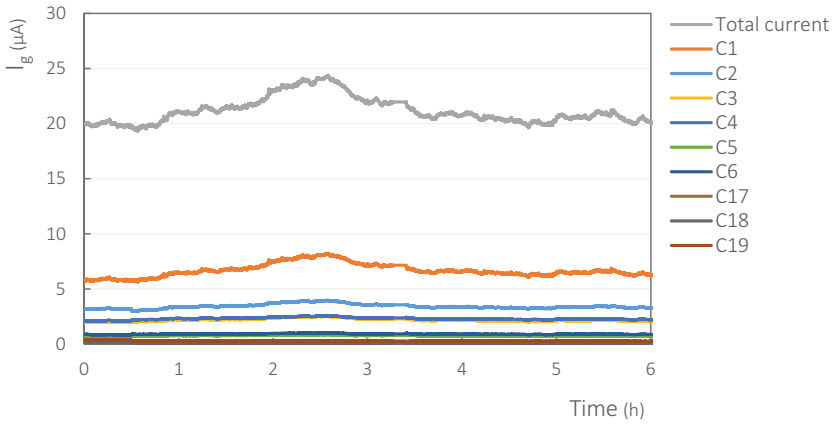


**Fig. 16.** Monitoring of the corrosion current of the system and its distribution in the reinforcement bars.

**Table 5**
Distribution of the currents received by each cathode bar according to the total current *I*.

| Cathode bar $C_i$ | After 10 min | | After 2.5 h | | After 6 h | |
|---|---|---|---|---|---|---|
| | $I_{Ci}$(μA) | $\alpha_{Ci}$(%) | $I_{Ci}$(μA) | $\alpha_{Ci}$(%) | $I_{Ci}$(μA) | $\alpha_{Ci}$(%) |
| $C_1$ | 5.9 | 29 | 8.0 | 33 | 6.3 | 31 |
| $C_2$ | 3.2 | 16 | 3.9 | 16 | 3.3 | 16 |
| $C_3$ | 2.0 | 10 | 2.5 | 10 | 2.1 | 10 |
| $C_4$ | 2.1 | 11 | 2.5 | 11 | 2.2 | 11 |
| $C_5$ | 0.7 | 4 | 0.9 | 4 | 0.7 | 4 |
| $C_6$ | 0.9 | 4 | 1.0 | 4 | 0.9 | 4 |
| $C_7$ | 0.7 | 4 | 0.8 | 3 | 0.7 | 4 |
| $C_8$ | 0.5 | 2 | 0.5 | 2 | 0.5 | 2 |
| $C_9$ | 0.4 | 2 | 0.5 | 2 | 0.4 | 2 |
| $C_{10}$ | 0.4 | 2 | 0.5 | 2 | 0.4 | 2 |
| $C_{11}$ | 0.3 | 1 | 0.3 | 1 | 0.3 | 1 |
| $C_{12}$ | 0.3 | 2 | 0.3 | 1 | 0.3 | 2 |
| $C_{13}$ | 0.3 | 1 | 0.3 | 1 | 0.2 | 1 |
| $C_{14}$ | 0.6 | 3 | 0.6 | 2 | 0.6 | 3 |
| $C_{15}$ | 0.4 | 2 | 0.4 | 2 | 0.3 | 2 |
| $C_{16}$ | 0.4 | 2 | 0.4 | 1 | 0.3 | 2 |
| $C_{17}$ | 0.3 | 2 | 0.3 | 1 | 0.3 | 1 |
| $C_{18}$ | 0.2 | 1 | 0.1 | 0.5 | 0.1 | 0.4 |
| $C_{19}$ | 0.4 | 2 | 0.3 | 1 | 0.2 | 1 |
| Total system | 20.0 | 100 | 24.0 | 100 | 20.1 | 100 |

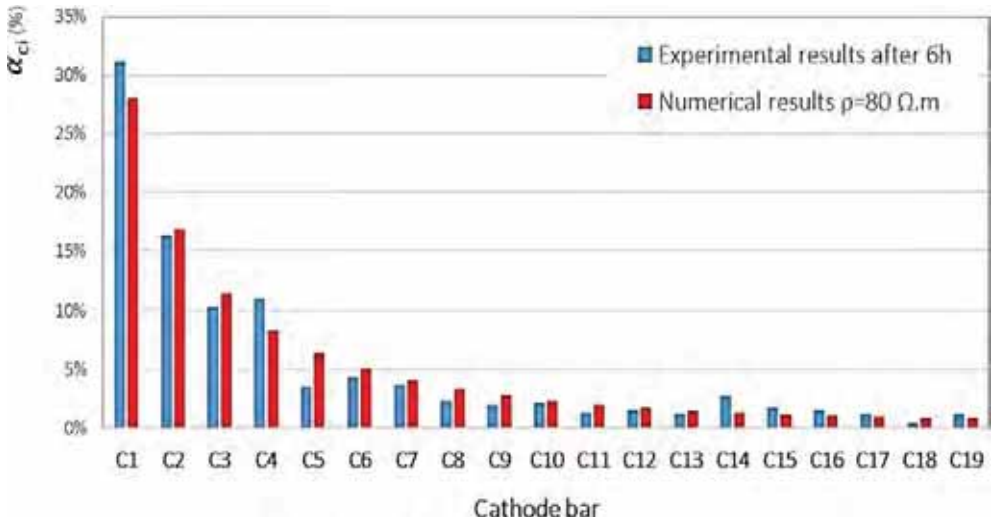


**Fig. 17.** Distribution of macrocell current delivered by the anode and received by the 19 cathode bars.

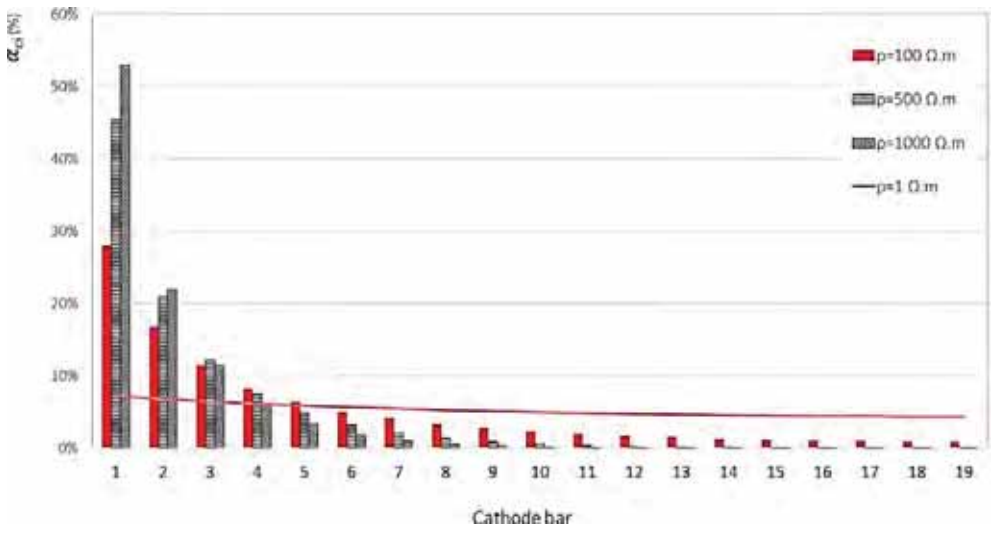


**Fig. 18.** Numerical results showing the impact of electrical resistivity on the corrosion current distribution.

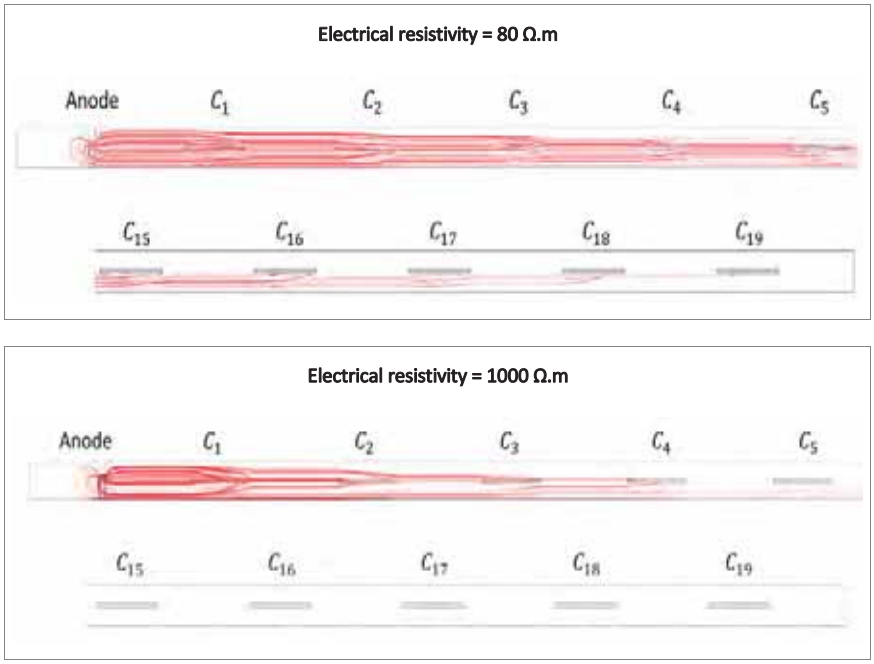


**Fig. 19.** Distribution of ionic current lines provided by cathodes located at both ends of the beam when all cathodes are connected to the anode in case of electrical resistivity of 80 and 1000 Ω·m, respectively (side view).

the current is collected by the closer steel bars which was demonstrated experimentally. The gradual decrease of the line concentration along the cathode–anode distance is due to an increase in ohmic resistance. By comparing both upper and lower images in Fig. 19, it can be clearly seen that the current is distributed differently when electrical resistivity is increased, in a way that the current becomes more concentrated next to the anode and subsequently a lower fraction of current is received by the more distant cathodes.

To infer the mobilizable distance in case of the second experiment (when cathodes are acting cathodically all together), it is possible to define the zone of influence of an anodic area '$D_{max}$' by fixing a reference criterion of, for example, 80% of the total current for the cumulative cathodic current provided in this zone, which means that only 20% (for the example chosen) of the total current goes to cathodes located outside the zone of influence.

Table 6 presents the lengths of the zone of influence for each electrical resistivity according to this criterion and shows that the zone of influence decreases with increasing resistivity. For instance, this zone extends over a length of 7.1 m for the lower resistivity of 1 Ω·m and is limited to 1.1 m for the higher resistivity of 1000 Ω·m. As stated above, the results correspond to a one-dimensional reinforcement arrangement.

Fig. 20 displays the evolution of $D_{max}$ with the electrical resistivity and the corresponding fitting model. The latter was determined by a power equation optimized with the aim of minimizing the Mean Square Error 'MSE' between the points in red and the fitted model.

Eq. (9) describes the relationship between $D_{max}$ and resistivity giving a correlation coefficient of 0.97 and an MSE equal to 1.

$$D_{max} = \frac{7}{\rho^{0.23}} \quad (9)$$

where:

$D_{max}$ is the Mobilizable distance corresponding to a cumulative cathodic current of 80% (m);

$\rho$ is the electrical resistivity (Ω.m).

According to this investigation, it can be concluded that, if closer bars are present next to the anode and are acting cathodically, then these cathodes receive more current than the more distant ones. The attenuation of cathodic current with the distance from the anode is strong and depends on the electrical resistivity of

**Table 6**
Cathode-anode distances where the relative current reaches 20%

| Electrical resistivity (Ω.m) | Mobilizable cathode $D_{max}$ corresponding to a cumulative cathodic current of 80% (m) |
|---|---|
| 1 | 7.1 |
| 80 | 3.3 |
| 300 | 1.8 |
| 500 | 1.5 |
| 1000 | 1.1 |

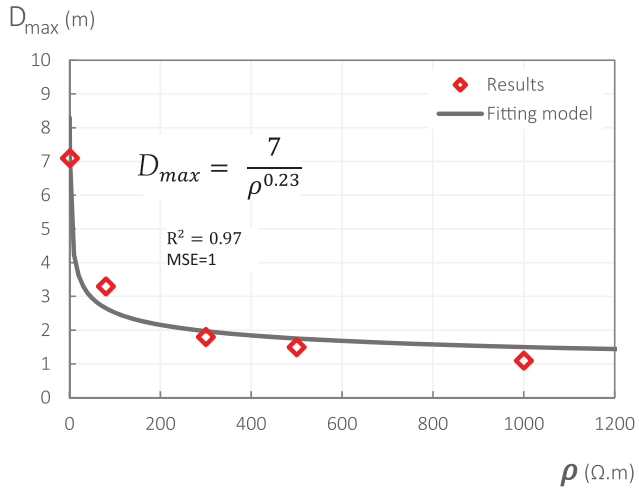


**Fig. 20.** Maximum mobilizable cathode–anode distance $D_{max}$ as a function of electrical resistivity.

the concrete which controls the distribution of macrocell current along with the rebar network in such a way that the proportion of corrosion current received by the closest cathode area increases with electrical resistivity and consequently the cathodic area involved in the macrocell corrosion process is reduced.

It is possible to make an analogy between the behavior of concrete and that of soil keeping in mind that concrete is a more complex material and usually more resistive than typical soils like humid and saline soils, clays, limestone, etc. In other words, the mobilizable cathode distance $D_{max}$ also known as "distance of influence" in case of macrocell corrosion of reinforcement steel bars embedded in concrete can be compared to the throwing power of galvanic (sacrificial) anodes $L_{max}$ of pipelines embedded in soils.

The former was calculated in this paper by means of an empirical model and is dependent on electrical resistivity and the latter was calculated by other researchers [2,10] by means of theoretical equations and is also a function of electrical resistivity.

In addition, the results show that, when all bars are acting cathodically, concrete with high electrical resistivity contributes to the limitation of the throwing power of the anode which engenders an obvious reduction in the area of the mobilizable cathode and subsequently reduces the corrosion current in concrete structures.

## 5. Conclusion

While traditional prospects for corrosion in submerged region proclaim that corrosion rate is limited by the absence of cathodic regions due to the restricted oxygen availability at the steel/concrete interface, the present work complements previously reported studies in the domain of chloride-induced macrocell corrosion in concrete and shows that corrosion can be provided by cathodes distant from the anode. This work also brings an added values to efforts previously made by allowing to test experimentally and numerically the impact of large cathode–anode distances on macrocell corrosion for the same anode and for the same cathode/anode ratio.

This work studied, firstly, the influence of the cathode–anode distance on the macrocell current independently of the cathode/anode ratio. The attenuation of the cathodic reaction according to the cathode–anode distance and the influence of electrical resistivity of concrete were also tested. Experimental campaigns were carried out on a 10 m long reinforced beam presenting a one-dimensional arrangement of rebars where cathode bars are identical but are located at different distances from the anode. The first campaign consisted of connecting the anode to each cathode separately which allows studying macrocell corrosion in case of partially submerged structures. On the other hand, the second part of the study consisted of connecting the anode to all the cathodes and determining the fraction of current received by each cathode. The experiments were followed by numerical simulations allowing to test the impact of electrical resistivity on corrosion current distribution.

It was found that:

- Whatever the electrical resistivity, in the absence of closer bars acting cathodically and connected to the anode, the macrocell corrosion current can be provided by cathode bars at large distances from the anode. This could mean that, in cases of partly immersed structures where corrosion is initiated in an immersed region of the structure, the mobilized cathodic area could be far away from the anode in aerated parts of the structure, where oxygen is available. These results are supported by the observations regarding localized corrosion in submerged regions of structures [14].
- The increase in electrical resistivity reduces the cathode–anode distance allowing a significant current flow (mobilizable C-A distance). As a result, a higher resistivity would restrain the extent of the reinforcement area in the submerged zone where anodic sites could be developed.
- If closer bars are present next to the anode and are acting cathodically, then these cathodes receive more current than the more distant ones. The attenuation of cathodic current with the distance from the anode is strong and depends on the electrical resistivity of the concrete.
- The electrical resistivity influences the distribution of macrocell current along with the rebar network in such a way that the proportion of corrosion current received by the closest cathode area increases with electrical resistivity and so the cathodic area involved in the macrocell corrosion process decreases.
- The 3D numerical modeling has proved to be a powerful tool for macrocell corrosion analysis. Qualitative and quantitative agreements between experimental measurements and numerical results based on this approach were also found in other studies [4,8,25]. Furthermore, the findings of this paper show that numerical simulation allows performing parametric studies rapidly which helps in a second step the enrichment of the available database as well as the coherent development of further experiments and the opportunity to substitute laboratory experiments by numerical computer simulations.

## Author contributions

Chantal Chalhoub planned and conducted all the experiments in the laboratory LMDC, Toulouse, France. Chantal Chalhoub did all the numerical simulations on the software Comsol Multiphysics, evaluated the results, and wrote the manuscript (original and revised version and answers to reviewers) and cover letter.

The co-authors Raoul François and Myriam Carcassès contributed with constructive criticism and helpful guidance that increased the scientific quality of the report. They also helped in the evaluation and discussion of the results.

The work was funded by the ANR MODEVIE project, grant ANR-14-CE22-0018 of the French National Research Agency (ANR) and by the French National Federation of Public Works (FNTP).

## Declaration of Competing Interest

The authors declare that they have no known competing financial interests or personal relationships that could have appeared to influence the work reported in this paper.

## Acknowledgments

This work was supported by the ANR MODEVIE project, grant ANR-14-CE22-0018 of the French National Research Agency (ANR) and by the French National Federation of Public Works (FNTP).

## References

[1] R. Francois, S. Laurens, F. Deby, in: Corrosion and Its Consequences for Reinforced Concrete Structures, Elsevier, 2018, https://doi.org/10.1016/B978-1-78548-234-2.50001-9.
[2] Pedeferri (Deceased), P. Macrocell, Corrosion Mechanism. In Corrosion Science and Engineering; Pedeferri, P., Ed.; Springer International Publishing: Cham, 2018; pp 169–182. https://doi.org/10.1007/978-3-319-97625-9_9
[3] M. Raupach, Chloride-induce macrocell corrosion of steel in concrete—theoretical background and practical consequences, Constr. Build. Mater. 10 (5) (1996) 329–338, https://doi.org/10.1016/0950-0618(95)00018-6.
[4] J. Warkus, M. Raupach, Modelling of reinforcement corrosion – corrosion with extensive cathodes, Mater. Corros. 57 (12) (2006) 920–925, https://doi.org/10.1002/maco.200604032.

[5] A. Arya, P.R.W. Vassie, Influence of cathode-to-anode area ratio and separation distance on galvanic corrosion currents of steel in concrete containing chlorides, Cem. Concr. Res. 25 (1995) 989–998, https://doi.org/10.1016/0008-8846(95)00094-S.
[6] Raupach, M.; Gulikers, J. A Simplified Method to Estimate Corrosion Rates - a New Approach Based on Investigations of Macrocells. Institute for Research in Construction, National Research Council Canada 1999, 376–385.
[7] Cavalier, P.; Vassie, P. Investigation and Repair of Reinforcement Corrosion in a Bridge Deck; Proceedings of the Institution of Civil Engineers ice, 1981; Vol. 70. https://doi.org/10.1680/iicep.1981.1784
[8] Jäggi, S.; Böhni, H.; Elsener, B. Macrocell Corrosion of Steel in Concrete-Experiments and Numerical Modelling. European Federation of Corrosion 2001.
[9] B. Elsener, Macrocell Corrosion of Steel in Concrete – Implications for Corrosion Monitoring, Cem. Concr. Compos. 24 (1) (2002) 65–72, https://doi.org/10.1016/S0958-9465(01)00027-0.
[10] L. Lazzari, Engineering Tools for Corrosion: Design and Diagnosis, Woodhead Publishing, 2017.
[11] A. Torres-Acosta, A. Sagues, Concrete cracking by localized steel corrosion – geometric effects, Mater. J. 101 (6) (2004) 501–507. https://doi.org/10.14359/13489.
[12] Broomfield, J. P. Corrosion of Steel in Concrete: Understanding, Investigation and Repair, Second Edition, 2nd ed.; T & F Books UK, 2009; Vol. 295.
[13] E. Busba, A. Sagues, Localized corrosion of embedded steel in cracked reinforced concrete pipes, Corrosion -Houston Tx 69 (4) (2013) 403–416, https://doi.org/10.5006/0871E.
[14] M. Walsh, A. Sagues, Steel corrosion in submerged concrete structures - part 1: field observations and corrosion distribution modeling, Corrosion -Houston Tx 72 (4) (2016) 518–533, https://doi.org/10.5006/1945.
[15] Thistlethwaite, C. Behaviour of Massive Reinforced Concrete Sections in Seawater. Ph.D., University of Dundee, 2014.
[16] J.L. Beaton, D.L. Spellman, R.F. Stratfull, Corrosion of steel in continuously submerged reinforced concrete piling, Highway Research Board 204 (1967) 11–21.
[17] C. Andrade, I. Maribona, S. Feliu, J. González, S. Feliu Jr, The effect of macrocells between active and passive areas of steel reinforcements, Corros. Sci. 33 (2) (1992) 237–249, https://doi.org/10.1016/0010-938X(92)90148-V.
[18] Elsener, B.; Hug, A.; Burchler, D.; Bohni, H. Evaluation of Localized Corrosion Rate on Steel in Concrete by Galvanostatic Pulse Technique. B. Elsener, A. Hug, D. Burchler, and H. Bohni,'Corrosion of Reinforcement in Concrete Construction',(Eds. Page C L, Bamforth P B & Figg J W), Royal Society of Chemistry(1996), 264-93,(WSCA Abstract 1996, 264–272.
[19] M. Raupach, J. Gulikers, Investigations on cathodic control of chloride-induced reinforcement corrosion, European Federation of Corrosion Publications(UK) 31 (2000) 13–23.
[20] Guilbaud, J.; Chahbazian, G.; Derrien, F.; Raharinaivo, A. Electrochemical Behaviour of Steel under Cathodic Protection in Medium Simulating Concrete; Swamy RN, editor. Corrosion and Corrosion Protection of Steel in Concrete, vol. 2. Sheffield Academic Press; 1994; pp 1382–1391.
[21] Bertolini, L.; Elsener, B.; Pedeferri, P.; Redaelli, E.; Polder, R. B. Corrosion of Steel in Concrete: Prevention, Diagnosis, Repair, 2nd edition.; Wiley-VCH VerlagGmbH & Co., 2013
[22] Angst, U.; Boschmann, C.; Wagner, M.; Elsener, B. Experimental Protocol to Determine the Chloride Threshold Value for Corrosion in Samples Taken from Reinforced Concrete Structures; 2017. https://doi.org/10.3791/56229.
[23] Palacky, G. Clay Mapping Using Electromagnetic Methods. First Break 1987, 5 (8), 295–306.
[24] A. Samouëlian, I. Cousin, A. Tabbagh, A. Bruand, G. Richard, Electrical resistivity survey in soil science: review, Soil Tillage Res. 83 (2) (2005) 173–193, https://doi.org/10.1016/j.still.2004.10.004.
[25] J. Warkus, M. Raupach, Modelling of reinforcement corrosion-geometrical effects on macrocell corrosion, Mater. Corros. 61 (6) (2010) 494–504, https://doi.org/10.1002/maco.200905437.

# Paper VI

## Influence of concrete electrical resistivity on corrosion propagation and its relationship with cathode/anode ratio and chloride contamination

**Chantal Chalhoub*, Raoul François, Myriam Carcasses**

**To be submitted**

# Influence of concrete electrical resistivity on corrosion propagation and its relationship with cathode/anode ratio and chloride contamination

Chantal Chalhoub*, Raoul François, Myriam Carcasses
LMDC, INSA, UPS, Université de Toulouse, France
* Corresponding author: chantal.chalhoub@insa-toulouse.fr

## Abstract

The electrical resistivity of concrete is an important durability indicator usually used to inspect the lifetime of reinforced concrete structures under the risk of corrosion. It is well documented in the literature that an inversely proportional relationship exists between corrosion rate and the electrical resistivity of concrete both for chloride-induced and carbonation-induced corrosion. This study investigates the influence of electrical resistivity of concrete on macrocell corrosion in the case of ''large'' anodes during the corrosion propagation phase. Different mortar and concrete compositions with different types of binder were used and had different electrical resistivity. The first experimental campaign consisted of measuring the electrical resistivity of samples in different chloride contamination levels. A relationship between resistivity and free chloride content was determined for all the formulations showing the decrease of resistivity with the increase in chloride content. The second campaign consisted of cathode-anode galvanic coupling and measurement of corrosion currents. The originality of this work was the use of a cathode permutation technique where the same anode is connected to a cathode from a different formulation. The permutation technique allows us to study, for the same anodic activity, the impact of parameters at the cathode, mainly the electrical resistivity. According to the results, a proportional relationship could exist between macrocell corrosion current and the electrical resistivity. Additionally, this paper studies the effect of electrical resistivity on the cathode/anode (C/A) ratio and the mobilizable cathode surface contributing to macrocell current. Results showed that corrosion current increased with C/A ratio but tended to stabilize for lower C/A ratio when electrical resistivity increases which could be linked to an ohmic control of corrosion limiting the mobilizable cathode surface. Finally, macrocell currents decreased with the increase in electrical resistivity and the results show an asymptotic behavior of current when electrical resistivity is very high.

## Keywords

Macrocell corrosion; Propagation; Chlorides; Electrical resistivity; Cathode to anode ratio.

## 1. Introduction

The electrical resistivity (ρ) characterizes the ability to conduct the flow of electric current in materials. This electric current can be realized either by electronic conduction through the flow of electrons in metals like reinforcement bars or by electrolytic or ionic conduction through the flow of ions in fluids and porous materials like concrete.

In the case of concrete, the electrolytic conduction depends on the characteristics of the interstitial solution such as the degree of saturation, the nature of ions and in particular, the concentration of chloride ions. It also depends on the capacity of ions to circulate which is a function of the porosity of concrete and tortuosity of the porous network.

Owing to the relatively simple measurement technique, concrete resistivity is an important durability indicator usually used to evaluate the transport properties of concrete and to inspect the lifetime of reinforced concrete structures under the risk of corrosion [1–11]. Indeed, it is well documented in the literature, that an inversely proportional relationship exists between corrosion rates and the electrical resistivity of concrete both for chloride-induced and carbonation-induced corrosion [1–11]. This linear relationship can be easily proved with numerical simulation [12].

For this purpose, the RILEM TC 154-EMC Benchmark was launched in 2000 to provide a background description and a technical guideline of the different existing on-site and some in situ methods used to evaluate electrical resistivity of concrete [13].

Alonso et al. [2] were the first researchers to highlight the impact of electrical resistivity on corrosion rate prediction by proposing an empirical model based on an inversely proportional relationship between corrosion rate and electrical resistivity.

After that, several corrosion rate models, like the Duracrete model [14], insisted on the relationship between corrosion rates of steel and concrete resistivity showing that electrical resistivity is a controlling factor of the propagation phase of corrosion.

The degree to which the corrosion rate is limited by concrete resistivity is mostly dependent on the anode size [25] and the cathode size and location.

The impact of concrete electrical resistivity on the limitation of the mobilizable surface of passive steel was studied in previous work [Paper V]. It was shown that the mobilizable cathode-anode distance allowing a significant current flow decreases with the increase in electrical resistivity [Paper V]. Another finding is that the mortar resistivity influences the distribution of macrocell current along with the reinforcement network, for instance, the part of current provided by the cathode area near the anode increased with resistivity which reduces the cathodic mobilizable surface involved in the macro cell corrosion process [Paper V].

The cathode/anode ratio which is the surface ratio between anode and cathode is another important parameter involved in the corrosion propagation phase. It is commonly known that the increase in the cathode/anode (C/A) ratio leads to the increase of the macrocell corrosion current since the anode is surrounded by a larger cathode surface [15–17]. However, the extent to which the C/A ratio stimulates macrocell corrosion is strongly dependent on electrical resistivity. Indeed, Warkus and Raupach [11] found numerically that high current densities were observed in the case of electrical resistivities between 100 and 1000 Ω.m. For all the tested geometries, they significantly decrease beyond 1000 Ω.m. This means that the electrolytic control also known as ohmic control becomes dominant at very high resistivities (higher than 1000 Ω.m). In [12], the authors stated that high electrical resistivity is responsible for low corrosion kinetics since it mobilizes a smaller passive area.

After corrosion initiation, comes the corrosion propagation phase which is influenced by several parameters. Electrical concrete resistivity is one of these factors known to affect the rate of corrosion propagation, and subsequently, the service life duration of the structures. Many researchers were interested in studying the impact of electrical resistivity on the corrosion rate of reinforcing steel in concrete [2,18] and found an inversely proportional relationship between both variables [1–11].

In this research field, this paper aims to study and understand the impact of electrical resistivity on macrocell corrosion propagation in mortar and concrete. It also investigates the influence of chloride contamination on electrical resistivity in the case of different types of binders. Most importantly, this paper studies the effect of electrical resistivity on the C/A ratio and the mobilizable cathode surface contributing to macrocell current.

Firstly, the electrical resistivity in different types of mortar and concrete formulations was measured according to two different methods; the first one consisting of a direct measurement of resistivity with a resistivity meter and the second one consisting of an indirect measurement using numerical simulation. These measurements were realized separately on cathodes (samples without chlorides) and anodes (samples contaminated with different levels of chlorides) to test the impact of chloride pollution on resistivity.

Then, an experimental campaign was carried out, consisting in the measurement of galvanic corrosion currents between anodes and cathodes from the same composition.

The second step consisted in keeping the same anode but replacing the cathodes with other cathodes from different formulations. This technique is called, in this paper, ''cathode permutation'' since only the cathode is changed or replaced and the anodes are kept the same. This technique allows studying the impact of the parameters at the cathode on macrocell current which is usually associated with the kinetics of the cathodic reaction and most importantly with the electrical resistivity of the cathode.

Finally, an anode sample was connected to larger cathodes consisting of two-layered reinforced concrete walls. The concrete walls allow testing different coupling systems associated with different C/A ratios which allow testing the impact of the C/A ratio on the mobilizable cathode surface. The ''cathode permutation'' technique was also applied in this case by connecting the same anode, each time, to a different wall with different concrete mix and subsequently different electrical resistivity. This method allowed us to test the influence of electrical resistivity on the effect of the C/A ratio.

## 2. Electrical resistivity measurement techniques

There are several non-destructive in situ and on-site techniques for electrical resistivity measurements. Hereafter, a brief review of the measurement techniques that are widely used for the measurement of electrical resistivity of concrete, is presented.

In laboratories, measurements can be realized on reference samples or concrete cores taken from real structures with devices based on two-electrode configuration using two metallic plates for injection of current on either side of the sample and the measurement of the corresponding potential difference between the same plates. Laboratory measurements can also be done with devices based on quadrupole configuration using the multi-ring device developed by Du Plooy et al [19] where the current is injected between two plates and the potential difference is measured between annular electrodes.

On construction sites and sometimes in laboratories, measurements can be realized on the surface of the concrete structures or even inside the structures using embedded devices. Superficial measurements, commonly known for their easy implementation, can be realized with multi-electrode devices such as the Wenner device [20] that was initially developed for soil resistivity measurements.

Wenner is a four-point set-up with four equally spaced electrodes which allows measuring the resistance. This measured resistance is then transformed into an apparent resistivity using the Wenner formula. Angst and Elsener [21] found, experimentally and numerically, that the application of this formula is acceptable even though the assumptions on which it is based are not respected (semi-infinite media). They also found experimentally that measurements with such devices overestimate the resistivity compared to bulk resistivity measurements likely because of the presence of coarse aggregates [21].

In addition to resistivity measurements, the multi-electrode devices allow having a profile of the electrical resistivities of concrete at different depth levels by an inversion calculation method [22–24].

On the other hand, the embedded devices in concrete are mainly used to quantify and monitor the electrical resistivity gradients in concrete mainly in the cover thickness [25–28].

These methods have the advantage of being relatively quick to set up and allow an immediate interpretation of the result. However, the quality of all of these measurement techniques is dependent on the electrical contact between concrete and the electrodes of the devices used [25] which represents a limitation of these methods if the contact was not good.

Moreover, these measurements can be disturbed by the presence and the volume of reinforcement rebars [13,29,30]. Indeed, the presence of (passive or active) rebars can disturb the electrical resistivity measurements since steel is a good electric conductor that could underestimate the real concrete resistivity.

## 3. Parameters influencing concrete electrical resistivity

The electrical resistivity of concrete can be significantly affected by several parameters [31]. Hereafter, a brief review of some important influencing parameters:

### 3.1. Water content

One of the most important parameters affecting concrete resistivity is the water content [24,29,32–37]. Lots of studies have established a direct relationship between the degree of water saturation and electrical resistivity where the resistivity decreases (according to a power-law) when the degree of saturation increases [3,31,38,39].

### 3.2. Characteristics of the porous network

It appears that the electrical resistivity is correlated with the nature, quantity, and characteristics of the interstitial solution in the concrete.

It seems logical that electrical resistivity can be associated with intrinsic parameters of the porous network like the water porosity, the degree of connectivity and tortuosity of the porous material [40]. These parameters influence the transfer properties of the porous volume and also the ability of ions to flow in the pore solution.

### 3.3. Chloride contamination and carbonation

Another important factor influencing concrete resistivity is chloride contamination. It has been shown that the electrical resistivity decreases when the concentration of chlorides in the interstitial solution increases [38,41–45]. This is due to the increase of ionic conductivity in the pore solution of concrete which favors the circulation of the ionic current.

As an example, Sbartaï et al. [43] measured the electrical resistivity of four concrete mixtures designed with Portland cement CEM I 52.5 R and made with different w/b ratios. The resistivity measurements were achieved with the four-point method in a Wenner configuration. The authors [43] found similar behavior in the case of all concrete mixtures where the resistivity is significantly reduced with the increase of NaCl concentrations. In this study, samples were oven-dried then saturated in NaCl solutions with different concentrations from 0 to 60 g/l [43].

Some researchers like Fares et al [41] used the electrical Resistivity Tomography (ERT) which is a non-destructive DC-electrical technique that allows determining electrical resistivity profiles versus depth. Then, Fares et al [41] used a calibration method to correlate electrical resistivity to chloride

contents to get the chloride profiles versus depth which are then compared to those measured with potentiometric titration to validate the method. This technique was applied to concrete and mortar samples based on CEMI and the chloride-resistivity relationship was modeled using an exponential law.

Conversely, concrete carbonation appears to have an opposite impact on electrical resistivity since resistivity increases with the carbonation level. This can be partially attributed to the precipitation of calcium carbonate, and ferric, alumina, and silica oxides causing the reduction of the number of ions in the interstitial solution [2].

### 3.4.Binder type and w/b ratio

The type of binder used is an important factor that can modify the microstructure of concrete, and thus, affects its electrical resistivity [46–48]. For instance, the use of fly ash or slag or silica fume in concrete increases significantly its resistivity [36,48] which is due to a refinement of the porosity and a significant lowering of the average pore diameter.

Additionally, the w/b ratio is an important parameter that governs the microstructure of the cement paste and the properties of its interstitial solution which impacts the concrete resistivity. Indeed, an increase of the w/b ratio is associated with the decrease of electrical resistivity [43,49–51] since the porosity and pore connectivity increases [44].

### 3.5.Temperature

Temperature influences the concentration and the mobility of the ions in the interstitial solution and also the ion-ion and ion-solid interactions [52] and therefore it influences the concrete electrical resistivity. Lopez et al. [40] indicated that, when considering the effect of temperature, it is always important to examine the relative humidity factor. For instance, in case of constant relative humidity, such as saturated environments, the increase in temperature implies an increase of the mobility of the ions in pore solution leading to a decrease of electrical resistivity [29,53]. On the other hand, in case of a limited supply of electrolyte, such as, dry or semidry environments, the electrical resistivity of concrete is high whatever the temperature.

## 4. Experimental details

### 4.1.Specimens and formulations

Three types of samples were used in the experiments presented in this paper: Anode samples, cathodes and larger cathodes (walls). The anodes are cylindrical samples $(\varphi 3.3\times 7\ \mathrm{cm})$. These samples are contaminated with different levels of chlorides and contain at their center a ϕ6 x 10 mm Fe-500 ribbed steel bar. Anodes were oven-dried and then saturated in aqueous NaCl solutions with concentrations ranging from 0 to 280 g/L. The cathodes are cylindrical samples $(\varphi 11\times 22\ \mathrm{cm})$. These samples are chloride-free and contain at their center a ϕ6 x 160 mm Fe-500 ribbed steel bar. The larger cathodes are parallelepiped walls $(75\times 20\times 100\ cm)$ embedding 18 Fe-500 ribbed steel bars with a diameter of 12 mm. 10 bars with a length of 70 cm are horizontally placed and 8 bars are vertical with a length of 102 cm with 5 cm emerging from the wall. The steel bars are separated with plastic spacers, to avoid electrical conductivity between the bars. Electric wires were tin welded to the horizontal bars and were coupled with a connection box making it possible to connect them as needed from outside the wall. A PVC pipe containing a sodium hydroxide solution (NaOH) was fixed to the wall and sealed with silicone to place the anode. The preparation of these samples and the details of the preconditioning of anodes are further detailed in previous work [54].

Table 1 presents the composition of the mortar and concrete formulations used for the anode and cathode samples. Two mortar mixes were realized and annotated with the letter M and three concrete mixes were used and are annotated with the letter B. The numbers indicated in the names of the formulations represent their w/b ratios. The formworks of all the samples were removed 24h after casting. After that, the cathode and anode samples were wet cured in a humidity room (relative humidity = 95%) and then the anode samples were dried and then polluted with chlorides by immersion in saline NaCl solutions. The detailed composition and characterization tests of these formulations are detailed in another work [Paper III] and the anode preconditioning procedure is presented in [54].

*Table 1. Composition of formulations used for anodes and cathodes*

| | Formulation | Composition | w/b |
|---|---|---|---|
| Mortar | M1-055 | 100% CEMI 52.5R | 0.55 |
| | M10SF-043 | 90% CEMI 52.5R+ 10% Silica Fume S95 DM | 0.43 |
| Concrete | B1-15L-049 | 85% CEM I 52.5 N + 15% Limestone | 0.49 |
| | B3-04 | 100% CEM III A 52.5 ES | 0.4 |
| | B3-15L-051 | 85% CEM III A 52,5 L PMES + 15% Limestone | 0.51 |

Table 2 presents the formulations of the larger cathodes. Three reinforced concrete walls are geometrically identical with three different compositions were realized. The wall W1-055 is based on CEMI, while the wall W15SF-043 contains 15% of silica fume substituting the cement and the wall W80S-047 contains slag with a level of substitution of 80%.

The formworks of the walls W1-055 and W15SF-043 were removed 24h after casting, while, the formwork of the wall W80S-047 was removed 90 days after casting. After that, the walls were placed in a temperature-controlled room at 20 °C (atmospheric exposure).

*Table 2. Formulations of the walls (larger cathodes)*

| Materials | Quantity (kg/m3) | | |
|---|---|---|---|
| | W1-055 | W15SF-043 | W80S-047 |
| Cement | 350<br>CEMI 52.5 N CE CP2 NF | 340<br>CEMI 52.5R | 80<br>CEMI 52.5R |
| Silica fume | 0 | 60 | 0 |
| Slag | 0 | 0 | 320<br>ECOCEM |
| Washed Sand | 700<br>0/4R ALL SILICE | 858<br>0/4 (SL0704) | 858<br>0/4 (SL0704) |
| Gravel | 1100<br>4/10 SR ALL SILICE | 945<br>4/12 (GL0412) | 945<br>4/12 (GL0412) |
| Superplasticizer | 0 | 4.8<br>Master glénium sky 537 | 2<br>Master glénium sky 537 |
| w/b | 0.55 | 0.43 | 0.47 |

## 4.2.Electrical resistivity measurements

The electrical resistivity in saturated conditions of all the formulations was measured using a direct measurement method and also an indirect measurement technique.

This first method is realized on non-reinforced reference samples which are identical to the test specimens but without rebars. The measurement is done with a resistivity meter according to RILEM TC-154 EMC.

The second method is realized on the test samples and consists of externally polarizing the specimens and using the instantaneous response of the system allowing to do the ohmic drop correction and using 3D numerical simulation to determine the electrical resistivity. This method is detailed in previous work [Paper II]. Both measurements are realized in a temperature-controlled room at 20 $^{o}$C.

## 4.3.Galvanic coupling and permutation technique

The experimental campaign consists of measuring the galvanic corrosion current between anodes and cathodes from the same formulation. Then, the same anode is connected to a cathode from a different formulation. This technique is called, in this paper, ‘’cathode permutation’’ since only the cathode is changed. The permutation technique makes it possible to study, for the same anodic activity, the impact of the parameters at the cathode, mainly the electrical resistivity.

Corrosion current monitoring was realized with a potentiostat using the Zero resistance ammeter ''ZRA'' technique for each galvanic coupling as shown in Fig. 1 for a duration of 7 days and the average corrosion current is calculated from the integral of the current signal and is annotated $I_g$. All the experiments were realized at a constant temperature of 20$^{o}$ C.

The second experiment consisted of the galvanic coupling of anode samples with larger cathodes consisting of three reinforced concrete walls. This connection allows testing different coupling systems associated with different C/A ratios which allow testing the impact of the C/A ratio on the mobilizable cathode surface. The ''cathode permutation'' technique was also applied in this case by connecting the same anode to different walls which are geometrically identical but were formed with different compositions and subsequently had different electrical resistivities. This method makes it possible to test the influence of electrical resistivity on the evolution of macrocell current with the C/A ratio. Corrosion currents were measured with a Multimeter ''Agilent'' as shown in Fig. 2 and the current values $I_g$ were recorded after their stabilization to a steady-state condition.

Knowing that in the corrosion initiation phase, the size of the anode is relatively small due to the low level of chlorides at the steel surface. During this phase, the corrosion is believed to be under anodic control [55] and independent of the bulk resistivity [56]. Hence, it must be emphasized that this paper only considers the cases where the anode is relatively "large". This indicates that the frame of this work is limited to the corrosion propagation phase and does not consider the initiation phase. Hence, the results with relatively high chloride contents were only used to analyze the experimental outcomes.


*Fig. 1. Experimental set-up of the anode-cathode connection*

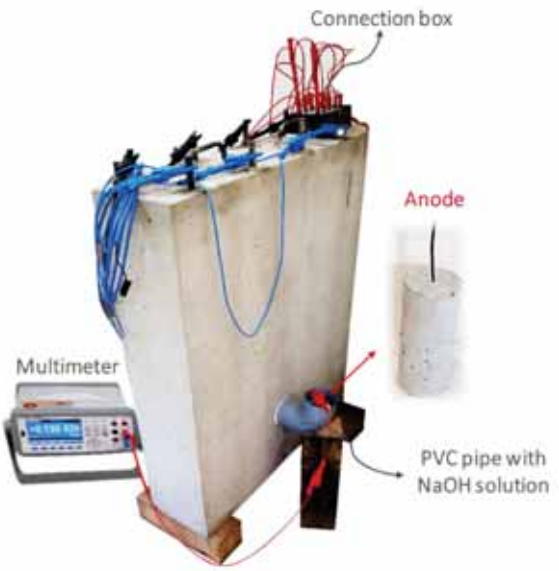


*Fig. 2. Experimental set-up of the anode-wall connection*

### 4.4.Determination of chloride content

After all the electrochemical measurements, the total chlorides were measured according to the NF-EN-14629 standard [57]. Since the total chlorides are the sum of free and fixed chlorides, the transition from total chlorides to free chlorides was achieved using empirical adsorption isotherm equations presented in previous work [Paper III]. In some cases, free chloride contents were directly measured according to the procedure recommended by GranDuBé [58].

In a study realized by Sbartaï et al. [43], similar preconditioning which consisted of oven-drying the samples then soaking them in NaCl solutions. The authors [43] stated that this preconditioning technique (oven-drying before contamination) allows, first, to accelerate chloride intrusion throughout the material by capillary processes, and also, to have a homogeneous distribution of the total chloride content inside the tested samples. This last statement was supported by a chemical investigation achieved according to (AFPCAFREM) standards [59]. Therefore, it is possible to say that the preconditioning adopted in this work likely allows having a homogenous distribution of chlorides in anode specimens. This statement was also confirmed experimentally with measurements of total chlorides achieved on mortar powders collected from different areas of the same anode sample. The obtained results indicated a variation of chlorides between 91 and 113% versus the chloride content measured in the area near the rebar (Appendix V). This observation is an indication of the reproducibility of the adopted procedure and most importantly the homogeneous distribution of the total chloride content inside the tested samples.

## 5. Results and discussion

### 5.1.Electrical resistivity as a function of chloride contamination

Table 3 summarizes the electrical resistivity of all the mortar and concrete formulations in the case of non-contaminated samples. The electrical resistivity of cathodes was realized on reinforced specimens using the indirect method, while, the resistivity of the walls was realized on non-reinforced samples using the direct method.

It can be seen that the electrical resistivity of the formulations containing silica fume, like M10SF-043 and W15SF-043, and formulations with slag, like B3-04, B3-15L-051, and W80S-047, presented

higher electrical resistivity compared to formulations containing CEMI, like M1-055, B1-15L-049, and W1-055. Additionally, for the same type of binder, electrical resistivity increased with the decrease of w/b, for example, B3-04 presented a resistivity 2.7 times higher than that of B3-15L-051.

*Table 3. Electrical resistivity measurements of samples without chlorides*

| Formulation | Electrical resistivity (Ω.m) (RILEM TC-154 EMC) | | |
|---|---|---|---|
| | Average | CV (%) | Age (d) |
| M1-055 | 113 | 7 | 40-300 |
| M10SF-043 | 737 | 10 | 80-108 |
| B1-15L-049 | 69 | 10 | 98 |
| B3-04 | 718 | 2 | 255 |
| B3-15L-051 | 267 | 1 | 289 |
| W1-055 | 110 | 10 | 90 |
| W15SF-043 | 990 | 3 | 90 |
| W80S-047 | 630 | 2 | 91 |

Fig. 3 presents the electrical resistivity results obtained in the case of contaminated samples with different formulations according to free chloride contents. Resistivity was measured using both direct and indirect methods. The sum of tested samples used for both measurement methods is indicated in the legend of each graph in Fig. 3.

The direct method is realized on non-reinforced reference samples (ϕ3.3×7 cm) contaminated with different chloride levels and the results are the points in blue. After the direct measurement, the samples were split and the free chlorides were directly measured.

The indirect method presented earlier is directly realized on anode samples (ϕ3.3×7 cm) after the galvanic coupling tests and the results are the points in red. After the indirect measurement, the samples were split and the total chlorides were measured and then transformed to free chlorides using chloride binding isotherms.

The results clearly show that the increase of chloride contamination causes a decrease in the electrical resistivity. This result is not very novel and it is consistent with previous research work [38,41–45].

According to previous work [Paper II], it was possible to determine a relationship between electrical resistivity and free chloride content in case of a mortar formulation based on CEMI as follows:

$$\rho = \frac{\rho_0}{1+1.3\times Cl} \qquad \text{Eq. 1}$$

Where:
- $\rho$ is the electrical resistivity of mortar or concrete (Ω.m);
- $\rho_0$ is the electrical resistivity of mortar or concrete non-contaminated with chlorides (Ω.m);
- $Cl$ is the free chloride content (%/wt. binder).

This model was applied in the case of the different mortar and concrete formulations used in this paper and is presented in the graphs of Fig. 3 as a black dashed curve. Also, Fig. 3 shows the values of correlation factors $R_d^2$ and $R_i^2$ calculated between this model and the resistivity experimentally measured with both direct and indirect methods, respectively.

Looking at the results, it is possible to argue that an intrinsic relationship between free chloride content and electrical resistivity (like the one presented in Eq. 1) might likely be applied whatever the concrete or mortar formulation which means that it is independent of the binder type used and the w/b ratio. This could be explained by the ionic activity in the interstitial solution being governed by chloride contamination.

It must be noted however that some scattering is observed in the case of concrete formulations B1-15L-049 and B3-04. Also, it must be noted that the resistivity measured during the direct method is, in most cases, lower than the ones determined with the indirect method, especially in the case of the formulations B1-15L-049 and B3-04. For instance, in the case of the formulation B3-04, the resistivity measured with the indirect method is sometimes twice as big as the one measured with the direct method. This indicates that the model might have overestimated the real resistivity since it was calculated according to $\rho_0$ which was determined with the indirect method.

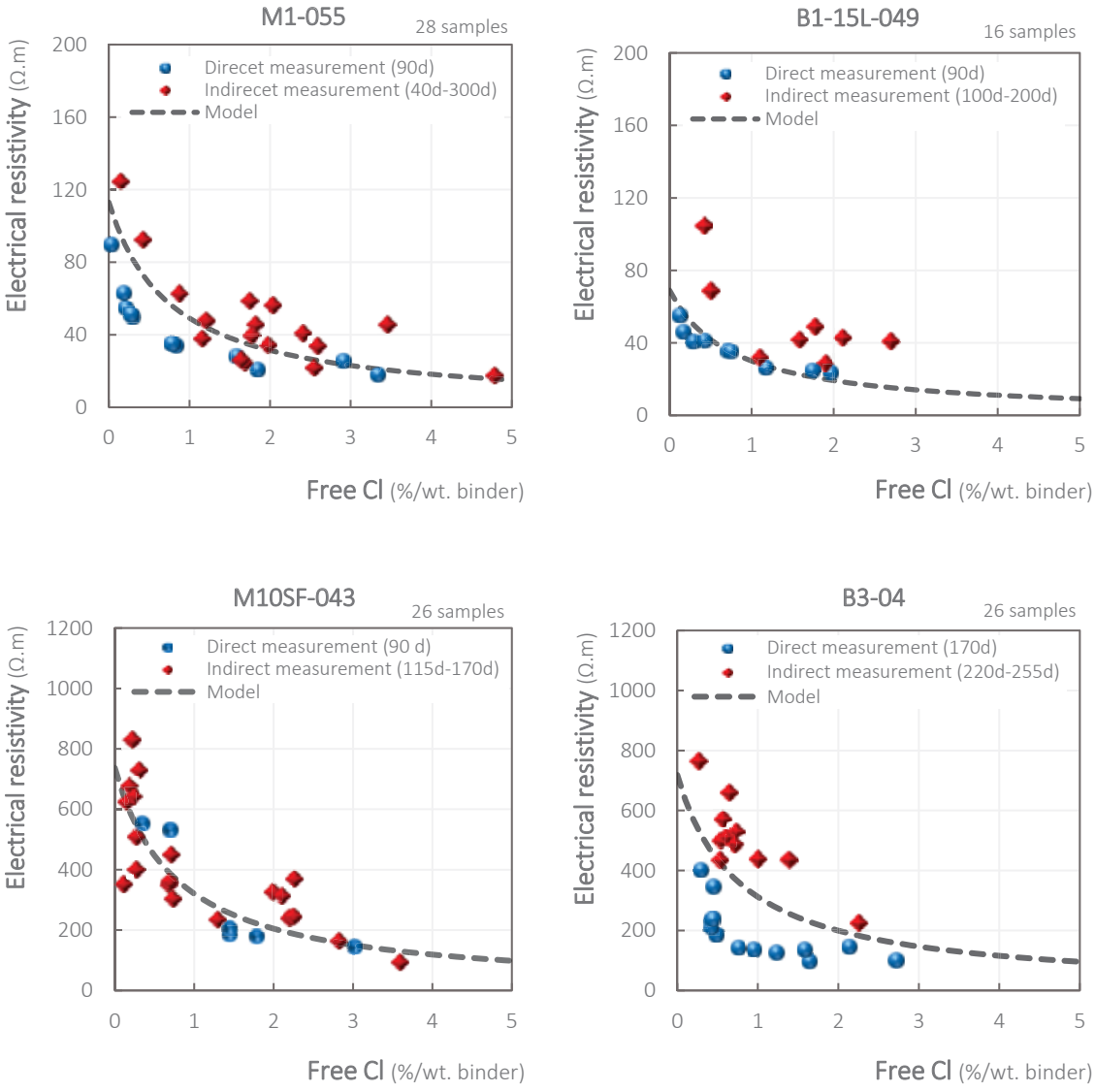

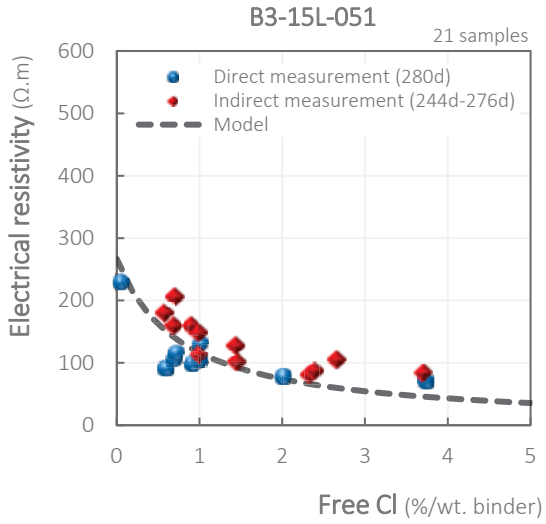


*Fig. 3. Electrical resistivity as a function of chloride contamination level in case of different formulations*

As mentioned earlier, Fares el al. [41] modeled the relationship between electrical resistivity and free chloride contamination levels (expressed in %/wt. concrete or mortar) in case of 2 concrete formulations (C1 and C2) and 1 mortar formulation (M2), all based on CEMI. The model obtained, for each formulation, was an exponential law with regression coefficients greater than 0.9 [41].

Therefore, it was interesting to compare the models developed by Fares el al. [41] with the one achieved in this paper. The model developed by Fares el al. [41] was realized according to free chloride contents expressed versus the weight of concrete, thus, the equations were transformed to be a function of the free chloride level expressed in percentage of the weight of cement and is presented in Eq. 2.

$$\rho = \rho_0 e^{-\alpha\, Cl} \qquad \textit{Eq. 2}$$

Where $\alpha$ is an empirical constant determined by [41] but changed in this paper to account for the free chlorides by mass of cement instead of concrete as follows:

$$\alpha = \begin{cases} 0.47 & in\ case\ of\ C1 \\ 0.51 & in\ case\ of\ C2 \\ 0.61 & in\ case\ of\ M2 \end{cases} \qquad \textit{Eq. 3}$$

Fig. 4 presents the normalized resistivity $\frac{\rho}{\rho_0}$ according to both approaches, which means that it presents the resistivity ratio versus $\rho_0$.

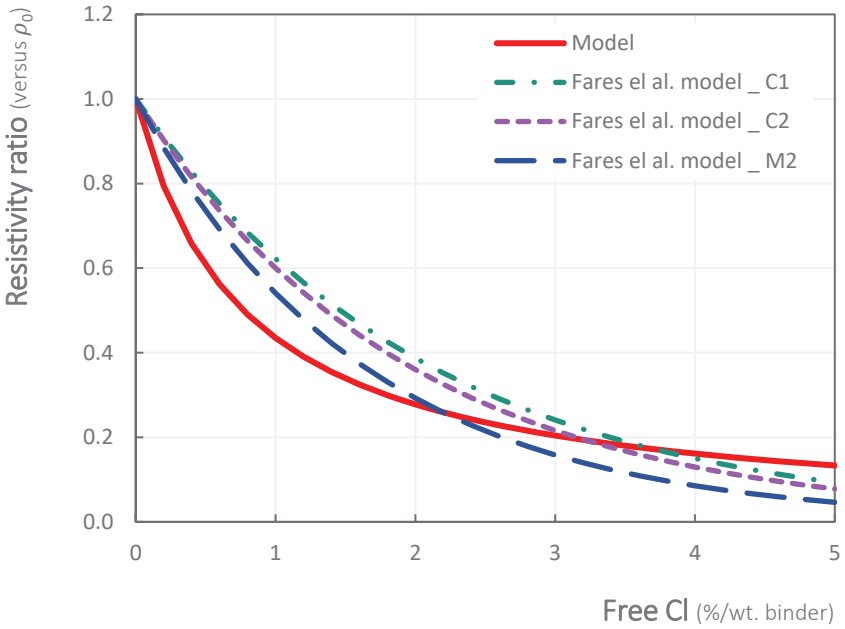


*Fig. 4 Comparison between Fares et al. models [41] and the model developed in this paper to link resistivity to chloride pollution*

It can be seen that the model presented in this paper underestimates the outcome values from models of Fares et al. [41] for chloride levels lower than almost 2.5 %/ wt. binder while it slightly overestimates values from models for higher chloride levels.

To sum up, the measurements of electrical resistivity in saturated conditions show a significant decrease in resistivity with the increase in chloride contamination which is believed to have a homogeneous distribution in the tested samples. As an illustration, for the mixture M1-055, the electrical resistivity decreased from 110 to 18 Ω.m as the free chloride content increased from 0 to 4.8 %/wt. cement. Similar behavior can be observed for the rest of the mortar and concrete mixtures. These findings are consistent with several studies in literature and can be explained by the high mobility of free chlorides in saturated concrete which increases the ionic conduction [38,41–45].

This relationship between electrical resistivity and chloride content is an indication of the presence of a time-dependent resistivity gradient in real structures, since, parts of the structure will be contaminated with chlorides while the rest remains intact.

Also, it was observed that the resistivity changed with the type of binder where it was the highest in cases of mixtures with mineral additions like silica fume. Furthermore, for the same type of binder, the decrease in w/c ratio, which reduced concrete porosity, increased the electrical resistivity.

Finally, whatever the model used to simulate the impact of chloride content on resistivity, all the results agree that the increase in chloride level leads to the decrease of the electrical resistivity which means that, in real structures, a resistivity gradient is partially induced by the diffusion of chlorides through the cover of the structure making it a spatial and time-dependent phenomenon.

## 5.2.Permutation results of mortar formulations

This section presents the results of the permutation tests. The idea is to experimentally validate the impact of resistivity on the macrocell corrosion current and to characterize, for the same anodic activity, the effect of electrical resistivity at the cathode, representing the sound part of the structure.

Fig. 5 presents the cathode permutation results of the mortar formulations M1-055 and M10SF-043, where M1-055 anode samples were connected with M1-055 cathode samples (points in blue) and then connected with M10SF-043 cathode samples (points in red). Additionally, three M1-055 anodes contaminated with chloride levels higher than 4.5%/wt. binder were only connected with M10SF cathodes. The measured currents were between 7.8 and 17.8 µA. It must be noted that M10SF-043 is almost **6.5** times more resistant than M1-055 when the tests were realized.

The results clearly show that macrocell corrosion currents were lower when anodes were connected to M10SF-043. The ratio between the currents measured during the connections with cathodes M1-055 and M10SF-043 was almost **6.5** which is equal to the resistivity ratio between both M1-055 and M10SF-043 formulations.

The low currents obtained when anodes are connected to M10SF cathodes can thus be explained by the higher electrical resistivity caused by the presence of silica fume and the lower w/b ratio.

Nevertheless, it is important to note that the macrocell current is dependent on the electrical resistivity only beyond the chloride threshold level. This observation could be interpreted as an indication of the anodic control of corrosion at initiation when the anode size is small and the chloride level is low [55] making the local parameters at anode the controlling engine of the corrosion process.

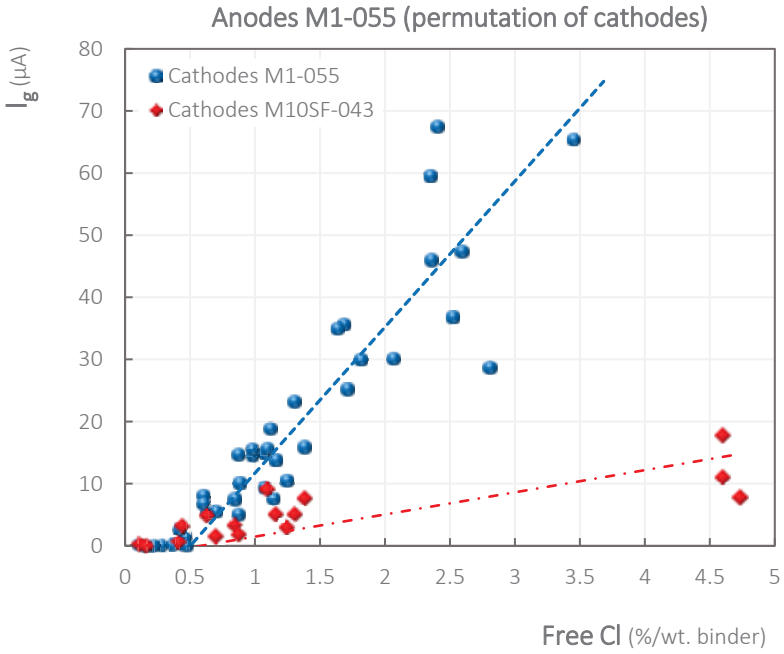


*Fig. 5. Anode M1 with cathodes M1-055 and M10SF-043*

## 5.3.Permutation results of concrete formulation

Fig. 6 presents the cathode permutation results of the concrete formulations B3-04 and B1-15L-049 where B3-04 anodes were connected with B3-04 cathode samples (points in blue) and then with B1-15L-049 cathodes (points in red). It must be noted that B3-04 is almost **10.4** times more resistant than B1-15L-049.

The results clearly show that, for chloride levels higher than 1.5%, macrocell corrosion currents were **5** times higher, when anodes were connected to cathodes B1-15L-049 presenting the formulation with the lower resistivity.

This big difference between the current ratio and resistivity ratio might be attributed to the overestimated resistivity in the case of the formulation B3-04. When considering the resistivity measured with the direct method presented in Fig. 3, the resistivity ratio between B3-04 and B1-15L-049 varies between **6** and **7**.

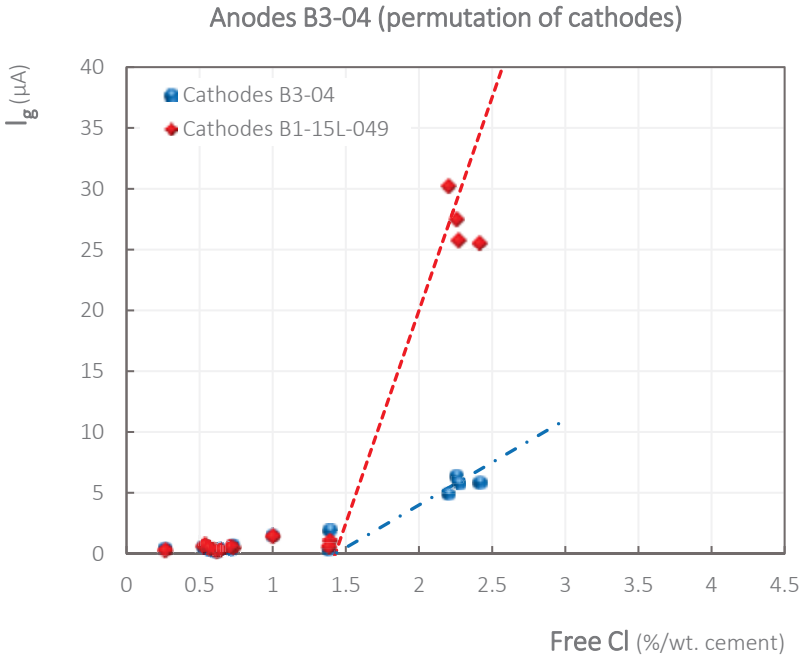


*Fig. 6. Anodes B3-04 with cathodes B3-04 and B1-15L-049*

Fig. 7 presents the cathode permutation results of the concrete B3-15L-051 and B1-15L-049 samples where B3-15L-051 anodes were connected with B3-15L-051 cathodes (points in blue) and then with B1-15L-049 cathodes (points in red).

Despite the presence of some scattering, the results show that, for chloride levels higher than 1.0 %, macrocell corrosion currents were **3.2** times higher when anodes were connected to cathodes B1-15L-049 which is **3.9** times less resistant than B3-15L-049.

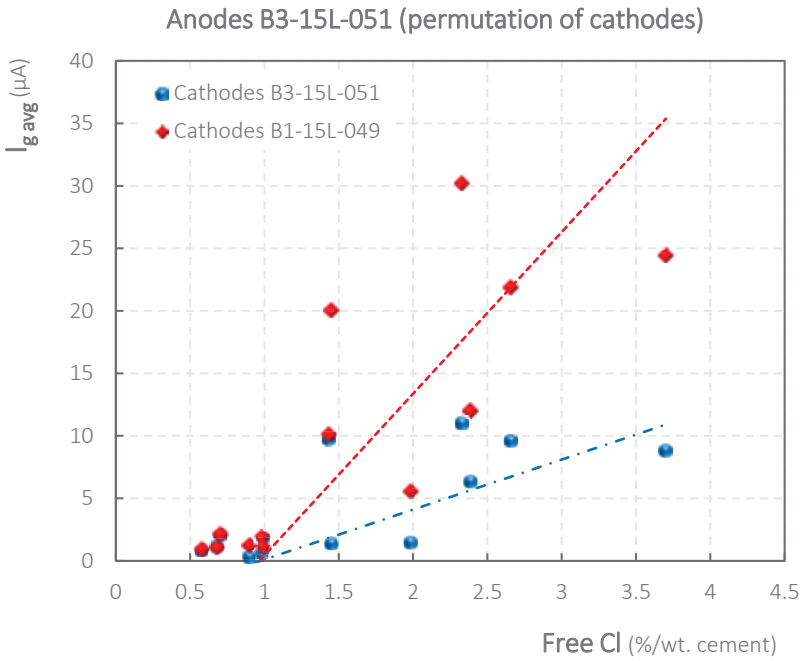


*Fig. 7. Anodes B3-15L-051 with cathodes B3-15L-051 and B1-15L-049*

The originality of this study lies in the cathode permutation technique which allows highlighting the impact of properties at the cathode which are mainly related to electrical resistivity which is influenced by several factors like the w/b ratio and binder type.

According to these observations, it can be concluded that a proportional relationship may exist between corrosion currents and electrical resistivity.

## 5.4.Macrocell current versus the cathode/anode ratio: influence of electrical resistivity

To test the effect of electrical resistivity on the effect of the C/A ratio and subsequently on the extent of the mobilizable cathode surface, two anode samples contaminated with 1.82 and 2.52 % of free chlorides per weight of cement were connected to each of the three walls described in section 4.1. A relatively high concentration of chlorides was chosen for this experiment to avoid the anodic corrosion control phenomenon mentioned earlier. The free chloride content of the anode sample was directly measured after the test.

The experimental set up achieved is described earlier (in section 4.3) and consists of the cathode permutation technique where the same anode is connected to different walls with different characteristics, in particular, different electrical resistivity. As an illustration, the wall W15SF-043 (W15SF) and W80S-047 (W80S) have electrical resistivities respectively 8.9 times and 5.7 times higher than that of the wall W1-055 (W1).

Fig. 8 shows the absolute (on the left) and relative (on the right) experimental currents obtained according to the C/A ratios. The relative current is determined, for each C/A ratio, by dividing the measured current with the maximum current obtained which is the current measured when connecting the anode to all the rebars of the wall. This maximum apparent C/A ratio is equal to 2950.

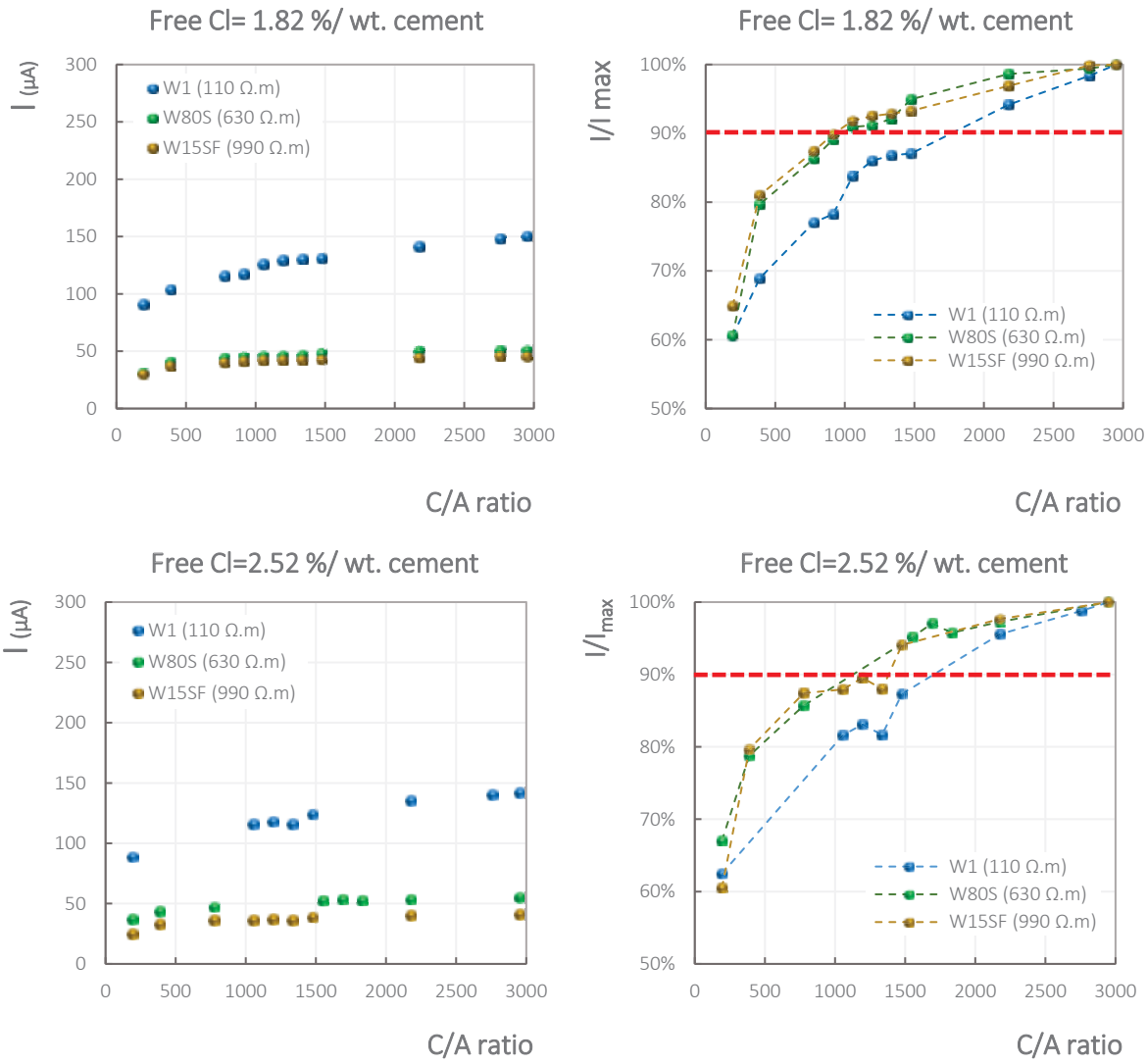


*Fig. 8. Results of the galvanic coupling of anode samples with each of the walls W1, W15SF and W80S (on the left are presented the relative currents and on the right the absolute currents)*

An overall vision of the results indicates that whatever the C/A ratio tested, the corrosion currents decrease when the anode is connected to the walls W15SF and W80S compared to when it is connected to wall W1. Moreover, when increasing the C/A ratio, the macrocell current increases but with a progressive reduction of the increasing rate. This means that there is a limitation of the mobilizable cathodic surface above which the efficiency of cathode becomes negligible.

As a first approach, this mobilizable cathode surface threshold could be defined when the macro-cell current reaches 90% of the maximal value experimentally recorded which means the one obtained for a C/A ratio of 2950. This relative current of 90% versus the maximum current obtained when connecting the anode to all the bars of the wall (C/A ratio= 2950) is indicated with a horizontal red dashed line.

Table 4 summarizes, for each electrical resistivity of the wall, the C/A ratio necessary to reach 90% of the maximum current obtained when connecting the anode to all the bars of the wall. It can be seen that the higher the electrical resistivity of the wall, the lower is the C/A ratio needed to reach 90% of the maximum current. This means that when electrical resistivity increases, the current starts to stabilize for lower C/A which could be linked to an ohmic control of corrosion limiting the mobilizable

cathode surface. Finally, macrocell currents decreased with the increase in electrical resistivity and the results show an asymptotic behavior of current when electrical resistivity is very high.

*Table 4. C/A ratio when $I/I_{max}$ is equal to 90% as a function of electrical resistivity*

| Free chloride content (%/ wt. cement) | Electrical resistivity of the wall (Ω.m) | Critical C/A ratio when $I/I_{max}$ = 90% |
|---|---|---|
| 1.82 | 110 | ≈1770 |
| | 630 | 920 |
| | 990 | 920 |
| 2.52 | 110 | ≈1700 |
| | 630 | 1200 |
| | 990 | 1200 |

## 6. Conclusion

The core of this study is the investigation of the influence of electrical resistivity of concrete and mortar on macrocell corrosion in the case of ''large'' anodes during the corrosion propagation phase. Firstly, an experimental campaign consisted of measuring the electrical resistivity of samples in different chloride contamination levels. The objective was to find a relation between resistivity and free chloride content. A second campaign was realized and consisted of cathode-anode galvanic coupling and measurement of corrosion currents. A cathode permutation technique was adopted to test the impact of parameters at cathode most importantly the electrical resistivity. Additionally, this paper studies the effect of electrical resistivity on the cathode/anode ratio and the mobilizable cathode surface contributing to macrocell current.

From this study, the following main conclusions were drawn:

- The increase in chloride levels in mortar or concrete leads to the decrease of electrical resistivity. A possible intrinsic relationship may exist between free chloride content and electrical resistivity whatever the concrete or mortar formulation in case of saturated conditions. This confirms the importance of ionic activity as a major influencing parameter.

- According to the results, a proportional relationship could exist between macrocell corrosion current and the electrical resistivity.

- The results show the importance of bearing in mind the spatial variability of electrical resistivity in concrete structures. Therefore, there is a need for using numerical simulations to model the corrosion propagation of reinforced concrete structures to take into consideration the spatial variability of several parameters like electrical resistivity.

- When increasing the cathode/anode ratio, the macrocell current increases but with a progressive reduction of the increasing rate. As a result, the effect of cathode decreases with the increase of cathode surface which means that there is a limitation of the mobilizable cathodic surface above which the efficiency of cathode becomes negligible.

- The increase in electrical resistivity leads to the stabilization of corrosion current for lower cathode/anode ratios which could be linked to an ohmic control of corrosion limiting the mobilizable cathode surface.

## Acknowledgment

This work was supported by the ANR MODEVIE project, grant ANR-14-CE22-0018 of the French National Research Agency (ANR) and by the French National Federation of Public Works (FNTP).

## References

[1] A. Molina, C. Andrade, C. Alonso and J.A. González, Tec. Ing. Univ. Zulia, 8 (1985), .
[2] C. Alonso, C. Andrade and J.A. González, *Relation between Resistivity and Corrosion Rate of Reinforcement in Carbonated Mortar Made with Several Cement Types*, Vol. 18, 1988.
[3] W. Lopez and J. Gonzalez, *Influence of the degree of pore saturation on the resistivity of concrete and the corrosion rate of steel reinforcement*, Cement and concrete research 23 (1993), pp. 368–376.
[4] T. Liu and R.W. Weyers, *Modeling the Dynamic Corrosion Process in Chloride Contaminated Concrete Structures*, Vol. 28, 1998.
[5] J. Gulikers, *Theoretical considerations on the supposed linear relationship between concrete resistivity and corrosion rate of steel reinforcement*, Materials and Corrosion 56 (2005), pp. 393–403.
[6] W. Morris, A. Vico and M. Vázquez, *Chloride induced corrosion of reinforcing steel evaluated by concrete resistivity measurements*, Electrochimica Acta 49 (2004), pp. 4447–4453.
[7] W. Morris, A. Vico, M. Vazquez and S. De Sánchez, *Corrosion of reinforcing steel evaluated by means of concrete resistivity measurements*, Corrosion Science 44 (2002), pp. 81–99.
[8] C. Andrade and C. Alonso, *Corrosion rate monitoring in the laboratory and on-site*, Construction and Building Materials 10 (1996), pp. 315–328.
[9] G. Glass, C. Page and N. Short, *Factors affecting the corrosion rate of steel in carbonated mortars*, Corrosion Science 32 (1991), pp. 1283–1294.
[10] R. Polder and L. Bertolini, *Concrete resistivity and reinforcement corrosion rate as a function of temperature and humidity of the environment*, TNO report 97- BT-R0574, TNO Building and Construction Research, Delft, The Netherlands, 1997.
[11] S. Feliu, J. Gonzalez, S. Feliu and C. Andrade, *Relationship between conductivity of concrete and corrosion of reinforcing bars*, British corrosion journal 24 (1989), pp. 195–198.
[12] R. Francois, S. Laurens and F. Deby, *Corrosion and Its Consequences for Reinforced Concrete Structures*, Elsevier, 2018.
[13] *RILEM TC 154-EMC: ELECTROCHEMICAL TECHNIQUES FOR MEASURING METALLIC CORROSION Test methods for on site measurement of resistivity of concrete | Scinapse | Academic search engine for paper*, Scinapse 33 (2000), pp. 603–611.
[14] DuraCrete, *Duracrete, Probabilistic Performance Based Durability Design: Modelling of Degradation*, The Netherlands, 1998.
[15] J. Warkus and M. Raupach, *Modelling of reinforcement corrosion – geometrical effects on macrocell corrosion*, Materials and Corrosion 61 (2009), .
[16] A. Arya and P.R.W. Vassie, *Influence of cathode-to-anode area ratio and separation distance on galvanic corrosion currents of steel in concrete containing chlorides*, Cement and Concrete Research 25 (1995), pp. 989–998.
[17] C. Cao, *3D simulation of localized steel corrosion in chloride contaminated reinforced concrete*, Construction and Building Materials 72 (2014), pp. 434–443.
[18] W. López and J.A. González, *Influence of the Degree of Pore Saturation on the Resistivity of Concrete and the Corrosion Rate of Steel in Concrete*, Vol. 23, 1993.
[19] R. Du Plooy, S. Lopes, G. Villain and X. Dérobert, *Development of a multi-ring resistivity cell and multi-electrode resistivity probe for investigation of cover*, NDT & E International 54 (2013), pp. 27–36.

[20] F. Wenner, *A method of measuring earth resistivity*, Journal of the Washington Academy of Sciences 5 (1915), pp. 561–563.
[21] U.M. Angst and B. Elsener, *On the Applicability of the Wenner Method for Resistivity Measurements of Concrete.*, ACI Materials Journal 111 (2014), .
[22] M.H. Loke, *Electrical imaging surveys for environmental and engineering studies*, A practical guide to 2D and 3D surveys (2001), .
[23] Y. Fargier, *Développement de l'Imagerie de Résistivité Électrique pour la reconnaissance et la surveillance des Ouvrages Hydrauliques en Terre*, Ecole Centrale de Nantes, 2011.
[24] M. Fares, *Evaluation de gradients de teneur en eau et en chlorures par méthodes électromagnétiques non-destructives.*, Université Nantes Angers Le Mans, France., 2015.
[25] J. Badr, Y. Fargier, F. Deby, G. Villain, S. Palma-Lopes, S. Delepine-Lesoille et al., *Design and implementation of embedded sensors based on electrical resistivity to determine water content profiles in thick concrete structures*, .
[26] R. Baessler, J. Mietz, M. Raupach and O. Klinghoffer, Corrosion monitoring sensors for durability assessment of reinforced concrete structures, in Materials Week, 3988 (2000), pp. 32–39.
[27] W. McCarter, T. Chrisp, A. Butler and P. Basheer, *Near–surface sensors for condition monitoring of cover-zone concrete*, Construction and Building Materials 15 (2001), pp. 115–124.
[28] D.F. Rucker, J.B. Fink and M.H. Loke, *Environmental monitoring of leaks using time-lapsed long electrode electrical resistivity*, Journal of Applied Geophysics 74 (2011), pp. 242–254.
[29] S. Millard, Reinforced concrete resistivity measurement techniques, 91 (1991).
[30] A. Nguyen, G. Klysz, F. Deby and J.-P. Balayssac, *Evaluation of water content gradient using a new configuration of linear array four-point probe for electrical resistivity measurement*, Cement and Concrete Composites 83 (2017), pp. 308–322.
[31] O.E. Gjørv, Ø.E. Vennesland and A.H.S. El-Busaidy, Electrical Resistivity Of Concrete In The Oceans, in OTC-2803-MS, 1977, pp. 8.
[32] S. Feliu, C. Andrade, J. González and C. Alonso, *A new method forin-situ measurement of electrical resistivity of reinforced concrete*, Materials and structures 29 (1996), pp. 362–365.
[33] R. Sriravindrarajah and R. Swamy, *Development of a conductivity probe to monitor setting time and moisture movement in concrete*, Cement, Concrete and Aggregates 4 (1982), pp. 73–80.
[34] R.L. Du Plooy, *The development and combination of electromagnetic non-destructive evaluation techniques for the assesment of cover concrete condition prior to corrosion*, Université Nantes Angers Le Mans, 2013.
[35] G. Villain, Z.M. Sbartaï, J.-F. Lataste, V. Garnier, X. Dérobert, O. Abraham et al., Characterization of water gradients in concrete by complementary NDT methods, 2015.
[36] S. Naar, *Evaluation non destructive du béton par mesures de résistivité électrique et thermographie infrarouge passive*, Bordeaux 1, 2006.
[37] K. Hornbostel, C.K. Larsen and M.R. Geiker, *Relationship between concrete resistivity and corrosion rate–a literature review*, Cement and Concrete Composites 39 (2013), pp. 60–72.
[38] M. Saleem, M. Shameem, Er.G. Hussain and M. Maslehuddin, *Effect of moisture, chloride and sulphate contamination on the electrical resistivity of Portland cement concrete*, Construction and Building Materials 10 (1996), pp. 209–214.
[39] C. Larsen, E. Sellevold, F. Askeland, J. Østvik and O. Vennesland, Electrical resistivity of concrete—Part II: influence of moisture content and temperature, 2006.
[40] C. Andrade, C. Alonso, A. Arteaga and P. Tanner, Methodology based on the electrical resistivity for the calculation of reinforcement service life, 2000, pp. 899–915.
[41] M. Fares, G. Villain, S. Bonnet, S.P. Lopes, B. Thauvin and M. Thiery, *Determining chloride content profiles in concrete using an electrical resistivity tomography device*, Cement and Concrete Composites 94 (2018), pp. 315–326.
[42] J. Enevoldsen, C. Hansson and B. Hope, *The influence of internal relative humidity on the rate of corrosion of steel embedded in concrete and mortar*, Cement and concrete research 24 (1994), pp. 1373–1382.

[43] Z. Sbartaï, S. Laurens, J. Rhazi, J. Balayssac and G. Arliguie, *Using radar direct wave for concrete condition assessment: Correlation with electrical resistivity*, Journal of applied geophysics 62 (2007), pp. 361–374.
[44] F. Hunkeler, *The resistivity of pore water solution—a decisive parameter of rebar corrosion and repair methods*, Construction and Building Materials 10 (1996), pp. 381–389.
[45] I.-S. Yoon, *Effect of Water and Chloride Content on Electrical Resistivity in Concrete*, NOT PEER-REVIEWED (2019), .
[46] A. Neville, *Propriétés des Bétons» Editions Eyrolles*, Paris 806 (2000), .
[47] V. Lakshminarayanan, P. Ramesh and S. Rajagopalan, *A new technique for the measurement of the electrical resistivity of concrete*, Magazine of Concrete research 44 (1992), pp. 47–52.
[48] J. Cabrera and P. Ghoddoussi, *Influence of Fly Ash on the Resistivity and Rate of Corrosion of Reinforced Concrete*, Special Publication 145 (1994), pp. 229–244.
[49] B. Hughes, A. Soleit and R. Brierley, *New technique for determining the electrical resistivity of concrete*, Magazine of concrete research 37 (1985), pp. 243–248.
[50] J.-F. Lataste, *Évaluation non destructive de l'état d'endommagement des ouvrages en béton armé par mesures de résistivité électrique*, Bordeaux 1, France. (2002), .
[51] G.E. Monfore, *The electrical resistivity of concrete*, Journal of the PCA Research and Development Laboratories 10 (2019), pp. 35–48.
[52] M. Castellote, C. Andrade and M.C. Alonso, *Standardization, to a reference of 25 C, of electrical resistivity for mortars and concretes in saturated or isolated conditions*, Materials Journal 99 (2002), pp. 119–128.
[53] R.B. Polder, *Test methods for on site measurement of resistivity of concrete—a RILEM TC-154 technical recommendation*, Construction and building materials 15 (2001), pp. 125–131.
[54] C. Chalhoub, R. François and M. Carcasses, *Determination of chloride threshold initiating corrosion: A new set-up taking the localized aspect of corrosion into account*, Cement and Concrete Research 124 (2019), pp. 105825.
[55] U. Angst, B. Elsener, C.K. Larsen and Ø. Vennesland, *Chloride induced reinforcement corrosion: rate limiting step of early pitting corrosion*, Electrochimica Acta 56 (2011), pp. 5877–5889.
[56] K. Hornbostel, U.M. Angst, B. Elsener, C.K. Larsen and M.R. Geiker, *Influence of mortar resistivity on the rate-limiting step of chloride-induced macro-cell corrosion of reinforcing steel*, Corrosion Science 110 (2016), pp. 46–56.
[57] *NF EN 14629 - Produits et systèmes pour la protection et la réparation des structures en béton - Méthodes d'essais - Mesurage du taux de chlorure d'un béton durci*. 2007.
[58] G. Arliguie and H. Hornain, *GranDuBé: grandeurs associées à la durabilité des bétons*, Presses des Ponts, 2007.
[59] Z.M. Sbartaï, *Caractérisation physique des bétons par radar: approche neuromimétique de l'inversion*, Paul Sabatier University (France) and Sherbrooke University (Canada)., 2005.

# Paper VII

## Influence of ground granulated blast furnace slag on macrocell corrosion of steel in reinforced mortar

**Chantal Chalhoub*, Raoul François, Myriam Carcasses**

**To be submitted**

# Influence of ground granulated blast furnace slag on chloride-induced corrosion of steel in reinforced mortar

Chantal Chalhoub*, Raoul François, Myriam Carcasses
LMDC, INSA, UPS, Université de Toulouse, France
* Corresponding author: chantal.chalhoub@insa-toulouse.fr

## Abstract

The core aim of this study is the evaluation of the corrosion behavior of steel embedded in mortars with high levels of slag (80%). The corrosion behavior was assessed using electrochemical measurements consisting of galvanic coupling between anode samples contaminated with chlorides and cathode specimens without any chlorides and polarization tests applied on chloride-free cathode specimens form different formulations and different curing and storing conditions. It was found that steel embedded in mortar with a high substitution level of slag (80%) presented a particular behavior. Highly negative potentials were measured despite the absence of chlorides which was considered as an indication of the absence of dissolved oxygen at the steel/mortar interface. It was assumed that these negative potentials were associated with the reaction of water reduction, while, in the presence of oxygen the reaction is the reduction of oxygen. During the galvanic coupling between highly negative cathodes and chloride contaminated anodes, corrosion currents were, in some cases, negative and then became positive. The change in sign of the measured current was always associated with the increase in the potentials of cathodes to more positive values which was considered as an indication of the oxidation of iron taking place at the cathode. These statements were only assumptions and needed further investigations.

## Keywords

Chloride-induced corrosion; Steel reinforcement; Mortar; Blast furnace slag; Oxygen; Cathodic reaction; Anodic reaction.

## 1. Introduction

In recent years, the emphasis on reducing environmental impact has grown. Hence, the use of mineral additives has increased owing to their different mechanical and chemical enhanced properties compared to ordinary Portland cement and their ecological and economic interests.

Slag is an example of innovative mineral additives used in concrete either in cement production, as a constituent of blended cement replacing clinker or in concrete production as a ground addition, as a mineral admixture partially replacing cement [1,2]. Slag is also used in the production of hydraulic aggregates for roads or as the main constituent of road hydraulic binders [2] and is used in aggregates for concrete, bituminous mixes, ballast, etc [2]. It is known for its low cost and clinker and energy saving which engenders environmental and economic benefits [3].

The contents of slag used in concrete vary from 6% to 95%. The use of high-content cement is usually considered in the context of nuclear waste conditioning. In effect, slag is capable of replacing cement in high percentages owing to its intrinsic cementitious characteristics [4].

Despite several benefits of slag, its incorporation in construction requires the study of its impact on the mechanical behavior of concrete along with its electrochemical behavior and influence on rebar

corrosion. Several studies have inspected the role of slag in the corrosion process of reinforced structures. Most of these studies used simple traditional electrochemical methods developed for plain Portland cement and found that these methods can cause misleading assumptions concerning the corrosion of rebars embedded in slag-containing concretes. The reason behind this different behavior, in presence of slag, could be attributed to different redox reactions that are happening and which are not distinguishable from the real corrosion process of embedded steel using these electrochemical measurements.

The core aim of this study is the evaluation of the corrosion behavior of steel embedded in slag-containing mortars. The corrosion behavior is assessed using electrochemical measurements, along with the extraction of the steel rebars.

In this study, mortars with high slag contents of 80% were inspected. Mortars with 0% and 40% of slag and 10% of silica fume were also tested for comparative purposes. The electrochemical measurement techniques consisted of galvanic coupling between anode samples contaminated with chlorides and cathode specimens without any chlorides. The macrocell current flowing between anode and cathode was monitored for almost 6 days and the amount of chlorides at the anode was also determined. Moreover, the measurement methods included steady-state polarization techniques applied to chloride-free cathode specimens form different formulations and different curing conditions. The experimental polarization curves deduced from this test were fitted to Butler-Volmer models and the electrochemical parameters of steel were determined to allow the investigation and characterization of the electrochemical behavior of steel to identify the different mechanisms governing the equilibrium system.

## 2. Review of the characteristics of slag when used in concrete

This section presents an overview of the different properties and characteristics of slag used in concrete and its role concerning chloride-induced corrosion in concrete structures, according to literature.

### 2.1. Production of blast-furnace slag

Slag is a nonmetallic byproduct of the steel industry left over from the manufacture of iron in a blast furnace, where it corresponds to the sterile gangue of iron ore, isolated from the liquid iron. Molten slag crystallizes if cooling is slow and is essentially amorphous if cooling is faster.

The principle basis of the modern production of slag goes back to practices dating from decades. The first step of the slag production consists of the gradual melting of iron ore, coke, and flux in a blast furnace. Pre-heated air, blown across the ports of the blast furnace, burns the coke and melts iron ore into metallic iron. Then, a chemical reaction occurs between the other mineral products of iron ore and flux to produce molten slag, called blast-furnace slag (BFS), separated from the liquid iron owing to their different densities. The BFS is then treated to the finished products.

### 2.2. Types of slag

There are three main types of slag usually manufactured and are differentiated according to the speed of cooling as follows:

1. Granulated Blast-Furnace Slag: the product is rapidly cooled by immersion in water which is responsible for its glassy granular texture.

2. Expanded Blast-Furnace Slag: the product is obtained by controlled cooling by immersion in water or with other cooling methods like air or by a combination of both.
3. Air Cooled Blast-Furnace Slag: this slag, used as aggregates, is cooled slowly under atmospheric conditions.

It is also possible to differentiate 2 types of slag according to their structure [2] as follows:

- Vitrified slags obtained by sudden cooling, usually with water which gives it a vitreous glassy structure allowing it to develop properties similar to those of cement. Vitrified slags are most often produced in the form of granulated slags because of their physicochemical characteristics.

- Crystallized slag obtained by a slow cooling where crystallization takes place during cooling which transforms it into an artificial and chemically stable hard rock with physical and mechanical characteristics comparable to those of natural materials.

The type of slag suitable for cement production is almost entirely amorphous and corresponds to the first category of each list.

## 2.3. Chemical composition

The chemical composition of slag mainly consists of silica, alumina, lime, and magnesia. Consequently, slag contains less calcium and alkalis ($K^+$,$Na^+$) compared to the composition of a Portland cement.

Nevertheless, the composition varies significantly according to the origin of slag and its production (the composition of flux and ore, coke consumption, type of iron produced) [5]. Even though, the ratio between silica plus alumina constituents and lime plus magnesia slightly varies between different slags [6].

## 2.4. Hydration

When slag is mixed with water, the hydration kinetics are extremely slow and the hydration of slag requires the use of an activator. Indeed, shortly after mixing slag with water, an impermeable layer of aluminosilicate is formed on the surface of anhydrous grains which blocks the hydration reaction [7]. The use of an activator, like Portland cement, NaOH solution, etc., engenders the increase in pH which allows the dissolution of this layer leading to the continuation of the hydration reaction [7]. Slag hydration kinetics decrease with the increase of the substitution level of slag [8].

Since the slag has a chemical composition close to clinker, the main hydration products obtained are similar to those of Portland cement: C-S-H, portlandite, AFm phases, and AFt phases [9–12].

However, slag is generally richer in aluminum, silicon, and magnesium, and lower in calcium [13]. According to some studies, slag has pozzolanic properties and partly consumes portlandite [8,14] (produced during clinker hydration) to bring the missing calcium to the CSH and to have an equal CaO / SiO2 ratio at 1.7. When portlandite is completely consumed, the CaO / SiO2 ratio of C-S-H is likely to decrease, which facilitates the incorporation of aluminum into C-S-H [15]. Other phases such as hydrotalcite [16–19] and strätlingite [20] can also be observed.

During hydration of sulfide-containing cement, like blast furnace slag, the sulfide can be partially oxidized to sulfate during the hardening process [21].

Yet, it has been stated that the blue-green coloration observed in concrete containing slag is caused by the oxidation of hydrated products like siderotilate (FeSO4_5H2O) and rosenite (FeSO4_7H2O) to ferric salts. These products are formed from the hydration of certain iron sulfides present initially in an

amorphous form in the anhydrous slag [22]. This particular coloration depends on the slag content, the curing conditions and the oxidation rate [22]. Chaouche et al [23] attributed this specific coloration found in blast furnace slag-based materials to the presence of polysulfide radical anions.

## 2.5. Microstructure and porosity

The microstructure of cementitious material is characterized by the total porosity, capillary porosity, nanoporosity, degree of connectivity and pore size distribution. The substitution of clinker by slag has a significant effect on the microstructure as follows:

- The slow hydration process of cement with slag mainly causes an overall increase in the total porosity at a given age [9,24–27] which is higher when the slag content is higher [24]. However, for the same degree of hydration, the porosity would be comparable or even greater for slag cement [24]. Nevertheless, whatever the material (with or without slag), the total porosity accessible to water decreases over time, due to the formation of hydrates [24].

- The capillary pore entry size is lower for slag cement than for cement formed with CEMI at a given age [10,28–30]. The capillary porosity accessible to mercury decreases with the addition of slag [24]. According to SEM observations, Daube and Bakker found that the capillary pores in concrete with 60% of GGBFS were lower than 10–50 µm compared to 0.05–60 µm found in OPC specimens. Moreover, the authors stated that pores could be occupied with C–S–H gel [31].

- The critical input diameter of the nanopores and the nanoporous volume increase in the presence of slag which is probably due to the larger amount and lower density of C-S-H phases [24,32–34].

- The refinement of the porosity induces a decrease in the degree of connectivity and an increase in the specific surface area [24,35,36]. Yet, Stephant [24] found, in his work, that the degree of pore connectivity, determined by mercury intrusion porosimetry, evolves only very little over time and as a function of slag content.

## 2.6. Mechanical strength

The partial substitution of cement with slag causes the decrease of mechanical strength at an early age, however, it improves the long term strength of concrete [37].

It seems that, in the case of concrete with high substitution levels of slag, the water penetration into concrete is prevented [3]. In effect, slag reacts with water in alkaline environments and reacts afterward with calcium hydroxide to produce hydration products and more C–S–H gel compared to CEMI concrete which retards the strength progress at an early age [3].

## 2.7. Chloride-ion diffusion coefficient

The diffusion of chloride ion into concrete is an important parameter for durability assessment of reinforced concrete structures.

The chloride-ion diffusion coefficient of concrete significantly decreases in presence of slag [27,38,39], as much as ten times smaller in case of concrete with 60% of GGBFS compared to concrete with pure Portland cement [39]. This result could be explained by the fineness of the porous network in the presence of slag which controls the transfer properties of cementitious materials despite the higher overall porosity [40].

Moreover, the study achieved by Song et al. [38] showed that the resistance to chloride ion penetration is more influenced by the substitution level than the level of fineness of GGBFS.

Another investigation was realized by Polder and De Rooij [33] on six concrete structures aged between 18 and 41 years located along the North Sea coast in The Netherlands. Most of the structures were made with blast furnace slag cement. Polder and De Rooij [33] found that all structures presented a significant chloride ingress with a big scatter within the comparatively small investigated areas.

## 2.8. Oxygen effective diffusion coefficient and permeability

Given the effect of slag on the microstructure and porosity of concrete, the transport properties should also be impacted by its presence in the mixture.

Tuutti et al. [41] have studied the evolution of the diffusion coefficient of oxygen as a function of relative humidity for cement pastes with different w/c ratios and slag contents. They found that, whatever the cement, the effective diffusion coefficient decreases with relative humidity with lower coefficients in the presence of slag [41].

Wong et al. [42] measured the apparent permeability of oxygen, for vacuum dried cement pastes (CEMI and CEMI+60% of slag) at different times and w/c ratios and found that permeability of oxygen decreases with the addition of slag.

The decrease in transport properties like the effective diffusion coefficient and gas permeability in the presence of slag can be explained by the refinement of porosity [24].

## 2.9. Electrical resistivity

As mentioned earlier, the presence of slag in concrete causes the refinement of the pore structure and changes the mineralogy of the hydration products. Consequently, the mobility of ions in pore solution, such as chloride ions, is reduced [43]. This means that in presence of slag the electrical conductivity is reduced (or the electrical resistivity is increased) which could explain, according to some authors [44,45], the inhibition of reinforcement corrosion in slag concrete.

## 2.10. Chloride binding capacity

The partial substitution of ground granulated blast-furnace slag (GGBFS) for ordinary Portland cement (CEM I) increases the chloride binding capacity through the increase in physical and chemical chloride binding [32,46–50].

Some research works indicated that the origin of the increase in the chemical chloride binding capacity is the increase in the aluminate content in concrete [47,48,50].

Also, Slag-blended Portland cement and alkali-activated slag cement produce hydrotalcite as a hydration product formed from the high amount of magnesium contained in slag [51] which improves chemical binding effects [50,52,53] and promote the restriction of chloride ingress.

## 2.11. pH of the interstitial solution

The measured pH In Portland cement is generally between 13 and 13.5 [13,54,55] due to the presence of alkalis. It is reported that the presence of slag reduces the pH of the pore solution [56]. Cheng found that the pH values obtained from concretes decreased with the increase in the substitution level of slag [56]. The reduction of pH could be caused by several reasons:

- The lower alkali content in the slag than in the clinker. As an illustration, Longuet [57] found that the pH is slightly lower in the case of slag cement (80% of slag) than that of Portland cement paste with a pH of 13.1 versus 13.9 in the case of Portland cement. Moreover, Stephant [22] stated the concentration of alkali decreases with the slag content because these elements (potassium and sodium) are mainly present in the clinker.

- The increase in the alkalis adsorption capacity of the C-S-H caused by the reduction of the CaO / SiO2 ratio of these hydrates.
- The higher quantity of capillary water at a given time in slag cement reduces the concentration of alkalis.

The reduction of pH of the interstitial solution because of the addition of slag in concrete seems to have no adverse effect on the resistance to corrosion [3].

# 3. Review of the impact of slag on reinforcement corrosion in concrete

## 3.1. Passive film

Kosalla and Raupach [58] studied polarization states and potential differences in reinforced concrete specimens in case of rebars in a passive state with OPC (CEMI) and blast furnace slag cement (BFSC and CEM III). They found that steel, in presence of slag, presents a strong response to variations in oxygen availability compared to OPC which may indicate that the passive layer formed in presence of slag is different from the one formed in OPC concrete.

Mcphee and Cao [59] stated that the efficiency of the passive film in the presence of slag may be weakened by the reducing agents existing in slag which can react with the iron. This process will inhibit the early development of the passive film on steel in concretes with high slag contents, and may progressively destroy previously formed oxide layers [59]. This means that the steel in slag cement is not protected as well as in OPC [59].

It is difficult to confirm the presence of iron sulfide compounds formed at the steel surface using Raman spectroscopy [60]. Yet, Mundra et al. [61] observed the formation of these iron sulfide compounds with X-ray photoelectron spectroscopy when steel was immersed in the simulated pore solution of alkali-activated slag cement [61].

According to the results obtained by Criado and Provis [60], the mechanisms of passivation of steel in the presence of chloride ions is different between steel embedded in alkali-activated slag mortars and steel in white Portland mortars whit a higher resistance to chloride-induced corrosion of steel provided by slag mortars.

## 3.2. Critical chloride content

While many studies have focused on the corrosion resistance of steels in the presence of slag, few studies have been conducted on the effect of slag on the critical chloride threshold value [62] and the results are unclear and controversial [63–65]. Indeed, some published papers found lower *Ccrit* in case of specimens containing slag in comparison with OPC specimens [66–70], while others reported higher *Ccrit* [68,71–74] or did not find any important impact [75–77].

To sum up, the impact on slag on the critical threshold values is dispersed and the tendencies vary from one study to another.

## 3.3. Redox potential of the interstitial solution of the cement paste

The main difference between the interstitial solution of a Portland cement and that of slag cement is the result of its redox potential, which is neutral or slightly reduced in the case of CEMI [78] and strongly reducing in the presence of slag [24,55,78,79]. Glasser et al. [78] indicated that the potential decrease is caused by the presence of sulfide in the interstitial solution and that the redox potential decrease with the increase in slag content.

As indicated by Stephant [24], the strongly reducing potential is a characterization of sulfur species. Indeed, according to the Pourbaix sulfur diagram [80] shown in Fig. 1, it is possible to identify several species of reduced sulfur ranging from thiosulfate ($S_2O_3^{2-}$) to sulfide ($S^{2-}$).

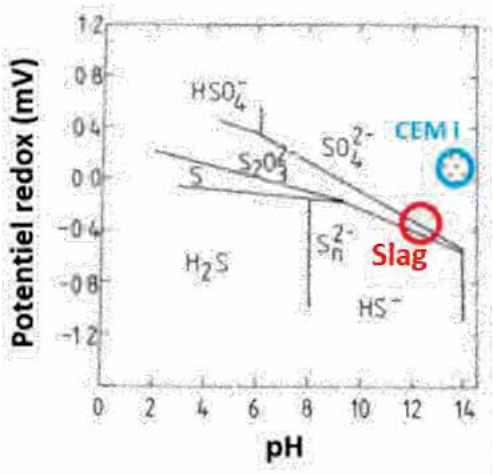


*Fig. 1. Representation of the Pourbaix sulfur diagram representing the majority species as a function of pH and redox potential* [80]
*Taken from* [24]

## 3.4. Sulfur species in slag and their influence

Sulfur in slag is mainly present in the form CaS, FeS, and MnS in a vitreous form with only a very small proportion in crystalline form. Sulfur in slag is mainly present in the form of sulfides (sulfides ion: $S^{2-}$) which can be oxidized to sulfates (sulfates ion: ${SO_4}^{2-}$) [81,82] determining the initial amount of sulfides difficult [83]. Indeed, the concentration of sulfides in the pore solution decreases with the progress of hydration [81].

Moreover, it has been shown that thiosulfate (thiosulfate ion: ${S_2O_3}^{2-}$), resulting from the oxidation of sulfides present in the anhydrous slag during the hydration process, may also be present in the pore solution [82].

There is a complex relationship between pH and oxidation reaction rates of sulfur species. According to some works, the reaction kinetics tend to increase with the increase of the pH (exponential increase between pH 10.5 and 13)[84]. Correspondingly, Roy [81] found that the kinetics of the reaction at pH equal to 13 are too fast to allow the release of sulfides trapped in the amorphous phases making the reaction rate less important at pH 13 than at pH 12.5.

Until now, it is still difficult to quantify the sulfide concentration in solution because of its instability in the presence of oxygen and because of the analytical methods used (ion chromatography, selective electrode, and UV-visible spectrometry) are not always sufficiently selective [24].

The concentration of sulfide in the interstitial solution increases with the slag content [24]. Yet, sulfide concentrations measured in literature do not exceed 10 mmol/L for hydration times greater than 2 years and materials with a slag content between 70 and 75% [24,41,55,85,86].

The presence of sulfur in slag has occasionally raised doubts for researchers dealing with corrosion in concrete [87]. Several studies [27,59,88–90] indicated that the presence of sulfides in slag concretes would influence the electrochemical behavior of steel reinforcement resulting in particular values of free potentials more negative than those measured on concretes with Portland cement despite the absence of aggressive agents. Some studies [91] attribute the negative potential found in the presence of slag to the equilibrium potential of the Fe/FeS redox couple. Other studies [59] suggested that sulfides could be oxidized to sulfates, resulting in a decrease in dissolved oxygen concentration at the steel/concrete interface which could explain the low potentials obtained for concretes with slag. Holloways and Sykes [90] showed that low measured potential values are attributed mainly to the presence of redox couples associated with sulfides and oxygen depletion. Despite very high chloride contents, no trace of corrosion was observed on the

surface of the steels. The assumption is that a larger amount of chlorides is needed to lower the pitting potential below the free potential of steel [90]. Stephant [24] stated that the potential measurements in the solution could only be explained by the sulfate/sulfide oxidation-reduction couple. Indeed, from the Nernst law, the calculated potential is - 592 mV (Ag/AgCl electrode) for CEM III/C cement, which is close to the measured potential [24].

The presence of sulfur or sulfides could be adsorbed, in the absence of oxides, on the surface of the metal, and have several consequences [92]. Indeed, Tromans [93] proposed that sulfides present in the pore water of slag concretes may be combined with the passivation layer (incorporated into magnetite) reducing the potential zone where the passive film is stable which reduces its ability to protect the steel. This result was also observed in the pastes pore solution analysis realized by Scott [66] and the investigation of the potential/pH diagram of sulfides adsorbed on the surface on the iron superimposed on the potential/pH diagram of the Fe-S-$H_2O$ system realized by Marcus [92]. Moreover, MacPhee and Cao [59] stated that the oxygen concentration at the steel/concrete interface could be decreased because of the oxidation of sulfides which would affect the nature of the passive film and explain the strongest passivity currents measured in comparison with the formulation with Portland cement.

Hence, it is possible to assume that the presence of sulfide in cement with slag indicates that the redox potential of the pore solutions will be much lower compared to the potential measured in OPC [60]. Therefore, sulfur must be analyzed carefully concerning electrochemical interactions, since they are redox-sensitive elements [94].

## 3.5. Oxygen availability

The relationship between oxygen availability at the steel/concrete interface and the presence of slag in concrete have been the subject of several studies [27,95].

Valentini et al. [95] measured the ohmic resistance and corrosion potential and corrosion rate using linear polarization resistance of steel bars embedded in mortar samples with different levels of slag (0, 20, 45, and 75% relative to the weight of cement) stored at 50 and 100% relative humidity. They found that samples with slag substitution levels of 20 and 45% had at first very negative potentials that tended to decrease over time particularly when stored at a relative humidity of 50% [95]. Samples with higher replacement levels of slag (75%) had the lowest initial potential that rapidly increased to values similar to those of samples formed without slag. The authors [95] underlined the probable influence of oxygen availability and electrical resistivity on these results.

Garcia et al. [27] measured the free potential in the case of slag concretes and found that it is influenced by the degree of substitution of slag and the age of the specimen. He also measured the linear polarization resistance (Rp) and found that the concrete with 60% of slag exhibits highly negative potential values and significantly higher 1/Rp values despite the absence of a trace of corrosion [27]. The authors also carried out a vacuum saturation of some reference samples made with CEMI in the absence of chlorides. The samples were removed from the desiccator and potential monitoring was realized while the sample was immersed in water and when placed in ambient air [27]. They found that the measured potential decreases very rapidly and stabilizes at very low values around -850mV/SCE. As soon as the sample is out of the water, the value of the potential rises to reach the measured value before saturation under vacuum [27].

Despite these high current values, no trace of corrosion is observed on the surface of the specimens. It could be envisaged that in the case of very low oxygen contents, the corrosion potential is shifted to very negative potential values due to the absence of oxygen [27].

Garcia et al. [27] indicated that it is possible to interpret the obtained results by 2 possibilities:

1. For sufficiently negative potential values the passivation layer is thermodynamically more stable if one refers to the Pourbaix diagram. The measured potential is lower than the potential at which the peak of oxidation associated with the formation of magnetite is observed [96–98]. If it is assumed that the passivation layer is destabilized due to the absence of oxygen, the high current values could then be associated with the $Fe/Fe^{2+}$ couple. Since a disturbance with respect to the equilibrium potential is imposed, no resistance is present to limit the passage of $Fe^{2+}$ ions in solution (even if in fact the corrosion current is very low).
2. The potential at the reinforcement is very close to the equilibrium potential of the $H_2O/H_2$ redox couple. This assumption is also mentioned in another study [91].

## 3.6. Corrosion resistance and corrosion rates

Several studies [32,99–104] reported that the use of cement replacement materials like blast furnace slag contributes to the reduction of the steel corrosion probability in addition to the permeability of concrete.

Some studies [105–107] reported that the effect of slags on corrosion resistance depends on several parameters like the w/b ratio, the type of cement used and the substitution level of slag, however, the impact of this parameter is still unclear and scattered. As an illustration, Baweja [107] found that for w/b ratio of 0.45 and a slag content of 30% presented less corroded areas than Portland cement, while, samples corresponding to a higher w/b ratio of 0.55 presented an opposite result. Also, Yeau and Kim [99] evaluated the corrosion resistance of two types of Portland cements with a slag substitution rate between 0 and 55%. The penetration of chlorides in the material consisted of drying/immersion cycles. The results show that the level of the corroded surface decreased with the increase of slag substitution rate [99]. Jau et al. [108] investigated the durability indicators (such as pore size distribution, permeability, electrical resistance, compressive strength, and concentration of chloride ions) and electrochemical measurements (like corrosion potentials) of slag cement subjected to seawater. They concluded that concretes with slag substitution levels between 20 and 30% represent the concrete with the best corrosion resistance durability parameters [108]. Huang et al. [102] and Arya and Xu [32] found that concrete with GGBS contents of 15% and 30% have high corrosion resistance. Hope and Ip [103] stated that rebar corrosion was lower when the GGBS content increased except during the first 7 days that followed casting.

Song and Saraswathy [3] did an overview of the impact of the presence of slag in concrete. Based on durability considerations, they concluded that replacing cement with 40% of GGBFS does not have any significant influence on corrosion rates of rebar in concrete, while, a substitution level of 60% significantly reduces the corrosion rate [3]. This result was supported by Mangat et al. [109] who found that the electrical resistivity of concrete increases with the slag content and concluded that there is no significant influence on rebar corrosion when cement is replaced with slag with levels up to 40%.

## 3.7. Long term durability of GGBFS concrete

At the Building Research Establishment, the long term performance of concrete with slag was investigated under field and laboratory conditions [110]. The study concluded that concrete with GGBFS contributed to the decrease of the heat evolution and chloride penetration and the increase of the resistance to sulfate attack and alkali-silica reaction and the increase of compressive strength at later ages [110].

Another study reported the concrete properties on the longer time durability [111] and showed that slag cement concrete mostly with high substitution levels of slag (70 and 80%), carbonated considerably compared to concrete with Portland cement of similar mixture proportions when samples were subsequently stored in dry internal environments [111]. On the other hand, when samples were

stored in saturated conditions like water or exposure sites under moist conditions, they showed little or no carbonation [111].

## 3.8. Electrochemical measurements in case of slag-containing mortar/concrete

One of the techniques used to determine corrosion initiation consists of an open circuit potential of the rebars where the criteria for corrosion initiation is a predefined potential drop during a certain time which remains at its level or lower for a minimum duration. Lots of studies used or developed such protocols to detect corrosion initiation [112–115], for instance, the protocol developed by the RILEM technical committee (TC) 235-CTC [116].

However, several studies reported that this simple electrochemical measurement cannot be applied in the case where the potential is very negative, such as in slag cement or other binders containing sulfide [27,117,118]. Moreover, the measurement of corrosion current density using the polarisation resistance technique, despite its several limitations when used in case of concretes with OPC, is also inapplicable and ineffective in cases of slag-containing matrices. Indeed, the measured current densities for the slag containing mortars were high, which is usually considered as an indication of a high risk of corrosion, yet, the extracted rebars did not show any sign of corrosion [60]. Criado and Provis [60] stated that this clear mismatch between actual observations of minimal corrosion on rebars and the results of electrochemical measurements is an indication that these high corrosion currents observed are not automatically generated by a corrosion process but could be the result of the oxidation of sulfides present in the slag (i.e., aqueous-phase related to the chemical reactions in the pore solution concerning sulfide species). As mentioned previously, the presence of sulfide anions can considerably reduce the redox potential of the pore solution around the steel. Hence, sulfide could react with iron and produce iron sulfides which passivate the steel surface and delays the corrosion process [94]. Hence, there is a need to further inspect the Tafel constants usually used for binders with Portland cement and determine if they are usable for slag-rich and/or alkali-activated cement [60].

This means that it is necessary to reevaluate some of the established electrochemical assessment of corrosion and criteria used to evaluate the corrosion probability when studying untraditional cement like the ones rich in redox-active elements like sulfide in blast furnace slag [94].

# 4. Experimental

## 4.1. Raw materials and their characterization

In this paper, four mortar formulations were used and their composition is presented in Table 1. These formulations were formed with the same type of cement CEMI 52.5R but were made with different substitution levels of slag 0%, 40%, and 80% and are called M1-055, M40S-055 and M80S-047 respectively. A commercial powdered blast furnace slag supplied by ECOCEM, France was used. A formulation with 10% of silica fume annotated M10SF-043 was also used for comparative purposes.

The w/b ratio of the formulations M1-055 and M40S-055 is equal to 0.55. For the substitution level of 80% of slag, two mixes were proposed with the same proportions but with different w/b ratios of 0.55 and 0.47. However, the formulation with the highest w/b ratio suffered from segregation and presented poor durability parameters. As a result, it was chosen to use the formulation with a lower w/b ratio of 0.47 to pursue the experimental campaign. Table 1 also shows the mass percentage of binder calculated by dividing the weight of binder with the calculated theoretical density. It also shows the theoretical content of sulfides present in binders according to the technical sheets of the materials used. Knowing that these values are not the result of any experimental measurements they are only considered here as indicative values showing that the amount of sulfide increases with the increase of the slag content in the formulation.

*Table 1. Composition of mortar formulations used*

| | Quantity (kg/m$^3$ of mortar) | | | |
|---|---|---|---|---|
| | **M1-055** "M1" | **M10SF-043** "M10SF" | **M40S-055** "M40S" | **M80S-047** "M80S" |
| **Sand** 0-4mm RL | 1408 | 1457 | 1408 | 1408 |
| **Binder** | 512 | 530 | 512 | 512 |
| **CEMI** 52.5 R | 512 | 477 | 307 | 102 |
| **Silica fume** (CONDENSIL S95 DM) | 0 | 53 | 0 | 0 |
| **Plasticizer** (CHRYSO®Fluid Optima 175) | 0 | 3.18 | 0 | 0 |
| **Granulated ground blast-furnace slag** (ECOCEM) | 0 | 0 | 205 | 410 |
| **Effective water** | 281.4 | 225.25 | 281.4 | 240.5 |
| **Theoretical density** | 2223 | 2232 | 2220 | 2179 |
| **Sand/Binder** | 2.75 | 2.75 | 2.75 | 2.75 |
| **Water/Binder** | 0.55 | 0.43 | 0.55 | 0.47 |
| **Mass percentage of binder** (%) | 23.03 | 23.75 | 23.04 | 23.48 |
| **Theoretical sulfide content in the binder** (%) | 0.01 | 0.02 | 0.33 | 0.64 |
| **Paste volume** (L) | 467 | 425 | 471 | 436 |

Table 2 shows the durability properties of the 4 mortar formulations presented earlier that were measured at 90 days except for the pH of the extracted interstitial solution that was measured after 90 days. The results presented consist of the average value (Avg) measured on 3 different non-reinforced reference samples except for the electrical resistivity of the formulation M1-055 was the measurement was only realized on 2 samples. The Standard deviation (SD) of the measured values is also presented in this table. No pH value was measured, in the case of M10SF-043, because it was not possible to extract the interstitial solution from the samples even after using very high pressure.

*Table 2. Properties of mortar formulations used*

| | M1-055 | | M10SF-043 | | M40S-055 | | M80S-047 | |
|---|---|---|---|---|---|---|---|---|
| **Characterization tests at 90 days** | **Avg** | **SD** | **Avg** | **SD** | **Avg** | **SD** | **Avg** | **SD** |
| **Electrical resistivity** (Ω.m) (RILEM TC-154 EMC [119]) | 128 | 8 | 737 | 48 | 148 | 15 | 395 | 24 |
| **Water porosity** (%) (AFREM [120]) | 21.0 | 0.15 | 15.0 | 0.32 | 19.7 | 0.47 | 23.6 | 0.63 |
| **Chloride migration coefficient** ($10^{-12}$ $m^2/s$) (NtBuild 492) | 16.73 | 0.52 | ---* | --- | 4.79 | 0.72 | 3.45 | 0.69 |
| **Compressive strength** (MPa) (NF EN 196-1) | 75.37 | 1.82 | ---* | --- | 71.88 | 1.02 | 51.34 | 2.73 |
| **pH of interstitial solution** (≥90 d) | 13.04 (21.9 °C) (767j) | --- | --- | --- | 13.05 (22.3 °C) (362 j) | --- | 13.04 (21.7 °C) (334 j) | --- |

*Tests only realized at 28 days

According to Table 2, it can be seen that a higher porosity and lower migration coefficient are found when adding slag to the mixture. This is due to the refinement of the porous network which causes a reduction in the degree of connectivity and an increase in the specific surface area [36,121]. According to [24], this variation seems to be directly related to the content and microstructure of C-S-H.

The compressive strength for the formulations with 80% of slag is lower than that of CEMI+40S at 90 days. This can be explained by a delay in hydration due to the higher substitution level of slag. CEMI and CEMI+40S have similar strengths at 90 days which can be explained by a similar hydration level at this maturity age.

The pH of the interstitial solution was also measured at maturity ages higher than 90 days mentioned in Table 2. The extraction of the interstitial solutions was carried on one reference sample per formulation taken from the wet curing room. The formulations M1-055, M40S-055, and M80S-047 with different slag contents had the same pH.

## 4.2. Description of test specimens

Two types of cylindrical mortar samples were realized: cathode sample (ϕ110 x 220 mm) which are chloride-free and anode samples (ϕ33 x 70 mm) which are polluted with different levels of chlorides through a test procedure detailed in a previous work [122] which consisted in drying the samples to constant weight defined by a predetermined weight loss criteria then soaking them for a duration of 48 h in several concentrations of sodium chloride solutions. Each cathode sample embeds, at its center, a ϕ6 x 160 mm Fe-500 ribbed steel bar, while, each anode sample contains, at its center, a ϕ6 x 10 mm steel bar. Steel bars were tin welded to electrical wires on the upper and lower parts of the rebar to ensure an electrical connection needed to realize the electrochemical measurements.

In this paper, the results corresponding to M80S-047 samples will only be presented. M1-055, M10SF-043, and M40S-055 cathode samples were only used for comparative purposes. Formworks of M1-055, M10SF-043, and M40S-055 samples were removed 24 h after casting while formworks of M80S-047 samples were removed 5 days after. After casting, the M80S-047 anode samples were wet cured for 90 days then moved to the oven to start the drying process.

On the other hand, the cathode samples were cured and stored in two different conditions: some of them were wet cured in a curing room with relative humidity (RH) of 95% and the rest were immersed in water directly after removing their formwork. This continual total immersion in water was chosen in the attempt to prevent oxygen from diffusing into the samples. The duration of curing before electrochemical experiments was at least 90 days. The number of cathodes stored in each of these conditions according to the different formulations is presented in Table 3.

Also, since cathode samples were not contaminated with chlorides and since they were kept in a very humid environment, it is possible to say that cathode specimens are protected from corrosion induced by chlorides and carbonation.

Since no cathodes from the formulation M1-055 were immersed after demolding, it was proposed to use an electrochemical set up as a fast method in the attempt to eliminate oxygen. Thus, a previously tested cathode M1-1 was selected for this experiment. The setup is similar to the polarization test presented earlier in part 4.3.3, yet, it only consists in polarizing the specimen cathodically with a potential drop of $400\ mV$ for a duration of $90\ h$. The polarization test was achieved twice on this cathode: one test was realized after the end of wet curing and the second one after its cathodic polarization.

*Table 3. Number of cathode samples for the different storing conditions and mortar formulations*

| | Number of cathode samples according to storing and curing conditions | |
|---|---|---|
| Formulation | Aerated conditions<br>Wet curing room<br>(RH≈ 95%) | Immersed in water<br>(annotated "IMM") |
| M1-055 | 6<br>(one cathode was polarized) | --- |
| M10SF-043 | 5 | 1 |
| M40S-055 | 5 | 1 |
| M80S-047 | 7 | 1 |

## 4.3. Methods

### 4.3.1. Measurement of macrocell currents between anode and cathode samples

The anode and cathode samples were placed in an alkaline sodium hydroxide solution and were electrically connected to a BioLogic SP-50 galvanostat-potentiostat. The macrocell current flowing between both samples was measured with an SP-50 ZRA function. The monitoring was realized under a constant temperature of 20 °C and was maintained for a duration of 160 h approximatively and the acquisition frequency was 1 Hz. The anode is connected to the terminal WE of the potentiostat and the cathode to the terminal CE.

Fig. 2 shows a schematic illustration of the connection achieved for the anode-cathode galvanic coupling tests showing the flow of electrons from the anode to the cathode when the measured current is positive. Conversely, Fig. 3 shows a schematic illustration of the connection achieved for the anode-cathode galvanic coupling tests showing the flow of electrons from the cathode to the anode when the measured current is negative.

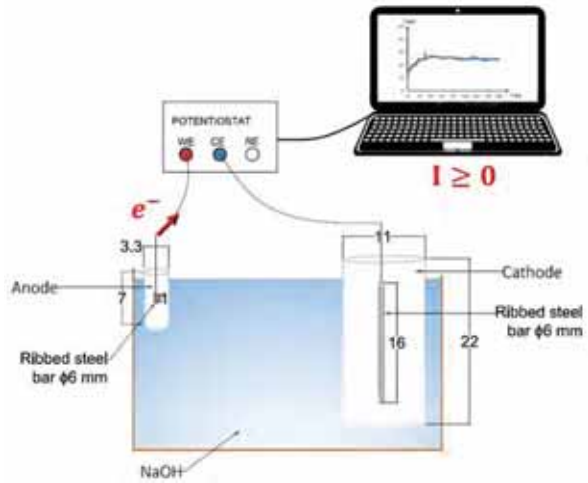


*Fig. 2. Schematic illustration of macrocell current monitoring when the current is positive*

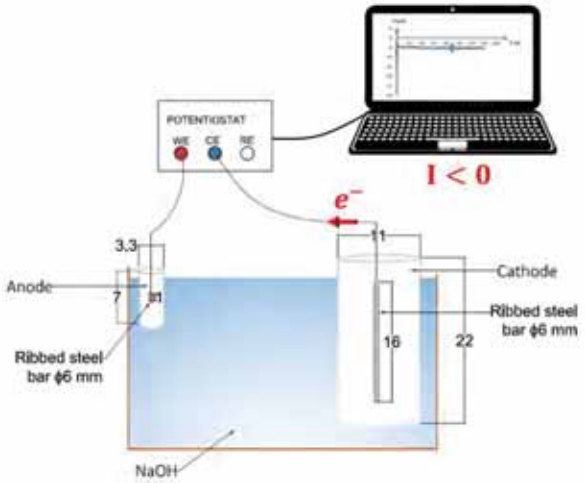


*Fig. 3. Schematic illustration of macrocell current monitoring when the current is negative*

The potential of anode and cathode samples were measured before the electrical connection of both samples and after the coupling test after disconnecting the samples and waiting at least one hour for depolarization. Potential measurements were realized with a silver chloride reference electrode Ag-AgCl-KCl sat annotated “ref” which was placed in the NaOH solution on the surface of the samples.

### 4.3.2. Measurement of chloride content

After the end of electrochemical tests, the anode samples were split in the middle, and mortar was collected from a predefined sampling area around the rebar. This powder was used to measure the total chloride content according to standard NF-EN-14629. The volumetric examination was performed using a titrator coupled with Ti amo software by precipitation with a silver nitrate solution.

Knowing that free chlorides mostly contribute to rebar corrosion, it was important to determine the relationship between total and free chlorides. This was realized by soaking 6 anodes reference samples in saline solutions and one in demineralized water for 48 h without their electrical connection with a cathode (therefore avoiding possible chloride accumulation generated by the potential gradient resulting from the coupling test). Afterward, Total and free chlorides were measured on these samples according to standard NF-EN-14629 and the GranDuBé method, respectively. Given that total chlorides

are the sum of bound and free chlorides, it is possible to model the shift from total to free chlorides could using empirical Freundlich adsorption isotherm equations as follows:

$$Bound\ Cl = \alpha\ Free\ Cl^{\delta} \qquad \text{Eq. 1}$$

where:
- $Bound\ Cl$ is the amount of bound chlorides in the solid phase in (%/wt. binder);
- $Free\ Cl$ is the quantity of free chlorides in the pore solution in (%/wt. binder);
- $\alpha$ and $\delta$ are empirical coefficients.

Fig. 4 shows the experimental results of the 7 reference samples (point in black) and the corresponding empirical relationship found between bound and free chlorides (curve in red). The initial total and free chlorides measured when soaking the sample with water were 0.04% and 0.03% per weight of the binder. The empirical coefficients obtained by fitting the Freundlich equation with the experimental results are $\alpha = 0.09$ and $\delta = 0.63$ with a correlation coefficient of $0.91$.

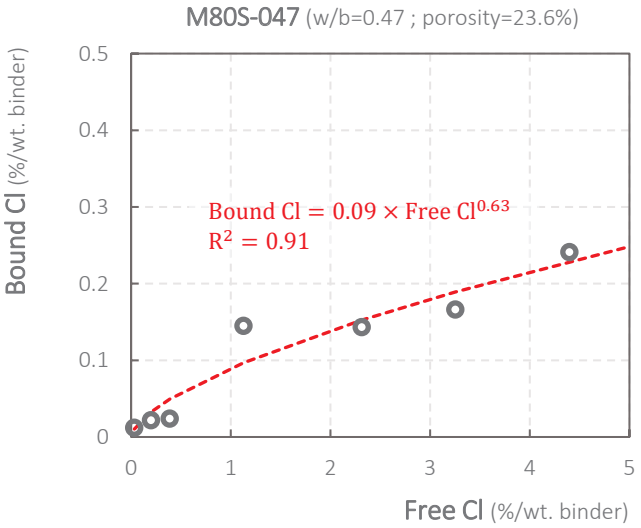


*Fig. 4. Chloride-binding isotherm and corresponding Freundlich equation for the fixation of chlorides after 48 h of soaking in saline solution in case of the formulation M80S-047*

### 4.3.3. Polarization tests on cathode samples

The polarization tests on cathode samples are an important measurement that could allow understanding the electrochemical behavior of chloride-free cathode samples. The polarization tests were achieved on cathode samples from the 4 mortar formulations which were stored under different conditions (curing room and completely submerged).

To realize a real-steady state measurement, a reversible potentiostatic step protocol developed by Laurens et al [123] was applied to obtain the polarization curves. The experimental set up was realized using a BioLogic SP-50 potentiostat and an Ag-AgCl-KCl sat reference electrode. The polarization cycle is programmed in the software and consists of applying potential increments and drops of 10, 20, 40, and then 3 steps of 80 mV with respect to the Open Circuit Potential (OCP). This means that the explored polarization range was $\pm\ 310\ \mathrm{mV}$ according to the free potential. For each potential step, a waiting period of $360\ s$ and an acquisition frequency of $1\ \mathrm{Hz}$ were selected.

It is possible to model the polarization behavior of a uniform corrosion system using the Butler-Volmer equation (Eq. 2) derived by John Alfred Valentine Butler, Max Volmer, and Tibor Erdey Grúz.

This equation describes the relationship between the potential $E$ of the system under polarization and the corresponding net current density $i$ created at the steel/electrolyte interface.

$$i = i_{corr}\left(\exp\left(\frac{\mathrm{Log}(10)}{\beta_a}(E - E_{corr})\right) - \exp\left(-\frac{\mathrm{Log}(10)}{\beta_c}(E - E_{corr})\right)\right) \quad \text{Eq. 2}$$

Where:

- $i$ is the net current density produced by the uniform corrosion system at the steel-electrolyte interface (A/m$^2$);
- $E$ is the potential of the uniform corrosion system under polarization (V/ref);
- $i_{corr}$ is the corrosion current density (A/m$^2$);
- $E_{corr}$ is the potential of the uniform corrosion system at equilibrium (V/ref);
- $\beta_a = \beta_{a,Red}$ is the anodic Tafel slope of the electrochemical system, expressing the oxidation reaction of the reducing agent (V/dec);
- $\beta_c = \beta_{c,Ox}$ is the cathodic Tafel slope of the electrochemical system, expressing the reduction reaction of the oxidant agent (V/dec).

In case of passive steel and when the flow of oxygen at the steel/concrete interface is considered unlimited, the reducing agent is the steel $Fe$ which undergoes oxidation while the oxidant agent is dissolved oxygen $O_2$ at the steel/concrete interface which undertakes the reduction reaction. However, in the absence of oxygen or the presence of other redox couples, other reactions may occur, therefore, other redox couples must be considered and investigated.

Since the cathode samples are chloride-free, it is possible to assume that the steel under investigation is entirely in a passive state. Thus, the characterization of the behavior of passive steel can be directly determined from the experimental polarization test by fitting a Butler-Volmer model on the experimental polarization curve. The anodic and cathodic Tafel slopes $\beta_a$ and $\beta_c$ were extracted graphically from the well-defined anodic and cathodic branches of the experimental polarization curve.

# 5. Results

## 5.1. Results of galvanic coupling between M80S cathode and M80S anode

This section presents the results of the monitoring of the macrocell corrosion current $\mathrm{I}$ over the test duration $\mathrm{t}$ of 10 coupling experiments obtained from 10 different anode specimens connected to the cathode samples from the formulation M80S-047 which were all stored and cured in aerated conditions.

The results obtained from the anode-cathode galvanic coupling tests realized with this formulation with high levels of slag showed an atypical behavior when compared to results from slag-free formulations or formulations with lower slag content. In the absence of slag or in case of a low slag content, the macrocell current measured between anode and cathode became constant after a few hours of measurements and was positive during the monitoring. On the other hand, in the case of the formulation M80S-047, the results of the macrocell current monitoring mainly do not represent a steady-state condition since corrosion currents, in most cases, were not stable.

The results of the macrocell current monitoring can be categorized into 3 different cases according to the sign of the measured current during the monitoring duration as follows:

CASE 1:

This case gathers the results where the measured macrocell currents were constantly positive $(I \geq 0)$ during the test, as shown in Fig. 5. According to the anode-cathode connection presented in part 4.3.1, a positive current means that the electrons are provided by the oxidation reaction at the anode and received by the cathode where the reduction reaction takes place.

The potentials of anode and cathode specimens measured before and after the test were also indicated. It can be seen that the potentials of the cathode samples before the test were between $-84$ and $-160\ \mathrm{mV/ref}$ which usually indicates steel in a passive state and in aerated conditions. After the galvanic coupling test, the potentials of the cathodes became slightly more negative between $-159$ and $-255\ \mathrm{mV/ref}$. The potentials of cathodes stayed mainly the same, yet slightly more negative. The corroded area was only measured on the anode 1 (from test 1) under microscopic observation and it was found equal to 8% of the total anode surface.

CASE 2:

This case gathers the results where the measured macrocell currents were constantly negative $(I < 0)$ during the test, as shown in Fig. 8. According to the anode-cathode connection, a negative macrocell current indicates that the electrons are provided by the oxidation reaction at the cathode and received by the anode when the reduction reaction happens.

In this case, the potentials of the cathodes before the test were between $-935$ and $-435\ \mathrm{mV/ref}$. The potentials of the cathode samples became more positive after the test but were lower than $-266\ \mathrm{mV/ref}$, mainly around $-400\ \mathrm{mV/ref}$. No corrosion was detected on all the rebars of these anode samples which were analyzed under microscopic observation. This is a confirmation that the measured current is linked to a reduction reaction at the anode. Nevertheless, no corrosion was observed on the cathode specimen, which means that the oxidation process at the cathode does not correspond to the oxidation of iron.

CASE 3:

This case gathers the results where the measured macrocell currents were negative at the beginning and then became positives after a certain period of time $(I < 0\ then\ I > 0\ )$, as shown in Fig. 7. The potentials of the cathode before the coupling test were between $-989$ and $-451\ \mathrm{mV/ref}$ and became more positive after the test; between $-338$ and $-172\ \mathrm{mV/ref}$. This case means that after a reduction phenomenon at the anode, the electrochemical process turns into the oxidation of iron at the anode.

CASE 1 $(I \geq 0)$

TEST 1

Cl at anode = 1.33 (%/ wt. binder)

$E_{anode}$ = -129 mV/ref → -490 mV/ref

$E_{cathode}$ = -160 mV/ref → -255 mV/ref

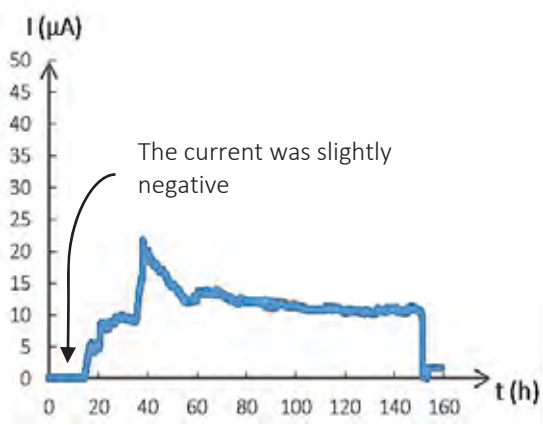


TEST 2

Cl at anode = 1.42 (%/ wt. binder)

$E_{anode}$ = -387 mV/ref → -410 mV/ref

$E_{cathode}$ = -84 mV/ref → -235 mV/ref

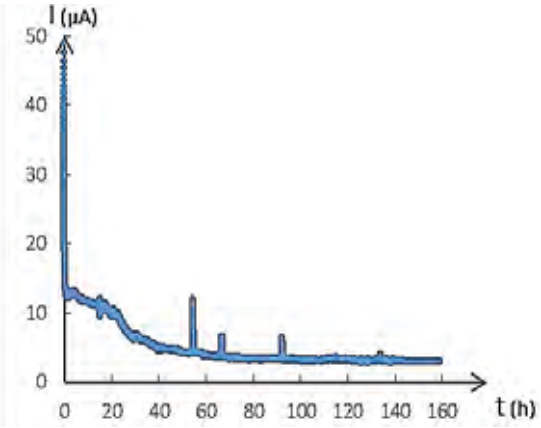


TEST 3

Cl at anode = 2.76 (%/ wt. binder)

$E_{anode}$ = -475 mV/ref → -610 mV/ref

$E_{cathode}$ = -147 mV/ref → -159 mV/ref

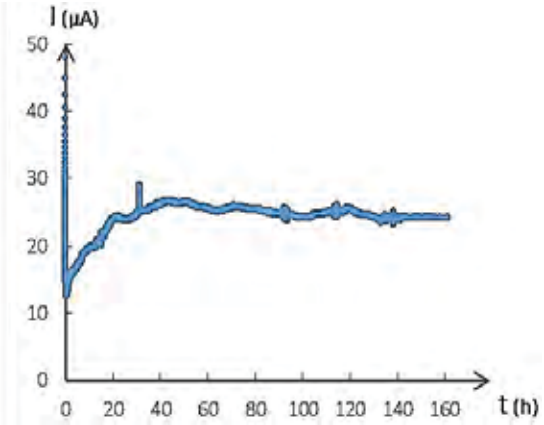


*Fig. 5. Results of macrocell corrosion currents of M80S-047 anode-cathode coupling, Case 1*

CASE 2 $(I < 0)$

TEST 4

Cl at anode = 0.56 (%/ wt. binder)

$E_{anode}$ = -136 mV/ref → NM*

$E_{cathode}$ = -522 mV/ref → NM

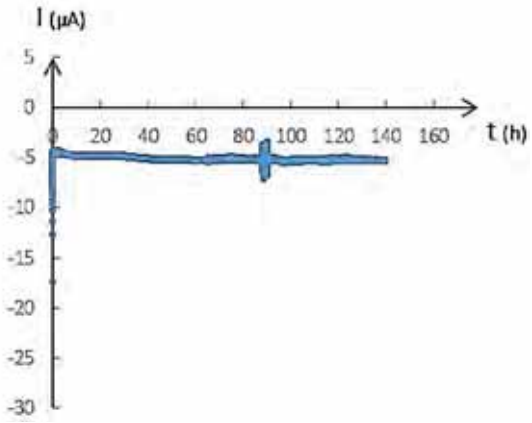


TEST 5

Cl at anode = 0.71 (%/ wt. binder)

$E_{anode}$ = -115 mV/ref → NM

$E_{cathode}$ = -435 mV/ref → -266 mV/ref

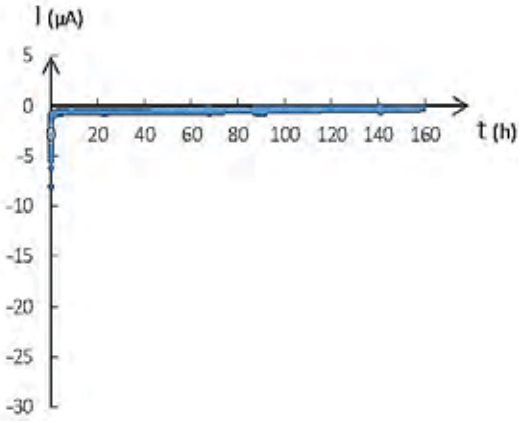


TEST 6

Cl at anode = 1.19 (%/ wt. binder)

$E_{anode}$ = -438 mV/ref → NM

$E_{cathode}$ = -700 mV/ref → -420 mV/ref

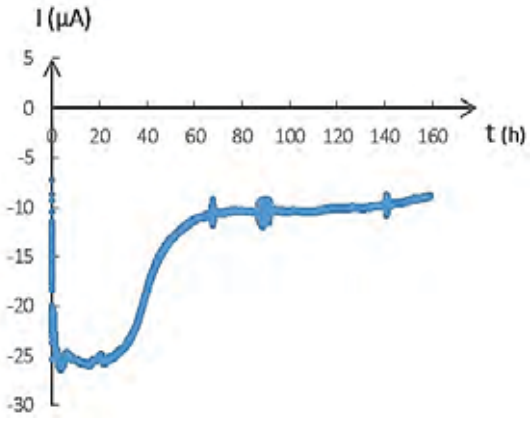


TEST 7

Cl at anode = 1.31 (%/ wt. binder)

$E_{anode}$ = -423 mV/ref → NM

$E_{cathode}$ = -935 mV/ref → -465 mV/ref

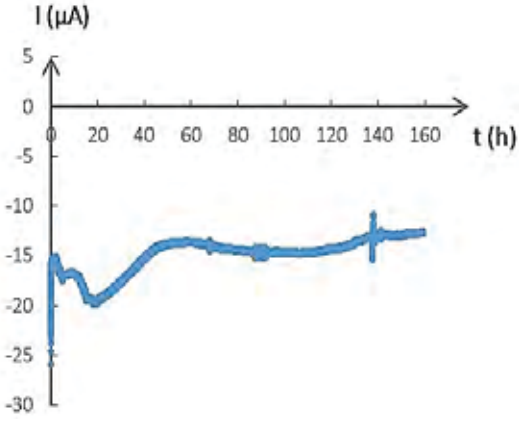


*Fig. 6. Results of macrocell corrosion currents of M80S-047 anode-cathode coupling, Case 2*

**NM means not measured*

CASE 3 $(I < 0 \; then \; I > 0)$

TEST 8

Cl at anode = 0.66 (%/ wt. binder)

$E_{anode}$ = -118 mV/ref → -404 mV/ref

$E_{cathode}$ = -989 mV/ref → -186 mV/ref

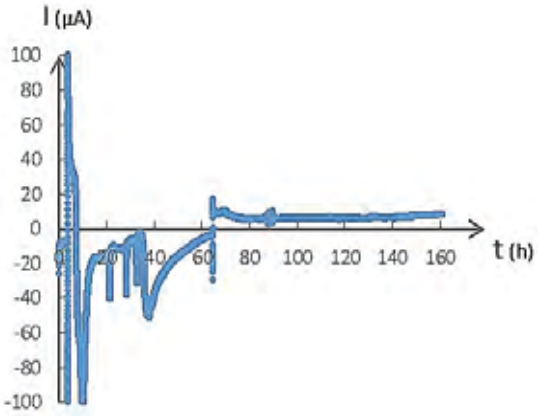


TEST 9

Cl at anode = 0.94 (%/ wt. binder)

$E_{anode}$ = -357 mV/ref → -455 mV/ref

$E_{cathode}$ = -940 mV/ref → -172 mV/ref

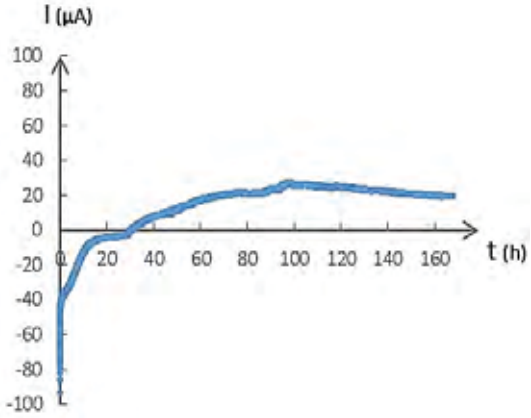


TEST 10

Cl at anode = 3.81 (%/ wt. binder)

$E_{anode}$ = NM → -576 mV/ref

$E_{cathode}$ = -451 mV/ref → -338 mV/ref

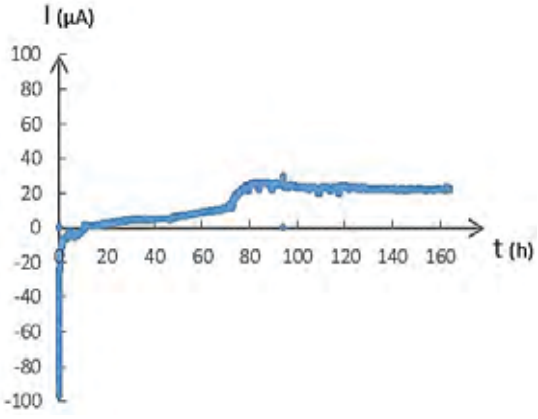


*Fig. 7. Results of macrocell corrosion currents of M80S-047 anode-cathode coupling, Case 3*

The results presented above were summarized in Table 4. In each case, the obtained results were interpreted as follows:

CASE 1:

Given the positive current measured and the potentials of cathodes before and after the tests, it is possible to assume that the oxidation reaction takes place at the anode (Eq. 3) where the reducing agent is iron $Fe$ and the reduction reaction is that of dissolved oxygen at the cathode (Eq. 4) with $O_2$ being the oxidant agent.

$$Fe \rightarrow Fe^{2+} + 2\,e^{-} \qquad \textit{Eq. 3}$$

$$\frac{1}{2}\,O_2 + H_2O + 2\,e^{-} \rightarrow 2\,OH^{-} \qquad \textit{Eq. 4}$$

The observations reported in this case were similar to those obtained from the galvanic coupling test on formulations without slag (like M1-055 and M10SF-043) or with lower slag contents [Paper III].

CASE 2:

Given the negative current measured and the highly negative potentials of cathodes which became more positive after the tests, it is possible to assume that the oxidation reaction takes place at the cathode and the reduction reaction takes place at the anode. The reduction reaction at the anode must be that of dissolved oxygen (Eq. 4) with $O_2$ being the oxidant agent. The oxidation reaction at the cathode is unknown. Yet, it is possible to assume that reactions at the cathode could be the oxidation of iron with a significant polarization for a weak current and therefore a rapid reduction of the galvanic current. Indeed at such low potential, the passive layer has disappeared but the anodic polarization of cathode led to both the increase of the potential of the cathode and the reformation of the passive layer.

The highly negative potentials are usually an indication of a high risk of corrosion as stated in ASTM [124]. However, in the case of our study, the highly negative potentials measured on lots of cathode samples do not indicate chloride-induced corrosion, since cathode samples were not contaminated with chlorides. These very negative potentials in concretes or mortars containing slag were also found in other studies in the literature [27,60,94].

CASE 3:

In this case, when the macrocell current was negative, the oxidation reaction was at the cathode and the reduction reaction was that of oxygen at the anode. As mentioned earlier, it is possible to assume that the oxidation reaction at the cathode is the oxidation of iron with a significant polarization for a weak current and therefore a rapid reduction of the galvanic current with a possible inversion but which also gives weak kinetics because of limited oxygen access. As mentioned for CASE 2, the anodic polarization of cathode lead to the reformation of the passive layer, then the cathode could act again as a real cathode. Then the measured current changed the sign from negative to positive, the oxidation reaction changed from being at the cathode to being at the anode and the potential of the cathode became more positive. The oxidation reaction at the anode corresponds to the oxidation of iron $Fe$ (Eq. 3).

A possible explanation why, in case 2, the current stayed negative during the test may be attributed to an insufficient connection time needed to reform the passive layer such as the potential of the cathode to become higher than that of the anode. Probably, a longer time would lead to obtaining the inversion of current, even if the lack of oxygen would lead to a very limited galvanic current.

*Table 4. Description and interpretation of the results obtained from M80S anode-cathode coupling tests*

| Case | Test | Description | Possible interpretation |
|---|---|---|---|
| 1 | 1<br>2<br>3 | $I \geq 0$<br>Before connection:<br>$E_{cathode} > E_{anode}$<br>After connection:<br>$E_{cathode} > E_{anode}$<br>$E_{cathode}$ slightly decreases | At anode:<br>Oxidation of iron<br>At cathode<br>Reduction of oxygen |
| 2 | 4<br>5<br>6<br>7 | $I < 0$<br>Before connection:<br>$E_{cathode} < E_{anode}$<br>After connection:<br>$E_{cathode}$ increases | At anode:<br>Reduction of oxygen<br>At cathode<br>Oxidation of iron and progressive reformation of the passive layer due to the increase of the potential at the cathode |
| 3 | 8<br>9<br>10 | $I < 0$ *then* $I > 0$<br>Before connection:<br>$E_{cathode} < E_{anode}$<br>After connection:<br>$E_{cathode} > E_{anode}$<br>$E_{cathode}$ increases | At anode:<br>Reduction of oxygen → Oxidation of iron<br>At cathode<br>Oxidation of iron and reformation of the passive layer due to the increase of the potential at the cathode, then reduction of oxygen (which could be released by aging in the redox process of sulfides) |

## 5.2. Results of galvanic coupling between M1 cathode and M80S anode

Additional experiments were realized by connecting 2 M80S anodes with 2 cathodes from the M1-055 formulation. These M80S anodes were connected previously to M80S cathodes in tests 9 and 10 (case 3 in part 5.1) and the macrocell currents during the test were negative at the beginning and then became positive. The corrosion monitoring between these anodes and M1 cathodes was maintained for 1600 h and the potentials of the cathodes were also measured before and after the test.

Fig. 8 presents the monitoring of macrocell currents obtained from both tests showing that the currents were positive during the entire test duration. The potentials of M1-055 cathode specimens were around $-100\ \mathrm{mV/ref}$ and remained constant before and after the test.

In this case, the oxidation reaction takes place at the anode and corresponds to the oxidation of iron (Eq. 3) and the reduction reaction is that of dissolved oxygen at the cathode (Eq. 4). Such behavior is similar to the one reported in case 1. The current measured during test A decreased with time, whereas, the current measured during the test B was mainly in a steady state.

TEST A

M80S Anode (Test 9) with M1 cathode

$E_{cathode}$ = -105 mV/ref → -110 mV/ref

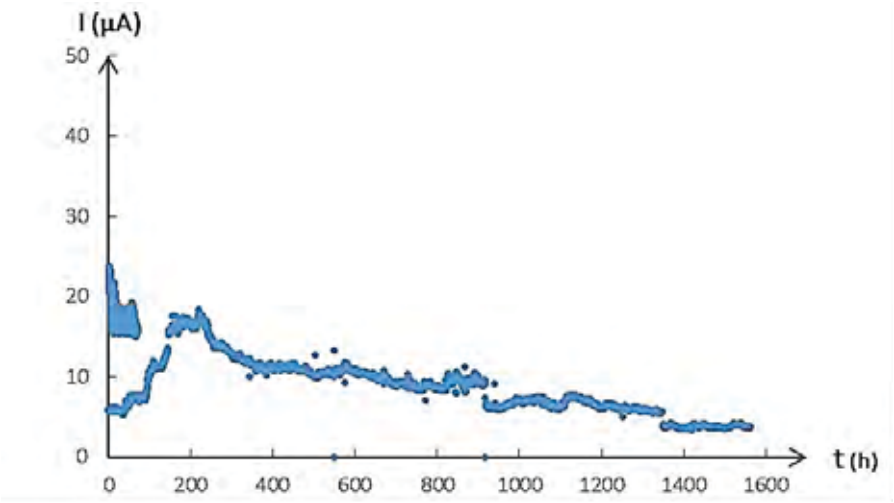


TEST B

M80S Anode (Test 10) with M1 cathode

$E_{cathode}$ = -112 mV/ref → -122 mV/ref

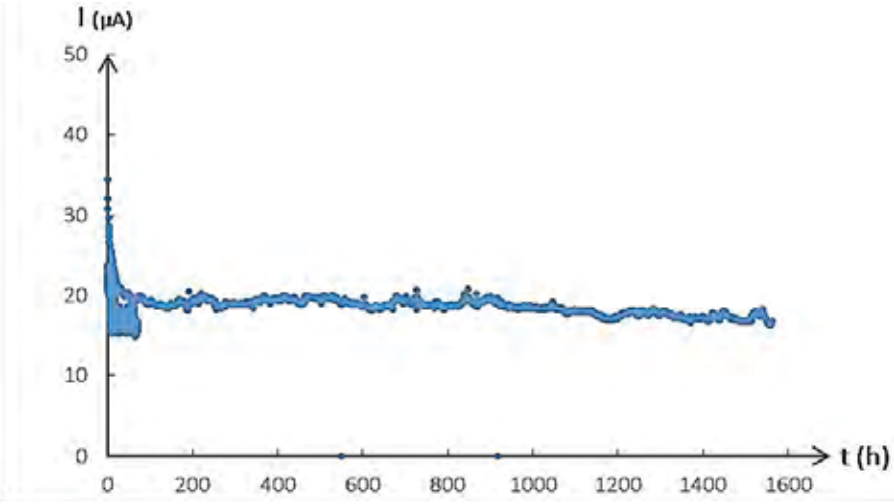


*Fig. 8. Monitoring of the macrocell current during the coupling of 2 M80S anodes with 2 M1 cathodes*

This experiment showed that the same M80S anodes which were connected to M80S cathodes presented a different behavior when they were connected to M1 cathodes with higher potentials. This is an indication that the atypical behavior observed in the case of the formulation M80S-047 is mostly linked to the atypical state of the cathode. Indeed, it can be seen that the sign of the current, and

subsequently the nature of the systems involved, is mainly linked to the type of the cathode, and more precisely to the potential of the cathode.

## 5.3. Results of galvanic coupling between M1 cathode and M80S cathode

Another additional test was realized by connecting 2 cathodes samples: cathode M1 from the formulation M1-055 which was cured and stored in aerated conditions (RH of 95%) and cathode M80S IMM from the formulation M80S-047 which was completely immersed in water directly after removing its formwork.

The corrosion monitoring was realized in the same conditions of the galvanic coupling setup described in part 4.3.1 but the measurement was maintained for almost 1500 h (63 days). Another difference is that the cathode M80S IMM (connected to the terminal $\mathrm{CE}$ of the potentiostat) was coupled with a cathode M1 (connected to the terminal $\mathrm{WE}$ of the potentiostat) instead of an anode.

Fig. 9 shows the current measured when connecting both cathodes. The galvanic current varied between $-0.5\ \mu\mathrm{A}$ and $-2\ \mu\mathrm{A}$. The cathodes remained connected for 4300 h (179 days) and the current was recorded. The current measured after 179 days was $-0.95\ \mu\mathrm{A}$.

The potential of the cathode M80S before the test was $-650\ \mathrm{mV/ref}$ while the potential of the cathode M1 was $-32\ \mathrm{mV/ref}$. After the coupling, the potential of the cathode M80S IMM increased and became $-200\ \mathrm{mV/ref}$. These observations are similar to the ones reported in case 2 when M80S anodes were connected to M80S cathodes.

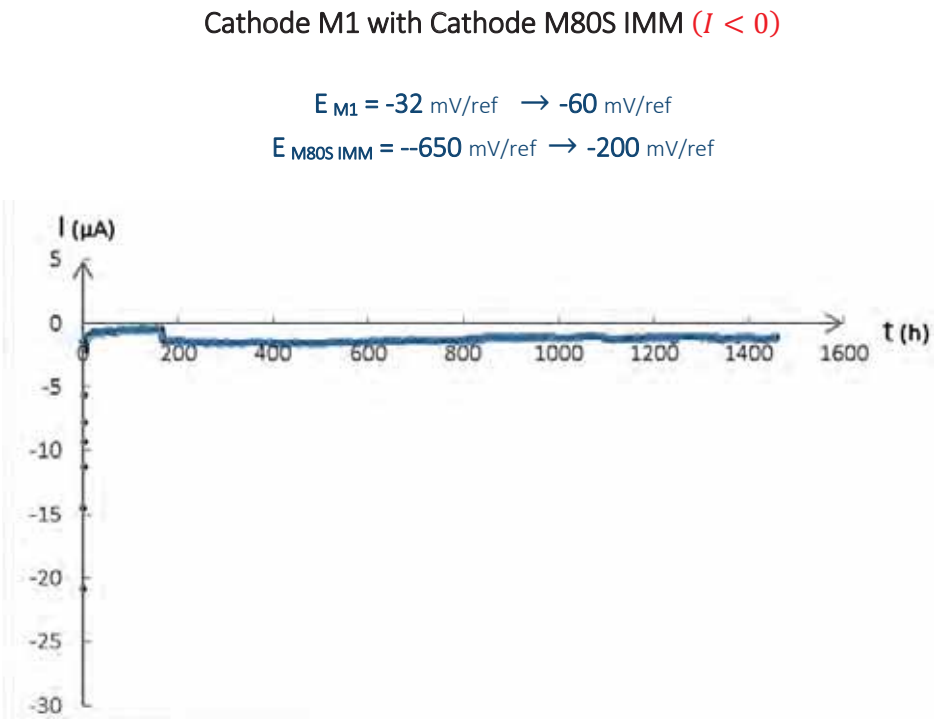


*Fig. 9. Monitoring of the macrocell current during the coupling of Cathode M1 with Cathode M80S IMM*

Fig. 10 shows a schematic illustration of the connection achieved between the cathodes M1 and M80S IMM showing the flow of electrons from the cathode M80S IMM to the cathode M1 associated with the negative current measured (Fig. 9). The cathode M80S IMM was kept immersed in the NaOH

solution during the entire test duration to prevent as much as possible the diffusion of oxygen inside the cathode.

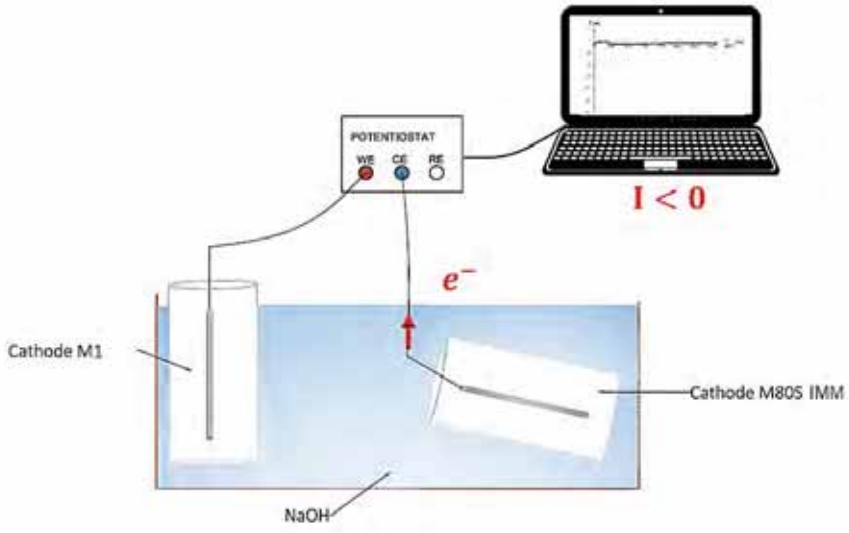


*Fig. 10. Schematic illustration of macrocell current monitoring when cathodes M1and M80S IMM are connected*

Since both samples were cathodes, it is possible to confirm that the "negative" current measured in this situation, and the negative currents measured between M80S anodes and cathodes corresponding to the cases 2 and 3, corresponds to the iron oxidation reaction, probably the reformation of the passive layer. The density of current is about 1 μA/cathode surface = 0,03 μA/cm$^2$ which corresponds to corrosion at passive state.

The negative current measured can only be justified by the fact that the oxidation reaction takes place at the cathode M80S IMM with the lowest initial potential. Given the potential of the cathode M1, it is possible to say that the reduction reaction occurring at the cathode M1 is the reduction of dissolved oxygen.

This experiment showed that the behavior observed when connecting the cathodes M1 and M80S was similar to the results obtained in the case 2 when M80S anodes were connected to M80S cathodes, which indicates that these phenomena are not induced by the anode but more likely by the state of the cathode.

## 5.4. Polarization curves of cathodes

To provide further insight into the electrochemical behavior of the steel embedded in mortar with a high level of slag, polarization tests were conducted on cathode specimens from the formulation M80S-047 and other formulations where the cathodes were stored and cured in different environments.

Fig. 11 shows images of some cathode samples formed with the formulations M1-055, M10SF-043, M40S-055, and M80S-047 according to the curing and storing environments. It is possible to see that M1-055 cathodes have a brown color and M10SF-043 cathodes are more grayish due to the presence of silica fume. A blue-green coloration is present in the case of M80S-047 cathodes aerated and immersed, while it only appears in the case of the formulation M40S-055 when the cathode was totally and continually immersed underwater. When the M40S-047 cathodes are cured and stored without immersion, their color is brown similar to that of M1-055 cathodes.

As stated in part 2.4, this coloration is usually the result of the formation of ferric salts resulting from the oxidation of hydrated products formed from the iron sulfides usually present in slag [22]. The authors [22] used slag contents form 50 to 70% and observed that the degree of the blue-green coloration increases with the slag content. They also found that continual submergence of concrete in water endorses the conservation of the blue-green coloration for a prolonged period of time because air cannot freely diffuse into the concrete to oxidize the ferrous salts to ferric salts [22]. However, when the samples are sealed in plastic bags and cured, their coloration was predominantly brown which could be explained by the ability of oxygen to enter these samples from an early age.

The results in [22] confronted with the visual observations realized in this study allow to confirm that, when samples formed with formulations containing slag are immersed in water, the diffusion of oxygen into the samples is mainly prevented, whereas, when these samples are stored in a humidity room, oxygen can still diffuse into the specimens. Hence, it is possible to assume that there is no oxygen in the cathode M40S IMM, and if any possible available oxygen entered, it could have been consumed by sulfides [90,125].

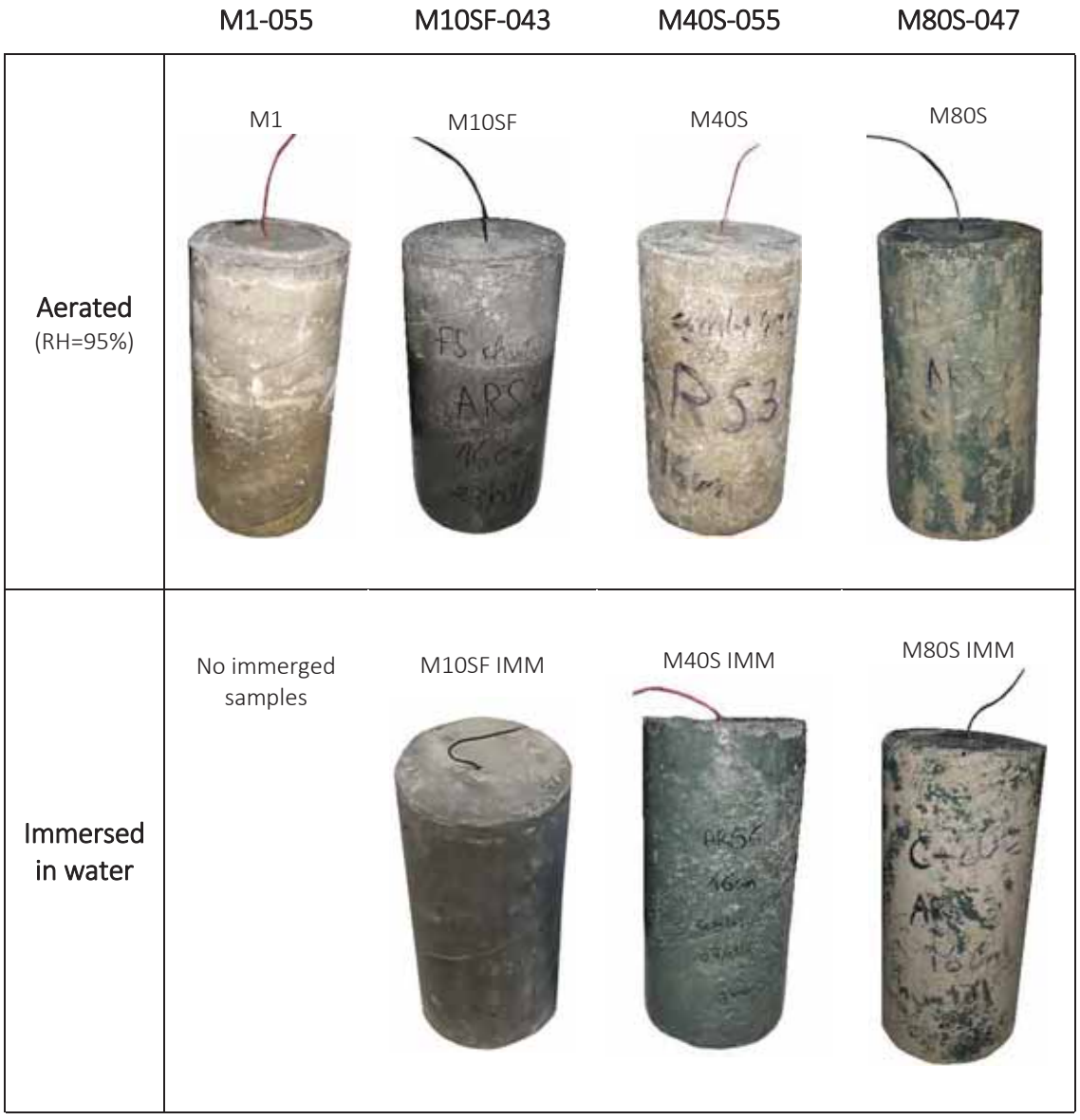


*Fig. 11. Images of cathode samples from different mixes and environments*

### 5.4.1. Case of the formulation M80S-047

Fig. 14 shows the experimental polarization curves of the M80S-047 cathodes after ohmic drop correction. All these cathodes were cured and stored in aerated conditions. The polarization test of the M80S-047 cathode specimen which was immersed in water (M80S-3) was not realized.

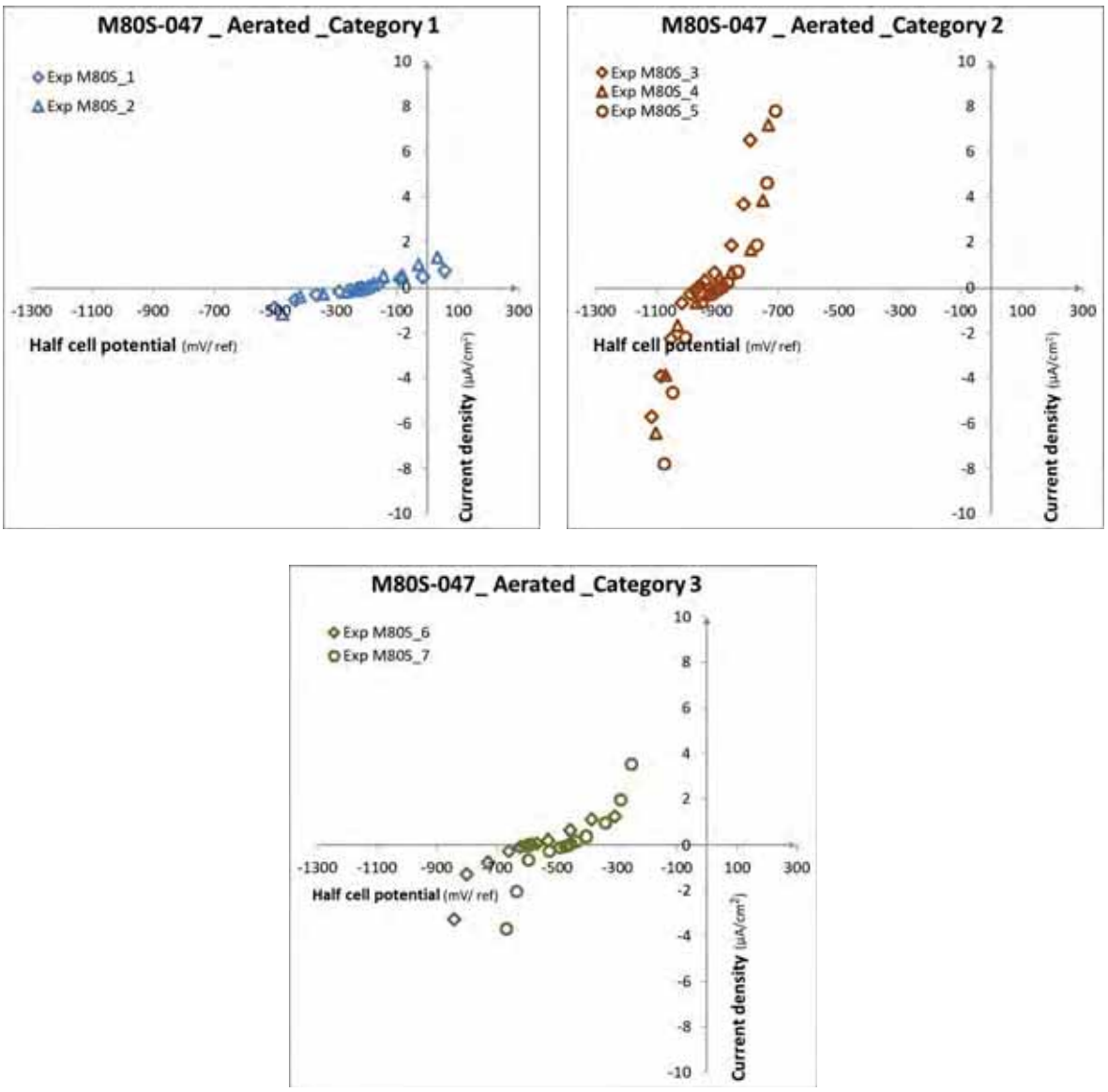


*Fig. 12. Experimental polarization curves of M80S aerated cathode specimens*

According to Fig. 12, it can be seen that the polarization curves obtained from aerated M80S-047 cathode specimens can be divided into 3 different categories according to their equilibrium potentials as follows:

CATEGORY 1:

In the first category, cathodes have free potentials higher than $-230\ \mathrm{mV/ref}$. Both anodic and cathodic slopes are moderately steep.

CATEGORY 2:

In the second category, potentials are around $-900\ \mathrm{mV/ref}$ and both anodic and cathodic slopes are very steep.

CATEGORY 3:

In the third category, potentials are between $-400\ \mathrm{mV/ref}$ and $-600\ \mathrm{mV/ref}$, and the polarization curves could be described as mixed state corresponding to an intermediate behavior between the behaviors observed in both categories 1 and 2.

For better comprehension, it is possible to globally fit the experimental results corresponding to each condition with one electrochemical model; the Butler-Volmer equation presented in Eq. 2 where the anodic and cathodic Tafel slopes $\beta_{a,p}$ and $\beta_{c,p}$ are determined graphically from the anodic and cathodic parts of the experimental polarization curves, respectively.

Fig. 13 shows, for each formulation, the Logarithm representation of the cathodic part of the polarization curves according to the polarization applied, and the corresponding cathodic Tafel slope $\beta_{c,p}$ expressed in mV/dec. It is possible to see that the cathodic Tafel slope $\beta_{c,p}$ can be ranked in the following order CATEGORY 1 > CATEGORY 2 > CATEGORY 3 where a lower $\beta_{c,p}$ is associated with a steeper cathodic response.

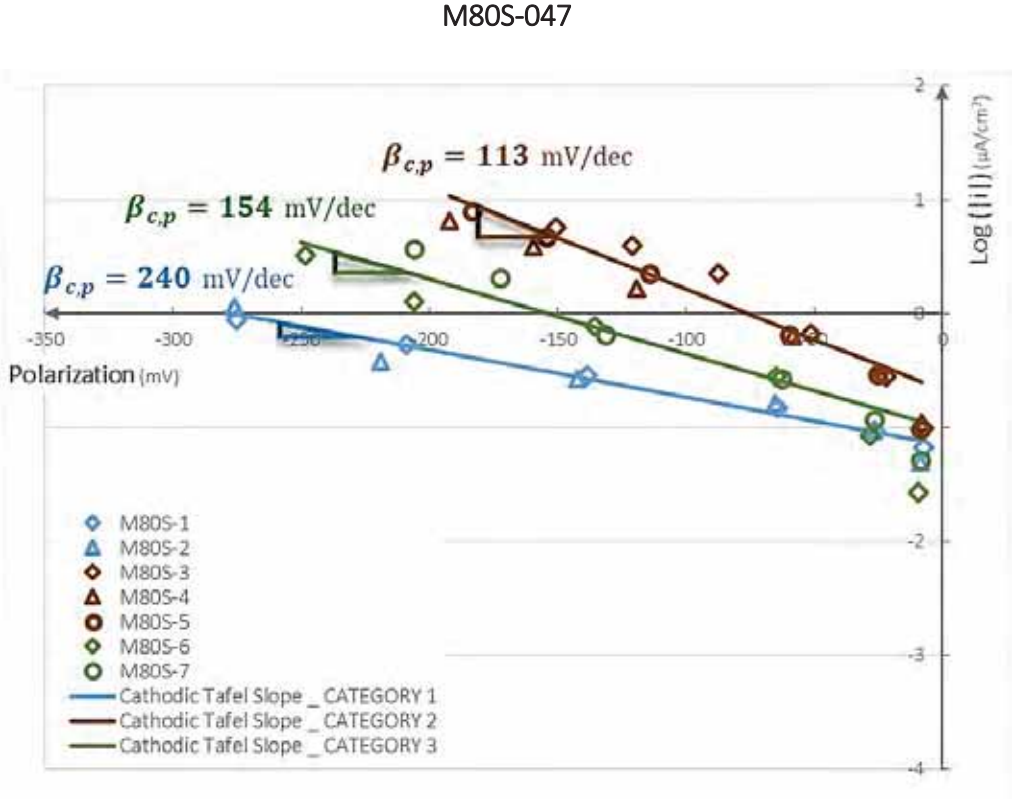


*Fig. 13. Logarithm representation of the cathodic part of polarization curves and the corresponding cathodic Tafel slope*

Table 7 presents the electrochemical parameters of passive steel of the M80S cathodes according to the 3 categories. Based on the results, it is clear that a decrease in $E_{corr,p}$ goes together with the decrease of $\beta_{c,p}$ and $\beta_{a,p}$.

*Table 5. Butler-Volmer parameters of passive steel of M80S cathodes*

| CATEGORY | $E_{corr,p}$ (V/ref) | $\beta_{c,p}$ (V/dec) | $\beta_{a,p}$ (V/dec) |
|---|---|---|---|
| CATEGORY 1 | $-0.213$ | $0.240$ | $0.227$ |
| CATEGORY 3 | $-0.529$ | $0.154$ | $0.194$ |
| CATEGORY 2 | $-0.922$ | $0.113$ | $0.104$ |

### 5.4.2. Case of the formulations M1-055 and M40S-055

Fig. 14 shows the experimental polarization curves of the M1 and M40S cathodes after ohmic drop correction. The results on the left correspond to cathodes which were cured and stored in aerated conditions. Conversely, on the right, it is possible to assume that the cathodes are associated with deaerated conditions.

It must be noted, however, that the cathode M1 in deaerated conditions was cured and stored in an aerated environment then it was polarized cathodically in the attempt to eliminate oxygen as stated in section 4.2.

Based on the findings in Fig. 14, it is possible to see that wet cured cathodes form formulations M1-055, and M40S-055 presented similar behavior characteristics of passive steel. Their free potentials (without external polarization) were between $-100\ \mathrm{mV/ref}$ and $-200\ \mathrm{mV/ref}$, yet, it is possible to notice a slight difference in the slope of their cathodic responses.

The polarization curve of cathode M1-1 after cathodic polarization was different form its polarization curve achieved after its wet curing. The free potential became highly negative (lower than $-900\ \mathrm{mV/ref}$) and both anodic and cathodic responses became steeper.

The same thing was noticed in the case of the cathode M40S IMM which was continually immersed in water. This cathode presented a different behavior from the other M40S cathodes which were stored in an aerated environment. The free potential became highly negative (close to $-900\ \mathrm{mV/ref}$) and both anodic and cathodic responses became steeper. The different behavior observed in case of this cathode goes along with its blue-green color compared to the brown color of aerated M40S cathodes.

A similarity can be observed between the curves in aerated conditions (blue curves on the left) and the curves obtained in case of the category 1 of the formulation M80S. The similarity is also observed between the curves in deaerated conditions (orange curves on the right) and the curves obtained in case of the category 2 of the formulation M80S.

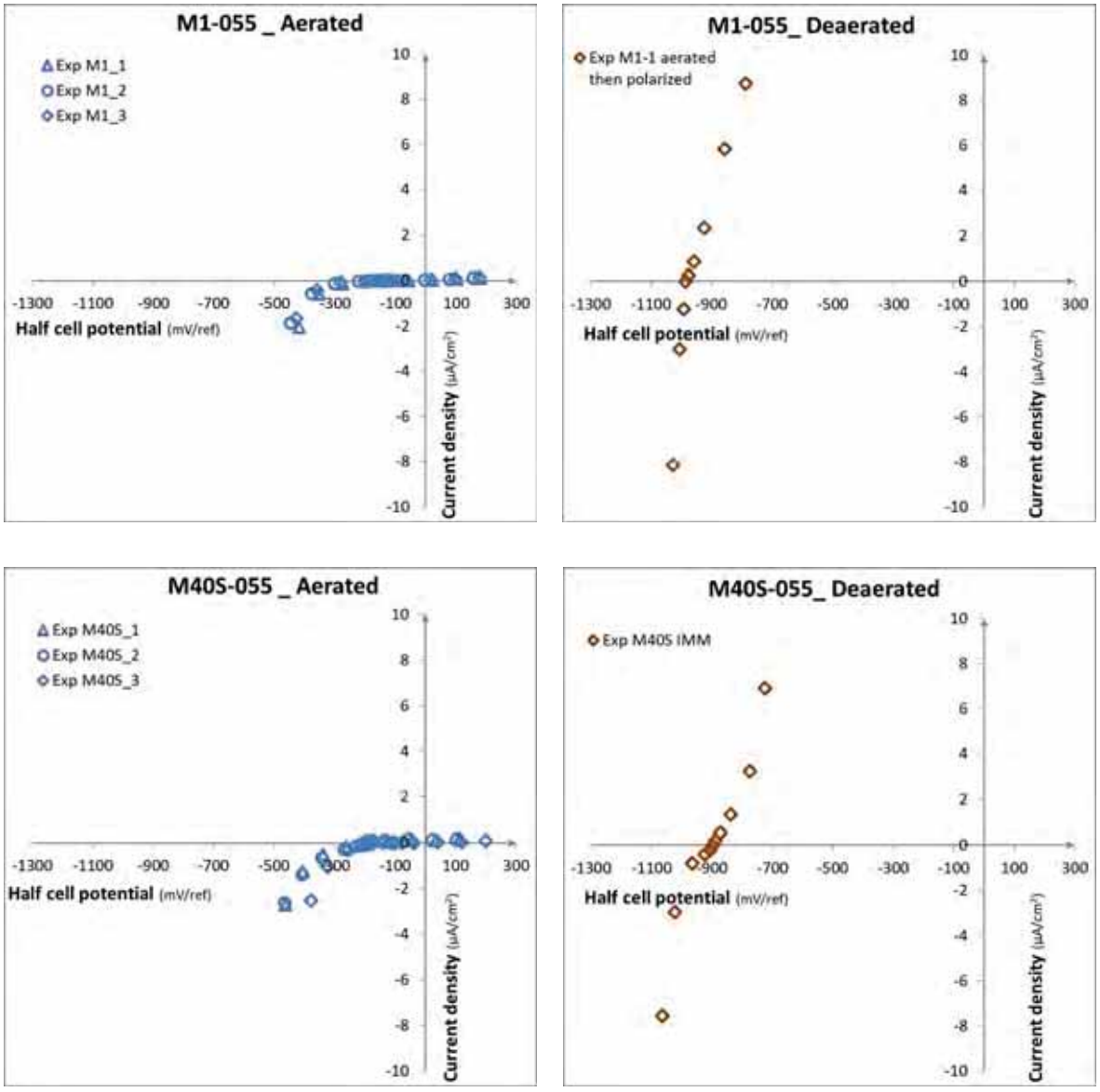


*Fig. 14. Experimental polarization curves of M1 and M40S cathode specimens*

Fig. 15 shows, for each formulation and condition, the Logarithm representation of the cathodic part of the polarization curves according to the polarization applied, and the corresponding cathodic Tafel slope $\beta_{c,p}$ expressed in mV/dec. It is possible to see that the cathodic Tafel slope $\beta_{c,p}$ are always lower in case of deaerated cathodes.

M1-055

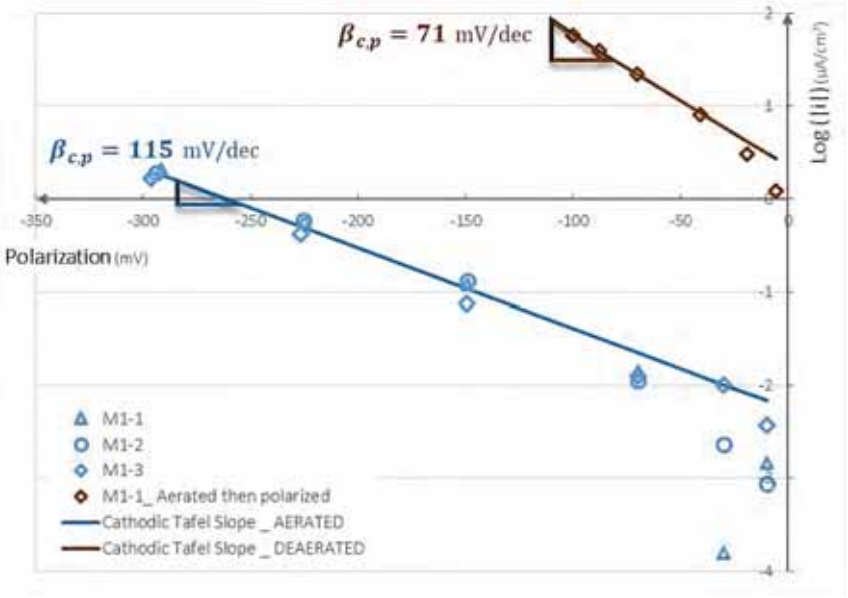


M40S-055

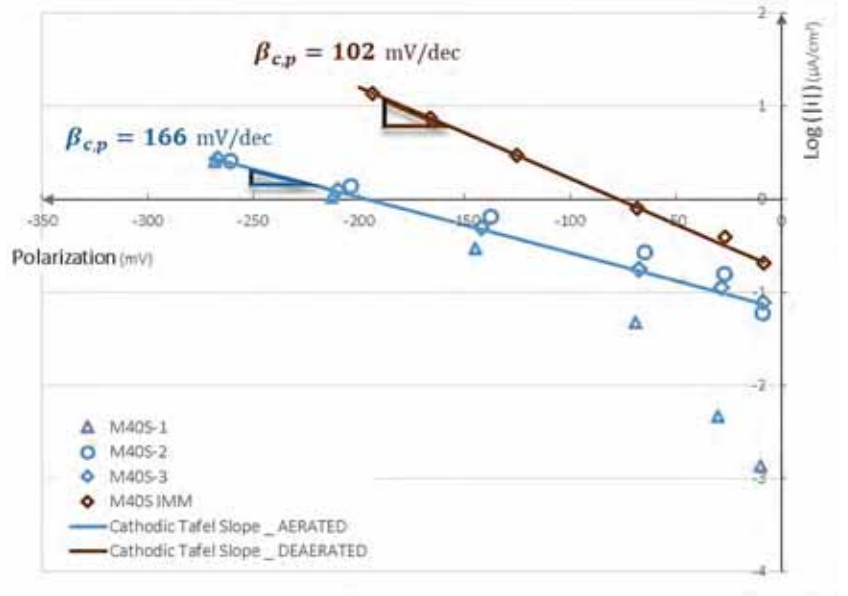


*Fig. 15. Logarithm representation of the cathodic part of polarization curves and the corresponding cathodic Tafel slope*

is clear that $\beta_{c,p}$ decreases when the curing condition changes form aerated to deaerated. The tendency observed in the case of the results obtained in this section are in agreement with the tendency observed in the case of the formulation M80S, where, a decrease of $\beta_{c,p}$ is always associated with a decrease of $\beta_{a,p}$ and $E_{corr,p}$.

All these results make it possible to assume that the atypical behavior shown in the case of the formulation M80S-047 could be associated with the lack of oxygen at the steel/mortar interface. The same behavior was observed in the case of the cathode samples made with formulations without slag or with a lower slag content (M1 and M40S) in deaerated conditions. Therefore, it can be deduced that the highly negative potentials and very steep anodic and cathodic responses are not linked to reactions associated with sulfides but more likely linked to the lack of oxygen.

Indeed, the presence of a high amount of slag, and subsequently a high amount of sulfides, plays an important role in the limitation of the amount of oxygen because of the oxidation of sulfides. This could explain the reason why the M40S cathodes stored in aerated conditions did not show any atypical behavior, yet, when stored underwater, the behavior changed.

Table 6 presents the electrochemical parameters of passive steel of all the tested cathodes. It is clear that $\beta_{c,p}$ decreases when the curing condition changes form aerated to deaerated. The tendency observed in the case of the results obtained in this section are in agreement with the tendency observed in the case of the formulation M80S, where, a decrease of $\beta_{c,p}$ is always associated with a decrease of $\beta_{a,p}$ and $E_{corr,p}$.

All these results make it possible to assume that the atypical behavior shown in the case of the formulation M80S-047 could be associated with the lack of oxygen at the steel/mortar interface. The same behavior was observed in the case of the cathode samples made with formulations without slag or with a lower slag content (M1 and M40S) in deaerated conditions. Therefore, it can be deduced that the highly negative potentials and very steep anodic and cathodic responses are not linked to reactions associated with sulfides but more likely linked to the lack of oxygen.

Indeed, the presence of a high amount of slag, and subsequently a high amount of sulfides, plays an important role in the limitation of the amount of oxygen because of the oxidation of sulfides. This could explain the reason why the M40S cathodes stored in aerated conditions did not show any atypical behavior, yet, when stored underwater, the behavior changed.

*Table 6. Butler-Volmer parameters of passive steel of M1 and M40S cathodes*

| Formulation and curing condition | | $E_{corr,p}$ (V/ref) | $\beta_{c,p}$ (V/dec) | $\beta_{a,p}$ (V/dec) |
|---|---|---|---|---|
| M1-055 | AERATED | $-0.138$ | $0.115$ | $0.240$ |
| | DEAERATED | $-0.986$ | $0.071$ | $0.167$ |
| M40S-055 | AERATED | $-0.169$ | $0.166$ | $0.250$ |
| | DEAERATED | $-0.898$ | $0.102$ | $0.155$ |

### 5.4.3. Case of the formulation M10SF-043

Table 7 presents the electrochemical parameters of passive steel of the M1 and M10SF cathodes in aerated conditions.

*Table 7. Butler-Volmer parameters of passive steel specimens*

| Formulation and curing condition | | $E_{corr,p}$ (V/ref) | $\beta_{c,p}$ (V/dec) | $\beta_{a,p}$ (V/dec) |
|---|---|---|---|---|
| M1-055 | AERATED | $-0.138$ | $0.115$ | $0.240$ |
| M10SF-043 | AERATED | $-0.196$ | $0.240$ | $0.442$ |

It can be seen that for the same curing condition, the electrochemical parameters are not the same between both formulations. In the case of M10SF-043, $E_{corr,p}$ is slightly lower, while $\beta_{c,p}$ and $\beta_{a,p}$ are

almost twice higher. This situation is different from what was previously observed between aerated and deaerated cathodes.

Indeed, in this case, the systems involved are the same since the potentials are in the same order of magnitude. However, the higher anodic and cathodic Tafel slopes are associated with a decrease in the kinetics of the oxidation reaction of iron and the reduction reaction of oxygen, respectively. The latter could be associated with a lower effective steel surface area accessible for cathodic reduction reaction owing to the lower porosity (lower w/b ratio) of the formulation M10SF-043. This decrease in $\beta_{c,p}$ could also be induced by a possible reduction in pH in the case of M10SF-043 (even though the pH of M10SF-043 was not measured in this study).

This interpretation is supported by an observation stated by Hornbostel et al [126] who found lower current densities by cathodes in fly ash mortar compared to Portland cement mortars [126]. One explanation of this observation, according to Hornbostel et al [126], may be related to the lower $OH^-$ concentration present in the pore solution of fly ash mortar known for its impact on oxygen reduction reaction [127]. Another explanation is the denser matrix in fly ash mortar resulting in a lower effective steel surface area accessible for cathodic reduction reaction [126].

## 6. Discussion

This section aims at discussing the overall observations found according to the obtained results using 1D illustrations of the galvanic coupling of active and passive steel. Indeed, the electrical coupling of two systems leads to their mutual polarization where the system with the lower free potential is polarized anodically, while, the system with the more positive potential is polarized cathodically.

Fig. 16 shows a 1D illustration of two different cases of galvanic coupling of active and passive steel. The current responses of these systems to an applied polarization are modeled by their polarizing curves where active steel is shown in red and passive steel in blue.

SITUATION 1

The first situation corresponds to the case where oxygen is available at the cathode. In this situation, the potential of active steel is lower than that of passive steel.

The anodic reaction of active steel corresponds to the oxidation of iron (Eq. 3) in active state conditions meaning that the oxidation kinetics correspond to those of active steel (depassivated steel). The cathodic reaction of active steel corresponds to the reduction of oxygen (Eq. 4).

On the other hand, the anodic reaction of passive steel corresponds to the oxidation of iron (Eq. 3) in passive state conditions meaning that the oxidation kinetics correspond to those of passive steel which is protected with a passivation film. The cathodic reaction of passive steel corresponds to the reduction of oxygen (Eq. 4).

When both uniform systems are coupled, the active steel is polarized anodically and passive steel cathodically. Hence, the reactions involved in this system correspond to the oxidation of iron at the anode and reduction of dissolved oxygen at the cathode.

In this situation, the polarization curve of passive steel is associated with the ones measured on all the cathodes which were aerated; hence oxygen was considered available. These curves are also similar to the ones encountered in CATEGORY 1 of the formulation M80S-047.

When connecting such cathode with an anode, the current measured was positive indicating that electrons are provided form the oxidation reaction at the anode and reduction of oxygen at the cathode.

This situation could be associated with the CASE 1 where M80S anodes were connected to M80S cathodes with potentials higher than $-160\ \mathrm{mV/ref}$ and the case where M80S anodes were connected to M1 cathodes with free potentials around $-100\ \mathrm{mV/ref}$.

In presence of oxygen, the kinetics of the reduction of oxygen at the cathode could be conditioned by properties of the cement matrix (like a lower porosity or pore size); this idea will be discussed later on. The kinetics of the oxidation of iron is conditioned by the level of chloride contamination at the anode [Paper II].

SITUATION 2

The second situation corresponds to the case where oxygen is not available at the cathode. In this situation, the potential of the passive steel is lower than that of the active steel.

The anodic reaction of passive steel is probably the oxidation of iron because the passive layer do not exist for such low potential. It could be assumed that the cathodic reaction of passive steel corresponds to the reduction of water (Eq. 5) because of the low potential of the steel.

$$2\,H_2O\ + 2\,e^- \rightarrow 2\,OH^- + \ H_2 \qquad \textit{Eq. 5}$$

When both uniform systems are coupled, the passive steel is polarized anodically and active steel cathodically. Hence, the reactions involved in this system correspond to an oxidation reaction of iron at the cathode and the reduction of dissolved oxygen at the anode.

In this case, the polarization curve of passive steel is associated with the ones measured on the CATEGORY 2 of M80S aerated cathodes and cathodes form other formulations which were considered in deaerated conditions such as M40S IMM and M1 cathode which was polarized.

The polarization curves corresponding to CATEGORY 3 of M80S aerated cathodes could be associated with a mixed state of the equilibrium systems of CATEGORIES 1 and 2. This means that in some areas of the steel oxygen is still available, while, in other areas, oxygen does not exist.

When connecting such cathode with an anode and even cathode, the current measured was negative indicating that electrons are provided form the oxidation reaction at the cathode. This situation could be associated to the CASES 2 and 3 where M80S anodes were connected to M80S cathodes with highly negative potentials.

The assumption that the oxidation reaction at the cathode is that of iron and reformation of the passive layer because the galvanic coupling allows the potential of the cathode to increase due to the polarization induced by the anode. According to possible oxygen diffusion to the cathode or possible release of oxygen due to the aging in the redox process involving Sulphur and sulfides, the galvanic current could in some cases, and after a certain time, become positive.

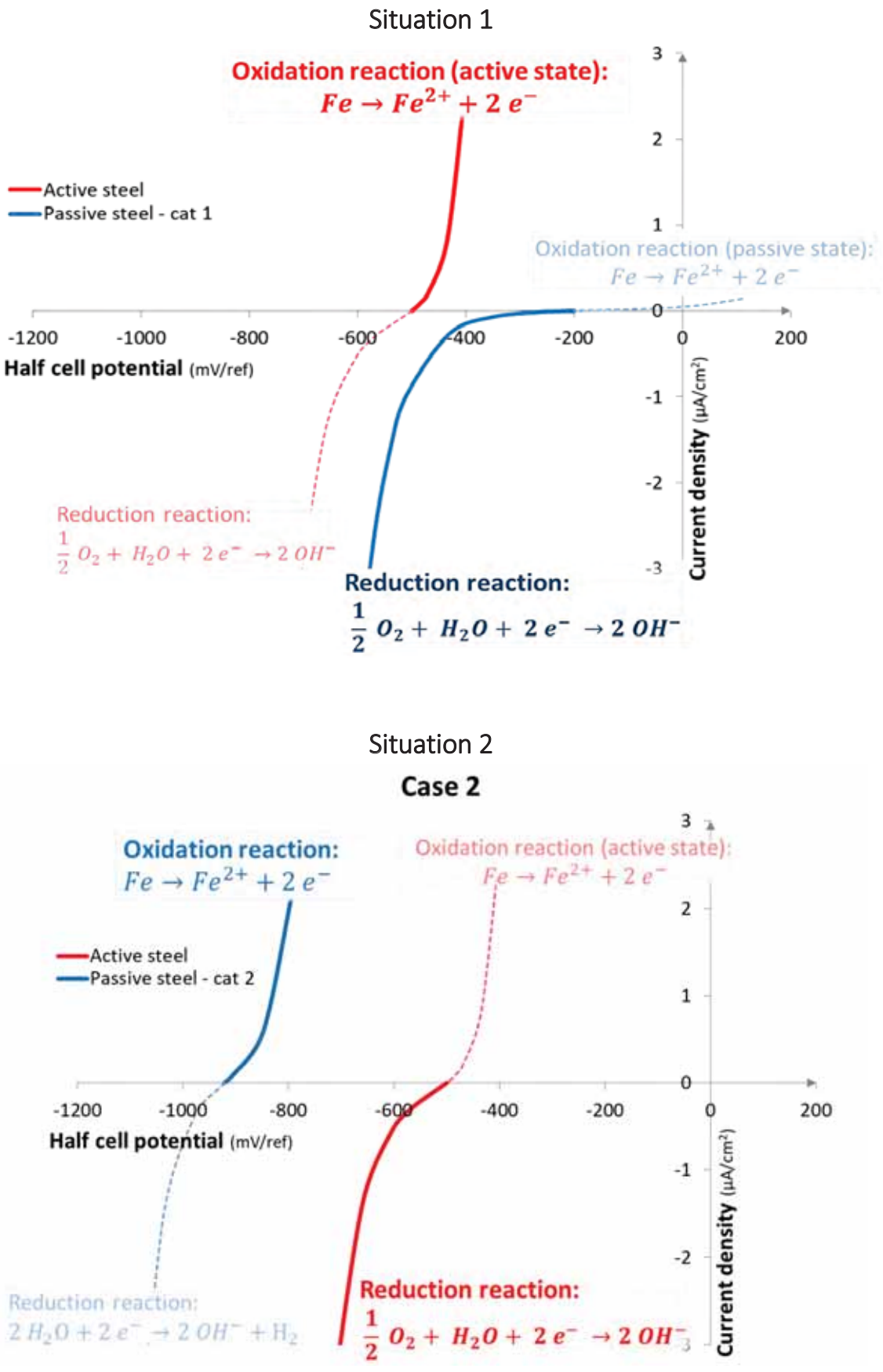


*Fig. 16. 1D representation of the electrical coupling of active and passive steel*

As stated earlier, in the presence of oxygen, the kinetics of the reduction of oxygen at the cathode could be conditioned by properties of the cement matrix.

Fig. 17 shows a polarization curve of passive steel where oxygen is considered present at the steel/concrete interface, yet, it is conditioned by some parameters in a way that a decrease in water porosity or a decrease in the size of pores cause an increase in the cathodic Tafel slope $\beta_{c,p}$ and a slight decrease of the potential $E_{corr,p}$. The increase in $\beta_{c,p}$ means that the kinetics of the reduction of oxygen become lower.

This situation is different from the case where oxygen was considered unavailable. In the second case, the potentials $E_{corr,p}$ were far more negative and $\beta_{c,p}$ sharply decreased instead of increasing. All these observations show that another redox system is involved when oxygen is unavailable.

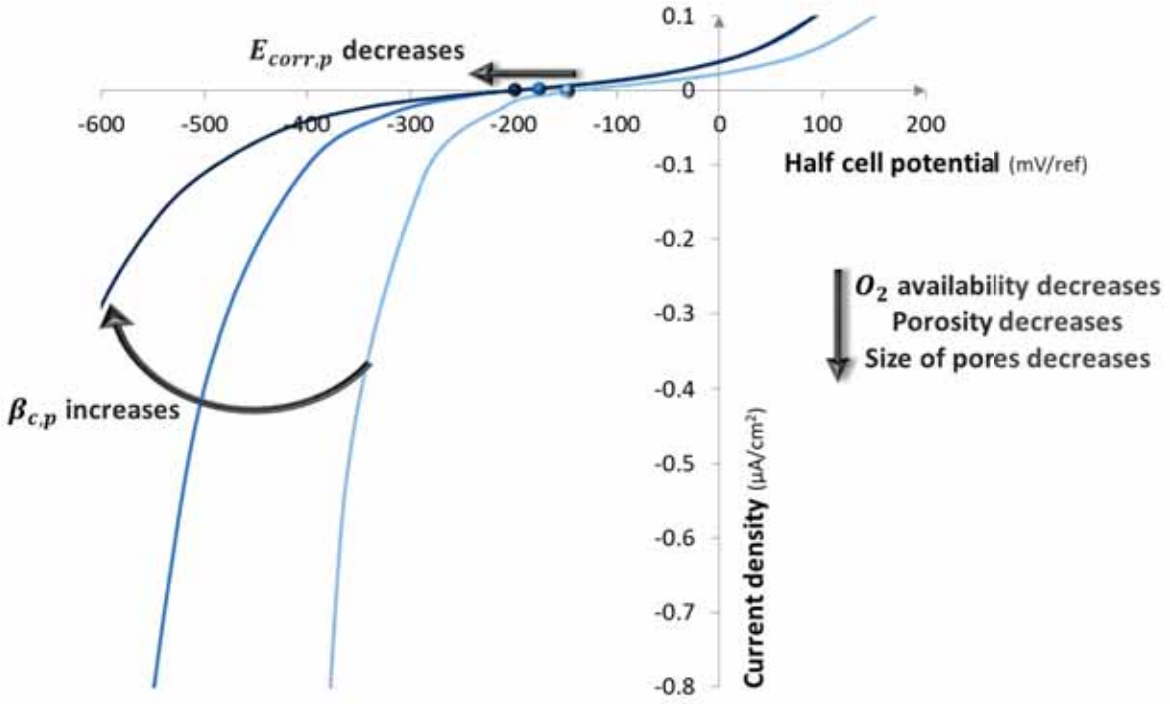


*Fig. 17. Impact of oxygen availability on the polarization curve of passive steel*

# 7. Conclusion

This study focused on studying the impact of slag on the behavior of passive steel and subsequently on the macrocell corrosion current. The results obtained in this study only concern the short term behavior of formulations with slag since the long term analysis was not studied.

The experiments consisted of realizing galvanic coupling on anode samples contaminated with chlorides and cathode samples without any chlorides made with a mortar formulation with 80% of slag and 20% of CEMI with w/b ratio of 0.47. The experiments were based on the test protocol developed in [122] which was applied on mortar samples with 100% of CEMI. Polarization tests were achieved on chloride-free cathode specimens with 80% of slag and the deduced polarization curves were compared to polarization curves of cathodes form different formulations (100%CEMI, 60%CEMI:40%Slag, 20%CEMI:80% Slag, and 90%CEMI:10%Silica fume) and w/b ratios (0.43, 0.47 and 0.55) and different curing conditions. The results showed an atypical behavior of mortar with 80% of slag when compared to other results obtained in case of formulations without slag or with a lower level of slag.

Based on the results of the polarization tests, it was possible to assume that this atypical behavior is mainly linked to the unavailability of oxygen at the steel/mortar interface which is linked to the refinement of the porous network and also to the oxidation of oxygen by the high amount of sulfides present in slag. Indeed, formulations with lower slag substitution level, and a subsequently lower amount of sulfides, did not show a similar behavior unless stored underwater. This means that such formulations did not contain enough sulfides allowing to consume, in aerated conditions, all the oxygen.

Indeed, highly negative free potentials were measured in the case of the cathode samples despite the absence of chlorides. High kinetics of anodic and cathodic reactions were also measured when the steel was polarized externally. It was assumed that the reduction reaction is that of water reduction, while, in the presence of oxygen, the reaction is the reduction of oxygen. It was also assumed that the oxidation reaction is that of iron at the cathode with a significant polarization for a weak current and therefore a rapid reduction of the galvanic current with a possible inversion but which also gives weak kinetics because of limited oxygen access, while, in the presence of oxygen, the oxidation of iron in passive conditions takes place.

Based on the results of galvanic coupling tests, it was found that when the potential of the cathode is higher (more positive) than that of the anode, the measured current was positive indicating that the oxidation reaction takes place at the anode and the reduction reaction at the cathode. This behavior was similar to that encountered in the case of formulations without slag (100% of CEMI) and lower slag content (40% of slag). On the other hand, when the potential of the cathode is lower than that of the anode, the macrocell current is positive which means that the electrons are provided by the oxidation of iron at the anode and received by the cathode where the reduction of oxygen takes place.

According to these findings, it is possible to assume that if a part of a structure made with a high level of slag, appears to have a very negative potential due to the lack of oxygen, there is no real risk of corrosion since an eventual macrocell current could be established with another part of the structure with a higher potential, which will lead to polarization and then an increase of the potential and the reformation of the passive layer.

Hence, the binder with a high level of slag usually known for its atypical behavior would, in the long term and aerated conditions, behave like an ordinary slag-free binder (such as CEMI). As a result, when studying the phase of corrosion propagation of steel in concrete with high levels of slag, it would be more conservative to consider that the slag inhibitory property is mainly linked to his higher electrical resistivity.

## Acknowledgments

This work was supported by the ANR MODEVIE project, grant ANR-14-CE22-0018 of the French National Research Agency (ANR), and by the French National Federation of Public Works (FNTP).

## References

[1] C. Shi and J. Qian, *High performance cementing materials from industrial slags—a review*, Resources, Conservation and Recycling 29 (2000), pp. 195–207.

[2] P. ROSSI, L. GAVOIS and G. RAOUL, *Laitiers de haut-fourneau Origine, production et caractéristiques*, Techniques de l'ingénieur Valorisation des sous-produits industriels en génie civil base documentaire : TIB826. (2014), .

[3] H.-W. Song and V. Saraswathy, *Studies on the corrosion resistance of reinforced steel in concrete with ground granulated blast-furnace slag—An overview*, Journal of hazardous materials 138 (2006), pp. 226–233.

[4] C. Hwang and C. Lin, Strength development of blended blast furnace slag cement mortars, in Proceedings of the 2nd International Conference on Fly Ash, Silica Fume, Slag and Natural Pozzolana in Concrete, 1986, pp. 1323–1340.

[5] M. Shoaib, S. Ahmed and M. Balaha, *Effect of fire and cooling mode on the properties of slag mortars*, Cement and Concrete Research 31 (2001), pp. 1533–1538.

[6] *SLAG AND ITS RELATION TO THE CORROSION CHARACTERISTICS OF FERROUS METALS*, NATIONAL SLAG ASSOCIATION NSA 172-13, .

[7] P.K. Mehta, 3rd International Conference on Fly Ash, Silica Fume, and Natural Pozzolans in Concrete, 1989, pp. 1–43, 1989.

[8] J. Escalante, L. Gomez, K. Johal, G. Mendoza, H. Mancha and J. Mendez, *Reactivity of blast-furnace slag in Portland cement blends hydrated under different conditions*, Cement and Concrete Research 31 (2001), pp. 1403–1409.

[9] G. Vanhamme, *Etude de la réactivité des alitiers du haut-fourneau dans les ciments de type CEM III*, Thesis, Université libre de Bruxelles., 2011.

[10] A. Darquennes, *Comportement au jeune âge de bétons formulés à base de ciment au laitier de haut-fourneau en condition de déformations libre et restreinte*, Thesis, Université libre de Bruxelles, 2009.

[11] M. Whittaker, M. Zajac, M.B. Haha, F. Bullerjahn and L. Black, *The role of the alumina content of slag, plus the presence of additional sulfate on the hydration and microstructure of Portland cement-slag blends*, Cement and Concrete Research 66 (2014), pp. 91–101.

[12] K. Luke and E. Lachowski, *Internal composition of 20-year-old fly ash and slag-blended ordinary Portland cement pastes*, Journal of the American Ceramic Society 91 (2008), pp. 4084–4092.

[13] H.F. Taylor, *Cement Chemistry*, Thomas Telford, 1997.

[14] I. Pane and W. Hansen, *Investigation of blended cement hydration by isothermal calorimetry and thermal analysis*, Cement and concrete research 35 (2005), pp. 1155–1164.

[15] B. Lothenbach and A. Nonat, *Calcium silicate hydrates: solid and liquid phase composition*, Cement and Concrete Research 78 (2015), pp. 57–70.

[16] S.A. Bernal, R. San Nicolas, R.J. Myers, R.M. de Gutiérrez, F. Puertas, J.S. van Deventer et al., *MgO content of slag controls phase evolution and structural changes induced by accelerated carbonation in alkali-activated binders*, Cement and Concrete Research 57 (2014), pp. 33–43.

[17] N. Collier and N. Milestone, *The encapsulation of Mg (OH) 2 sludge in composite cement*, Cement and Concrete Research 40 (2010), pp. 452–459.

[18] A. Harrisson, N. Winter and H.F. Taylor, *Microstructure and microchemistry of slag cement pastes*, MRS Online Proceedings Library Archive (1987), .

[19] S.-D. Wang and K. Scrivener, *Hydration Products of Alkali Activated Slag Cement*, Cement and Concrete Research - CEM CONCR RES 25 (1995), pp. 561–571.

[20] W. Chen, *Hydration of slag cement: theory, modelling and application*, Université de Twente., 2006.
[21] A. Brückner, R. Lück, W. Wieker, A. Winkler, C. Andreae and H. Mehner, *Investigation of redox reactions proceeding during the hardening process of sulfide containing cement*, Cement and concrete research 22 (1992), pp. 1161–1169.
[22] B. Sioulas and J. Sanjayan, *The coloration phenomenon associated with slag blended cements*, Cement and concrete research 31 (2001), pp. 313–320.
[23] M. Chaouche, X.X. Gao, M. Cyr, M. Cotte and L. Frouin, *On the origin of the blue/green color of blast-furnace slag-based materials: Sulfur K-edge XANES investigation*, Journal of the American Ceramic Society 100 (2017), pp. 1707–1716.
[24] S. Stephant, *Etude de l'influence de l'hydratation des laitiers sur les propriétés de transfert gazeux dans les matériaux cimentaires*, 2015.
[25] V. Kocaba, *Development and evaluation of methods to follow microstructural development of cementitious systems including slags*, Thèse de l'École polytechnique fédérale de Lausanne, École polytechnique fédérale de Lausanne, 2009.
[26] B. Kolani, *Comportement au jeune âge des structures en béton armé à base de liants composés aux laitiers*, Thesis, Université Toulouse 3., 2012.
[27] V. Garcia, *Contribution à l'étude du taux de chlorures pour l'amorçage de la corrosion des armatures du béton armé*, Université Toulouse III-Paul Sabatier, 2013.
[28] R.F. Feldman, Significance of porosity measurements on blended cement performance, in Proceedings of the CANMETIACI 1st International Conference on the use of fly ash, silica fume, slag and other mineral by-products in concrete, 1 (1983), pp. 415–433.
[29] M.M.C. Canut, *Pore structure in blended cement pastes*, Thesis, Université technique du Danemark, 2011.
[30] T. Häkkinen, *The influence of slag content on the microstructure, permeability and mechanical properties of concrete Part 1 Microstructural studies and basic mechanical properties*, Cement and Concrete Research 23 (1993), pp. 407–421.
[31] J. Daube and R. Bakker, *Portland blast-furnace slag cement: a review*, in *Blended Cements*, ASTM International, 1983, .
[32] C. Arya and Y. Xu, *Effect of cement type on chloride binding and corrosion of steel in concrete*, Cem. Concr. Res. 25 (1995), pp. 893–902.
[33] R.B. Polder and M.R. De Rooij, *Durability of marine concrete structures: field investigations and modelling*, Heron, 50 (3) (2005), .
[34] G. Glass, B. Reddy and N. Buenfeld, *Corrosion inhibition in concrete arising from its acid neutralisation capacity*, Corrosion Science 42 (2000), pp. 1587–1598.
[35] H. Wong, N. Buenfeld, J. Hill and A. Harris, *Mass transport properties of mature wasteform grouts*, Advances in cement research 19 (2007), pp. 35–46.
[36] M. Auroy, *Impact de la carbonatation sur les propriétés de transport d'eau des matériaux cimentaires*, thesis, Université Paris-Est, 2014.
[37] V.M. Malhotra, *Properties of fresh and hardened concrete incorporating ground granulated blast furnace slag*, Supplementary Cementing Materials for Concrete, Minister of Supply and Services, Canada (1987), pp. 291–336.
[38] H.-W. Song, S.-J. Kwon, S.-W. Lee and K.-J. Byun, *A study on resistance of chloride ion penetration in ground granulated blast-furnace slag concrete*, Journal of the Korea Concrete Institute 15 (2003), pp. 400–408.
[39] R. Huang and C. Yang, *Condition assessment of reinforced concrete beams relative to reinforcement corrosion*, Cement and Concrete Composites 19 (1997), pp. 131–137.
[40] C. Perlot, *Influence de la décalcification de matériaux cimentaires sur les propriétés de transfert: application au stockage profond de déchets radioactifs*, U.F.R P.C.A, 2005.
[41] K. Tuutti, *Corrosion of Steel in Concrete*, Stockholm: Lund University (1982), .

[42] H. Wong, R. Zimmerman and N. Buenfeld, *Estimating the permeability of cement pastes and mortars using image analysis and effective medium theory*, Cement and Concrete Research 42 (2012), pp. 476–483.
[43] S. Li and D.M. Roy, *Investigation of relations between porosity, pore structure, and chloride diffusion of fly ash and blended cement pastes*, Cement and Concrete Research 16 (1986), pp. 749–759.
[44] C. Dehghanian, *Corrosion behavior of steel in concrete made with slag-blended cement*, Corrosion 55 (1999), pp. 291–296.
[45] P. Gu, J. Beaudoin, M.-H. Zhang and V. Malhotra, *Performance of reinforcing steel in concrete containing silica fume and blast furnace slag ponded with sodium chloride solution*, Materials Journal 97 (2000), pp. 254–262.
[46] C. ARYA, N. Buenfeld and J.B. Newman, *Factors Influencing Chloride-Binding in Concrete*, Cement and Concrete Research 20 (1990), pp. 291–300.
[47] R. Luo, Y. Cai, C. Wang and X. Huang, *Study of chloride binding and diffusion in GGBS concrete*, Cement and Concrete Research 33 (2003), pp. 1–7.
[48] R. Dhir, M. El-Mohr and T. Dyer, *Chloride binding in GGBS concrete*, Cement and Concrete Research 26 (1996), pp. 1767–1773.
[49] K. Kopecskó and G.L. Balázs, *Concrete with improved chloride binding and chloride resistivity by blended cements*, Advances in Materials Science and Engineering 2017 (2017), .
[50] O. Kayali, M. Khan and M.S. Ahmed, *The role of hydrotalcite in chloride binding and corrosion protection in concretes with ground granulated blast furnace slag*, Cement and Concrete Composites 34 (2012), pp. 936–945.
[51] J. Lumley, R. Gollop, G. Moir and H. Taylor, *Degrees of reaction of the slag in some blends with Portland cements*, Cement and Concrete Research 26 (1996), pp. 139–151.
[52] X. Ke, S.A. Bernal, O.H. Hussein and J.L. Provis, *Chloride binding and mobility in sodium carbonate-activated slag pastes and mortars*, Materials and Structures 50 (2017), pp. 252.
[53] X. Ke, S.A. Bernal and J.L. Provis, *Uptake of chloride and carbonate by Mg-Al and Ca-Al layered double hydroxides in simulated pore solutions of alkali-activated slag cement*, Cement and Concrete Research 100 (2017), pp. 1–13.
[54] K. Andersson, B. Allard, M. Bengtsson and B. Magnusson, *Chemical composition of cement pore solutions*, Cement and Concrete Research 19 (1989), pp. 327–332.
[55] M. Angus and F. Glasser, *The chemical environment in cement matrices*, MRS Online Proceedings Library Archive 50 (1985), .
[56] A. Cheng, R. Huang, J.-K. Wu and C.-H. Chen, *Influence of GGBS on durability and corrosion behavior of reinforced concrete*, Materials Chemistry and Physics 93 (2005), pp. 404–411.
[57] P. Longuet, *La Phase Liquide du Ciment Hydrate Rev. des Materiaux de Constructions et des Travaux Publics*, Ciments et Betons 676 (1973), pp. 35–41.
[58] M. Kosalla and M. Raupach, *Potential differences between passive reinforcement segments in concrete components in dependency of binder type, aeration conditions and quality of the steel/concrete-interface*, Materials and Corrosion 67 (2016), pp. 639–651.
[59] D.E. MacPhee and H. Cao, *Theoretical Description of Impact of Blast-Furnace Slag (BFS) on Steel Passivation in Concrete*, Magazine of Concrete Research 45 (1993), pp. 63–69.
[60] M. Criado and J.L. Provis, *Alkali activated slag mortars provide high resistance to chloride-induced corrosion of steel*, Frontiers in Materials 5 (2018), .
[61] S. Mundra, S. Bernal and J. Provis, *Durability of steel reinforced alkali-activated concretes in the presence of chloride*, The future of cement 200 (2017), .
[62] K.Y. Ann and H.-W. Song, *Chloride threshold level for corrosion of steel in concrete*, Corrosion Science 49 (2007), pp. 4113–4133.
[63] U. Angst, B. Elsener, C. K. Larsen and Ø. Vennesland, *Critical chloride content in reinforced concrete — A review*, Cement and Concrete Research, 39 (2009), pp. 1122–1138.

[64] U.M. Angst, M.R. Geiker, M.C. Alonso, R. Polder, O.B. Isgor, B. Elsener et al., *The effect of the steel–concrete interface on chloride-induced corrosion initiation in concrete: a critical review by RILEM TC 262-SCI*, Materials and Structures 52 (2019), pp. 88.
[65] Y. Cao, C. Gehlen, U. Angst, L. Wang, Z. Wang and Y. Yao, *Critical chloride content in reinforced concrete — An updated review considering Chinese experience*, Cement and Concrete Research 117 (2019), pp. 58–68.
[66] A.N. Scott, *The Influence of Binder Type and Cracking on Reinforcing Steel Corrosion in Concrete*, 2004.
[67] J. Ryou and K. Ann, *Variation in the chloride threshold level for steel corrosion in concrete arising from different chloride sources*, Magazine of Concrete Research 60 (2008), pp. 177–187.
[68] W. Breit, *Kritischer korrosionsauslösender Chloridgehalt - Neuere Untersuchungsergebnisse (Teil 2). 8:511*, Beton 48 (1998), .
[69] V. Gouda and W. Halaka, *Corrosion and corrosion inhibition of reinforcing steel: II. Embedded in concrete*, British Corrosion Journal 5 (1970), pp. 204–208.
[70] Q. Zhang, W. Sun and J. Shi, *Influence of mineral admixtures on chloride threshold level for corrosion of steel in mortar*, Guisuanyan Xuebao(Journal of the Chinese Ceramic Society) 38 (2010), pp. 633–637.
[71] Z. Meng, *Research on Chloride Threshold Level for Reinforcement Corrosion in Concrete and the Impact of Corrosion Inhibitor*, Ph.D. Master thesis Harbin Institute of Technology, 2012.
[72] H. Ba and M. Zhang, *Study of critical concentration of chloride ion on concrete reinforcement corrosion*, Eighth Natl. Symp. Durab. Concr. (2012), pp. 485–492.
[73] P.-F. Wang, M.-T. Tsai and Y.-W. Chan, *A study on critical chloride ion concentration for corrosion of reinforcing steel in mortar*, J. Chin. Inst. Civil Hydraul. Eng. 26 (2014), pp. 211–214.
[74] P. Schiessl and W. Breit, Local repair measures at concrete structures damaged by reinforcement corrosion-aspect of durability, 1996, pp. 525–534.
[75] B. Oh, S. Jang and Y. Shin, *Experimental Investigation of the Threshold Chloride Concentration for Corrosion Initiation in Reinforced Concrete Structures*, Mag. Concr. Res. 55 (2003), pp. 117–124.
[76] Y. Li, Y. Zhu and J. Fang, *Experimental study of chloride ion's critical content causing reinforcement corrosion in concrete*, Hydro-Science and Engineering (2004), pp. 24–28.
[77] Y. Li, *The study of chloride ions penetration capacity and critical content concrete*, Master thesis Nanjing Hydraulic Research Institute, 2003.
[78] F.P. Glasser, K. Luke and M. Angus, *Modification of cement pore fluid compositions by pozzolanic additives*, Cement and Concrete Research 18 (1988), pp. 165–178.
[79] B. Lothenbach, G. Le Saout, M. Ben Haha, R. Figi and E. Wieland, *Hydration of a low-alkali CEM III/B–SiO2 cement (LAC)*, Cement and Concrete Research 42 (2012), pp. 410–423.
[80] M. Pourbaix and A. Pourbaix, *Potential-pH equilibrium diagrams for the system S-H2O from 25 to 150°C: Influence of access of oxygen in sulphide solutions*, Geochimica et Cosmochimica Acta 56 (1992), pp. 3157–3178.
[81] A. Roy, *Sulfur speciation in granulated blast furnace slag: An X-ray absorption spectroscopic investigation*, Cement and Concrete Research 39 (2009), pp. 659–663.
[82] P. Nadarajah, *Chemistry and corrosion mechanisms of steels embedded in high-dendity slag concrete for storage of used nuclear fuel Department of Chemical Engineering and Applied Chemistry*, University of Toronto, 2011.
[83] M. Radwan, *Influence of the type of blast furnace slag on some characteristics of high slag cement*, Silicates industriels (2002), pp. 89–95.
[84] K.Y. Chen and J.C. Morris, *Kinetics of oxidation of aqueous sulfide by oxygen*, Environmental Science & Technology 6 (1972), pp. 529–537.
[85] P. Longuet, L. Burglen and A. Zelwer, *La phase liquide du ciment hydraté*, n° 219, 1973.
[86] C. Vernet, Comportement de l'ion S2- au cours de l'hydratation des ciments riches en laitiers, in Proceeding de la Conférence sur les laitiers et ciments aux ajouts, Mons, 1981.
[87] *NATIONAL SLAG NSA 172-13 ASSOCIATION*, .

[88] V. Bouteiller, C. Cremona, V. Baroghel-Bouny and A. Maloula, *Corrosion initiation of reinforced concretes based on Portland or GGBS cements: Chloride contents and electrochemical characterizations versus time*, Cement and Concrete Research 42 (2012), pp. 1456–1467.
[89] N. Jarrah, O. Al-Amoudi, M. Maslehuddin, O. Ashiru and A. Al-Mana, *Electrochemical behaviour of steel in plain and blended cement concretes in sulphate and/or chloride environments*, Construction and Building Materials 9 (1995), pp. 97–103.
[90] M. Holloway and J. Sykes, *Studies of the corrosion of mild steel in alkali-activated slag cement mortars with sodium chloride admixtures by a galvanostatic pulse method*, Corrosion science 47 (2005), pp. 3097–3110.
[91] G. Taché, *Méthodes électrochimiques d'étude et de detection de la corrosion des armatures dans le béton*, 1986.
[92] P. Marcus, *Corrosion Mechanisms in Theory and Practice*, CRC press, 1995.
[93] D. Tromans, *Anodic Polarization Behavior of Mild Steel in Hot Alkaline Sulfide Solutions*, Vol. 127, 1980.
[94] M. Criado, S.A. Bernal, P. Garcia-Trinanes and J.L. Provis, *Influence of slag composition on the stability of steel in alkali-activated cementitious materials*, Journal of materials science 53 (2018), pp. 5016–5035.
[95] C. Valentini, L. Berardo and I. Alanis, *Influence of Blast Furnace Slags on the Corrosion Rate of Steel in Concrete*, 1990.
[96] L. Freire, X. Nóvoa, M. Montemor and M. Carmezim, *Study of passive films formed on mild steel in alkaline media by the application of anodic potentials*, Materials Chemistry and Physics 114 (2009), pp. 962–972.
[97] S. Joiret, M. Keddam, X. Nóvoa, M. Pérez, C. Rangel and H. Takenouti, *Use of EIS, ring-disk electrode, EQCM and Raman spectroscopy to study the film of oxides formed on iron in 1 M NaOH*, Cement and Concrete Composites 24 (2002), pp. 7–15.
[98] M. Sánchez, J. Gregori, C. Alonso, J. García-Jareño, H. Takenouti and F. Vicente, *Electrochemical impedance spectroscopy for studying passive layers on steel rebars immersed in alkaline solutions simulating concrete pores*, Electrochimica Acta 52 (2007), pp. 7634–7641.
[99] K. Yeau and E. Kim, *An Experimental Study on Corrosion Resistance of Concrete with Ground Granulate Blast-Furnace Slag*, Cement and Concrete Research 35 (2005), pp. 1391–1399.
[100] A. Ramezanianpour and V. Malhotra, *Effect of curing on the compressive strength, resistance to chloride-ion penetration and porosity of concretes incorporating slag, fly ash or silica fume*, Cement and concrete composites 17 (1995), pp. 125–133.
[101] G. Osborne, *Durability of Portland blast-furnace slag cement concrete*, Cement and Concrete Composites 21 (1999), pp. 11–21.
[102] R. Huang, J.-J. Chang and J.-K. Wu, *Correlation between corrosion potential and polarization resistance of rebar in concrete*, Materials Letters 28 (1996), pp. 445–450.
[103] B.B. Hope and A.C. Ip, *Corrosion of steel in concrete made with slag cement*, Materials Journal 84 (1987), pp. 525–531.
[104] O.S.B. Al-Amoudi, M. Maslehuddin and A.I. Al-Mana, *Prediction of long-term corrosion resistance of plain and blended cement concretes*, Materials Journal 90 (1993), pp. 564–570.
[105] İ.B. Topçu and A.R. Boğa, *Effect of ground granulate blast-furnace slag on corrosion performance of steel embedded in concrete*, Materials & Design 31 (2010), pp. 3358–3365.
[106] K.O. Ampadu, K. Torii and T. Kubota, *Chloride induced corrosion of steel bars embedded in ecocement blast-furnace slag mortars*, Special Publication 199 (2001), .
[107] D. Baweja, H. Roper and V. Sirivivatnanon, *Chloride-induced steel corrosion in concrete: part 1-corrosion rates, corrosion activity, and attack areas*, ACI Materials Journal, Technical paper 95 (1998), pp. 207–217.
[108] W.-C. Jau and D.-S. Tsay, *A study of the basic engineering properties of slag cement concrete and its resistance to seawater corrosion*, Cement and Concrete Research 28 (1998), pp. 1363–1371.

[109] P. Mangat and B. Molloy, *Influence of PFA, slag and microsilica on chloride induced corrosion of reinforcement in concrete*, Cement and Concrete Research 21 (1991), pp. 819–834.
[110] G.J. Osborne, *Durability of Portland Blast-Furnace Slag Cement Concrete*, Building Research Establishment Information Paper, IP6/92, Building Research Establishment, Garston 21 (1992), pp. 11–21.
[111] K. Hollinshead, G.J. Osborne, and D.J. Bigland, Tees Barrage: durability assessment of concrete, in Proceedings of the Instr. Civil Engineers Mun. Engineers 115, 1996, pp. 203–208.
[112] P. Sandberg, *Chloride initiated reinforcement corrosion in marine concrete*, Division of Building Materials, LTH, Lund University, 1998.
[113] U. Angst, B. Elsener, C. Larsen and Ø. Vennesland, *Chloride Induced Reinforcement Corrosion: Electrochemical Monitoring of Initiation Stage and Chloride Threshold Values*, Vol. 53, 2011.
[114] N. R. Jarrah, O. Al-Amoudi, M. Maslehuddin, O. A. Ashiru and A. Ibrahim Al-Mana, *Electrochemical Behaviour of Steel in Plain and Blended Cement Concretes in Sulphate and/or Chloride Environments*, Vol. 9, 1995.
[115] V. Bouteiller, C. Cremona, V. Baroghel-Bouny and A. Maloula, *Corrosion Initiation of Reinforced Concretes Based on Portland or GGBS Cements: Chloride Contents and Electrochemical Characterizations versus Time*, Vol. 42, 2012.
[116] L. Tang, J.M. Frederiksen, U. Angst, R. Polder, M. Cruz Alonso, B. Elsener et al., *Experiences from RILEM TC 235-CTC in Recommending a Test Method for Chloride Threshold Values in Concrete*, Vol. 3, 2018.
[117] U. Angst, C. Boschmann, M. Wagner and B. Elsener, *Experimental Protocol to Determine the Chloride Threshold Value for Corrosion in Samples Taken from Reinforced Concrete Structures*, 2017.
[118] V. Garcia, R. Francois, M. Carcasses and P. Gegout, *Potential Measurement to Determine the Chloride Threshold Concentration That Initiates Corrosion of Reinforcing Steel Bar in Slag Concretes*, Vol. 47, 2014.
[119] *RILEM TC 154-EMC: ELECTROCHEMICAL TECHNIQUES FOR MEASURING METALLIC CORROSION Test methods for on site measurement of resistivity of concrete | Scinapse | Academic search engine for paper*, Scinapse 33 (2000), pp. 603–611.
[120] J.P. OLLIVIER, *Durabilité Des Bétons. Compte Rendu Des Journées Techniques AFPC-AFREM*, 1997.
[121] H. Wong, N. Buenfeld, J. Hill and A. Harris, *Mass transport properties of mature wasteform grouts*, Advances in cement research 19 (2007), pp. 35–46.
[122] C. Chalhoub, R. François and M. Carcasses, *Determination of chloride threshold initiating corrosion: A new set-up taking the localized aspect of corrosion into account*, Cement and Concrete Research 124 (2019), pp. 105825.
[123] S. Laurens, P. Hénocq, N. Rouleau, F. Deby, E. Samson, J. Marchand et al., *Steady-state polarization response of chloride-induced macrocell corrosion systems in steel reinforced concrete — numerical and experimental investigations*, Cement and Concrete Research 79 (2016), pp. 272–290.
[124] C. ASTM, *876-15 Standard Test Method for Corrosion Potentials of Uncoated Reinforcing Steel in Concrete*, American Society for Testing and Materials, Philadelphia, Pa, USA (2015), .
[125] Q. Ma, S.V. Nanukuttan, P.M. Basheer, Y. Bai and C. Yang, *Chloride transport and the resulting corrosion of steel bars in alkali activated slag concretes*, Materials and Structures 49 (2016), pp. 3663–3677.
[126] K. Hornbostel, U.M. Angst, B. Elsener, C.K. Larsen and M.R. Geiker, *Influence of mortar resistivity on the rate-limiting step of chloride-induced macro-cell corrosion of reinforcing steel*, Corrosion Science 110 (2016), pp. 46–56.
[127] H. Kaesche, *Corrosion of Metals: Physicochemical Principles and Current Problems*, Springer Science & Business Media, Berlin, 2012.

# Paper VIII

## Lifetime prediction model based on a service limit state criteria associated with a corrosion current density corresponding to the appearance of the first corrosion-induced cracking

**Chantal Chalhoub*, Raoul François, Myriam Carcasses**

**To be submitted + ANR Report**

# Lifetime prediction model of reinforced concrete structures under the risk of corrosion based on service limit state criteria associated with a corrosion current density corresponding to the appearance of the first corrosion-induced cracking

Chantal Chalhoub*, Raoul François, Myriam Carcasses
LMDC, INSA, UPS, Université de Toulouse, France
* Corresponding author: chantal.chalhoub@insa-toulouse.fr

## Abstract

In the last 30 years, several empirical prediction models were developed for the determination of corrosion current density used for the estimation of the duration of corrosion propagation. Each model incorporated additional input parameters of factors influencing corrosion propagation. This paper presents a summary of some of these models and their possible limitations. An examination of significant elements influencing the corrosion current density was also detailed. The objective was the development of a simplified empirical model for the prediction of the corrosion current density in the case of chloride-induced macrocell corrosion in uncracked reinforced concrete structures. The model is based on experimental results obtained from an experimental test that physically separates the anode from the cathode. The current densities obtained are apparent, relative to the ratio of the anodic and cathodic parts of the experimental device. The corrosion current density predicted by the model makes it possible to calculate the duration of the propagation phase before the appearance of the first corrosion cracks. The originality of the model is that the corrosion current density is taken into account only partly to obtain a local reduction of the reinforcement section, the other part of the corrosion current density is used for the extension of the anodic zones in their length. The link between loss of local section and the appearance of a corrosion crack is empirical. This method will allow forming a simplified propagation service life model of relevance to the engineer.

## Keywords

Macro-cell; Corrosion current density; Propagation phase; Chlorides; Cathode over anode ratio; Electrical resistivity; Cross-section reduction; Exposure class; Performance-based approach.

## 1. Introduction

Corrosion is one of the main causes of degradation of reinforced concrete structures especially marine structures. It is, therefore, an essential element to study for understanding the long-term behavior of materials used in the construction and improve the repair of reinforced concrete structures. When dealing with reinforcement corrosion, the service life ($t_{service}$) of reinforced concrete structures is the sum of the corrosion initiation phase and corrosion propagation phase (Eq. 1).

$$t_{service} = t_{ini} + t_{prop} \qquad Eq.\ 1$$

The time to initiation ($t_{ini}$) through local depassivation of steel is defined as the time needed for chlorides to reach a critical threshold value ($C_{crit}$). During the initiation phase, the chloride threshold value is one of the most important input parameters that govern the outcome of the prediction of the initiation stage. However, there is still no agreement on a reliable method for its determination and several mechanisms are still not well understood [1].

Most methods for lifetime prediction only discuss the initiation stage which is a conservative approach concerning the design of structures. However, recently, several works mentioned the importance of incorporating a part of the propagation period in the life of the structure ($t_{prop}$). As an example, for XS exposure according to EN 206, if the initiation phase is only considered, then corrosion risk is higher for XS1 than XS2, however, norm and experience say the opposite. Indeed, for XS2 exposure, due to the lack of oxygen, corrosion risk is lower than XS1. Therefore, the attention of the scientific community has shifted to the propagation phase, but without neglecting the initiation period.

The localized nature of corrosion in concrete leads to the propagation stage of corrosion with a corrosion current density that depends on numerous elements and several processes: anodic, cathodic, ohmic and geometric. In the propagation phase, the corrosion is said to be active. The duration of the propagation phase must be associated with a level of deterioration related to a pre-defined limit state corresponding to structural or durability performance. The propagation phase can also be divided into several sub-phases that correspond each to predefined limit criteria. The damages caused by corrosion can be related to steel cross-section loss, loss in ductility or damage of the steel/concrete interface bond, cracking of the concrete cover and also the collapse of the structure. The limit states of a structure are either service limit states (SLS) or ultimate limit states (ULS). There are several definitions of service limit state that could depend on an aesthetic criterion or excessive deflections or delamination risk. The ultimate limit state could, for example, correspond to excessive loss of bearing capacity or risk of brittle failure. However, limit states must take into account the element of safety and the cost of repair. Hence, it is more suitable to adopt an adequate service limit state related to an acceptable damage indicator in case of the propagation phase such as the longitudinal corrosion-induced crack openings on the concrete surface or the cross-section loss corresponding to the appearance of the first corrosion-induced crack.

Several models were developed to predict times to different corrosion-induced limit states with little focus on the calculation and prediction of corrosion density ($i_{corr}$). Though, $i_{corr}$ is one of the most important parameters that influence the output results of these models [2]. This implies that even when dealing with the most refine prediction models, the outcome mainly depends on the accuracy and credibility of the prediction of the corrosion current density. Consequently, in the last 30 years, several corrosion density prediction models were developed and they can be classified according to their type: empirical, analytical or numerical. Furthermore, the other key factor of these models is the relationship between corrosion density and the loss of steel cross-section. Nowadays, all existing approaches are based on the assumption that all the corrosion current density contributes to the reduction of the cross-section, which could be a wrong approach in the case of non-uniform corrosion.

This work is part of the ANR MODEVIE research program which corresponds to the modeling part of French National Project PERFDUB aiming at developing a methodology for justifying the durability of concrete structures using a performance-based approach. This project is mainly interested in the corrosion in reinforced concrete structures under the influence of chlorides and carbonation. Starting from scientific models available for the different phenomena in play, its output is an overall engineering model able to provide a reliable assessment of concrete structures service life by calculating the sum of initiation period and propagation period. The engineering models adapted to the performance-based approach must describe both phases, initiation, and propagation. Furthermore, the material input data will be mainly durability and environmental indicators.

This study begins with a review of some empirical models developed for the prediction of corrosion current densities in reinforced concrete structures that are used to determine the duration of corrosion propagation. This section was followed by a literature overview of the different parameters influencing corrosion propagation.

This paper addresses the prediction of the duration of the corrosion propagation phase based on the observation that in a concrete structure before the appearance of corrosion-induced cracks, the preponderant component of corrosion is that related to the macro-cell process (localized corrosion).

This first step consisted of developing a model for the assessment of the corrosion current density which was considered constant during the early phase of corrosion propagation before the appearance of the first cracks. The proposed model takes into consideration the parameters affecting the corrosion propagation phase which are related to anodic, cathodic and ohmic processes governing chloride-induced corrosion propagation.

The proposed model takes into consideration the impact of parameters related to:

- The anodic behavior like the concentration in free chlorides and the steel/concrete interface;
- The influence of parameters related to cathodic behavior like oxygen availability;
- The parameters related to the ohmic interaction between anodic zones and cathodic zones, in particular, the electrical resistivity of the concrete which accounts for the relative humidity and the type of binder, the surface ratio between cathode and anode (very high in real structures), and the distance between aerated cathode and anode (important parameter for XS2 type exposures).
- The influence of temperature.

The model was initially expressed in terms of macrocell corrosion current and was calibrated from experimental results obtained from previous studies, mainly from an experimental test that physically separates the anode contaminated with chlorides from the cathode which is chloride-free [3]. After calibration, the transition from corrosion current to corrosion current density was achieved. These current densities were considered as apparent densities since they were calculated by considering the entire surface of the anode.

It must be noted that several definitions of corrosion current density models annotated "$i_{corr}$" exist in the literature, where most of them assume a uniform corrosion state. In this paper, the developed model takes explicitly into account the localized aspect of corrosion. Hence, the developed corrosion current density model was initially called "$i_{ge}$" but was later on annotated "$i_{corr}$" to simplify the notations.

The service limit criterion chosen in this study was the appearance of the first corrosion-induced cracks which was considered as a conservative and practice-related approach. The link between loss of local section and the appearance of corrosion cracks was deduced from other literature studies but was updated to take into account the fluid nature of corrosion products in submerged regions. The model is empirical and allows the determination of the steel cross-section loss initiating cracking knowing the diameter of the reinforcement bar and the concrete cover.

After the determination of the corrosion current density and the steel cross-section loss initiating cracking in concrete, it was possible to calculate the duration of the propagation phase before the appearance of the first corrosion cracks using Faraday's law. The originality of the model is that the corrosion current density is taken into account only partly to obtain a local reduction of the reinforcement section, the other part of the corrosion current density is used for the extension of the anodic zones in their length.

## 2. Chloride-induced corrosion in concrete

In the presence of chlorides, corrosion in reinforced concrete structures is localized. Chlorides cause a local depassivation of reinforcement bars that firstly occurs on the first layers of rebars next to the exposed concrete surface. This localized corrosion, also known as macrocell corrosion, engenders a galvanic coupling between active depassivated rebars and passive rebars because of potential gradient. Once initiated, the corrosion process becomes self-maintained and self-propagating due to the migration of chlorides toward active areas under the generated electrical field. An ionic current flow circulates in concrete and electronic current is exchanged through the network of reinforcement between active (anode) and passive (cathode) zones (Fig. 1).

Macrocell corrosion characterized by the physical separation between anode and cathode is different from microcell corrosion where anodic and cathodic sites are spatially combined. In the case of chloride-induced corrosion, both microcell and macrocell corrosion may coexist during the propagation phase with microcell corrosion densities relatively negligible compared to macrocell current densities [4].

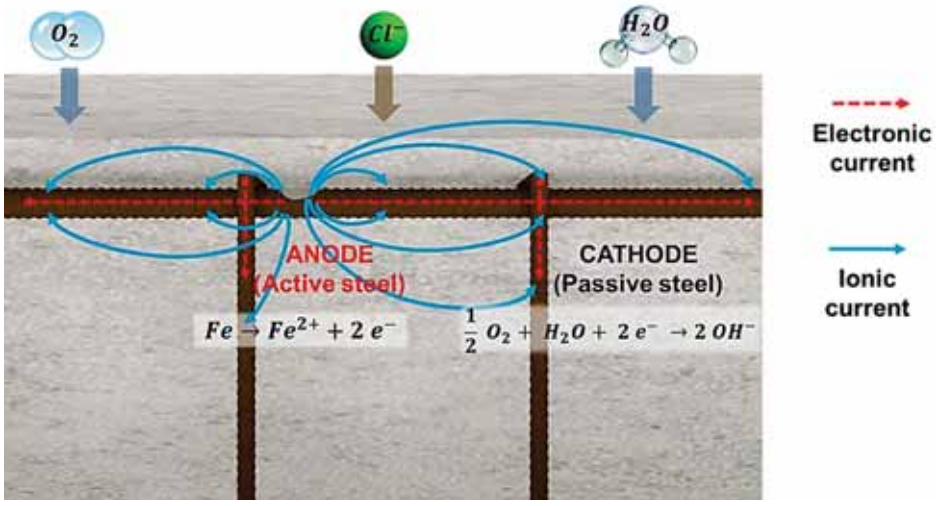


*Fig. 1. Schematic illustration of localized chloride-induced corrosion in concrete*

## 3. RILEM TC-154-EMC standard approach to calculate $i_{corr}$ and estimate service life of reinforced concrete structures

The measurement of polarization resistance $R_p$ through linear polarization technique is widely used to evaluate corrosion current densities in concrete structures. Lots of empirical corrosion current density predictive models used this non-destructive electrochemical technique to quantify corrosion densities. It was then important to understand this approach before presenting the predictive models. The RILEM TC-154-EMC [5] discusses, in detail, the protocol adopted for on-site corrosion density measurement of steel reinforcement in concrete which consists of several steps presented hereafter.

### 3.1. Measurement of Rp:

The measurement is made with a three-electrode set-up with reinforcing steel as Working Electrode (WE), a Counter Electrode (CE) and a Reference Electrode (RE). The principle of measurement is to impose an overvoltage ΔE in both anodic and cathodic direction and measure a variation of current Δi (potentiostatic) or on the contrary to impose a current Δi and measure a difference of potential ΔE (galvanostatic). The potential-current polarization curve can be modeled by the Butler-Volmer equation

and Rp is defined as the slope of this curve at the corrosion potential at equilibrium ($E_{corr}$). $R_p$ can thus be calculated using Eq. 2 and it also can be obtained from the analysis of the transitory period (coulostatic or transient methods). When measuring $R_p$, the potentiostat used can automatically compensate the ohmic drop due to concrete resistance with two methods: positive feedback and current interruption.

$$R_p\ [\Omega] = \frac{\Delta E\ [V]}{\Delta i\ [A]} \qquad \textit{Eq. 2}$$

## 3.2. Calculation of instantaneous corrosion current density $i_{corr}$:

In the case of uniform corrosion and for a weak polarization, limited first-order development of the Butler-Volmer equation allows linearizing the relation between the overvoltage ΔE and the corrosion current density called by the RILEM committee [5] instantaneous corrosion current density. The density is then based on the assumption of uniform corrosion and is calculated using the Stern-Geary [6] equation as follows:

$$i_{corr}\ [A/cm^2] = \frac{B\ [V]}{R_p\ [\Omega]\ \ S_p[cm^2]} \qquad \textit{Eq. 3}$$

Where B is a constant deduced from a combination of anodic and cathodic Tafel slopes and is considered for on-site measurements equal to 26 mV (case of active steel) or 52 mV (case of passive steel) and $S_p$ is the area of steel surface supposed to be polarized.

An external circular Guard Ring GR concentric to the CE is usually supposed to confine the current for the delimitation of the polarized area. The GR counterbalances the central electrical field and the intensity of the confining current is controlled so that the potential difference between two reference electrodes (S1, S2) placed between CE and GR is equal to 0. If the potential is constant on the surface this means that the current lines are normal to the surface and that the polarization current is confined, however, in reality, the mechanisms are much more complex. Also, the GR used in some LPR instruments to confine the current may generate an additional current around the counter-electrode [7].

Fig. 2 illustrates the RILEM protocol for on-site corrosion measurement showing the confinement of the current when using a GR to counterbalance the electrical field. The supposedly polarized area $S_p$ is a measurement constant associated with the diameter of the reinforcement under examination and the dimensions of the measurement system. This representation does not consider the interaction between injected currents and galvanic currents which tends to interpret a measurement realized on localized corrosion by considering it like a uniform corrosion system [4].

Fig. 3 illustrates the distribution of current lines obtained in case of localized corrosion when numerically simulating anodic polarization with a GECOR – type measurement [8]. Fig. 3 clearly shows that, in the case of an anodic polarization, both polarizing and confining currents ( $I_{CE}$ and $I_{gr}$, respectively) are collected by the area of active steel. This also implies that the additional current contributes entirely to the polarization, whereas it is not taken into account in polarization resistance calculation [8].

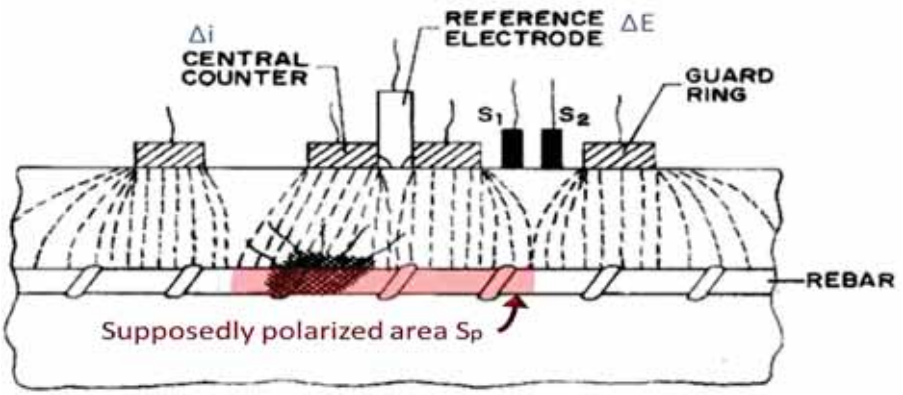


*Fig. 2 RILEM protocol for on-site corrosion measurement and the assumed polarized area (modified image taken from* [5]*)*

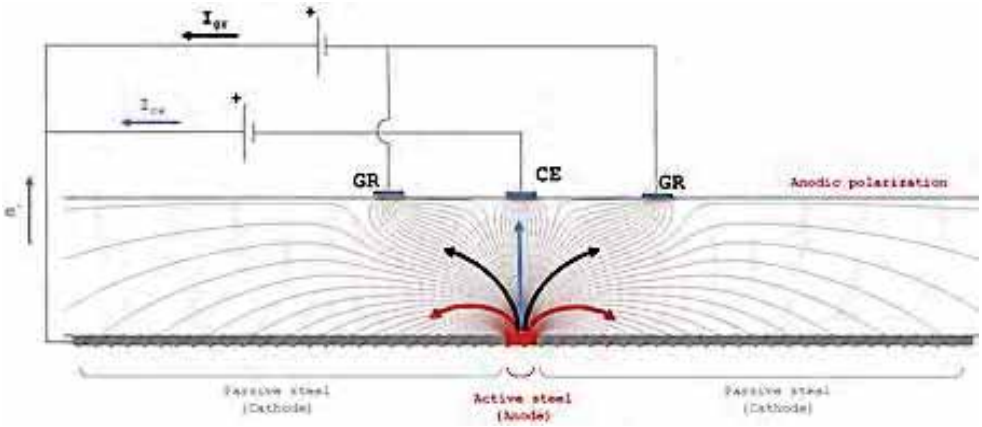


*Fig. 3. Simulated shapes of current lines obtained in case of localized corrosion when simulating an anodic polarization with a GECOR-type measurement (taken from [8])*

## 3.3. Calculation of non-uniform current density $I_{corr}$:

In the case of localized corrosion, corrosion density $I_{corr}$ is used instead of $i_{corr}$ to account for the non-uniform morphology of corrosion. However, because of the impossibility of direct visual inspection of the corroded part of the structure, it is difficult to determine the actual surface of active rebar. Therefore, the RILEM TC-154-EMC [5] decided to consider that the non-uniform corrosion density is equal to the instantaneous corrosion density which is derived from the $R_p$ measurement (Eq. 4). It was also suggested to use a magnification factor α to account for pitting corrosion which results in another corrosion current density at the pitting site defined as $I_{pit}$ (Eq. 5). The factor α varies from 3 (several scattered pits) to 10 (severe localized corrosion) [9–11]. The authors confirmed the possible presence of a galvanic corrosion current $I_{galv}$ between anodic and cathodic zones which is only expressed according to the active surface. However, they also stated that microcell corrosion may permanently exist which prevents to have a direct correlation between $I_{corr}$ and $I_{galv}$ with $I_{corr}$ being greater than $I_{galv}$ (Eq. 6).

$$I_{corr}=i_{corr} \ [A/cm^2] \qquad \textit{Eq. 4}$$

$$I_{pit}=\alpha \ I_{corr} \ [A/cm^2] \qquad \textit{Eq. 5}$$

$$I_{corr} \geq I_{galv} \ [A/cm^2] \qquad \textit{Eq. 6}$$

## 3.4. Calculation of the penetration of attack (steel cross-section loss)

The penetration rate $V_{corr}$ is deduced from the corrosion current density $I_{corr}$ using Faraday's law as presented in Eq. 7.

$$m = \frac{M\ I\ t_{prop}}{Z\ F} \qquad \textit{Eq. 7}$$

Where:

- m is the metal loss (g);
- M is the molar mass of steel equal to 55.8 g/mol;
- I is the corrosion current (A);
- $t_{prop}$ is the corrosion propagation duration (s);
- Z is the metal valence equal to 2 [12];
- F is the Faraday constant equal to 96500 A.s/mol.

All the corrosion current is supposed to reduce the steel cross-section. Hence, it is supposed that a density of current of 1µA/cm² corresponds entirely to a loss of steel section $V_{corr}$ of 11.6 µm/year (Eq. 8). The penetration of attack $P_x$ for a propagation duration can be calculated with Eq. 9. The maximum penetration depth $P_{pit}$ corresponding to maximum cross-section loss is calculated by multiplying the uniform penetration depth with the factor α (Eq. 10). This factor can be considered equal to 2 in case of uniform loss in diameter around the bar.

$$V_{corr}\ [\mu m/year] = 11.6\ I_{corr}\ [\mu A/cm^2] \qquad \textit{Eq. 8}$$

$$P_x\ [\mu m] = V_{corr}[\mu m/year]\ t_{prop}\ [year] \qquad \textit{Eq. 9}$$

$$P_{pit} = \alpha\ P_x\ [\mu m/year] \qquad \textit{Eq. 10}$$

## 3.5. Ranges of corrosion current densities associated with the service life of reinforcement

Table 1 presents the ranges of corrosion and penetration rates with the corresponding corrosion levels. It can be seen that the threshold corrosion density for a high level of corrosion is 1 µA/cm$^2$ corresponding to a penetration attack of 0.01 mm/year or 0.1 mm/year in the pitting zone.

Fig. 4 presents a flowchart summarizing the different steps for the estimation of the service life of reinforced concrete structures according to the corrosion density measurement protocol and the service life approach that is detailed in the RILEM TC-154-EMC paper [5].

*Table 1. Ranges of corrosion and penetration rates with the corresponding corrosion levels [5]*

| $I_{corr}$ [$\mu A/cm^2$] | $V_{corr}$ [mm/year] | Corrosion level |
|---|---|---|
| $\leq 0.1$ | $\leq 0.001$ | Negligible |
| 0.1-0.5 | 0.001-0.005 | Low |
| 0.5-1 | 0.005-0.010 | Moderate |
| >1 | >0.010 | High |

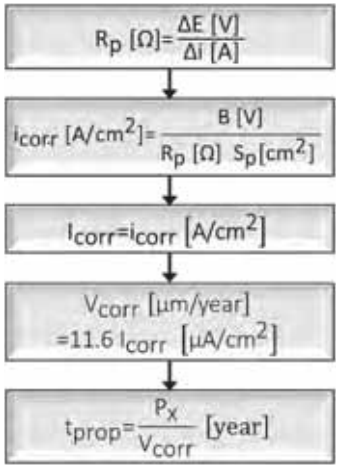


*Fig. 4. Flowchart of steps used for the estimation of the service life of reinforced concrete structures under risk of corrosion*

## 3.6. Shortcomings and limitations of this approach

Some possible limitations of the measurement methodology presented in the RILEM TC-154-EMC report [5]:

- The linear polarization resistance (LPR) technique used to determine the corrosion current density suffers from a lack of reliability. To improve the physical understanding of this technique, Clément et al [7] used finite element modeling to highlight the limitations of the approach. It was found that the polarizing current is not uniformly distributed on the steel surface causing an important source of error not taken into account by the experimental protocols [7]. This result was also found by Elsener [13] who stated that this measurement could lead to an erroneous corrosion current density of the anode to a factor of 10.
- Clément et al [7] also found that the measurement with an annular counter-electrodes with confining devices was a three-dimensional physical problem only solvable with numerical simulation. Besides, the numerical simulation highlights an additional complexity induced by the use of a guard ring that does not confine the current of polarization injected by the counter electrode but polarizes itself the reinforcement network [7].
- The Stern-Geary equation [6] used to estimate the rate of corrosion, is based on the hypothesis of uniform corrosion which is not representative of non-uniform corrosion commonly encountered in reinforced concrete. Indeed, Angst and Büchler [14] analyzed theoretically and experimentally the applicability of the Stern-Geary equation in case of galvanic corrosion and found that two main errors compensate each other out, making this equation applicable in case of specific conditions [14].
- Another doubt concerning LPR measurements is the ohmic drop between the three electrodes [13]. If correction of the ohmic drop is not well realized, the uncompensated polarization resistance is hence always greater than the real one and may thus be dependent on the electrical resistivity of concrete. The LPR devices usually have a built-in feature of ohmic drop correction. Usually, such devices attempt to separate the instant potential drop from the slower potential decrease and use the instant drop for ohmic drop compensation. However, the separation of these two effects may be questionable [15].
- Finally, observations of localized corrosion patterns of reinforcement bars show that the extension of the anodic area on the length of the rebars (longitudinal extension) is always more marked than the cross-section steel loss (the extension at depth) [4]. Indeed, the corrosion current densities are always higher at the boundary of the anodic site resulting in a higher galvanic coupling at the surface than at depth. Hence, it can be assumed that the total anodic corrosion current contributes not only to cross-section steel loss (extension at depth) but also and mainly to the extension of the anodic area on the

length of the rebars (longitudinal extension). Consequently, the use of the total current density to calculate the cross-section mass loss is conservative [4].

# 4. Empirical models for corrosion propagation in reinforced concrete

Empirical models are based on experimental results which are usually deduced from laboratory tests realized in controlled environments. The main advantage of these models is that they are simple and easy to use especially in the case of engineering purposes. Moreover, the input parameters needed are usually easy to measure. Besides, these models can be used as a foundation for other mathematical and numerical models. One of the main disadvantages of all the empirical models is that they are, in most cases, dependent on the conditions of the experimental set-up used. The experiments are usually realized in controlled environments which engenders the isolation of some parameters from the others leading to the neglect of possible interaction between them. Hence, the application of empirical models may be limited to some conditions but they can be enhanced using numerical approaches. In the case of such models, it is important to indicate the conditions of the experimental investigation and more specifically the limitations of the model itself.

## 4.1. Experimental work of Alonso et al. (1988)

The beginning of all empirical models for corrosion current density prediction is based on a work realized by Alonso et al. [16]. The authors realized a statistical analysis of carbonation-induced experiments. The reinforced test specimens (20 x 55 x 80 mm) were made of mortar with six different types of binders (Portland cement (PC), slag cement, pozzolanic cement, sulfate resistant PC, fly ash (FA) cement and 70/30 PC/FA) with a water/binder ratio of 0.50. After 8 days of curing (RH=100% and T=20±2°C), the specimens were carbonated in a CO2-filled chamber with different relative humidity (between 50 and 70%) followed with exposure to successive humidity periods of 100 and 50% and partial immersion. Carbonation was considered complete when the samples' weight stabilized. The authors transformed $R_p$ determined from LPR measurements in terms of corrosion current densities based on the Stern-Geary equation [5] using a predefined constant B equal to 26 mV.

The potentiostat, used for electrochemical monitoring, measures the ohmic drop between the reference electrode and the steel bar and compensates automatically the ohmic drop from the polarization resistance measurements (positive feed-back method). The authors [16] found a direct relation between calculated corrosion current densities and electrical resistance of concrete measured by the potentiostat. The electrical resistance measured by the potentiostat was not transformed into resistivity because of the difficulty of the calculation of the transformation factor from the geometrical position of the electrodes.

The step between corrosion current and resulting corrosion current density $i_{corr}$ is always questionable, and here, authors used a surface of 6 $cm^2$ which was not clearly defined but could probably be the total surface of the tested rebar.

Even though in this work, corrosion is induced by carbonation, the presented procedure is similar to another experimental study which was realized by Molina et al. [17] in the presence of chlorides. The authors also showed, in their work, the relationship between current densities of steel and electrical resistivity and ambient humidity.

While the aim of this work was not to arise with a corrosion current density prediction model, the corrosion-resistivity relation was considered by other researchers as a propagation prediction model with electrical resistance as an input parameter.

The experimental results of this work showed a strong relationship between corrosion current density and concrete electrical resistance that was determined as the ohmic drop compensation. This implies that electrical resistivity could act as a controlling element of the corrosion propagation process.

$$i_{corr} = \frac{K_{corr}}{R_c} \qquad \text{Eq. 11}$$

Where:

- $i_{corr}$ is the corrosion current density (µA/cm$^2$);
- $K_{corr}$ is the constant with a value of $10^4$ µA. Ω /cm$^2$;
- $R_c$ is the electrical resistance of concrete measured using the potentiostat (Ω).

## 4.2. Model by Liu et Weyers (1998)

### 4.2.1. Description of the experimental set-up

Liu and Weyers's empirical model [18] was developed based on statistical analyses of a 5-year corrosion study realized on 44 uncracked reinforced concrete bridge decks (1180 x 1180 x 216 mm) with covers of 25, 51 and 76 mm which were exposed to outdoor conditions. The cement contents ranged from 337 to 382 kg/m$^3$ and water/cement ratios of 0.41, 0.42, 0.43 and 0.45. Different amounts of sodium chlorides were mixed in the fresh concrete (from 0 to 7.2 kg/m$^3$). The type of cement used was not indicated in the study but could probably be an ordinary Portland cement.

Corrosion current density measurements were performed using the linear polarization technique using both 3LP and Gecor devices. Both devices measure the resistance of the concrete cover with potentiostatic and galvanostatic tests respectively and deduct it from the polarization resistance measurements. The Stern-Geary equation [6] is then used to calculate the corrosion intensity using a predefined Tafel slope constant (40 and 26 mV/dec for 3LP and Gecor respectively). The corrosion current density is then obtained by dividing corrosion intensity with the corresponding area of polarized steel. In the case of the 3LP device, the polarized surface is assumed to be the surface area of the tested reinforcing bar over the length of the rectangular counter electrode which was 178 mm. while, in the case of the Gecor device, the surface is considered to be the surface area of the bar over a length midway between two outer half cells which was 130 mm. The results of corrosion densities obtained with the two devices have a difference of one order of magnitude (factor of 15).

Type T thermocouples placed at the depth of the steel surface allowed the measurement of the internal temperature of the steel/concrete interface. Metal loss measurements were also realized and compared with the corrosion current densities of samples that showed corrosion-induced cracks.

### 4.2.2. Corrosion current density prediction model

The corrosion current density derived from this study was a non-linear regression prediction model presented as shown in Eq. 12.

$$i_{corr} = 0.92 \cdot \exp\left(7.89 + 0.7771 \ln(1.69Cl) - 3006\left(T^{-1}\right) - 0.000116R_c + 2.24t^{-0.215}\right) \qquad \text{Eq. 12}$$

Where:

- $i_{corr}$ is the corrosion current density (µA/cm$^2$);
- Cl is the total chloride content at the steel/concrete interface (acid-soluble) (kg/m$^3$);
- T is the temperature at the steel surface (K);
- $R_c$ is the electrical resistance of the concrete cover (Ω);
- t is the corrosion time (years).

They also derived another corrosion current density model for water soluble chloride contents (free chlorides $Cl_{Free}$):

$$i_{corr} = 0.92 \cdot \exp\left(8.37+0.618 \ln\left(1.69Cl_{Free}\right) -3034\left(T^{-1}\right)-0.000105R_c+2.32t^{-0.215}\right) \quad \textit{Eq. 13}$$

### 4.2.3. Input parameters

The input parameters of the model are summarized in Table 2.

*Table 2. Input parameters of Liu and Weyers's model*

| Category | Subcategory | Input parameter |
|---|---|---|
| Material | Concrete | Cover resistance |
| Environment | Chlorides | Total chloride content at the steel/concrete interface |
| | Temperature | The temperature at the steel surface |
| Time | | Time of active corrosion |

### 4.2.4. Major findings of this work

- The authors found a correlation between current densities measured with the 3LP technique and the chloride content, resistivity, temperature and active corrosion time.
- The authors calculated average corrosion current densities from the weight loss measurements and found that the 3LP device overestimates current densities whereas the Gecor underestimates them. Hence, the model obtained with the 3LP method could be calibrated with the weight loss measurements and divided with a factor of 1.55.

### 4.2.5. Some limitations of the model

Similar to Alonso et al.'s model [16], the determination of corrosion current densities was realized using methods based on LPR techniques and the Stern-Geary equation and the polarized surface is supposed to be in correlation with the size of the measurement device.

### 4.2.6. Upgrade of the model - Balafas and Burgoyne's model

Balafas and Burgoyne [19] revisit this model then Balafas interpreted the results obtained by Lopez et al. [20] and proposes the following relationship between $R_c$ (in Ω) and relative humidity (RH) (Eq. 14). This equation can be substituted in Eq. 12 and Eq. 13.

$$R_c = 90.537\ RH^{-7.2548}\left(1 + \exp\left(5-50(1-RH)\right)\right) \quad \textit{Eq. 14}$$

A French national project EVADEOS ANR [21] presented a synthesis of the simplified models used for the prediction of current densities of reinforcement in concrete, in carbonated and chloride medium. The project developed an experimental campaign based on slabs tested during the ANR APPLET program from 2007 to 2010 to compare the existing models and recommend the best model for corrosion prediction.

The test specimens used were reinforced slabs (300 x 300 x 50 mm) with steel bars with a diameter of 6 mm and a length of 400 mm where only a length of 200 mm is exposed to corrosion. The slabs were prepared using a Portland cement-based concrete (275 kg/m3) with a cover thickness of 22 mm and a high water/cement ratio of 0.7 to promote corrosion. Parts of the slabs were doped with 5% NaCl

by weight of cement then exposed for 2 years to the outside atmosphere of Saclay, France. After almost 2 years, autopsies were performed and average corrosion current densities were quantified using gravimetric measurements.

It was found that the Balafas model predicts the closest steel weight loss induced by corrosion to that determined on test samples [21]. The advantage of this model is that it integrates the majority factors influencing the kinetics of corrosion. Besides, it takes into account the decrease in corrosion kinetics over time [21].

## 4.3. Model by DuraCrete (1998)

### 4.3.1. Corrosion current density prediction model

The DuraCrete model [22] is an extension of Alonso's corrosion-resistance relation (1988) [16]. Influencing factors were added to the old model to take into account the galvanic aspect of corrosion and also the impact of chloride content, growth of oxide layer and availability of oxygen giving the model presented in Eq. 15

$$i_{corr} = \frac{K_{corr}}{\rho\,(t)}\; F_{Cl}\; F_{galv}\; F_{Oxyde}\; F_{Oxy} \qquad \textit{Eq. 15}$$

where:

- $i_{corr}$ is the corrosion current density (µA/cm$^2$);
- $K_{corr}$ is the constant regression parameter equal to $10^4$ ;
- $F_{Cl}$, $F_{Galv}$, $F_{Oxyde}$, $F_{oxy}$ are parameters of adjustment to take into account respectively the chloride content, the galvanic corrosion effect, the growth of the oxide layer and the availability of oxygen;
- ρ(t) is the electrical resistivity of concrete (Ω.m) at time t presented in Eq. 16.

$$\rho\,(t) = \rho_0\; f_e\; f_t \left(\frac{t}{t_0}\right)^n \qquad \textit{Eq. 16}$$

where:

- $\rho_0$ is the electrical resistivity of concrete at time $t_0$ (Ω.m);
- N is the factor taking into account the influence of aging on $\rho_0$;
- $f_e$ is the factor that modifies $\rho_0$ to account for the environmental exposure conditions;
- $f_t$ is the factor that reflects the influence of the test method for measuring the resistivity.

In the work developed by Alonso et al [16], $i_{corr}$ is implicitly supposed to take into account the non-uniform morphology of corrosion mainly because of the limited steel surface used for measurement. However, the model Duracrete [22] proposed an extension of the model presenting explicitly the non-uniform characteristics of corrosion using parameters linked to the cathode ($F_{oxy}$), the anode ($F_{Cl}$, $F_{Oxyde}$) and the galvanic aspect of corrosion ($F_{Galv}$).

### 4.3.2. Some limitations of the model

- While the model takes explicitly into account the non-uniform aspect of corrosion, the surface used to calculate the corrosion current density density is not defined.
- While influencing factors were mentioned in this model, no quantitative value is given and no procedures are specified on how to obtain or predict these factors.

## 4.4. Model by Scott (2004)

### 4.4.1. Description of the experimental set-up

Scott's model [23] was developed using experimental results based on cracked beam specimens (120 x 120 x 375 mm) with concrete covers of 20 and 40mm and crack widths of 0.2 and 0.7mm. Scott realized a variety of binder type with a constant w/b ratio of 0.58 and used ordinary Portland cement (PC) and formulations with different percentages of slag (25/75 PC/GGBS, 50/50 PC/GGBS, 75/25 PC/GGBS) and formulations with fly ash (70/30 PC/FA) and silica fume (93/7 PC/SF) and a combination of slag and silica fume (50/43/7 PC/GGBS/SF). The author used smooth and ribbed steel bars with a diameter of 16 mm and a length of 355 mm. The steel was wire brushed then cleaned before casting with acetone to remove the mill scale layer. The electrical connection was realized by a copper wire attached to the steel at one end of the bars. The concrete specimens were cast face down then cured for 14 days at 23 °C then moved to a climate control room set at 30 °C where they were subjected to cycles of 3 days of ponding in 5% NaCl solution followed with 4 days of drying.

The authors used a coulostatic method to determine the polarization resistance $R_p$ which is calculated using the applied current density and is expressed in $\Omega.cm^2$. The coulostatic method is based on an LPR technique that measures the relaxation of the potential under charge after a known duration. The corrosion current densities were then calculated using the Stern-Geary [6] equation with a constant Tafel slope equal to 26.

### 4.4.2. Corrosion current density prediction model

The proposed corrosion current density prediction model is presented in Eq. 17:

$$i_{corr} = \left(1.43\frac{C_c}{f} + 0.02\right) e^{\left[\left(\frac{40-x}{20}\right)1.2\left(\frac{C_c}{f}\right)^3\right]} \qquad \text{Eq. 17}$$

where:

- $i_{corr}$ is the corrosion current density ($\mu A/cm^2$);
- F is the slag correction factor equal to $10^{(|0.5-S|-0.5+S)}$;
- S is slag substitution level expressed as a decimal;
- $C_c$ is the chloride conductivity index value at 90 days (mS/cm);
- x is the concrete cover depth between 20 and 40 mm (mm).

### 4.4.3. Input parameters

The input parameters of this model were all related to concrete and are presented in Table 3.

*Table 3. Input parameters of Scott's model*

| Category | Subcategory | Input parameter |
|---|---|---|
| Material | Concrete | Cover thickness |
| | | Substitution level of slag |
| | | Chloride conductivity |

### 4.4.4. Major findings of this work

The work realized by Scott et al. particularly focused on the impact of cement additions on multiple characteristics of corrosion of steel in concrete. The authors found that:

- Analysis of the chemistry of pore solution derived from pastes showed an important dependence of hydroxide concentration on binder type with SF having the lowest concertation.
- Samples with slag had significant levels of sulfides and thiosulfate, low levels of dissolved oxygen and very negative redox potentials which could limit the development and effectiveness of the passive layer.
- Experiments realized in concrete and simulated pore solutions under passive conditions (before adding chlorides) allowed to find that very high corrosion current densities compared to other binder types were found in case of materials containing slag.
- Corrosion current densities were more sensitive to electrical resistivity (inverse of conductivity) than the composition of pore solution and the oxygen availability linked to the cover depth except when the resistivity is low such as in the case of PC.
- The corrosion density was more sensitive to the type of binder than to the crack width.
- No important correlation was found between corrosion current densities and oxygen diffusion and water sorptivity indexes which provides information on pore geometry of concrete.

#### 4.4.5. Some limitations of the model

- The model was built on results from cracked specimens hence it is probable that only fast corrosion initiation occurring at crack location influences the measurements of $R_p$ making this model not representative of the behavior of uncracked structures.
- The reinforcement bars used in the experimental set-up were round smooth and ribbed steel bars and they were cleaned with acetone to remove the mill scale layer. This type of surface condition of steel (without mill scale) does not represent a realistic surface condition and could have an influence on the corrosion currents obtained [3].
- The experimental investigation was realized for a fixed chloride concentration (5% NaCl solution) and temperature (30$^{o}$C) and the impact of both parameters was not studied.
- Similar to previous models, the determination of corrosion current densities was realized using methods based on LPR techniques and the Stern-Geary equation.

### 4.5. Other models

Other empirical models were also developed to predict the corrosion density in concrete. Some of these models were based on accelerated corrosion tests (with initially admixed chlorides or the use of impressed current) or depend on parameters linked to the composition of the formulation used instead of durability indicators or environmental parameters.

#### 4.5.1. Vu and Stewart's model (2000, 2005)

The model proposed by Vu and Stewart in the year 2000 [24] is based on a lifetime analysis of a reinforced concrete slab bridge and is built on the assumption that oxygen availability at the steel surface is the controlling element and may not be valid in case of anodic and ohmic controls of corrosion propagation. Moreover, this model is proposed in the context of accelerated corrosion which does not represent corrosion in real structures. More importantly, the prediction model is only a function or w/b ratio, cover depth (C in cm), time to corrosion initiation ($t_i$) and time (t) and is not a function of durability indicators nor cement type. The corrosion current density $i_{corr}$ for a RH of 75% and a temperature of 20 $^{o}$C is expressed in ($\mu A/cm^2$) as follows:

$$i_{corr} = \left( \frac{32.13(1- w/b)^{-1.64}}{C} \right) (t-t_i)^{-0.29} \qquad \textit{Eq. 18}$$

An attempt to improve the model was realized by Vu et al in 2005 [25] to take into account the time-variant nature of corrosion current density as follows:

$$i_{corr} = \left( \frac{37.8(1- w/b)^{-1.64}}{C} \right) \alpha (t-t_i)^{\beta} \qquad \textit{Eq. 19}$$

with:

$$\alpha = \begin{cases} 0.85 & \text{if corrosion is time-invariant} \\ 1 & \text{if corrosion is time-variant} \end{cases} \qquad \beta = \begin{cases} -0.29 & \text{if corrosion is time-invariant} \\ 0 & \text{if corrosion is time-variant} \end{cases}$$

### 4.5.2. Yalcyn and Ergun's model (1996)

Yalcyn and Ergun [26] determined the corrosion current density using the LPR technique in concrete with admixed chloride and acetate ions (accelerated corrosion). The predictive models based on experimental investigations carried out on uncracked concrete cylindrical specimens (ϕ150 × 150 mm) formed with 10 % of pozzolanic cement is presented in Eq. 20.

$$i_{corr} = i_0 e^{-Ct} \qquad \textit{Eq. 20}$$

where:

- $i_{corr}$ is the corrosion current density at time t (μA/cm$^2$);
- $i_0$ is the initial corrosion current density (μA/cm$^2$);
- C is the constant evaluated from experimental curves and is a function of pH, permeability, degree of concrete pore saturation and cover thickness and was find equal to $1.1\times10^{-3}$ day$^{-1}$.

## 4.6. Summary and discussion

Fig. 5 shows a timeline of the previously presented empirical models developed for the prediction of corrosion current density and the chronological order of the different influencing factors that were implemented in these models.

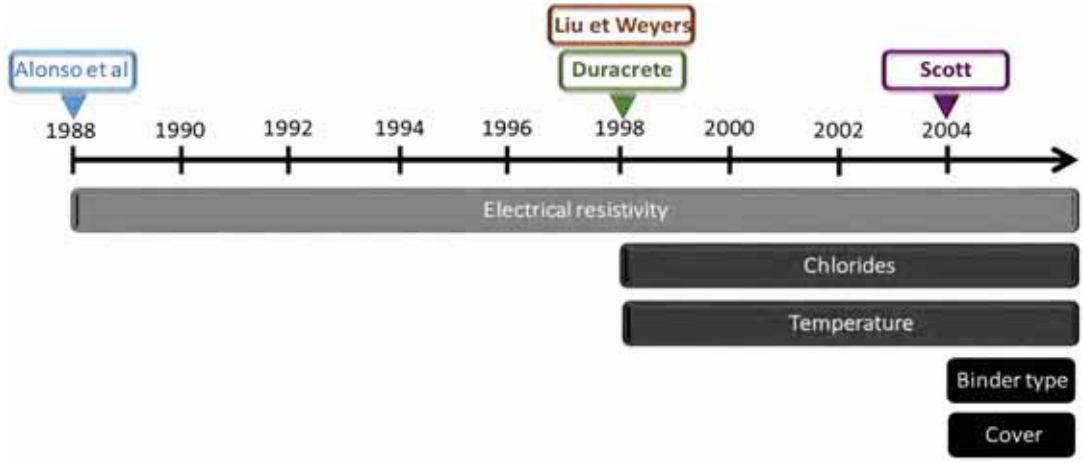


*Fig. 5. Timeline of the contribution of the previously presented empirical models and the influencing parameters implemented in these models*

Table 4 summarizes the different techniques and measurement devices used to quantify corrosion current densities according to the procedures adopted by these models.

Lots of these models supposed to implicitly take into account the non-uniform characteristics of corrosion but used the LPR technique or a method based on this technique to determine the polarization resistance accounting only for uniform corrosion. Some were completed by additional influencing factors to account for macrocell corrosion (such as DuraCrete [22]). Also, the models used

the Stern-Geary equation to calculate $i_{corr}$. The major difference between measuring techniques is the considered area of the polarized steel surface.

To compare the output of the models, corrosion current densities were calculated using the corrosion rate equations for the same preselected conditions mentioned below:

- Concrete based on ordinary Portland cement (OPC);
- T=20 °C (ambient temperature is considered equal to the temperature at the depth of the rebar);
- Total chloride content= 3.4 kg/m$^3$ which is equivalent to 1%/wt. cement for a cement content of 340 kg/m$^3$;
- Chloride conductivity index= 0.8 mS/cm;
- Concrete cover= 20 mm with a resistance of 10000 Ω;
- Corrosion time t= 1 year.

According to Table 4, it can be seen that the corrosion current densities obtained are in the same order of magnitude.

*Table 4. Comparison between the measurement techniques and corrosion current densities of the presented models*

| Model | Alonso et al. (1988) [16] | Liu et Weyers (1998) [18] | Scott (2004) [23] |
|---|---|---|---|
| LPR Technique | Potentiostatic technique + Stern-Geary equation | Potentiostatic technique + Stern-Geary equation | Coulostatic method + Stern-Geary equation |
| Measuring device | Potentiostat | 3LP | not mentioned |
| B (mV) | 26 | 40 | 26 |
| Polarized area | $S_p$=6 cm$^2$ | $S_p$=89 cm$^2$ Surface area of rebar over the length of rectangular counter electrode, 178 mm | not mentioned |
| $i_{corr}$ (µA/cm$^2$) | 1 | 1 | 2 |

## 5. Parameters affecting macrocell corrosion propagation

There is a great number of factors that could affect the chloride-induced corrosion current density of steel in concrete. In the next section, an overview of many influencing parameters and their impact on the corrosion current density will be presented.

It must be noted that most of these parameters may interact making it complicated to completely isolate the impact of each element. Yet, the examination of the individual influence of several parameters on corrosion propagation will allow to better understand the nature of the corrosion process.

### 5.1. Chloride content

Liu and Weyers [18] studied the influence of chloride contents on corrosion propagation. They found that corrosion current densities increased with the level of chloride content in concrete. The authors stated that this could be explained by the increase in conductivity of concrete induced by chloride ions. They also indicated that chloride ions can react with ferrous ions and form a water-soluble product that can accelerate corrosion. Arya and Xu [27] suggested that for a given mix, the free chloride content is a major factor influencing the corrosion current density. Indeed, a high free chloride content is associated with high concrete conductivity.

## 5.2. Electrical resistivity

The corrosion reaction requires both a flow of electrons and ions to complete the circuit. Hence, electrical resistivity and resistance of the concrete to the flow of ions will also affect the corrosion current density as demonstrated by Alonso et al. (1988) [16]. Many researchers were interested in studying the impact of electrical resistivity on the corrosion current density of reinforcing steel in concrete [16,20]. Several factors (like relative humidity, temperature, cement and binder type, presence of ions in pore water such as chlorides) can considerably affect the electrical resistivity of concrete [28]. It is more likely to establish a direct relationship between water saturation and resistivity [28]. Indeed, Tuutti [29] stated that for RH greater than 90%, cathodic control becomes effective thus the maximum expected corrosion current density would occur where the RH of the concrete is between about 85 and 90%.

The electrical resistivity of concrete gives indications on the pore connectivity of concrete and consequently, on its resistance to the penetration of gaseous or liquid elements. Concrete resistivity is dependent on concrete quality, pore connectivity, degree of saturation (SR) of concrete, chloride contamination, carbonation, and temperature, etc. The ohmic resistance of the same concrete may vary considerably between dry and saturated environments. Knowing that the pore connectivity mainly depends on the binder type, the resistivity also varies significantly between concretes with different binder types for the same environmental conditions. Carbonation and chloride concentration have also a direct important impact on electrical resistivity. In the case of carbonation, an increase of electrical resistance is observed and may be attributed to the precipitation of $CaCO_3$, and alumina, silica and ferric oxides, which causes the decrease of the quantity of ions in the pore water [16]. Whereas, in the presence of chlorides, the electrical resistance of concrete decreases due to the increase of ionic conductivity in the pore solution of concrete.

Corrosion of steel in concrete is a reaction that needs a sufficient degree of saturation that corresponds to a sufficient amount of electrolyte for the flow of the ionic current and a sufficient amount of oxygen for the cathodic reaction. The quantity of oxygen at the steel/concrete interface is usually abundant [16]. Consequently, the corrosion current density increases when the concrete resistivity decreases. On the other hand, in the case of totally immersed structures, the corrosion current density is usually weak since it is controlled by oxygen availability also known as cathodic control even if the ohmic resistance is very low.

## 5.3. Binder type

The use of cement additions and substitutions with different binder types has become very popular and encouraged due to economic and environmental benefits. The use of these materials has a significant effect on the chemical and physical properties of concrete which indicates their possible impact on corrosion propagation of steel in concrete.

The corrosion process is dependent on the chemical environment at the steel/concrete interface which is affected by the cement matrix, while the nature of the corrosion products is determined by the availability of oxygen. Corrosion propagation is also dependent on the ionic flow in concrete and the electrochemical properties of the steel-concrete interface. Moreover, in the presence of chlorides, the chloride binding capacity is also affected by the type of binder. Therefore, it is expected that the type of binder used in concrete can have a significant effect on the corrosion behavior of steel.

Table 5 presents the ranking order of corrosion current densities for different binder types (Portland Cement (PC), Blast furnace Slag (BFS), Fly Ash (FA), Silica Fume (SF)) according to results published by different researchers. A more detailed overview of these findings is presented in the next section followed by a detailed explanation of the possible impact of each binder type on corrosion in concrete.

Schiessl and Raupach [30] found a reduction in macrocell corrosion when substituting the OPC with different binder types in concrete made with 2% of chlorides by mass of cement however there were relatively small differences in corrosion current densities between the various binder types.

Arya and Xu [27] studied a range of mixes by measuring the macrocell galvanic current using a zero resistance ammeter between steel bars embedded in two layers of concrete: the lower layer dosed with different levels of chloride at the time of mixing contains a mild steel electrode (ϕ8 x 50 mm) acting as anode and the upper layer, which is chloride free, contains two mild steel electrodes (ϕ8 x 500 mm) acting as cathode. They found that for a 3% addition of chlorides at the time of mixing, the ranking order of corrosion current density was FA>PC>S>SF, whereas, for 1% of chlorides the order became FA>SF>S> PC.

Sirivivatnanon et al. [31] investigated the effect of various replacement levels of cement with other binders with machined and polished steel on the corrosion current density of steel in mortars exposed to 3% NaCl with a 10 mm cover. The authors found corrosion current densities ranked as follows: PC > 5% SF > 20% FA > 40% FA > 40% BFS > 60% BFS > 60% FA > 80% BFS > 10% SF.

Scott [23] calculated, with the Stern-Geary equation, corrosion current density measured, with a coulostatic method based on the LPR technique, on cracked beam specimens crack widths of 0.2 and 0.7mm with concrete covers of 20 and 40mm. He tested several concrete mixes and found the corrosion current density in the following ranking order PC>7%SF>25%S>30%FA>50%S>75%S.

*Table 5. Summary of the ranking order of corrosion current density according to different binder types*

| Ranking order of corrosion current density according to different binder types | References |
|---|---|
| FA>PC | [27,32] |
| PC>FA | [33] |
| PC > 20%S > 10% SF > 26% FA > 42% S<br>(at 100 days) | [30] |
| PC > 5% SF > 20% FA > 40% FA > 40% S > 60% S > 60% FA > 80% S > 10% SF | [31] |
| PC>7%SF>25%S>30%FA>50%S>75%S | [23] |
| 35%FA>PC>65%S>10%SF (3% addition of chlorides at the time of mixing)<br>35%FA>10%SF>65%S> PC (1% addition of chlorides at the time of mixing) | [27] |
| PC>SF | [32,34] |

### 5.3.1. Silica fume

Arya and Xu [27] measured the galvanic current in samples with different mixes of concrete (with Portland cement, silica fume, slag and fly ash) where chloride was introduced as NaCl at the time of mixing. They stated that lower corrosion current densities with SF may be linked to the physical characteristics of the matrix (for instance diffusion of ferrous ions and oxygen) rather than the chemistry of pore solution [27]. Page and Havdahl [34] studied corrosion behavior of steel in microsilica cements by corrosion potential and linear polarization measurements. They found that when increasing the replacement levels of microsilica in pastes for a constant total chloride content and water content, the $[Cl^-]/[OH^-]$ ratio in pore water increases. The authors [34] suggested that this tended to destabilize the passivity of steel at the beginning but the effect became less significant with curing and the growth of anodic sites was restrained indicating the good resistance of microsilica to corrosion. This result was also found by Mangat et al. [32]. Page and Havdahl [34] explained this result by the fine pore structure of the material which limits the mobility of chloride ions near the embedded steel surface.

### 5.3.2. Slag

Arya and Xu [27] found that mixes with slag had higher chloride binding capacity than that of PC resulting in lowering the Cl- concentration in pore solution which could induce lower corrosion current densities. Valentini et al. [35] measured the corrosion potential of steel in mortar specimens with different levels of slag stored at 100% RH. They found that potentials, in slag bearing samples with substitution levels of 20 and 45%, were initially highly negative but tended to decrease over time especially when stored at 50% RH. Samples with a replacement level of 75% had the lowest initial potential that quickly risen to values similar to those of PC. The authors measured the corrosion current density of the steel bars using the polarization resistance method and found that current densities were approximately 10 times greater for material with slag and quickly dropped with time and became similar to those of PC samples [35]. The authors [35] highlighted the possible impact of oxygen availability and electrical resistivity on these experimental outcomes. Tromans [36] suggested that in the case of slag concretes, sulfides present in the pore water may be combined with the passivation layer reducing its ability to protect the steel. This result was also observed in the pastes pore solution analysis realized by Scott [23]. Scott also found that, in presence of slag, lower dissolved oxygen contents were measured due to the conversions of sulfide to thiosulfate and finally sulfate causing incomplete passivation of rebars and thus inducing higher passivation corrosion current densities and lower Ccrit [23].

### 5.3.3. Fly ash

Arya and Xu [27] found higher corrosion current densities with FA and justified this result with the reduction in the concentration of $OH^-$ due to pozzolanic reactions of FA. This result was also provided by Mangat et al. [32] with FA having a higher corrosion current density than PC at a cover of 10 mm.

Thomas et al. [33] found lower metal loss for higher substitution levels of fly ash (FA) for reinforcement bars at cover depths of 10 and 20 mm.

When evaluating the reported results in the literature concerning the impact of binder type on corrosion, it appears that there is still no agreement on the influence of binder type on the corrosion current density of steel in concrete. The results were often inconsistent and contradictory. Some of these results could be majorly influenced by the test procedure (such as the linear polarization technique) rather than the impact of the binder type itself. The effect of binder type and cement additions needs further study to more accurately apprehend their chemical and physical impact on corrosion in the presence of chlorides.

## 5.4. Cathode to anode ratio

The cathode to anode (C/A) ratio is the ratio between the surfaces of passive steel and that of active steel. This factor usually depends on the volumetric density rebars in concrete but it varies with time. In fact, in real structures, the C/A ratio is initially very high but decreases with time due to the extension of the anodic area. Warkus and Raupach [37] studied experimentally and numerically the effect of this ratio and found that the increase in the C/A ratio caused the increase in macrocell galvanic current. Arya and Vassie [38] tested the influence of the C/A ratio by connecting different sets of rebars of a 4m long concrete beam containing 7 rebars bar which could be externally electrically connected. 3% of chlorides by weight of cement were added to mix water to initiate corrosion. The current flowing between different sets of rebars was monitored with a zero resistance ammeter. The authors [38] found that the current increased with the increase of C/A ratio up to a ratio of 190 with a variation slope that decreased with increasing C/A ratio.

## 5.5. Oxygen availability

Oxygen is an essential parameter for corrosion propagation, without oxygen no corrosion occurs. Alonso et al. (1988) state that cathodic control related to a limited supply of oxygen is only an issue when the concrete is underwater or soil, or the cover is sufficiently thick in was that the pores remain saturated. In the work realized by Lay et al. [39], it was stated that the effect of the availability of oxygen can be taken into account in corrosion propagation models by introducing a factor $F_{O_2}$ that is, in most cases, equal to 1 since oxygen availability is usually not limited except in case of submerged concrete. Oxygen availability is also affected by the binder type such as slag cement or cement substituted with different levels of BFS and alkali-activated slag cement [35,40–43].

## 5.6. Temperature

Temperature is an important element affecting the corrosion current density. The relation between the temperature and several thermally stimulated processes are usually described by the Arrhenius [44] equation as follows:

$$K=Ae^{\left(\frac{-E_A}{RT}\right)} \qquad \textit{Eq. 21}$$

where:

- K is the rate constant;
- A is the pre-exponential factor;
- $E_A$ is the activation energy (J/mol);
- R is the gas constant equal to 8.31 J/mol/K;
- T is temperature (K).

In reinforced concrete, temperature influences the electrolyte resistance [45], the electrochemical reactions at the cathode where it was found that the oxygen reduction current density increases with temperature [45,46] and finally the reactions at anode [45]. The relation between the temperature and these processes can be described by an equation similar to the Arrhenius [44] equation presented in Eq. 21 as follows:

$$I = I_0\, e^{b\left(\frac{1}{T_0}-\frac{1}{T}\right)} \qquad \textit{Eq. 22}$$

where:

- I and $I_0$ are corrosion current densities at T and $T_0$, respectively ($\mu A/cm^2$);
- b is the constant of Arrhenius law (K) which is equal to $\frac{E_A}{R}$;
- $T_0$ is the reference temperature (K);
- T is the temperature at measurement (K).

When considering the impact of temperature on electrolyte resistance and for reference temperature of 20 °C, the constant b is in the range of 1700 K (in case of synthetic pore solution with a pH of 13.5) and 3800 K (in case of concrete exposed at 60% of RH) [47]. Several researchers [45,48,49] have described the impact of temperature using the same relationship presented in Eq. 22. Constant b was found equal to 2283 K by Liu et al. [48].

Jäggi et al. [45] tested the impact of temperature on anodic and cathodic electrochemical reactions and macrocell currents. They measured the cathodic polarization curves on polished mild steel in synthetic pore solution with pH of 13.5 and on reinforced cylindrical (1D mortar samples) mortar samples (w/c=0.6) embedding at their center a degreased rebar. Also, the authors [45] measured macrocell current on mortar blocks (2D mortar samples) as a function of temperature. The coefficient

of the Arrhenius equation describing the temperature dependence were all in the same order of magnitude as shown in Table 6. The results they obtained were in good agreement with ones measured between an anode in instrumented cores and the rebar network bridge decks [50].

*Table 6. Arrhenius temperature dependence coefficient for anodic, cathodic and total macrocell current in solutions, (1D - 2D) mortar tests and field experiments (Taken from [45])*

| Current\Media | Solution | 1D mortar samples | 2D mortar samples | Field 3D |
|---|---|---|---|---|
| Macrocell | 4350 ± 80 | --- | 4210 ± 90 | 4000 ± 250 [50] |
| Anodic | 4300 | --- | --- | --- |
| Cathodic | 4310 | 4250 | --- | --- |

In general, a temperature increase leads to the increase of corrosion current density if the other influencing parameters are held constant. However, in reality, changes in temperature will result in changes of other parameters. For instance, the increase in temperature may lead to the drying of concrete causing the increase of its electric resistivity but also causes the increase of oxygen diffusion coefficient. Therefore, the effect of temperature on corrosion current density in concrete is very complicated and the direct application of the Arrhenius equation to the steel corrosion process in concrete may not be entirely simple because it could be controlled by interactions with other parameters and the environmental conditions of the reinforced structure. Lopez et al. [51] stated that the effect of temperature must always be considered with the moisture availability. This means that in case of continuous supply of electrolyte for example in case of saturated conditions in presence of chlorides, the rise in temperature is associated with a significant increase of the corrosion current densities since no concrete drying occurs. On the other hand, in case of a limited supply of electrolyte, such as dry or semidry environments, the corrosion current density can be comparatively low even at a high temperature owing to the high resistance of concrete.

## 5.7. Defects at the steel/concrete interface: “Top-bar effects”

Fresh concrete can settle in the formwork due to its own weight which usually promotes segregation and bleeding. These mechanisms induce defects usually located on the lower part of horizontal reinforcement bars according to the casting direction [52,53]. These settlements and bleeding regions may be entirely air-filled or partly water-filled and their size increases with the height of concrete below the reinforcing steel. Also, they usually occur when the steel bars are positioned at depths higher than 15 cm [54–56]. Top-cast horizontal bars show more defects on their lower side than the bottom-cast horizontal bars. This effect is called the "top-bar effect" and presents a common engineering situation known for its negative impact on steel/concrete bond properties. Defects at the steel/concrete interface are also known for being a critical factor influencing the corrosion of reinforced concrete [53–64]. They accelerate corrosion initiation and propagation in the re-bar [52,62]. Indeed, in the presence of defects, the cement hydration products are modified [65]. The lower side of the reinforcement bar in presence of defects behaves as an anode, whereas the rest of the bar is protected with denser concrete, mainly acts as the cathode [52,54]. This explains why corrosion is always initiated at the regions with defects [63]. In the unpublished work of Yu et al. [unpublished], four beams with the same concrete and cover depth were realized but were achieved with different casting directions and exposure conditions. The work focused on the study of load-induced cracks which were also coupled with the presence of top-casting-induced defects in the case of two beams. The authors realized cracking maps and measured the cross-sectional loss and chloride profiles of concrete. They found that in the presence of top-casting-induced defects, corrosion started at cracks and then propagated more easily. After corrosion initiation, the average weight loss, for the same exposure time, was almost twice bigger in the beams with top-casting-induced defects.

## 5.8. Summary and discussion

The localized nature of chloride-induced corrosion in concrete leads to the propagation stage which is influenced by several parameters related to materials (concrete and steel bars), environment (temperature, relative humidity, chloride concentration…), geometry (density and length of rebars), casting conditions, etc. Fig. 6 presents a flow chart of the different parameters affecting the corrosion current density and their possible interaction.

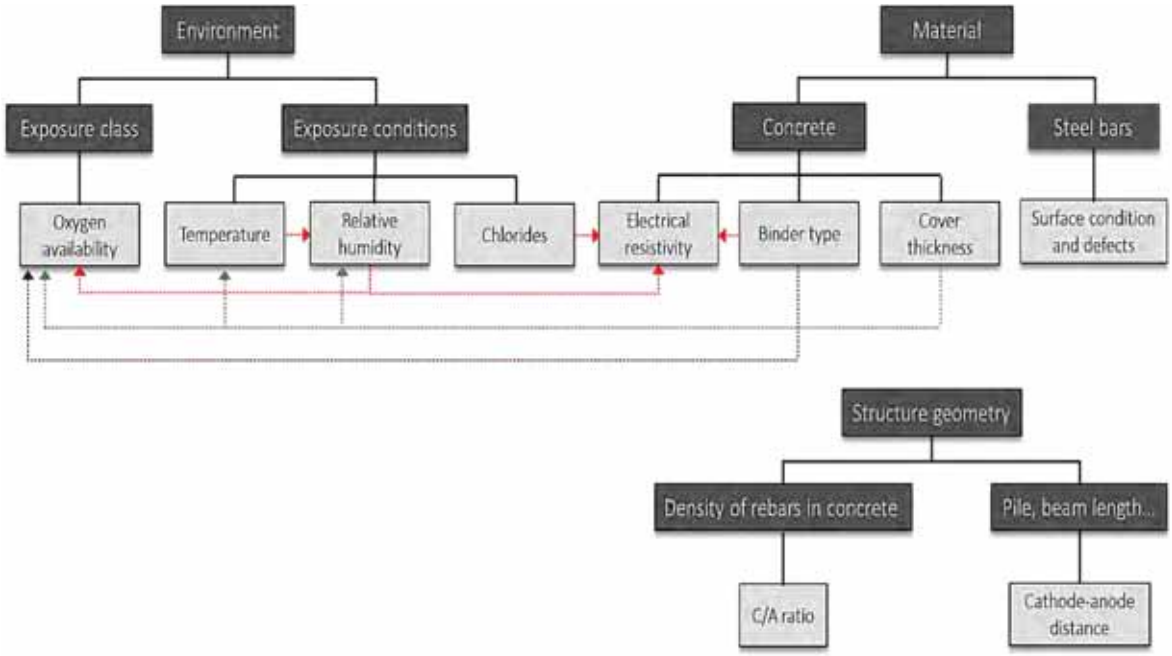


*Fig. 6. Flow chart of the different parameters affecting corrosion current density and their possible interaction*

Those parameters can also be classified as anodic, cathodic, geometric, ohmic and environmental parameters according to their impact on controlling corrosion propagation. For instance, the anodic parameters can be associated with steel surface conditions and defects, growth of corrosion products, chloride content, the cathodic process are mainly linked to oxygen availability and the ohmic process is controlled by the electrical resistivity. The geometric factors correspond to the C/A ratio and C-A distance. Finally, the environmental conditions are generally associated with temperature.

Table 7 summarizes the influencing parameters which were detailed earlier and their impact on corrosion current density $i_{corr}$.

*Table 7. Overview of the influence of several parameters on corrosion current density*

| Category | Parameter | | Effect on $i_{corr}$ | Relationship between parameter and corrosion current density | References |
|---|---|---|---|---|---|
| Anodic parameters | Chloride content | | ↑ | Corrosion current density proportional to the logarithm of chlorides | [18] |
| | | | | --- | [1] |
| | | | | Corrosion current density proportional to chloride conductivity index | [23] |
| | Binder type | FA | ↑ | No agreement on the influence of binder type | [27,32] |
| | | | ↓ | | [23,31,33] |
| | | SF | ↑ | | [27] |
| | | | ↓ | | [23,27,30–32,34] |
| | | S | ↑ | | [27] |
| | | | ↓ | | [23,27,30,31,35] |
| Cathodic parameters | Oxygen availability | | ↑ | oxygen availability is usually not limited except in case of submerged concrete | [39] |
| | | | | oxygen availability is affected by the binder type such as sulfide containing materials like slag | [35,40–43] |
| Ohmic parameters | Electrical resistivity | | ↓ | Inverse relationship | [16,22] |
| Geometric parameters | C/A ratio | | ↑ | --- | [37,38] |
| | C-A distance | | ↓ | --- | [38] |
| Environmental parameters | Temperature | | ↑ | Arrhenius law | [30,48,49] |
| Casting conditions | Top-bar effect | | ↑ | Accelerates corrosion initiation and propagation | [52,62] Yu et al. [unpublished] |

*↑ (↓) indicates an increase (decrease) in corrosion current density with an increase of the corresponding variable;*

# 6. Corrosion rate prediction model and its interpretation

## 6.1. Corrosion rate prediction model

A simplified empirical model was formed allowing to evaluate a part of the service life of reinforced concrete structures. The developed model allows to predict the maximum corrosion rate (directly after initiation) and is based on experimental results obtained from an experimental test, developed by Chalhoub et al. [3], based on the galvanic coupling between a cathode sample (ϕ110 x 220 mm) without chlorides representing passive steel and an anode sample (ϕ33 x 70 mm) which is oven-dried then soaked in sodium chloride solutions with different concentrations from 12 to 280 g/L. Several mortar and concrete formulations and different types of ribbed steel surface conditions were evaluated. The test was realized in a temperature-controlled room at 20 $^{o}$C.

In this paper, the results obtained with the specimens embedding as received rebars were only evaluated. The preparation of test specimens and their preconditioning is not presented in this paper but is detailed in previous work [3]. The developed model is based on the study of the separate influence of each parameter alone without coupling the effect of the interdependent factors.

The macrocell galvanic current density $i_{corr}$ between active corroding steel and passive steel is expressed in A/m$^2$ in Eq. 23. The detailed interpretation of the following corrosion density model will be discussed subsequently.

$$i_{corr} = \gamma_{Cl} \frac{K_{Cl} \; \frac{K_C}{A} \; K_T \; K_{O_2} \; K_f}{\rho} \qquad \textit{Eq. 23}$$

The corrosion current density parameters are presented in Table 8 and the input data needed to calculate these parameters are summarized in Table 9.

*Table 8. Factors of the corrosion propagation model*

| Factor | Meaning | Value or expression | Unit |
|---|---|---|---|
| $\gamma_{Cl}$ | Calibration constant | 0.173 | A.Ω./m |
| $K_{Cl}$ | Parameter related to free chloride contamination | $K_{Cl} = \frac{(\lvert Cl\text{-}C_{crit}\rvert + Cl\text{-}C_{crit})^{0.89}}{0.08}$ | ---- |
| $K_{\frac{C}{A}}$ | Parameter related to C/A ratio | 4 | ---- |
| $K_T$ | Parameter related to temperature | $K_T = e^{4220\left(\frac{1}{293} - \frac{1}{T}\right)}$ | ---- |
| $K_{O_2}$ | Parameter corresponding to the impact of oxygen availability | 0 or 1 | ---- |
| $\rho$ | Electrical resistivity of concrete | $\rho = \rho_0 K_{RH}$ | Ω.m |
| $K_{RH}$ | Factor related to the impact of RH on electrical resistivity | $K_{RH} = \left(\left(\frac{100}{RH}\right)^4\right)^d$ | ---- |
| $K_f$ | Parameter corresponding to the impact of the top-bar effect | $K_f = \begin{cases} 1 \rightarrow \text{No Top-bar effect} \\ 2 \rightarrow \text{Top-bar effect} \end{cases}$ Deduced from unpublished results of Yu et al. | ---- |

*Table 9. Input parameters of the corrosion propagation model and their corresponding data source*

| Input data | Meaning | Data source | Unit |
|---|---|---|---|
| $C_{crit}$ | Critical chloride threshold value | Depends on several parameters | %/wt. binder |
| Cl | Free Cl content | $Cl = C_{crit} + 0.3$ | %/wt. binder |
| T | Temperature | Determined from a meteorological Station near the studied structure | Kelvin |
| $\rho_0$ | Electrical resistivity in saturated conditions realized at 20 °C | Laboratory measurement according to RILEM TC-154 EMC techniques [66] | Ω.m |
| RH | Relative humidity at the steel/concrete interface | ≥ 90 % | % |
| d | Time of dry periods factor | $d = \begin{cases} 0 \rightarrow \text{wetted concrete} \\ 1 \rightarrow \text{not wetted concrete} \end{cases}$ | ---- |

## 6.2. Interpretation of the model

The model was initially expressed in terms of macrocell corrosion current and was calibrated from experimental results obtained from previous experimental studies. After calibration, the transition from corrosion current to corrosion current density was achieved. These current densities were considered as apparent densities since they were calculated by considering the entire surface of the anode.

### 6.2.1. Chlorides

The impact of chlorides on corrosion was based on results of the experimental test developed by Chalhoub et al. in [3] where galvanic corrosion currents $(I_g)$ measured between anode and cathode were investigated according to free chloride contents $(\text{Free Cl})$ in case of CEMI mortar samples (water/cement ratio of 0.55 and sand/cement ratio of 2.75). The critical content of free chlorides $C_{crit}$ was found equal to 0.5 %/ wt.cement [3].

Indeed, below critical content, the measured macrocell currents were relatively negligible whereas, for higher chloride contents, a proportional relationship existed between galvanic current and chloride contamination level. This result could be explained by the increase in active corroded area with the chloride content, the increase in the oxidation kinetics at the anode (decrease of the anodic Tafel coefficient) [Paper II] and also the decrease of electrical resistivity at the anode with the increase in chloride contamination level.

The calibration of the factor $K_{Cl}$ is realized according to these results. The fitting model is illustrated in Fig. 7 (red curve) and presented in Eq. 24.

$$K_{Cl} = \frac{(|Cl\text{-}C_{crit}|+Cl\text{-}C_{crit})^{0.89}}{0.08} \qquad \textit{Eq. 24}$$

where:

- Cl is the free chloride content (%/wt. cement) ;
- $C_{crit}$ is the critical threshold value of free chlorides which is equal to 0.5 %/wt. cement in the case of the tested formulation based on CEMI [3].

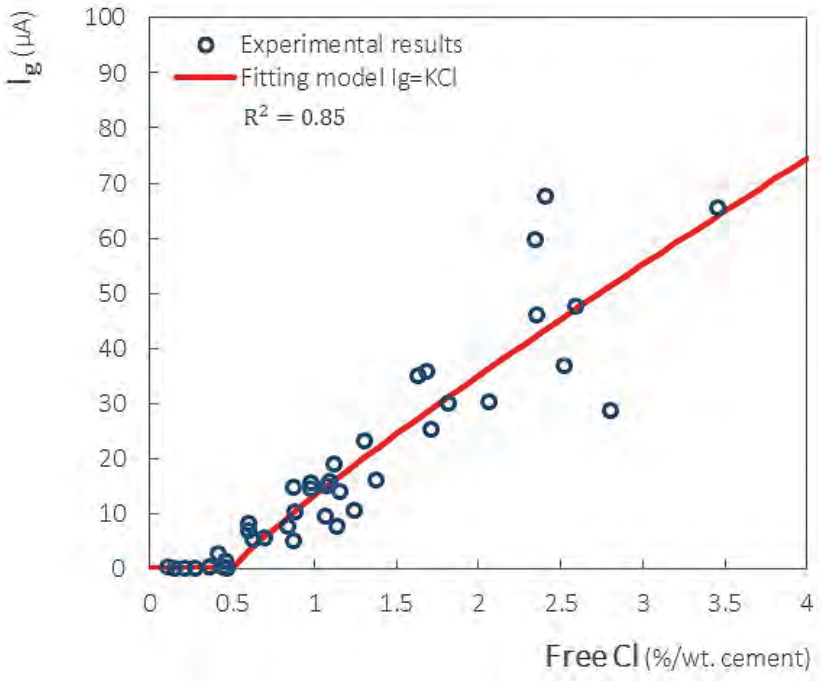


*Fig. 7. Experimental results and fitting model of galvanic current according to chloride contamination*

After corrosion initiation, an electrical field is generated and causes the migration of chlorides towards the anode. The migration of chlorides under the effect of the electrical field was not investigated in this thesis but is under study in another Ph.D. thesis [D. Garcia, under progress].

As a first step, the chloride level at the steel/concrete interface at the beginning of corrosion propagation was considered to exceed the critical chloride content by an amount of 0.3 % per weight of the binder, as shown in Eq. 25.

$$Cl = C_{crit} + 0.3 \qquad \textit{Eq. 25}$$

### 6.2.2. C/A ratio

The model is based on the experimental test presenting a C/A ratio of 16. However, at the beginning of corrosion in real structures, the C/A ratio is very high. Therefore, it is important to take into consideration the impact of this parameter in the corrosion rate model. In the same research paper [3], an experimental campaign was realized to test the impact of the C/A ratio. Galvanic cathode-anode connections were realized between anode samples and different rebars of a reinforced wall to test C/A ratios from 200 till 2952. It was found that the increase in the C/A ratio leads to the increase in the galvanic corrosion current and that the evolution of the current is not linear but tends to stabilize [3]. It must be noted that, in this experiment, the effect of the C/A ratio is coupled with the effect of the distance between cathode and anode. Consequently, it is possible to use a factor $K_{C/A}$ as shown in Eq. 26 which allows taking into account the impact of C/A ratio on corrosion current measured in the experimental protocol corresponding to a C/A ratio of 16.

$$K_{C/A} = \frac{I_{g\,C/A}}{I_{g\,16}} \qquad \textit{Eq. 26}$$

where:

- $K_{C/A}$ is the factor related to the effect of the cathode to anode ratio “C/A”;

- $I_{g\ 16}$ is the galvanic current for C/A ratio equal to 16 (µA);
- $I_{g\ C/A}$ is the galvanic current for a C/A ratio higher than 16 (µA).

Fig. 8 shows the evolution of factor $K_{C/A}$ presented in Eq. 26 according to the apparent C/A ratio for samples with different free chloride contents (indicated in the legend of the graph in %/wt. cement).

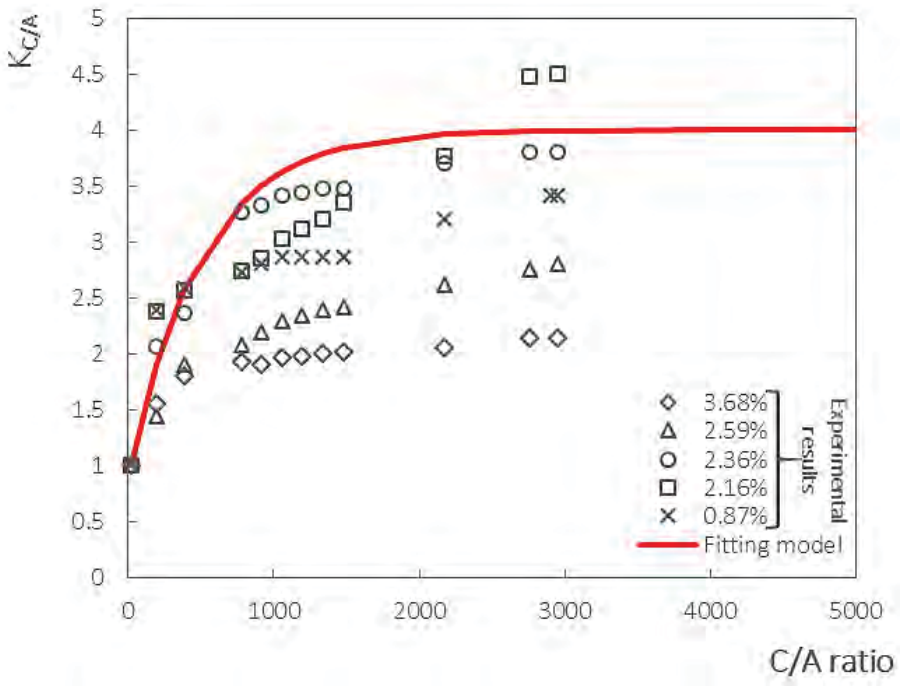


*Fig. 8. Evolution of factor $K_{C/A}$ according to C/A ratio _ Experimental results and fitting model*

A conservative fitting model of $K_{C/A}$ was chosen and is presented in Eq. 27 and illustrated in Fig. 8 as red curve. The latter is similar to an envelope curve of the worst-case scenario with a factor $K_{C/A}$ approaching a value of 4 when the C/A ratio tends towards infinity. Knowing that at the beginning of corrosion propagation the C/A ratio is very high, it is suitable to consider $K_{C/A}$ equal to 4.

$$K_{C/A} = 3 \times \left(1\text{-}e^{-0.002(C/A\ -16)}\right) + 1 \qquad \textit{Eq. 27}$$

### 6.2.3. Temperature

To evaluate the impact of temperature, the same experimental procedure described in part 6.1 was used, however, in this case, the test was realized outside the laboratory and was exposed to the outdoor temperature. The galvanic corrosion current was monitored and maintained for 120 hours. The temperature of air and the temperature of the NaOH solution were measured with thermocouples T of the thermometer instrument HANNA HI 98804 which is equipped with a microprocessor for accurate temperature readings and acquisition of results. The recording time step was 15 min for the temperature and 1 min for the current measurements.

Fig. 9 shows the galvanic current and temperature monitoring of the experimental test of an anode sample contaminated with a chloride level of 0.87 %/wt. cement. There is a similar variation between the galvanic current and the temperature of the NaOH solution. The highest measured values were 12.5 µA at a solution temperature of 11.4 °C and the lowest values were 8.8 µA at 3.2 °C. A phase shift

exists between the temperature of the air and that of the solution and consequently the corrosion current which is produced by the temperature lag between the atmosphere and stagnant liquids. During the measurement, the outdoor temperature was low and did not exceed 20 °C. The variation of the corrosion current obtained is mainly dependent on the temperature variation.

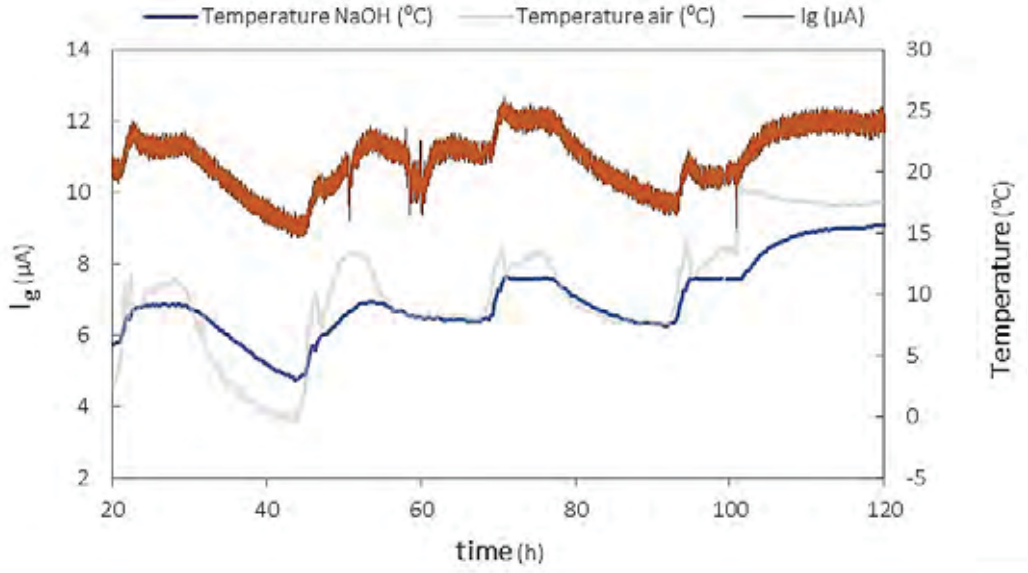


*Fig. 9. Example of galvanic current and temperature monitoring over time*

The factor $K_T$ related to temperature dependence is calculated with Eq. 28 as follows:

$$K_T = \frac{I_g}{I_{g0}} \qquad \textit{Eq. 28}$$

where:
- $I_g$ is the corrosion current at temperature T (µA);
- $I_{g0}$ is the corrosion reference current at a reference temperature of 20°C (µA);

Hence, the corresponding Arrhenius-type relationship model used to fit the experimental results can be determined as shown in Eq. 29.

$$K_T = e^{b\left(\frac{1}{T_0} - \frac{1}{T}\right)} \qquad \textit{Eq. 29}$$

where:
- $T_0$ is the reference temperature equal to 20 °C or 293 K;
- T is the temperature at measurement (K);
- b is the constant of Arrhenius law (K).

The experimental current results were normalized to current at 20 °C. This value of galvanic corrosion current $I_{g0}$ was deduced from the experimental result obtained when this specimen was tested at 20°C (form part 6.2.1). A similar experiment was also realized with another anode sample contaminated with 1.16%/ wt. cement. Fig. 10 presents the evolution of currents normalized to 20 °C which is equivalent to $K_T$ calculated with Eq. 28 according to the temperature. The results were also compared with literature results [18,38,45,67]. Additionally, Fig. 10 presents the model $K_T$ calculated with Eq. 29 with a constant b equal to 4220 ± 250. Since the experimental results obtained in this work

were limited to a small range of temperatures, it was decided to use a constant b equal to 4220 which fitted well literature data.

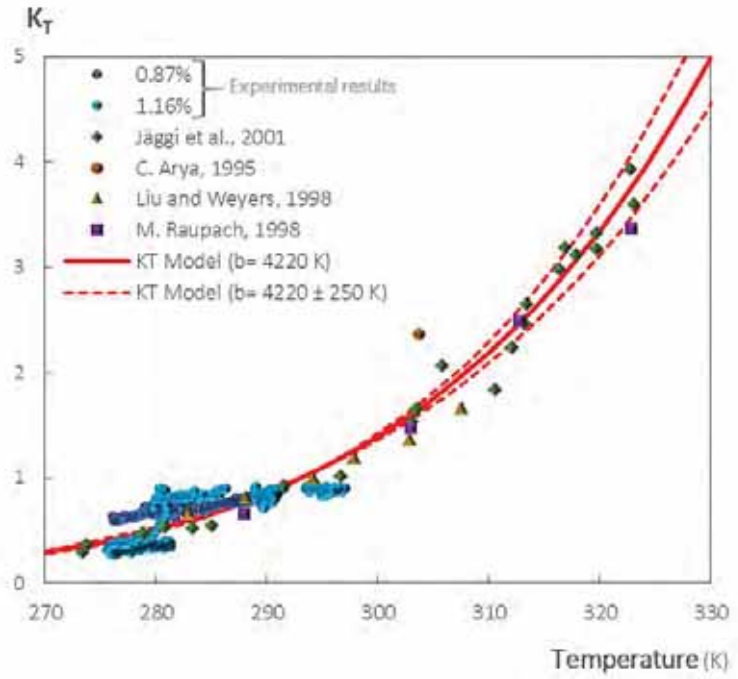


*Fig. 10. Relationship between the normalized macrocell current and temperature for the experimental results and the corresponding model*

### 6.2.4. Electrical resistivity

In [Paper VI], it was stated that a proportional relationship could exist between corrosion currents and the overall resistivity when considering both resistivities at cathode and anode. As a result, the electrical resistivity was considered inversely proportional to the corrosion current density.

In the experiments reported in [Paper VI], samples were partially immersed during corrosion measurements and electrical resistivity was measured in the laboratory under saturated conditions (RH=95%). It is then important to correct the resistivity to account for the real RH at the steel/concrete interface as follows:

$$\rho = \rho_0 \times K_{RH} \qquad \text{Eq. 30}$$

where:

- ρ is the electrical resistivity of concrete (Ω.m);
- $\rho_0$ is the electrical resistivity measured in saturated conditions (RH≥95%) at 20 °C (Ω.m);
- $K_{RH}$ is a factor related to the impact of relative humidity.

In the LIFECON project [39], an experimental campaign was realized by comparing the electrical resistivity of concrete at different RH (between 50% and 95%) with a reference RH of 100%. The study was only realized on two different types of binders (CEM I and CEM III) with w/c between 0.45 and 0.65. The results of the statistical determination of $K_{RH}$ indicate that the average value of $K_{RH}$ increases exponentially when reducing relative humidity expressed in %, as shown in the following equation:

$$K_{RH} = \left(\frac{100}{RH}\right)^4 \quad \text{Eq. 31}$$

In our model, the relative humidity was that of concrete at the level of steel. Thus, the relative humidity was always considered to be higher than 90% and varies between 90 and 95% according to the exposure class.

It is important to take into consideration the rain duration and condensation at the surface of the concrete. According to the same project [39], it is possible to consider the wet periods in the model by introducing a parameter d which is related to the time of dry periods as follows:

$$K_{RH} = \left(\left(\frac{100}{RH}\right)^4\right)^d \quad \text{Eq. 32}$$

Knowing that concrete is rapidly saturated but needs more time to dry out subsequently, and since there is not enough data for the estimation of the time needed for the concrete to dry after wetting, it was proposed to consider d equal to 0 when concrete is not protected from rain or wetted by other sources and to take d equal to 1 when concrete is not wetted [39].

Knowing that the binder type affects the electrical resistivity of concrete, its impact on the corrosion current density was taken implicitly in the electrical resistivity $\rho_0$ measured in saturated conditions.

Moreover, electrical resistivity is a function of chloride contamination. Indeed, the increase in free chloride content leads to the decrease of electrical resistivity as shown in several reported research papers [68–73] and in [Paper VI]. Nevertheless, the effect of chloride contamination on electrical resistivity will not be explicitly taken into account in this model since it is implicitly considered in the factor $K_{Cl}$ (presented in part 0). Also, at the beginning of corrosion propagation, the concrete cover is only contaminated with chlorides and the rest of the concrete remains intact.

### 6.2.5. Oxygen availability

To study the parameter related to oxygen availability $K_{O_2}$ , structures are categorized according to their exposure class presented in Table 10.

*Table 10. $K_{O_2}$ according to exposure classes of structures or parts of the structures.*

| Exposure class | Methods of contamination | $K_{O_2}$ |
|---|---|---|
| XS1 | Parts of the structure exposed to sea spray | 1 |
| XS2 | Parts of structure immersed permanently in seawater | Depends on the length of the submerged zone |
| XS3 | Tidal areas subjected to projections or spray | 1 |

In cases of structures in XS1 and XS3 conditions, it is supposed that oxygen is always available at the steel/concrete interfaced and $K_{O_2}$ is considered equal to 1. On the other hand, in the case of the XS2 environment, it is important to note that, almost all structures are not entirely immersed. This implies that even if a part of the structure is entirely immersed, it is always electrically connected to the rest of the structure which is located in the atmospheric area.

In [Paper V], the impact of C-A distance on corrosion current was experimentally and numerically evaluated on a 10 m length beam. It was found that whatever the electrical resistivity, in the absence of closer bars acting cathodically and connected to the anode, the galvanic corrosion current can be provided by cathode bars at large distances from the anode. This means that, in cases of partly immersed structures where corrosion is initiated in an immersed region of the structure (exposure class XS2), the mobilized cathodic area could be far away from the anode in aerated parts of the structure, where oxygen is available. These results are supported by observations regarding localized corrosion in submerged zones [74]. It was also found that the increase in electrical resistivity reduces the cathode-anode distance allowing a significant current flow (mobilizable C-A distance). As a result, a higher resistivity would restrain the extent of the reinforcement area in the submerged zone where anodic sites could be developed. An equation describing the relationship between the maximum mobilizable C-A distances '$d_{max}$' and electrical resistivity 'ρ' was developed for numerical results and is presented in Eq. 33.

$$d_{max} = \frac{80}{\rho^{0.42}} \qquad \textit{Eq. 33}$$

where:

- $d_{max}$ is the mobilizable distance corresponding to a relative current threshold of 20% (m);
- ρ is the electrical resistivity (Ω.m).

However, it must be noted that the results correspond to the geometry of the test beam presenting a one-dimensional reinforcement arrangement, while, in actual reinforced concrete structures, the reinforcement network could be three dimensional. Hence, further investigations are needed to study the impact of resistivity on the mobilizable cathode in partially submerged structures with a three-dimensional reinforcement network.

Nevertheless, it would be reasonable to use, in case of XS2 exposure class, and oxygen coefficient $K_{O_2}$ which depends on the immersed length of the structure. It is then possible to use a conservative approach by considering $K_{O_2}$ equal to $1$ when the submerged length of the structure is lower than $d_{max}$ and $0$ when the submerged length of the structure is higher than $d_{max}$.

### 6.2.6. Calculation of corrosion current density

The corrosion current density is obtained when dividing the corrosion current with steel surface area. It is logical to divide the current with the area of passive steel in case of passive corrosion and with the area of active steel in case of active corrosion.

Yet, it is possible to define several densities according to the concerned steel surface area. Most approaches from literature (presented in part 4) defined the density as a result of the current divided by the area of steel supposed to be polarized without taking into account the real surface of active steel because it is unknown.

In the test set-up adopted in this work, it is possible to define 2 arbitrary densities: the first one by dividing the current by the apparent surface of anode (entire anode surface) and the second one by the sum of anode and cathode surface involved in the test. It is also possible to divide the current by the surface of the real part of the anode which is in an active state and finally it is possible to calculate through numerical simulation a density corresponding to a hypothetical full active surface of the anode. This leads to the identification of 4 different densities presented in Eq. 34, Eq. 35, Eq. 36 and Eq. 37, respectively and illustrated in Fig. 11.

- Apparent current density $i_{g\ app}$:

$$i_{g\ app} = \frac{I_g}{S_{anode}} \qquad \textit{Eq. 34}$$

- Global current density $i_{g\ a+c}$:

$$i_{g\ a+c} = \frac{I_g}{S_{anode} + S_{cathode}} \qquad \textit{Eq. 35}$$

- Real current density $i_{g\ real}$:

$$i_{g\ real} = \frac{I_g}{S_{active}} \qquad \textit{Eq. 36}$$

- Limit current density $i_{g\ num}$:

$$i_{g\ num} = \frac{I_{num}}{S_{anode}} \qquad \textit{Eq. 37}$$

where:

- $I_g$ is the measured marcocell (galvanic) current between anode and cathode (μA);
- $S_{anode}$ is the area of the anode which is equal to 1.88 $cm^2$;
- $S_{cathode}$ is the area of the cathode which is equal to 30.16 $cm^2$;
- $S_{active}$ is the area of corroded (active) steel ($cm^2$);
- $I_{num}$ is the numerically calculated marcocell (galvanic) current corresponding to a hypothetical full active surface of anode (μA).

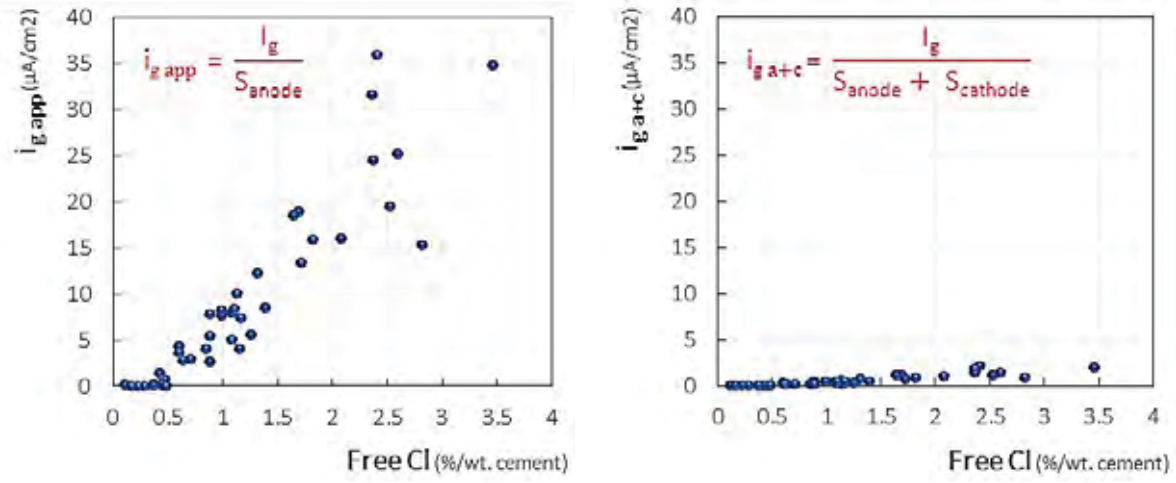

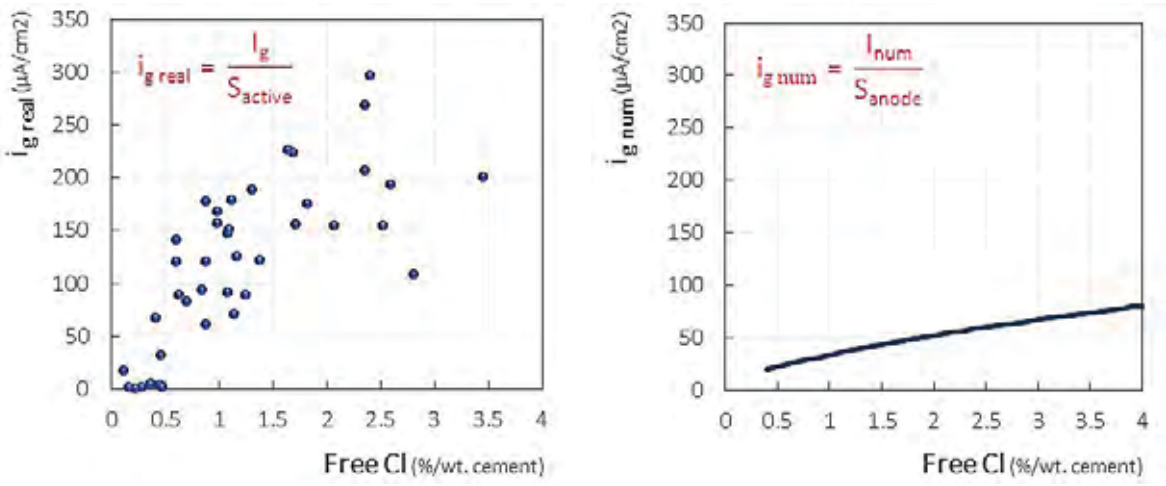


*Fig. 11. Corrosion current densities according to the different definitions (different steel surface areas)*

It is interesting to compare the difference between the order of magnitude of the current densities obtained with Eq. 34, Eq. 36 and Eq. 37 versus the densities obtained with Eq. 35 which presents current densities in the same order of magnitude of the ones obtained with previously presented corrosion rate predictive models (Table 4).

Nonetheless, the corrosion density with a physical signification is $i_{g\ real}$ corresponding to the real anodic surface. However, since the model is designed for engineering purposes and due to the difficulty of direct visual measurement of the real active area of steel at the anode, it was more practical to determine the current density model in terms of an apparent corrosion density. A calibration constant $\gamma_{Cl}$ equal to 0.173 A.Ω/m was used to calibrate the model.

## 7. Prediction of corrosion propagation duration

Corrosion initiation is followed by the phase of corrosion propagation. To determine the service life of a structure, it is necessary to define an acceptable service limit state "SLS" criterion, for instance, a criterion corresponding to the appearance of the first corrosion-induced (C-I) crack. Cracks induced by corrosion are parallel to the reinforcement bars and are caused by the expansive nature of the corrosion products that are formed during the propagation period.

### 7.1. Section loss initiating cracking

There are several approaches adopted for the prediction of the occurrence of the first C-I crack. Some of these approaches are based on accelerated tests under the electrical field [25,75–77] and do not represent real corrosion. Several predictive models are based on a uniform expansion of the reinforcement surface [78,79]. This approach does not represent the localized aspect of chloride-induced corrosion in concrete.

Vidal et al. [80] implemented an empirical model based on experimental results of local corrosion measurements obtained from the autopsy of two naturally corroded reinforced beams for durations of 14 and 17 years. The implemented method considers that the local cross-section loss is associated with the pressure caused by corrosion products. This model was validated by a third beam which was kept under load and cycles of spraying with a salt solution followed by drying [62]. Two cross-section loss were observed and measured. The first cross-section generated a corrosion crack, whereas, the second one did not generate any corrosion crack. The cross-section loss calculated with the model of Vidal et al. was well enclosed by both measured cross-section losses [4].

In this work, this model [80] has been retained. Knowing the reinforcement bar diameter and the concrete cover (distance between the rebars and the surface of concrete), it is possible to determine the local cross-section loss initiating corrosion cracking as follows:

$$S_a = A_s \left[1-\left[1-\frac{2\,Pr_{O_2}\,pf_g}{D}\left(7.53+9.32\frac{c}{D}\right)10^{-3}\right]^2\right] \qquad \textit{Eq. 38}$$

where:

- $S_a$ is the local cross-section loss leading to the initiation of corrosion cracking ($m^2$);
- D is the steel bar nominal diameter (m);
- $A_s$ is the cross-section of the rebar which is equal to $\frac{\pi D^2}{4}$ ($m^2$);
- c is the concrete cover thickness between reinforcement and the concrete surface (m);
- $pf_g$ is the geometric pitting factor [81] with $pf_g = \begin{cases} 1 & \text{Carbonation-induced corrosion} \\ 4 & \text{Chloride-induced corrosion} \end{cases}$
- $Pr_{O_2}$ is the parameter which considers the pressure of corrosion products according to oxygen availability with $Pr_{O_2} = \begin{cases} 1 & \text{Exposure class XS1 and XS3} \\ 2.5 & \text{Exposure class XS2 (no experimental background)} \end{cases}$

It must be noted that in the case of underwater corrosion (exposure class XS2), no corrosion-induced cracking exists despite important steel cross-section loss. In fact, in high-humidity conditions with low oxygen content, fluid and non-expansive corrosion products are more generally expected, which may not induce concrete cracking, therefore, there is no visual manifestation of corrosion during a usual design service period [82–84].

As a result, in the case of submerged structures, it is important to define a substitute to the classical widespread service limit-state such as the visible external cracks. However, since the developed model is achieved for engineering purposes, visual inspections are needed as a limit state criterion. Therefore, a factor ($Pr_{O_2}$) was introduced in Eq. 38 to account for the lower pressure of corrosion products produced during underwater corrosion allowing to differentiate between the different exposure classes. In the case of an exposure class XS2, the value of this factor was set to 2.5, however, there is no real experimental nor theoretical background behind this choice. From this point, this assumption needs further investigation.

## 7.2. Calculation of the anodic area and volume

Fig. 12 shows a cross-section of a CEMI mortar anode sample polluted with a free Cl content of 2.07 %/wt. cement that was observed by X-ray Tomography at the CEA laboratory in Sacaly, France. The cross-section clearly shows the corrosion pit indicating the localized nature of chloride-induced corrosion in mortar.

Knowing the localized aspect of corrosion, it was adequate to use the method presented in [4] where the corrosion pit was considered to be based on a triangular cross-section with an opening angle of $2\varphi$ on the rebar diameter with a pitting depth $e_p$ and a length $L_a$ as shown in Fig. 13.

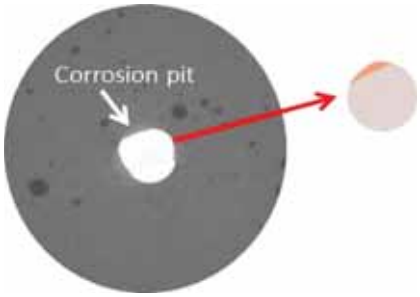


*Fig. 12. Cross-section of CEMI anode sample (X-ray Tomography (CEA Saclay France))*

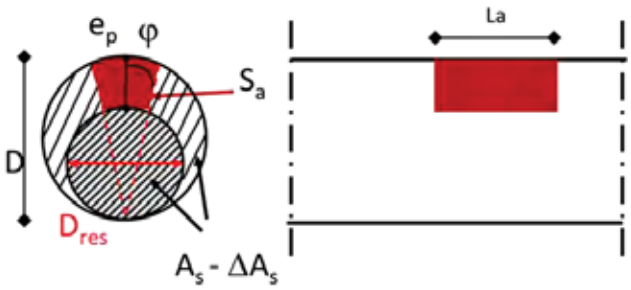


*Fig. 13. Localized corrosion of reinforcement rebar [4]*

The extension area of the anodic active steel is given in Eq. 39 and the volume of the anodic zone can be calculated with Eq. 40.

$$A_a = 2\, L_a\, D \tan(\varphi) \qquad \textit{Eq. 39}$$

$$V_a = S_a L_a \qquad \textit{Eq. 40}$$

where:

- $A_a$ is the surface of the lateral extension of the active anodic area ($m^2$);
- $L_a$ is the length of the active anodic area (m);
- $\Phi$ is half of the opening angle of the triangle that is considered equal to $\frac{\pi}{12}$ (according to [4]);
- $V_a$ is the volume of the anodic zone ($m^3$).

It must be mentioned that the shape of the pitting corrosion and the opening angle certainly affects the prediction of the structure's service life. Moreover, the length of the anodic area $L_a$ is usually unknown. This variable will be compensated when calculating the propagation duration.

## 7.3. Mass loss and corrosion rate - Faraday's law

Traditionally, the overall mass loss of a metal that is induced by corrosion propagation is calculated using Faraday's law (Eq. 7). However, the corrosion of steel in concrete is not uniform. Therefore, it is more adequate to calculate the local mass loss instead of a global average value. In some studies, this overall mass loss was transformed into a uniform cross-section steel thickness loss. This approach is not correct since corrosion steel loss is not uniform around the steel bar cross-section. Also, the total anodic corrosion current contributes to penetration at depth and also to the lateral extension of the anodic area(s). Consequently, only a part of the total current density will be used to calculate the cross-section mass loss. The corrosion propagation duration $t_{prop}$ corresponding to the occurrence of first corrosion crack can be calculated using the Faraday's relation as follows:

$$m = V_a\, \rho_s \qquad \textit{Eq. 41}$$

$$t_{prop} = \frac{V_a\, \rho_s\, Z\, F}{M\, I_{corre}} \qquad \textit{Eq. 42}$$

$$I_{corre} = k\, I_{corr} = k\, i_{corr}\, A_a \qquad \textit{Eq. 43}$$

where:

- $V_a$ is the volume of the anodic zone ($m^3$).
- $\rho_s$ is the density of iron equal to $7.86\times10^6$ g/$m^3$;
- $I_{corre}$ is the corrosion current contributing to the weight loss of the anodic volume (A);
- K is the factor corresponding to the portion of current leading to steel cross-section loss which is taken equal to 0.5 (assumption of the model taken without any experimental nor theoretical background).
- $i_{corr}$ is the galvanic corrosion current density obtained from Eq. 23 (A/m2) ;

The equation associating the service propagation period to corrosion rate can thus be can be expressed in years as follows:

$$t_{prop} = \mu \left(\frac{S_a}{D}\right)\left(\frac{1}{K\, i_{corr}}\right) \qquad \textit{Eq. 44}$$

Where the first term is a constant ($\mu = \frac{\rho_s Z F}{2 M \tan(\phi)}$ = 5.07E+10 A.s/$m^3$ = 1629 A.year/$m^3$), the second term depends on the concrete structure (rebar diameter and cover) with $S_a$ in $m^2$ and D in m and the third term is related to corrosion density.

The penetration of attack can be calculated as follows where $V_{corr}$ is expressed in µm/year, $i_{corr}$ in A/$m^2$ and t in years.

$$V_{corr} = \frac{D^2 - (D - e_p)^2}{t\, D} \qquad \textit{Eq. 45}$$

The localized penetration depth $e_{p\ localized}$ can be calculated, according to the chosen geometry of the pitting, using Eq. 46, whereas, the uniform penetration depth $e_{p\ uniform}$ is usually calculated as shown in Eq. 47 and both penetration depth are expressed in m.

$$e_{p\ localised} = D - \sqrt{D^2 - \frac{S_a}{\tan\phi}} \qquad \textit{Eq. 46}$$

$$e_{p\ uniform} = P_x = \frac{S_a}{\pi\, D} \qquad \textit{Eq. 47}$$

For a structure having rebars with a diameter of 12 mm and a cover of 26 mm, $e_{p\ localized}$ is equal to 660 µm while $e_{p\ uniform}$ is equal to 110 µm. This comparison highlights the major difference between both approaches and stresses the need to take into account the localized aspect of corrosion.

# 8. Summary and discussion

Fig. 14 presents a flowchart summarizing the different steps proposed to estimate the service life of concrete structures which consists of 3 steps:

1. Determination of corrosion rate;
2. Calculation of the steel cross-section loss causing the appearance of the first C-I crack;
3. Estimation of the duration of corrosion propagation.

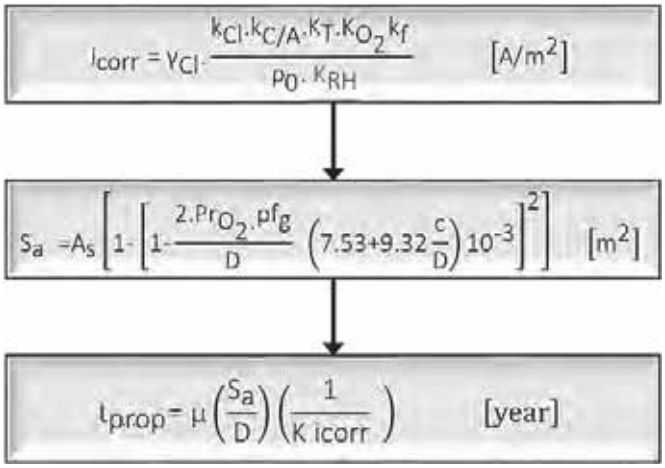


*Fig. 14. Flowchart of the different steps proposed to estimate the service life of concrete structures*

## 8.1. Application of the empirical model

To test the application of the presented model, input parameters were selected arbitrarily and the data are summarized in Table 11. Regarding the geometry of the structure, a cover thickness of 40 mm and a rebar diameter of 20 mm were proposed. It was considered that there is a "top bar effect" in the studied structure. The selected concrete was chosen to be based on CEMI and electrical resistivity of 70 Ω.m was suggested. As for the environment of the structure, three exposure classes were tested: XS1, XS2, and XS3. The temperature was supposed to be equal to 20 °C and the concrete was considered wetted (d=0) in the case of XS2 and XS3 and was considered not wetted (d=1) in case of XS1. The submerged length in the case of an XS2 structure was considered to be 3 m.

*Table 11. Selected input data of the model*

| Input data | Value | Unit |
|---|---|---|
| T | 293 | Kelvin |
| $\rho_0$ | 70 | Ω.m |
| RH | 95 (if XS2 and XS3)<br>90 (if XS1) | % |
| d | 0 (if XS2 and XS3)<br>1 (if XS1) | --- |
| D | 20 | mm |
| c | 40 | mm |
| Submerged length (XS2) | 3 | m |
| $K_f$ | 2 (presence of defects) | --- |

Table 12 presents the outputs of the model, $i_{corr}$, and $t_{prop}$, according to the different exposure classes. The results clearly show that for exposure classes XS2 and XS3, having the same corrosion rate, the propagation duration was higher in XS2 which is explained by the chosen criterion related to the first C-I cracking. It must be noted that this statement is only true in case of a submerged length lower than the maximum mobilizable cathode as stated in part 6.2.5.

Results for compared with values found in literature according to AFNOR normalization documents [85,86] where the corrosion propagation duration was considered from experts' opinion. In [86], the authors stated that the reason why XS3 showed the lowest $t_{prop}$ is that the corrosion rate is the highest in XS3 exposure conditions where both oxygen and water are available, and salty water can evaporate leading to high surface concentrations. The authors [86] also indicated that $t_{prop}$ is significantly higher under XS2 conditions because of the limited oxygen availability and $t_{prop}$ is intermediate under XS1 conditions because of reduced water availability and absence of salty water.

*Table 12. Outputs of $i_{corr}$ and $t_{prop}$ according to electrical resistivity and exposure class*

| Exposure class | $i_{corr}$ ($\mu A/cm^2$) | $t_{prop}$ (years) | $t_{prop}$ (years) according to [85] | $t_{prop}$ (years) according to [86] |
|---|---|---|---|---|
| XS1 | 13.3 | 8 | 2 | 10 |
| XS2 | 20.3 | 13 | 6 | 15 |
| XS3 | 20.3 | 5 | 1 | 5 |

## 8.2. Sensibility study of the model

During the construction of any model, sensitivity analysis of the model variables must be realized since it allows us to know the parameters that contribute the most to the variability of the model's response. The input data were considered similar to those presented in Table 11 with an exposure class XS3. Each parameter is varied according to a predefined marge of variation and the outputs are calculated according to these input data. All the results are summarized in Table 13. As expected, according to these results, it is possible to see that the model is most sensitive to electrical resistivity.

*Table 13. Sensibility analysis of input data*

| Input data | Input value | $t_{prop}$ (years) |
|---|---|---|
| T | [-5 ; 40] °C | [20 ; 2] |
| $\rho_0$ | [50 ; 500] Ω.m | [4 ; 38] |
| D | [10 ; 40] mm | [9 ; 3] |
| c | [20 ; 75] mm | [3 ; 9] |

## 8.3. Assumptions of the chosen model

- The corrosion current corresponds to the measurements of localized galvanic corrosion but the galvanic corrosion density is apparent and is calculated according to the entire surface of the anode.
- The corrosion current leads both to the extension of the anodic zones and to the reduction of the cross-section of the reinforcement bar with the assumption that 50% of the current leads to the loss of cross-section (value taken without any experimental support).
- Half of the opening angle of the triangle limiting the loss of the cross-section is assumed to be equal to $\frac{\pi}{12}$ (value taken without any experimental background according to [4]). It is important to note that

the shape of the corrosion pit and the chosen opening angle certainly affect the prediction of the service life of the structure.

- The influence of the top-bar effect on the propagation of corrosion is a parameter not studied in this work but was taken into account by using the factor $K_f$ supposed to be equal to 2 in the presence of defects (value is taken considering the unpublished work of Yu et al.).
- The factor $Pr_{O_2}$ introduced in the equation of the cross-section loss initiation the first C-I crack in case of submerged structures was set to 2.5, however, there is no real experimental nor theoretical background behind this choice.
- The results corresponding to the mobilizable cathode (used for the assessment of $K_{O_2}$ in exposure class XS2) correspond to a one-dimensional reinforcement arrangement, while, in actual reinforced concrete structures, the reinforcement network could be three dimensional.

All the assumptions considered in this model need further investigation.

### 8.4. Aspects not treated by the empirical model

- The model is only studied on lab specimens. It is then important to calibrate this model using data from long-term field tests.
- The model does not consider the influence of cracks on the corrosion rate.
- The model presented in this paper is only applied to non-carbonated concretes.

## 9. Conclusion

The prediction of the corrosion current density is based on the observation that in a concrete structure before the appearance of corrosion-induced cracks, the preponderant component of corrosion is that related to the macro-cell process also known as localized corrosion. This work contributed to the objectives of the French ANR Modevie project aiming for the development of an overall engineering model for the assessment of concrete structures service life by calculating the sum of initiation period and propagation period.

The engineering model developed in this paper is adapted to the performance-based approach allowing to describe the corrosion propagation phase with input data based on durability and environmental indicators. The assessment of the propagation period was associated with a service limit state corresponding to a loss of steel cross-section linked to the appearance of the first corrosion-induced crack. The developed model is an empirical simplified service life predictive model of relevance to the engineer and is based on experimental results obtained on an experimental test that physically separates the anode from the cathode. The model takes into account the influence of the parameters related to the anodic behavior: concentration in free chlorides mainly; the influence of parameters related to the cathodic behavior: oxygen availability and the ohmic interaction between anodic zones and cathodic zones, in particular: the surface ratio between cathode and anode (very high in real structures), the distance between aerated cathode and anode (important parameter for XS2 type exposures), and the electrical resistivity of the concrete which takes into account the impact of the relative humidity at the steel/concrete interface and the influence of the type of binder. The current densities obtained are either apparent, relative to the ratio of the anodic and cathodic parts of the experimental device, or real, compared to the proportion of anode surface corroded. The corrosion current density predicted by the model then makes it possible to calculate the duration of the propagation phase before the appearance of the first corrosion cracks. The originality of the model is that the corrosion current density is taken into account only partly to obtain a local reduction of the reinforcement section, the other part of the corrosion current density is used for the extension of the zones anodic in their length. The link between loss of local section and the appearance of a corrosion crack is empirical.

The output of the model was compared to values found in literature according to AFNOR normalization documents [85,86] where the corrosion propagation duration was considered from experts' opinion. A series of tests were carried out to evaluate the sensitivity of the model and to estimate the lifetime of real structures in various environments with classical rebar cover design and concrete complying with corresponding exposure class.

The limitations and assumptions of the model were also highlighted indicating that future corrosion studies, as well as developments towards predicting the duration of corrosion propagation in concrete, would benefit from considering those aspects.

Further development of this model towards predicting corrosion propagation in carbonated concrete would benefit from considering this work. The development of a simplified engineering model for the estimation of the propagation duration of reinforced concrete structures subjected to carbonation is currently under development. The model will be calibrated with a similar experimental protocol based on the separation of cathode and anode. The only difference between both protocols is the preconditioning of anode samples which are carbonated instead of being contaminated with chlorides.

## Acknowledgments

This work was supported by the ANR MODEVIE project, grant ANR-14-CE22-0018 of the French National Research Agency (ANR) and by the French National Federation of Public Works (FNTP).

## Appendices

This paper is completed with a summarized report in French describing the developed engineering model and Excel spreadsheets designed for engineering calculations based on the corrosion propagation prediction model.

## References


[1] U. Angst, B. Elsener, C. K. Larsen and Ø. Vennesland, *Critical chloride content in reinforced concrete — A review*, Cement and Concrete Research, 39 (2009), pp. 1122–1138.

[2] C.Q. Li, R.E. Melchers and J. Zheng, *Analytical Model for Corrosion-Induced Crack Width in Reinforced Concrete Structures*, Vol. 103, 2006.

[3] C. Chalhoub, R. François and M. Carcasses, *Determination of chloride threshold initiating corrosion: A new set-up taking the localized aspect of corrosion into account*, Cement and Concrete Research 124 (2019), pp. 105825.

[4] R. Francois, S. Laurens and F. Deby, *Corrosion and Its Consequences for Reinforced Concrete Structures*, Elsevier, 2018.

[5] RILEM TC-154-EMC, *Recommendations of RILEM TC-154-EMC: "Electrochemical techniques for measuring metallic corrosion"Test methods for on-site corrosion rate measurement of steel reinforcement in concrete by means of the polarization resistance method*, Mater. Struct. 37 (2004), pp. 623–643.

[6] M. Stern and A.L. Geary, *Electrochemical Polarization I. A Theoretical Analysis of the Shape of Polarization Curves*, Vol. 104, 1957.

[7] A. Clément, S. Laurens, G. Arliguie and F. Deby, *Numerical Study of the Linear Polarisation Resistance Technique Applied to Reinforced Concrete for Corrosion Assessment*, Vol. 16, 2012.

[8] S.L. J. Marchand Y. Protière, E. Samson, *A Numerical Study of Polarization Tests Applied to Corrosion in Reinforced Concrete*, Special Publication 312 (2016), pp. 1–12.

[9] J.A. González, C. Andrade, C. Alonso and S. Feliu, *Comparison of rates of general corrosion and maximum pitting penetration on concrete embedded steel reinforcement*, Cement & Concrete Research 25 (1995), pp. 257–264.

[10] C. Andrade and C. Alonso, *On-site measurement of corrosion rate of reinforcements*, Construction and Building Materials 15 (2001), pp. 141–145.

[11] C. Andrade, C. Alonso, J.A. Gonzalez and J. Rodriguez, *REMAINING SERVICE LIFE OF CORRODING STRUCTURES*, DURABILITY OF STRUCTURES. IABSE SYMPOSIUM, SEPTEMBER 6-8 1989, LISBON (IABSE REPORT VOLUME 57/1) (1989), pp. 359–363.

[12] *Handbook of Chemistry and Physics, 90th Ed., CRC Press*, 2009.

[13] B. Elsener, *Macrocell Corrosion of Steel in Concrete - Implications for Corrosion Monitoring*, Vol. 24, 2002.

[14] U. Angst and M. Büchler, *On the applicability of the Stern–Geary relationship to determine instantaneous corrosion rates in macro-cell corrosion*, Materials and Corrosion 66 (2014), pp. 1017–1028.

[15] U. Angst, *Chloride induced reinforcement corrosion in concrete: Concept of critical chloride content – methods and mechanisms*, Norwegian University of Science and Technology Faculty of Engineering Science and Technology Department of Structural Engineering, 2011.

[16] C. Alonso, C. Andrade and J.A. González, *Relation between Resistivity and Corrosion Rate of Reinforcement in Carbonated Mortar Made with Several Cement Types*, Vol. 18, 1988.

[17] A. Molina, C. Andrade, C. Alonso and J.A. González, Tec. Ing. Univ. Zulia, 8 (1985), .

[18] T. Liu and R.W. Weyers, *Modeling the Dynamic Corrosion Process in Chloride Contaminated Concrete Structures*, Vol. 28, 1998.

[19] I. Balafas and C. Burgoyne, *Environmental Effects on Cover Cracking Due to Corrosion*, Vol. 40, 2010.

[20] W. López and J.A. González, *Influence of the Degree of Pore Saturation on the Resistivity of Concrete and the Corrosion Rate of Steel in Concrete*, Vol. 23, 1993.

[21] *Evaluation non destructive pour la prédiction de la Dégradation des structures et l'Optimisation de leur Suivi*. Agence nationale de la recherche, 2011.

[22] DuraCrete, *Duracrete, Probabilistic Performance Based Durability Design: Modelling of Degradation*, The Netherlands, 1998.

[23] A.N. Scott, *The Influence of Binder Type and Cracking on Reinforcing Steel Corrosion in Concrete*, 2004.

[24] K. Anh T. Vu and M. Stewart, *Structural reliability of concrete bridges including improved chloride-induced corrosion models*, Struct. Saf 22 (2000), pp. 313.
[25] K. Vu, M. Stewart and J. Mullard, *Corrosion-induced cracking: Experimental data and predictive models*, ACI Struct. J 102 (2005), pp. 719.
[26] H. Yalçyn and M. Ergun, *The prediction of corrosion rates of reinforcing steels in concrete*, Cem. Concr. Res 26 (1996), pp. 1593–1599.
[27] C. Arya and Y. Xu, *Effect of cement type on chloride binding and corrosion of steel in concrete*, Cem. Concr. Res. 25 (1995), pp. 893–902.
[28] O.E. Gjørv, Ø.E. Vennesland and A.H.S. El-Busaidy, Electrical Resistivity Of Concrete In The Oceans, in OTC-2803-MS, 1977, pp. 8.
[29] K. Tutti, *Corrosion of steel in concrete*, Swedish Cement and Concrete Research Institute (1982), pp. 17–21.
[30] P. Schiessl and M. Raupach, *Influence of Concrete Composition and Microclimate on the Critical Chloride Content in Concrete*, 1990.
[31] V. Sirivivatnanon, L. Bucea, E. Meck, S. Yozghatlian and H. Cao, *Influence of Fly Ash, Ground Granulated Blast Furnace Slag and Silica Fume on Chloride Induced Corrosion of Steel Reinforcement, 2nd International Symposium on Blended Cements*, 2nd International Symposium on Blended Cements, Malaysia (1994), pp. 114–120.
[32] P.S. Mangat, J. Khatib and B.T. Molloy, *Microstructure, Chloride Diffusion and Reinforcement Corrosion in Blended Cement Paste and Concrete*, Vol. 16, 1994.
[33] M.D.A. Thomas, J.D. Matthews, C.A. Haynes, C.L. Page, K.W.J. Treadway and P. Bamforth, *Chloride diffusion and reinforcement corrosion in marine exposed concretes containing pulverized-fuel ash.*, Society of Chemical Industry, London (1990), pp. 198–212.
[34] C. L. Page and J. Havdahl, *Electrochemical Monitoring of Corrosion of Steel in Microsilica Cement Paste*, Vol. 18, Materials and Structures, 1985.
[35] C. Valentini, L. Berardo and I. Alanis, *Influence of Blast Furnace Slags on the Corrosion Rate of Steel in Concrete*, 1990.
[36] D. Tromans, *Anodic Polarization Behavior of Mild Steel in Hot Alkaline Sulfide Solutions*, Vol. 127, 1980.
[37] J. Warkus and M. Raupach, *Modelling of reinforcement corrosion – geometrical effects on macrocell corrosion*, Materials and Corrosion 61 (2009), .
[38] A. Arya and P.R.W. Vassie, *Influence of cathode-to-anode area ratio and separation distance on galvanic corrosion currents of steel in concrete containing chlorides*, Cement and Concrete Research 25 (1995), pp. 989–998.
[39] S. Lay, P. Schießl and J. Cairns, *Lifecon deliverable D 3.2*, Service life model, Technical research center of Finland (2003), .
[40] V. Garcia, *Contribution à l'étude du taux de chlorures pour l'amorçage de la corrosion des armatures du béton armé*, Université Toulouse III-Paul Sabatier, 2013.
[41] H. Wong, R. Zimmerman and N. Buenfeld, *Estimating the permeability of cement pastes and mortars using image analysis and effective medium theory*, Cement and Concrete Research 42 (2012), pp. 476–483.
[42] D.E. MacPhee and H. Cao, *Theoretical Description of Impact of Blast-Furnace Slag (BFS) on Steel Passivation in Concrete*, Magazine of Concrete Research 45 (1993), pp. 63–69.
[43] M. Holloway and J. Sykes, *Studies of the corrosion of mild steel in alkali-activated slag cement mortars with sodium chloride admixtures by a galvanostatic pulse method*, Corrosion science 47 (2005), pp. 3097–3110.
[44] S. Arrhenius, *On the Reaction Velocity of the Inversion of Cane Sugar by Acids*, Vol. 4, 1889.
[45] S. Jäggi, H. Böhni and B. Elsener, *Macrocell corrosion of steel in concrete-Experiments and numerical modelling*, European Federation of Corrosion (2001), .
[46] S. Jaggi, B. Elsener and H. Bohni, *Oxygen reduction on mild steel and stainless steel in alkaline solutions*, European Federation of Corrosion Publications(UK) 31 (2000), pp. 3–12.

[47] D. Bürchler, B. Elsener and H. Böhni, *Electrical resistivity and dielectric properties of hardened cement paste and mortar*, MRS Online Proceedings Library Archive 411 (1995), .
[48] Y. Liu, Y. Liu, R.E. Weyers and C. Chairman, *Modeling the Time-to-Corrosion Cracking of the Cover Concrete in Chloride Contaminated Reinforced Concrete Structures*, 1996.
[49] Y. P. Virmani, K. C. Clear, T. J. Pasko Jr, W. Jones and D. Jones, *Time-to-Corrosion of Reinforcing Steel in Concrete Slabs. Volume 5: Calcium Nitrite Admixture or Epoxy-Coated Reinforcing Bars as Corrosion Protection Systems*, 1983.
[50] Y. Schiegg, B. Elsener and H. Böhni, Online-monitoring of the corrosion in reinforced concrete structures, in Proc. EUROCORR, 2001.
[51] W. López, J.A. González and C. Andrade, *Influence of Temperature on the Service Life of Rebars*, Vol. 23, 1993.
[52] T.U. Mohammed and H. Hamada, *Corrosion of horizontal bars in concrete and method to delay early corrosion*, ACI materials journal 103 (2006), pp. 303.
[53] A. Castel, T. Vidal, R. Francois and G. Arliguie, *Influence of steel–concrete interface quality on reinforcement corrosion induced by chlorides*, Magazine of Concrete Research 55 (2003), pp. 151–159.
[54] R. Zhang, A. Castel and R. François, *Influence of steel–concrete interface defects owing to the top-bar effect on the chloride-induced corrosion of reinforcement*, Magazine of Concrete Research 63 (2011), pp. 773–781.
[55] T.A. Soylev and R. François, *Quality of steel–concrete interface and corrosion of reinforcing steel*, Cement and Concrete Research 33 (2003), pp. 1407–1415.
[56] T.A. Söylev and R. François, *Corrosion of reinforcement in relation to presence of defects at the interface between steel and concrete*, Journal of Materials in Civil Engineering 17 (2005), pp. 447–455.
[57] L. Yu, R. François and R. Gagné, *Influence of steel–concrete interface defects induced by top-casting on development of chloride-induced corrosion in RC beams under sustained loading*, Materials and Structures 49 (2016), pp. 5169–5181.
[58] T.U. Mohammed, N. Otsuki, H. Hamada and T. Yamaji, *Chloride-induced corrosion of steel bars in concrete with presence of gap at steel-concrete interface*, Materials Journal 99 (2002), pp. 149–156.
[59] J. Ryou and K. Ann, *Variation in the chloride threshold level for steel corrosion in concrete arising from different chloride sources*, Magazine of Concrete Research 60 (2008), pp. 177–187.
[60] U.M. Angst, M.R. Geiker, M.C. Alonso, R. Polder, O.B. Isgor, B. Elsener et al., *The effect of the steel–concrete interface on chloride-induced corrosion initiation in concrete: a critical review by RILEM TC 262-SCI*, Materials and Structures 52 (2019), pp. 88.
[61] T. Vidal, A. Castel and R. Francois, *Corrosion process and structural performance of a 17 year old reinforced concrete beam stored in chloride environment*, Cement and Concrete Research 37 (2007), pp. 1551–1561.
[62] L. Yu, R. Francois, V. Hiep Dang, V. L'Hostis and R. Gagné, *Development of Chloride-Induced Corrosion in Pre-Cracked RC Beams under Sustained Loading: Effect of Load-Induced Cracks, Concrete Cover, and Exposure Conditions*, Vol. 67, 2015.
[63] A. Michel, A.O.S. Solgaard, B.J. Pease, M.R. Geiker, H. Stang and J.F. Olesen, *Experimental investigation of the relation between damage at the concrete-steel interface and initiation of reinforcement corrosion in plain and fibre reinforced concrete*, Corrosion Science 77 (2013), pp. 308–321.
[64] R. Zhang, A. Castel and R. François, *Concrete cover cracking with reinforcement corrosion of RC beam during chloride-induced corrosion process*, Cement and Concrete Research 40 (2010), pp. 415–425.
[65] A. Horne, I. Richardson and R. Brydson, *Quantitative analysis of the microstructure of interfaces in steel reinforced concrete*, Cement and Concrete Research 37 (2007), pp. 1613–1623.

[66] *RILEM TC 154-EMC: ELECTROCHEMICAL TECHNIQUES FOR MEASURING METALLIC CORROSION Test methods for on site measurement of resistivity of concrete | Scinapse | Academic search engine for paper*, Scinapse 33 (2000), pp. 603–611.
[67] M. Raupach, *Results from laboratory tests and evaluation of literature on the influence of temperature on reinforcement corrosion*, Institute of Materials, Corrosion of Reinforcement in Concrete: Monitoring, Prevention and Rehabilitation(UK), (1998), pp. 9–20.
[68] M. Saleem, M. Shameem, Er.G. Hussain and M. Maslehuddin, *Effect of moisture, chloride and sulphate contamination on the electrical resistivity of Portland cement concrete*, Construction and Building Materials 10 (1996), pp. 209–214.
[69] M. Fares, G. Villain, S. Bonnet, S.P. Lopes, B. Thauvin and M. Thiery, *Determining chloride content profiles in concrete using an electrical resistivity tomography device*, Cement and Concrete Composites 94 (2018), pp. 315–326.
[70] J. Enevoldsen, C. Hansson and B. Hope, *The influence of internal relative humidity on the rate of corrosion of steel embedded in concrete and mortar*, Cement and concrete research 24 (1994), pp. 1373–1382.
[71] Z. Sbartaï, S. Laurens, J. Rhazi, J. Balayssac and G. Arliguie, *Using radar direct wave for concrete condition assessment: Correlation with electrical resistivity*, Journal of applied geophysics 62 (2007), pp. 361–374.
[72] F. Hunkeler, *The resistivity of pore water solution—a decisive parameter of rebar corrosion and repair methods*, Construction and Building Materials 10 (1996), pp. 381–389.
[73] I.-S. Yoon, *Effect of Water and Chloride Content on Electrical Resistivity in Concrete*, NOT PEER-REVIEWED (2019), .
[74] M. Walsh and A. Sagues, *Steel Corrosion in Submerged Concrete Structures - Part 1: Field Observations and Corrosion Distribution Modeling*, Corrosion -Houston Tx 72 (2016), pp. 518–533.
[75] C. Andrade, C. Alonso and F. Molina, *Cover Cracking as a Function of Bar Corrosion: Part I-Experimental Test*, Vol. 26, 1993.
[76] T. El Maaddawy and K. Soudki, *A Model for Prediction of Time from Corrosion Initiation to Corrosion Cracking*, Vol. 29, 2007.
[77] John A. Mullard and Mark G. Stewart, *Corrosion-Induced Cover Cracking: New Test Data and Predictive Models*, Structural Journal 108 (2011), .
[78] K. Lundgren, *Bond between Ribbed Bars and Concrete. Part 2: The Effect of Corrosion*, Vol. 57, 2005.
[79] Andres A. Torres-Acosta and Alberto A. Sagues, *Concrete Cracking by Localized Steel Corrosion--Geometric Effects*, Materials Journal 101 (2004), pp. 501–507.
[80] T. Vidal, A. Castel and R. Francois, *Analyzing Crack Width to Predict Corrosion in Reinforced Concrete*, Vol. 34, 2004.
[81] R. Francois, G. Arliguie and J.C. Maso, *Durability of Reinforced Concrete, Internal Synthesis Report*, L.M.D.C. I.N.S.A.-U.P.S., Toulouse, France, 1994.
[82] A. Torres-Acosta and A. Sagues, *Concrete cracking by localized steel corrosion - Geometric effects*, Materials Journal 101 (2004), pp. 501–507.
[83] J.P. Broomfield, *Corrosion of Steel in Concrete: Understanding, Investigation and Repair, Second Edition*, 2nd ed.Vol. 295, T & F Books UK, 2009.
[84] E. Busba and A. Sagues, *Localized Corrosion of Embedded Steel in Cracked Reinforced Concrete Pipes*, Corrosion -Houston Tx 69 (2013), pp. 403–416.
[85] *CEN/TC 250/SC 2/WG 1/TG 10 _ Summary for Reliability analysis of German & Spanish DtS Rules for Durability vs Maximum Corrosion Threshold*. AFNOR/P18B/GE CR, 2018.
[86] *Béton – Classes de résistance aux expositions _ Contribution française aux travaux du TG 10, préparée par François TOUTLEMONDE*. AFNOR/P18B/GE CR, 2019.

# Part III- Appendices

# Appendix I

## Technical sheets of materials

Appendix in: Study of the initiation and propagation phases of chloride induced corrosion in reinforced concrete structures

Realized by: Chantal Chalhoub

Thesis for the degree of Philosophiæ doctor

Université Toulouse 3 Paul Sabatier (UT3 Paul Sabatier)

Laboratoire Matériaux et Durabilité des Constructions de Toulouse

Appendix I

# FICHE TECHNIQUE PRODUIT

CIMENTS

LAFARGE
Construire des villes meilleures

**52,5R**

USINE DU TEIL

## CEM I 52,5 R CE CP2 NF

*NF EN 197-1 NF P 15-318*

**Déclaration de Performance n°**
**0333-CPR-1201**

CE NF

**SERVICES EXCLUSIFS**
Centre de Relation Clientèle :
0825 888 057*
Numéro indigo : 0,15€ TTC/mn

## CARACTERISTIQUES PHYSIQUES ET MECANIQUES

| | DP (min) | Stabilité (mm) | Résistances mécaniques (MPa) 2 jours | 28 jours | | | MV (g/cm3) | SSB (cm²/g) | Demande en eau (%) | Q41 (J/g) | L* | |
|---|---|---|---|---|---|---|---|---|---|---|---|---|
| Val. moyenne | 126 | 1,0 | 40,6 | 71,8 | | | 3,15 | 4150 | 28,7 | 363 | 64 | |
| Val. garantie | > 60 | < 10 | > 28 | > 50 | | | | | | | | |

## CARACTERISTIQUES CHIMIQUES

| | Valeur moyenne | Valeur garantie | | Valeur moyenne |
|---|---|---|---|---|
| SO3 (%) | 3,50 | < 4,5 | Alcalins équivalents [Na2O + 0,658 K2O] (%) | 0,2 |
| Chlorures Cl- (%) | 0,04 | < 0,1 | Alcalins actifs [suivant la norme NF P 18-454] (%) | 0,2 |
| Perte au feu 950°C (%) | 2,00 | < 5 | Vc coefficient de variation des alcalins actifs | 0,13 |
| Insolubles (%) | 0,40 | < 5 | | |
| S-- (%) | 0,01 | < 0,2 | | |

## CONSTITUANTS PRINCIPAUX ET SECONDAIRES :

| Clinker Portland Le Teil | 95,0% |
|---|---|
| C3S + C2S (%) | 78 |
| CaO/SiO2 | 3,1 |
| MgO (%) | 0,8 |
| C3S (%) | 67 |
| C2S (%) | 10 |
| C3A (%) | 9 |
| C4AF (%) | 8 |

| Constituant secondaire | 5,0% |
|---|---|
| Calcaire | |
| **Total des constituants** | **100%** |

## AUTRES CONSTITUANTS

| | |
|---|---|
| Gypse (%) | 4,7 |
| Agent de mouture AMA14E - Teneur sous forme d'extrait sec (%) | 0,07 |
| ou Agent de mouture AMA32E - Teneur sous forme d'extrait sec (%) | 0,07 |

## LIVRAISON EN SAC

ISO 9001 BUREAU VERITAS Certification

ISO 14001 BUREAU VERITAS Certification

Date de révision : **01/04/2015**

Holcim France

# FICHE TECHNIQUE

## Fabriqué à LUMBRES

Mise à jour du 19/12/2014

## Ciment Portland

| | | |
|---|---|---|
| *NF EN 197-1/A1* | CEM I 52,5 N | 01/06/2001 |
| | N° de certificat : 0333-CPR-2701 | |
| ***CE+NF*** | **CEM I 52,5 N CE CP2 NF** | **05/02/1998** |
| *NF P15-318* | Ciments à teneur en sulfures limitée pour béton précontraint | CP2 |
| *CE+BENOR* | CEM I 52,5 N CE HES BENOR | 13/09/2000 |
| | N° de certificat : 15/33/239 | |
| *NBN B12-110* | Ciment Portland à haute résistance initiale | HES |

Disponibilités : Sac 25 kg, Vrac

## COMPOSITION DÉCLARÉE (en %)

**Constituant**

| | |
|---|---|
| Clinker (K) | **97** |
| Laitier de haut-fourneau (S) | _ |
| Schiste calciné (T) | _ |
| Sulfate de calcium (Cs) | _ |
| Pouzzolanes naturelles (P) | _ |
| Cendres volantes siliceuses (V | _ |
| Cendres volantes calciques (W) | _ |
| Calcaires (L ou LL) | _ |
| Constituants secondaires | **3** |

**Régulateur de prise**

| | |
|---|---|
| Gypse | **5,0** |
| Anhydrite | _ |
| Autre sulfate de calcium | _ |

**Additif**

| | | |
|---|---|---|
| Agent de mouture | CXN2 | **0,06** |
| Sulfate ferreux | _ | **0,25** |

## RESISTANCES A LA COMPRESSION (en MPa)

| 1 jour | 2 jours | 7 jours | 28 jours |
|---|---|---|---|
| **24** | **37** | _ | **60** |

## CARACTÉRISATION PHYSIQUE

| Sur poudre | | Sur pâte pure | | Sur mortier | |
|---|---|---|---|---|---|
| Masse volumique (en g/cm$^3$) | **3,09** | Besoin en eau (en %) | **30,5** | Chal. hydr. 41h (en J/g) | _ |
| Surface massique (en cm$^2$/g) | **4600** | Stabilité (en mm) | **0,5** | | |
| Indice de clarté | **66,5** | Début de prise (en min) | **160** | | |

## CARACTÉRISATION CHIMIQUE (en %)

| PAF | INS | $SiO_2$ | $Al_2O_3$ | $Fe_2O_3$ | CaO | MgO | $SO_3$ | $K_2O$ | $Na_2O$ | $S^{--}$ | $Cl^-$ | $CO_2$ | $CaO_{libre}$ | $Na_2O$ éq actif |
|---|---|---|---|---|---|---|---|---|---|---|---|---|---|---|
| **1,8** | **0,5** | **20,1** | **5,2** | **3,3** | **64,1** | **0,8** | **3,0** | **0,76** | **0,28** | **0,01** | **0,07** | **1,0** | **1,7** | **0,78** |

Composition potentielle du clinker : C3A **8,6** C3S **61** C4AF **11,1**

Usine de fabrication afaq ISO 9001 ISO 14001 ISO 9001

**Ciments Calcia**
Italcementi Group

**Direction Industrielle et Technique**
Les Technodes
B.P. 01
78931 Guerville cedex

**Direction Commerciale**
Assistance
et Prescription Clients
Tél. : 01 34 77 78 81
Fax : 01 30 98 73 50

Version du : 26/01/2015

N° certificat CE : 0333-CPR-2204

# Fiche produit de Rombas

## CEM III/A 52,5 L CE PM-ES-CP1 NF

### Caractéristiques physiques et mécaniques

| Compression en MPa | | | | Eau pâte pure en % | Début de prise en mn à 20 °C | Chaleur en J/g à 41h | Masse volumique en g/cm$^3$ | Surface Blaine en cm$^2$/g | Stabilité en mm |
|---|---|---|---|---|---|---|---|---|---|
| 1j | 2j | 7j | 28j | | | | | | |
| nd | 20 | 40 | 63 | 33.0 | 210 | 288 | 2.96 | 4150 | 1 |

### Composition élémentaire (%)

| | |
|---|---|
| Perte au feu | 0.7 |
| $SiO_2$ | 29.0 |
| $Al_2O_3$ | 9.2 |
| $Fe_2O_3$ | 1.4 |
| $TiO_2$ | 0.5 |
| MnO | 0.3 |
| CaO | 50.5 |
| MgO | 4.5 |
| $SO_3$ | 2.6 |
| $K_2O$ | 0.70 |
| $Na_2O$ | 0.38 |
| $P_2O_5$ | 0.1 |
| $S^{--}$ | 0.56 |
| $Cl^-$ | 0.26 |
| Insoluble CEN | 0.4 |
| $Na_2O$ éq. Totaux | 0.80 |
| Colorimétrie (L*) | 74 |

### Constituants (%)

| | |
|---|---|
| **Principaux** | |
| Clinker (K) de | 36.0 |
| *Couvrot* | |
| Laitier (S) | 64.0 |
| Cendres (V) | |
| Calcaire (L ou LL) | |
| Fumées de silice (D) | |
| **Secondaires** | |
| Calcaire (L ou LL) | |
| Total | 100.0 |
| **Sulfate de calcium** | |
| Gypse | |
| Anhydrite | 4.0 |
| **Additifs** | |
| *Chlorure de sodium* | 0.4 |
| *Agent de mouture* | 0.020 |
| *Agent réducteur* | |
| *Sulfate de fer* | 0.13 |

### Caractéristiques des constituants

| Nature | Caractéristiques | |
|---|---|---|
| Clinker (K) | $CaO/SiO_2$ | 3.1 |
| Couvrot | C3S+C2S | 79 |
| | MgO (%) | 1.0 |
| | C3S (%) | 68 |
| | C2S (%) | 11 |
| | C3A (%) | 10 |
| | C4AF (%) | 8 |
| Laitier (S) | | |
| | Laitier vitreux (%) | 98.7 |
| | $(CaO+MgO)/SiO_2$ | 1.3 |
| | $CaO+MgO+SiO_2$ (%) | 83.6 |
| Cendres (V) | | |
| | PF (%) | |
| | CaO réactive (%) | |
| | $SiO_2$ réactive (%) | |
| Calcaire (L ou LL) | $CaCO_3$ (%) | |
| | Adsorption bleu méthylène (g/100g) | |
| | TOC (%) | |
| Fumées de silice (D) | $SiO_2$ amorphe (%) | |
| | PF (%) | |
| | Aire massique BET (m²/kg) | |

### Mouture

| | |
|---|---|
| Broyeur(s) | 6 et 5 |

### Stockage

| | |
|---|---|
| Silo(s) | cf plan de silotage |

| Etablissement | Vrac | Ensachage |
|---|---|---|
| Usine de Rombas | Oui | Non |
| Dépôt de Gennevilliers | Oui | Non |

**Ces valeurs ne sont données qu'à titre indicatif. Les résultats d'auto-contrôle sont disponibles sur demande à la Direction Commerciale Assistance et Prescription Clients**

Siège social :
Rue des Technodes
78930 Guerville
Tél. : 01 34 77 78 00
Fax : 01 34 77 79 06

SAS au capital de 593 836 525 €
Siren 654 800 689 RCS Versailles

CE
0333

# Certificat
Certificate

## Certificat de constance des performances d'un ciment courant

Délivré conformément au Règlement (UE) 305/2011 du Parlement Européen et du Conseil du 9 mars 2011 (Règlement Produits de Construction ou RPC)

**Délivré par :**

| | |
|---|---|
| Organisme de Certification | AFNOR Certification |
| Numéro d'identification | 0333 |
| Adresse | 11, rue Francis de Pressensé<br>F - 93571 LA PLAINE SAINT-DENIS CEDEX |

**Délivré à :**
**Fabricant**

| | |
|---|---|
| Nom | CIMENTS CALCIA |
| Adresse | Les Technodes - BP 01<br>78931 GUERVILLE CEDEX |

**Produit certifié**

| | |
|---|---|
| Désignation du ciment selon la norme | CEM III/A 52,5 L |
| Identification supplémentaire du ciment | |
| Lieu de production du ciment | Rombas |

**AFNOR Certification atteste que toutes les dispositions relatives à l'évaluation et à la vérification de la constance des performances et aux performances décrites dans l'annexe ZA de la norme EN 197-1 : 2011 sont appliquées selon le système 1+ et que ce ciment répond aux dispositions de l'annexe ZA de la norme EN 197-1 : 2011.** La conformité est établie conformément à la norme EN 197-2 comme indiquée dans l'annexe ZA de la norme EN 197-1 : 2011.

Numéro du certificat : **0333 - CPR - 2204**

**Conditions et période de validité du certificat :** ce certificat a été délivré pour la première fois le 01/07/2013. Sauf suspension ou annulation, ce certificat demeure valide tant que les conditions précisées dans les spécifications techniques harmonisées ou les conditions de fabrication en usine ou le contrôle de la production des produits ne sont pas modifiés de manière significative.

Directrice Générale
Florence MÉAUX

Date d'émission du certificat
01/07/2013

cofrac
CERTIFICATION DE PRODUITS ET SERVICES
ACCRÉDITATION N° 5-0020 PORTÉE DISPONIBLE SUR WWW.COFRAC.FR

005 - 2011/01 -

CE

0333

# Certificat
Certificate

## Zertifikat der Leistungsbeständigkeit der Normalzement

Ausgestellt gemäß der Verordnung (EU) Nr. 305/2011 des Europäischen Parlaments und des Rates vom 9. März 2011 (Bauprodukteverordnung - CPR)

**Ausgestellt durch :**

| | |
|---|---|
| Zertifizierungsstelle : | AFNOR Certification |
| Identifikationsnummer | 0333 |
| Adresse | 11, rue Francis de Pressensé<br>F - 93571 LA PLAINE SAINT-DENIS CEDEX |

**Ausgestellt für :**

**Hersteller :**

| | |
|---|---|
| Name | CIMENTS CALCIA |
| Adresse | Les Technodes - BP 01<br>78931 GUERVILLE CEDEX |

**Zertifiziertes Produkt**

| | |
|---|---|
| Normbezeichnung | CEM III/A 52,5 L |
| Zusätzliche Produktbezeichnung | |
| Herstellwerk | Rombas |

AFNOR Certification bescheinigt, dass alle Vorschriften zur Bewertung und Überprüfung der Leistungsbeständigkeit und die Leistungen beschrieben im Anhang ZA der EN 197-1 : 2011 Norm entsprechend System 1+ angewendet werden und dass das normalzement alle darin vorgeschriebenen Anforderungen des Anhanges ZA der EN 197-1 : 2011 Norm erfüllt.

Die Konformität wurde gemäß der EN 197-2 Norm (wie im Anhang ZA der EN 197-1 : 2011 Norm beschrieben) festgelegt.

Nummer des Zertifikats : **0333 - CPR - 2204**

Gültigkeitsbedingungen und -dauer des Zertifikates: Dieses Zertifikat wurde erstmals am 01.07.2013 ausgestellt.
Dieses Zertifikat gilt, solange es nicht erlöscht oder ausgesetzt wurde und solange die in der harmonisierten Norm vorgeschriebenen Anforderungen, die Bedingungen der Herstellung im Werk oder die Anforderungen der werkseigenen Produktionskontrolle nicht wesentlich modifiziert werden.

Die Beauftragte Generaldirektorin von AFNOR Certification
Florence MÉAUX

Datum der Ausstellung des Zertifikats
01/07/2013

cofrac
CERTIFICATION DE PRODUITS ET SERVICES
ACCRÉDITATION N° 5-0030 PORTÉE DISPONIBLE SUR WWW.COFRAC.FR

005 - 2011/01 -

Fiche technique

Omya International AG
P.O. Box 335
CH-4665 Oftringen

+41 62 789 29 29
+41 62 789 20 77

www.omya.com

# Betocarb® - GY

SITE: GY, France

DESCRIPTION DU PRODUIT: Addition calcaire de catégorie A-FM selon la norme NF P 18-508 pour bétons hydrauliques. Utilisable en tant que filler pour bétons hydrauliques hautes performances (EN 12620+ A1).

COMPOSITION DU PRODUIT:

| | | |
|---|---|---|
| $CaCO_3$ | 95 | % |
| Carbonates totaux | 96 | % |
| Chlorures | 0.0008 | % |
| Sulfates | 0.003 | % |
| Soufre total | 0.05 | % |
| Matières organiques | 0.05 | % |
| Essai au bleu de méthylène | 1.5 | g/kg |
| Alcalins équivalents | 0.02 | % |
| Silice totale | 1 | % |
| Réactivité aux alcalins | NR | |

CARACTERISTIQUES TYPES DU PRODUIT:

| | | |
|---|---|---|
| Granulométrie: | | |
| · Particules < 2 mm | 100 | % |
| · Particules < 0.125 mm | 91 | % |
| · Particules < 0.063 mm | 77 | % |
| Surface spécifique Blaine (DIN 66126) | 596 | $m^2/kg$ |
| Indice d'activité à 28 jours | 0.77 | |
| Taux d'humidité départ usine (ISO 787-2) | 0.2 | % |

CARACTERISTIQUES GENERALES DU PRODUIT:

| | | |
|---|---|---|
| Densité (ISO 787-10) | 2.7 | g/ml |
| Densité apparente tassée (ISO 787-11) | 1.5 | g/ml |

APPLICATIONS PRINCIPALES:

Produits en béton
- Pavés
- Blocs
- Autres produits

Béton prêt à l'emploi
Eléments préfabriqués

REPARTITION GRANULOMETRIQUE (Malvern Mastersizer 2000):

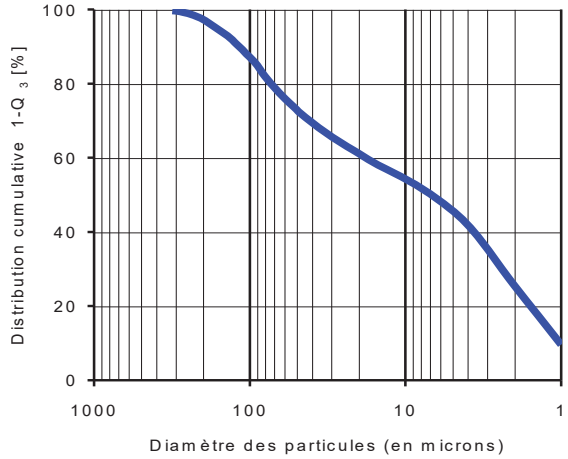


CONDITIONNEMENT STANDARD:
- VRAC
- SAC (papier) de 25 kg sur palette



édition : 04.05.2015
Product Information :
S08.03.01_FR_CORP\FRGY
I28002_02_F
version : 14

# FICHE DE DONNEES DE SECURITE
**Selon 1907 /2006/CE, Article 31**

*Date d'édition : 01.10.2010* *Révision : 02.05.2013*

## 1. IDENTIFICATION DE LA SUBSTANCE/ DU MELANGE ET DE LA SOCIETE/ L'ENTREPRISE

### ➢ Identificateur du produit :

- **Nom du produit** : **CONDENSIL® S95 DM**
- **Utilisations identifiées pertinentes de la substance ou du mélange et utilisations déconseillées.**
  Utilisation principale : addition pour bétons, mortiers et coulis

- **Fournisseur** : **CONDENSIL 1327 avenue de la Houille Blanche F 73024 CHAMBERY CEDEX**

**Usine** : **265 rue des Epinettes F 73000 CHAMBERY**

Tél. **: 33 4 79 62 74 03**
Fax **: 33 4 79 96 35 94**
E-mail **condensil@vicat.fr**

## 2. IDENTIFICATION DES DANGERS

### ➢ Classification de la substance ou du mélange :

- **Classification selon le règlement (CE) n° 1272/2008**
  Le produit n'est pas classifié selon le règlement CLP.
- **Classification selon la directive 67/548/CEE ou directive 1999/45/CE :** Néant
- **Indications particulières concernant les dangers pour l'homme et l'environnement :**
  Aucun danger particulier à mentionner. Veuillez, néanmoins, respecter les informations figurant dans cette fiche de données de sécurité.
  Veuillez respecter les conditions de stockage et d'utilisation. Une forte concentration dans l'air peut occasionner une irritation des yeux, de la peau, des muqueuses et de l'appareil respiratoire.
  Le risque de fibrose pulmonaire est minime. Toutefois, on pense qu'une exposition de longue durée (plusieurs années) à des concentrations supérieures aux limites recommandées peut occasionner une bronchopneumopathie chronique obstructive (BPCO).
- **Système de classification :**
  La classification correspond aux listes CEE actuelles et est complétée par des indications tirées de publications spécialisées et des indications fournies par l'entreprise.

### ➢ Eléments d'étiquetage :

- **Marquage selon les directives CEE :**
  Bien que ce produit ne soit pas soumis à l'obligation d'identification, nous recommandons d'observer les conseils de sécurité.
  Le produit n'est pas identifié suivant les directives de la Communauté européenne/les lois respectives nationales.
  2004/73/CE ; 2006/8/CE
- **Identification particulière de certaines préparations :**
  Fiche de données de sécurité disponibles sur demande pour les professionnels

### ➢ Autres dangers :

- **Résultats des évaluations PBT et vPvB**
  **PBT (Persistant/Bioaccumulable/Toxique)** : Non applicable
  **vPvB** (très persistant/très bioaccumulable) : Non applicable

## 3. COMPOSITION/INFORMATIONS SUR LES COMPOSANTS

### ➢ Caractérisation chimique : Mélanges

- **Description** : micro-billes de Silice SiO2

- **Composants** :

| | | | |
|---|---|---|---|
| 1) | CAS : 69012-64-2<br>EINECS : 273-761-1 | Silice amorphe | 80-100% |
| 2) | CAS : 14464-46-1<br>EINECS : 238-455-4<br>RTECS VV7325000 | Silice cristalline : cristobalite | < 0,5% |
| 3) | | Oxydes métalliques divers | 0-20% |

## 4. PREMIERS SECOURS

### ➢ Description des premiers secours :

Les secouristes doivent veiller à leur propre protection. Retirer les vêtements souillés.

- **Après inhalation :**
  Après inhalation des poussières : Repos, air frais.

- **Après contact avec la peau :**
  Après contact avec la peau, se laver immédiatement et abondamment avec de l'eau et du savon. En aucun cas n'utiliser de solvant. En cas d'irritation consulter un médecin.

- **Après contact avec les yeux :**
  Après contact avec les yeux, laver à fond à l'eau courante pendant 15 minutes en maintenant les paupières écartées, faire procéder à un contrôle par un ophtalmologue.

- **Après ingestion:**
  Après ingestion, rincer immédiatement la bouche et faire boire de grandes quantités d'eau, secours médical. Ne provoquer les vomissements que si cette recommandation provient d'un centre anti-poison ou d'un médecin.

### ➢ Principaux symptômes et effets, aigus et différés :

Symptômes : Des symptômes significatifs ne sont pas attendus car le produit n'est pas classé.

### ➢ Indications des éventuels soins médicaux immédiats et traitements particuliers nécessaires:

Traitement : Traitement symptomatique (décontamination, fonctions vitales), aucun antidote spécifique connu.

## 5. MESURES DE LUTTE CONTRE L'INCENDIE

### ➢ Moyens d'extinction :

- **Moyens d'extinction** : Sans objet. Le produit n'est pas inflammable.

### ➢ Conseils aux pompiers :

- **Equipement spécial de sécurité** : porter un appareil respiratoire autonome

Autres informations :

Le danger dépend des produits et des conditions de combustion. L'eau d'extinction contaminée doit être éliminée conformément aux réglementations officielles locales.

## 6. MESURES A PRENDRE EN CAS DE DISPERSION ACCIDENTELLE

### ➢ Précautions individuelles, équipement de protection et procédures d'urgence :

Veiller à une aération suffisante (milieu non confiné).
Eviter la formation de poussière
Porter un équipement de sécurité (voir chapitre 8). Eloigner les personnes non protégées.

### ➢ Précautions pour la protection de l'environnement :

Ne pas rejeter dans les canalisations, dans les eaux de surface et dans les nappes d'eau souterraines.

### ➢ Méthodes et matériel de confinement et de nettoyage :

Pour de petites quantités : Ramasser à l'aide d'un moyen adapté (balai, pelle,…)
Pour de grandes quantités : Ramasser a l'aide d'un moyen adapté (aspirateur, pelle mécanique,….)
Le produit doit être récupéré dans des conteneurs appropriés et éliminé conformément à la réglementation en vigueur.

### ➢ Référence à d'autres sections :

Afin d'obtenir des informations pour une manipulation sûre, consulter le chapitre 7.
Afin d'obtenir des informations sur l'exposition et la protection individuelle, consulter le chapitre 8.
Afin d'obtenir des informations sur l'élimination, consulter le chapitre 13.

## 7. MANIPULATION ET STOCKAGE

### ➢ Manipulation :

- **Précautions à prendre pour une manipulation sans danger**
  Eviter la formation de poussière
  Les formations de poussière qui ne peuvent être évitées doivent être régulièrement ramassées et/ou aspirées..
  N'employer que dans des secteurs bien aérés. En cas de transvasement, il faut le faire dans la direction du vent et éviter les pertes autant que possible.
  En cas de formation de poussière importante, prévoir une aspiration.
  Prévoir pour le personnel des protections respiratoire.
- **Préventions des incendies et des explosions** : le produit n'est pas inflammable ni explosif.

### ➢ Conditions d 'un stockage sûr, y compris d'éventuelles incompatibilités :

- **Stockage**
- **Exigences concernant les lieux et conteneurs de stockage :**
  Stocker dans un endroit aéré et sec. Protéger de l'action directe des rayons du soleil.
  Matériaux adaptés : Polyéthylène haute densité (PEHD)
- **Indications concernant le stockage commun :**
  Eviter tout risque de contact avec l'acide fluorhydrique (HF)
- **Autres indications sur les conditions de stockage :**
  Prudence en cas de réouverture d'emballage entamés
  Conserver les emballages dans un endroit bien aéré et sec.

## 8. CONTRÔLES DE L'EXPOSITION/PROTECTION INDIVIDUELLE

### ➢ Indications complémentaires pour l'agencement des installations techniques :

Sans autre indication, voir point 7

### ➢ Paramètres de contrôle :

69012-64-2 : fumées, silice

- **Composants présentant des valeurs-seuils à surveiller par poste de travail :**

**1) Poussières :**
VME (France) Valeur momentanée : 10 mg/m³
Valeur à long terme : 5 mg/m³

**2) 14464-46-1 silice cristalline : cristobalite :**
VME (France) 0,05 a mg/m³
a pour la fraction alvéolaire

### 3) 14808-60-7 quartz (SiO2) :

VME (France) 0,1 a mg/m³
a pour la fraction alvéolaire

### 4) 15468-32-3 tridymite :

VME (France) 0,05 a mg/m³
a pour la fraction alvéolaire

- **Remarques supplémentaires :**
Le présent document s'appuie sur les listes en vigueur au moment de son élaboration.

## ➢ Contrôles de l'exposition :

Eviter l'inhalation de poussières. Assurer une bonne ventilation des locaux lors de la manipulation et de l'utilisation du produit.

- **Equipement de protection individuel:**

1) **Protection des yeux :** le port de lunettes de sécurité avec protection latérale est **vivement recommandé** pour éviter le contact avec les yeux (p.ex. EN 166).

2) **Protection respiratoire :** l'utilisation des masques filtrants pour poussières ultra-fines pendant les opérations pouvant générer de la poussière est **obligatoire (p.ex. EN 143 ou 149, Type P1 ou FFP1)**.

3) **Protection des mains :** l'utilisation des gants de protection adaptés pour éviter tout contact avec la peau est **recommandée**.

4) **Protection du corps :** le port de vêtements de travail protecteurs et adaptés est **obligatoire**.

- **Mesures générales de protection et d'hygiène :**
Afin d'éviter une contamination lors de la manipulation, une combinaison de travail fermée et des gants devraient être portés. Appliquer les mesures habituelles de précaution aux poudres ultra fines. Lors de l'utilisation, ne pas manger, ni boire, ni fumer. Se laver les mains et/ou le visage avant les pauses et après le travail. Après le travail, veiller à la propreté et au soin de la peau. Les gants doivent être contrôlés régulièrement et avant chaque usage. Remplacer si nécessaire (en cas de petites fuites p.ex.).

## 9. PROPRIETES PHYSIQUES ET CHIMIQUES

### ➢ Informations sur les propriétés physique et chimiques essentielles:

- **Indications générales :**

**1) <u>Aspect</u>**

- **Forme :** poudre ultra-fine. Taille des particules élémentaires : environ 150nm.
- **Couleur :** Gris (Luminance L* entre 40 et 75)
- **Odeur :** Inodore
- **Valeur du pH :** neutre

**2) <u>Changement d'état</u>**

- **Point de fusion** : 1550-1700°C
- **Point d'ébullition** : Non déterminé

**3) <u>Point d'inflammation</u>**
Non applicable

**4) <u>Auto-inflammation</u>**
Le produit ne s'enflamme pas spontanément

**5) <u>Danger d'explosion</u>**
Le produit n'est pas explosif

**6) <u>Densité à 20°C</u>**
150-750 kg/m³

**7) <u>Solubilité dans/miscilité avec l'eau</u>**
Non soluble

**8) <u>Teneur en solvants</u>**

- **Teneur en substances solides** : 100%

## 10. STABILITE ET REACTIVITE

### ➢ Stabilité:

Le produit est inerte et stable dans les prescriptions/indications pour le stockage et la manipulation préconisée par le fournisseur.

**<u>Indications complémentaires :</u>** Une élévation de températures au-delà de 1000°C peut engendrer la transformation en silice cristalline (cristobalite/tridymite), produit présentant un risque de silicose. Le taux de transformation augmente avec la température et la durée d'exposition du produit.

### ➢ Réactivité:

Le produit peut réagir avec l'acide fluorhydrique(HF) pour libérer un gaz toxique ($SiF_4$)

### ➢ Matières incompatibles :

Acide fluorhydrique (HF), acides forts, bases fortes, oxydants puissants.

### ➢ Produits de décomposition dangereux :

Aucun produit de décomposition dangereux, si les prescriptions/indications pour le stockage et la manipulation sont respectées.

## 11. INFORMATIONS TOXICOLOGIQUES

- **Informations sur les effets toxicologiques :**
  **Toxicité aiguë :** aucune (pratiquement pas toxique après une ingestion unique. Le produit n'a pas été testé. Les informations proviennent de produits de structure ou de composition analogue).
- **Effet primaire d'irritation :**
  **De la peau** : Possibilité d'irritation en cas d'action prolongée sur la peau.
  **Des yeux** : peut entrainer de légères irritations aux yeux..
- **Sensibilisation :**
  Aucun effet de sensibilisation connu.
- **Indications toxicologiques complémentaires :**
  Selon le procédé de calcul de la dernière version en vigueur de la directive générale CEE de classification des préparations, le produit n'est soumis à aucune obligation de marquage.
  En cas de manipulation et d'utilisations conformes, le produit n'a aucun effet nocif pour la santé selon notre expérience et les informations dont nous disposons.

Autres informations sur la toxicité:

Selon notre expérience et les informations dont nous disposons, le produit ne provoque aucun effet nocif, dans les conditions normales de manipulation et de mise en œuvre.

## 12. INFORMATIONS ECOLOGIQUES

- **Toxicité :**
  **Toxicité aquatique :** pas d'informations importantes disponibles.
  **Autres indications écologiques** : d'après les connaissances actuelles, des effets écologiques négatifs ne sont pas attendus.
- **Résultats des évaluations PBT et VPVB :**
  **PBT** : non applicable.
  **vPvB** : non applicable.

## 13. CONSIDERATIONS RELATIVES A L'ELIMINATION

- **Méthode de traitement des déchets :**
  **Recommandation :** ne doit pas être évacué avec les ordures ménagères. Ne pas laisser pénétrer dans les égouts. Les prescriptions locales et nationales doivent être respectées. Les résidus sont à éliminer comme le produit.

- **Emballages non nettoyés :**
  **Recommandation :** évacuation conformément aux prescriptions légales.

## 14. INFORMATIONS RELATIVES AU TRANSPORT

- **Transport par terre ADR/RID (ordonnance sur le transport des produits dangereux – route et train)(transfrontalier):**
  **Classe ADR/RID** : Non

- **Transport maritime IMDG (ordonnance sur le transport de produits dangereux) :**
  **Polluant marin :** Non

- **Transport aérien ICAO-TI et IATA-DGR**
  **Classe ICAO/IATA :** No ID ONU ("Règlement type de l'ONU: Précautions particulières à prendre par l'utilisateur: Non applicable)

## 15. INFORMATIONS REGLEMENTAIRES

### ➢ Réglementations/législation particulières à la substance ou au mélange en matière de sécurité, de santé et d'environnement

- **Prescriptions nationales :** non
- **Autres prescriptions, restrictions et règlements d'interdiction :** non
- **Substances extrêmement préoccupantes (SVHC) selon REACH, article 57 :** non
- **Evaluation de la sécurité chimique :** une évaluation de la sécurité chimique n'a pas été réalisée.

## 16. AUTRES INFORMATIONS

- Ces indications sont fondées sur l'état actuel de nos connaissances, mais ne constituent pas une garantie quant aux propriétés du produit et ne donnent pas lieu à un rapport juridique contractuel.
- L'attention des utilisateurs est en outre attirée sur les risques éventuellement encourus lorsqu'un produit est utilisé à d'autres usages que ceux pour lesquels il est conçu.
- Elle ne dispense en aucun cas l'utilisateur de connaitre et d'appliquer l'ensemble des textes réglementant son activité. Il prendra sous sa seule responsabilité les précautions liés à l'utilisation qu'il fait du produit.
- Cette énumération ne doit pas être considérée comme exhaustive et n'exonère pas le destinataire de s'assurer qu'éventuellement d'autres obligations ne lui incombent pas en raison de textes autres que ceux cités concernant la détention et la manipulation du produit pour lesquels il est seul responsable.

### ➢ Acronymes et abréviations :

ADR: Accord européen sur le transport des marchandises dangereuses par route
RID : Règlement international concernant le transport des marchandises dangereuses par chemin de fer
IMDG ; International Maritime Code for Dangerous Goods
IATA : International Air Transport Association
IATA-DGR : Dangerous Goods Regulations by the "International Air Transport Association"(IATA)
ICAO : International Civil Aviation Organization
ICAO-TI : Technical Instructions by the "International Civil Aviation Organization" (ICAO)
GHS : Globally Harmonized System of Classification and Labelling of Chemicals

**Signature** *Date d'édition : 01.10.2010* *Révision : 02.05.2013*

**Alain PICOT**
**Directeur CONDENSIL**

## 1. DEFINITION

Ecocem, le laitier granulé de haut fourneau moulu CE produit par ECOCEM France à Fos sur Mer (13), répond à la norme européenne **NF EN 15167-1**, 2006 : Laitier granulé de haut-fourneau moulu pour utilisation dans le béton, mortier et coulis - Partie 1 : définitions, exigences et critères de conformité.
Le certificat CE de constance des performances 1164-CPR-LGM001, a été renouvelé le 10 Janvier 2017, par le CERIB, organisme notifié n°1164.
Ecocem est un laitier moulu de classe A, suivant les distinctions faites dans la norme NF EN 206/CN, classe confirmée, en date du 28 Juin 2013, par le CERIB.

## 2. FABRICATION

Ecocem est produit par le séchage et le broyage du laitier granulé de haut-fourneau.
Le laitier granulé est obtenu par trempe à l'eau du laitier à la sortie des hauts-fourneaux de Fos sur Mer, au moyen de granulateur de nouvelle génération (INBA®).
Le taux de vitrification moyen obtenu est supérieur à 90% (mesure par diffraction de rayons X).
Ecocem est livré en vrac.

## 3. COMPOSITION CHIMIQUE (centésimale moyenne)

| | |
|---|---|
| **CaO** | 42,9 |
| **$SiO_2$** | 38,0 |
| **$Al_2O_3$** | 10,8 |
| **MgO** | 6,6 |

| | |
|---|---|
| **$Fe_2O_3$** | 0,7 |
| **$TiO_2$** | 0,7 |
| **$SO_3$** | 0,1 |
| **$S^{2-}$** | 0,7 |

| | |
|---|---|
| **$Na_2O$** | 0,28 |
| **$K_2O$** | 0,35 |
| **$Na_2O$ éq.** | 0,51 |
| **$Cl^-$** | 0,01 |

Module chimique $(CaO+MgO)/SiO_2$ : > 1,25 *(≥1,2 : classe A selon NF EN 206-1/CN)*

## 4. CARACTERISTIQUES PHYSIQUES (valeurs indicatives représentatives)

| **FORMULATION** | | **Résistances en Compression** (MPa) | | | **Indice d'activité** | | | **Temps de prise initial** (min) |
|---|---|---|---|---|---|---|---|---|
| **Ecocem** | **Ciment référence** | 7 jrs | 28 jrs | 90 jrs | 7 jrs | 28 jrs | 90 jrs | |
| **0%** | **100%** | 46 | 58 | 62 | - | | | 143 |
| **50%** | **50%** | 32 | 56 | 69 | 69% | 97% | 111% | 174 |
| *Limites de la Norme produit NF EN 15167-1* | | | | | *≥ 45%* | *≥ 70%* | - | *< 2 × Tps Ciment* |
| *Limites Classe A selon Norme NF EN 206/CN* | | | | | *≥ 65%* | *≥ 85%* | - | - |

## 5. AUTRES CARACTERISTIQUES

Surface spécifique Blaine : 4450 ± 250 $cm^2/g$
*≥ 2750 cm2/g : NF EN 15167-1*
*≥ 4200 cm2/g : classe A selon NF EN 206/CN*

Passant à 32 µm : ≥ 95%
Diamètre médian indicatif (d50) : 11µm

Indice [CIE L*ab] avec CR410 : L* = 89,5 ± 2
Perte au feu (950°C) : < 1,5%
Humidité (100°C) : < 0,5%
Masse volumique ($g/cm^3$) : 2,90 ± 0,03
Densité apparente : 0,8 ± 0,1

L'emploi du laitier Ecocem contribue à la réduction de la solubilité des résidus tels que chlorures, sulfates et fluorures.

A02
**CERTIFICAT DE RECEPTION** **3.1-EN 10204 : 2004**
**INSPECTION CERTIFICATE 3.1**

DATE / Date 21/06/19 Page: 01

A03 N° de DOCUMENT
*Document Nr* 10545

A01
**SOCIETE DES ACIERS D'ARMATURE POUR LE BETON S.A.S.**
Capital social 47.275.000 Euro
B.P.1 222, rue Victor de Lespinats 54230 NEUVES-MAISONS
Téléphone 03 83 50 29 00 - Télécopie 03 83 47 08 54
RC. Nancy 389 517 061 - Siret 389 517 061 00021
NAF 2410Z - TVA/FR 52 389 517 061

| A07 N° COMMANDE Client *Customer Order Nr.* | A08 N° COMMANDE *Order Works Nr.* | A11 N° AVIS EXPEDITION *Dispatching Nr.* | A06 CLIENT *Customer* | A12 DESTINATION *Destination* |
|---|---|---|---|---|
| 543 150519 | IM087 | 10665 19 | FIMUREX AQUITAINE | 82400 GOLFECH |

| B03 NORME / *Standard* | B02 TYPE / *Type* | B01 QUALITE / *Grade* | B04 PROCESSUS DE FABRICATION / *Working Process* |
|---|---|---|---|
| NF A35-052 | BKR | TSB/SAE1012/B10 | |

A10 SPECIFICATIONS TECHNIQUES / *Specification covering shipment*

Nous certifions que les produits enumeres ci dessous sont controles et exempts de radioactivite
This material has been inspected and found to be free from radioactivity

Z01 DECLARATION DE CONFORMITE
*Conformity attestation*

Nous certifions que les produits enumeres ci dessous sont conformes aux stipulations de la commande
We certify hereby that the below mentioned products are consistent with the order prescriptions

COMPOSITION CHIMIQUE / *Chemical composition*

| B07 COULEES *Heat* | C71 C % | C72 Mn % | C73 Si % | C74 P % | C75 S % | C76 Cr % | C77 Ni % | C78 Cu % | C79 Mo % | C80 | C81 N2 % | C82 B % | C83 | C84 | C85 | C86 | Ceq % |
|---|---|---|---|---|---|---|---|---|---|---|---|---|---|---|---|---|---|
| 92165 | 0,120 | 0,735 | 0,164 | 0,020 | 0,027 | 0,111 | 0,069 | 0,218 | 0,026 | | 0,010 | 0,0002 | | | | | 0,289 |
| 92857 | 0,130 | 0,749 | 0,195 | 0,027 | 0,029 | 0,139 | 0,071 | 0,290 | 0,020 | 0,001 | 0,011 | 0,0002 | 0,002 | | | | 0,311 |
| | | | | | | | | | | | | | | | | | |
| | | | | | | | | | | | | | | | | | |
| | | | | | | | | | | | | | | | | | |

PROPRIETES MECANIQUES / *Mechanical properties*

| B07 COULEES *Heat* | C00 n° essai *Test Nr.* | B09 ∅ (mm) | B10 ou B12 Longeur *Length (m)* | B13 | B13 P/m (Kg/m) | C11 Re ( MPa ) | C12 Rm ( MPa ) | C14 | C15 | C13 Agt (%) | C13 A5 (%) | C13 | B15 | B16 | B17 | B17 | B19 | B10 | B21 | B22 PLIAGE Bend | B22 DEPLIAGE Rebend |
|---|---|---|---|---|---|---|---|---|---|---|---|---|---|---|---|---|---|---|---|---|---|
| 92165/ | 1 | 6,30 | | | 0,250 | 372,0 | 512,0 | | | 19,30 | 38,8 | | | | | | | | | | |
| 92857/ | 1 | 6,30 | | | 0,249 | 362,0 | 498,0 | | | 19,80 | 39,9 | | | | | | | | | | |
| | | | | | | | | | | | | | | | | | | | | | |
| | | | | | | | | | | | | | | | | | | | | | |
| | | | | | | | | | | | | | | | | | | | | | |
| | | | | | | | | | | | | | | | | | | | | | |
| | | | | | | | | | | | | | | | | | | | | | |
| | | | | | | | | | | | | | | | | | | | | | |
| | | | | | | | | | | | | | | | | | | | | | |
| | | | | | | | | | | | | | | | | | | | | | |
| | | | | | | | | | | | | | | | | | | | | | |
| | | | | | | | | | | | | | | | | | | | | | |
| | | | | | | | | | | | | | | | | | | | | | |
| | | | | | | | | | | | | | | | | | | | | | |

B11

B14

B06 MARQUES D'IDENTIFICATION / *Identification Marks*

B14 SERVICE QUALITE
*Quality Department*

NOM
*Name* A. POPPE

RIQQ001A

# Appendix II

## Description and preparation of samples

Appendix in: Study of the initiation and propagation phases of chloride induced corrosion in reinforced concrete structures

Realized by: Chantal Chalhoub

Thesis for the degree of Philosophiæ doctor

Université Toulouse 3 Paul Sabatier (UT3 Paul Sabatier)

Laboratoire Matériaux et Durabilité des Constructions de Toulouse

Appendix II

Appendix II

# Contents

# 1. Introduction

The aim of this report is to describe the preparation of the different samples used in the thesis report.

# 2. Preparation of cathode samples

## 2.1. Description

Cathode samples are cylindrical reinforced samples with dimensions of ϕ = 110 and h= 220 mm and a cover of 5.2 cm having one steel bar with dimensions of ϕ = 6 and h = 160 mm embedded at their center. As shown in Fig. 1 some cathodes embedded at their center rebars with dimensions of ϕ = 6 and h = 50 and 10 mm. The latter were used to test lower cathode to anode ratios.

These samples were chloride-free and are used as cathodes for galvanic coupling tests.

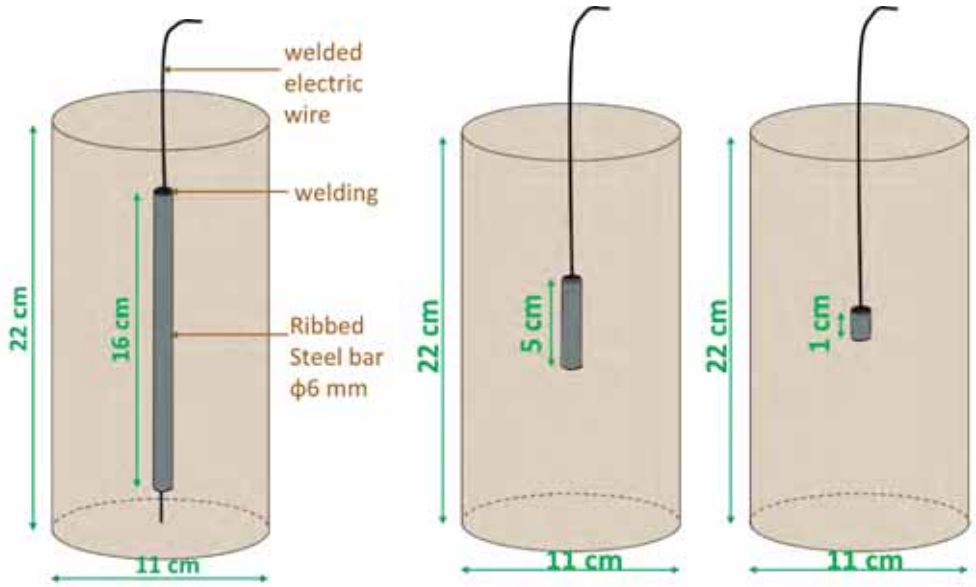


*Fig. 1. Dimensions of cathode samples*

## 2.2. Electric wire welding and installation of reinforcement bars

Steel reinforcements Fe-500 ribbed steel bar 6 mm in diameter are sawn into pieces of 160 mm in length. Two electrical wires were tin welded to each steel bar, one to the upper part and one to the lower, leaving only the lateral surface of then steel uncovered (Fig. 2). The upper wire was used to guarantee a good electrical connection during electrochemical testing. Each wire must be stripped some mm from the edge to do the welding. It is important to ensure that no part of the bare wire remains outside the weld to avoid contact between bare wire and concrete.

The length of the electrical wire on the underside of the steel that will fix the reinforcement in the center of the mold must be at least 5 cm and that of the wire of the upper part must exceed 3 cm. Each wire was held in place by a hole made in the middle of the upper and lower part of the mold (Fig. 3).

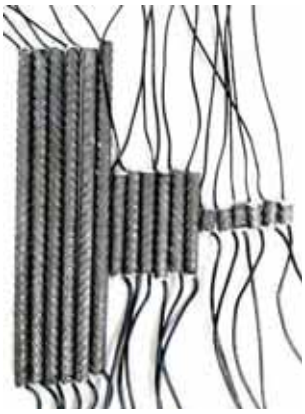

*Fig. 2. Steel centered in the ''Cathode'' and ''Anode'' molds respectively*

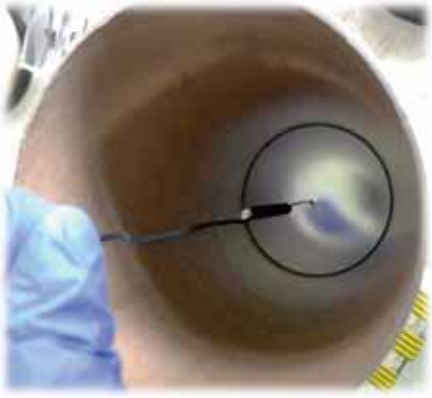

*Fig. 3. Steel centered in the ''Cathode'' molds*

## 2.3.Preparation

Carton molds with dimensions of 11x22 $cm^3$ are used for the casting of cathodic specimens. The molds must be drilled at the center of the base and cover using a drill with a Ø 2 mm drill bit. The determination of the center of the surfaces to be pierced is carried out by marking the center of the disc of the base of a single mold (intersection of 2 diameters) which will be used as a support to pierce the rest of the molds.

The lower wire was fixed to the hole of the base of the mold with a knot, which was then covered in silicone. This will allow to maintain the rebars in the center of the specimen. This means that a gap of 3 cm should be left on the underside of the rebar.

During the casting, the mold is filled by half while keeping the steel in the center. Then, the samples must be vibrated for 10s on a concrete molds table/Plate Vibrato or with a concrete vibrator. Then, the mold is entirely filled and vibrated again for 10s. The mold is then covered with a pierced plastic lid and the upper wire welded to the steel is introduced through the centered hole of the lid and then fixed with a tape. The specimen is then vibrated for 2 to 5 s.

Fig. 4 illustrates the different steps adopted for the preparation of cathodes.

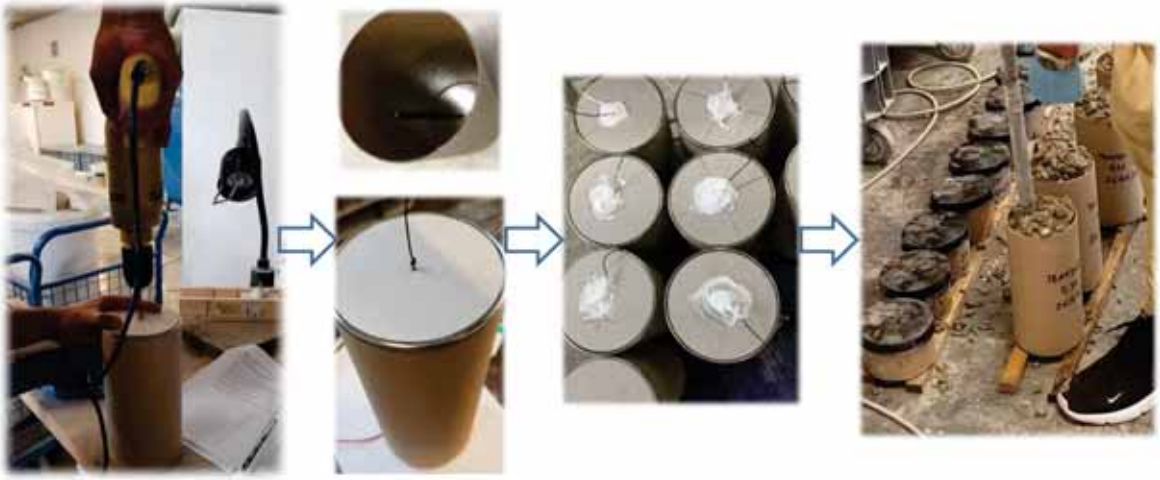

*Fig. 4. Preparation of concrete cathode samples*

## 2.4.Wet curing

As shown in Fig. 5, the cathode samples are placed after casting in a wet curing room (relative humidity= 95%). The time needed for demolding and the duration of wet curing depend on the mortar or concrete formulation. While some cathodes were subjected to wet curing, other cathodes were entirely immerged in water directly after demolding as presented in Fig. 6.

*Fig. 5. Cathodes in wet curing room after casting before demolding*

*Fig. 6. Wet curing of cathodes (on the left) and water immersion of cathodes samples (on the right)*

# 3. Preparation of anode specimens

## 3.1. Description

The anodic samples are also cylindrical (ϕ33 x 70 mm) with diameters, ϕ, of 33 mm and heights, h, of 70 mm having one steel bar embedded at their center, with dimensions of ϕ = 6 mm and h = 10 mm, thus having a cover of 1.35 cm.

As shown in Fig. 7, the mortar samples (on the left) were directly realized in small plastic molds. However, anode concrete samples were casted as cylindrical concrete specimens with a diameter of 110 mm instead of 33 mm and a height of 70 mm were made because of the size of aggregates. After curing, the final anode (ϕ 33 x h 70 mm) was extracted from the cylindrical specimen by coring.

These samples were contaminated with chlorides before being used either as test samples for corrosion tests or as reference samples for chloride-binding isotherms or for imbibition duration verification tests.

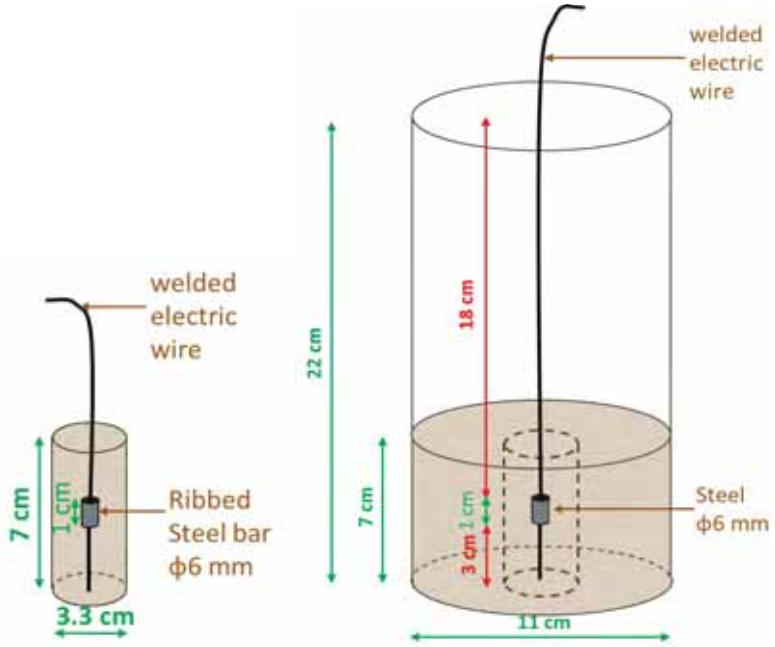


*Fig. 7. Description of mortar (on the left) and concrete (on the right) anode samples*

## 3.2. Preparation

Firstly, Fe-500 ribbed steel reinforcements 6 mm in diameter are sawn into pieces of 10 mm in length. The mass of the anode steels must be measured before welding and casting and the anodes must be identified. Similarly to cathodes, electrical wires were welded to the rebars on the upper and lower side of the bars and the length of the wire on the lower side must be at least 5 cm and that of the wire of the upper part must exceed 18 cm.

The lower wire was fixed to the hole of the base of the mold with a knot, which was then covered in silicone. This will allow to maintain the rebars in the center of the specimen. This means that a gap of 3 cm should be left on the underside of the rebar.

Fig. 8 shows the different steps of the preparing of mortar anodes, while, Fig. 9 illustrates the preparation of concrete anode specimens.

*Fig. 8. Preparation of mortar anode samples*

*Fig. 9. Preparation of concrete anode samples*

## 3.3.Preconditioning

After casting, samples are placed in a wet curing room (relative humidity= 95%). The time needed for demolding and the duration of wet curing depend on the mortar or concrete formulation.

After curing, the final concrete anode is extracted from the centrally located cylindrical specimen with a diameter of 33 mm (Fig. 9).

After the end of curing, anodes are dried in a “WEISS” heating drying oven at a constant temperature of 45 °C and a controlled relative humidity of 25% until their mass was constant, i.e. until 2 successive weighings before and after 24 h in the oven did not differ by>0.05%. The temperature was limited to 45 °C to avoid the destabilization of hydrates and cracking.

After the end of drying, the chlorides were introduced by soaking the anodes in 1 L of sodium chloride solutions having controlled chloride contents using demineralized water. The electrical wires

welded to the bars and the lower part of the samples were coated with silicone to avoid the penetration of chloride into the samples through the wires or the holes. The samples were entirely immersed for 48 h in saline solutions with 5 different concentrations of NaCl: 12.25, 22.75, 70, 140 and 280 g/L.

Fig. 10 presents a schematic representation of the preconditioning protocol adopted to accelerate the chloride diffusion into the samples.


*Fig. 10. Preconditioning of anode samples (drying then soaking in NaCl saline solution)*

# 4. Preparation of reinforced walls

## 4.1.Description

As presented in Fig. 11, the wall is a concrete parallelepiped of 75x20x100 cm containing 18 embedded steel bars of 12 mm diameter: 10 horizontal bars each having a length of 70 cm and 8 vertical bars having a length of 102 cm with 5 cm emerging from the concrete.

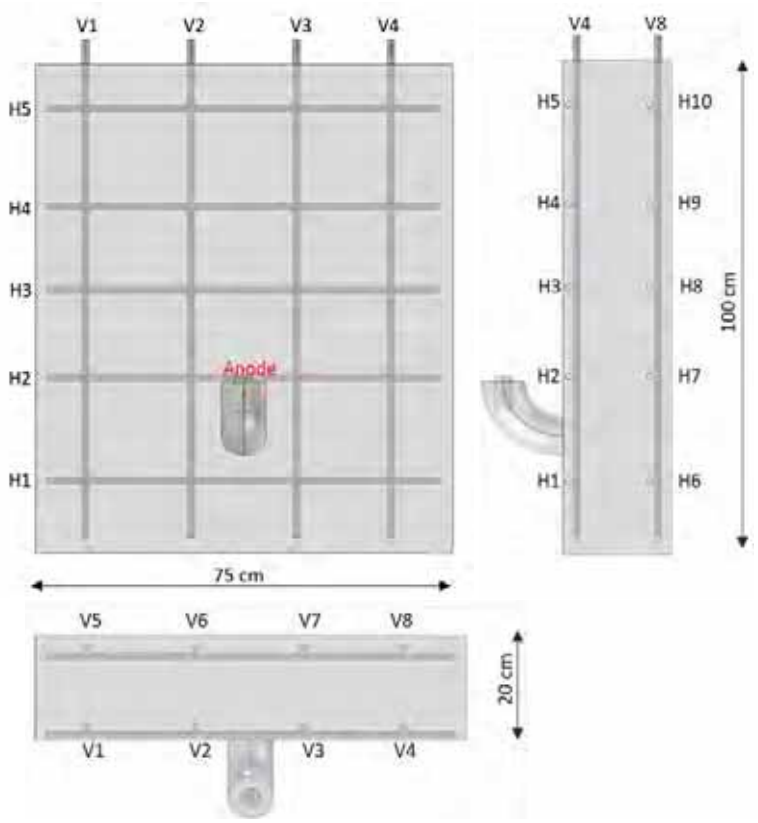


*Fig. 11. Description of the concrete wall*

## 4.2.Preparation

As shown in Fig. 12, the network of frames was completely electrically disconnected using plastic spacers to connect the bars which could be electrically connected externally with a connection box.

*Fig. 12. Installation of reinforcement bars in the formwork*

Appendix II

As illustrated in Fig. 13, the wall is filled with fresh concrete in four stages. Each time, each layer is vibrated with a concrete vibrator.

*Fig. 13. Formwork and casting of the wall*

After demolding a PVC pipe containing a sodium hydroxide solution was connected to the wall with silicone (Fig. 14). The pipe must be supported for 1 to 2 days to allow the silicone to dry and to make sure the connection is completely sealed.


*Fig. 14. Wall after demolding and installation of PVC tube*

## 5. Preparation of reinforced 10 m length beam

The geometry of the beam is illustrated in Fig. 15. Note that the scale in the horizontal direction is different from that in the vertical direction to make the scheme clearer. The beam had a length of 10 m and a square cross section of 10x10 $cm^2$. It contained a single bed of reinforcement bars that was composed of 20 ribbed steel bars with a diameter of 12 mm, 19 of which had a length of 20 cm and one a length of 2 cm. This last bar, representing the anode, was exposed to chloride contamination in order to initiate its corrosion. The length of this bar was kept short in order to limit the cathodic area within the anode.

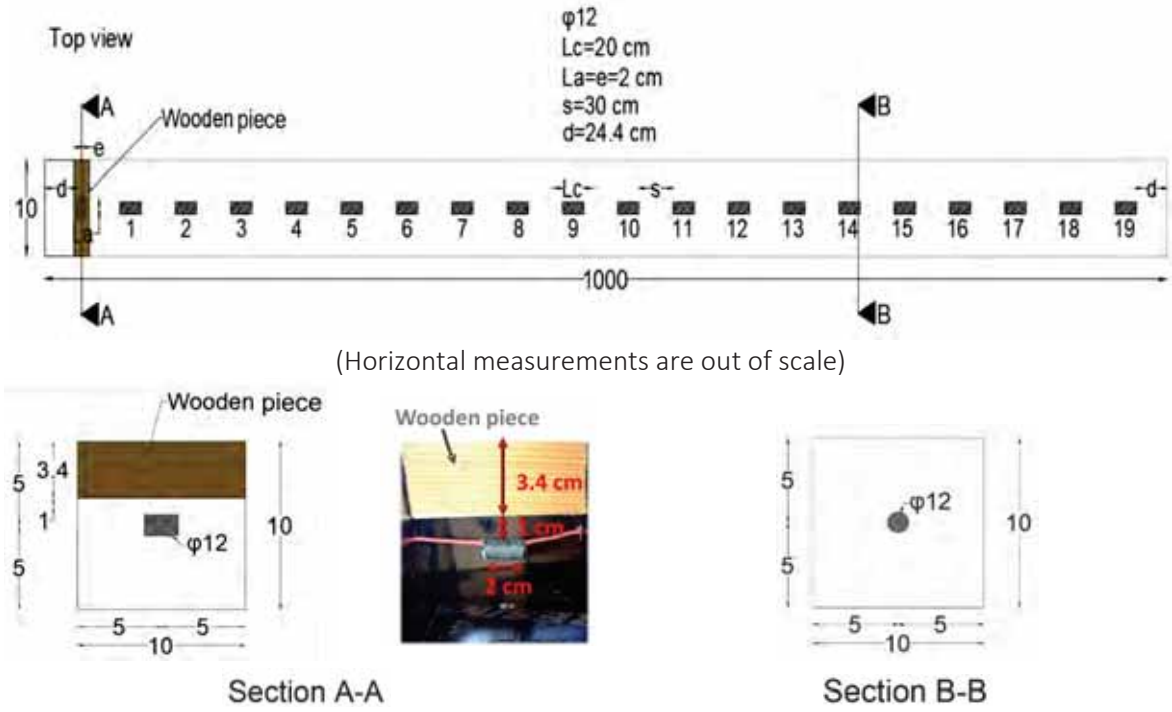


*Fig. 15. Details of reinforcement of the mortar beam (dimensions are in cm except for ϕ12 in mm)*

As shown in Fig. 16, all the 19 bars of 20 cm length were aligned, centered and parallel to the length of the beam, and were in an entirely passive state: they acted as cathodes. The total area of cathode bars is approximatively 1,437 $cm^2$. The first bar on the left was centered but transversal to the direction of the other bars. It formed the anode with a surface of 7.5 $cm^2$. The spacing (s) between two consecutive bars was 30 cm and the last bar at each extremity of the beam was 24.4 cm from the end.

The electrical contact was made with electrical wires that were tin welded to each bar. A piece of wood was fixed above the anode bar before casting, to leave a space of only 1 cm between its lower part and the upper part of the anode bar. This was done in order to reduce the cover thickness to 1 cm instead of 4.4 cm at the level of the anode bar.

Fig. 17 shows an image taken during the casting of the beam which was filled with fresh mortar in four stages. Each time, each layer is vibrated with a concrete vibrator.

Given the large span of the beam, it was decided to keep it in its formwork throughout all the tests to avoid any damage that demolding might have caused.

Appendix II

**Error! Reference source not found.** shows how the beam with hafly covered with aluminum paper. This step was realized after finishing all the experimental measurements and is a part of the future projects and perspectives.

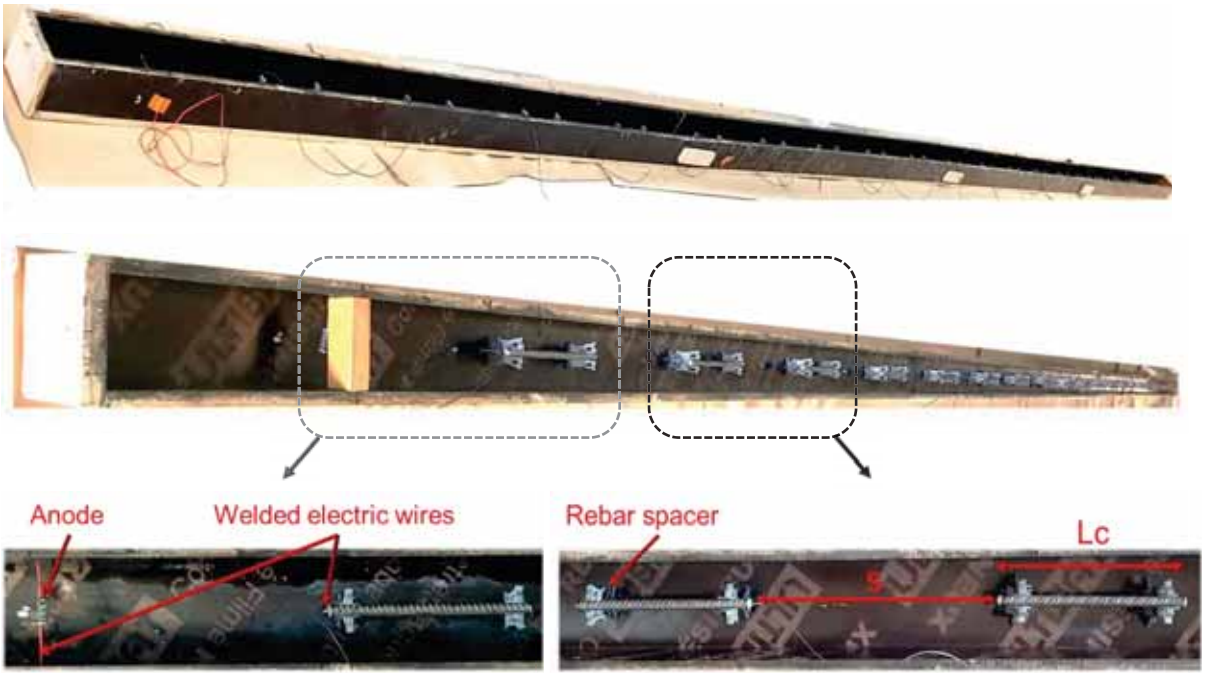


*Fig. 16. Formwork of the mortar beam*

*Fig. 17. Casting of the beam*

# Appendix III

## Characterization tests

Appendix in: Study of the initiation and propagation phases of chloride induced corrosion in reinforced concrete structures

Realized by: Chantal Chalhoub

Thesis for the degree of Philosophiæ doctor

Université Toulouse 3 Paul Sabatier (UT3 Paul Sabatier)

Laboratoire Matériaux et Durabilité des Constructions de Toulouse

Appendix III

Appendix III

# Contents

## 1. Introduction

The aim of this report is to describe the different characterization tests to analyze the behavior of materials. The characterization tests used in thus study are the measurements of electrical resistivity, water porosity, chloride migration coefficient and compressive strength. These measurements were realized for each formulation at different maturity ages. The report only presents the test procedures realized at the LMDC laboratory in Toulouse, France.

## 2. Electrical resistivity

The electrical resistivity (ρ) characterizes the ability to conduct the flow of electric current in materials. This electric current can be realized either by electronic conduction through the flow of electrons in metals like reinforcement bars or by electrolytic or ionic conduction through the flow of ions in fluids and porous materials like concrete.

Owing to the relatively simple measurement technique, concrete resistivity is an important durability indicator usually used to evaluate the transport properties of concrete and to inspect the lifetime of reinforced concrete structures under the risk of corrosion [1–11].

For this purpose, the RILEM TC 154-EMC Benchmark was launched in 2000 in order to provide a background description and a technical guideline of the different existing on site and some in situ methods used to evaluate electrical resistivity of concrete [12]. This section descirbes the test adopted in the thesis which was used for directly measuring the electrical resisivity.

The test is carried out, for each formulation and maturity age, on three $(\emptyset 11 \times 5\ cm)$ specimens sliced from three $(\emptyset 11 \times 22\ cm)$ cylindrical samples. Fig. 1 shows the device used for measuring the electrical resistivity on mortar/concrete samples. Each specimen is placed between 2 stainless steel grids that are connected to the terminals of the ohmmeter Ohmega Ω. Wet sponges separate the grids from the specimens to promote electrical coupling. The number of measurement cycles was 5 and the imposed current used was 0.5 mA.

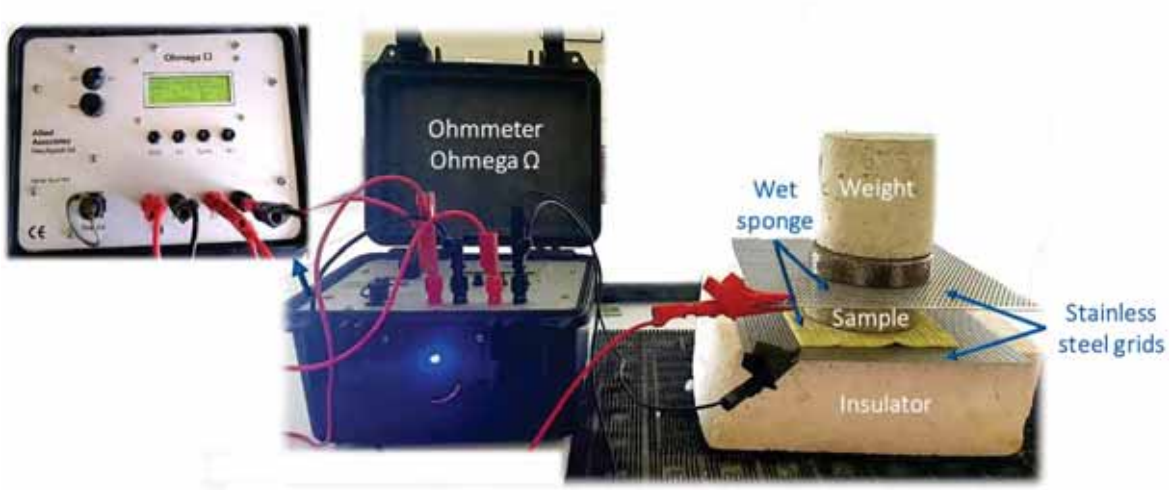


*Fig. 1. Parallel plate device for measuring electrical resistivity*

The ohmmeter displays the average value of electrical resistance obtained according to the values measured with the 5 cycles. The electrical reissitance is then transformed into electrical resistivity which is calculated as follows:

$$\rho = R \times \frac{S}{L} \qquad \textit{Eq. 1}$$

where:

- $\rho$ is the electrical resistivity of the material (Ω.m);
- $R$ is the measured electrical resistance (Ω);
- $S$ is the section of the sample ($m^2$);
- $L$ is length of the sample (m).

## 3. Water porosity

Porosity accessible to water is an indicator of overall sustainability. The overall technique used to measure the water porosity is recommended by AFREM [13] presenting a very reproducible and repeatable measurement [14].

For each mixture and maturity age, 3 disks of approximately 5 cm thickness and 11 cm diameter were cut using a diamond saw from 3 different samples of approximately 22 cm thickness and 11 cm diameter. These samples are vacuum saturated under water following the recommended protocol GranDuBé [15]. The saturation consists in placing the samples in a desiccator (Fig. 2) and maintaining the vacuum for 4 hours. The water is then gradually introduced over a duration of 15 minutes until the sample is covered with about 2 cm of water. The reduced pressure is maintained in the desiccator for 48 hours and the specimens are then removed for hydrostatic weighing.


*Fig. 2. Saturation device*

Water porosity (open porosity) is equal to the ratio between the total volume of open pores in a porous body and the apparent volume of the body. The water porosity is given by the following equation:

$$p_w = \frac{(M_{atmospher} - M_{dry})}{(M_{atmospher} - M_{water})} \times 100 \qquad \text{Eq. 2}$$

where:
$p$ is the porosity accessible to water (%);
$M_{atmospher}$ is the mass of saturated specimen measured in air;
$M_{dry}$ is the mass of the dried specimen;
$M_{water}$ is the apparent mass of the submerged specimen.

The mass of the immersed test sample $M_{water}$ is measured by hydrostatic weighing of the sample totally submerged in water. The mass of the saturated sample $M_{atmospher}$ is measured in the air after gently wiping the sample to remove the surface water without removing the water from the pores. In order to measure the mass of the dried sample $M_{dry}$, the specimen is dried according to the French norm NF P18-459. The drying is achieved in an oven at $(105 \pm 5)$ °C temperature until constant weight. The mass is considered constant when two successive weighings carried out 24 hours apart have a mass variation lower than 0.05%. The mass thus determined is the dry mass $M_{dry}$.

This protocol allows also to determe the density of the materials using Eq. 3, where $\rho_{water}$ is the water density.

$$\rho = \frac{M_{atmospher}}{(M_{atmospher} - M_{water})/\rho_{water}} \qquad \text{Eq. 3}$$

## 4. Chloride migration coefficient

The chloride migration coefficient was measured, according to standard NtBuild 492 for mortar mixes, and according to the French standard XP P18-462 for concrete mixes. This section presents a summary of the procedure realized, according to NtBuild 492 standard, on mortar mixtures annotated with letter “M” at the LMDC laboratory in Toulouse, France. For each formulation and maturity age, 3 cylindrical samples of 110 mm diameter and 50 mm thickness were tested. These samples were cut using a diamond saw from 3 different samples of approximately 22 cm thickness and 11 cm diameter.

Firstly, samples are placed in a desiccator where the vacuum is maintained for 3 h. Then, the desiccator still running is filled with saturated calcium hydroxide solution with a concentration of 2 g/L so as to immerse all the specimens. The vacuum is maintained for a further hour before allowing air to re-enter the container and the specimens are saturated under vacuum for $18 \pm 2$ hours.
Afterwards, specimens are fixed in rubber sleeves secured with two stainless steel clamps as shown in Fig. 3 and the perimeter of the sample/sleeve connection was sealed with a line of silicone sealant to improve the tightness. It is important to make sure that the sleeves are completely sealed to avoid any leakage.

Appendix III

*Fig. 3. Samples fixed in rubber sleeves*

As shown in Fig. 4, samples are placed in a plastic reservoir (h) which contains a catholyte solution (e) made with 10 % sodium chloride (NaCl) by mass in tap water (100 g NaCl in 900 g water, about 2 N). Then, the sleeve are filled with 300 ml of anolyte solution (b) made with sodium hydroxide with a concentration of 12g/L NaOH. Solutions are prepared with demineralized water and stored at a temperature of 20–25 °C. The anode (c) is immersed in the anolyte solution (b) and is connected to the positive pole of the power supply while the cathode (f) is connected to the negative pole.

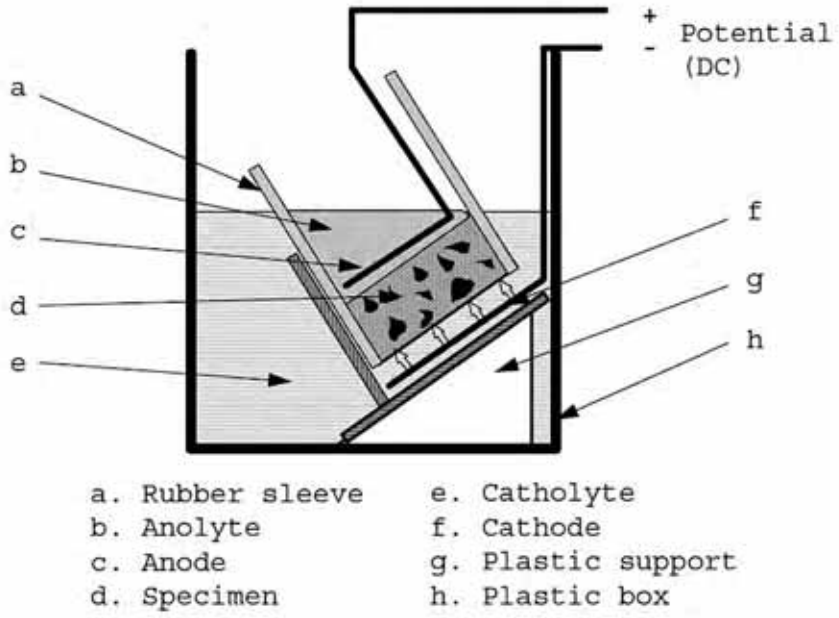


*Fig. 4. One arrangement of the migration set-up (Taken from Nt Build 492)*

Fig. 5 shows an image taken during the migration test showing the connections of anode and cathode where a potential difference of 30 V is applied to each sample forcing the chloride ions to migrate inside the specimen. The voltage is adjusted according to the initial current and a new value of the current is noted. The test time is set according to the new value of the initial current. The final current and temperature must be recorded.

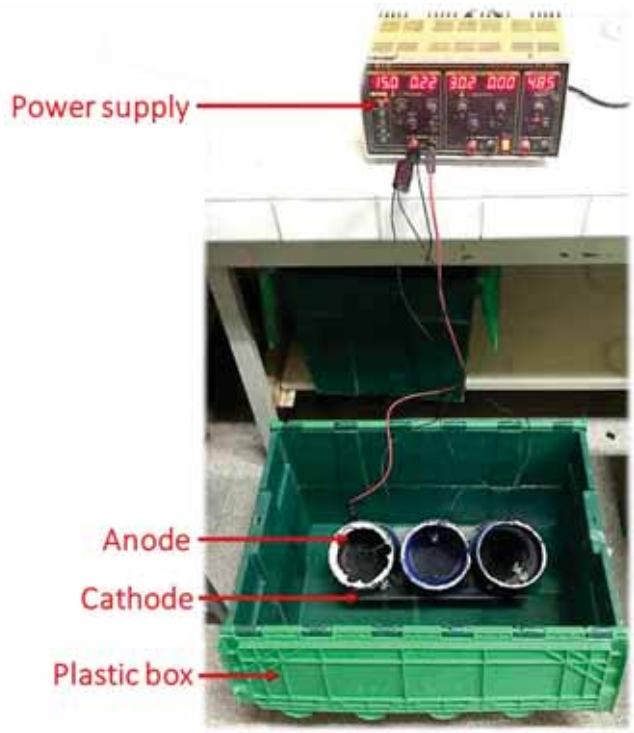


*Fig. 5. Experimental set-up of the migration test*

At the end of the test, the specimen is split axially into two pieces and a solution of silver nitrate is sprayed on both parts. The chloride penetration can thus be evaluated from the white precipitation of silver chloride. The chloride penetration front is measured, by means of a suitable ruler, from the center of the cross section of the sample to both edges at intervals of 10 mm to obtain seven depths. The depth measurement must be realized with an accuracy of 0.1 mm and the depth pf the areas located at 10 mm from the ends are not considered.

The chloride migration coefficient can be calculated from the penetration depth according to the following equation:

$$D_{nssm} = \frac{0.0239(273 + \mathrm{T})\mathrm{L}}{(\mathrm{U} - 2)\mathrm{t}} \times \left( xd - 0.0238 \sqrt{\frac{(273 + T)Lx_d}{U - 2}} \right) \qquad \textit{Eq. 4}$$

where:

- $D_{nssm}$ is the apparent migration coefficient ($10^{-12}$ $m^2/s$);
- $\mathrm{U}$ is the absolute value of the applied voltage (V);
- $\mathrm{T}$ is the average value of the initial and final temperatures in the anolyte solution (° C);
- $\mathrm{L}$ is the thickness of the sample (mm);
- $x_d$ is the average value of the penetration front (mm);
- $\mathrm{t}$ is the duration of the test (h).

. Fig. 6 shows results of chloride migration coefficients obtained on some mortar formulations which were used in the thesis report and Fig. 7 presents examples of chloride penetration fronts of these mortar formulations at the same maturity ages.

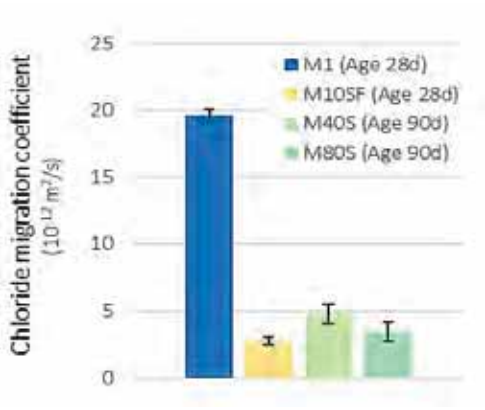


*Fig. 6. Chloride migration coefficient of mortar formulations*


*Fig. 7. Examples of chloride penetration fronts of mortar formulations*

## 5. Compressive strength

The compressive strength of the mortar formulations was measured according to NF EN 196-1 and that of concrete formulations was measured according to NF EN 206-1.

The compression tests of concrete were carried out, for each mortar composition and maturity age, on three adjusted $(\emptyset 11 \times 22\ cm)$ specimens. Tests are performed with a concrete press machine shown in Fig. 8 with a press load speed of 0.5 MPa/s. The concrete specimen is subjected to a compressive force increasing to failure: the maximum force that can withstand the specimen corresponds to the compressive strength.

*Fig. 8. Concrete press machine*

The compression tests of mortar were carried out, for each mortar composition and maturity age, on 3 $(4 \times 4 \times 16\ cm)$ prismatic specimens. First, a bending test is performed on the prismatic samples

resulting in 2 halfs per prism as shown in Fig. 9. The 6 half-prisms obtained form the bending test are then tested in compression on the lateral faces under a $(4 \times 4\ cm^2)$ section. A load is applied on the samples and is increased until rupture. At failure, the pressure applied corresponds to the compressive strength. The test result corresponds to the arithmetic mean of the 6 values of the compressive strength performed on the 3 prisms.

*Fig. 9. Two half-prisms obtained from bending test*

## 6. References


[1] A. Molina, C. Andrade, C. Alonso and J.A. González, Tec. Ing. Univ. Zulia, 8 (1985), .

[2] C. Alonso, C. Andrade and J.A. González, *Relation between Resistivity and Corrosion Rate of Reinforcement in Carbonated Mortar Made with Several Cement Types*, Vol. 18, 1988.

[3] W. Lopez and J. Gonzalez, *Influence of the degree of pore saturation on the resistivity of concrete and the corrosion rate of steel reinforcement*, Cement and concrete research 23 (1993), pp. 368–376.

[4] T. Liu and R.W. Weyers, *Modeling the Dynamic Corrosion Process in Chloride Contaminated Concrete Structures*, Vol. 28, 1998.

[5] J. Gulikers, *Theoretical considerations on the supposed linear relationship between concrete resistivity and corrosion rate of steel reinforcement*, Materials and Corrosion 56 (2005), pp. 393–403.

[6] W. Morris, A. Vico and M. Vázquez, *Chloride induced corrosion of reinforcing steel evaluated by concrete resistivity measurements*, Electrochimica Acta 49 (2004), pp. 4447–4453.

[7] W. Morris, A. Vico, M. Vazquez and S. De Sánchez, *Corrosion of reinforcing steel evaluated by means of concrete resistivity measurements*, Corrosion Science 44 (2002), pp. 81–99.

[8] C. Andrade and C. Alonso, *Corrosion rate monitoring in the laboratory and on-site*, Construction and Building Materials 10 (1996), pp. 315–328.

[9] G. Glass, C. Page and N. Short, *Factors affecting the corrosion rate of steel in carbonated mortars*, Corrosion Science 32 (1991), pp. 1283–1294.

[10] R. Polder and L. Bertolini, *Concrete resistivity and reinforcement corrosion rate as a function of temperature and humidity of the environment*, TNO report 97- BT-R0574, TNO Building and Construction Research, Delft, The Netherlands, 1997.

[11] S. Feliu, J. Gonzalez, S. Feliu and C. Andrade, *Relationship between conductivity of concrete and corrosion of reinforcing bars*, British corrosion journal 24 (1989), pp. 195–198.

[12] *RILEM TC 154-EMC: ELECTROCHEMICAL TECHNIQUES FOR MEASURING METALLIC CORROSION Test methods for on site measurement of resistivity of concrete | Scinapse | Academic search engine for paper*, Scinapse 33 (2000), pp. 603–611.

[13] J.P. OLLIVIER, *Durabilité Des Bétons. Compte Rendu Des Journées Techniques AFPC-AFREM*, 1997.

[14] F. Cassagnabère and M. Carcasses, *Les indicateurs de durabilité ou comment caractériser la durabilité des bétons ?*, 2014, .

[15] G. Arliguie and H. Hornain, *GranDuBé: grandeurs associées à la durabilité des bétons*, Presses des Ponts, 2007.

# Appendix IV

## Steel surface preparation

Appendix in: Study of the initiation and propagation phases of chloride induced corrosion in reinforced concrete structures

Realized by: Chantal Chalhoub

Thesis for the degree of Philosophiæ doctor

Université Toulouse 3 Paul Sabatier (UT3 Paul Sabatier)

Laboratoire Matériaux et Durabilité des Constructions de Toulouse

Appendix IV

Appendix IV

# Contents

# 1. Introduction

Reinforcement bars are often covered with a layer of mill scale which is a high temperature phase formed during the cooling of iron which may or may not be combined with a layer of corrosion related to the action of rainwater or formed during prolonged outdoor exposure on site. The mill scale mostly encountered on rebars used for construction is non-uniform and irregular with cracks and crevices [1,2]. This mill scale layer is usually known to reduce the protecting features of the passive layer which protects the steel form corrosion [3].

The non-uniformity of mill scale could lead to the concept of weakest spot. The weakest spot could be related to the geometry of the rebar such as the presence of ribs which can induce different cooling kinetics during the industrial process. On the other hand, the weakest spot could be related to damages after manufacture for instance during the handling or during the assembly of the bars on construction site. It could also be related to size effect in casting process for instance the heterogeneity of the steel/concrete interface.

If the weakest point is induced by the rebar damages or size effect, this limitation cannot be resolved in a laboratory experimental test even if a bigger length of anode rebar was used. Knowing that, in reality, the length of the bars is approximately 6m whereas the length of the bars used as anodes, in experimental works, usually do not exceed 0.1 m [4]. However, if the weakest point is associated with the geometry, it is possible to resolve this issue by using different types of steel surface conditions.

Moreover, the surface condition of the reinforcing steel has an important influence on $Ccrit$. On site, the type of rebars used is as-received, which means that rebars are generally covered with a non-uniform layer of mill scale or pre-rusted when the mill scale layer is combined with rust products. It is then important to understand the impact of these layers on corrosion initiation.

In the thesis four types of reinforcement bars were used. The aim of this report is to describe the methods used for the preparation of steel bars and the different treatment used.

## 2. Types of reinforcement bars and their treatments

Fig. 1 presents a briefing of the different types of rebars used according to their surface preparation and shows photographs of these reinforcement bars.

### As Received Steel "ARS"

Steel without any treatment

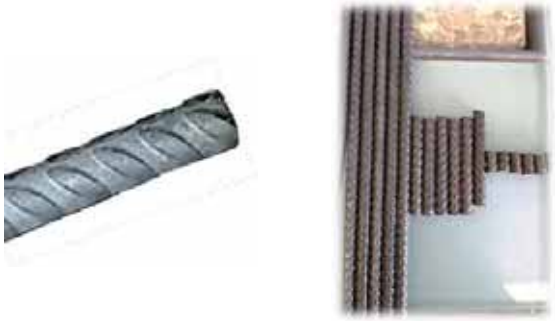

### Cleaned Steel "CS"

Steel cleaned with a chemical cleaning procedure detailed afterwards in part 3

### Cleaned Steel Pre-oxidized by high Temperature "CSPT"

Steel cleaned then oxidized with a heat treatment detailed afterwards in part 4

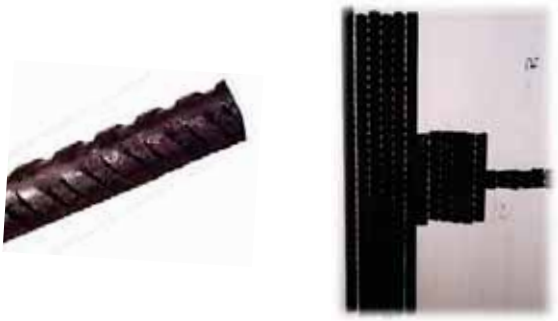

### Cleaned Steel Pre-oxidized by exposure to Humid environment "CSPH"

Steel cleaned then oxidized in a humid environment

*Fig. 1. Photographs of the different types of steel bars used: ARS, CS, CSPT and CSPH*

## 3. Chemical cleaning protocol

The chemical cleaning procedure is based on standard ISO 8407 [5], which uses an acid solution to remove the mill scale layer and/or corrosion products usually present on reinforcement bars. However, Even if the calamine layer is removed, the homogeneity of the surface of the steel after cleaning remains a matter of uncertainty. The cleaning procedure is realized at a temperature of 20 $^{o}$C ± 2 $^{o}$C.

The first step of the cleaning protocol consists in dipping the steel for 30 seconds in Clark's solution whose composition for 1l of solution is: 1L of chloridric acid + 20 g of antimony trioxide + 50 g of tin (II) chloride (Fig. 2).


*Fig. 2. Reinforcement bar soaked in a Clark solution*

After that, the steel bar is rinsed thoroughly with distilled water, then, it is brushed very lightly with a very soft brush which allows to remove any remaining surface products (Fig. 3). Afterwards, the rebar is dried in acetone or ethanol as shown in Fig. 4.

*Fig. 3. Rinsing with water and brushing steel after cleaning with Clark solution*

*Fig. 4. Rebar totally immerged in acetone*

The reinforcement bar is then placed in a desiccator containing silica gel (moisture absorber) until the mortar/concrete sample preparation which is realized on the casting day.

Fig. 5. Desiccator containing cleaned steels

The weight difference of the steel bar before and after the cleaning treatment was measured on 96 different bars and had an average value of 2.23 mg with a coefficient of variation of 28.8%. This value could represent the weight of the mill scale layer at the steel surface.

## 4. Heat treatment protocol

The pre-oxidation of steel using the heat treatment consists in placing the reinforcement bars in an oven at a temperature of 400 °C for a duration of 72 h as shown in Fig. 6. This protocol was inspired form a test procedure developed in 2012 in a technical document issued by CEA in the framework of the ANDRA/CEA agreement [6].

Fig. 6. Heat treatment of reinforcement bars placed in an oven

This technique allows to obtain a homogeneous layer of corrosion products having a composition close to that of the mill scale found in the case of ARS bars, which is made up mostly of magnetite with a little hematite.

The weight difference after cleaning of the samples was measured before and after the heat treatment on 48 different steel bars. The weight difference was around 0.67 mg with a coefficient of variation of 38.4% and represented the weight of the layer of corrosion products formed at the surface of the steel bars during the heating treatment.

## 5. Pre-oxidation procedure in humid environment

The pre-oxidation of steel in humid environment consists in placing the reinforcement bars in a humidity room $(RH = 95\%)$ for almost two weeks as shown in Fig. 7. The rebars were placed in plastic moulds which contained holes to allow oxygen and water to reach the rebars. The reason for using the moulds was to protect the rebars from the strong rain showers in the humidity room which could remove the corrosion products formed.

Fig. 7. Reinforcement bars placed in humidity room (photograph taken directly after placing the rebars in the room)

## 6. References

[1] P. Ghods, O. Isgor, G. A. McRae, J. Li and G.P. Gu, *Microscopic investigation of mill scale and its proposed effect on the variability of chloride-induced depassivation of carbon steel rebar*, Corr. Sci. 53 (2011), pp. 946–954.

[2] F. YANG, *Corrosion protection of steel embedded in new sustainable cementitious materials*, Politechnico Milano., 2018.

[3] E. Mahallati and M. Saremi, *An Assessment on the Mill Scale Effects on the Electrochemical Characteristics of Steel Bars in Concrete under DC-Polarization*, Vol. 36, 2006.

[4] C. Chalhoub, R. François and M. Carcasses, *Determination of chloride threshold initiating corrosion: A new set-up taking the localized aspect of corrosion into account*, Cement and Concrete Research 124 (2019), pp. 105825.

[5] *ISO 8407:2009(en), Corrosion of metals and alloys — Removal of corrosion products from corrosion test specimens*.

[6] *Corrosion à l'état passif en milieu cimentaire - Etat d'avancement de la fiche technique 5621 pour l'année 2012*. CEA/ANDRA, 2012.

# Appendix V

## Determination of the contents of total and free chlorides in concrete and mortar

Appendix in: Study of the initiation and propagation phases of chloride induced corrosion in reinforced concrete structures

Realized by: Chantal Chalhoub

Thesis for the degree of Philosophiæ doctor

Université Toulouse 3 Paul Sabatier (UT3 Paul Sabatier)

Laboratoire Matériaux et Durabilité des Constructions de Toulouse

Appendix V

Appendix V

# Contents

# 1. Introduction

The following report describes the methodology adopted in the thesis for the determination of the total (acid-soluble) and free (water-soluble) chloride contents by potentiometric technique in mortar and concrete specimens used during the thesis. The experimental tests were realized by Chantal Chalhoub in the laboratory LMDC in Toulouse, France. The report also presents a small overview on the different techniques adopted for measuring the chloride content in cementitious materials. This overview is inspired form the thesis report realized by Silva [1] and Angst [2].

# 2. State of the art: current practice and techniques used for the measurement of chloride content

The measurement of chloride content in cementitious materials is a very important topic especially in the domain of chloride-induced corrosion in reinforced concrete structures. This measurement is a very challenging task because of the high heterogeneity of concrete [1]. The determination of the level chloride contamination in concrete is documented in different technical documents [3] and standards [4–6]. Yet, many laboratories have developed their own procedures for instance the recommendations of GranDuBé [7]. The determination of chlorides is very complex and the measurement techniques produce large uncertainty between the different laboratories [8]. Moreover, the results obtained from the same procedure performed by the same laboratory showed a high scatter with an uncertainty in the range of 10–25% (with the highest uncertainty at low chloride contents) even for constant method and laboratory [9].

There are several destructive and non-destructive methods for the assessment of chloride content in cementitious materials. The traditional method consists in the measurements of chlorides on powder samples dissolved with nitric acid for total chlorides and water for free chlorides. Subsequently, the quantification of chlorides is achieved by several procedures such as titration or spectrophotometric methods.

Ion selective electrodes (ISEs) are non-destructive electrochemical sensors used for direct potentiometry technique allowing the determination of chloride ion activity in a solution. This method allows to continuously monitor the chloride ingress providing information well before corrosion initiates. Ag/AgCl electrodes were found suitable to be used as chloride sensors embedded in concrete or mortar to monitor the free chloride concentration in pore solution [10–13]. Yet, the accuracy of this measurement technique in the concrete pore solution might be disturbed by diffusion potentials between reference electrode and (ISE) [10,14,15]. Hence, the measurement system must be optimized for example by using combined sensors containing both ISE and reference electrode [2].

Other techniques can also be used for measuring the chloride content allowing to considerably save time by reducing the time needed for the preparation of samples. As an example, X-ray fluorescence spectrometry (XRF) technique can be used to evaluate the total chloride content [16,17]. Laser-induced breakdown spectroscopy (LIBS) is another technique used for surface scanning and depth profiling of chlorides in concrete [18]. Other techniques like near-infrared (NIR) spectrometry [19,20], electron probe micro analyzer (EPMA) [21–24] and the innovative technique of Laser ablation inductively coupled plasma mass spectrometry (LA-ICP-MS) [25] can also be used.

## 3. Sampling area

To determine the chloride content in mortar or concrete, a sample size between 1 and 5 g is required. The cylindrical contaminated anode samples are first split in half as shown in Fig. 1. Then mortar or concrete is collected from a sampling area surrounding the rebar embedded in the center of the specimen as illustrated in Fig. 2.

*Fig. 1. Anode sample split in half*

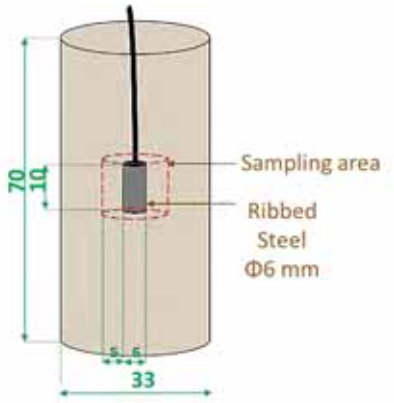


*Fig. 2. Sampling area in anode specimens*

## 4. Grinding

Mortar or concrete samples were oven dried at a temperature of $105 \pm 5\ ^{0}C$, then crushed to a fine powder with RETSCH – RS 100 machine presented in Fig. 3. Afterwards, the obtained powder must be filtered in a sieve of a smaller or equal diameter of 315 micrometer.


*Fig. 3. Grinding machine used to transform mortar/concrete samples into fine powder*

# 5. Chemical analysis

## 5.1. Dissolution of total chlorides

The following methods are realized according to standards NF EN 14629 stated in 2007 [4]. This standard describes the methods for measuring the content of total chlorides which is the sum of free and bound chlorides. Total chlorides are soluble in acid. Fig. 4 summarizes the different steps of the adopted experimental protocol. The following tests must be carried out under a temperature of 20 $^{o}$C ± 2 $^{o}$C.

Firstly, the mortar or concrete powder sample is weighed using a particular scale with a precision of 0.0001 g and the mass of the samples must be indicated in grams to the nearest 0,0001 g.

Then, the sample is introduced into a 250 mL beaker in which 100 mL of demineralized water are added. The beaker is placed on a magnetic stir plate for two minutes to homogenize the solution. Then, 10 mL of diluted nitric acid nitric acid $HNO_3$ with a concentration of 5 mol/L of are added to the beaker. The addition of concentrated acid allows the laboratory to use a dispenser. This operation saves time and avoids cross-contamination. It is also recommended to add 50 mL of demineralized water and 50 mL of hot water in order to accelerate the boiling and avoid any projection. The mixture should be heated to boiling, the latter being maintained for at least 3 minutes, stirring the solution continuously.

The mixture must then be filtered immediately using a medium-textured paper filter. The beaker, the agitator and the residue on the filter must be rinsed with demineralized water at least 7 times each. The filtrate is diluted in a 250 mL volumetric flask by adding demineralized water until the total volume of solution reaches the line marked on the volumetric flask. The sealed volumetric flask must be inverted 12 times to thoroughly mix the solution. The latter is transferred form the volumetric flask to a PVC tube until testing.

1 -Measure the weight of the samples using a scale with a precision of 0.0001 g.

2 -Introduce the powder into a 250 mL beaker and add 100 mL of demineralized water and 10 mL of diluted nitric acid.

3 -Heat the mixture to boiling.

-After boiling, maintain the solution for at least 3 minutes.

4 -Filter the solution using a medium-textured paper filter.

5 -Rinse the agitator, the beaker, and the residue on the filter with demineralized water at least 7 times each.

-Add water in the 250 mL volumetric flask which contains the filtrate until the total volume of solution reaches the line marked on the volumetric flask.

-Use a pipette or dropper to fill the volumetric flask and use the meniscus of the solution and the line on the flask to determine the endpoint.

-Seal the volumetric flask and invert it 12 times to thoroughly mix the solution.

-Add the solution in a PVC tube and seal it.

*Fig. 4. Description of the methodology used to prepare solutions for measuring the total chloride contents*

## 5.2.Dissolution of free chlorides

The following methods are realized according to standards recommended in GranDuBé [7]. This standard describes the methods for measuring the content of free chlorides which are soluble in water. The following tests must be carried out under a temperature of 20 $^{o}$C ± 2 $^{o}$C. For each prepared solution, 2 samples must be tested and the final chloride content is the average value of both chloride contents measured.

Firstly, the mortar or concrete powder sample is weighed using a particular scale with a precision of 0.0001 g and the mass of the samples must be indicated in grams to the nearest 0,0001 g.

Next, the sample is introduced into a 250 mL beaker in which 200 mL of deionized water is added. The beaker is then placed on a magnetic plate for stirring for a duration of 3 minutes.

After that, the obtained solution is filtered and the filter and beaker are rinsed only once using 10 ml of demineralized water. It is possible to rinse the equipment 7 times, however, this must be done only with extremely small volume of demineralized water. This volume has been scarcely limited to avoid any further chloride extraction by dissolving the chloroaluminates.

Finally, 2 mL of concentrated nitric acid is added to the final solution to acidify the medium to stabilize the chlorides in solution and the filtrate is completed to a volume of 250 mL in a volumetric flask. The sealed volumetric flask must be inverted 12 times to thoroughly mix the solution. The latter is transferred form the volumetric flask to a PVC tube until testing.

## 6. Measurements with chloride titrator

The measurement of chloride content is carried out by potentiometric method by means of a chloride titrator (Fig. 5). The test is performed using a combined electrode consisting in a silver electrode, in contact with the solution to be tested, and a reference electrode whose potential is fixed. This makes it possible to follow the evolution of the potential difference between both electrodes.

*Fig. 5. Titrator used to measure the chloride content*

The titrator is connected to the software *Tiamo* which allows to visualize the results of the experiments. Before using the titrator, the solution $AgNO_3$ must be calibrated using demineralized water. Afterwards, between 5 and 50 mL of solution are removed form PVC tubes and added in beakers for testing. 1 mL of orthophosphoric acid is added in the tested solution which is diluted with demineralized water until reaching a volume of 100 mL.

The input data inserted in the software for each tested solution are shown in Fig. 7 and consist in the name and location of the beaker, the volume of the solution and the initial weight of mortar or concrete powder filtered.

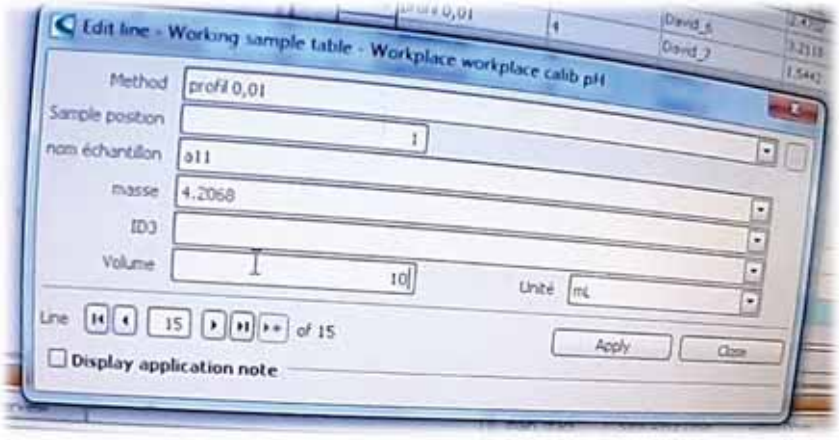


*Fig. 6. Titrator used to measure the chloride content*

Appendix V

The potential of the silver electrode depends on the concentration of $Ag^+$ ions according to the Nernst relationship. In the presence of chloride ions $Cl^-$, the concentration of $Ag^+$ is limited by the solubility constant of silver chloride as follows:

$$[Ag^+] = \frac{K_{sp}}{[Cl^-]} \qquad \textit{Eq. 1}$$

Where:
$[Ag^+]$ and $[Cl^-]$ are the concentrations of silver ions and chlorides, respectively;
$K_{sp}$ is the solubility constant of silver chloride AgCl.

According to Nernst relationship, Eq. 2 shows the potential of the silver electrode according to the reference electrode which is a function of $[Ag^+]$ and subsequently a function of $[Cl^-]$ as follows:

$$E_{Ag/AgCl}/ref = E^0_{Ag/AgCl}/ref + 0.059 \log\left(\frac{K_{sp}}{[Cl^-]}\right) \qquad \textit{Eq. 2}$$

Silver nitrate is added gradually to the solution until all the chloride ions are consumed by precipitation. The equilibrium is reached when the number of moles of $Ag^+$ ions is equal to the number of $Cl^-$ ions in the solution.

Fig. 7 shows the titration curve which presents the variation of the measured potential of the tested solution expressed in mV using the silver electrode with respect to the reference electrode according to the volume of silver nitrate added expressed in mL. The equilibrium is translated into a sudden jump of potential just before reaching the equivalence point.

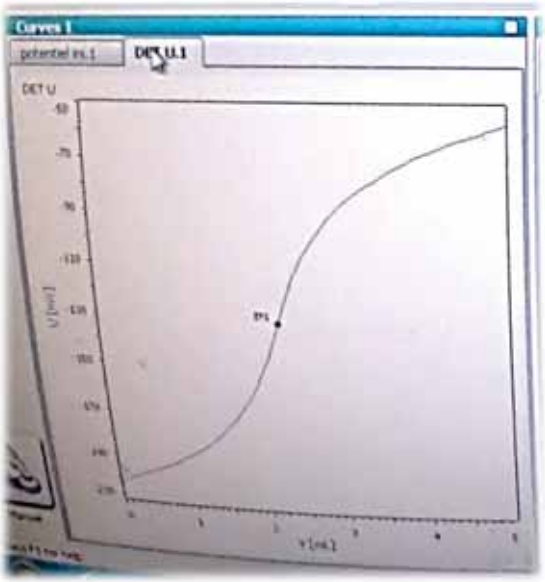


*Fig. 7. Example of the evolution of the potential of the solution according to the volume of silver nitrate added by titrator*

The number of moles of chloride ions corresponds to the product between the volume of solution of $AgNO_3$ added and its concentration. Knowing the volume of the tested solution, the concentration of the solution and the total number of moles contained in the 250 mL solution prepared from the filtrate can thus be calculated. Having the initial mortar powder mass, the total chloride content per

mortar mass is displayed by the software. From this value, the percentage of total chlorides per mass of binder can then be calculated.

The reproducibility of the adopted procedure was estimated one several specimens based on 2 identical powder samples taken from the same mortar or concrete powder. The coefficient of variation between the results did not exceed 12 %.

## 7. Spatial variation of chloride content in anode samples

In the work realized in the thesis, anode samples were oven dried then soaked in saline NaCl solutions. In order to evaluate the spatial variation in chloride contamination in anode samples, a reference reinforced anode sample was soaked in a saline solution with a concentration of 280 g/L for a duration of 48 hours.

Then, the specimen was split in half and one of the parts of the anode was used to collect mortar powder form different areas. This part was divided into 6 parts and 6 mortar powders were collected and tested. The level of total chloride contents was measured with the titrator and the percentages of chloride contents were calculated versus the level of chloride measured in the area surrounding the rebar.

As shown in Fig. 8, the obtained results indicate a variation of chlorides between 91 and 113% versus the chloride content measured in the area near the rebar. This observation is an indication of reproducibility of the adopted procedure and most importantly the homogeneous distribution of the total chloride content inside the tested samples.

This results is consistent with observations from the study realized by Sbartaï et al. [26] where the same preconditioning of samples was used. The authors [26] stated that this preconditioning technique (oven drying before contamination) allows, first, to accelerate chloride intrusion throughout the material by capillary processes, and also, to have a homogeneous distribution of the total chloride content inside the tested samples. This last statement was supported by a chemical investigation achieved according to (AFPCAFREM) standards [27].

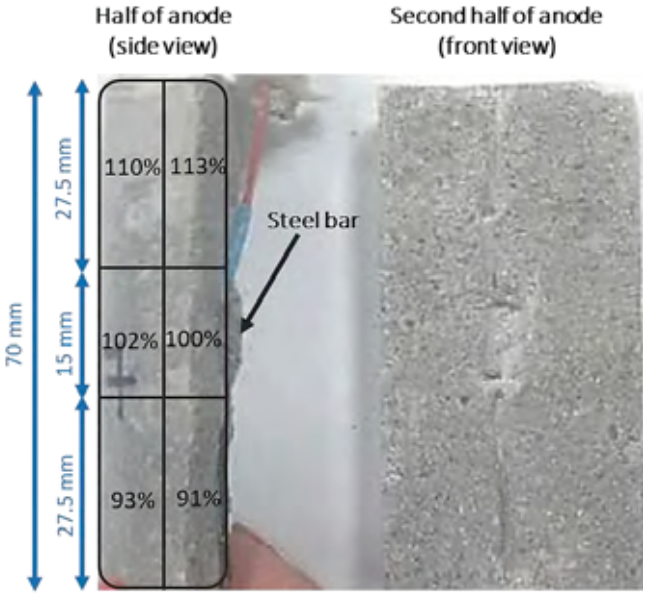


*Fig. 8. Spatial variation of the percentages of total chloride contents versus the chloride level measured around the rebar*

## 8. References


[1] N.F. da Silva, Chloride Induced Corrosion of Reinforcement Steel in Concrete - Threshold Values and Ion Distributions at the Concrete-Steel Interface, 2013.

[2] U. Angst, Chloride induced reinforcement corrosion in concrete: Concept of critical chloride content–methods and mechanisms, 2011.

[3] RILEM TC 178-TMC, RILEM TC 178-TMC: 'Testing and modelling chloride penetration in concrete'Analysis of total chloride content in concrete, Mater. Struct. 35 (2002), pp. 583–585.

[4] NF EN 14629 - Produits et systèmes pour la protection et la réparation des structures en béton - Méthodes d'essais - Mesurage du taux de chlorure d'un béton durci. 2007.

[5] European Standard EN196-21, Methods for testing cement: determination of the chloride, carbon dioxide and alkali content of cement, European Committee for Standardization. 1989.

[6] AASHTO-T260, Standard method of test for sampling and testing for chloride ion in concrete and concrete raw materials, American Association of State Highway and Transportation Officials. 1997.

[7] H. Hornain, GranDuBé: grandeurs associées à la durabilité des bétons, Presses des Ponts, 2007.

[8] M. Castellote and C. Andrade, Round-Robin test on chloride analysis in concrete—Part I: Analysis of total chloride content, Materials and structures 34 (2001), pp. 532–549.

[9] U. Angst, A. Rønnquist, B. Elsener, C.K. Larsen and Ø. Vennesland, Probabilistic considerations on the effect of specimen size on the critical chloride content in reinforced concrete, Corrosion Science 53 (2011), pp. 177–187.

[10] U. Angst, B. Elsener, C.K. Larsen and Ø. Vennesland, Potentiometric determination of the chloride ion activity in cement based materials, Journal of applied electrochemistry 40 (2010), pp. 561–573.

[11] M. Montemor, J. Alves, A. Simoes, J. Fernandes, Z. Lourenço, A. Costa et al., Multiprobe chloride sensor for in situ monitoring of reinforced concrete structures, Cement and Concrete Composites 28 (2006), pp. 233–236.

[12] B. Elsener, L. Zimmermann and H. Böhni, Non destructive determination of the free chloride content in cement based materials, Materials and Corrosion 54 (2003), pp. 440–446.

[13] Y. Femenias, U. Angst, F. Moro and B. Elsener, Development of a novel methodology to assess the corrosion threshold in concrete based on simultaneous monitoring of pH and free chloride concentration, Sensors 18 (2018), pp. 3101.

[14] U. Angst and Ø. Vennesland, Detecting critical chloride content in concrete using embedded ion selective electrodes–effect of liquid junction and membrane potentials, Materials and corrosion 60 (2009), pp. 638–643.

[15] U. Angst, Ø. Vennesland and R. Myrdal, Diffusion potentials as source of error in electrochemical measurements in concrete, Materials and Structures 42 (2009), pp. 365–375.

[16] E. Proverbio and F. Carassiti, Evaluation of chloride content in concrete by X-ray fluorescence, Cement and concrete research 27 (1997), pp. 1213–1223.

[17] R. Dhir, M. Jones and H. Ahmed, Determination of total and soluble chlorides in concrete, Cement and Concrete Research 20 (1990), pp. 579–590.

[18] G. Wilsch, F. Weritz, D. Schaurich and H. Wiggenhauser, Determination of chloride content in concrete structures with laser-induced breakdown spectroscopy, Construction and building materials 19 (2005), pp. 724–730.

[19] V.S. Ban, B.L. Volodin and S. Dolgi, Determination of chloride ion concentration in concrete by means of near infra-red spectroscopy, 7983 (2011), pp. 1–7.

[20] V. Burakov, V. Kiris and S. Raikov, Optimization of conditions for spectral determination of chlorine content in cement-based materials, Journal of Applied Spectroscopy 74 (2007), pp. 321–327.

[21] O.M. Jensen, A.M. Coats and F.P. Glasser, Chloride ingress profiles measured by electron probe micro analysis, Cement and Concrete Research 26 (1996), pp. 1695–1705.

[22] O.M. Jensen, P.F. Hansen, A.M. Coats and F.P. Glasser, Chloride ingress in cement paste and mortar, Cement and Concrete Research 29 (1999), pp. 1497–1504.
[23] P.P. Win, M. Watanabe and A. Machida, Penetration profile of chloride ion in cracked reinforced concrete, Cement and concrete research 34 (2004), pp. 1073–1079.
[24] H. Wall and L.-O. Nilsson, A study on sampling methods for chloride profiles: simulations using data from EPMA, Materials and Structures 41 (2008), pp. 1275–1281.
[25] S.F. Boulyga and K.G. Heumann, Direct determination of halogens in powdered geological and environmental samples using isotope dilution laser ablation ICP-MS, International Journal of Mass Spectrometry 242 (2005), pp. 291–296.
[26] Z. Sbartaï, S. Laurens, J. Rhazi, J. Balayssac and G. Arliguie, Using radar direct wave for concrete condition assessment: Correlation with electrical resistivity, Journal of applied geophysics 62 (2007), pp. 361–374.
[27] Z.M. Sbartaï, Caractérisation physique des bétons par radar: approche neuromimétique de l'inversion, Paul Sabatier University (France) and Sherbrooke University (Canada)., 2005.

# Appendix VI

## Steady state polarization test

Appendix in: Study of the initiation and propagation phases of chloride induced corrosion in reinforced concrete structures

Realized by: Chantal Chalhoub

Thesis for the degree of Philosophiæ doctor

Université Toulouse 3 Paul Sabatier (UT3 Paul Sabatier)

Laboratoire Matériaux et Durabilité des Constructions de Toulouse

Appendix VI

Appendix VI

# Contents

# 1. Introduction

This reports aims to present the steady state polarization test which was performed on cathode specimens and anode specimens in several papers of the thesis report in in order to characterize the electrochemical properties of passive and active steel.

# 2. Double layer model and electrical analogy

Corrosion of the steel in the interstitial solution of the concrete involves oxidation-reduction reactions at the interface between the electrode and the electrolyte. The nature of this interface is in particular conditioned by absorption phenomena.

When a metal is immersed in an electrolyte, there is a separation of the electrical charges. The distribution of mobile charges depends on the absorption of water molecules and ions (anions and hydrated cations) on the surface of the metal.

Water is formed of dipolar molecules that is to say that the barycenter of the positive charges does not coincide with that of the negative charges because of its dissymmetry. These molecules will therefore orient themselves according to the charges present on the surface. The dissolved cations are generally hydrated and therefore cannot approach the surface a distance less than the radius of the hydration sphere. Conversely, anions are rarely hydrated and can therefore be close enough to the surface to be chemically absorbed.

The metal-solution interface can be considered as the superposition of 2 thin layers, one positively charged and the other negatively. Its electrical behavior can be assimilated to that of a capacity capacitor (double layer) in parallel with a polarization resistance. This resistance reflects the ability of the electrode to polarize under the application of external stress.

# 3. Steady state polarization test protocol

## 1.1. Measurement device

Polarization tests were achieved by potentiostatic tests thanks to a BioLogic SP-50 potentiostat (Fig. 1).


*Fig. 1. BioLogic SP-50 potentiostat*

The experimental setup is illustrated in Fig. 2 for cathode specimens and the same setup was also applied to anode specimens as shown in Fig. 3. The test is achieved with a measurement cell consisting of 3 electrodes:

- Working electrode (WE) which is the reinforcement bar embedded in the samples;
- Reference electrode (RE) which is an Ag/AgCl/KCl (sat) electrode;
- Counter electrode (CE) which is a titanium mesh surrounding the sample.

The test piece is placed in a tank filled with water or sodium hydroxide (NaOH) to ensure the electrical continuity of the measuring circuit.

With this device, it is possible to realize a potentiostatic test which consists in imposing a constant potential difference between the counter electrode and the working electrode and measuring the evolution of the current over time.

In other words, this test allow to unbalance the equilibrium state of the WE by applying an overvoltage $(\Delta E)$ which shifts the equilibrium and favors one reaction with respect to the other. This is called polarization and it could be done in two different ways:

- Anodic polarization by applying a potential increment $(\Delta E > 0)$ which enhances the oxidation (anodic) reaction;
- Cathodic polarization by applying a potential drop $(\Delta E < 0)$ which enhances the reduction (cathodic) reaction.

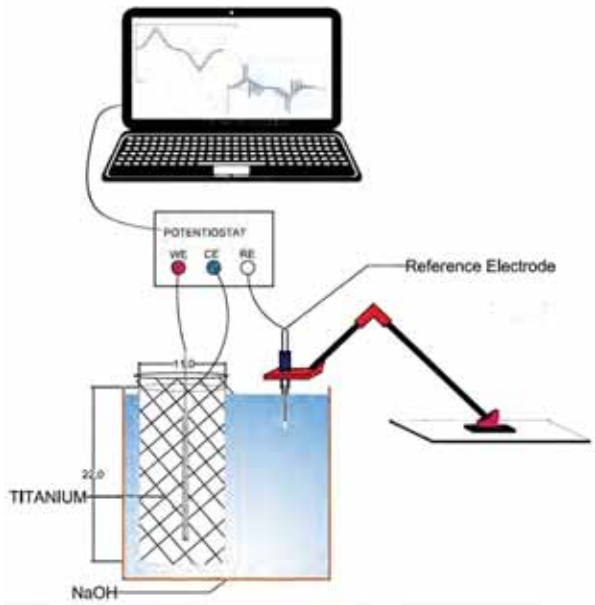


*Fig. 2. Assembly of the steady state polarization test on cathode specimen*

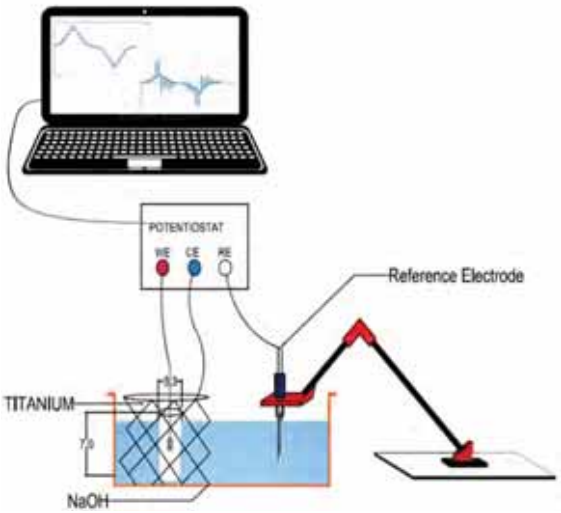


*Fig. 3. Assembly of the steady state polarization test on anode specimen*

## 1.2. Potentiostatic test

A steady state polarization test makes it possible to obtain a polarization curve which is a potential-intensity curve $I_{CE} = f\ (E)$ expressing the variation of the current according to an imposed polarization. This test makes it possible to characterize the electrochemical behavior of an electrode/electrolyte system and to determine the corresponding Butler-Volmer parameters.

In order to achieve real-steady state measurement, a reversible potentiostatic step protocol introduced by Laurens et al [1] was implemented to get the polarization curves. In such a protocol, the instantaneous responses (annotated to with "$0$") for each step allowed for estimating the electrical properties of mortar or concrete, while the asymptotic response (annotated with "$\infty$") qualifies the polarization behavior of the steel. Fig. 4 shows the instantaneous and steady state response of the electrochemical polarized system.

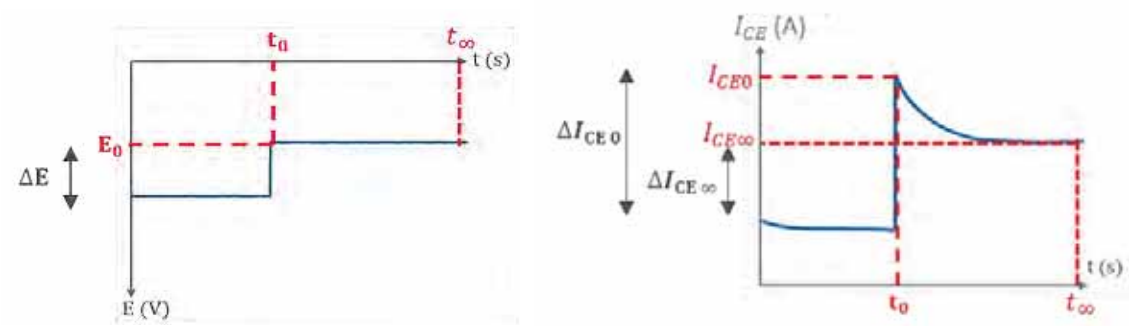


*Fig. 4. Instantaneous and steady state response of the electrochemical polarized system*

Fig. 5 presents a 1D electrical circuit diagram known as the Randles circuit [2] proposed to model the electrical response over time of the electrochemical system between both electrodes (represented by parts 1 and 4) by integrating ohmic, capacitive and electrochemical effects.

As discussed in part 2, the metal-solution interface (zone 2) can be considered as the superposition of 2 thin layers with one layer positively charged and the second one negatively charged. Its electrical behavior can be modelled by a capacitor (capacitive effect) in parallel with a polarization resistance (electrochemical effect). This system is connected in series with a resistance that represents the electrical resistivity of the concrete existing between the interface of the working electrode and the counter electrode (zone 3).

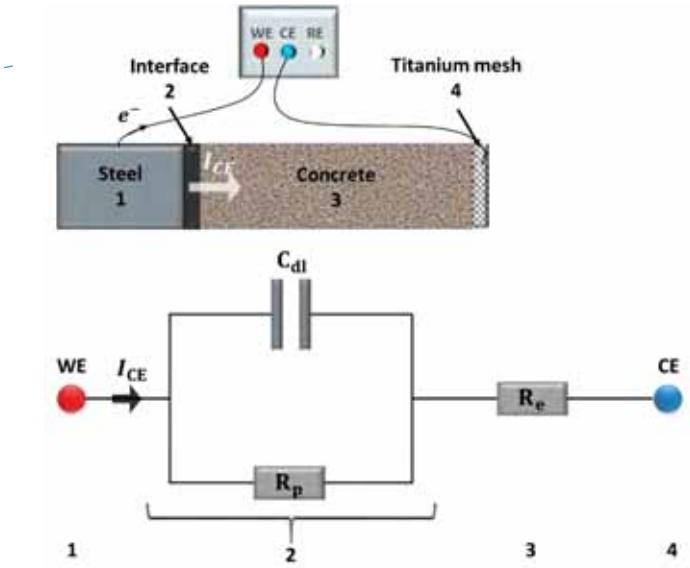


*Fig. 5. Electric circuit of Randles [2] and its application in the polarization test (example of an anodic polarization)*

The initial behavior of the interface is only capacitive and not electrochemical. At $t$ = 0, the current passes only through the capacitor (Fig. 6) and the apparent resistance of the system is then equal to the resistance of the electrolyte $R_e$ (Eq. 1). Thus, the instantaneous response of a system under polarization makes it possible to characterize the resistivity of the electrolyte between the working electrode and the counter electrode. This method will be used and detailed later on to determine the electrical resistivities of the test samples.

At t=0:

$$\Delta E = \frac{\Delta I_{CE\,0}}{R_e} \qquad \textit{Eq. 1}$$

In steady state, the capacitor is fully charged and the current goes only through the polarization resistance (Fig. 7). Apparent resistance increases gradually during time until reaching the maximum value corresponding to the sum of the polarization resistance $R_p$ and the ohmic resistance $R_e$ (Eq. 2) (Fig. 4).

At t=∞:

$$\Delta E = \frac{\Delta I_{CE\,\infty}}{R_e + R_p} \qquad \textit{Eq. 2}$$

The samples used are axisymmetric. Therefore, the assumption of a one-dimensional distribution of the current according to the equivalent model of Randles can be applied and the current lines are perpendicular to the counter electrode and the working electrode and the field of potential is "concentric".

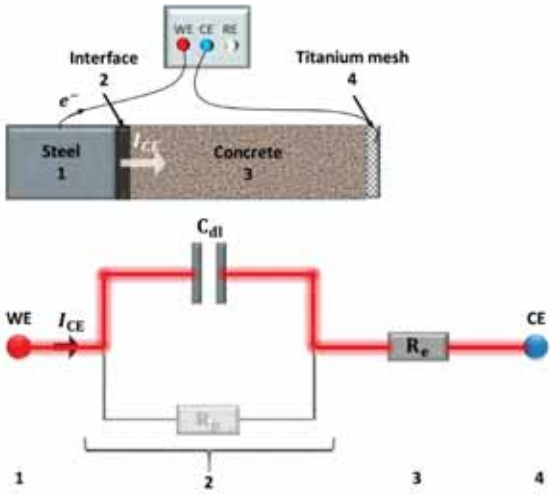


*Fig. 6. Instantaneous behavior of electric circuit of Randles*

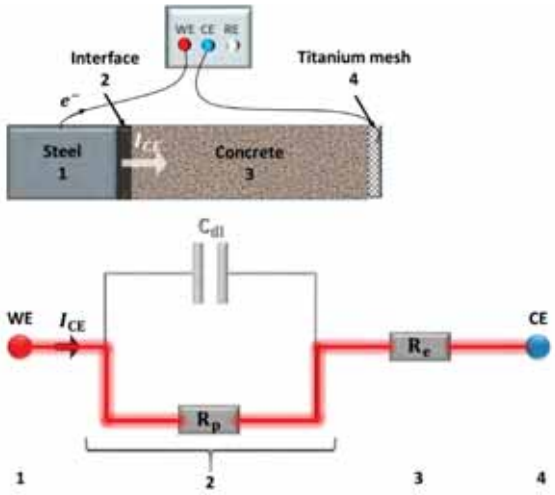


*Fig. 7. Steady state behavior of electric circuit of Randles*

The objective of this test is to determine the electrochemical behavior of the working electrode in steady state. However, depending on the level of polarization applied, the time required to achieve this steady state can be very long. The reversible potentiostatic step protocol developed by Laurens et al [1] allows for quickly and accurately estimating asymptotic responses and consequently for building polarization curves in real steady-state condition.

In fact, when polarizing in the anodic direction $(\Delta E > 0)$, the current $I_{CE}$ decreases as the capacitor charges. The value of the current measured before reaching the steady state $I_{\infty+}$ is therefore an overestimated value of the asymptotic response of the system. On the other hand, in the cathodic polarization $(\Delta E < 0)$, the current increases and the value of the current measured before reaching the steady state $I_{\infty-}$ is therefore an underestimated value of the asymptotic response of the system. Thus, the average value of the two current limit values will be the closest to the steady current in permanent mode $I_{CE\,\infty}$ (Eq. 3).

$$I_{CE\,\infty} = \frac{I_{CE\infty+} + I_{CE\infty-}}{2} \qquad \textit{Eq. 3}$$

It is important to emphasize that when the reference electrode is not positioned near the working electrode, the current $I_{CE}$ passes through a volume of concrete located between both electrodes that has a significant resistance that leads to the establishment of a potential gradient in the cell measurements (Ohm's law). It is, therefore, necessary to correct the values measured by subtracting the ohmic effect that is determined using the instantaneous behavior of the polarized system (Eq. 4) (ohmic drop correction).

$$\Delta E_{corrected} = \Delta E - R_e \times I_{CE\,\infty} \qquad \text{Eq. 4}$$

## 1.3. Polarization cycle

The first step of the polarization cycle consists in measuring the free potential system (OCP) for a stabilization time of 60 seconds. This potential corresponds to the native potential of the corrosion system noted $E_{corr}$ in the Butler-Volmer equation.

As showed in Fig. 8, the polarization cycle programmed in the software consists in applying potential increments and drops of 10, 20, 40 and then 3 steps of 80 mV with respect the Open Circuit Potential (OCP). For each potential step, a waiting time of $360\ s$ was chosen with an acquisition frequency of 1 Hz. Therefore, with respect to the free potential, a polarization range of $\pm\ 310\ mV$ was explored.

*Table 1. Steps of Potential imposed over time*

| | $\Delta E$ (mV) |
|---|---|
| Anodic polarization | +10 |
| | +20 |
| | +40 |
| | +80 |
| | +80 |
| | +80 |
| | +80 |
| | -80 |
| | -80 |
| | -80 |
| | -80 |
| | -40 |
| | -20 |
| | -10 |

| | $\Delta E$ (mV) |
|---|---|
| Cathodic polarization | -10 |
| | -20 |
| | -40 |
| | -80 |
| | -80 |
| | -80 |
| | -80 |
| | +80 |
| | +80 |
| | +80 |
| | +80 |
| | +40 |
| | +20 |
| | +10 |

It was chosen to start the cycle with the cathodic polarization in case of cathode samples (classic cathodes with no highly negative potential). This is done in order to avoid any possible alteration at the steel-electrolyte interface caused by the anodic polarization. Inversely, the cycle was initiated with the anodic polarization in case of anode samples or sulfide containing cathode samples which showed highly negative potentials (below -300 mV / Ag/AgCl/KCl). Between anodic and cathodic polarization of the same specimen a waiting time between 20 min and 1 hour is needed to make sure the WE was depolarized.

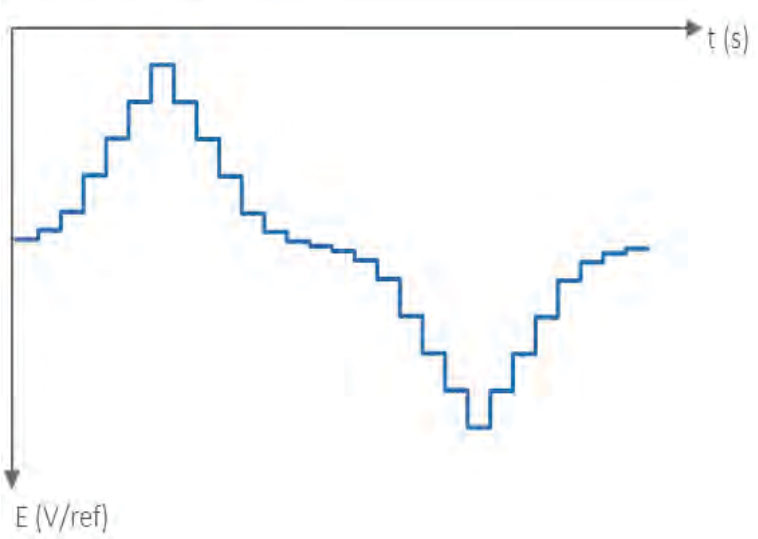


*Fig. 8. Potentiostatic routine used: potential steps imposed over time*

Fig. 9 represents the evolution of the counter electrode current during the polarization. As explained in Part 1.2, it is necessary to evaluate the asymptotic response of the steady state system $I_{CE\,\infty}$ by framing.

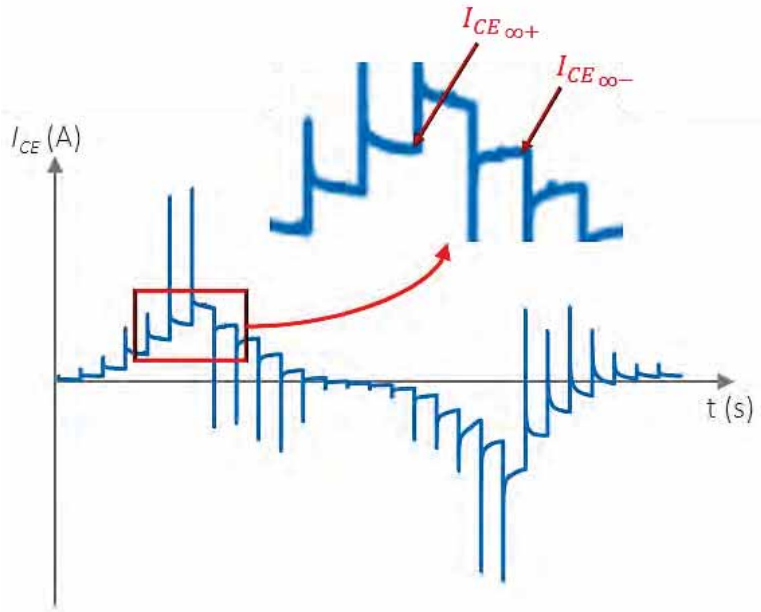


*Fig. 9. Measured current $I_{CE}$ during the polarization test*

## 1.4. Application and interpretations

As an illustration of the test protocol, hereafter (Table 2) an example of a polarization test result in case of a cathode sample (steel in passive state). The polarization curve is generally represented by the current density as a function of the overvoltage applied. The current density $i_{CE}$ is calculated as the electrochemical exchange surface of the steel. In case of cathode samples (passive steel), this surface is 30.16 $cm^2$. The current density is then equal to the measured current divided by the steel surface.

*Table 2. Results of obtained currents according to applied overvoltage*

| | $\Delta E$ (mV) | $i_{CE\infty+}$ (μA/cm²) | $i_{CE\infty-}$ (μA/cm²) | $i_{CE\,\infty}$ (μA/cm²) |
|---|---|---|---|---|
| Anodic polarization | 0 | 0.00 | 0.00 | 0.00 |
| | 10 | 0.00 | 0.00 | 0.00 |
| | 30 | 0.00 | 0.00 | 0.00 |
| | 70 | 0.01 | -0.01 | 0.00 |
| | 150 | 0.04 | 0.00 | 0.02 |
| | 230 | 0.08 | 0.02 | 0.05 |
| | 310 | 0.16 | 0.07 | 0.12 |
| Cathodic polarization | 0 | 0.00 | 0.00 | 0.00 |
| | -10 | 0.00 | 0.00 | 0.00 |
| | -30 | 0.00 | 0.00 | 0.00 |
| | -70 | -0.01 | -0.01 | -0.01 |
| | -150 | -0.11 | -0.13 | -0.12 |
| | -230 | -0.54 | -0.61 | -0.57 |
| | -310 | -2.05 | -2.08 | -2.06 |

The reference electrode and the counter-electrode are not positioned near the working electrode. The electrolyte of the concrete has a significant resistance which leads to the establishment of a potential gradient in the measuring cell according to Ohm's law. Due to the potential gradient in the concrete, the potential value measured at the surface of the specimen does not reflect the potential at the steel. It is therefore necessary to correct the measured value by subtracting the ohmic effects (ohmic drop correction).

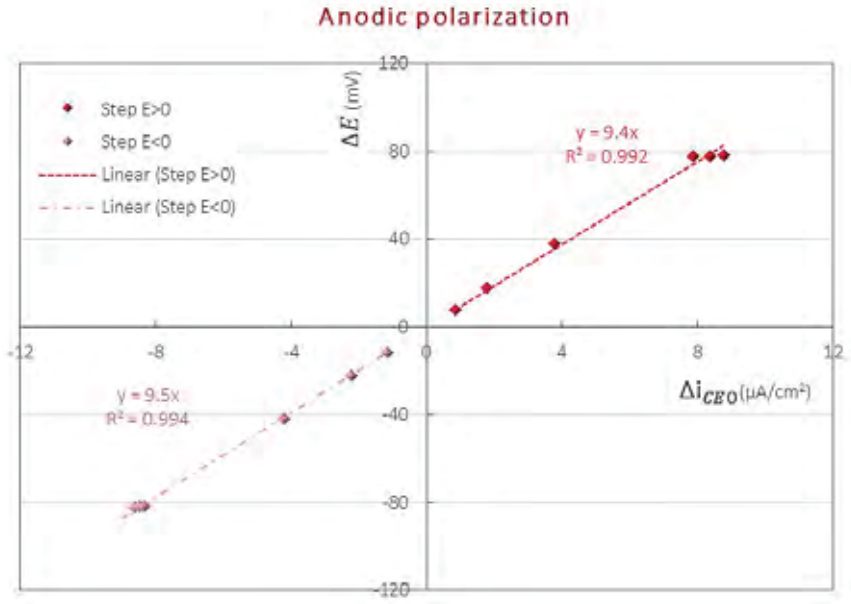

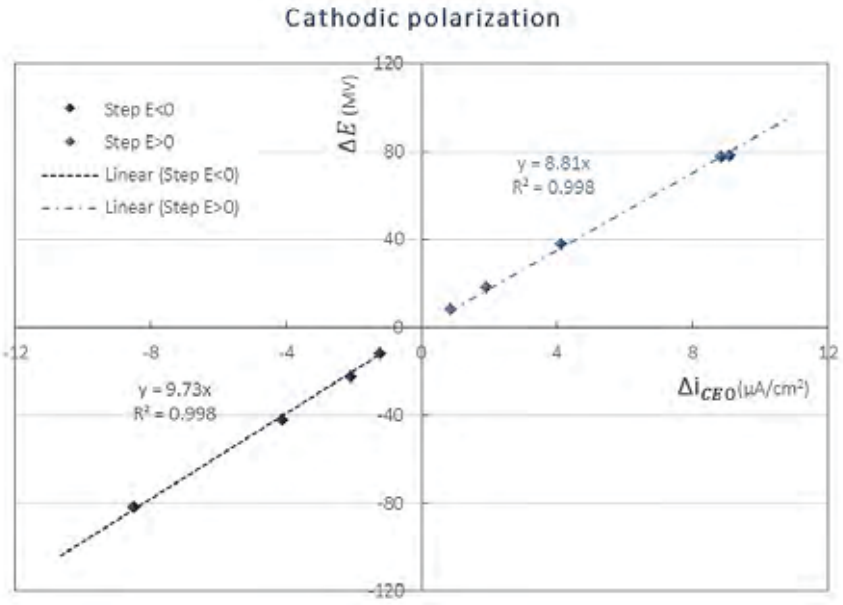


*Fig. 10. Determination of the resistance of the electrolyte $R_e$*

According to Eq. 1, it is possible to determine the resistance of the electrolyte. Fig. 10 presents the plots of $\Delta E$ as a function of the current density $\Delta i_{CE\,0}$. The linear fitting of the experimental points allows to determine the directing coefficient of the linear relationship. The coefficient $R^2$ is greater than 0.99, which reflects a perfect linearity between the overvoltage and the counter electrode current density for both anodic and cathodic polarizations. The average of all the directing coefficient multiplied by 1000 and divided by the surface of WE corresponds to the resistance of the electrolyte $R_e$ which is equal to 310 Ω. This value is a function of the geometry of the specimen and is therefore not intrinsic to the material. Table 3 gathers the raw and corrected results which are used to construct the polarization curves.

*Table 3. Raw and corrected results of obtained currents and overvoltage*

| | $\Delta E$ (mV) | $i_{CE\,\infty}$ (μA/cm²) | $\Delta E_{corrected}$ (mV) |
|---|---|---|---|
| Anodic polarization | 0 | 0.00 | 0 |
| | 10 | 0.00 | 10 |
| | 30 | 0.00 | 30 |
| | 70 | 0.00 | 70 |
| | 150 | 0.02 | 150 |
| | 230 | 0.05 | 230 |
| | 310 | 0.12 | 309 |
| Cathodic polarization | 0 | 0.00 | 0 |
| | -10 | 0.00 | -10 |
| | -30 | 0.00 | -30 |
| | -70 | -0.01 | -70 |
| | -150 | -0.12 | -149 |
| | -230 | -0.57 | -225 |
| | -310 | -2.06 | -292 |

Appendix VI

There are several methods to determine the electrochemical parameters of the Butler-Volmer equation presented in Eq. 5.

$$i = i_{corr}\left(\exp\left(\frac{\mathrm{Log}(10)}{\beta_a}(E - E_{corr})\right) - \exp\left(-\frac{\mathrm{Log}(10)}{\beta_c}(E - E_{corr})\right)\right) \quad \text{Eq. 5}$$

Where:
- $i$ is the net current density produced by the uniform corrosion system at metal-electrolyte interface (A/m$^2$);
- $E$ is the potential of the uniform corrosion system under polarization (V/ref);
- $i_{corr}$ is the corrosion current density (A/m$^2$);
- $E_{corr}$ is the potential of the uniform corrosion system at equilibrium (V/ref);
- $\beta_a$ is the anodic Tafel slope of the electrochemical system, expressing the oxidation reaction of iron (V/dec);
- $\beta_c$ is the cathodic Tafel slope of the electrochemical system, expressing the reduction reaction of oxygen (V/dec).

The first method consists in in plotting the corrected polarization curve on a semi-log scale as shown in Fig. 11 where are plotted the Tafel lines. The slopes of these lines and the coordinates of their intersection points are graphically determined. The intersection point corresponds to the operating point of the free system for which the overvoltage is zero and the anode current and cathode are equal in absolute value. The ordinate value of the intersection point correspond to $\log_{10} i_{corr}$.

The directing coefficients of these straight lines correspond directly to the anodic and cathodic slopes $\beta_a$ and $\beta_c$, respectively. It takes at least three points aligned to ensure the validity of this graphical method.

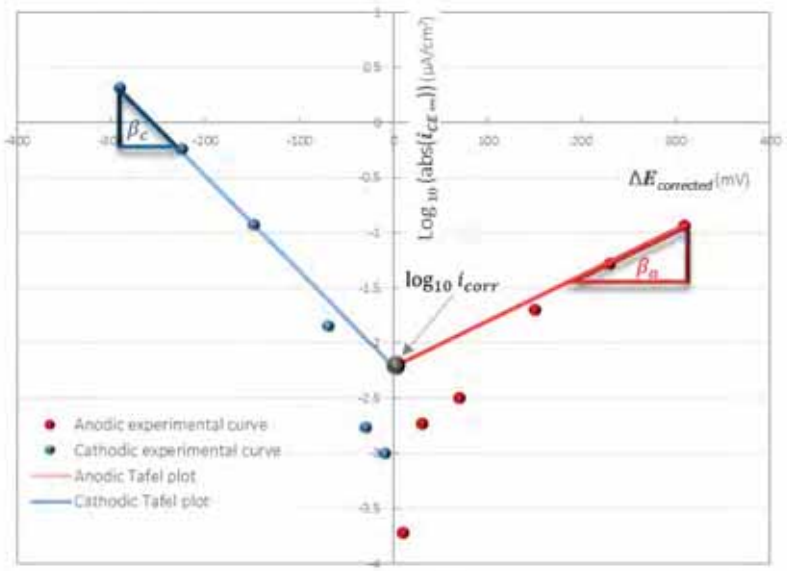


*Fig. 11. Anodic and cathodic Tafel plot*

A second method is to determine the Butler-Volmer parameters by adjusting the theoretical model of Butler-Volmer to the experimental curves. The objective is to determine the 4 parameters of Butler-Volmer allowing to minimize the Mean Square Error (MSE). The Excel solver (non-linear GRC) is used

to determine the optimal set of parameters. Fig. 12 shows the theoretical model adjusted to the experimental curve. Note that the parameters obtained with both methods must be identical.

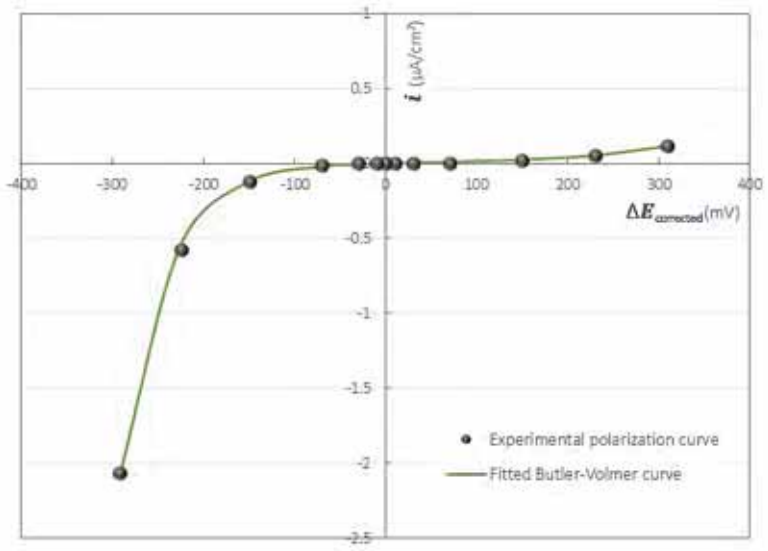


*Fig. 12. Butler-Volmer theoretical model adjusted to the experimental curve*

A third method can also be adopted by fitting of electrochemical parameters on the reversible electrode level and the parameters associated to the corrosion system can be deduced from theoretical equations. This method was performed in $paper\ 2$.

### 1.5. Some remarks

Since the cathode samples are chloride-free, the steel is indeed entirely in passive state. Therefore, the characterization of the passive behavior can be directly deduced from the experimental polarization test by fitting a Butler-Volmer model on the polarization curve.

Conversely, the anode specimens are contaminated with chlorides. Hence, the steel cannot be considered uniformly active despite the chloride presence. Therefore, regarding the anode specimen, the polarization response expresses the behavior of a galvanic system in which only a part of the steel surface is active. In this condition, the usual ohmic drop correction is no longer valid since the electrochemical solicitation, as well as the electrochemical state is not uniform. Consequently, no ohmic drop correction was applied on the polarization measurements relative to the anode specimens. As expressed in $paper\ 2$, the polarization behaviors of the anode specimens were used to infer active steel electrochemical properties from an optimization procedure based on inverse numerical modelling.

### 1.6. Impact of polarization test on chloride levels

It was important to test if the polarization experiment had an impact on the chloride contents measured at the level of the rebar. In other words, it was important to check if the polarization test, realized on samples after the galvanic coupling and before the chloride measurements, caused a migration of chlorides towards the steel bar causing an overestimation of the chloride content responsible for the galvanic corrosion current measured earlier.

Hence, several anode samples were contaminated with the same concentration of saline solutions and undertook the same cathode-anode galvanic coupling experiment, however, after the

galvanic coupling, one anode was polarized according to the polarization test while the other one wasn't. Chloride measurements were then realized on both samples. Table 4 presents the results of total chloride contents measured on polarized and non-polarized anode samples at the level of the rebar. It is expected that the chloride content for the same imbibition solution is not exactly the same between two different anodes. The results show that there is no specific tendency related to the impact of polarization on the chloride level around the steel bar.

*Table 4. Comparison of chloride contents between polarized and non-polarized anode*

| Concentration of the NaCl imbibition solution (g/L) | Total chloride content (%/wt. cement) | |
|---|---|---|
| | Polarized anode | Non polarized anode |
| 12.25 | 0.32 | 0.39 |
| 22.75 | 0.61 | 0.59 |
| 70 | 1.07 | 1.17 |
| 140 | 2.09 | 2.67 |
| 280 | 3.12 | 2.84 |

## 4. References

[1] S. Laurens, P. Hénocq, N. Rouleau, F. Deby, E. Samson, J. Marchand et al., *Steady-state polarization response of chloride-induced macrocell corrosion systems in steel reinforced concrete — numerical and experimental investigations*, Cement and Concrete Research 79 (2016), pp. 272–290.

[2] J.E.B. Randles, *Kinetics of rapid electrode reactions*, Discuss. Faraday Soc. 1 (1947), pp. 11–19.

# Appendix VII

## pH measurement of interstitial solution

Appendix in: Study of the initiation and propagation phases of chloride induced corrosion in reinforced concrete structures

Realized by: Chantal Chalhoub

Thesis for the degree of Philosophiæ doctor

Université Toulouse 3 Paul Sabatier (UT3 Paul Sabatier)

Laboratoire Matériaux et Durabilité des Constructions de Toulouse

Appendix VII

Appendix VII

# Contents

# 1. Introduction

This report presents the methods and equipment used for the extraction of interstitial solution form mortar samples in order to measure their pH.

# 2. Extraction of interstitial solution

The extraction of the interstitial solutions was carried on one reference sample $(11 \times 5\ cm)$ per formulation taken from the wet curing room. The apparatus presented in Fig. 1 developed by Cyr et al in 2008 [1] was used to extract the solutions. The device is composed of two thick inner (1) and outer cylinders (2) which are fitted into each other. The cylinders are located on the base plate of the device (3) which comprises a solution collector (4). The sample is placed in a chamber where it is crushed by an axial load produced by a hydraulic press on a set of pistons ((5), (6), (7)). The solution is collected in a small polypropylene recipient (8), which can be removed with a drawer system (9).

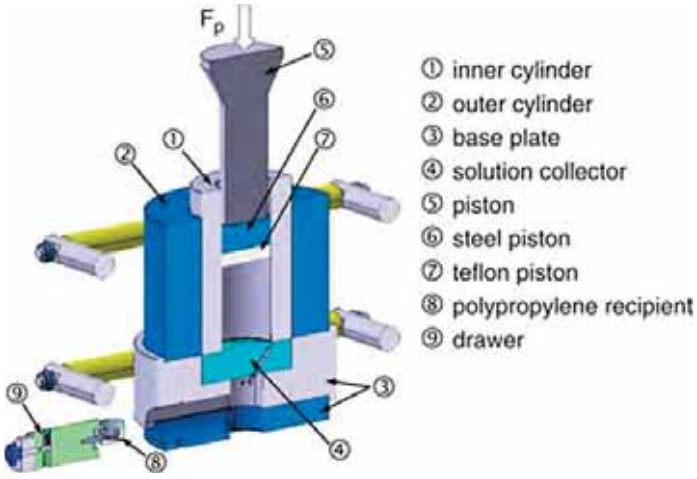


*Fig. 1. On the left: Extraction device set up to carry out the extraction of the pore solutions (from* [1]*)*

*Fig. 2. Sintco press and an extraction mold to extract interstitial solution from concrete*

The solutions were extracted using a Sintco 600 T press and an extraction mold at LMDC Toulouse, France (Fig. 2). The applied pressure profile considers pressure rise of 3 KN/s up to 1000 kN. The maximum pressure is maintained for 1 minute then it is decreased with a rate of 3 KN/s. It is necessary to maintain the maximum pressures for a few minutes in order to be able to extract between 5 and 10 ml of pore solution. The interstitial solution is then collected in a small polypropylene recipient and the pH of extracted solution should be directly measured.

It must be noted that the application of a pressure for the extraction of the pore solutions is known for having an influence on the concentrations of the ions present in solution [1,2]. In effect, the application of a strong pressure can lead to a change in the structure of hydrates such as ettringite and thus influence the chemical composition of extracted solutions. It is therefore necessary to minimize the pressure applied to extract the pore solution, but also ensure repeatability pressures, with the aim of allowing a comparison between each solution extracted by this method.

## 3. pH measurement

At the end of the extraction test, the pH of the pore solution was measured as soon as possible after collection using a standard pH meter HACH with a combined pH electrode as shown in Fig. 3. This device consists of a glass electrode connected to a digital converter. To ensure that the probe functions properly, a calibration of the system was done using two standard solutions: pH 10 and pH 13. This calibration makes it possible to calculate the slope of the calibration curve and the zero. This calibration method provides a pH accuracy of ± 0.001. The temperature of the solution was measured with a temperature probe coupled to the pH meter at the time of measurement. The pH meter converts the difference in potential established between the outer and inner walls of the glass into a pH unit and indicates values to 2 decimal place.

*Fig. 3. pH meter with a combined pH electrode.*

## 4. References

[1] M. Cyr, P. Rivard, F. Labrecque and A. Daidie, *High-Pressure Device for Fluid Extraction from Porous Materials: Application to Cement-Based Materials*, Journal of the American Ceramic Society 91 (2008), pp. 2653–2658.

[2] J. Bizzozero, *Hydration and dimensional stability of calcium aluminate cement based systems*, Ecole polytechnique fédérale de lausanne, 2014.

# Appendix VIII

## Conference and Workshop Communications
## Oral presentations

Appendix in: Study of the initiation and propagation phases of chloride induced corrosion in reinforced concrete structures

Realized by: Chantal Chalhoub

Thesis for the degree of Philosophiæ doctor

Université Toulouse 3 Paul Sabatier (UT3 Paul Sabatier)

Laboratoire Matériaux et Durabilité des Constructions de Toulouse

Appendix VIII

Appendix VIII

# Contents

Appendix VIII

# 1. 5th International Conference on Concrete Repair, Rehabilitation, and Retrofitting

## Conference paper and Oral presentation

| | |
|---|---|
| **Date** | 19-21 November 2018 |
| **Location** | Cape Town, South Africa |
| **Title** | A new approach to determine the chloride threshold initiating corrosion: preliminary results [1] |
| **Authors** | Chantal Chalhoub*, Raoul François, Myriam Carcasses<br>LMDC, INSA, UPS, Université de Toulouse, France |

**Abstract** The initiation of corrosion by chlorides is traditionally based on the existence of a threshold that would lead to corrosion. Almost all existing approaches considered implicitly that corrosion induced by chlorides is uniform and take not into account the intrinsic localized character of corrosion in reinforced concrete structures. This work aims to implement a new test protocol that takes explicitly into account the localized nature of chlorides-induced corrosion by inducing physical separation between anode and cathode thus permitting to measure the corrosion current. The anodic part allows to test different levels of chlorides and the cathodic part to highlight the ohmic (limiting ionic current by low porosity) and cathodic (restricting access to oxygen due to saturation of porosity, low porosity, dioxygen consumption by additions) control of corrosion. The chloride threshold is set on the basis of a threshold corrosion current that is considered acceptable with respect to the structure's life. The first results provide a preliminary idea of the variation of corrosion rate in function of chlorides content. This method also highlights the influence of surface condition of the steel-concrete interface on the corrosion current.

**Keywords** Chloride; Localized corrosion; Steel surface; Critical chloride content.

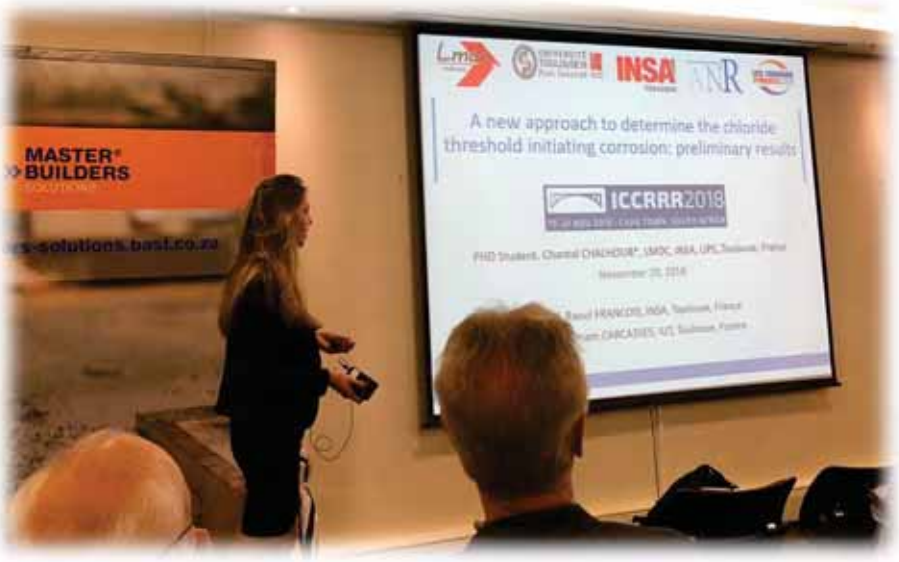

## 2. FIB workshop: mathematical models on reinforcement corrosion and its consequences for structural performance

### Oral presentation

| | |
|---|---|
| **Date** | 28-29 October 2019 |
| **Location** | Paris, France |
| **Title** | Prediction of corrosion current density during the propagation phase of corrosion density and its duration before the appearance of first corrosion-induced cracks as a function of environmental conditions |
| **Authors** | Chantal Chalhoub*, Raoul François, Myriam Carcasses<br>LMDC, INSA, UPS, Université de Toulouse, France |
| **Abstract** | This paper presents a methodology for predicting the corrosion current density during propagation phase of corrosion current and the duration of this phase before the appearance of the first corrosion-induced cracks. The prediction of the corrosion current density is based on the observation that in a concrete structure before the appearance of corrosion-induced cracks, the preponderant component of corrosion is that related to the macro-cell process (localized corrosion). The proposed model takes into account the influence of the parameters related to the anodic behavior: concentration in free chlorides mainly; the influence of parameters related to the cathodic behavior: oxygen availability and the ohmic interaction between anodic zones and cathodic zones with in particular: the resistivity of the concrete, the surface ratio between cathode and anode (very high in real structures), the distance between aerated cathode and anode (important parameter for XS2 type exposures). The model is based on experimental results obtained on an experimental test which physically separates the anode from the cathode. The current densities obtained are either apparent, relative to the ratio of the anodic and cathodic parts of the experimental device, or real, compared to the proportion of anode surface actually corroded. The corrosion current density predicted by the model then makes it possible to calculate the duration of the propagation phase before the appearance of the first corrosion cracks. The originality of the model is that the corrosion current density is taken into account only partly to obtain a local reduction of the reinforcement section, the other part of the corrosion current density is used for the extension of the zones anodic in their length. The link between loss of local section and appearance of a corrosion crack is empirical. |
| **Keywords** | Macro-cell; Chloride; Cathode over anode ratio; Resistivity; Cross-Section reduction. |

## 3. CEFFRACOR – GT2 Modélisation

### Presentation

| | |
|---|---|
| **Date** | 3 June 2019 |
| **Location** | Paris, France |
| **Title** | Etude numérique et expérimentale des effets d'échelle dans la corrosion des armatures du béton armé : influence du ratio Cathode/Anode et la distance Cathode-Anode |
| **Authors** | Chantal Chalhoub*, Raoul François, Myriam Carcasses (presented by R. François)<br>LMDC, INSA, UPS, Université de Toulouse, France |
| **Keywords** | Chloride-induced corrosion; Macrocell; Numerical simulation: Cathode to anode ratio; Cathode to anode distance. |

## 4. CSI PERFDUB-GT2b

### Oral presentation

| | |
|---|---|
| **Date** | 30 October 2019 |
| **Location** | Paris, France |
| **Title** | 1-Experimental protocol for the determination of critical chloride content<br>2- GT2b: Service life modeling of concrete structures - MODEVIE project |
| **Authors** | Chantal Chalhoub*, Raoul François, Myriam Carcasses<br>LMDC, INSA, UPS, Université de Toulouse, France |
| **Keywords** | Chloride; Localized corrosion; Critical chloride content; Lifetime of reinforced structures; Engineering model. |

# 6. ANR Modevie Project - Task 4 – Corrosion propagation phase

## Report + Oral presentations

**Date** 2016- 2020

**Location** Paris-Nanterre- Marne la vallée-Toulouse-Lyon-Nantes, France

**Title** "MODEVIE" PROJECT: PROPOSAL OF NEW SERVICE-LIFE MODEL

**Authors** Myriam Carcassès[1]*, Chantal Chalhoub[1], Jonathan Mai-Nhu[2], Philippe Turcry[3], Anass El Farissi[3], Abdelghafour Ait-Alaiwa[4]* and François Cussigh[5]*

[1] LMDC, INSA, UPS, Université de Toulouse, France
[2] Cerib, Epernon, France
[3]LaSIE, UMR 7356 CNRS, Université de La Rochelle, France
[4] VINCI Construction Grands Projets, Rueil, France
[5] VINCI Construction France, Nanterre, France

**Abstract** MODEVIE research program is the modelling part of French National Project PERFDUB aiming at setting up a methodology for justifying durability of concrete structures using a performance-based approach. Starting from scientific models available for the different phenomena in play, its output is an overall engineer model able to provide a reliable assessment of concrete structures service life (as far as rebars corrosion is concerned) by calculating the sum of initiation period and propagation period. Initiation period modelling is based on fib model laws and propose explicit values for every input data, avoiding as much as possible to refer to tabulated values depending on concrete mix design but relying on laboratory short term tests (typically less than 90 days). New formulas are given for very important parameters like chloride surface concentration in the case of marine or deicing salts environments. For corrosion propagation, a first approach is developed taking into account ambient relative humidity, temperature, chloride concentration at rebar level, oxygen availability and concrete resistivity. The duration of acceptable corrosion propagation period is defined as the one corresponding to first appearance of corrosion cracks. MODEVIE models are semi-probabilistic, based on characteristic values for concrete properties and limit conditions. They have been calibrated both from literature data and experimental ones (with a new test method for determining critical chloride concentration) and compared to classical rebar cover design with concrete complying with corresponding exposure class.

**Keywords** Performance-based approach; Corrosion; Semi-probabilistic model; Carbonation; Chlorides.

## 7. ANR Modevie - Task4 - FIB Shanghai, China

**Date** 27-29 April 2020

**Location** Shanghai, China

**Title** Service life modeling of concrete structures - MODEVIE project : engineering model for time of corrosion propagation

**Authors** Myriam Carcasses[1]*, François Cussigh[3]*, Chantal Chalhoub[1], Raoul François[1], Anass El Farissi[2], Philippe Turcry[2]

[1]LMDC, INSA, UPS, Université de Toulouse, France
[2]LaSIE, La Rochelle Université, UMR 7356 CNRS, France
[3]VINCI Construction France, Nanterre, France

**Abstract** The objective of MODEVIE research program is to define a common engineering model able to predict lifetime of reinforced concrete structures and adapted to the performance-based approach. It is interested in the corrosion of the reinforcement under the influence of chloride and carbonation in partially saturated conditions. It has been decided to define structure lifetime as the sum of the time of initiation ($t_{ini}$) and the time of propagation ($t_{prop}$). The engineering models adapted to the performance-based approach must describe the both phases, initiation and propagation. To complete this project, exposure classes have to be described: this description is a part of the model input data. Furthermore the material input data will be mainly durability indicators. The limit state, corresponding to the end of service life, is defined as the time of appearance of the first corrosion induced cracks. Our approach for modelling is based on a critical review of existing models and constructive proposals for their possible improvement. For $t_{ini}$, we use models based on the fib models proposed for chloride ingress and carbonation depth. The model of propagation time is the result of several experimental studies, whose purpose was to evaluate the effect of various parameters influencing the propagation of corrosion related to the types of materials (binder in particular), the environment and the geometry of the structure in reinforced concrete, but has also considered an important bibliographic review. For a given geometry of the structure, the quantity of corrosion products initiating the appearance of the first crack is determined. This quantity is usually expressed as a loss of section DeltaS. This loss of section is distributed either in uniform form (decrease in diameter) over a length L (case of carbonation) or in localized form on a more little length l (chloride). The corrosion current density necessary to obtain this section loss is then calculated, and finally linked to parameters related to the environment, the material and the structure… and time of propagation is then evaluated. A series of tests is carried out to evaluate the sensitivity of the model and to estimate the lifetime of real structures in various environments e.g. Rion-antirion bridge.

**Keywords** Lifetime of reinforced structures; Engineering model, Performance-based approach; Impact of material and exposure environment; Penetration depth and Corrosion rates.